Foldamer Catalysis

By

Zebediah C. Girvin

A dissertation submitted in partial fulfillment

of the requirements for the degree of

Doctor of Philosophy

(Chemistry)

at the

UNIVERSITY OF WISCONSIN-MADISON

2020

Date of final oral examination: 07/28/2020

The dissertation is approved by the following members of the Final Oral Committee:

Samuel H. Gellman, Professor, Chemistry

Tehshik P. Yoon, Professor, Chemistry

Clark R. Landis, Professor, Chemistry

Jeffrey D. Martell, Assistant Professor, Chemistry

To:

DG – for showing me a work ethic that cannot be matched.

Wilson – for teaching me how to read, an invaluable skill.

Unit – my best friend, even though you're a beta.

You've made it all possible.

Fred Potts – have a read.

Acknowledgement

Mom and Dad - I am forever grateful for a family that has always supported me in every possible way. Without the three of you none of this would be possible. Mom and Dad, you are the best parents I could have ever asked for, I have supreme confidence and know anything can be achieved because of you two, thank you. Sharing this journey with you both has made it so special, and without that I wouldn't have made it.

Boss – You'll never know the impact you've had on me, as a person and a scientist. The ability to barge into your office each day and discuss anything is something I don't take for granted. You always backed me and supported all my ideas, no matter how bad.

Unit – I hope you figure out how to light a cigar and which end to smoke, so MJ and I don't have to keep helping you. Now that I'm back East, I'll show you how to dovetail a joint, bench, work a radial arm saw, and check your oil. Every alpha needs a beta, so thank you. Take your hand off the bumblebee can.

MK – You did it…you convinced me Walgreens products far exceed CVS, nothing beats St. Louis BBQ, Derek Carr's skillset surpasses Mahomes, and umbrellas are a must.

Lei – You old dog. Best malt liquor salesman I ever met, with the nose of a bloodhound. Sell dumplings and put old Chen out of business. Take care of that bad boy you use for hydrogenations, big dog.

Naomi – I never minded lifting vacuum pumps for you, it's the least I could do for an Ivy-leaguer. Your welcome for being such a great co-TA.

Philip – thanks for the desk during quarantine, we'll be in touch.

Xinyu – NMR expert. I will not touch your computer again!

Gellman Group – Make sure whoever moves into Daddy's hood is worthy.

Tehshik – Thank you for being a second mentor, especially in photocatalysis.

Aris – You can always sleep on my floor.

Chase – What a character.

Jamie – I could not have made it without you.

Over the five years at UW-Madison I have been lucky enough to meet so many fantastic people that have helped me in countless ways. My time in Madison has been incredible and I will cherish the memories for a lifetime.

Table of Contents

Chapter 1

Foldamer Catalysis: 22 Years Since the Manifesto

1.1 Abstract

The extraordinary rate accelerations and control of reactivity exhibited by enzymes have long inspired efforts to develop synthetic catalysts. Foldamers, which are oligomers with a strong tendency to adopt a specific conformation, represent unique platforms for efforts to harness principles of enzyme function for catalyst design. Well-defined helical structures that have been identified in several foldamer families can serve as scaffolds for the predictable spatial arrangement of functional groups. The chirality of these helices offers a basis for asymmetric catalysis. Thus, foldamer-based approaches to catalyst development represent an attractive alternative to well-developed strategies involving small molecules or conventional peptides.

1.2 Introduction

The remarkable selectivities and rate accelerations achieved by natural enzymes result from evolutionary selection over billions of years.[1] These enzymes show chemists how effective catalysis can be, establishing benchmarks for efforts to develop non-biological catalysts.[2] High-resolution enzyme structures can inspire new design strategies in synthetic systems.[3] Contemporary efforts to build from these biological precedents are limited, however, because human designs cannot yet mimic the ability of a folded polypeptide to envelop a substrate (or substrates) within a pocket that precisely orients multiple functional groups while maintaining flexibility. Nevertheless, significant progress has been made by using synthetically malleable molecular frameworks to arrange functional group sets in a manner that promotes catalysis.[4]

Enzymatic catalysis often depends on the positioning of an array of functional groups within an active site. Protein catalysis has inspired many efforts to use small molecules to display sets of two or even three functional groups in a manner that allows coordinated action on a substrate or set of substrates.[4] Significant successes have been recorded, but such efforts collectively highlight

limitations of small-molecule frameworks. For example, cinchona alkaloids have provided the basis for a wide variety of useful catalysts, involving, for example, conjugate additions, Mannich reactions and cyanation reactions.[5] However, the rigid skeletons of these alkaloids are generated by biosynthetic machinery and not easy to modify, which means that the chemist must be shrewd to find reactions that can be catalyzed by functional group arrangements accessible with these skeletons.

In contrast to the non-periodic backbones of rigid, polycyclic molecules, peptides offer a modular backbone from which a variety of reactive groups can be displayed. Miller and coworkers have pioneered the use of β-turn peptidic catalysts for enantio- and site-selective catalysis.[4d] Reactivity control is often achieved through catalyst-substrate noncovalent interactions, which is reminiscent of substrate engagement among enzymes.[4d,6] Jacobsen and coworkers have elegantly shown that oligomeric catalysts, typically containing a urea or thiourea group for hydrogen bonding with substrates, are valuable catalysts for a plethora of asymmetric processes, including glycosylations, S_N1 substitutions and Picet-Spengler reactions.[7] Wennemers et al. have provided other relevant examples.[8] Peptides and other oligomers are amenable to the generation of large groups of candidates that can be screened for desired catalytic activities.[9]

Most α-amino acid residues are inherently flexible, a feature that can work against catalytic efficacy. Peptide flexibility can be modulated, however, in several ways, including (1) use of constrained residues, such as proline or non-proteinogenic analogues; (2) strategic combination of L and D residues; and (3) use of nonpolar solvents, which allow internal H-bonds to drive folding. Many significant advances in asymmetric catalysis and in site-specific modification of complex substrates have been achieved with catalysts composed entirely or primarily of α-amino acid residues.[4d, 6]

As interest in late-stage modification of polyfunctional molecules grows, it will be necessary to develop catalysts that contain not only a catalytic group or set of catalytic groups that provides the desired reactivity, but also ancillary functionality to control the location within the substrate at which the catalytic component operates. Numerous catalyst-substrate interactions may be necessary to achieve differentiation among sites that have similar inherent reactivity within a complex substrate.[10] In particularly challenging cases, specific modes of catalyst-substrate engagement will be required to overcome intrinsic reactivity trends among potential modification sites within a substrate. Work from the groups of Miller, Jacobsen and others, in which easily-modified peptidic or other oligomeric backbones were used to develop catalysts that manifest regio- and/or enantiocontrol,[11-13] has inspired our interest in trying to harness novel foldamer secondary structures. The continuously expanding collection of foldamer scaffolds broadens the ways in which sets of functional groups can be arranged in space to promote catalysis (Figure 1).
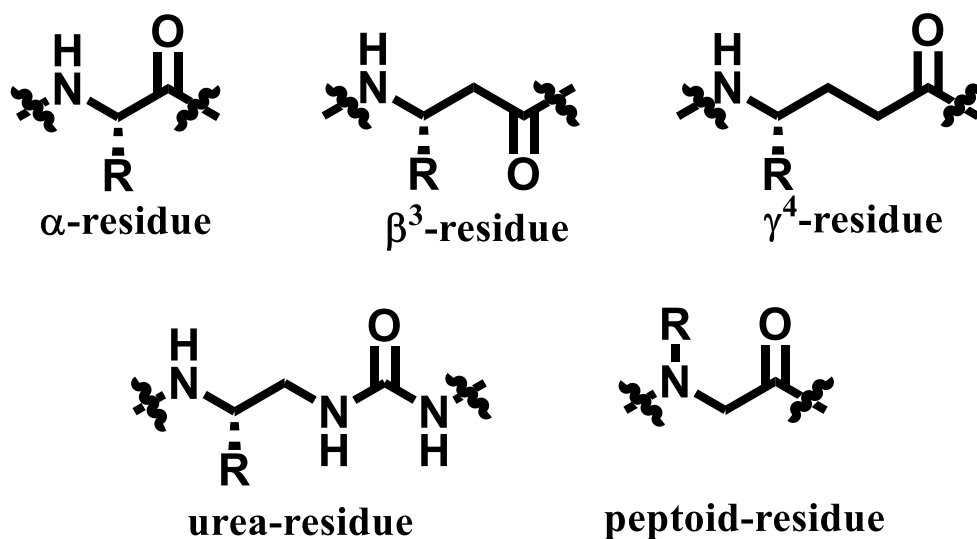
Figure 1. Selected natural and non-natural monomers utilized in foldamer backbones. R = generic side chain group.

1.3 Foldamers "Foldamers" are oligomers or polymers that are strongly disposed to adopt specific conformations.[14] Interest in synthetic foldamers was inspired by the recognition that biology relies

heavily on well-folded oligomers and polymers for catalysis and other sophisticated molecular tasks. Polypeptides and polyribonucleotides are the "biofoldamers", and the substantial differences between proteins and RNA at the backbone level have motivated chemists to survey non-biological backbones for discrete folding behavior. As conformational preferences have been elucidated for various types of unnatural backbones, it has been possible to endow these scaffolds with specific functions.[15] Here we review efforts to develop foldamers that catalyze reactions. The number of studies in this area has been modest so far, but the accomplishments to date suggest great potential for further development, particularly if chemists who specialize in solving synthetic problems are motivated to take up these non-traditional tools.

Most well-characterized foldamer scaffolds that are currently known adopt helical secondary structure.[15] In some cases, these helices can be engineered to undergo self-assembly, typically based on a hydrophobic driving force, which requires aqueous solution.[16] Intermolecular helix association could be a prelude to formation of helix-bundle tertiary structure, but progress toward foldamer tertiary structure has been limited, perhaps because of the technical challenges associated with constructing long oligomers. Therefore, efforts to devise foldamers that catalyze reactions have so far mostly been focused at the level of secondary structure, helices in particular. It should be noted that progress in the better-developed field of conventional peptide catalysis has been largely focused on relatively short oligo-α-peptides that adopt hairpin or helix conformations.[4d, 6,8b]

The relationship between subunit identity and helix geometry is well-established for several types of synthetic foldamers. This knowledge allows a chemist to design linear sequences that will bring a specific pair of side-chain functional groups into proximity upon helical folding (Figure 2). Proteins, of course, offer a much broader range of possibilities in terms of the number of catalytic

groups that can be arranged and the geometric relationships that can be accessed among those groups. However, despite important advances, the dream of purely rational design of protein catalysts has not yet been realized. As an alternative, directed evolution and selection, sometimes with computational guidance, have proven effective at generating novel protein catalysts for diverse reactions, as demonstrated by creative contributions from the groups of Arnold, Baker, Hilvert and others.[17-19] Considering foldamer secondary structures in the context of contemporary protein catalyst design suggests that the constraints of the foldamer systems (side chains and substrates remain largely solvent-exposed, and available side chain arrangements are limited) are balanced by an advantage relative to proteins: foldamers can be engineered to display predictable secondary structures that are very stable at short lengths. These systems allow the chemist to
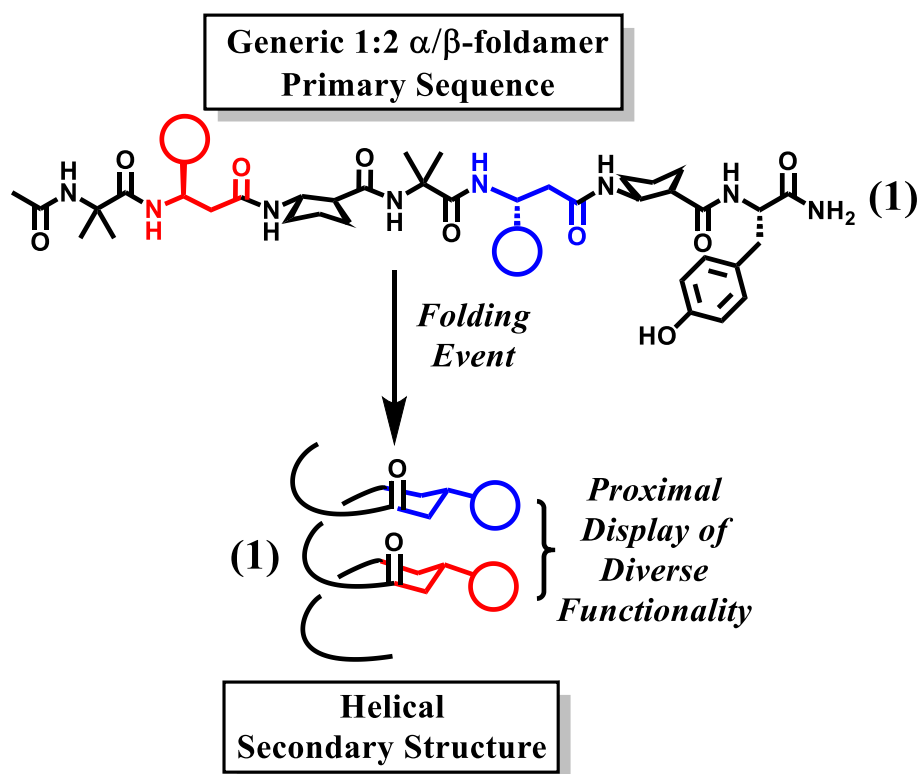
Figure 2. Primary sequence of generic 1:2 α/β-foldamer (1), and carton depiction of the helical secondary structure adopted upon folding, that results in the display of functional groups from a common helical face.

achieve predictable spatial arrangement of reactive groups, selected from a wide variety of possibilities, based on sequence-level design. As the range of well-characterized foldamer secondary structures grows, the opportunities for catalyst development will expand. Recent studies from the groups of Nicewicz, Miyake, and Kwon have highlighted the importance of understanding molecular shape in photocatalyst development and seem to suggest a new avenue for foldamer application.[20-22]

Potential benefits of foldamer-based design strategies can be illustrated by comparing α- and β-amino acid residues as building blocks. The familiar α-helix (pure α residue backbone) has ~3.6 residues per turn; therefore, residue pairs with i,i+3 or i,i+4 spacing will be approximately aligned along one side of an α-helix.[23] Use of other subunits provides access to helices with different structural parameters, which enables the designer to explore three-dimensional arrangements of a functional group diad that cannot be achieved with a conventional peptide. For example, β-amino acid oligomers (β-peptides) comprised entirely of β^3 residues adopt a helix with approximately three residues per turn ("14-helix", because the characteristic H-bonds involving 14-atom rings).[24] The 14-helix allows a closer angular alignment of an appropriately spaced pair of side chains (i,i+3) than can be achieved with an α-helix. This β-peptide helix brings the two side chains closer to one another in space, because the 14-helix has a rise of ~4.5 A per turn, while the α-helix has a rise of ~5.4 A per turn.

In addition to differences in the geometry of diad arrangement, changes at the backbone level can allow alteration of other important structural parameters. For example, a β-peptide comprised entirely of β^3 residues has only a modest propensity to fold because this type of residue is quite flexible.[24b] However, β-peptide 14-helix stability can be substantially enhanced by incorporating preorganized subunits derived from *trans*-2-aminocyclohexanecarboxylic acid

(ACHC).[24a] Short β-peptides containing ACHC residues appear to be fully helical in aqueous solution,[25] a feat that is impossible to achieve for an α-helix without side chain crosslinking. This distinction between the familiar α-helix and the β-peptide 14-helix illustrates a benefit offered by foldamer backbones: the degree of folding propensity can be modulated over a much wider range among β-peptides than is readily accessible among conventional peptides. Ramifications of this β-peptide feature in terms of catalysis are discussed below.

Not only can a specific helical conformation be stabilized by appropriate subunit preorganization, as illustrated by the impact of ACHC incorporation into 14-helical β-peptides, but also the nature of the helix can be altered by choice of subunit. Among β-peptides, replacing the six-membered ring constraint with a five-membered ring constraint, provided by *trans*-2-aminocyclopentanecarboxylic acid (ACPC), leads to formation of the 12-helix, which has ~2.5 residues per turn and a rise of ~5.4 A per turn (Figure 3).[26]

ACHC   ACPC   APC
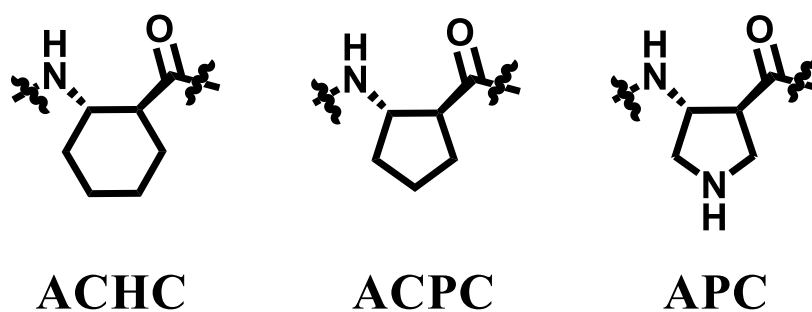
Figure 3. Representative five and six membered cyclically constrained β-amino acid residues.

In addition, the β-peptide 12- and 14-helices vary in the directionality of their H-bonds (C=O(*i*)—H-N(*i+3*) in the former vs. C=O(*i*)—H-N(*i+2*) in the latter). These two helices represent distinct scaffolds for display of functional group sets that might collectively display catalytic activity; each helix provides access to different (and therefore complementary) spatial arrangements

of a given reactive group cluster. The ability to fine-tune functional display through subunit identity and conformational preorganization may be useful in terms of asymmetric catalysis, where only a few kcal/mol difference between diastereomeric transition states can lead to substantial asymmetric induction.

Pushing beyond α-amino acid subunits in the quest for new foldamers offers an opportunity to explore heterogeneous backbones, a dimension of variation that has no parallel among the biological foldamers. Thus, for example, α- and β-amino acids can be combined to generate α/β-peptides with diverse patterns of α and β residues along the backbone, a dimension of sequence variation that is distinct from the more familiar variation that involves only side chains. A range of helical secondary structures has been identified among α/β-peptides with different proportions and arrangements of α and β subunits.[27] In general, these helices are stabilized by use of ACPC. As discussed below, the superfamily of ACPC-containing foldamers provides a fertile basis for catalyst discovery.

The preceding paragraphs have focused on foldamers containing β-amino acid residues because this group is particularly well characterized, but comparable possibilities emerge as more extended amino acids and related subunits are employed for foldamer construction. Thus, for example, several helical secondary structures have been identified among oligomers containing γ-amino acids, including γ-peptides, α/γ-peptides, β/γ-peptides and α/β/γ-peptides.[28] Fundamental structural studies have begun to provide a basis for γ-peptide catalyst development, as described below.

1.4 Carbon-Carbon Bond Chemistry

The controlled formation or cleavage of carbon-carbon bonds is of central importance in metabolism and in synthetic organic chemistry. Both types of reaction have been explored in the context of foldamer catalysis.

In one of the earliest examples, Hilvert et al. showed that a β-peptide decamer could serve as an effective catalyst for the retroaldol reaction of 4-phenyl-4-hydroxy-2-oxobutyrate in aqueous buffer (Figure 4).[29] This effort was inspired by earlier work with designed lysine-containing α-peptides that adopt an α-helical conformation and display retroaldol catalysis.[30,31] The catalytic mechanism appears to involve imine formation between the keto group of the substrate and a lysine side chain, the latter in the amino rather than ammonium form. The β-peptide designs featured β^3-homolysine (β^3-hLys) as the source of the catalytic group.

The most effective β-peptide featured the repeating sequence triad ACHC-ACHC-β^3-hLys, which generates a globally amphiphilic 14-helix with nonpolar cyclohexyl side chains dominating two-thirds of the circumference and a stripe of amine/ammonium side chains on the opposite side of the helical cylinder. The ACHC residues fulfill two roles, stabilizing the helical secondary structure and providing a composite hydrophobic surface that drives self-assembly in aqueous solution. Both features proved to be important for maximizing catalysis. A sequence isomer in which the β^3-hLys and ACHC residues were distributed around the entire helix circumference did not self-assemble and was a poor catalyst of the retroaldol reaction. An analogue of the most effective β-peptide in which all of the preorganized ACHC residues were replaced by flexible but hydrophobic β^3-hVal residues was an inferior catalyst. It was proposed that self-assembly enhances catalysis by bringing positive charges near one another, thereby lowering the pK_a of at least one side chain ammonium group.

Guichard et al. have characterized urea-based foldamers that form a helix with ~2.5 residues per turn.[32] This helix is stabilized by bifurcated H-bonds between each backbone carbonyl and both N-H groups of the urea group at position i+2. Palomo, Guichard and coworkers have shown that oligourea 2 catalyzes the enantioselective addition of malonates to nitro-olefins (Figure 5A).[33]
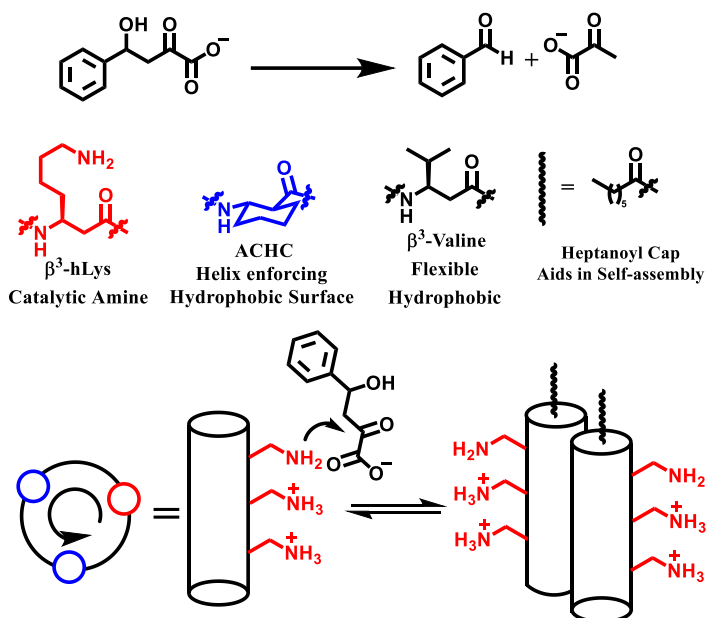
Figure 4. β-peptide catalyzed retroaldol reaction. Cartoon depiction of helical wheel with ACHC and β³-hLys residues clustered on respective helical faces.
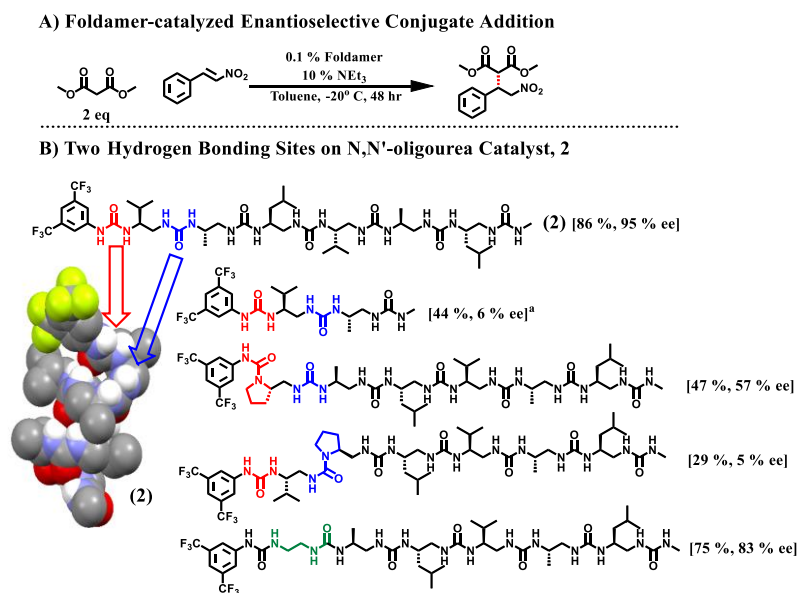
Figure 5. A) Foldamer-catalyzed, enantioselective conjugate addition. B) Selected N,N'-oligoureas for catalyst structure-activity relationship. Crystal Structure of 2. aReaction run at room temperature. Hydrogen bonding (or disrupted hydrogen bonding) sites are

highlighted in red and blue. Unsubstituted urea monomer in green. Crystal structure: black – carbon, red = oxygen, white = hydrogen, blue = nitrogen, green = fluorine. Only N-H hydrogens are shown.

Useful reactivity and high enantioselectivity (up to 99 % ee) were achieved at extremely low catalyst loading (0.1 mol % urea oligomer, along with 10 mol % Et_3N), a significant feat in comparison to traditional organocatalytic loadings (10-20 mol %).[34] Helix formation generates two neighboring urea groups at the N-terminus, both of which are double H-bond donor sites. The authors propose that this NH-rich site is responsible for substrate recognition and activation.

Because they harness an active site involving the helical oligourea backbone rather than functional groups provided by side chains, the reactivity achieved by Palomo, Guichard et al. is reminiscent of the Juliá-Colonna epoxidation.[35] This enone epoxidation is catalyzed by polyleucine, and the array of amide NH groups aligned at the N-terminus of the α-helix is proposed to be the site of substrate binding and activation. Roberts et al. have shown that poly-β^3-hLeu has comparable catalytic capabilities.[36]

Nitro-olefins are highly reactive electrophiles, and these molecules can be considered "privileged substrates" in the organocatalysis community because conjugate additions to nitro-olefins have been so widely studied.[37] Wennemers et al. have shown that the tri-α-peptide D-Pro-Pro-Glu-NH₂ (**3**)

is an excellent catalyst for aldehyde additions to nitro-olefins (Figure 6A).[38]
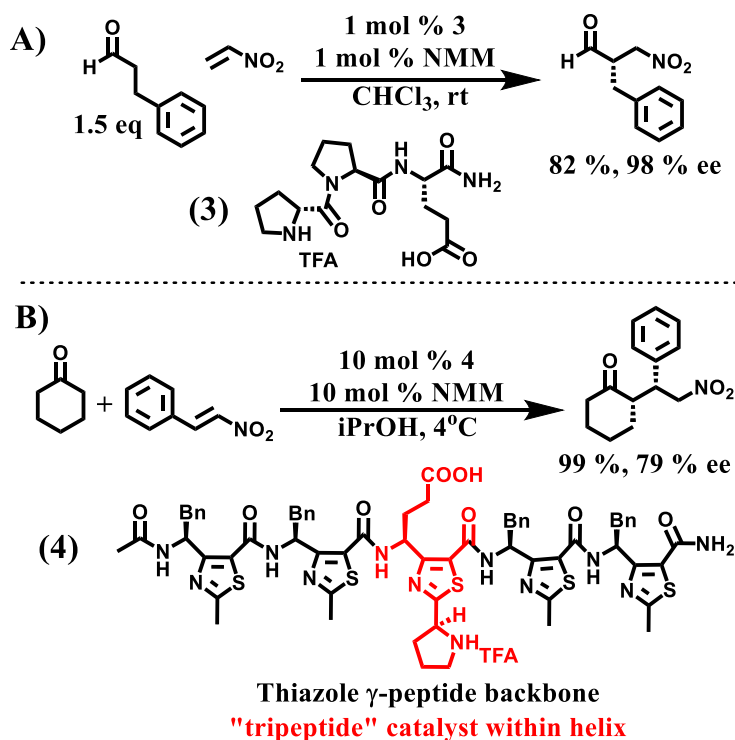
Figure 6. Conjugate additions to nitro-olefins by A) tri-α-peptide D-Pro-Pro-Glu-NH₂ and B) thiazole-based peptide. TFA = trifluoroacetic acid.

Recently this group systematically evaluated the effect of replacing α residues with β homologues; only the Glu residue could be substituted without loss of reactivity or stereoselectivity.[39] Figueiredo, Maillard et al. have reported that helical γ-peptides (**4**) containing thiazole-based subunits catalyze the stereospecific conjugate addition of ketones to nitro-olefins.[40] In this system, the two reactive groups required for bifunctional catalysis, a pyrrolidine and a carboxylic acid, are located within a single γ residue (Figure 6B). However, the authors demonstrated that yield and stereoselectivity increased modestly as the foldamer in which that γ residue was embedded grew longer, suggesting that the helical secondary structure is beneficial in terms of reaction outcome.

Price, Michaelis et al. have developed helical α-peptides that serve as bifunctional catalysts of enantioselective Diels-Alder and indole alkylation reactions.[41] These catalysts can be considered "foldamers" because they are feature non-proteinogenic residues not only to provide catalytic functionality (an imidazolidinone and a thiourea, projecting from side chains) but also to promote a helical conformation (Aib residues). The Diels-Alder reaction between 2-butenal and a carbamate-functionalized diene occurred with high yield and enantioselectivity with this peptide catalyst (**5**) (Figure 7A). The imidazolidinone was intended to provide electrophilic activation for 2-butenal (via iminium formation).[42] The thiourea was positioned to be approximately aligned with the imidazolidinone upon helix formation;[4e,f] H-bonds from the thiourea to the carbamate carbonyl were intended to hold the diene near the iminium dienophile.

Control studies supported the authors' bifunctional catalysis hypothesis. For example, insertion of proline residues, expected to disrupt helical folding, led to a loss of catalysis (**6**). Another control experiment involved competition between two dienes, one bearing a carbamate, which can H-bond to the thiourea, and the other (cyclopentadiene) lacking an H-bonding site (Figure 7B). With a simple imidazolidinone catalyst (**7**), cyclopentadiene was modestly preferred

over the carbamate-bearing diene, but the Diels-Alder reaction catalyzed by the bifunctional peptide

showed a strong selectivity for the carbamate-bearing diene.
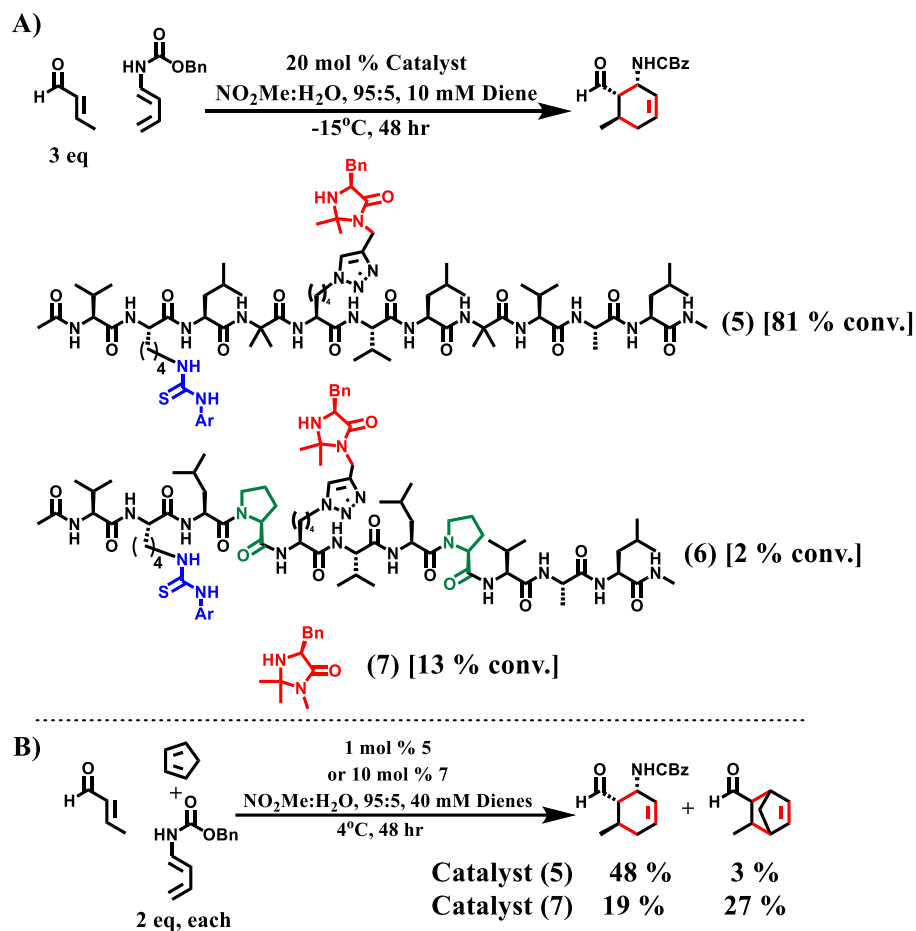
Figure 7. A) Peptide catalyzed Diels-Alder reaction. B) Diene competition experiments comparing bifunctional peptide catalyst (**5**) and small molecule imidazolidinone (**7**).

The use of Aib to stabilize helix formation in the work of Price, Michaelis et al. is

reminiscent of very clever work from Clayden et al. involving Aib-rich α-peptides.[43] This group

has shown that stereochemical information, as manifested in an sp³ stereocenter at one end of the

peptide, can be transmitted across 60 bonds contained in a locally achiral Aib-rich segment, to

influence the stereochemical outcome of a carbon-carbon bond-forming reaction that generates a

new sp^3 stereocenter at the other end of the peptide (Figure 8). This remarkable achievement reflects

the influence on helix screw sense exerted by terminal stereogenic centers.
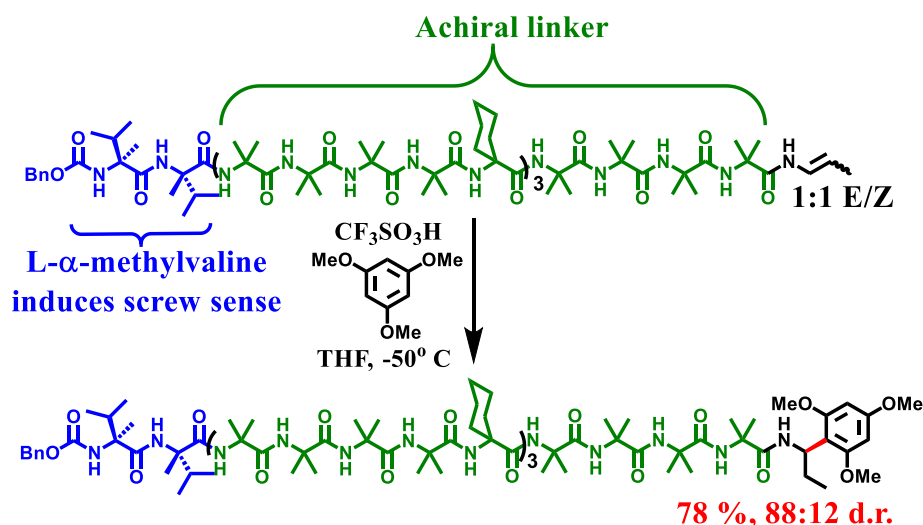
Figure 8. Asymmetric induction over 60 bonds.

Recent work in our laboratory has focused on bifunctional catalysis of aldol reactions by

foldamer helices bearing amine diads. In the first phase of these studies, we employed a well-known

type of selective crossed aldol condensation, in which formaldehyde is the obligate electrophile, to

probe the different diad geometries that could be achieved across a superfamily of ACPC-based β-

and α/β-peptides.[44] The crossed aldol reaction provided an assay for judging which backbone and

sequential spacing enabled the most effective coordination between the two side chain amino

groups.

These experiments built upon an extensive literature on amine catalysis of aldol and related

reactions.[4a,45] In particular, we were inspired by mechanistic analysis by Erkkila and Pihko of

pyrrolidine-catalyzed crossed aldol reactions involving formaldehyde. These researchers

demonstrated second-order catalysis by pyrrolidine and concluded that both reactants are

activated.[46] Specifically, formaldehyde is activated as an electrophile (iminium) by one pyrrolidine

molecule, and the other aldehyde is activated as a nucleophile (enamine) by the other pyrrolidine

molecule. The cyclopentane-based β residue ACPC can be replaced by pyrrolidine-based analogue APC while retaining helical propensity.[47] Therefore, the mechanistic insights from Erkkila and Pihko led us to hypothesize that foldamers containing two properly spaced APC residues would be effective catalysts of the crossed aldol reaction.

We evaluated this hypothesis by examining three series of APC-containing foldamers, one with a pure β residue backbone, one with a 1:1 alternation of α and β residues, and one with a 1:2 alternation of α and β residues. Each backbone had well-established conformational behavior, and we could be confident that examining bis-APC sequence variants for all three backbones would, collectively, explore a variety of spatial arrangements of the pyrrolidine units.

Our experimental design is illustrated for two of the backbones (pure β and 1:2 α:β) in Figure 9. We compared relative initial rates of the crossed aldol condensation involving hydrocinnamaldehyde as nucleophile among foldamers with a common backbone. In each case, the initial rate was normalized to that observed for the foldamer bearing a single APC residue (**8** or **12**). In both series, placing the two APC residues adjacent in sequence (**9** or **13**) caused no increase in initial rate.
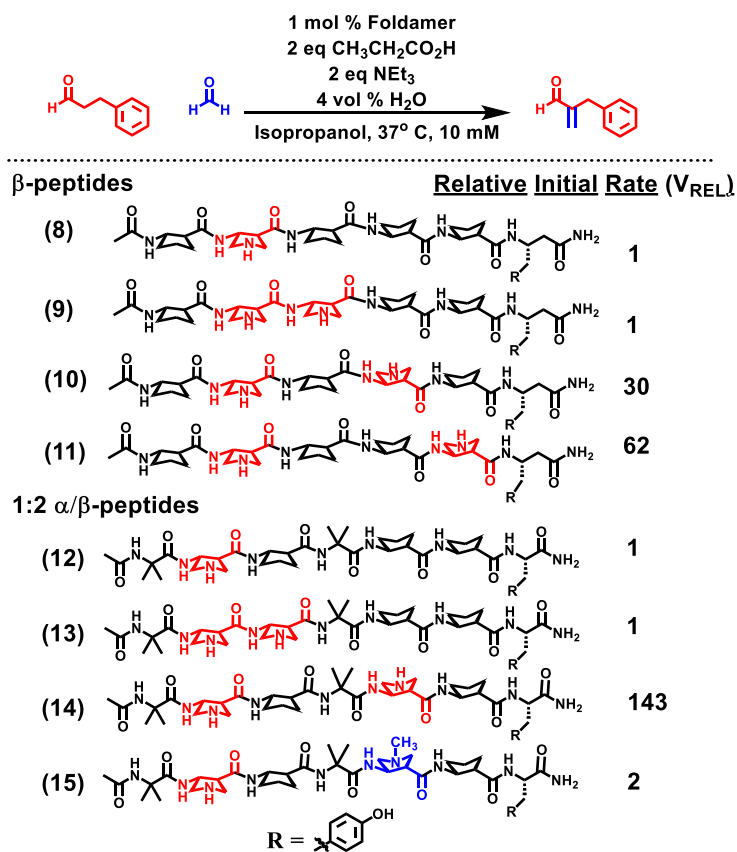
Figure 9. Evaluation of β- and 1:2 α/β-peptide amine diad geometries for the crossed aldol reaction.

These outcomes were expected, because helix formation causes the pyrrolidine nitrogen atoms to splay apart when the APC residues are adjacent in sequence. Further separation along the sequence allows the two pyrrolidine rings to approach alignment in the helical conformation. Thus, for the pure β backbone, which forms the 12-helix, with ~2.5 residues per turn, i,i+2 spacing (**10**) causes the pyrrolidines to be a little less that one turn apart, while i,i+3 spacing (**11**) causes them to be a little more than one turn apart. Both arrangements lead to a significant increase in initial rate of the crossed aldol reaction. The most substantial initial rate enhancement was observed in the 1:2 α:β series, when the pyrrolidines had i,i+3 spacing (**14**). This foldamer backbone forms a helix with ~3 residues per turn, and this sequential spacing should cause nearly perfect angular alignment of the pyrrolidine rings.

Mechanistic studies provided strong support for our hypothesis that α/β-peptide **14** acts as a bifunctional catalyst of the crossed aldol reaction, covalently activating formaldehyde as the iminium and hydrocinnamaldehyde as the enamine. For example, replacing one secondary amine with a tertiary amine (**15**) largely abolished the rate enhancement relative to mono-APC reference foldamer **12**, as predicted by this hypothesis. In addition, catalysis was shown to be first-order in terms of foldamer **14**.

The activity manifested by α/β-peptide **14** is significant in terms of the young field of foldamer catalysis, but this activity is not useful in a practical sense. If one needed to prepare the enal product generated from hydrocinnamaldehyde and formaldehyde, one would use pyrrolidine rather than synthesizing **14**. However, the identification of **14** as a bifunctional catalyst led us to wonder how this foldamer system might be used to achieve catalytic reactivity that was not accessible with simple amines. These considerations led us to explore intramolecular aldol reactions intended to form medium-sized rings.

Exploratory studies with dialdehyde **16** revealed that bis-APC foldamer **14** caused very little reaction.[48] However, when we examined analogue **17**, in which the catalytic diad has been altered to feature a primary amine in addition to a secondary amine, dialdehyde **16** was induced to form cyclodimers and cyclotrimers, containing 16- and 24-membered rings. (Another possible product, cyclo-octene-1-aldehyde, was not detected.) This unexpected outcome was intriguing because large carbocycles can be challenging to prepare, and because there was no way to predict that altering the composition of the catalytic diad would so profoundly affect reactivity. Control reactions with a 1:1 combination of pyrrolidine and n-butylamine provided very little product, which demonstrated that the foldamer catalyst displays activity distinct from smaller and more conventional catalysts.
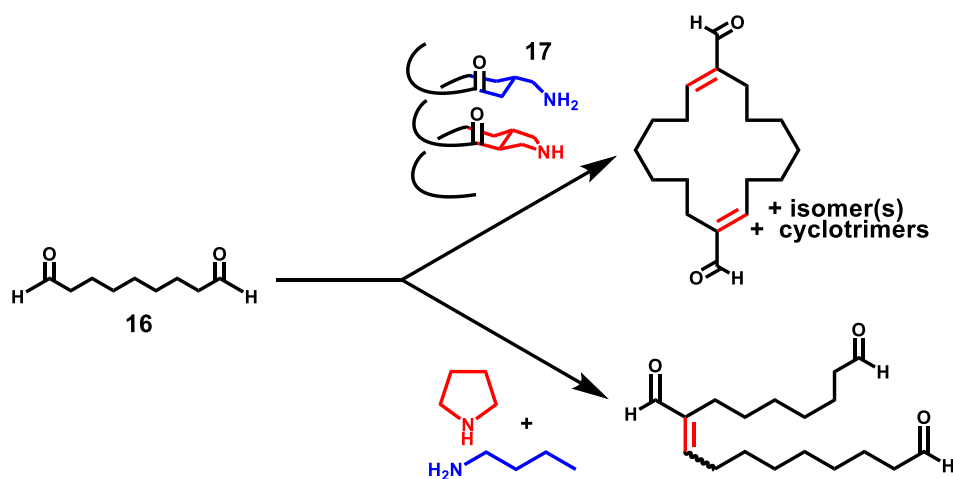
Figure 10. Observation of foldamer-catalyzed cyclodimerization of dialdehyde **16**, and small molecule control reaction.

We turned to longer dialdehydes to evaluate the effects of ring size on catalytic efficacy of macrocyclizations. Good yields could be achieved for 14-, 16- and 18-membered ring formation, but 12-membered ring formation in this series was accompanied by significant cyclodimerization. We speculate that ring strain associated with medium-sized rings (conventionally identified as those containing 8-11 atoms) makes it hard to effect their closure.[49] The observed catalysis of larger ring formation is attributed to a templation effort of the foldamer, which forms transient covalent

intermediates (iminium and enamine) with both ends of a long-chain dialdehyde and facilitates ring-closing bond formation (Figure 11A).
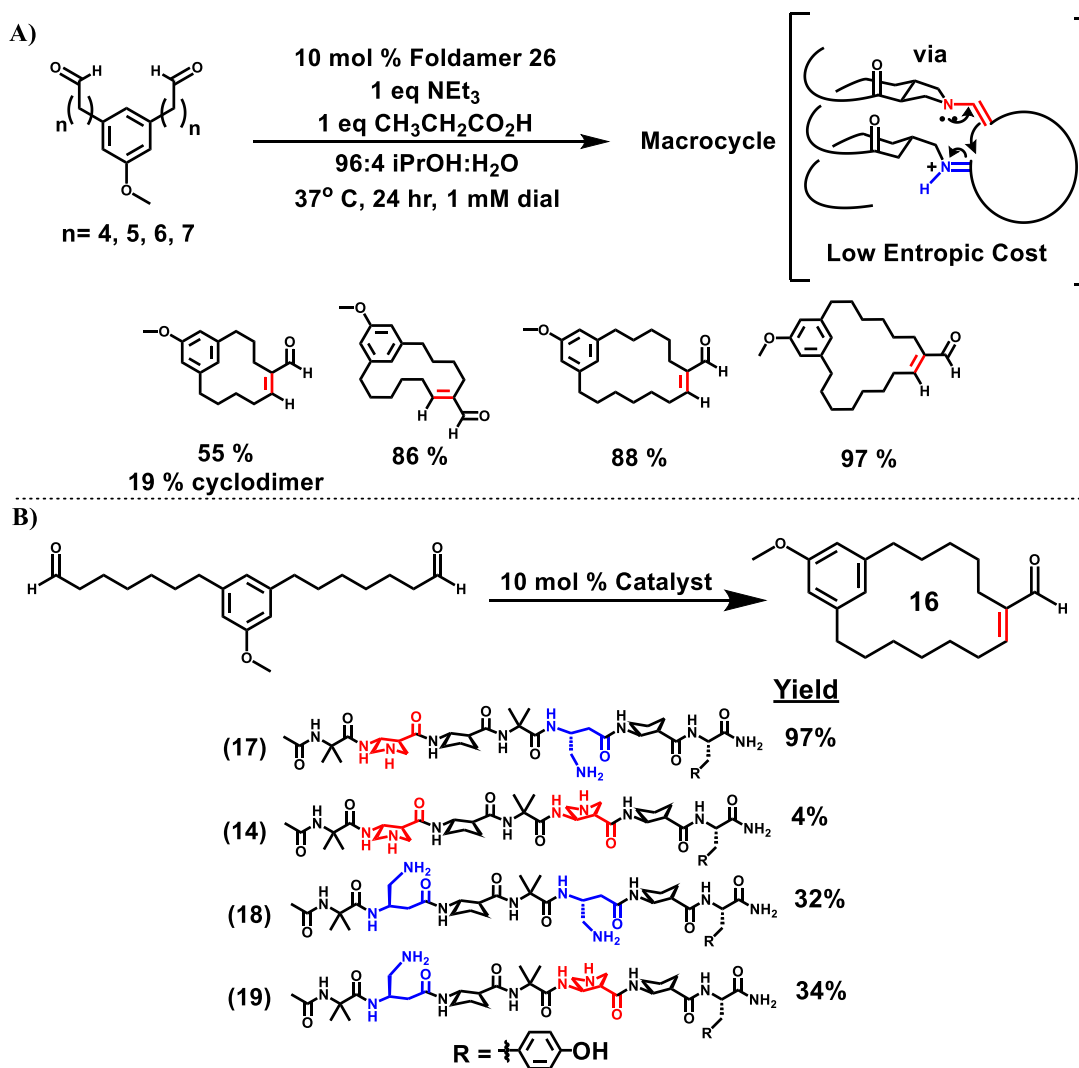
Figure 11. A) Foldamer-templated macrocyclization of dialdehydes. B) Foldameric structural aspects that effect catalysis.

The unimolecular cyclization to form a 16-membered ring enal provided the basis for exploring the impact of foldamer structure on reaction outcome (Figure 11B). Consistent with results from the crossed aldol study, we found that the i i+3 spacing of the two amino groups is required for efficient macrocyclization. A diad comprised of two secondary amines was almost

completely ineffective (**14**), and the yield was poor when the diad comprised two primary amines (**18**). Swapping the positions of the secondary and primary amines within the sequence caused a substantial decline in macrocycle yield (**19**), which shows that catalysis is very sensitive to the spatial arrangement of the two catalytic groups.

To illustrate the utility of this new type of macrocyclization reaction, we used foldamer **17** in the synthesis of the natural product robustol, which contains a 22-membered ring.[50] The cyclization step produced two regio-isomeric enals, because the starting dialdehyde was unsymmetrical. Subjecting this mixture to decarbonylation followed by hydrogenation, however, provided a single product, which could then be converted to robustol.
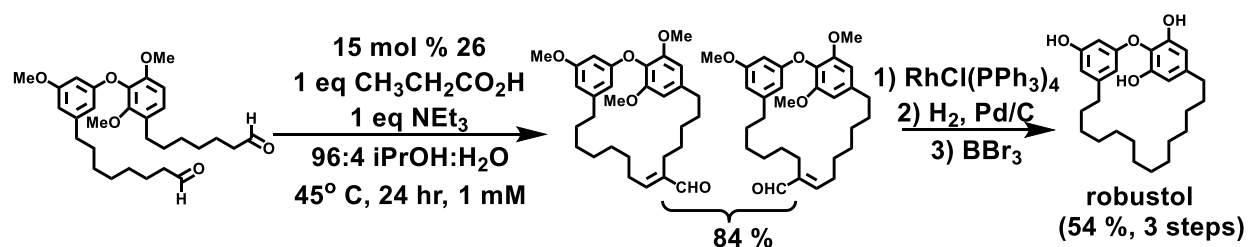
Figure 12. Total synthesis of robustol via foldamer-catalyzed macrocyclization.

1.5. Other Reactions

One of the earliest examples of foldamer catalysis featured the peptoid backbone. Peptoids are N-alkyl-glycine oligomers; therefore, the backbone contains only tertiary amide groups.[51] Because the peptoid backbone lacks H-bond donors, avoidance of steric repulsion plays a major role in determining secondary structure, although other non-covalent interactions contribute.[52]

Mayaan, Ward and Kirshenbaum explored the oxidative kinetic resolution of racemic 1-phenyl-ethanol with peptoids bearing a nitroxyl group derived from TEMPO (Figure 13).[53,54] The peptoid subunits contained a stereogenic center in the side chain. Peptoids in this class had earlier been shown to adopt a helical conformation. When the nitroxyl group was placed on a peptoid heptamer (**20**), a kinetic resolution was observed (after 84% of the starting alcohol had been consumed, the remaining alcohol displayed 99% ee). The presence of the peptoid helix was important, because a peptoid dimer linked to the nitroxyl group (**21**), did not achieve any kinetic resolution of the alcohol enantiomers.
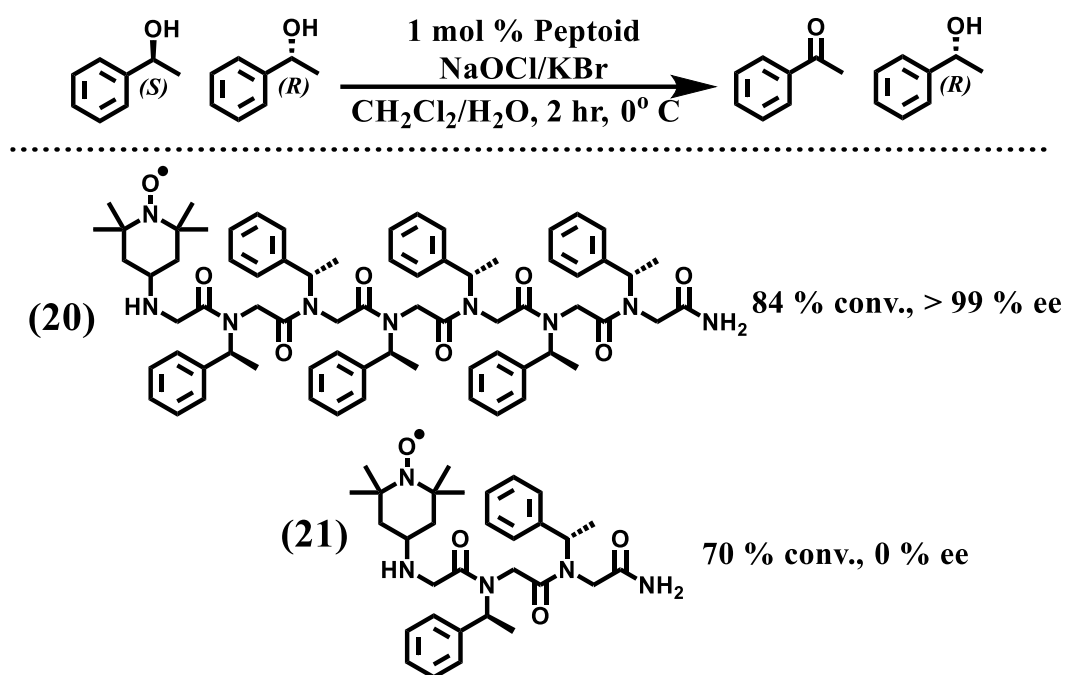
Figure 13. Oxidative kinetic resolution via peptoid catalysis.

Reactions of activated ester substrates have been popular subjects for enzyme-mimetic catalysis studies. Substantial rate accelerations have been achieved for the transesterification of vinyl trifluoroacetate to methyl trifluoroacetate with "spiroligomers" that display rigid but readily diversifiable backbones. This family of oligomers with controlled shapes has been developed by Schafmeister et al. In collaboration with the Houk group, Schafmeister and colleagues designed a

"spiroligozyme" that adopts a curved shape and projects three reactive groups from the concave surface (Figure 14A).[55] The transacylation reaction proceeds through an acyl-spiroligozyme intermediate that is reminiscent of the covalent intermediates formed by serine proteases. In subsequent work, this group developed a spiroligomer that catalyzes a Claisen rearrangement.[56]

Schepartz et al. have developed self-assembling β-peptides that catalyze the hydrolysis of 8-acetoxypyrene-1,3,6-trisulfonate (Figure 14B).[57] Unlike the β-peptides mentioned above that catalyze a retroaldol reaction, the β-peptides of Schepartz et al. form discrete helix-bundles in aqueous solution. Catalysis was promoted by engineering a high positive charge density on the β-peptides, to attract the anionic substrate. The α-amino acid residue histidine was incorporated into these designs to provide a side chain imidazole group critical for catalysis.

A)

Acylation 2,700 X Faster Than Small Molecule

B)

β³-octameric bundle
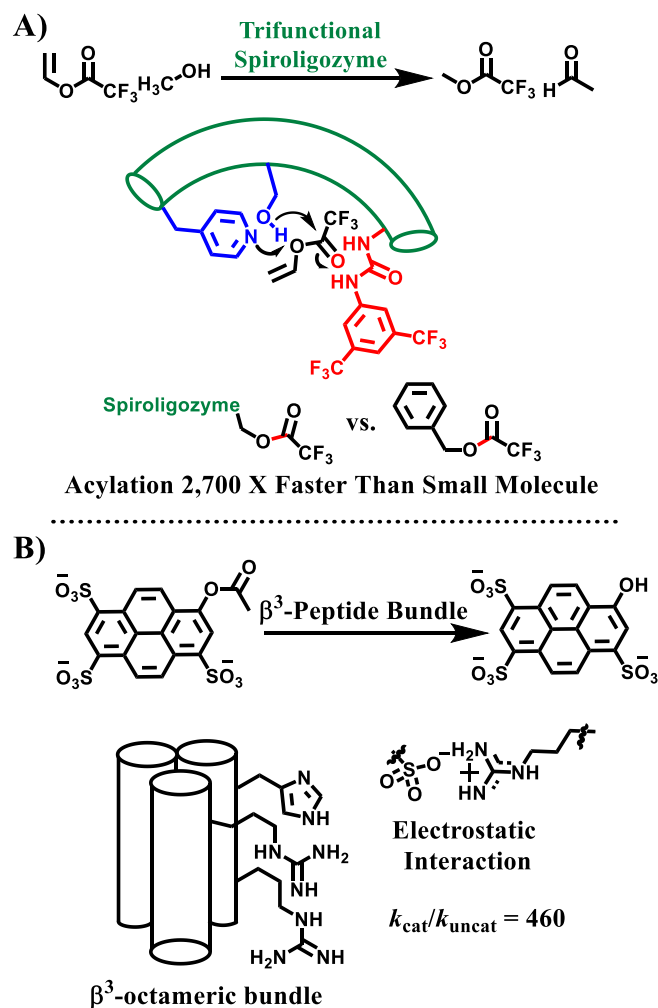
Figure 14. A) Spiroligozyme accelerated acylation/transesterification. B) Self-assembling β-peptide-catalyzed activated ester hydrolysis.

1.6. Recent lessons from conventional peptides

As noted above, pioneering accomplishments from Miller et al. and other groups have demonstrated the catalytic prowess that can be elicited from relatively short peptides containing exclusively α residues, and these precedents have helped to inspire the foldamer-based efforts discussed above.[4d,6,8,9,38,39] Here we highlight recent

advances with conventional peptide catalysts that suggest potentially productive paths for future foldamer-based studies.

Foldamers that adopt defined tertiary structure remain elusive, but combining two or more secondary structural motifs into a single catalyst scaffold represents an interesting alternative. Kudo et al. have taken this approach among α-peptides by linking a β-turn segment with a helical segment to develop a catalyst for regio- and enantioselective reductions of α,β,γ,δ-unsaturated aldehydes mediated by a dihydropyridine reagent (Figure 15).[58] Resin-supported catalyst **22** utilizes a proline residue for iminium activation of unsaturated aldehyde **23**, and the tandem turn/helix motif provides an asymmetric environment for the reduction. Control peptides that lacked either the turn or helix segment resulted in decreased regio- and enantioselectivity. The catalyst-controlled reduction was utilized in the enantioselective synthesis of (S)-citralis and (S)-phenoxanol, from a E/Z-α,β,γ,δ-unsaturated aldehyde **23**.
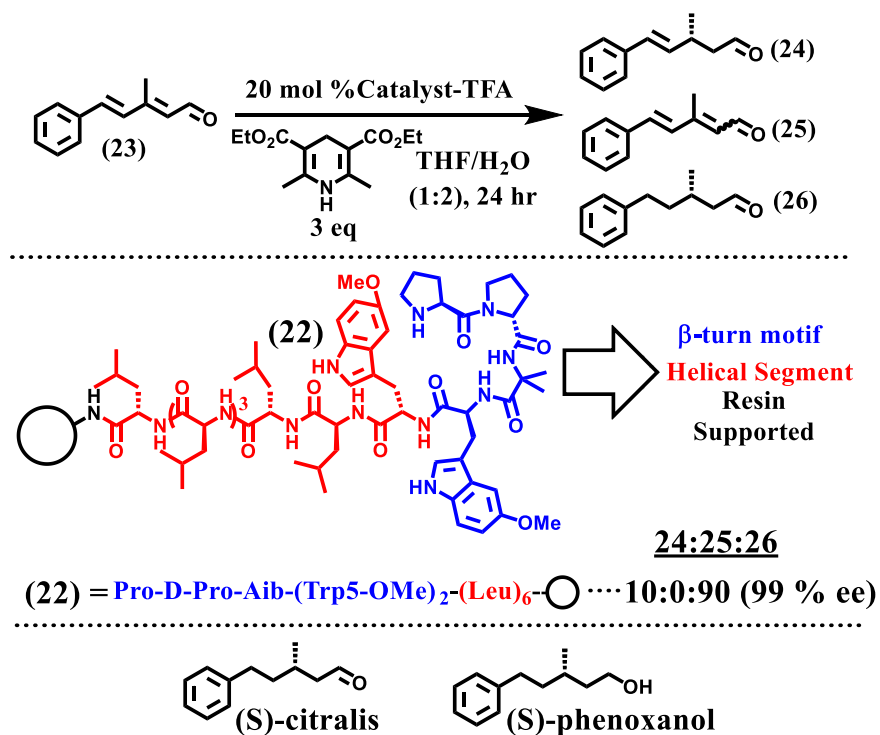
Figure 15. Regio- and enantioselective reduction of α,β,γ,δ-Unsaturated aldehydes.

Foldamers containing tandem helical and turn structural motifs may offer an avenue toward catalysts that begin to surround their substrates in an enzyme-like manner. This approach could lead to foldamers that contain elements intended to engage substrates in ways that guide the operation of the reactive groups. An alternative approach to this challenge that does not require creation of an authentic tertiary structure is suggested by work of Huc et al.[59] This group developed aromatic oligoamides with large internal cavities that could be modified with H-bonding groups in a site-specific manner to generate substrate-selective carbohydrate binders. Placement of reactive groups on the cavity walls could lead to catalysis. Most examples of foldamer catalysis have employed organic functionality to engage substrates ("organocatalysis"), but foldamer scaffolds could be powerful tools in the context of metal-mediated catalysis. The ability of chiral foldamer backbones to project metal-ligating groups in specific geometric orientations might support asymmetric catalysis.

Ball et al. have provided an elegant conventional peptide example with peptide **27**, which adopts an α-helical conformation and that aligns two side chain carboxylates, from Asp residues with *i,i+4* spacing, for multidentate coordination to a dirhodium core. Two peptide ligands, oriented antiparallel to one another, provide a complete coordination sphere of four carboxylates. The resulting complex, **28**, catalyzes enantioselective carbenoid insertion into Si-H bonds (Figure 16).[60,61]

Mechanistic studies identified side chains near the coordinated metal ions as important for enantioselectivity. The modularity of these α-peptide ligands makes them attractive for optimizing asymmetric catalysis, since many alternative side chains, natural or unnatural, could be employed. Foldamers would offer comparable benefits as metal ion ligands and offer side chain arrangements complementary to those accessible with α-peptides.
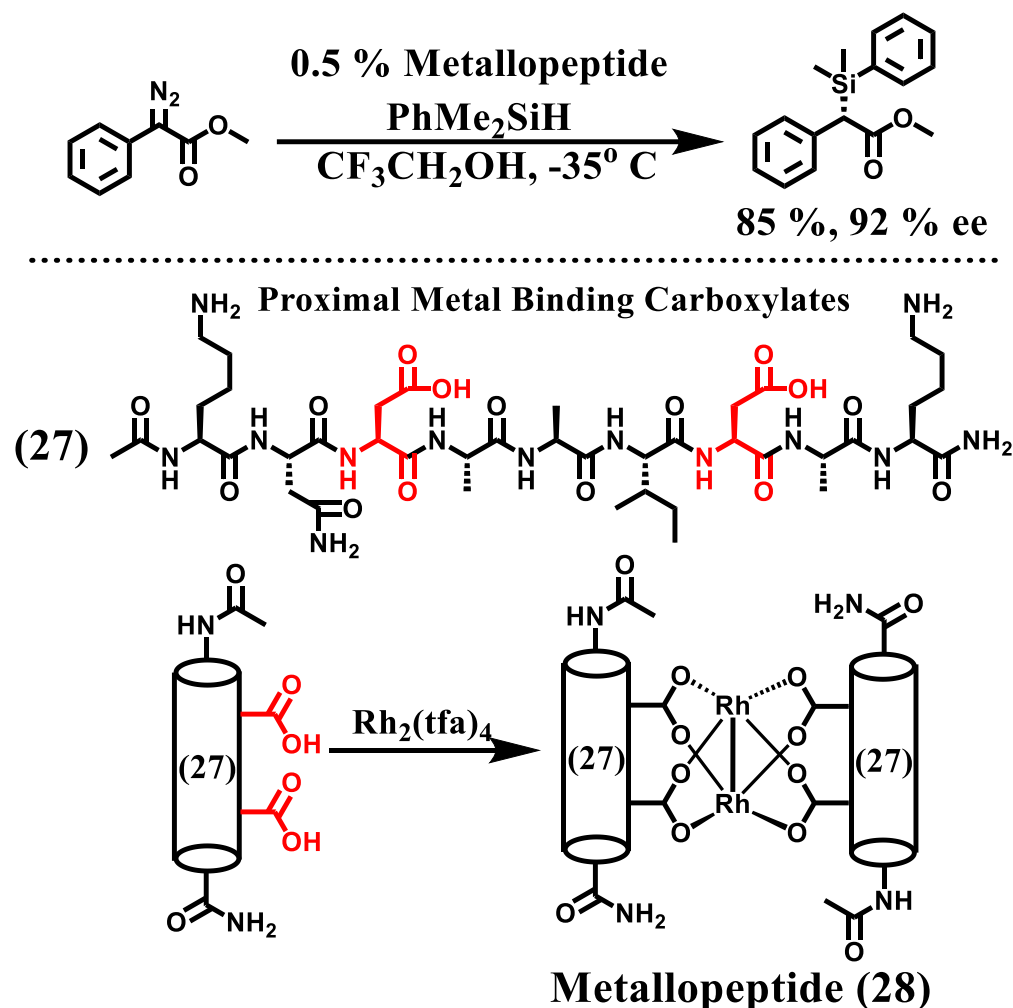
Figure 16. Metallopeptide-catalyzed enantioselective carbenoid insertion into Si-H bonds.

Substrate activation via reversible covalent bonding is an attractive strategy for catalysis because key bond-forming steps can be rendered intramolecular in this way.[62] The entropic benefit of this approach can lead to accelerated rates relative to comparable intermolecular reactions. Several of the foldamer-based catalysts described above rely on amines for reversible covalent activation of substrates, such as aldehydes or ketones, but other modes of covalent activation should be fruitful as well.

Ghadiri et al. demonstrated the ability of a quaternary structure formed by peptides that adopt a specific secondary structure, an α-helical coiled-coil dimer, to serve as a basis for catalyst

development. This system promoted diketopiperazine formation from thioester derivatives of α-amino acids via cysteine-based substrate anchoring (Figure 17).[63]
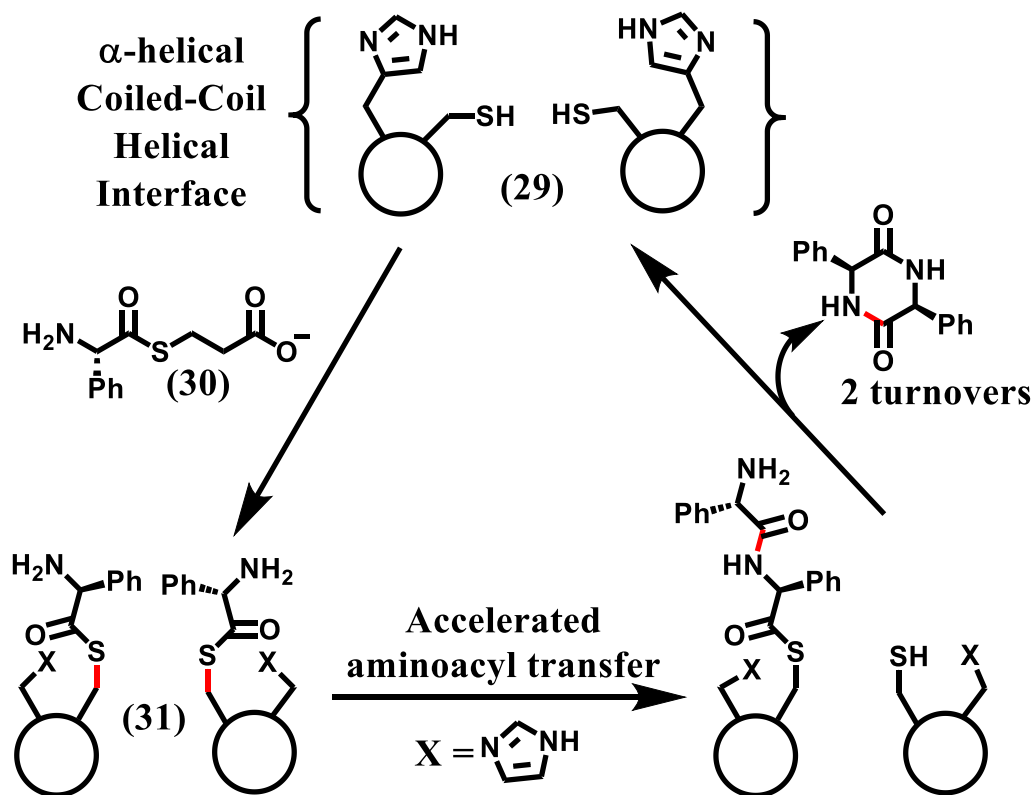
Figure 17. α-helical coiled-coil catalyzed diketopiperazine formation.

The coiled-coil dimer (**29**) was suggested to mimic a nonribosomal peptide synthetase in the juxtaposition of two cysteine side chains, each of which can capture a substrate (**30**) via transthiolesterification (**31**). Subsequent C-N bond formation was accelerated by the proximity of the two acyl-Cys units, as well as the nearby histidine residues, which may have a general base function. Cyclization generates the diketopiperazine by detaching the substrate, thus turning over the catalyst. In this example, formation of a transient thioester on the catalytic peptide does not intrinsically alter acyl group reactivity, relative to the thioester substrate, which contrasts with the activating effects of enamine or iminium intermediate formation in examples discussed above.

Nevertheless, the benefit of bringing two thioesters together, as accomplished by quaternary structure formation, is clearly established in this example, which raises the possibility that foldamer quaternary structures might be harnessed for catalyst development.[64] It is noteworthy that cysteine itself has been used as a catalyst for enantioselective Rauhut-Currier reactions,[65] which suggests other ways to use cysteine or other thiol-bearing subunits in foldamer catalysis.

Additional inspiration can be found in very creative work from Arora et al. that has resulted in redox-active multifunctional catalysts of peptide bond formation from N-protected α-amino acid substrates.[66] This chemistry is compatible with conventional solid-phase synthesis and sets a standard toward which future foldamer catalysis efforts can strive.

1.7. Perspective

The work summarized above suggests that foldamers offer a unique approach for development of new catalysts that are complementary to those accessible from small-molecule frameworks or conventional peptide scaffolds. Stable secondary structures established for diverse foldamer backbones expand the geometries available for orienting sets of reactive side chains in a manner that promotes multifunctional catalysis. As the folding "rules" for new foldamer systems are elucidated, the range of possible side chain arrangements will grow. The inherently modular nature of foldamers at the covalent level, a feature shared with conventional peptides, facilitates the exploration of new geometries for side chain clusters and new identities of the side chains in those clusters.

One potentially productive new path under examination in our group involves the creation of foldamer-based photocatalysts for organic transformations. Photocatalytic methods have exerted a profound effect on organic synthesis over the past decade, enabling a wide range of transformations to be driven by visible light.[67] Developments in this field can be hindered, however,

by the fact that the excited states of many popular photocatalytic moieties are too short-lived to support efficient Dexter energy transfer or single-electron transfer, which results in low quantum yields.[68] We hypothesize that a properly chosen foldamer scaffold might allow efficient energy or electron transfer by enforcing proximity between a photocatalytic moiety and a substrate. Ultimately, juxtaposing photoactive and substrate-binding functionality along a foldamer backbone might enable catalysis of stereoselective and/or chemoselective reactions.

Bifunctional Foldamers = Light Harvest + Chiral Helix
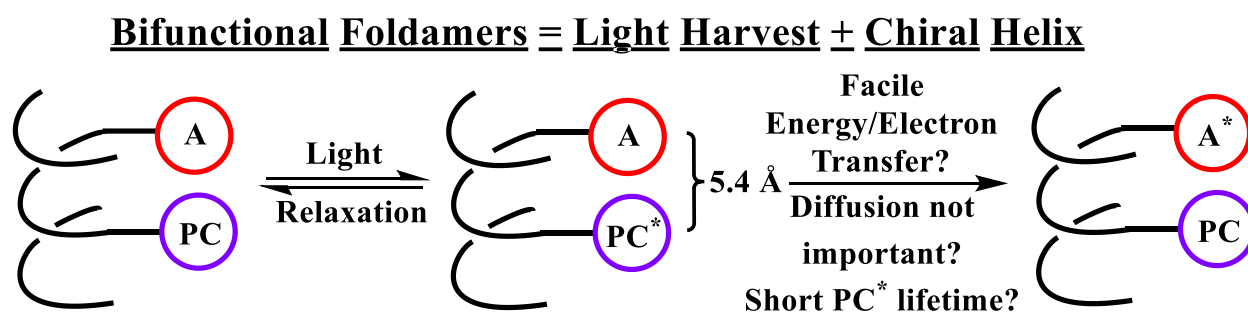
Figure 18. Cartoon depiction of efficient energy or electron transfer from a excited state photocatalyst to a ground state acceptor. A = acceptor, PC = photocatalyst.

Foldamers enable programmable variation of side-chain display, which supports applications that span molecular recognition,[15,69] medicine,[15,70] and catalysis. Here we have highlighted foldamers that facilitate organic reactions and display desirable features such as stereoselectivity or templation of macrocycle formation. We speculate that future efforts will support the hypothesis that foldamers, collectively, provide a very diverse set of possibilities for orienting specific sets of functional groups to achieve catalytic goals.

As with many efforts to develop new catalysts, foldamer-based approaches are ultimately inspired by the extraordinary properties of enzymes and ribozymes that have been elicited by natural evolutionary processes. In this regard, it is noteworthy that laboratory-based evolution has been harnessed by Holliger et al. to generate "xeno nucleic acid" oligomers, which could be viewed

as RNA-inspired foldamers, that display remarkable catalytic prowess.[71] In addition to the conceptual foundation provided by biopolymer catalysts, experimental work directed toward foldamer catalyst development benefits from the many impressive accomplishments of organic chemists who employ small molecules or conventional peptides as the basis for catalyst design or discovery.

1.8 References

1. a) Silverman, R. B. *Organic Chemistry of Enzyme-Catalyzed Reactions,* 2nd Edition.; Academic Press, 2002, p. 1-800. b) Drauz, K.; Groger, H.; May, Oliver, *Enzyme Catalysis in Organic Synthesis,* 3rd edition.; Wiley-VCH, Weinheim, 2012.

2. a) Wolfenden, R. *Annu. Rev. Biochem.* **2011**, *80*, 645-667. b) Herschlag, D.; Natarajan, A. *Biochemistry,* **2012**, *52*, 2050-2067. c) Khersonky, O.; Tawfik, D. S. *Annu. Rev. Biochem.* **2010**, *79*, 471-505.

3. Anantharaman, V.; Aravind, L.; Koonin, E. V. *Current Opinion in Chemical Biology* **2003**, *7*, 12-20.

4. a) Mukherjee, S.; Yang, J. W.; Hoffmann, S.; List, B. *Chem. Rev.* **2007**, *107*, 5413-5415. b) Yoon, T.P.; Jacobsen, E. N. *Science* **2003**, *299*, 1691-1693. c) Desper, J. M.; Breslow, R. J. *J. Am. Chem. Soc.* **1994**, *116*, 12081-12082. d) Colby Davie, E. A.; Mennen, S. M.; Xu, Y.; Miller, S. J. *Chem. Rev.* **2007**, *107*, 5759-5812. e) Pihko, P. M.; Rapakko, S.; Wierenga, R. K. *Hydrogen Bonding in Organic Synthesis,* Wiley-VCH, Weinheim, **2009**, pp. 43-71. f) Brak, K.; Jacobsen, E. N. *Angew. Chem. Int. Ed.* **2013**, *52*, 534-561.

5. a) Li, H.; Wang, Y.; Tang, L.; Deng, L. *J. Am. Chem. Soc.* **2004**, 126, 9906-9907. b) Song, J.; Wang, Y.; Deng, L. *J. Am. Chem. Soc.* **2006**, 128, 6048-6049. c) Tian, S.; Deng, L. *J. Am. Chem. Soc.* **2001**, 123, 6195-6196.

6. a) Sculimbrene, B. R.; Miller, S. J. *J. Am. Chem. Soc.*, **2001**, 123, 10125-10126. b) Barrett, K. T.; Metrano, A. J.; Rablen, P. R.; Miller, S. J. *Nature*, **2014**, 509, 71-75. c) Han, S.; Miller, S. J. *J. Am. Chem. Soc.*, **2013**, 135, 12414-12421.

7. a) Wendlandt, A. E.; Vangal, P.; Jacobsen, E. N. *Nature*, **2018**, 556, 447-451. b) Park, Y.; Harper, K. C.; Kuhl, N.; Kwan, E. E.; Liu, R. Y.; Jacobsen, E. N. *Science,* **2017**, 355, 162-166. c) Raheem, I. T.; Thiara, P. S.; Peterson, E. A.; Jacobsen, E. N. *J. Am. Chem. Soc.*, **2007**, 129, 13404-13405.

8. a) Krattiger, P.; Kovasy, R.; Revell, J. D.; Ivan, S.; Wennemers, H. *Org. Lett.*, **2005**, *7*, 1101-1103. b) Wennemers, H. *Chem. Commun.*, **2011**, *47*, 1236-12041.

9. Krattiger, P.; McCarthy, C.; Pfaltz, A.; Wennemers, H. *Angew. Chem. Int. Ed.*, **2003**, *42*, 1722-1724.

10. Hilton, M. J.; Brackett, C. M.; Mercado, B. Q.; Blagg, B. S. J.; Miller, S. J. *ACS Cent. Sci.*, **2020**, *6*, 426-435.

11. Park, Y.; Harper, K. C.; Kuhl, N.; Kwan, E. E.; Liu, R. Y.; Jacobsen, E. J. *Science*, **2017**, *355*, 162-166.

12. Li, J; Grosslight, S.; Miller, S. J. *ACS Catalysis*, **2019**, *9*, 9794-9799.

13. Toste, F. D.; Sigman, M. S.; Miller, S. J. *Acc. Chem. Res.*, **2017**, *50*, 609-615.

14. Gellman, S. H. *Acc. Chem. Res.* **1998**, *31*, 173-180.

15. a) Hecht, S.; Huc, I. *Foldamers: Structure, Properties, and Applications*, Wiley-VCH, Weinheim, **2007**, pp.1-435. b) Hill, D. J.; Mio, M. J.; Prince, R. B.; Hughes, T. S.; Moore, J. S. *Chem. Rev.* **2001**, *101*, 3893-4011. c) Guichard, D.; Huc, I. *Chem. Commun.* **2011**, *47*, 5933-5941. d) Martinek, T. A.; Fulop, F. *Chem. Soc. Rev.* **2012**, *41*, 687-702. e) Cheng, R. P.; Gellman, S. H.; DeGrado, W. F. *Chem. Rev.* **2011**, *101*, 3219-3252.

16. Horne, W. S.; Price, J. L.; Gellman, S. H. *PNAS*, **2008**, *105*, 9151-9156.

17. Arnold, F. H. *Acc. Chem. Res*., **1998**, *31*, 125-131.

18. Jiang, L.; Althoff, E. A.; Clemente, F. R.; Doyle, L.; Rothlisberger, D.; Zanghellini, A.; Gallaher, J. L.; Betker, J. L.; Tanaka, F.; Barbas III, C. F.; Hilvert, D. J.; Houk, K. N.; Stoddard, B. L.; Baker, D. *Science*, **2008**, *319*, 1387-1391.

19. Studer, S.; Hansen, D. A.; Pianowski, Z. L.; Mittl, P. R. E.; Debon, A.; Guffy, S. L.; Der, B. S.; Kuhlman, B.; Hilvert, D. *Science*, **2018**, *362*, 1285-1288.

20. MacKenzie, I. A.; Wang, L.; Onuska, N. P. R.; Williams, O. F.; Begman, K.; Moran, A. M.; Dunietz, B. D.; Nicewicz, D. A. *Nature*, **2020**, *580*, 76-80.

21. a) Theriot, J. C.; Lim, C- H.; Yang, H.; Ryan, M. D.; Musgrave, C. B.; Miyake, G. M. *Science*, **2016**, *352*, 1082-1086. b) McCarthy, B. G.; Pearson, R. M.; Lim, C- H.; Sartor, S. M.; Damrauer, N. H.; Miyake, G. M. *J. Am. Chem. Soc*., **2018**, *140*, 5088-5101. c) Sartor, S. M.; Lattke, Y. M.; McCarthy, B. G.; Miyake, G. M.; Damrauer, N. S. *J. Phys. Chem. A*, **2019**, *123*, 4727-4736.

22. Singh, V. K.; Yu, C.; Badujar, S.; Kim, Y.; Kwon, Y.; Kim, D.; Lee, J.; Toheed, A.; Thangavel, G.; Park, L. S.; Lee, J.; Nandajan, P. C.; Wannemacher, R.; Milian-Medina, B.; Luer, L.; Kim, K. S.; Gierschner, J.; Kwon, M. S. *Nature Catalysis*, **2018**, *1*, 794-804.

23. Pauling, L.; Corey, R. B.; Branson, H. R. *PNAS*, **1951**, 37, 205-211.

24. a) Appella, D. H.; Christianson, L. A.; Karle, I. L.; Powell, D. R.; Gellman, S. H. *J. Am. Chem. Soc.* **1996**, *118*, 13071-13072. b) Seebach, D.; Overhand, M.; Kuhnle, F. N. M.; Martinoni, B.; Oberer, L.; Hommel, U.; Widmer, H. *Helv. Chim. Acta.*, **1996**, 79, 913-941.

25. Raguse, T. L.; Lai, J. R.; Gellman, S. H. *J. Am. Chem. Soc.*, **2003**, 125, 5592-5593.

26. Appella, D. H.; Christianson, L. A.; Klein, D. A.; Powell, D. R.; Huang, X.; Barchi Jr., J. J.; Gellman, S. H. *Nature*, **1997**, 387, 381-384.

27. a) Schmitt, M. A.; Choi, S. H.; Guzei, I. A.; Gellman, S. H. *J. Am. Chem. Soc.*, **2006**, 128, 4538-4539. b) Choi, S. H.; Guzei, I. A.; Spencer, L.; Gellman, S. H. *J. Am. Chem. Soc.*, **2009**, 131, 2917-2924.

28. a) Guo, L.; Chi, Y.; Almeida, A. M.; Guzei, I. A.; Parker, B. K.; Gellman, S. H. *J. Am. Chem. Soc.*, 2009, 131, 16018-16020. b) Shin, H. Y.; Gellman, S. H. *J. Am. Chem. Soc.*, **2018**, 140, 1394-1400. c) Fisher, B. F.; Gellman, S. H. *J. Am. Chem. Soc.*, **2016**, 138, 10766-10769. d) Giuliano, M. W.; Maynard, S. J.; Almeida, A. M.; Guo, L.; Guzei, I. A.; Spencer, L. C.; Gellman, S. H. *J. Am. Chem. Soc.*, **2014**, 136, 15046-15053. e) Shin, Y. H.; Mortenson, D. E.; Satyshur, K. A.; Forest, K. T.; Gellman, S. H. *J. Am. Chem. Soc.*, **2013**, 135, 8149-8152. f) Guo, L.; Zhang, W.; Reidenbach, A.; Giuliano, M. W.; Guzei, I. A.; Spencer, L. C.; Gellman, S. H. *Angew. Chem. Int. Ed.*, **2011**, 50, 5843-5846. g) Fisher, B. F.; Guo, L.; Dolinar, B. S.; Guzei, I. A.; Gellman, S. H. *J. Am. Chem. Soc.*, **2015**, 137, 6484-6487. h) Guo, L.; Almeida, A. M.; Zhang, W.; Reidenbach, A. G.; Choi, S. H.; Guzei, I. A.; Gellman, S. H. *J. Am. Chem. Soc.*, **2010**, 132, 7868-7869.

29. Muller, M. M.; Windsor, M. A.; Pomerantz, W. C.; Gellman, S. H.; Hilvert, D. *Angew. Chem. Int. Ed.* **2009**, *48*, 922-925.

30. Johnsson, K.; Allemann, R. K.; Widmer, H.; Benner, S. A. *Nature*, **1993**, *365*, 530-532.

31. Tanaka, F.; Fuller, R.; Barbas III, C. F. *Biochemistry*, **2005**, *44*, 7583-7592.

32. Semetey, V.; Rognan, D.; Hemmerlin, C.; Graff, R.; Briand, J.; Marraud, M.; Guichard, G. *Angew. Chem. Int. Ed.*, **2002**, 41, 1893-1895.

33. Becart, D.; Diemer, V.; Salaun, A.; Oiarbide, M.; Nelli, Y. R.; Kauffmann, B.; Fischer, L.; Palomo, C.; Guichard, G. *J. Am. Chem. Soc.* **2017**, *139*, 12524-12532.

34. Dalko, P. I. Comprehensive Enantioselective Organocatalysis: Catalysts, Reactions, and Applications, Wiley-VCH-Weinheim, **2009**, pp. 1-1383.

35. Julia, S.; Guixer, J.; Masana, J.; Rocas, J.; Colonna, S.; Annuziata, R.; Molinari, H. *J. Chem. Soc. Perkin Trans.* **1982**, *1*, 1317-1324.

36. Coffey, P. E.; Drauz, K. H.; Roberts, S. M.; Skidmore, J.; Smith, J. A. *Chem. Commun.* **2001**, 2330-2331.

37. Allgauer, D. S.; Jangra, H.; Asahara, H.; Li, Z.; Chen, Q.; Zipse, H.; Ofial, A. R.; Mayr, H. *J. Am. Chem. Soc.*, **2017**, 139, 13318-13329.

38. Wiesner, M.; Revell, J. D.; Tonazzi, S.; Wennemers, H. *J. Am. Chem. Soc.*, **2008**, 130, 5610-5611.

39. Schnitzer, T.; Wennemers, H. *Helv. Chim. Acta.*, **2019**, 102, e1900070.

40. Aguesseau-Kondrotas, J.; Simon, M.; Legrand, B.; Bantignies, J- L.; Kang, Y. K.; Dumitrescu, D.; Van der Lee, A.; Campagne, J- M.; Marcia de Figueiredo, R.; Maillard, L. T. *Chem. Eur. J.* **2019**, *25*, 7396-7401.

41. Kinghorn, M. J.; Valdivia-Berroeta, G. A.; Chantry, D. R.; Smith, M. S.; Ence, C. C.; Draper, S. R. E.; Duval, J. S.; Masino, B. M.; Cahoon, S. B.; Flansburg, R. R.; Conder, C. J.; Price, J. L.; Michaelis, D. J. *ACS Catal.* **2017**, *7*, 7704-7708.

42. Ouellet, S. G.; Walji, A. M.; MacMillan, D. W. C. *Acc. Chem. Res.* **2007**, *40*, 1327-1339.

43. Byrne, L.; Sola, J.; Boddaert, T.; Marcelli, T.; Adams, R. W.; Morris, G. A.; Clayden, J. *Angew. Chem. Int. Ed.* **2014**, *53*, 151-155.

44. Girvin, Z. C.; Gellman, S. H. *J. Am. Chem. Soc.* **2018**, *140*, 12746-12483.

45. Erkkila, A.; Majander, I.; Pihko, P. M. *Chem. Rev.*, **2007**, 107, 5416-5470.

46. Erkkila, A.; Pihko, P. M. *Eur. J. Org. Chem.* **2007**, 4205-4216.

47. Johnson, L. M.; Gellman, S. H. *Methods Enzymol.*, **2013**, *523*, 407-429.

48. Girvin, Z. C.; Andrews, M. K.; Liu, X.; Gellman, S. H. *Science*, **2019**, *366*, 1528-1531.

49. Galli, L.; Mandolini, L. *Eur. J. Org. Chem.* **2000**, 3117-3125.

50. Cannon, J. R.; Chow, P. W.; Fuller, M. W.; Hamilton, B. H.; Metcalf, B. W.; Power, A. J. *Aust. J. Chem.* **1973**, *26*, 2257-2275.

51. Gangloff, N.; Ulbricht, J.; Lorson, T.; Schlaad, H.; Luxenhofer, R. *Chem. Rev.* **2016**, *116*, 1753-1802.

52. Gorske, B. C.; Stringer, J. R.; Bastian, B. L.; Fowler, S. A.; Blackwell, H. E. *J. Am. Chem. Soc.* **2009**, *131*, 16555-16567.

53. Maayan, G.; Ward, M. D.; Kirshenbaum, K. *PNAS*, **2009**, *106*, 13679-13684.

54. Nutting, J. E.; Rafiee, M.; Stahl, S. S. *Chem. Rev.* **2018**, *118*, 4834-4885.

55. Kheirabadi, M.; Celebi-olcum, N.; Parker, M. F. L.; Zhao, Q.; Kiss, G.; Houk, K. N.; Schafmeister, C. E. *J. Am. Chem. Soc.* **2012***, 134,* 18345-18353.

56. Parker, M. F. L.; Osuna, S.; Bollot, G.; Vaddypally, S.; Zdilla, M. J.; Houk, K. N.; Schafmeister, C. E. *J. Am. Chem. Soc.*, **2014**, 136, 3817-3827.

57. Wang, P. S. P.; Nguyen, J. B.; Schepartz, A. *J. Am. Chem. Soc.* **2014**, 136, 6810-6813.

58. Akagawa, K.; Sen, J.; Kudo, K. *Angew. Chem. Int. Ed.* **2013**, *52*, 11585-11588.

59. Chandramouli, N.; Ferrand, Y.; Lautrette, G.; Kauffmann, B.; Mackereth, C. D.; Laguerre, M.; Dubreuil, D.; Huc, I. *Nature Chemistry*, **2015**, *7*, 334-341.

60. Xia, Y.; Qiu, D.; Wang, J. *Chem. Rev.* **2017**, *117*, 13810-13889.

61. Sambasivan, R.; Ball, Z. T. *J. Am. Chem. Soc.* **2010**, *132*, 9289-9291.

62. Tan, K. L. *ACS Catal.*, **2011**, 1, 877-886.

63. Huang, Z- Z.; Leman, L. J.; Ghadiri, M. R. *Angew. Chem. Int. Ed.* **2008**, *47*, 1758-1761.

64. a) Mortenson, D. E.; Steinkruger, J. D.; Krietler, D. F.; Perroni, D. V.; Sorenson, G. P.; Huang, L.; Mittal, R.; Yun, H. G.; Travis, B. R.; Mahanthappa, M. K.; Forest, K. T.; Gellman, S. H. *PNAS*, **2015**, *112*, 13144-13149. b) Wang, P S. P.; Schepartz, A. *Chem. Commun.,* **2016**, 52, 7420-7432. c) Collie, G. W.; Pulka-Ziach, K.; Lombardo, C. M.; Fremaux, J.; Rosu, F.; Decossas, M.; Mauran, L.; Lambert, O.; Gabelica, V.; Mackereth, C. D.; Guichard, G. *Nature Chem.*, **2015**, 7, 871-880.

65. Aroyan, C. E.; Dermenci, A.; Miller, S. J. *J. Org. Chem.* **2010**, *75*, 5784-5796.

66. a) Handoko, Satishkumar, S.; Panigrahi, N. R.; Arora, P. S. *J. Am. Chem. Soc.*, **2019**, *141*, 15977-15985. b) Wu, H.; Handoko, R. Monika, Arora, P. S. *Org. Lett.* **2017**, *19*, 5122-5125.

67. a) Yoon, T. P.; Ischay, M. A.; Du, J. *Nature Chem.* **2010**, *2*, 527-530. b) Prier, C. K.; Rankic, D. A.; MacMillan, D. W. C. *Chem. Rev.*, **2013**, *113*, 5322-5363. c) Narayanam, J. M. R.; Stephenson, C. R. J. *Chem. Soc. Rev.* **2011**, *40*, 102-113. d) Blum, T. R.; Miller, Z. D.; Bates, D. M.; Guzei, I. A.; Yoon, T. P. *Science*, **2016**, *354*, 1391-1395. e) Holzl-Hobmeier, A.; Bauer, A.; Vieira Silva, A.; Huber, S. M.; Bannwarth, C.; Bach, T. *Nature*, **2018**, *564*, 240-243.

68. a) Dexter, D. L. *J. Chem. Phys.* **1953**, *21*, 836-850. b) Strieth-Kalthoff, F.; James, M. J.; Teders, M.; Pitzer, L.; Glorius, F. *Chem. Soc. Rev.* **2018***, 47*, 7190-7202. c) Arias-Rotondo, D. M.; McCusker, J. K. *Chem. Soc. Rev.* **2016**, *45*, 5803-5820. d) Romero, N. A.; Nicewicz, D. A. *Chem. Rev.* **2016**, *116*, 100075-10166.

69. Prince, R. B.; Barnes, S. A.; Moore, J. S. *J. Am. Chem. Soc.*, **2000**, *122*, 2758-2762.

70. Gopalakrishnnan, R.; Frolov, A. I.; Knerr, L.; Drury III, W. J.; Valeur, E. *J. Med. Chem.* **2016**, *59*, 9599-9621.

71. Taylor, A. I.; Pinheiro, V. B.; Smola, M. J.; Morgunov, A. S.; Peak-Chew, S.; Cozens, C.; Weeks, K. M.; Herdewijn, P.; Holliger, P. *Nature*, **2015**, 518, 427−430.

Chapter 2

Exploration of Diverse Reactive Diad Geometries for Bifunctional Catalysis via Foldamer Backbone Variation
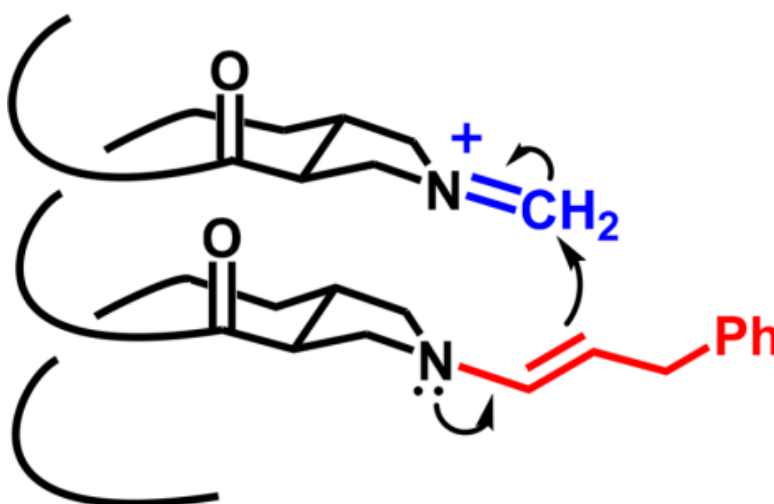
Portions of this chapter are published in:

2.1 Abstract

What is the best spatial arrangement of a pair of reactive groups for bifunctional catalysis of a chemical transformation? The conformational versatility of proteins allows reactive group geometry to be explored and optimized via evolutionary selection, but it has been difficult for chemists to identify synthetic scaffolds that allow broad comparative evaluation among alternative reactive group geometries. Here we show that a family of helices, adopted predictably by oligomers composed partially or exclusively of β-amino acid residues, enables us to explore a range of orientations for a pair of pyrrolidine units that must work in tandem to catalyze a crossed aldol reaction. Thus, the crossed aldol reaction serves as an assay of reactive diad efficacy. We have chosen a test reaction free of stereochemical complexity in order to streamline our study of reactivity. The best geometry enhances the initial rate of product formation by two orders of magnitude. Our findings raise the possibility that rudimentary catalysts involving an isolated secondary structure might have facilitated the development of prebiotic reaction networks.

2.2 Introduction

Life depends upon poly-α-amino acid catalysts (enzymes) that promote a wide array of reactions, frequently with extraordinary rate accelerations relative to the uncatalyzed processes.[1] Despite extensive study, however, the origins of the large catalytic rate enhancements that are commonly encountered remain unclear, in terms of both specific mechanisms and the evolutionary path from prebiotic catalysts to the efficient enzymes that abound in biology.[2,3] Considerable enzyme-inspired research has been directed toward simpler systems that display properties thought to be important for enzymatic catalysis. This approach has been motivated by the prospect that decreasing catalyst complexity should facilitate mechanistic analysis[4–6] and by the desire for new and efficient methods to synthesize organic molecules.[7–10] Proper spatial

organization of two or more reactive groups appears to be a critical feature of many enzyme mechanisms,[2,3] and bifunctional or multifunctional catalysis has been explored in smaller synthetic systems.[4–12] Here we introduce a new strategy for evaluating diverse orientations of a pair of reactive groups, with the goal of identifying arrangements that enable coordinated catalytic action. Our approach makes use of "foldamers", protein-inspired oligomers that feature unnatural backbones and display discrete conformational preferences.[13–15] We employ foldamers that contain β-amino acid residues and that adopt distinct helical secondary structures. These helices are used to position pairs of pyrrolidine units in different three-dimensional arrangements that are assessed for bifunctional catalysis of a crossed aldol reaction. The goal of this work is not to develop a new method for conducting crossed aldol reactions, but rather to use the crossed aldol reaction to compare alternative reactive diad geometries and identify an optimum in terms of bifunctional catalysis.

2.3 Results

Our experiments build on careful kinetic studies by Erkkilä and Pihko that established that pyrrolidine plays a dual role in catalyzing crossed aldol condensations involving formaldehyde as the electrophile.[16] The nucleophilic aldehyde is activated via enamine formation, and formaldehyde is activated via iminium formation (**Figure 1**).
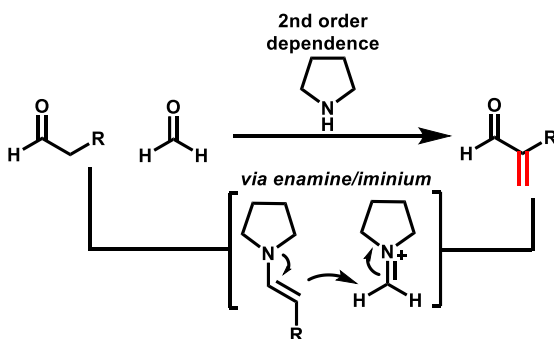
Figure 1. Second order dependence on pyrrolidine in crossed aldol reactions studied by Erkkilä and Pihko.[16]

This finding encouraged us to look to foldamers containing pairs of pyrrolidine-derived β-amino acid residues as a basis for probing the relationship between spatial organization of a reactive diad and catalysis of the crossed aldol condensation. We focused on hydrocinnamaldehyde as the nucleophile. Cyclically constrained β-amino acid residues enable tuning of foldamer secondary structure preference and stability via control of ring size and stereochemistry.[17–20] *trans*-2-Aminocyclopentanecarboxylic acid (ACPC) residues (**Figure 2**), for example, support formation of a β-peptide helix characterized by C=O(i)···H-N(i+3) H-bonds.[21]
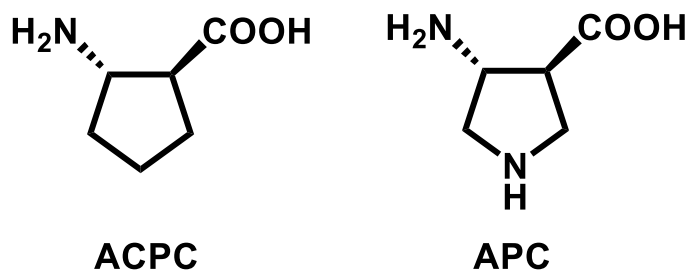
Figure 2. Cyclic β-amino acid ACPC and pyrrolidine derivative APC.

Combining (S,S)-ACPC residues with L-α-amino acid residues in varying proportions and patterns engenders a family of related helical secondary structures that feature C=O(i)···H-N(i+3) or C=O(i)···HN(i+4) H-bonds.[22–24] The pyrrolidine-based APC (**Figure 2**) residue displays conformational propensities indistinguishable from those of ACPC, as established by NMR analysis of diverse foldamers and numerous α/β-peptide crystal structures in the Protein Data Bank.[25] **Figure 3** shows three examples from the substantial set of ACPC-containing foldamer crystal structures in the Cambridge Structure Database. These examples illustrate helical secondary structures containing C=O(i)···H-N(i+3) H-bonds formed by three backbones, one containing exclusively β residues (**Figure 3A**),[21] a second with a 1:1 α:β repeat (**Figure 3B**),[23] and a third with a 1:2 α:β repeat (**Figure 3C**).[24] Collectively, these three helical secondary

structures should provide access to diverse arrangements of a pyrrolidine diad, because ACPC →

APC replacements are not expected to cause conformational changes.[25,26]

	(i,i+1)	(i,i+2)	(i,i+3)	(i,i+4)	(i,i+6)
β-peptide	8.2 Å, 142°	7.6 Å, 99°	6.6 Å, 33°	11.9 Å, 163°	—
1:1 αβ-peptide	—	8.1 Å, 134°	—	11.3 Å, 106°	13.6 Å*, 6°*
1:2 αβ-peptide	8.3 Å, 146°	9.0 Å, 148°	5.5 Å, 10°	10.8 Å, 141°	10.5 Å, 5°
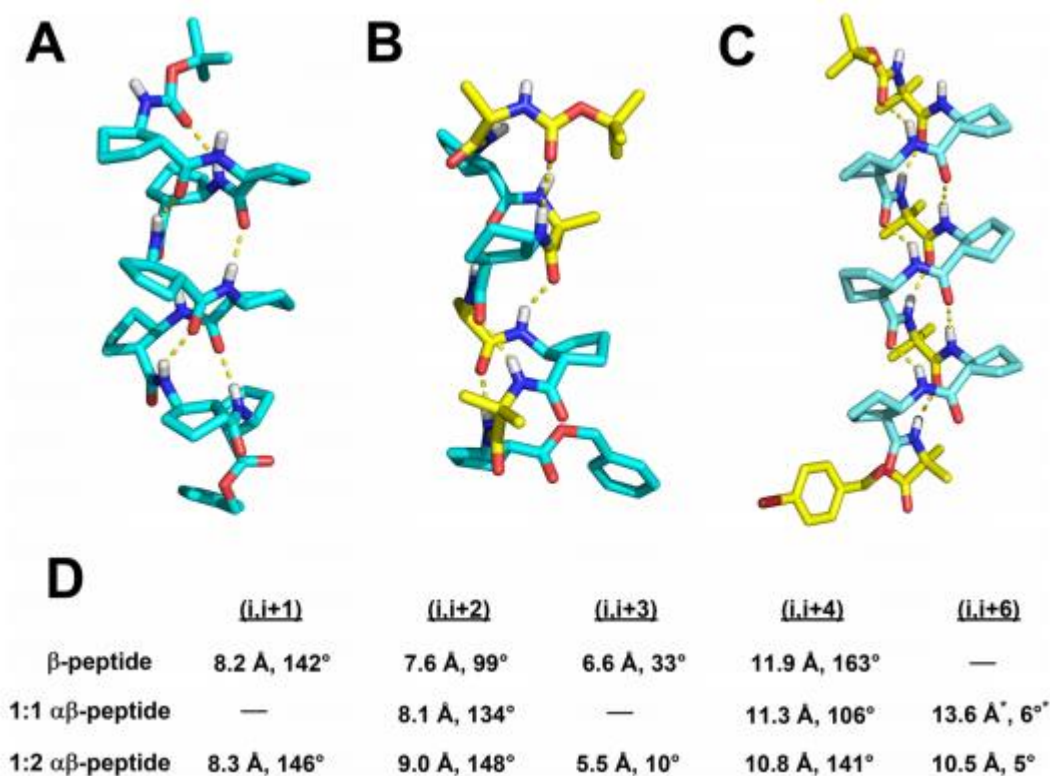
Figure 3. Crystal structures illustrating helical secondary structures adopted by ACPC-containing foldamers with different β residue content: (A) pure β (CSD: WELNOQ), (B) 1:1 α/β (CSD: OGAVAU), (C) 1:2 α/β (CSD: PUCDEX). Yellow and cyan represent carbon atoms in α and β residues, respectively. Blue represents nitrogen atoms, and red represents oxygen atoms. Hydrogen atoms other than those bound to nitrogen are omitted for clarity. Hydrogen bonds are depicted with dashed lines. (D) Three-dimensional relationships expected for the pair of side chain nitrogen atoms in foldamers containing two APC residues with varied sequential separation, based on the crystal structures shown in (A−C). Distances were measured between carbon-4 in the cyclopentane rings of appropriately spaced ACPC residues. For each ACPC residue, we defined a vector based on the positions of carbon-4 and carbon-2 (**Figure 4**). The angle between these two vectors, when the structure is viewed along the helix axis, is given. Values refer to average distance or average angle based on all possible measurements in the given structure; standard deviations can be found in **Figure 75**. Only one possible i, i+6 diad can be measured in 1:1 α/β-peptide (B). See experimental procedures section below for detailed description of distance/angle measurements.
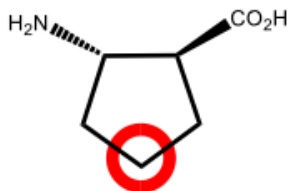
Figure 4. Carbon-4 in the cyclopentane ring of ACPC, highlighted in red, was used to define the average distance and dihedral angle between a pair of ACPC residues.
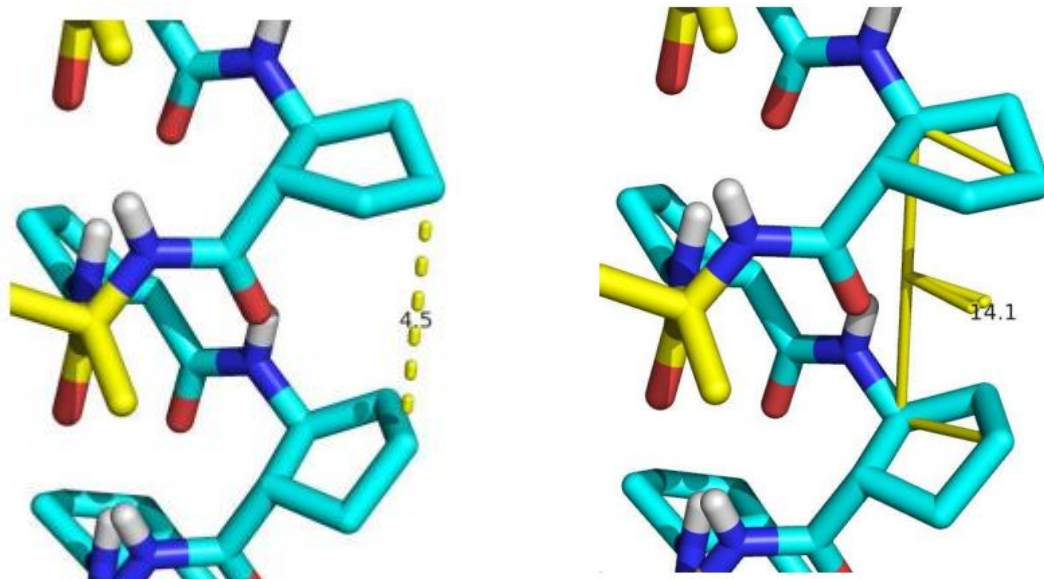
Figure 5 (Left). Close-up of 1:2 α/β-peptide crystal structure shown in **figure 3C**, depicting the distance measured (Å) between one pair of ACPC residues with the (i,i+3) diad arrangement.

Figure 6 (Right). Close-up of 1:2 α/β-peptide crystal structure shown in **figure 3C**, depicting the dihedral angle measured between one pair of ACPC residues with the (i,i+3) diad arrangement.

We constructed a series of APC-containing oligomers based on each of the three foldamer families illustrated in **Figure 3** to explore distinct pyrrolidine diad geometries for catalysis of the selected crossed aldol condensation (**Figure 7**). Each oligomer contains a C-terminal β^3-homotyrosine (β^3-hTyr) residue to facilitate concentration determination via UV absorbance, and the remaining β subunits are derived from ACPC or APC. Catalytic activities for the α-methylenation of hydrocinnamaldehyde were compared by assessing relative initial rates (≤1% reaction completion) under a set of conditions suggested by precedent (**Figure 7**).[16]
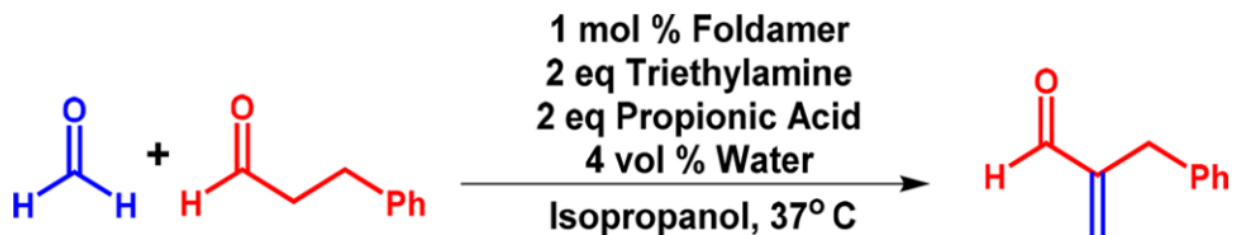
Figure 7. The crossed aldol reaction used in these studies.
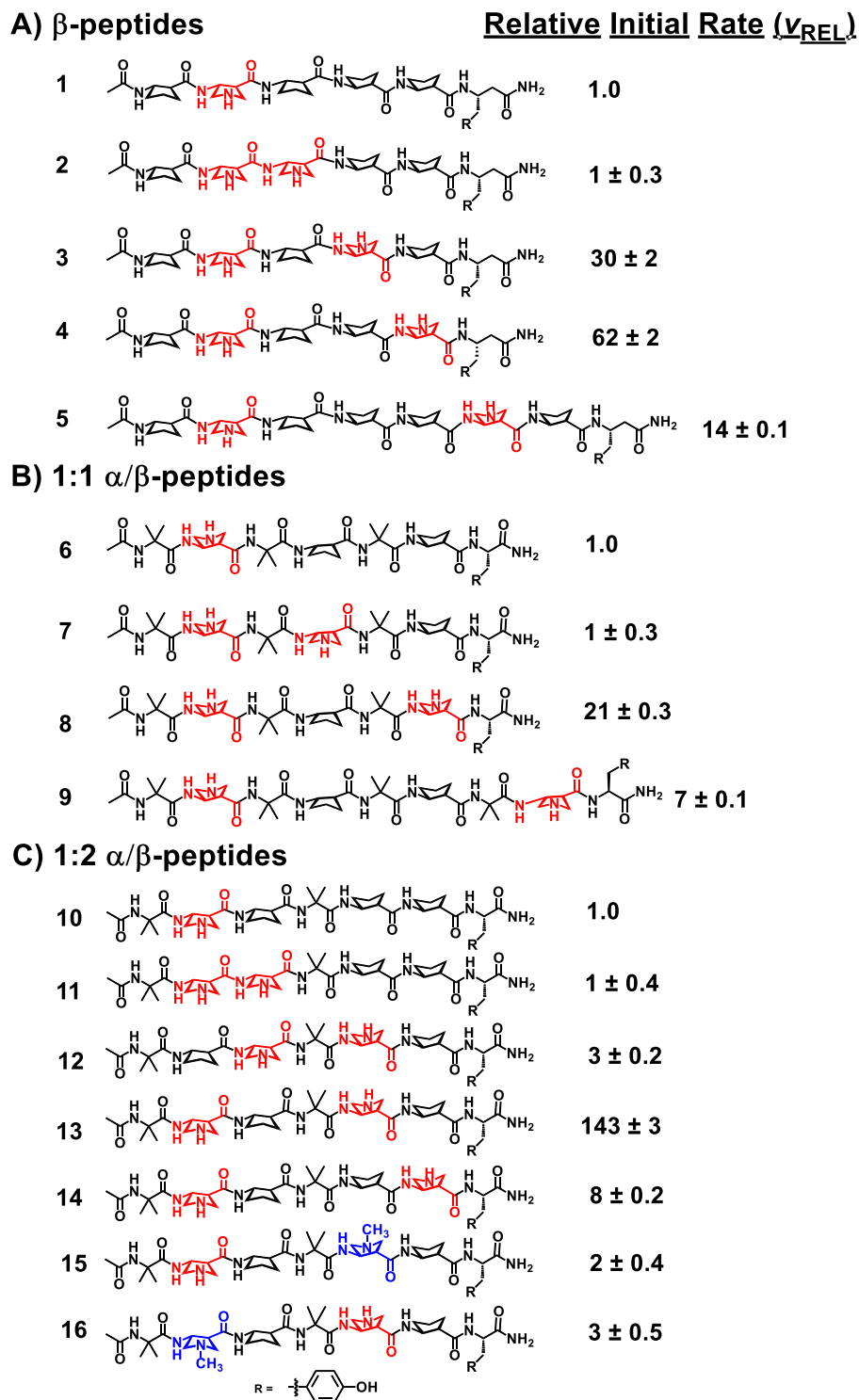
Figure 8. Foldamers used to evaluate different APC diad geometries. (A) β-peptides, (B) 1:1 α/β-peptides, and (C) 1:2 αβ-peptides. vREL represents average initial rate ± standard deviation relative to the initial rate for the mono-APC peptide in each series (i.e., **1**, **6**, or **10**), based on a minimum of three independent measurements for each value. APC residues are highlighted in red, and N-methyl APC residues are highlighted in blue (for control compounds **15** and **16**).

Product formation was monitored by UPLC. The two aldehyde substrates were used in equimolar

quantities. Reactions were conducted in isopropanol at 37 °C, with 4 vol % water and 2 equiv of

triethylamine and propionic acid relative to the aldehyde starting materials. The first set of studies

involved β-peptides **1−5** (**Figure 8A**). β-Peptide **1**, containing a single APC residue, was used as

the reference for this series. Comparison of **1** with pyrrolidine revealed that the secondary amine

within an APC residue is intrinsically less effective for crossed aldol catalysis relative to the

secondary amine within pyrrolidine itself: the initial rate of product formation was 216-fold larger

for pyrrolidine than for **1**. This difference in reactivity may reflect the presence of two electron-

withdrawing substituents on the APC ring.

β-Peptides **2−5** contain two APC residues with varied sequential spacing, which leads to

different three-dimensional orientations of the secondary amines upon formation of the

C=O(i)···H-N(i+3) H-bonded helix.[21] The catalytic efficacies of the different APC diads were

compared in terms of initial reaction rates normalized to the initial rate observed with mono-APC

β-peptide **1**. Specifically, the initial rate of product formation measured for each bis-APC β-

peptide (**2−5**), at 1 mol % β-peptide with reference to each of the aldehyde substrates, was divided

by the initial rate observed with 2 mol % **1** to generate v_{REL}. This approach ensured that the

concentration of APC units was constant across these measurements. The data for β-peptide **2**

show that placing two APC residues adjacent in sequence has no effect on v_{REL}, which suggests

that two pyrrolidine rings juxtaposed in this way cannot work cooperatively to catalyze the

crossed aldol condensation. This conclusion is expected based on the helical conformation

established for these β-peptides,[21] which has ~2.5 residues per turn and should induce a divergent

orientation of the pyrrolidine ring nitrogen atoms of the sequentially adjacent APC residues.

Significant enhancements in initial rates were observed for β-peptides **3** and **4**. The larger effect

(v_{REL} = 62) was measured for β-peptide **4**, which features i, i+3 spacing of the APC residues. This sequence relationship corresponds to a little more than one turn of the expected helix; thus, helical folding of **4** should cause a convergent orientation of the pyrrolidine ring nitrogen atoms. A smaller enhancement was observed for i, i+2 APC spacing (**3**, v_{REL} = 30).

β-Peptides **3** and **4** exclusively contain cyclically constrained ACPC residues in the linker region between the catalytic amines of the primary sequence. The modular nature of the foldamer backbone allows for replacement of these linker residues with relaxed, acyclic $β^3$-residues, while retaining the overall 12-helical secondary structure. In order to systematically probe the effect of relaxed linker residues on reactivity for peptides **3** and **4**, we synthesized the series of peptides shown in **Figure 9** that increasingly introduce flexibility. Our results suggest that alterations in the linker region between the catalytic amines have only modest effects on initial rate (**Figure 9**). It is possible that comparable linker residue changes would have much larger effects on other reactions, or on enantioselectivity in reactions that produce a stereogenic center. Energetic differences between diastereomeric transition states ($\Delta\Delta G^{\ddagger}$) that lead to alternative enantiomers need be only a few kcal/mol at room temperature to provide substantial enantioselectivity.

For i, i+4 APC spacing, significantly greater than one helical turn, the enhancement was more modest (**5**, v_{REL} = 14). Collectively, the initial rate data for this series support our premise that a well-established foldamer secondary structure represents a scaffold that can be used to compare the catalytic propensities of distinct reactive group diad geometries.

β-peptides: Effect of Relaxing Linker Residues: (i, i+2, and i, i+3) diads
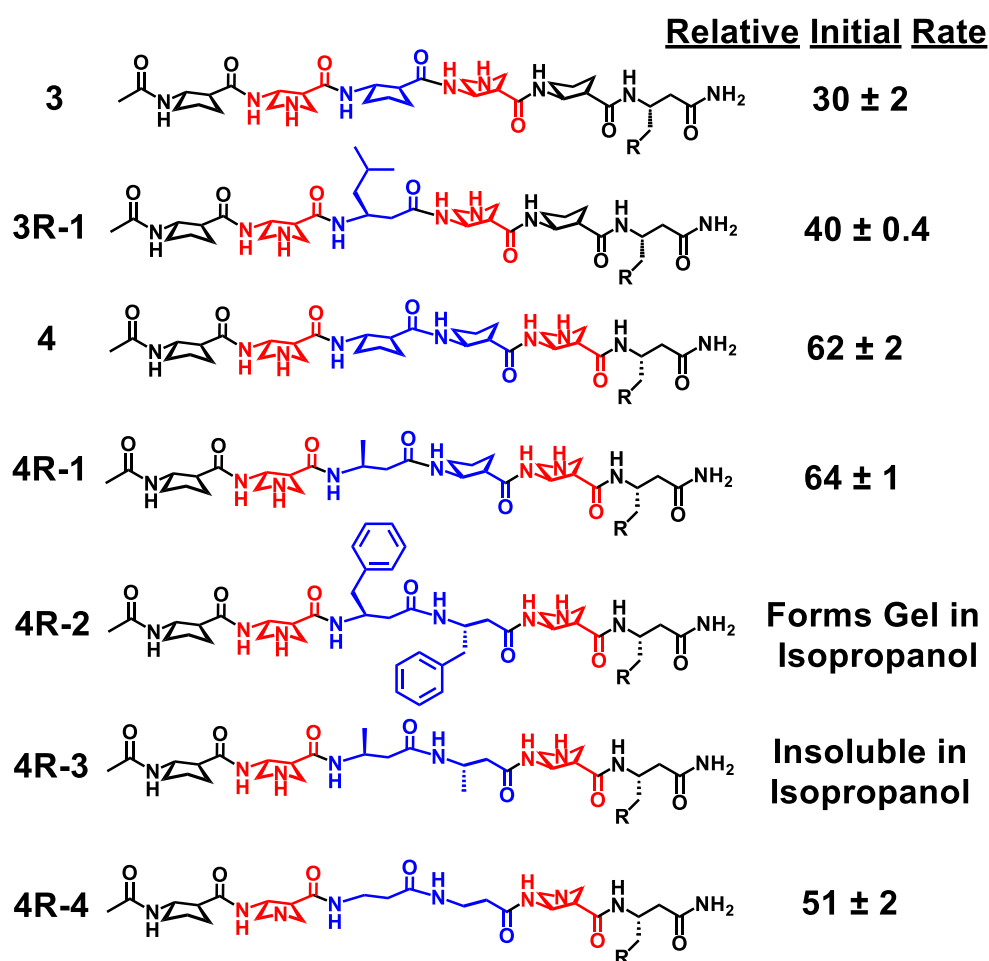
Figure 9. β-Peptides containing either i,i+2, or i, i+3 APC diad. The APC residues are highlighted in red. Highlighted in blue is the "relaxed" linker residues. For example, the β³-homoleucine residue in **3R-1** is expected to be more conformationally flexible than is the ACPC residue at the corresponding position in **3**. v_{REL} corresponds to the slope of the plot of product concentration (μM) vs. time (minutes) from 0.5 to 70.5 minutes for peptides **3-4R-4**, divided by the slope of the analogous plot for mono-APC catalyst **1**. Each v_{REL} is an average of three measurements ± standard deviation.

Series **6−9** (**Figure X8B**) features 1:1 α:β residue alternation. Crystallographic studies of this α/β-peptide family, including the example shown in **Figure 8B**, indicate that oligomers in the length range of **6−8** favor a helix containing C=O(i)···H-N(i +3) H-bonds and ~3 residues per turn.[23] (Longer 1:1 α/βpeptides, such as **9**, can also access a different helix containing C=O(i)···H-N(i+4) H-bonds and ~4.5 residues per turn.[23]) Mono-APC α/β-peptide **6** was used as

a reference for assessing cooperative catalysis by bis-APC analogues **7−9** (**Figure 8**). No initial rate enhancement was detected when APC residues were placed as close together as possible in terms of sequence (i, i+2; **7**). A modest enhancement was observed for i, i+4 APC spacing (**8**; $\nu_{REL} = 21$), which corresponds to a little more than one turn of the expected helix. Further sequential separation of the APC residues (i, i+6) caused a diminution in initial rate enhancement (**9**; $\nu_{REL} = 7$) (**Figure X**). The general pattern of an increase in ν_{REL} followed by a decrease as the APC residues are moved farther apart in sequence, with a maximum catalytic effect for spacing near one helical turn, is common to this 1:1 α/β-peptide series and the β-peptide series **2−5**. However, the maximum ν_{REL} is higher for the β-peptide series, which suggests that the helix formed by the pure β backbone can achieve a more favorable geometry for the secondary amine diad than is accessible with the 1:1 α:β backbone. One intriguing feature of the 1:1 α/β-peptide for future catalysis efforts is the opportunity to incorporate both α- and β-based catalytic residues into the primary sequence. An obvious advantage of α-derived catalytic residues is the broad side chain diversity and lower cost relative to β-derived residues. Furthermore, if a diad composed of different catalytic residues were achieved, one could imagine different activity due to side chain placement if the diad positions were swapped (**Figure 10**).

Two theoretical diads for a 1:1 α/β-peptide

Diad 1

Diad 2
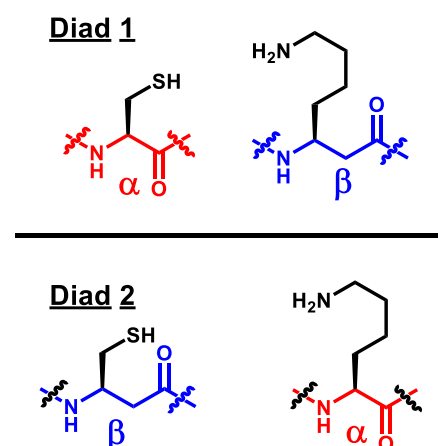
Figure 10. Two theoretical compositions of a cysteine-lysine diad within a 1:1 β-peptide. Each component of the diad could be incorporated into an α- or β-residue, introducing another level of diversification. For a given reaction, diad 1 may show reactivity different from that of diad 2 due to different geometric arrangements in the secondary structure.

α/β-Peptides **10−14** (**Figure 8C**) have a 1:2 α:β backbone repeat, and available crystal structures indicate that these foldamers favor a helix containing C=O(i)···H-N(i+3) H-bonds and ~3 residues per turn.[22,24] In this conformation, i, i +3 spacing should place APC residues almost exactly one

turn apart. Initial rate data for the 1:2 α/β-peptide series suggest that this secondary amine diad arrangement is particularly favorable for promoting the crossed aldol condensation, as **13** displayed an initial rate enhancement relative to mono-APC α/ β-peptide **10** (v_{REL} = 143) that was larger than any seen in the previous two peptide series. In contrast, placing the two APC residues adjacent in sequence, as in **11**, offered no rate enhancement, behavior that matches observations with the other two foldamer backbones. An APC pair with i, i+2 spacing was also catalytically ineffective (**12**). Lengthening the separation between APC residues beyond one helical turn, to i, i+4 (**14**), resulted in very limited reactivity (v_{REL} = 8).

To probe the importance of the helical secondary structure, we synthesized **13R-5**, where the achiral Aib-residues of **13** were replaced with chiral (L)-alanine residues, while retaining the i, i+3 APC diad. These changes preserve the helical secondary structure, which was confirmed via initial rate measurements (v_{REL} = 174) (**Figure 11**). Next, we synthesized **13R-5(D-Ala)**, where the (L)-alanine residues of **13R-5** were replaced with (D)-alanine residues. Incorporation of (D)-alanine residues should diminish alignment of the APC residues through destabilization of the helical secondary structure. When we measured the initial rate of crossed aldol reaction in the presence of **13R-5(D-Ala)**, we observed a decrease in reactivity (v_{REL} = 88) relative to the (L)-alanine containing diastereomer, **13R-5** (**Figure 11**). These results suggest that destabilizing the helical secondary structure in a catalyst that aligns the bis-APC diad on a common helical face, one turn apart, is detrimental to catalysis.

Peptide **13**, provides a geometry that is quite favorable for catalysis of the crossed aldol reaction. In order to better understand the exact features required for effective catalysis, we evaluated **17**, which displays a bis-APC diad from a common helical face, but the pyrrolidine rings are two turns apart.
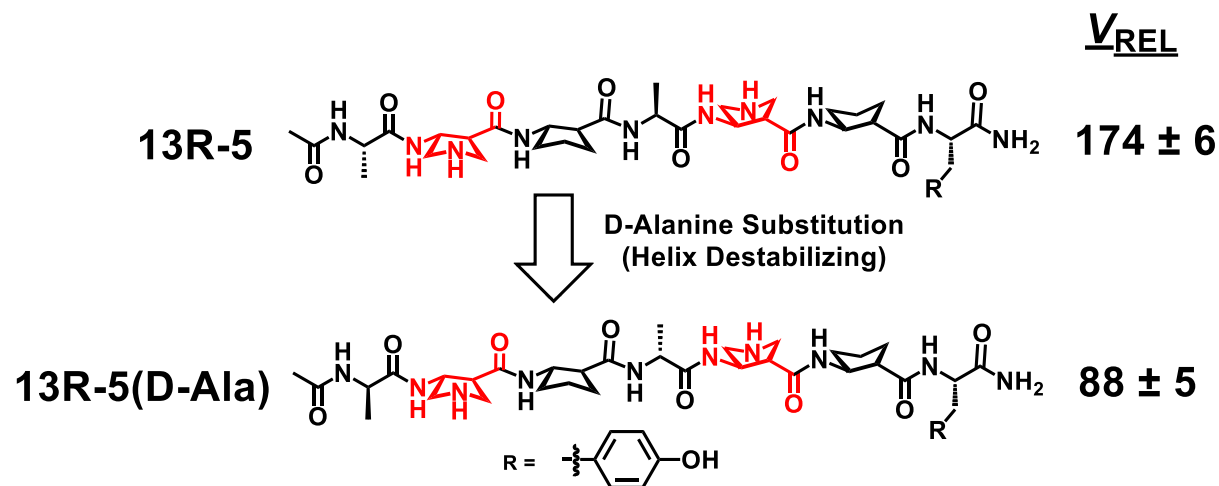
Figure 11. Structures of 1:2 α/β-peptides containing an i,i+3 APC diad. APC residues are highlighted in red. Highlighted in blue is the α residue in the linker between the two APC residues of **13R-5(D-Ala)** that was changed from L-Ala in (**13R-5**) to D-Ala. This change is expected to disrupt the helical secondary structure. The L-Ala in **13R-5** should result in a helical secondary structure that positions the two APC residues a single helical turn apart. Disruption of this helical secondary structure, via D-Ala incorporation should diminish alignment of the APC residues which presumably explains why the D-Ala containing diastereomer is less effective catalyst of the cross aldol reaction relative to the L-Ala-containing diastereomer.

Catalyst **17** resulted in substantially decreased reactivity (v_{REL} = 4) compared to **13**, highlighting the importance of having the amine diad not only presented from a common helical face, but also a single helical turn apart for this aldol reaction. Perhaps if the iminium ion were extended (**Figure 12**), a diad spanning two helical turns would be effective.

Figure 12. Hypothetical iminium ion that may benefit from a bis-amine diad two helical turns apart.

We evaluated the effect of replacing the (L)-alanine residues of **17** with (D)-alanine residues. In the i, i+3 arrangement (ideal diad arrangement for crossed aldol formation) as in **13R-5**, incorporation of D-alanine residues leads to helical destabilization and a decrease

in relative rate (**13R-5** vs. **13R-5(D-Ala)**). In contrast, **17** adopts a helical conformation that arranges the diad in n i, i+6 arrangement, roughly 10.5 Å apart, which is apparently ineffective for catalysis. We would expect that destabilization of this helical secondary structure could favor non-helical conformations that may allow some sort of cooperative catalysis, since a helix containing a i, i+6 diad is ineffective for this crossed aldol reaction. Interestingly, **17(D-Ala)** and **17(D-Ala)(D-Ala)** resulted in increased relative rates compared to **17** (**Figure 13**), suggesting that destabilizing a helix that arranges the diad in a non-effective geometry can result in non-helical conformations of the diad that enables the two groups to cooperate to some extent.
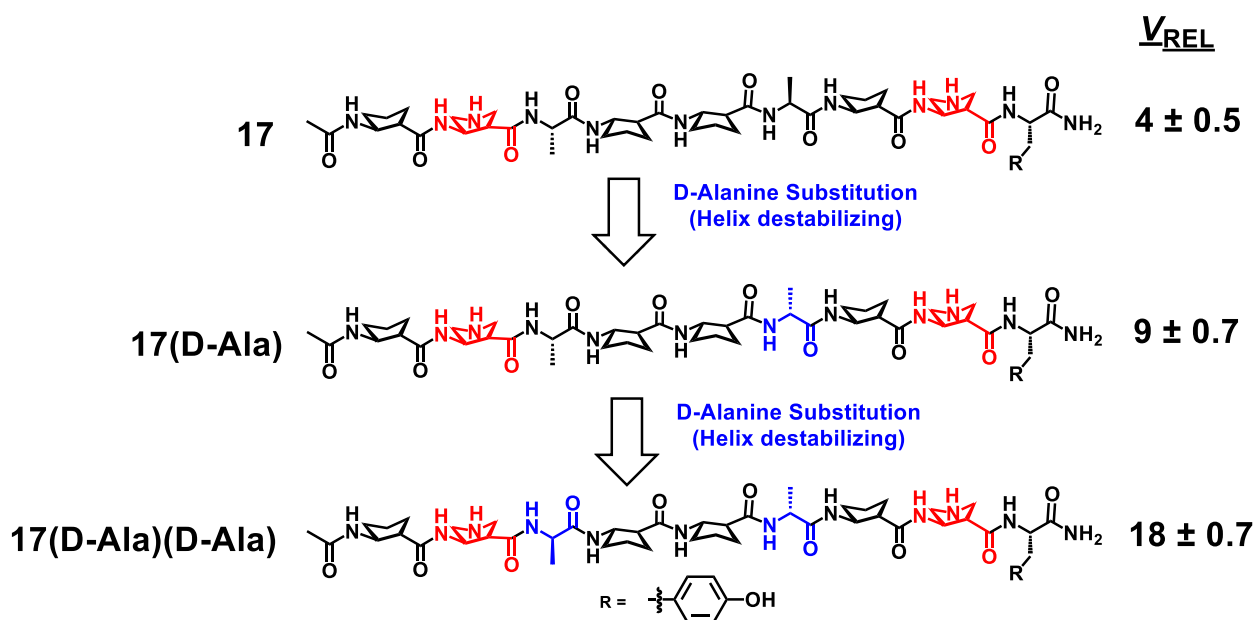
Figure 13. Structures of 1:2 α/β-peptides containing an i,i+6 APC diad. APC residues are highlighted in red. Highlighted in blue is the α-residues between the two APC residues of **17(D-Ala)** and **17(D-Ala)(D-Ala)** that were changed from L-Ala in (**17**) to D-Ala. This change is expected to disrupt helical secondary structure. In the i,i+3 H-bonded helical conformation expected for **17**, the two APC residues would be positioned on the same side of the helix separated by two helical turns, i.e., roughly 10.5 Å apart. This distance would presumably be too large to support bifunctional catalysis of the crossed aldol reaction. We hypothesize that the very small rate enhancement observed for **17** arises from a minor non-helical conformation where the two APC residues are closer together relative to the expected helix. Replacing L-Ala residues with D-Ala should destabilize the helical conformation that holds the two APC residues too far apart for effective crossed aldol catalysis. We interpret the small increases in vREL that emerge upon changing L-Ala to D-Ala in the linker to result from increased population of nonhelical conformers featuring APC-APC arrangements that support catalysis.

In order to isolate the variable responsible for the differences in catalysis observed between catalyst **13** and **17**, we conducted CD measurements in isopropanol, at the concentration of catalyst used for the initial rate measurements (0.12 mM). The CD spectra for **13** and **17** share a common signature, indicative of a common helical secondary structure. These results indicate that for effective catalysis of the crossed aldol reaction, an amine diad must not only be projected from a common helical face, but also a single helical turn apart.

We conducted further studies with α/β-peptide **13** because this foldamer appears to provide a particularly favorable secondary amine diad geometry for bifunctional catalysis of the crossed aldol condensation. To ask whether catalytic efficacy was specific to hydrocinnamaldehyde, we examined the crossed aldol reaction between hexanal and formaldehyde. Based on comparison with the mono-APC α/β-peptide **10**, α/β-peptide **13** displayed a relative initial rate of 154 ± 8, which is very similar to the value measured for hydrocinnamaldehyde (**Figure 14**).
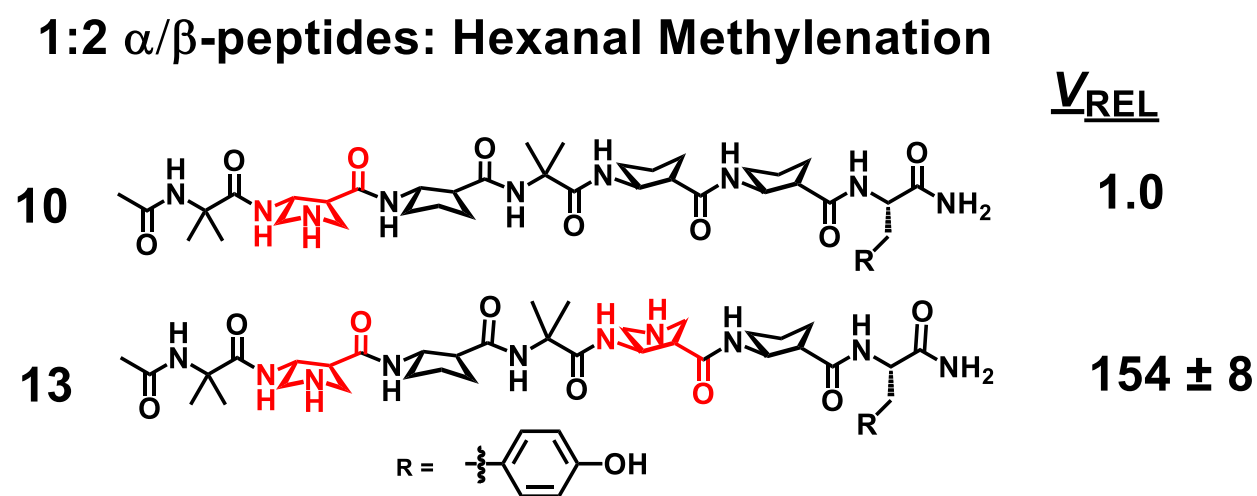
1:2 α/β-peptides: Hexanal Methylenation

	V_{REL}
10	1.0
13	154 ± 8

Figure 14. 1:2 α/β-Peptide catalysts **10**, and **13**. For the bis-APC peptide **13**, initial rate (v_{REL}) values relative to mono-APC catalyst **10** are shown.

Thus, catalytic efficacy of **13** does not seem to depend on the identity of the nucleophilic aldehyde.

Our studies were not motivated by preparative considerations, but we nevertheless established that **13** is competent to drive the crossed aldol reaction to completion. After 22 h, a 98% yield of the α-methylenation product was obtained in the presence of 5 mol % **13** (**Figure 15**). In contrast, only a 6% yield was obtained after the same period in the presence of 10 mol % mono-APC α/β-peptide **10**. Yields for other α/β-peptides were also determined (**Figure 15**).

Peptide	Mol %	Time (hour)	% Yield
10	10	22	5.6
11	5	22	0.44
13	5	22	98.2
13	10	17	100
14	5	22	19.5
17	5	22	19
13R-4	5	22	86.8
13R-5	1	22	14.6
13R-5	3	22	83.3
13R-5	5	22	96
13R-5	10	7	100

Figure 15. Yields measured for various catalysts using the calibration curve shown in the experimental section of this chapter. Although the main goal of our study was to understand the relationship between three-dimensional molecular structure and reactivity, we wanted to determine whether our most effective catalysts were competent to drive the crossed aldol reaction to completion.

Altering the dipeptide linking segment between the i, i+3- spaced APC residues caused modest but significant changes in the initial rate of product formation. Replacing the intervening ACPC residue of **13** with (S)-β^3-hLeu (**13R-1**, **Figure 16**) caused a decline in relative initial rate ($\nu_{REL} = 73$).
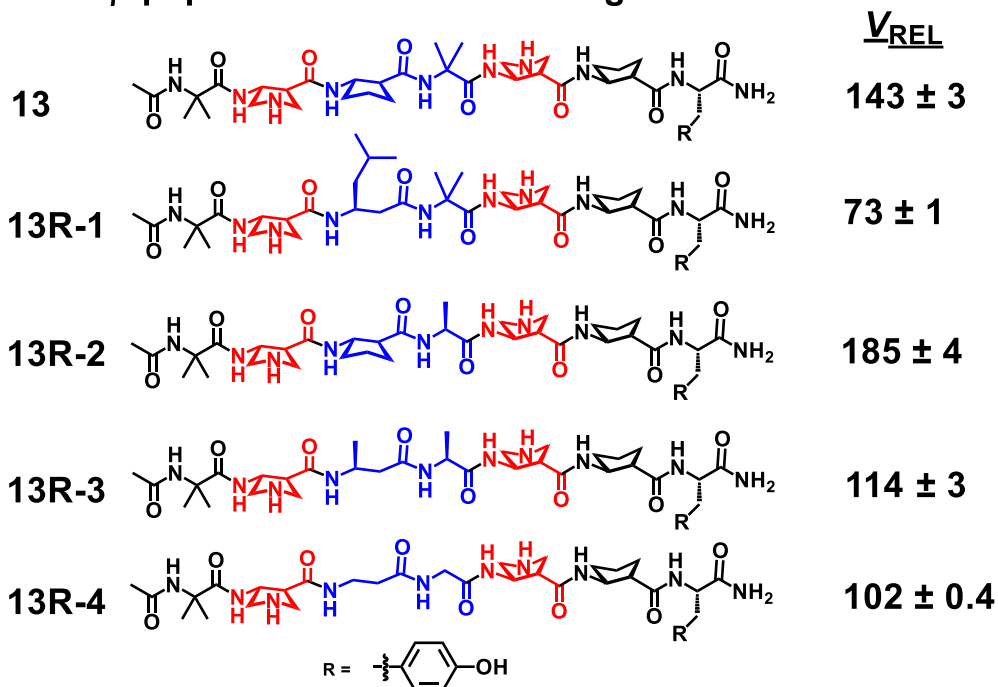
Figure 16. 1:2 α/β-Peptides containing a i,i+3 APC diad. The APC residues are highlighted in red. Highlighted in blue are "relaxed" linker residues between the APC residues in **13R-1**, **13R-2**, **13R-3**, and **13R-4**. All of the residues in blue are expected to be more conformationally flexible than ACPC or Aib. The vREL values reported above are derived from the slope of the graph product concentration (μM) vs. time (minutes) to 1% reaction completion. Each vREL is an average of three measurements ± standard deviation.

This β residue replacement would be expected to decrease helical propensity, based on comparison of cyclic and β^3 residues in other α/βpeptide backbones.[25,27] In contrast, an increase in initial rate ($\nu_{REL} = 185$) was observed upon replacement of the intervening Aib residue with L-Ala (**13R-2**), a change that should enhance conformational freedom. The α/β-peptide containing both changes showed intermediate reactivity (**13R-3**) ($\nu_{REL} = 114$).

Removal of all side chains, that is, replacement of ACPC-Aib with β-hGly-Gly (**13R-4**), resulted

in intermediate reactivity as well (v_{REL} = 102). The variation in crossed aldol reactivity observed

among **13** and the analogues with "relaxed" linkers spans <3-fold difference in v_{REL}, but these

findings suggest that modulating the conformational mobility of the segment between the reactive

sites offers a path to improving the efficiency of bifunctional foldamer catalysis.

The crossed aldol condensation is first order in catalyst: varying the concentration of α/β-

peptide **13** between 1 mol % and 10 mol % caused a linear change in the initial rate of product

formation (**Figure 17**).
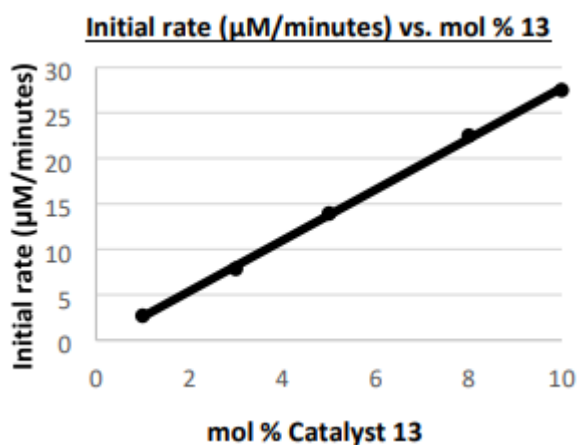
Figure 17. Initial rate (μM/minutes) vs. mol % **13** for the reaction shown in **Figure X**. The linear relationship observed is consistent with the hypothesis that the catalytic reaction is first order in catalyst **13**, i.e., that only one molecule of **13** is involved in the rate determining transition state.

Reactions run with 1 mol % **13** relative to formaldehyde and varying amounts of

hydrocinnamaldehyde revealed that the initial rate of product formation increased as

hydrocinnamaldehyde was increased from 1 mol % to 100 mol % (relative to formaldehyde);

however, further increases in the amount of hydrocinnamaldehyde had little effect on initial rate

(**Figures 18**). Reactions run with 1 mol % **13** relative to hydrocinnamaldehyde and varying

amounts of formaldehyde, between 50 mol % and 1000 mol %, showed that rising formaldehyde

concentration exerts a mild inhibitory effect on the initial rate of product formation (**Figure 19**).

This inhibition may indicate that formaldehyde reacts more avidly than does

hydrocinnamaldehyde with the APC side-chain nitrogen atoms.
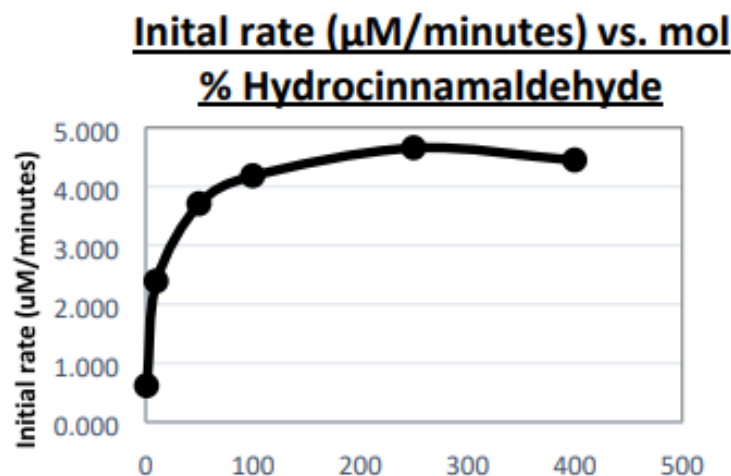
Figure 18. Initial rate (µM/min) vs. mol % hydrocinnamaldehyde relative to formaldehyde. The graph shows an increase in initial rate with increasing hydrocinnamaldehyde to 100 mol % (1:1 hydrocinnamaldehyde:formaldehyde), followed by a plateau in rate. The data points are shown to the right. Catalyst **13** was used for each reaction.

Mol% Formaldehyde	Rate (µM/minutes)
50	5.067
100	4.1784
300	3.4441
600	2.889
1000	2.217
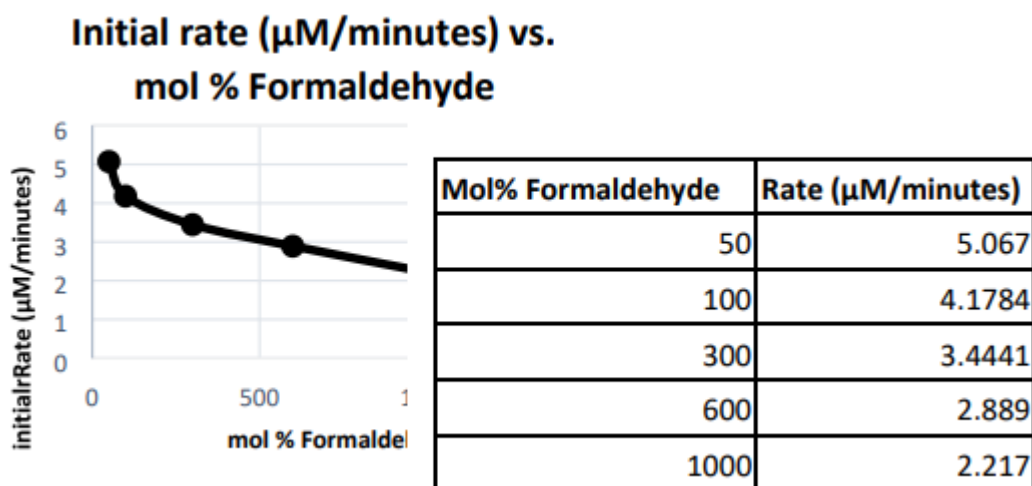
Figure 19. Initial rate (µM/minutes) vs. mol % formaldehyde. The data reveal an inhibitory effect on initial rate of high formaldehyde concentrations. Catalyst **13** was used for each reaction.

Monitoring of reaction progress by UPLC (equimolar aldehydes, 1 or 10 mol % **13**) revealed that

the α/β-peptide peak disappears upon mixing with the starting materials and reappears only after

product formation is complete (**Figure 20**; reaction conducted with 10 mol % 13).
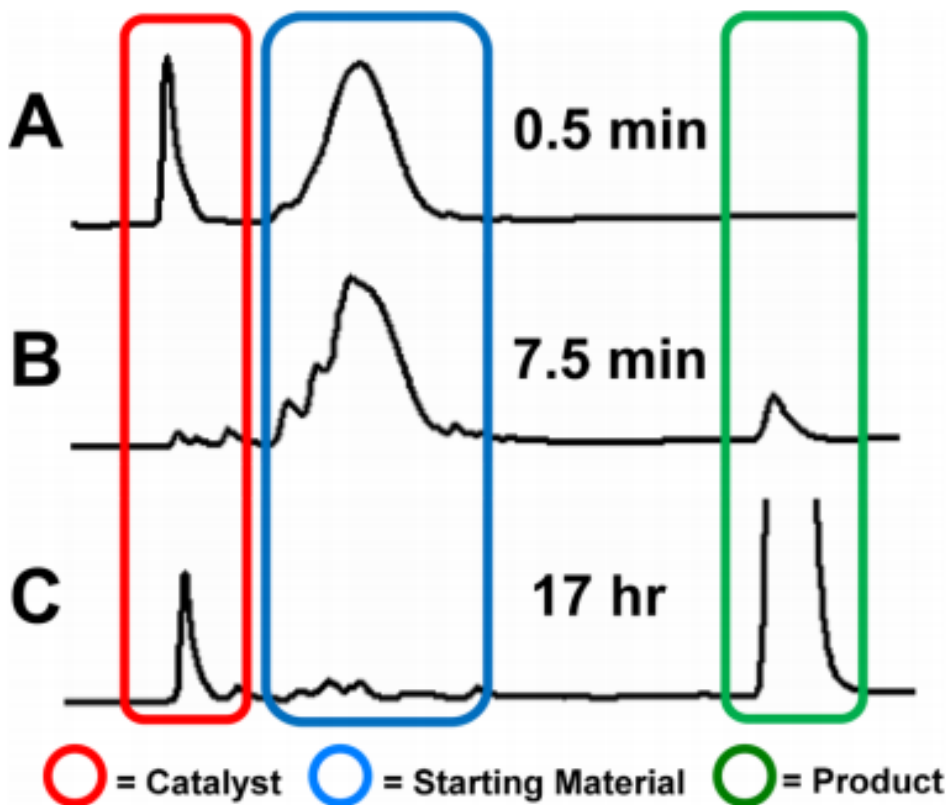
Figure 20. UPLC data (220 nm) depicting reaction progress. Red, blue, and green boxes highlight the regions containing peaks for catalyst **13**, hydrocinnamaldehyde + peptide intermediates, and the crossed aldol product, respectively. Reaction mixture (A) at 0.5 min after mixing, (B) at 7.5 min, and (C) at 17 h, after the starting materials have been fully consumed. Catalyst **13** rapidly disappears after exposure to the reaction conditions (A → B), and the peak for the catalyst reappears upon reaction completion (C).

In contrast, α/βpeptide **13** is fully detectable by UPLC when mixed with 100 equiv of either

formaldehyde or hydrocinnamaldehyde (**Figures 21** and **22**). These observations support the

hypothesis that catalysis requires the coordinated action of two secondary amine units, and they

raise the possibility that the catalytic mechanism proceeds via a relatively stable intermediate that

is formed only in the presence of both aldehyde substrates. This hypothetical intermediate might

contain a transient cross-link between the APC residues, a possibility that is supported by the

observations discussed below.
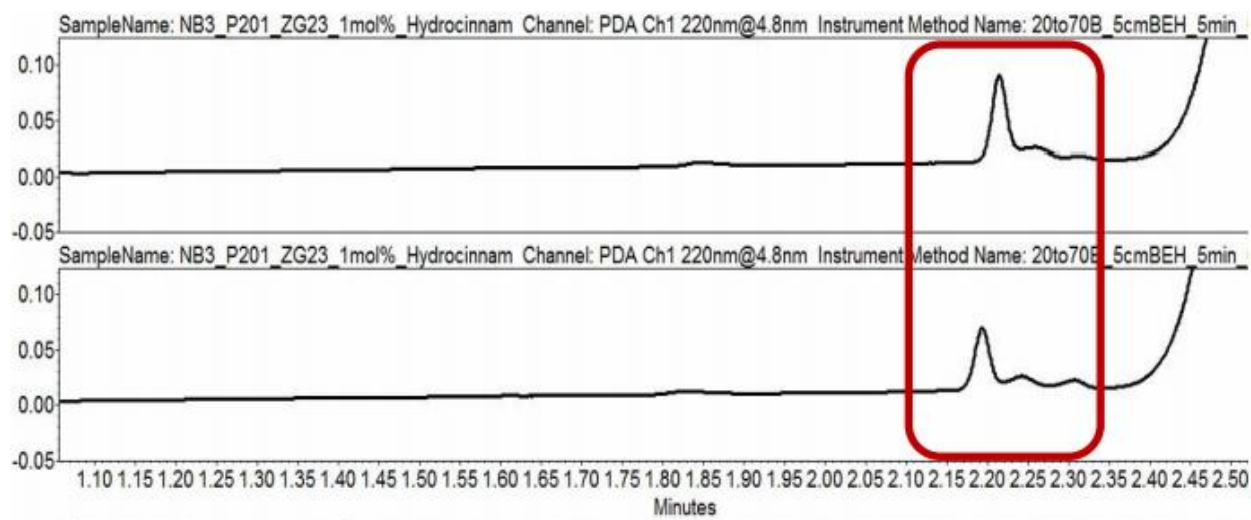
Figure 21. UPLC traces for catalyst **13** in the presence of 100 equivalents of hydrocinnamaldehyde (no formaldehyde). The upper trace was obtained 0.5 minutes after mixing, and the lower trace was obtained 60 minutes after mixing. The peptide peak is not affected by the excess of hydrocinnamaldehyde during this time. To the right of the peptide peak is the beginning of the hydrocinnamaldehyde peak. We cannot exclude the possibility that the peptide is reacting to generate enamine/iminium species which are hydrolyzed once an aliquot of the reaction mixture is injected onto the UPLC column.
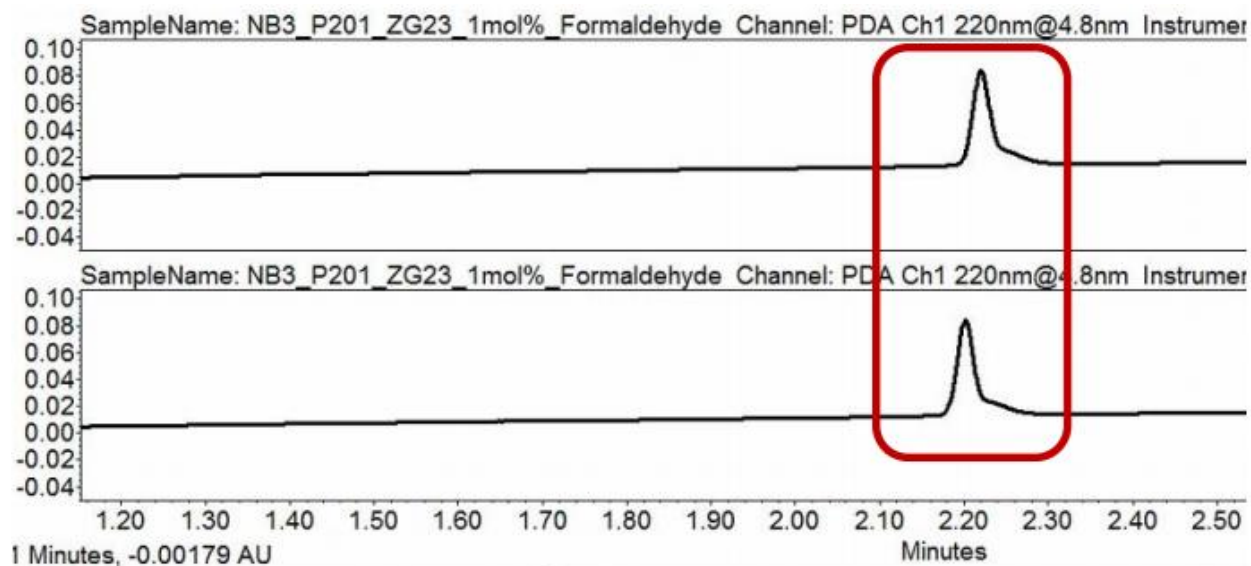
Figure 22. UPLC traces for catalyst **13** in the presence of 100 equivalents of formaldehyde (no hydrocinnamaldehyde). The upper trace was obtained 0.5 minutes after mixing, and the lower trace was obtained 60

minutes after mixing. The peptide peak is not affected by the excess of formaldehyde during this time. We cannot exclude the possibility that the peptide is reacting with formaldehyde to generate iminium species which are hydrolyzed once an aliquot of the reaction mixture is injected into the UPLC column.

Our experimental observations are accommodated by the catalytic cycle proposed in **Figure 23A**.
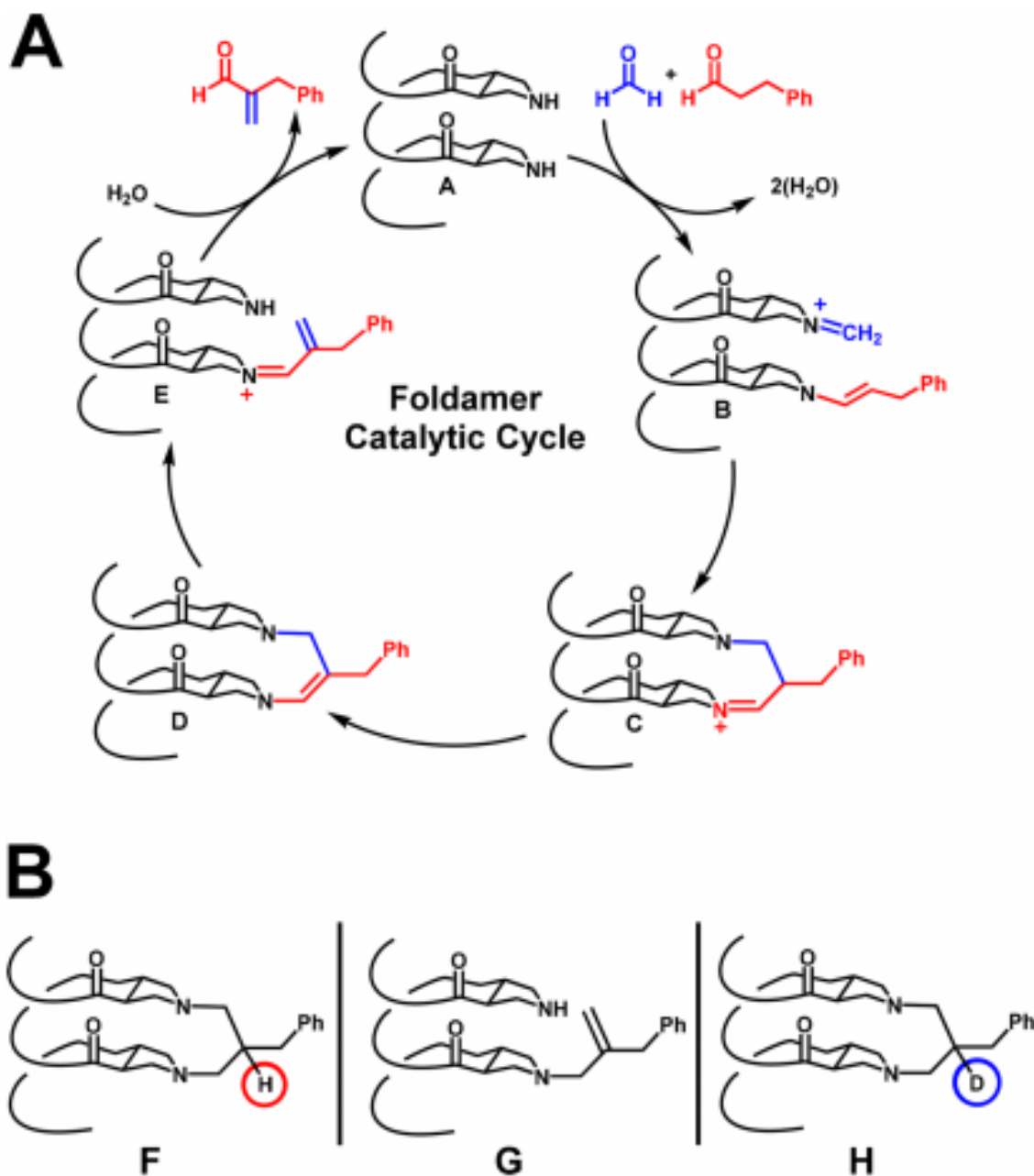
Figure 23. (A) Proposed catalytic cycle for the foldamer-catalyzed crossed aldol reaction. Hydrocinnamaldehyde-derived atoms are shown in red, and formaldehyde-derived atoms are shown in blue. (B) Possible products from reductive trapping of the catalytic reaction mixture. Circled in red in intermediate **F** is the α-hydrogen derived from

hydrocinnamaldehyde. Circled in blue in intermediate H is the α-deuterium derived from α,α-dideutero-hydrocinnamaldehyde.

The bis-APC foldamer catalyst **13** is represented generically by structure **A**. The hypothetical

catalytic mechanism involves condensation of one APC nitrogen with hydrocinnamaldehyde and

the other APC nitrogen with formaldehyde to generate enamine-iminium intermediate **B**.

Intramolecular attack of the enamine on the iminium forms iminium **C**, which contains a transient

crosslink. **C** could tautomerize to **D**, followed by N-protonation and C−N bond scission to

generate **E**. Alternatively, **C** could be transformed directly to **E**. Hydrolysis of the iminium in **E**

would liberate the product and regenerate **A**. The cross-linked intermediate proposed above could

correspond to **C** or **D**, or a mixture of the two. The proposed mechanistic cycle corresponds to

intramolecular dual covalent catalysis. We tested this hypothesis by preparing isomeric

α/βpeptides **15** and **16** (**Figure 24**), each of which is derived from **13** and bears a methyl group on

one of the APC ring nitrogens.

1:2 α/β-peptides: Support for Dual Covalent Catalysis
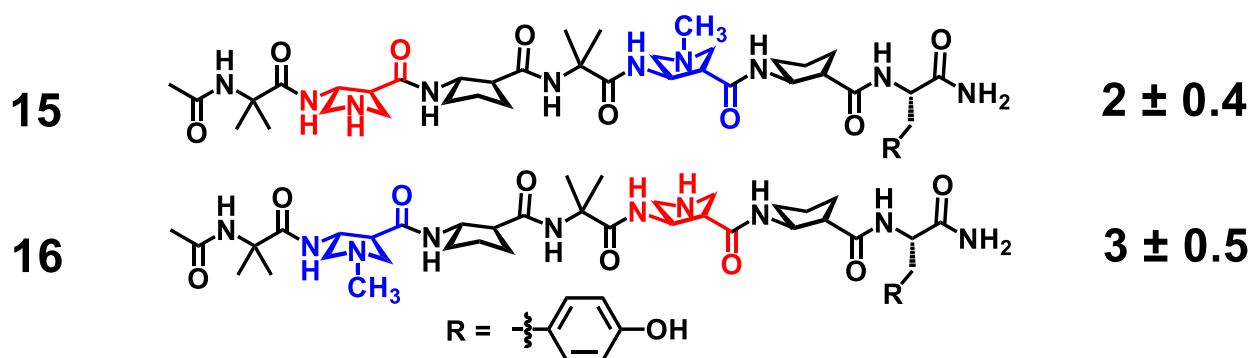
Replacing either of the secondary amino groups in **13** with a tertiary amino group precludes

formation of enamine-iminium intermediate **B**. Neither **15** nor **16** displays a significant increase in

initial rate relative to mono-APC α/β-peptide **10**. These observations support our hypothesis that

the crossed aldol rate enhancement observed for **13** emerges from dual covalent catalysis. We

sought further support for the mechanism proposed in **Figure 23A** by introducing NaBH4 after

partial completion of the crossed aldol condensation catalyzed by **13**. This reagent should reduce

the proposed iminium intermediates to tertiary amines, which are stable and therefore amenable to

detection via mass spectrometry. MS analysis of reaction mixtures generated via reductive

trapping revealed species with diverse m/z values, including 969.263, which for z = +1 could

correspond to the cross-linked α/β-peptide **F** (from reaction of **C** with NaBH4), the alkene **G**

(from reaction of **E** with NaBH4), or a mixture of **F** and **G** (**Figure 23B**). We distinguished

among these possibilities by conducting the reductive trapping experiment with α,α-dideutero-

hydrocinnamaldehyde. In this case, the cross-linked product generated via reduction of **C** would

be predicted to retain one deuterium (species **H**), while the alkene generated via reduction of **E**

would be predicted to contain no deuterium, leading to a difference between these products of 1

amu. MS analysis revealed that both the cross-linked α/β-peptide H (monodeuterated) and alkene

G are formed (**Figure 25**).
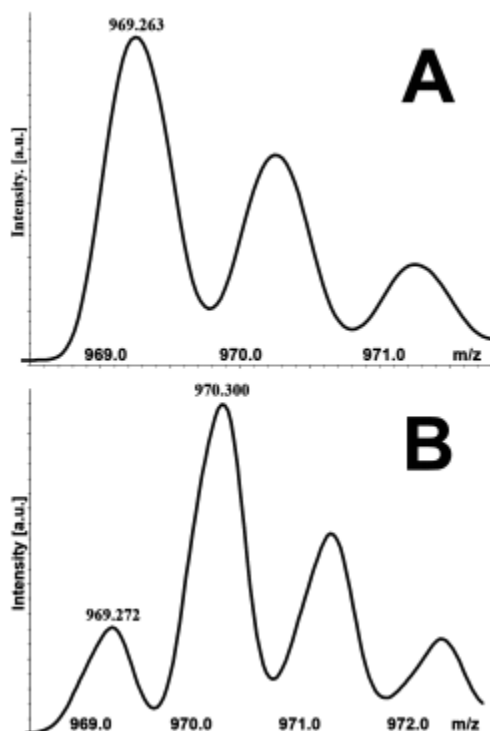
Figure 25. MALDI-TOF MS spectra depicting reduced intermediates. (A) Reaction carried out with hydrocinnamaldehyde as the nucleophile. Observed mass of 969.263 corresponds to **F**, **G**, or both. (B) Reaction carried out with α,α-dideutero-hydrocinnamaldehyde as the nucleophile. Mass corresponding to **G** is observed, as well as 970.300, corresponding to deuterated macrocyclic intermediate **H**.

We conducted analogous reductive trapping studies after exposure of α/β-peptide **13** to 100 equiv of only one of the aldehyde substrates under the reaction conditions (**Figure 26**, **27**). In each case, MS analysis of the product mixture detected the presence of mono- and dialkylated derivatives of **13** (e.g., when formaldehyde was used, m/z values consistent with mono- and dimethyl derivatives of **13** were observed). Thus, failure of UPLC to detect iminium/enamine derivatives of **13** after exposure to 100 equiv of one aldehyde substrate or the

other, described above, suggests that these types of intermediates hydrolyze rapidly under the

chromatographic conditions.
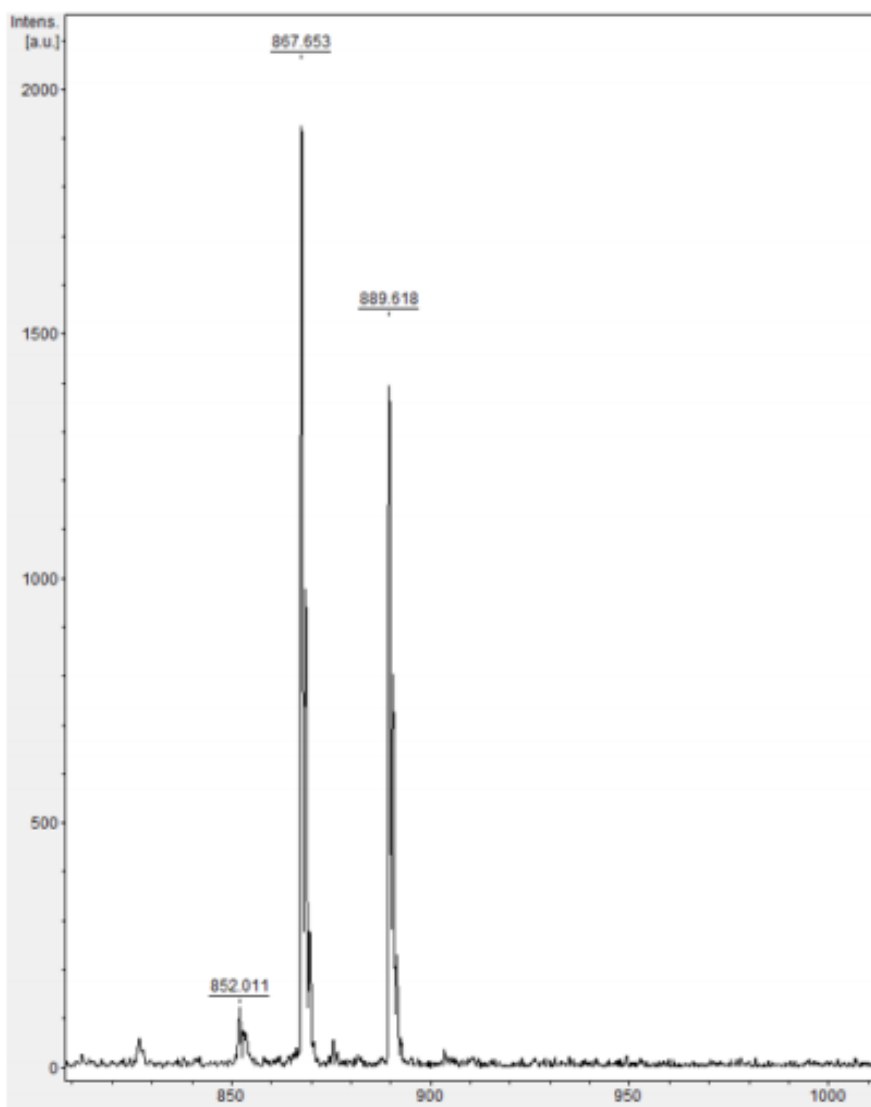
Figure 26. A portion of the MALDI-TOF MS spectrum obtained after mixing 100 equivalents of formaldehyde with 1 mol % **13** under the reaction conditions (no hydrocinnamaldehyde). The reaction was allowed to proceed for 2 hours and then the reaction solution was mixed with NaBH4. The spectrum shown corresponds to the mass expected for mono- and dimethyl derivatives of **13**. (Mono methyl M + H = 852.486, Dimethyl M + H = 867.062, M + Na = 890.052).
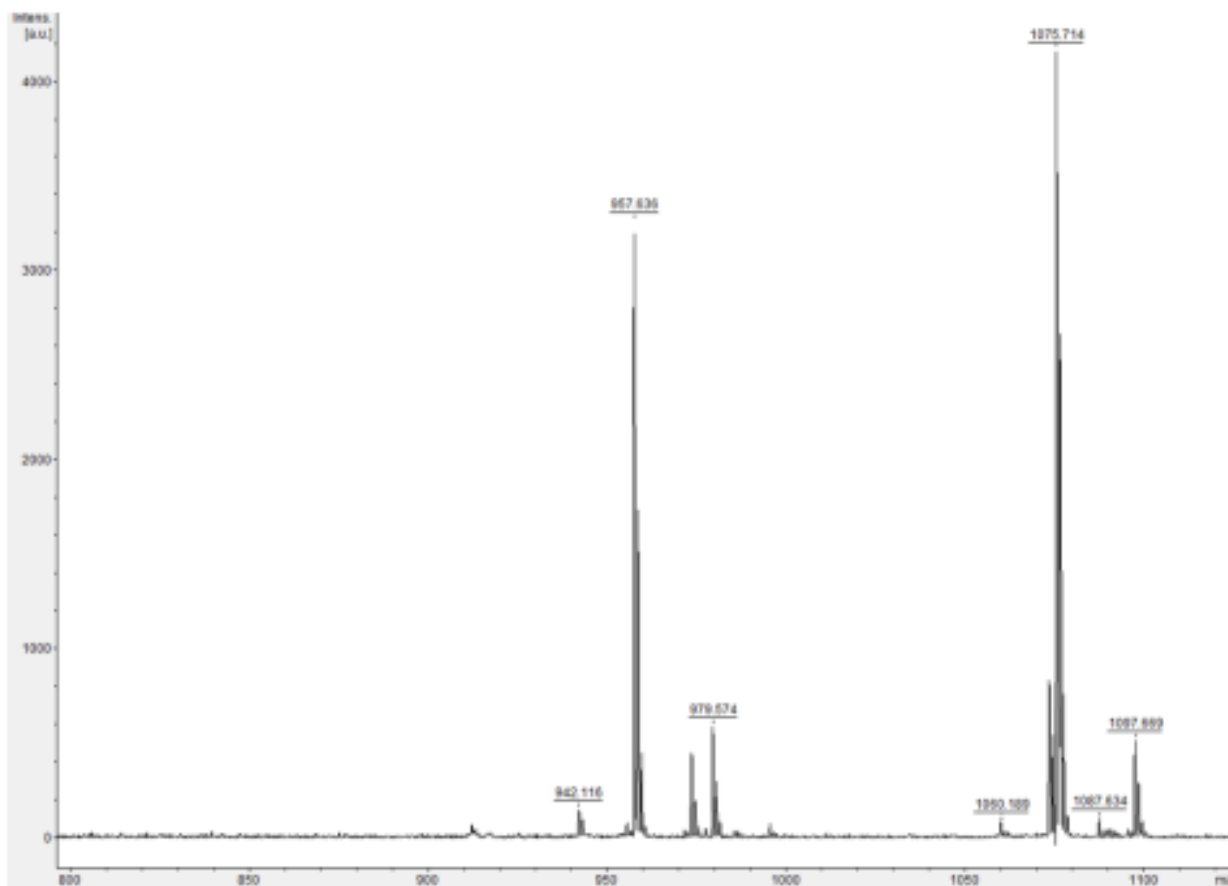
Figure 27. A portion of the MALDI-TOF MS spectrum obtained after mixing 100 equivalents of hydrocinnamaldehyde with 1 mol % **13** under the reaction conditions (no formaldehyde). The reaction was allowed to proceed for 2 hours and then the reaction solution was mixed with NaBH4. The spectrum shown corresponds to the mass expected for mono- and dialkylated derivatives of **13**. Mono alkylated M + H = 957.187, M + Na = 979.538. Dialkylated M + H = `1075.366, M + Na = 1097.616.

The ability of UPLC to detect transiently modified forms of α/βpeptide **13** in the presence of both

aldehyde substrates suggests that a particularly stable intermediate is formed under the reaction

conditions. We speculate that a transient cross-link, as in **C** or **D**, explains this level of stability.

Since α/β-peptide **13** can be detected via UPLC after complete consumption of the aldehyde

starting materials, we hypothesize that the proposed cross-linked intermediate is not sufficiently

stable to inhibit catalysis. Exposure of α/β-peptide **13** to the enal product under the reaction

conditions (in the absence of formaldehyde or hydrocinnamaldehyde), followed by reductive

trapping and MS analysis, led to detection of an adduct between the enal and **13** (**Figure 28**).
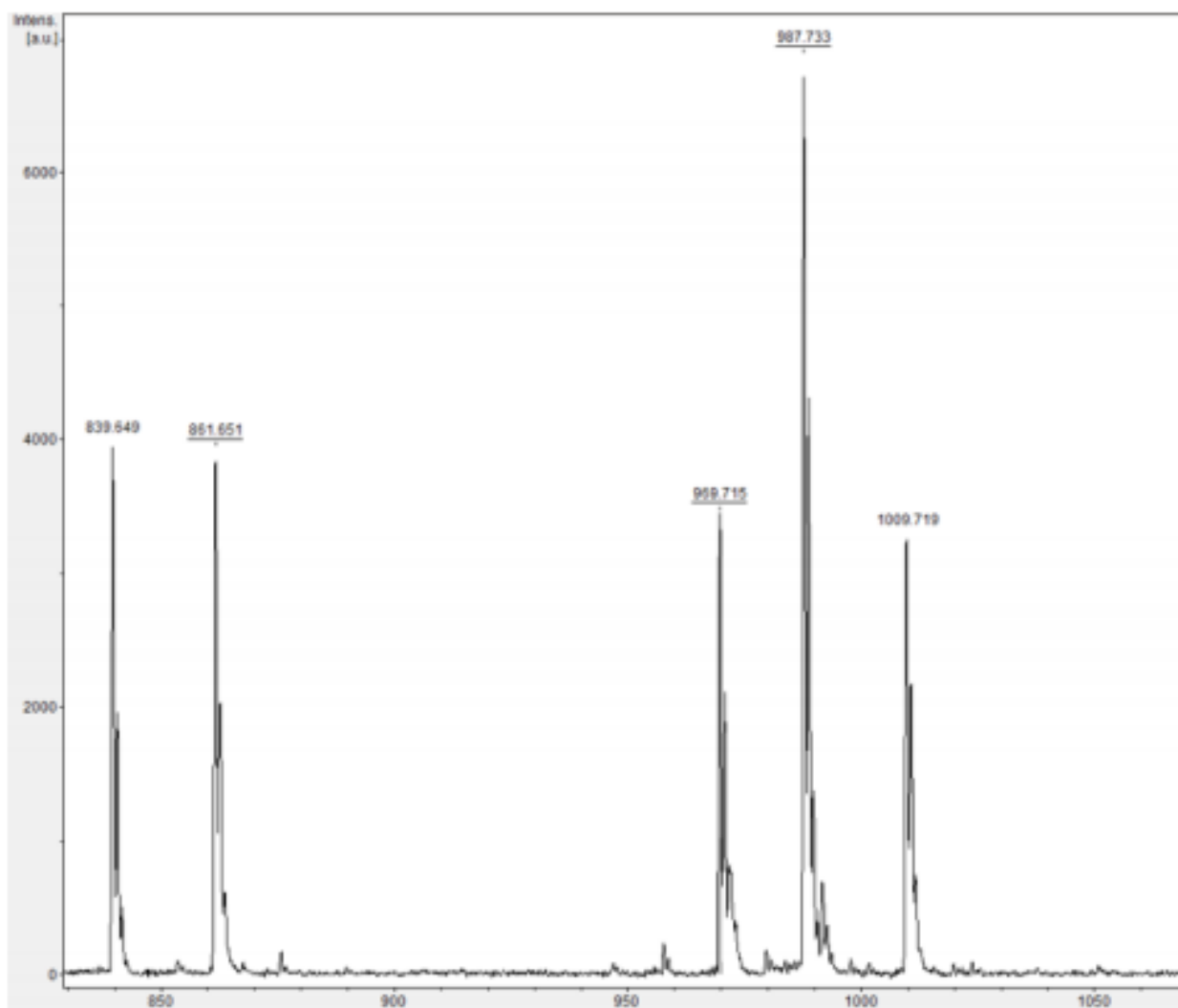
Figure 28. A portion of the MALDI-TOF MS spectrum obtained after mixing 100 equivalents of the enal product formed from hydrocinnamaldehyde and formaldehyde with 1 mol % **13** under the reaction conditions (no formaldehyde or hydrocinnamaldehyde). The reaction was allowed to proceed for 2 hours and then the reaction solution was mixed with NaBH4. The spectrum shown corresponds to the mass expected for catalyst **13**, mono-alkylated and/or cross-linked derivative of **13**. Catalyst **13** M + H = 839.008, M + Na = 861.460. Monoalkylated and or cross-linked derivative of **13**, M + H = 969.198, M + Na = 987.237, M + NH4 = 987.237, M + K = 1009.296.

This observation motivated us to explore the possibility that the crossed aldol reaction process is

fully reversible via a crossover experiment. α/β-Peptide **13**, hydrocinnamaldehyde, and the enal

formed from hexanal were combined under the reaction conditions. However, no crossover

product, i.e., neither hexanal nor the enal expected from hydrocinnamaldehyde, was detected after

70 min (**Figure 29**). Moreover, when this reaction was monitored by LC-MS, the peak for **13** did

not disappear, which suggests that the reaction between catalyst **13** and an enal, which was

detected via reductive trapping, does not lead to formation of the cross-linked intermediate. These

results led us to conclude that the crossed aldol reaction is not reversible under our conditions.
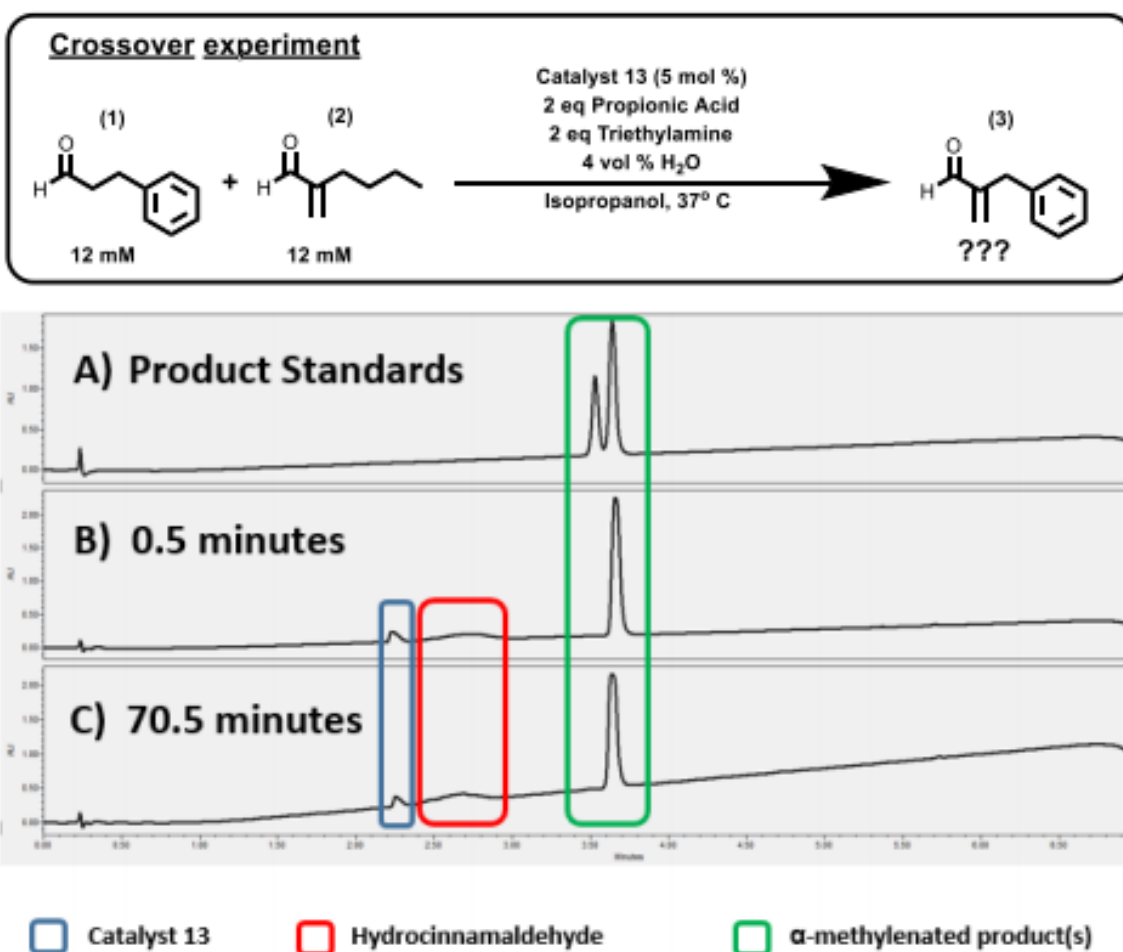
Figure 29. Crossover experiment to observe whether 2-benzylacrylaldehyde forms in the presence of Catalyst **13** with hydrocinnamaldehyde and 2-methylenehexanal. A) LC trace of **2** (right peak) and **3** (left peak). B) LC trace of reaction mixture at 0.5 minutes, showing catalyst **13**, **1**, and **3**. C) LC trace of reaction mixture after 70 minutes at 37° C. No crossover product was observed, suggesting that 2-methylenehexanal does not appear to re-enter the catalytic cycle and revert to hexanal and formaldehyde.

The proposed crossed aldol mechanism (**Figure 23A**) raises the possibility that a bifunctional catalyst would be effective for an aldol-based cyclization. Indeed, under the conditions employed for the crossed aldol reaction, combining 1,8-octanedialdehyde with 10 mol % of the best catalyst, α/β-peptide **13**, generates a 75% yield of cycloheptene-1- carbaldehyde after 140 min (**Figure 30**). Under identical conditions, isomeric α/β-peptide **12** generates an 8% yield of the cyclic enal. Previously, this intramolecular aldol reaction has been achieved by refluxing the dialdehyde in dichloromethane for 2 days with 76 mol % proline.
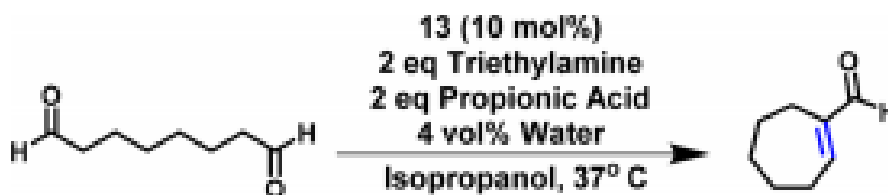
Figure 30. Aldol-based cyclization of 1,8-octanedialdehyde.

This intramolecular aldol reaction in the presence of other 1:2 α/β-peptides in which the diad geometry was altered (**12-14**) or dual covalent catalysis was precluded via introduction of a tertiary amine (**15**) exhibited product yields that follow the trend observed in the v_{REL} measurements above (**Figure 8**).
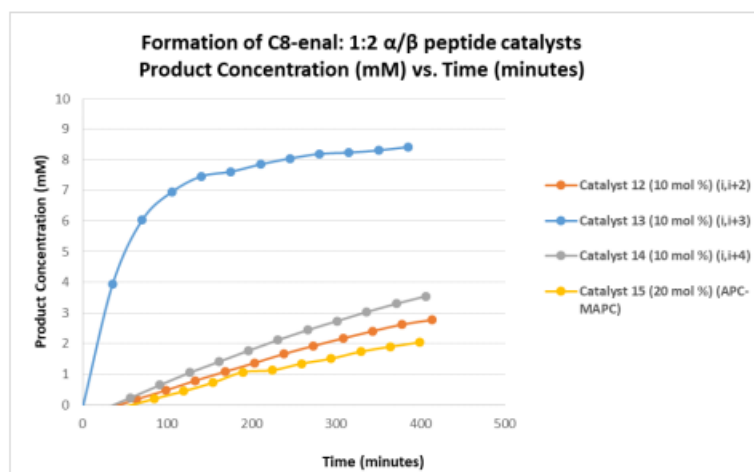
Figure 31. Reaction progress data for the intramolecular aldol cyclization reaction in the presence of 1:2 α/β-peptides **12**, **13**, **14**, and **15**. Reaction progress was monitored up to 400 minutes. Reaction conditions are described above. Catalyst **15**, which contains an i,i+3 APC-MAPC diad was loaded at 20 mol %, while bis-APC catalysts **12**, **13**, and **14** were loaded at 10 mol %. Therefore, the total concentration of APC residues was constant across these reactions. 10 mM product corresponds to quantitative yield.

Catalyst, mol %	% Yield @ 180 minutes	
12	11	
13	76	
14	18	
15	11	

Figure 32. Percent yields measured for various catalysts based on the UPLC data shown in **Figure 31** using the calibration curve shown in the experimental procedures section.

2.4 Conclusions

We have employed a crossed aldol condensation to compare the abilities of different helical scaffolds to achieve pyrrolidine (APC) diad geometries that support bifunctional catalysis. The lack of stereochemical complexity in this crossed aldol reaction streamlines initial rate analysis via product formation and therefore renders the crossed aldol process particularly useful for assessment of reactivities among catalyst candidates.[29,30] Variations in the sequential spacing between APC units strongly affect catalytic efficacy, as would be predicted if distinct sequential juxtapositions of reactive groups are translated by folding into distinct spatial relationships of those groups. The best bis-APC α/β-peptide catalysts enhance the initial rate of product formation by two orders of magnitude relative to a mono-APC control compound. This observation is encouraging in terms of ongoing exploration of foldamer-based catalysis. Our work complements other efforts to develop foldamer catalysts by highlighting the way that access to multiple related secondary structures, via predictable sequence-design strategies, enables evaluation of alternative reactive group geometries.[31,32] β^3-Homoleucine oligomers have been used in place of α-leucine oligomers to promote asymmetric enone epoxidation with hydrogen peroxide; exposed helix termini are presumed to be sites of H-bond-mediated catalysis.[33] Attachment of a catalytically active nitroxyl unit to a helical peptoid enabled kinetic resolution of 1-phenylethanol via preferential oxidation of one enantiomer.[34] In this case, the chiral foldamer presumably plays a

steric role, selectively impeding approach of one alcohol enantiomer to the nitroxyl unit. Two examples of catalysis by self-assembling helical β-peptides have been reported. One involves a retro-aldol reaction that depends upon nucleophilic reactivity of a β^3-hLys side chain.[35] The other case involves activated ester hydrolysis that requires terminal α-histidine residues.[36] Recently described helical oligo-urea foldamers promote the asymmetric conjugate addition of dimethyl malonate to nitroalkenes, apparently via H-bond-mediated activation of the acceptor.[37] In conceptually related work, rigid polycyclic molecular scaffolds have been used to develop catalysts for reactions such as aldol condensations.[6] Oligomers based on four different xenonucleic acid backbones that display endoribonuclease activity have been selected from large candidate pools generated via engineered polymerase enzymes.[38] This type of selection-based catalyst discovery is presently impossible with peptidic foldamers.

Our work is distinctive relative to these precedents because of our focus on and evidence for bifunctional catalysis. We have shown that the availability of a family of distinct but related helices (**Figure 3**) enables rapid assessment of alternative spatial organizations of the reactive diad. This aspect of our work highlights the value of continued efforts to identify new foldamer scaffolds. Previous catalyst development efforts with foldamers have typically been based on a single folding pattern.[34−37] Analogous designs with conventional peptides have focused on the α-helix,[39,40] although selections of short α-peptide catalysts from combinatorial libraries have shown that nonhelical conformations can be effective for reactive group organization.[41] Our foldamer-based approach is advantageous because multiple helical scaffolds with complementary shapes are available among β- and α/β-peptides, and the intrinsic modularity of peptides makes it straightforward to alter diad geometry within each scaffold via sequence changes. Much of the prior work with synthetic α-peptide and foldamer catalysts has emphasized stereo- and

regioselectivity in product formation,[7–12,29,34,39–41] while the studies reported here focus on reactivity.

The best catalytic enhancements we observed are small relative to those of highly evolved natural enzymes;[1] however, our approach has necessarily been limited to short, isolated secondary structures as scaffolds for reactive group organization (six or seven residues). In contrast, all known enzyme active sites are embedded within tertiary structures. This distinction is significant, because concave active sites allow control over substrate solvation,[42,43] but an active site created along the side of a single helix is solvent exposed. Noteworthy progress in de novo enzyme design has been reported, but these efforts have not yet achieved the rate enhancements manifested by proficient enzymes.[44] The favorable reactivity we observe for an aldol-based cyclization with the optimal foldamer suggests that even rudimentary catalysts involving an isolated secondary structure might have facilitated the maturation of prebiotic reaction networks. Enzymes typically contain hundreds of α-amino acid residues, which are necessary to generate globular folds with enclosed active sites. It is unlikely, however, that such long polypeptides existed in the prebiotic period. We therefore speculate that exploring the capabilities of isolated unnatural secondary structures as scaffolds for bifunctional catalysis represents a first step, inspired by prebiotic hypotheses regarding the origins of enzymes,[45] toward development of larger foldamers that adopt discrete tertiary structures and approach enzyme-like reactivities.

2.5 Experimental

2.5.1. Materials and Instrumentation

a. Materials and Reagents

Solvents and reagents obtained from Sigma-Aldrich included 37 wt. % formaldehyde in water, hydrocinnamaldehyde 90 % technical grade, propionic acid, and triethylamine. Hydrocinnamaldehyde was distilled prior to experiments, with purity checked via NMR. Isopropanol was HPLC grade obtained from Fisher Chemical. Filtered Millipore water was used for kinetics experiments. Protected amino acids and coupling reagents were obtained from ChemImpex Interantional, Inc. Solid phase peptide synthesis (SPPS) resins were obtained from EMD Millipore. ACS-grade DMF from Sigma-Aldrich was used as a washing solvent during SPPS, and biotech-grade DMF from Sigma-Aldrich was used during amino acid coupling.

b. Instrumentation

Solid-phase peptide synthesis was performed using a CEM MARS microwave system in Torviq polypropylene syringes fitted with a porous polypropylene disc at the bottom. Preparative HPLC was performed using a Shimadzu HPLC system (SCL-10VP system controller, LC-6AD pumps, SIL-10ADVP autosampler, SPD-10VP UV-vis detector, FRC-10A fraction collector) equipped with a Waters XSelect CSH Prep C18 column (5 μm particle size, 19 mm × 250 mm) operating at 12 mL/min. Peptide purity and concentration measurements and kinetic measurements were performed on a Waters Acquity H-Class UPLC equipped with an Acquity UPLC BEH C18 column (130 Å pore size, 1.7 μm particle size, 2.1 mm × 50 mm) operating at 0.4 mL/min. Circular dichroism measurements were performed using an Aviv Biomedical Model 420 circular dichroism spectrometer.

c. Instrument acknowledgements

(Instrument Name Instrument, Type, Grant, Award Year) Bruker microflex LRF, MALDI-TOF-MS, Generous gift from the Bender Fund. Waters Acquity H-Class, UPLC, DARPA N66001-15-

2-4023, 2014. Bruker Advance III-400, NMR Spectrometer, NSF CHE-1048642, 2010. Bruker

Advance III-500, NMR Spectrometer, Generous gift from Paul J. Bender, 2012

2.5.2 General Procedures

a. General Procedure: Peptide Synthesis and Purification

NovaPEG Rink Amide resin (50 µmol by amine loading [0.49 mmol/g], 102 mg) is added to a

Torviq solid-phase peptide synthesis vessel along with a micro stir bar. Resin is swelled in DCM

for 30 minutes before beginning synthesis. Fmoc amino acid (3.5 eq., 175 µmol) and HATU (3.45

eq., 172.5 µmol) are weighed into 10 mL glass vials. Amino acid and coupling reagent are pre-

activated by adding 3 mL biotech grade DMF, DIEA (8 eq., 70 µL, 400 µmol), and vortexing. The

pre-activated amino acid sits at room temperature for 5 minutes. DCM used to swell the resin is

aspirated from the vessel, the resin is washed 5X with DMF and then capped at the bottom. The

pre-activated amino acid solution is added to the vessel.

b. Coupling of amino acids (α, α-disubstituted, and β-amino acids):

 The reaction vessel containing the resin and pre-activated amino acid is transferred to the

microwave reactor, and the temperature sensor is placed in the vessel. The microwave coupling

program is initiated which S3 ramps to 70°C over two minutes, and holds at 70°C for thirteen

minutes. After the coupling, the vessel is taken out of the microwave and aspirated. The resin is

then washed 5X with ACS grade DMF. The vessel is then capped.

c. Deprotection of amino acids (α, α-disubstituted, and β-amino acids):

To the reaction vessel is added 6 mL of 20 %v/v piperidine in ACS DMF, and the vessel is moved

to the microwave reactor. The temperature probe is placed in the vessel. The microwave

deprotection program is initiated, which ramps to 80ºC over two minutes and holds at 80ºC for

four minutes. After deprotection, the vessel is aspirated and the resin is washed 5X with ACS

DMF. Subsequent coupling and deprotection steps are carried out until the final residue has been

coupled. N-terminal acetylation of peptides: To the reaction vessel, whose terminal residue has

been deprotected, is added 3 mL Biotech grade DMF, 50 eq DIEA and 50 eq acetic anhydride.

The mixture is allowed to stir for 45 minutes at room temperature. The solution is then aspirated,

and the resin is washed 3X with DMF, followed by 5X DCM, and 5X MeOH. The resin is dried

by leaving it on the aspirator for 15 minutes.

d. Cleavage of peptides from resin:

 Cleavage is performed by withdrawing 3 mL of 2.5 % TIPS, 2.5 % Water, 95% TFA into the

reaction vessel using the syringe plunger and rocking the vessel for 3 hours at room temperature.

Crude peptide solution is expunged into a 50-mL centrifuge tube, resin is washed 3X with TFA,

and TFA is blown off under a stream of N2. Once most of the TFA is removed, the crude peptide

is precipitated by addition of 40 mL cold diethyl ether and pelleted using a centrifuge at 4,300

rpm for 5 minutes. The supernatant ether is decanted, and the crude peptide solid is dried under a

stream of N_2. Crude peptide is prepared for HPLC purification by dissolving the solid in about 4

mL of 1:1 H2O-MeCN and transferring to an HPLC vial. HPLC solvent A is 0.1 % TFA in

filtered and degassed Millipore H_2O, and solvent B is 0.1 % TFA in acetonitrile. A linear gradient

of 10-60 %B is used to identify product peaks (determined by MALDI on collected fractions).

e. General procedure: concentration determination and purity of stock solutions

Collected peptide fractions are frozen over dry ice and lyophilized. The lyophilized powder is

dissolved in about 1.5 mL of isopropanol, and the solution is sonicated for 30 minutes. 5 µL of the

peptide stock solution is added to a UPLC vial containing 45 μL isopropanol (10-fold dilution) and mixed. A 2 μL injection is run on a UPLC equipped with a 5 cm BEH C18 column with 1.7 μm pore size at a flow rate of 0.4 mL/min. The method used is 10-50 %B over 5 minutes. UPLC Solvent A is 0.1 % TFA in filtered/degassed Millipore H_2O, and Solvent B is 0.1 % TFA in acetonitrile. Purity is assessed by UPLC via integration of the 220 nm and 275 nm channels (UPLC traces of peptides are provided below). Concentration of pure peptide solutions is determined by correlating the integral of the peptide peak in the 275 nm chromatogram with a calibration curve generated with known concentrations of Ac-Tyr-OH (each peptide contains a C-terminal tyrosine for determination of concentration). Catalyst loadings for all reactions were based on concentration determined in this way, which agreed with concentration measurements by UV-Vis absorbance at 275 nm. Stock solutions of catalysts in isopropanol were stored in a 20°C freezer. Purity analysis over several months showed no degradation of any peptide catalyst.

f. General procedure: initial rate, v_{REL}, and percent yield measurements for the crossed aldol reaction

Representative procedure for initial rate measurement for the crossed aldol reaction using 2 mol% catalyst **6**: To a 1 mL UPLC vial was added 185.82 μL isopropanol via pipette, followed by 10 μL H_2O (10 μL H_2O correspond to 4 vol% of the 250 μL total reaction volume). To the UPLC vial was then added: 26.8 uL (3 μmol) of a 0.112 M solution of distilled hydrocinnamaldehyde in isopropanol, 37 %w/v formaldehyde solution in H_2O (3 μmol, 0.243uL), propionic acid (6 μmol, 0.449 μL), triethylamine (6 μmol, 0.836 μL). Added last was Catalyst **6** (2 mol%, 25.86 μL of a 2.321 mM solution in isopropanol). All reactions were run at a total volume of 250 μL. The UPLC vial was immediately capped and shaken manually for 30 seconds. The UPLC vial was placed in the sample manager of the UPLC, which had been previously heated to 37°C. The

UPLC method was initiated, which performed chromatographic analysis of the reaction mixture every 7 minutes. For initial rate measurements, the UPLC method employed was a gradient of 20-70-%B over 5 minutes, followed by a 1 minute 95 %B flush and 1 minute re-equilibration to 20 %B. Solvent A is 0.1 % TFA in filtered/degassed Millipore H2O, and solvent B is 0.1 % TFA in acetonitrile. The sample manager was kept shut which maintained the temperature at 37⁰C throughout the reaction. A 1 µL aliquot was removed from the reaction mixture and injected onto the UPLC every 7 minutes. Product concentration was monitored via the 220 nm channel (the enal product absorbs at 220 nm). The product peak (220 nm) was integrated and converted to concentration in µM using a calibration curve generated with a pure synthetic standard of 2-benzylacrylaldehyde. Eleven data points were taken corresponding to the first 70 minutes of the reaction. The amount of isopropanol added to the UPLC vial is calculated by subtracting the sum of the volumes of all reaction components added (in µL) from 250 µL. Stock solutions of peptide ranged from 1.5 to 6 mM, with concentration determined as explained above. The reaction solution contained the following components: 12 mM hydrocinnamaldehyde, 12 mM formaldehyde, 4 vol % water, 24 mM propionic acid, and 24 mM triethylamine. For mono-APC peptides used for controls or peptides containing a methylated APC, 2 mol% peptide was used, giving a final secondary amine concentration of 0.12 mM. Peptides bearing two APC residues were loaded at 1 mol%, giving a final secondary amine concentration of 0.12 mM. This approach ensures that each initial rate measurement is performed with the same amount of secondary amine in solution. All kinetic experiments were performed at least three times, with different stock solutions of peptides made from different synthetic batches. The initial rate of the reaction was determined by plotting product concentration (µM) vs. time (minutes). The slope of the best fit line was used as the initial rate of the reaction in µM/minute. Time points only up to 1 % product

formation (often ~ 20-30 minutes reaction time) were used, to ensure that each reaction remained in the initial rate regime. For the mono-APC peptides, as well as several bis-APC peptides, 1% product formation was not achieved after 70.5 minutes, reflecting low catalytic activity. In these cases, eleven data points collected during the 70 min period were used to determine the initial rate of the reaction.

To determine the relative initial rate of reaction, v_{REL}, the initial rate measured for each bis-APC peptide at 1 mol% loading, was divided by the initial rate measured for the relevant mono-APC peptide at 2 mol% loading. Each of the three backbones we studied (pure β, 1:1 α:β, and 1:2 α:β) had an appropriate mono-APC peptide to serve as the reference for determination of v_{REL}. The three mono-APC peptides, **1**, **6**, and **10**, displayed very similar initial rates of crossed aldol reaction, which indicates that differences among the helical secondary structures adopted by these β- and α/β-peptides have little or no effect on the intrinsic reactivity of a single APC residue. Determination of percent yield for the crossed aldol reaction was determined using a calibration curve. Reagents were added in the same order as described above, with only the amount of peptide catalyst changing. For example, instead of 1 mol% bis-APC peptide, 5 mol% or 10 mol% was used, to ensure that the reaction would proceed to completion within a day. Determination of product concentration via UPLC was problematic as the reaction approached completion (12 mM product), because the UV detector limit was exceeded when a 1 μL injection volume was used (as in kinetic experiments). Therefore, 0.5 μL injections were used for reactions that were run to completion. A calibration curve was generated using a pure synthetic standard of 2-benzylacrylaldehyde. Using 0.5 μL injections allowed for a linear calibration curve without exceeding the detector limit up to ~ 14mM product (which is above 100% conversion for our reaction conditions).

g. General procedure: reductive trapping of crossed aldol reaction intermediates

α/β-Peptide **13** was allowed to react under standard initial rate conditions (0.12 mM **13**, **12** mM hydrocinnamaldehyde (or α,α-dideutero-hydrocinnamaldehyde), 12 mM formaldehyde, 24 mM propionic acid, 24 mM triethylamine, 4 vol % water, in isopropanol; 250 μL total reaction volume, 37°C). After one hour, 5 eq NaBH4 was added (relative to hydrocinnamaldehyde). Gas began to evolve. After gas evolution stopped, 1 μL of the reaction mixture was spotted on a MALDI plate and mixed with 1 μL of matrix (70 % acetonitrile, 30 % water, 0.1% trifluoroacetic acid, saturated solution of α-cyano-4-hydroxycinnamic acid). MALDI-TOF MS data were acquired; these data were calibrated using angiotensin II as an internal standard.

2.5.3 Small molecule synthesis

Synthesis of β-amino acid monomers: Fmoc-APC(Boc)-OH (**APC**) and Fmoc-MAPC-OH TFA (**M^APC**).
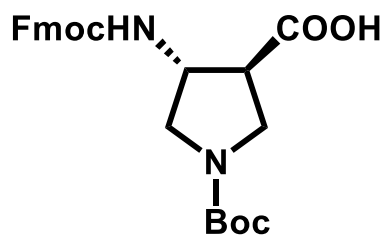
Fmoc-APC(Boc)-OH

APC was prepared following a published protocol.[46]

Fmoc-MAPC-OH TFA (**M^APC**): To a 100 mL round bottom flask equipped with a stir bar was added 800 mg of **Fmoc-APC(Boc)-OH** (1.77 mmol) followed by 8 mL of 4 M HCl in dioxane. The mixture was allowed to stir at room temperature for two hours, at which point a stream of nitrogen was blown on the reaction mixture to remove
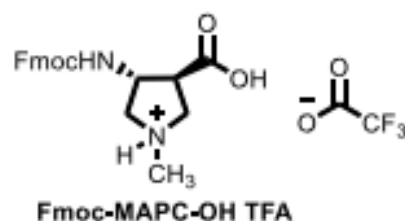
Fmoc-MAPC-OH TFA

dioxane, yielding the HCl salt of **Fmoc-APC(Boc)-OH** as a white solid that was carried forward without purification. To the HCl salt of **Fmoc-APC(Boc)-OH** was added 30 mL of ethanol, DIEA (3.54 mmol, 2 eq, 619 μL) and acetic acid (5.31 mmol, 3 eq, 304 μL). The mixture, a white slurry was stirred for ten minutes. 37 % w/v formaldehyde in water (37 mmol, 20.9 eq, 3mL) was then added, which caused the mixture to turn opaque brown. After another ten minutes, sodium cyanoborohydride (17.7 mmol, 10 eq, 1.12 g) was added, and the mixture was allowed to stir at room temperature under nitrogen overnight (12 hours). Solvent was removed to provide an off-white solid, which was dissolved in 5 mL MeOH for purification via preparative HPLC. Ultimately, 142 mg of **Fmoc-MAPC-OH TFA** was obtained (16.6 % yield). UPLC analysis indicated that this material was > 98 % pure (based on data monitoring of the UPLC run at 220 nm and 275 nm). ^{1}H NMR (400 MHz, d6-DMSO) δ 7.91 (d, J = 7.51 Hz, 2H), δ 7.86 (d, J = 6.67 Hz, 1H), δ 7.69 (dd, J = 7.48, 2.89 Hz, 2H), δ 7.43 (t, J=7.43 Hz, 2H), δ 7.35 (t, J = 7.46 Hz, 2H), δ 4.44 – 4.35 (m, 3H), δ 4.25 (t, J = 6.45 Hz, 1H), δ 3.70 – 3.26 (m, 6H), δ 2.82 (s, 3H). ^{13}C NMR (125 MHz, d6-DMSO) δ 171.98, δ 159.49, δ 159.24, δ 158.98, δ 158.72, δ 144.23, δ 144.13, δ 141.22, δ 128.13, δ 127.55, δ 125.57, δ 125.54, δ 120.62, δ 66.14, δ 55.81, δ 52.72, δ 47.07, δ 41.24, δ 25.93. HRMS m/z (ESI): calculated for [$C_{21}H_{22}N_2O_4$] + ([M+H]) 367.1652, found 367.1654. UPLC trace of monomer showed > 98.9 % purity via the 220 nm channel (See Spectra: MALDI-TOF MS, 1H NMR, 13C NMR, UPLC traces).

Synthesis of 2-benzylacrylaldehyde:
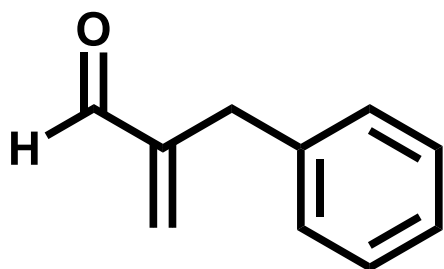
2-Benzylacrylaldehyde was synthesized using a published procedure,[47] and purified via high vacuum distillation. ^{1}H and ^{13}C NMR spectra matched those reported, and UPLC indicated that the material was pure.

Synthesis of α,α-dideuterated hydrocinnamaldehyde:
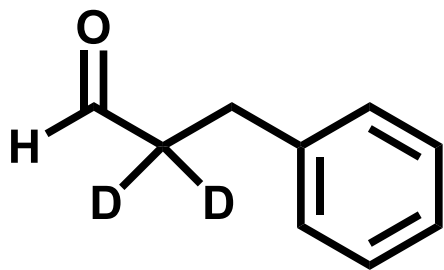
α,α-Dideuterated hydrocinnamaldehyde was synthesized using a published procedure.[48] Distilled hydrocinnamaldehyde (500 μL, 3.8 mmol) was added to a round bottom flask charged 500 μL D2O (1 μL per 1 μL of aldehyde) and DMAP (0.046 g, 0.1 eq). The mixture was heated to 100° C for 1 hr. After the solution had cooled, it was extracted twice with DCM. The combined DCM layers were washed with twice 1 M HCL, and then with sat. aq. Sodium bicarbonate and brine, and then dried with MgSO$_4$. The solvent was removed via rotary evaporation to provide the crude product as a yellow oil. The crude product was purified via high-vacuum distillation. ^{1}H and ^{13}C NMR spectra matched those reported.[48]

2.5.4 Tabulated initial rate measurements
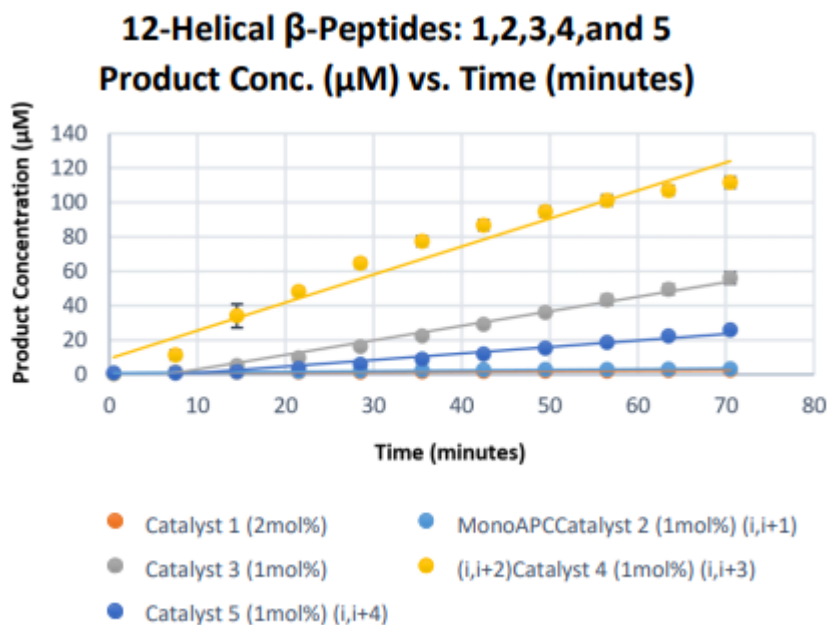
Figure 32. Reaction progress data for the crossed aldol reaction in the presence of β-peptide **1**, **2**, **3**, **4**, or **5**, between 0.5 and 70.5 minutes after catalyst addition. Each reaction was run in triplicate, and error bars denote standard deviation among product concentration measurements at a given time point. Reaction conditions are described above. Mono-APC βpeptide **1** was used at 2 mol % relative to the aldehyde starting materials, while each of the bisAPC β-peptides was used at 1 mol %. Therefore, the total concentration of APC residues was constant across these reactions. The maximum amount of product detected, 112 µM, corresponds to 1 % yield.

Peptide		Rate (1)	Rate (2)	Rate (3)	Avg Rate (µM/minutes)	StDev (µM/minutes)
	1	0.031	0.021	0.028	0.026	0.003
	2	0.026	0.052	0.034	0.037	0.01
	3	0.866	0.722	0.861	0.816	0.05
	4	1.55	1.75	1.58	1.63	0.06
	5	0.37	0.38	0.38	0.38	0.00

Peptide		vREL(1)	vREL(2)	vREL(3)	Avg vREL	StDev vREL
	1	n/a	n/a	n/a	Control Peptide	n/a
	2	0.966	1.97	1.29	1.41	0.30
	3	30.9	27.3	32.6	30.3	1.6
	4	58.7	66.3	59.8	61.6	2.4
	5	14.2	14.2	14.5	14.3	0.1

Figure 33. Initial rates measured for each reaction with catalysts **1-5**, along with the average v_{REL} and standard deviation for **2-5** (1 mol %) relative to **1** (2 mol %).
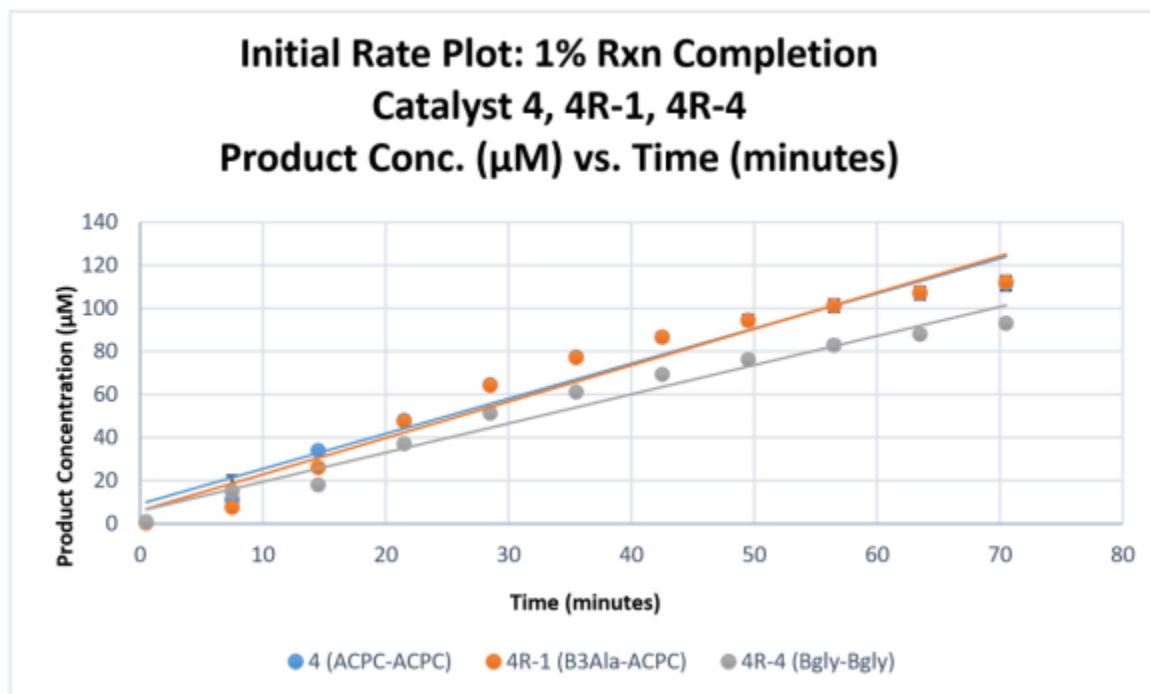
Figure 34. Reaction progress data for the crossed aldol reaction in the presence of β-peptide **4**, **4R-1**, or **4R-4** (each at 1 mol % relative to aldehyde starting materials), between 0.5 and 70.5 minutes after catalyst addition. Each reaction was run in triplicate, and error bars denote standard deviation among product concentration measurements at a given time point. Reaction conditions are described above. The maximum amount of product detected, 112 μM, corresponds to 1 % yield.

Peptide		Rate (1)	Rate (2)	Rate (3)	Avg Rate (μM/minutes)	StDev (μM/minutes)
	4	1.55	1.75	1.58	1.63	0.06
4R-1		1.76	1.65	1.66	1.69	0.04
4R-4		1.40	1.23	1.43	1.35	0.06
Peptide		vREL(1)	vREL(2)	vREL(3)	Avg vREL	StDev vREL
	4	58.7	66.3	59.8	61.6	2.4
4R-1		66.6	62.5	62.8	63.9	1.3
4R-4		53.1	46.8	54.0	51.3	2.3

Figure 35. Initial rates measured for each reaction with catalysts **4**, **4R-1**, and **4R4**, along with the average v_{REL} and standard deviation for **4**, **4R-1**, and **4R-4** (1 mol %) relative to mono-APC reference peptide **1** (2 mol %).
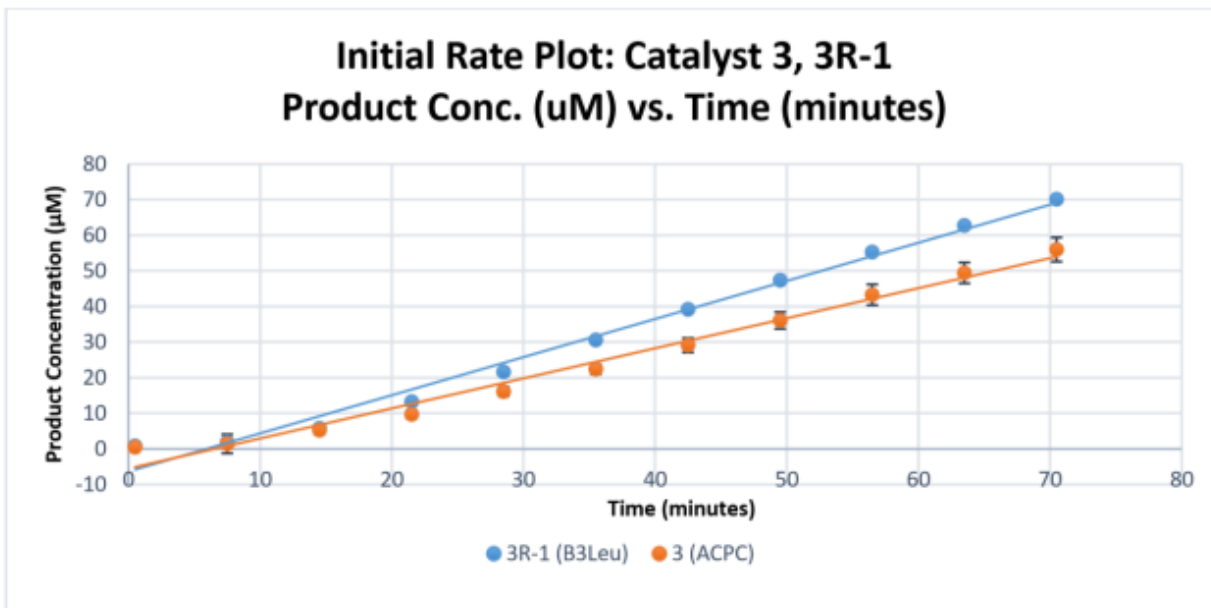
Figure 36. Plot of the product concentration (μM) vs. time (minutes) for 12- helical β-peptides **3** and **3R-1**. Error bars correspond to the standard deviation over three reactions. The rate used to determine the v_{REL} corresponds to the slope of the line from 0.5 to 70.5 minutes. Catalysts **3** and **3R-1**, at 1 mol % relative to aldehyde starting materials, do not reach 1 % product formation after 70 minutes. All v_{REL} values are relative to the initial rate of mono-APC peptide **1**, at 2mol%.

Peptide		Rate (1)	Rate (2)	Rate (3)	Avg Rate (μM/minutes)	StDev (μM/minutes)
	3	0.866	0.722	0.861	0.816	0.05
3R-1		1.05	1.07	1.09	1.07	0.01
Peptide		**vREL(1)**	**vREL(2)**	**vREL(3)**	**Avg vREL**	**StDev vREL**
	3	30.9	27.3	32.6	30.3	1.6
3R-1		40.0	40.6	41.2	40.6	0.35

Figure 37. Initial rates measured for each reaction with catalysts **3**, and **3R-1**, along with the average v_{REL} and standard deviation for **3** and **3R-1** (1 mol %) relative to mono-APC reference peptide **1** (2 mol %).
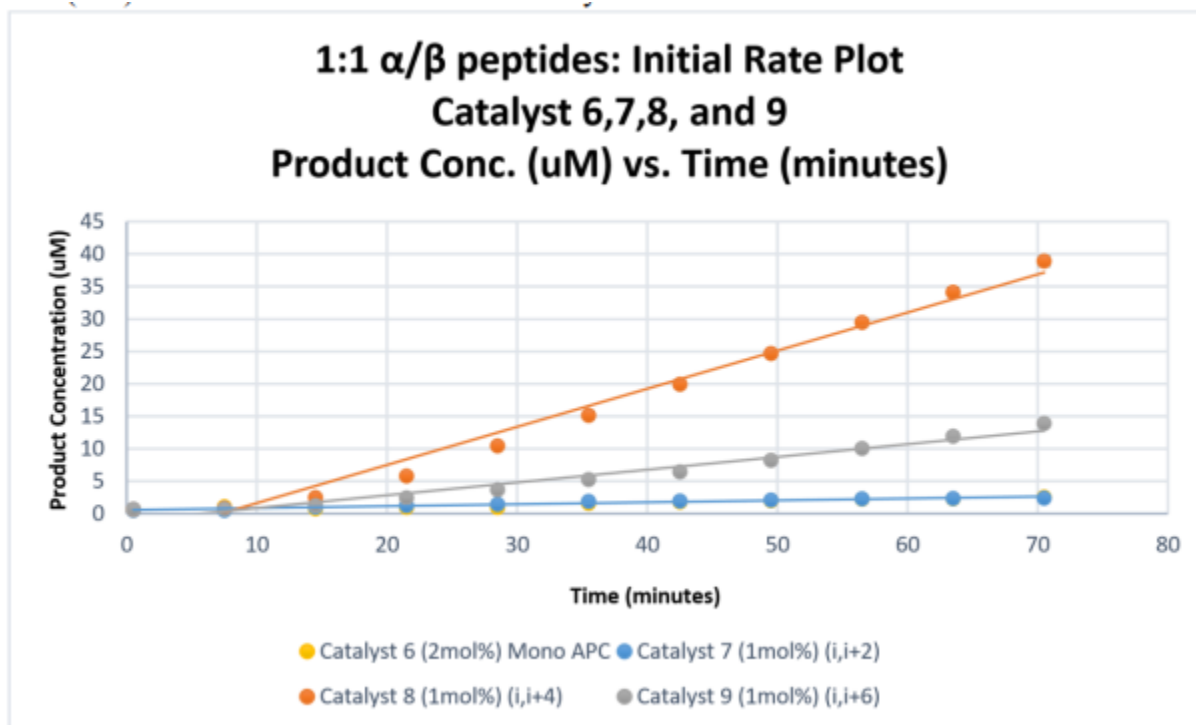
Figure 38. Reaction progress data for the crossed aldol reaction in the presence of 1:1 α/β-peptide **6**, **7**, **8**, or **9** between 0.5 and 70.5 minutes after catalyst addition. Each reaction was run in triplicate, and error bars denote standard deviation among product concentration measurements at a given time point. Reaction conditions are described above. Mono-APC α/β-peptide **6** was used at 2 mol % relative to the aldehyde starting materials, while each of the bis-APC α/β-peptides was used at 1 mol %. Therefore, the total concentration of APC residues was constant across these reactions.

Peptide	Rate(1)	Rate(2)	Rate(3)	Avg Rate (µM/minutes)	StDev (µM/minutes)
6	0.0308	0.0237	0.0309	0.028	0.002
7	0.046	0.024	0.018	0.029	0.01
8	0.598	0.568	0.597	0.587	0.01
9	0.191	0.202	0.197	0.197	0.003
Peptide	vREL (1)	vREL(2)	vREL(3)	Avg vREL	StDev vREL
6	n/a	n/a	n/a	Control Peptide	n/a
7	1.61	0.853	0.642	1.03	0.29
8	21.0	19.9	20.9	20.6	0.34
9	6.71	7.09	6.92	6.91	0.11

Figure 39. Initial rates measured for each reaction with catalysts **6**, **7**, **8**, and **9**, along with the average v_{REL} and standard deviation for **7**, **8**, and **9** (1 mol %) relative to mono-APC catalyst **6** (2 mol %).
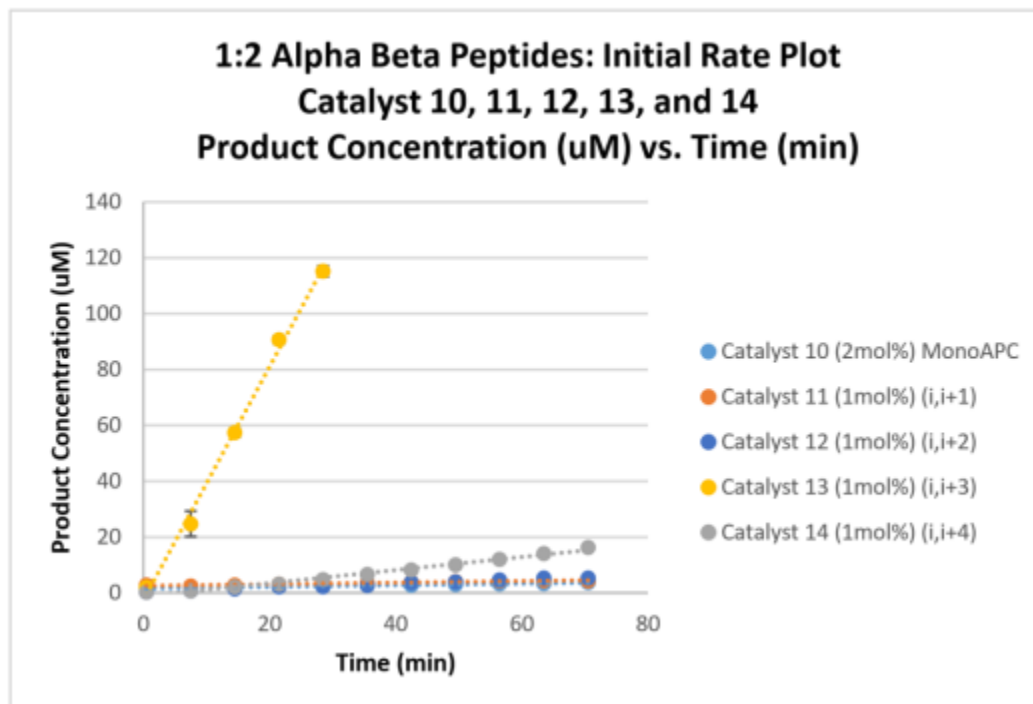
Figure 40. Reaction progress data for the crossed aldol reaction in the presence of 1:2 α/β-peptides **10**, **11**, **12**, **13**, and **14**. For **10**, **11** and **12**, reaction progress was monitored between 0.5 and 70 minutes after catalyst addition. For peptide **13**, reaction progress was monitored up to 1 % reaction completion (< 30 min). Each reaction was run in triplicate, and error bars denote standard deviation among product concentration measurements at a given time point. Reaction conditions are described above. Mono-APC 1:2 α/β-peptide **10** was used at 2 mol % relative to the aldehyde starting materials, while each of the bis-APC 1:2 α/β-peptides was used at 1 mol %. Therefore, the total concentration of APC residues was constant across these reactions. The maximum amount of product detected, 112 μM, corresponds to 1 % yield.

Peptide	Rate(1)	Rate(2)	Rate(3)	Rate (4)	Rate(5)	Rate(6)	Rate(7)	Avg Rate (µM/minutes)	StDev (µM/minutes)
10	0.12	0.15	0.08	0.12	0.0195	0.02	0.03	0.0293	0.003
11	0.047	0.011	0.053					0.037	0.01
12	0.065	0.0842	0.0781					0.076	0.006
13	3.99	4.33	3.99	4.37	4.21			4.18	0.08
14	0.24	0.24	0.22					0.233	0.01

Peptide	vREL (1)	vREL(2)	vREL(3)	vREL(4)	vREL(5)	vREL(6)	vREL(7)	Avg vREL	StDev vREL
10	n/a	n/a	n/a	n/a	n/a	n/a	n/a	Control Peptide	n/a
11	1.60	0.38	1.8					1.27	0.45
12	2.2	2.9	2.7					2.59	0.19
13	136.2	147.8	136.1	149.3	143.8			142.6	2.8
14	8.12	8.20	7.49					7.94	0.23

Figure 41. Initial rates measured for each reaction with catalysts **10**, **11**, **12**, **13**, and **14**, along with the average v_{REL} and standard deviation for **11**, **12**, **13**, and **14** (1 mol %) relative to mono-APC catalyst **10** (2 mol %). The first four rates reported for mono-APC peptide **10** are from one synthetic batch of the catalyst, while the last three reported rates are from a separate batch of the catalyst.
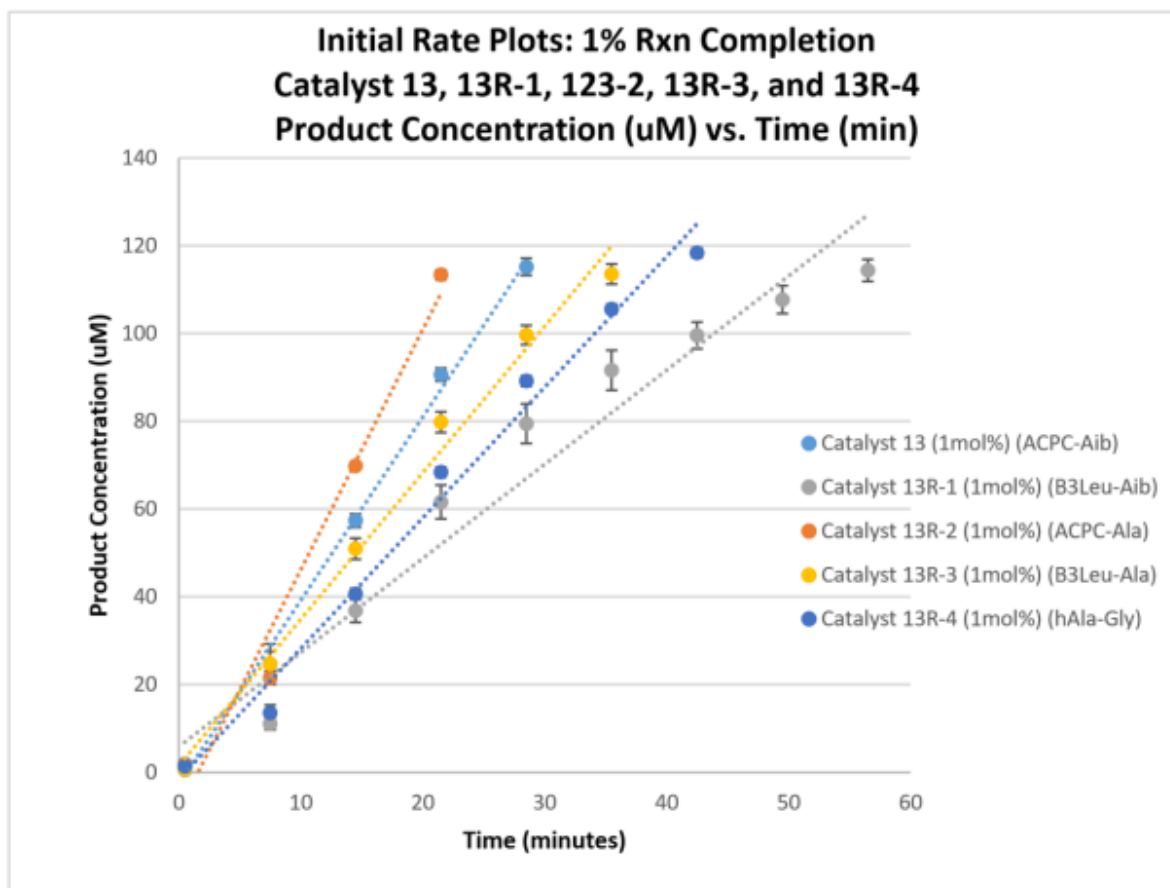
Figure 42. Reaction progress data for the crossed aldol reaction in the presence of 1:2 α/β-peptides **13**, **13R-1**, **13R-2**, **13R-3**, **13R-4**, and **13R-5** up to 1 % reaction completion. Each reaction was run in triplicate, and error bars denote standard deviation among product concentration measurements at a given time point. Reaction conditions are described above. Mono-APC 1:2 α/β-peptide **10** was used at 2 mol % relative to the aldehyde starting materials, while each of the bis-APC 1:2 α/β-peptides was used at 1 mol %. Therefore, the total concentration of APC residues was constant across these reactions.

Peptide	Rate(1)	Rate(2)	Rate(3)	Rate (4)	Rate(5)	Avg Rate (µM/minutes)	StDev (µM/minutes)
13	3.9898	4.3297	3.9869	4.3736	4.212	4.1784	0.081965206
13R-1	2.0804	2.1416	2.2138			2.145266667	0.038552879
13R-2	5.276	5.6177	5.336			5.4099	0.105333803
13R-3	3.175	3.3213	3.5159			3.3374	0.098738054
13R-4	2.9764	2.9574	3.0016			2.978466667	0.012801215

Peptide	vREL (1)	vREL(2)	vREL(3)	vREL(4)	vREL(5)	Avg vREL	StDev vREL
13	136.1706	147.771331	136.07167	149.2696246	143.7542662	142.6075085	2.797447305
13R-1	71.00341	73.0921502	75.556314			73.21729238	1.315797903
13R-2	180.0683	191.730375	182.11604			184.6382253	3.595010332
13R-3	108.3618	113.354949	119.99659			113.9044369	3.369899458
13R-4	101.5836	100.935154	102.44369			101.6541524	0.436901543

Figure 43. Initial rates measured for each reaction with catalysts **13**, **13R-1**, **13R2**, **13R-3**, **13R-4**, and **13R-5**, along with the average v_{REL} and standard deviation for **13**, **13R-1**, **13R-2**, **13R-3**, **13R-4**, and **13R-5** (1 mol %) relative to mono-APC peptide **10** (2 mol %).
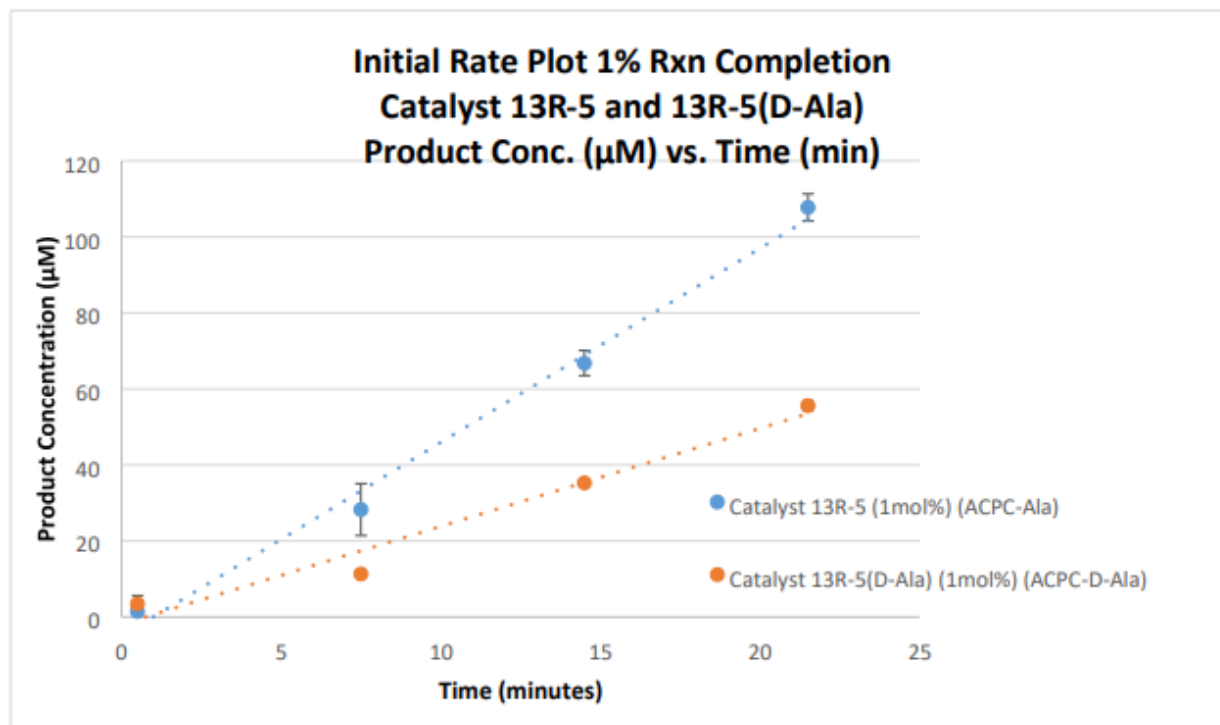
Figure 44. Reaction progress data for the crossed aldol reaction in the presence of 1:2 α/β-peptides **13R-5** and **13R-5(D-Ala)**. Each reaction was run in triplicate, and error bars denote standard deviation among product concentration measurements at a given time point. Reaction conditions are described above. At the final time point, 21.5 minute, **13R-5** displayed 1 % product formation, while diastereomer **13R-5(D-Ala)** displayed only 0.5 % product formation.

Peptide	Rate(1)	Rate(2)	Rate(3)	Rate(4)	Avg Rate (μM/minute	StDev (μM/minutes)
13R-5	4.94	4.65	5.48	5.35	5.10	0.19
13R-5(D-Ala)	2.30	2.77	2.67		2.58	0.14
Peptide	vREL (1)	vREL(2)	vREL(3)	vREL(4)	Avg vREL	StDev vREL
13R-5	169	159	187	183	174.2	6.5
13R-5(D-Ala)	78	94	91		88.0	4.9

Figure 45. Initial rates measured for each reaction with catalysts **13R-5** and **13R5(D-Ala)**, along with the average v_{REL} and standard deviation for **13R-5** and **13R-5(D-Ala)** (1 mol %) relative to 10 (2 mol %).
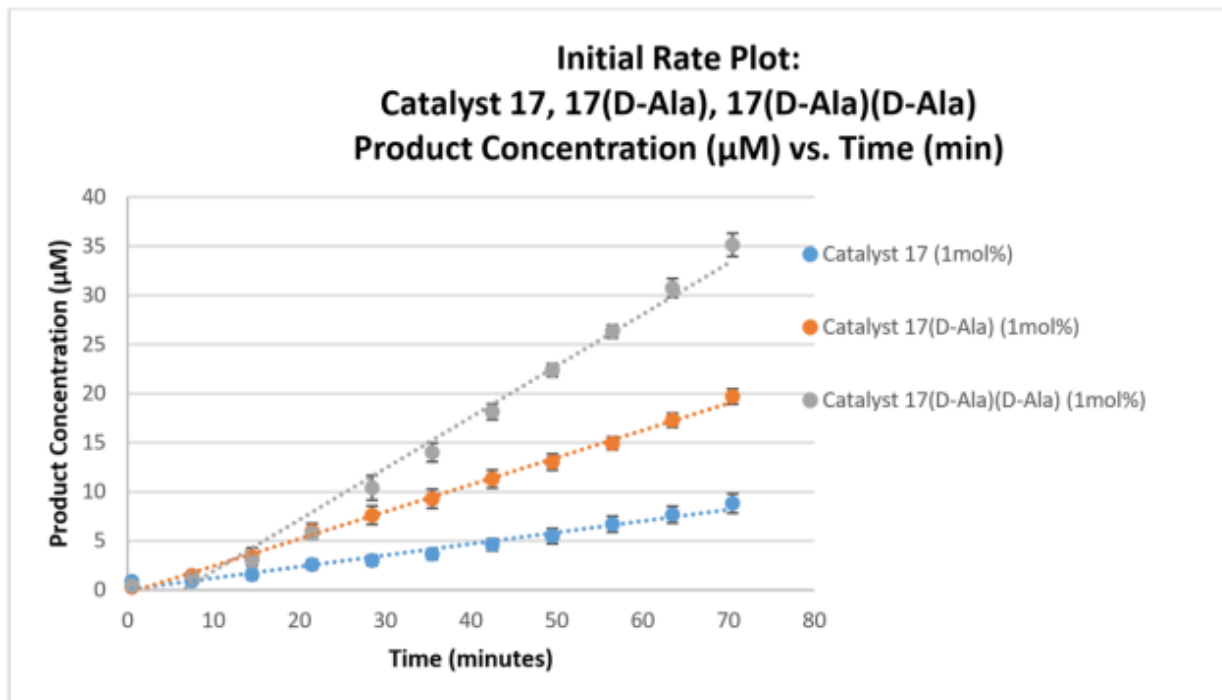
Figure 46. Reaction progress data for the crossed aldol reaction in the presence of 1:2 α/β-peptides **17**, **17(D-Ala)**, and **17(D-Ala)(D-Ala)** between 0.5 and 70.5 minutes after catalyst addition. Each reaction was run in triplicate, and error bars denote standard deviation among product concentration measurements at a given time point. Reaction conditions are described above.

Peptide	Rate(1)	Rate(2)	Rate(3)	Rate(4)	Rate(5)	Avg Rate (μM/minutes)	StDev (μM/minutes)
17	0.121	0.148	0.080	0.116	0.116	0.116	0.01
17(D-Ala)	0.187	0.307	0.292	0.255	0.286	0.265	0.02
17(D-Ala)(D-Ala)	0.5518	0.481	0.5345			0.522	0.02

Peptide	vREL (1)	vREL(2)	vREL(3)	vREL(4)	vREL(5)	Avg vREL	StDev vREL
17	4.11	5.04	2.74	3.97		3.96	0.47
17(D-Ala)	6.38	10.48	9.98	8.69	9.74	9.05	0.73
17(D-Ala)(D-Ala)	18.8	16.4	18.2			17.8	0.73

Figure 47. Initial rates measured for each reaction with catalysts **17**, **17(D-Ala)**, and **17(D-Ala)(D-Ala)** along with the average v_{REL} and standard deviation for **17**, **17(D-Ala)**, and **17(D-Ala)(D-Ala)** (1 mol %) relative to **10** (2 mol %).
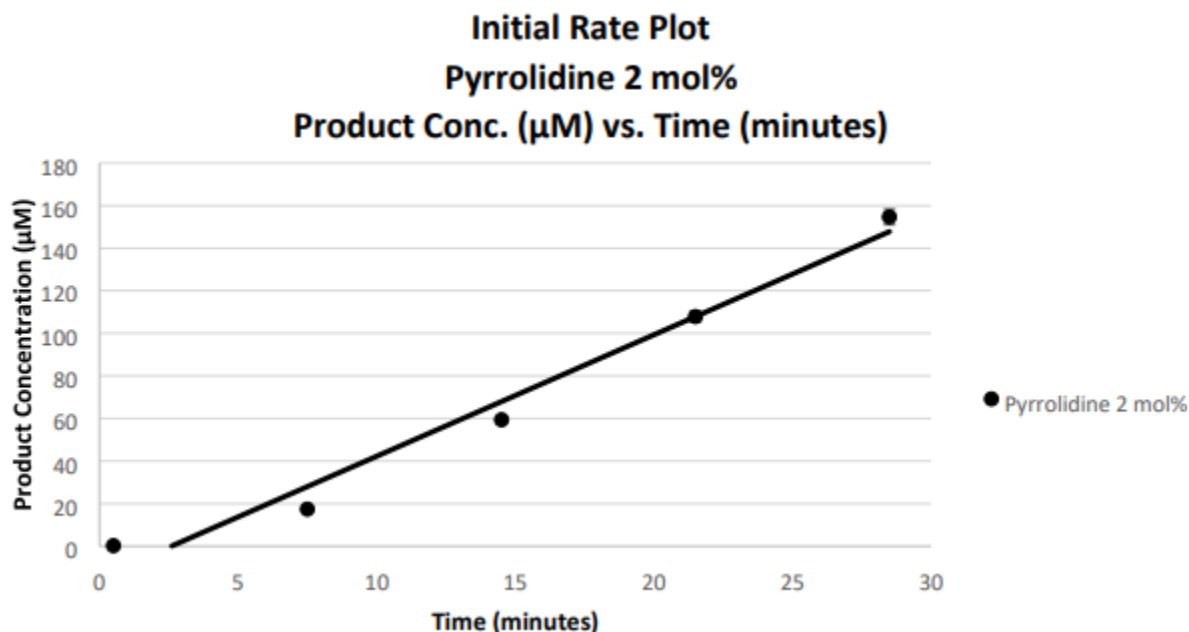
Figure 48. Initial rate for pyrrolidine. The initial rate was monitored to 1 % reaction completion. Experiments were run in triplicate, with error bars denoting standard deviation. Experiments run using general procedure for initial rates, substituting a peptide catalyst for pyrrolidine. The key denotes the catalyst and the mol % which it was loaded at. This initial rate provides a basis for comparing the reactivity of pyrrolidine with the reactivity of mono-APC peptide **10** (2 mol %).

Pyrrolidine 2 mol%				
Rate (1)	Rate (2)	Rate (3)	Avg Rate (µM/minutes)	StDev (µM/minutes)
5.5	5.7	5.9	5.71	0.1
vREL (1)	vREL (2)	vREL (3)	Avg vREL	StDev vREL
186.6	195.0	202.6	194.7	4.6

Figure 49. Initial rates measured for each reaction with pyrrolidine along with the average v_{REL} and standard deviation for pyrrolidine (2 mol %) relative to mono-APC 1:2 α/βpeptide **10** (2 mol %). The data shows that pyrrolidine is intrinsically more reactive than an APC residue.
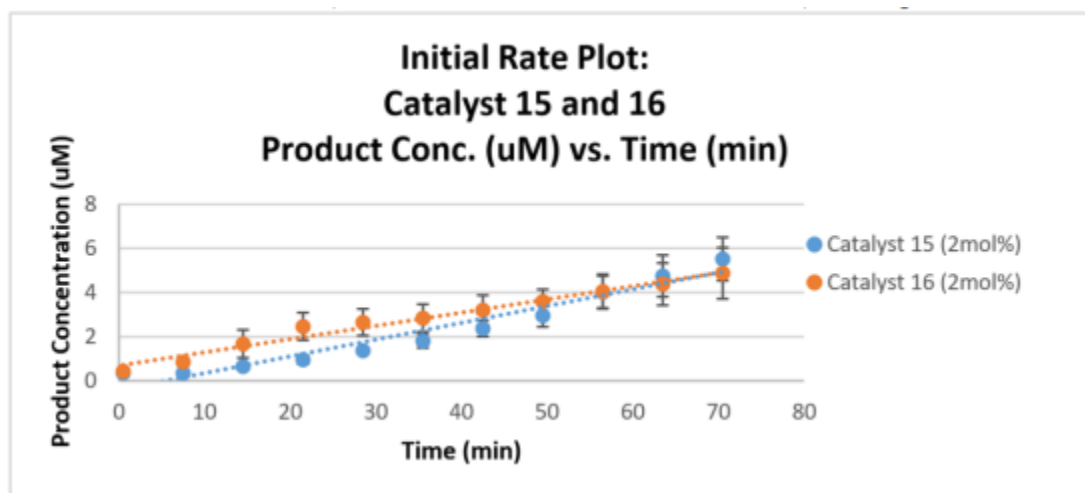
Figure 50. Reaction progress data for the crossed aldol reaction in the presence of 1:2 α/β-peptide **15** or **16** between 0.5 and 70.5 minutes after catalyst addition. Each reaction was run in triplicate, and error bars denote standard deviation among product concentration measurement at a given time point. Reaction conditions are described above.

Peptide	Rate(1)	Rate(2)	Rate(3)	Avg Rate (µM/minutes)	StDev (µM/minutes)
15	0.103	0.066	0.059	0.076	0.01
16	0.085	0.051	0.044	0.060	0.01
Peptide	vREL (1)	vREL(2)	vREL(3)	Avg vREL	StDev vREL
15	3.52	2.24	2.02	2.59	0.47
16	2.90	1.73	1.73	2.12	0.39

Figure 51. Initial rates measured for each reaction with catalysts **15** and **16** along with the average v_{REL} and standard deviation for **15** and **16** (2 mol %) relative to **10** (2 mol %).
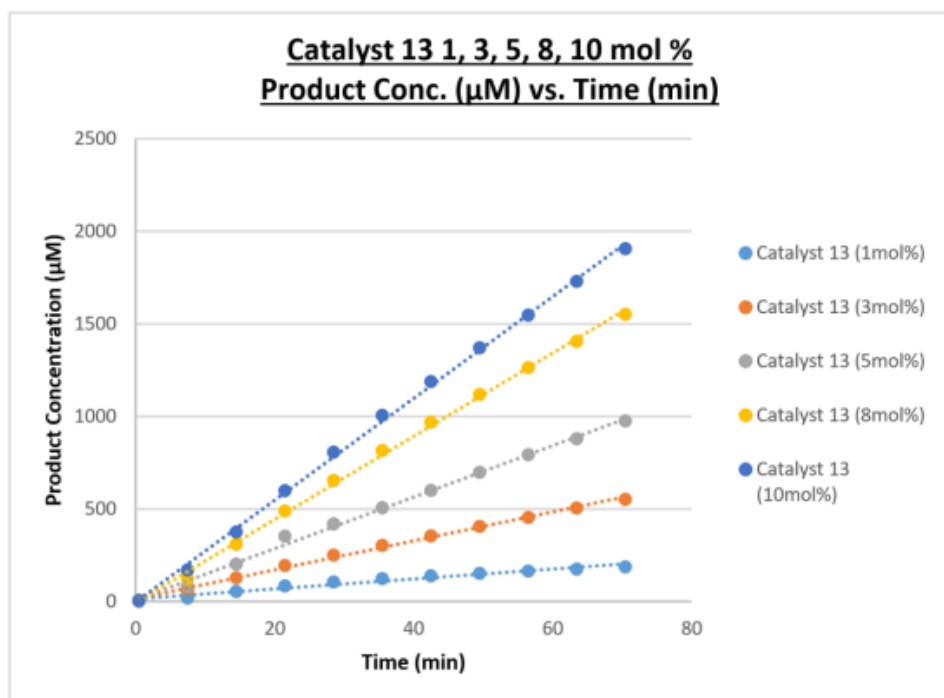
Figure 52. Reaction progress data for the crossed aldol reaction in the presence of 1:2 α/β-peptide: **13** between 0.5 and 70.5 minutes after catalyst addition. The mol % loading of **13** was varied from between 1 and 10 mol %.
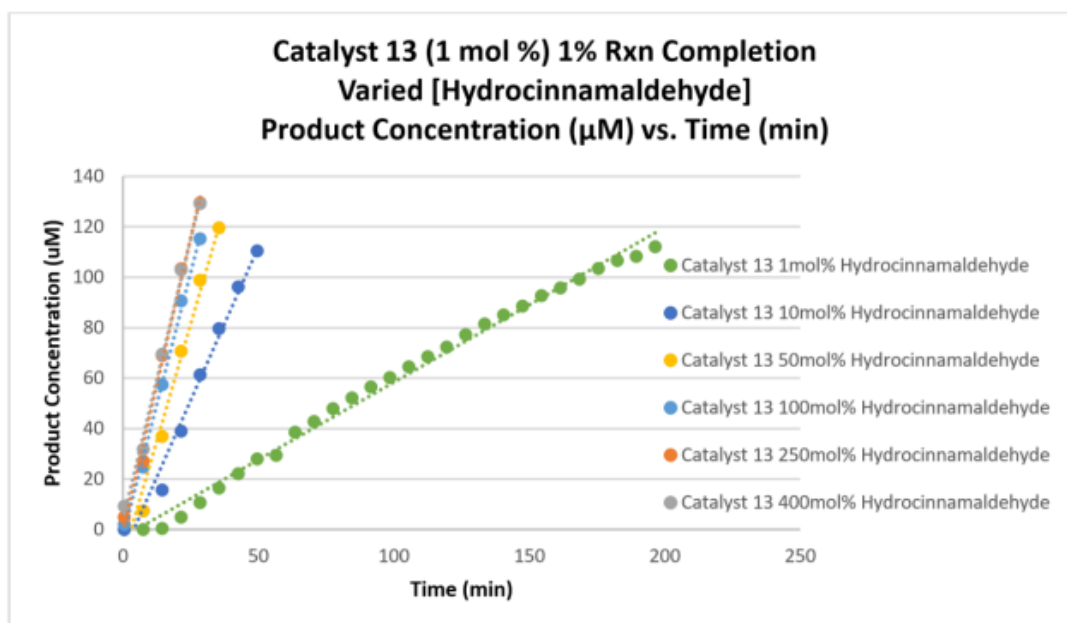
Figure 53. Reaction progress data for the crossed aldol reaction, to 1% product formation, in the presence of 1:2 α/β-peptide **13**, with different starting concentrations of hydrocinnamaldehdye. Lower amounts of hydrocinnamaldehyde resulted in a longer time to reach 1 % product formation. Hydrocinnamaldehyde was varied between 1 and 400 mol %, relative to formaldehyde concentration, which was held constant. For example, 100 mol % hydrocinnamaldehyde consists of a 1:1 ratio of hydrocinnamaldehyde and formaldehyde.

Mol% Hydrocinnamaldehyde	Rate (µM/minutes)
1	0.610
10	2.39
50	3.70
100	4.18
250	4.65
400	4.44

Figure 54. Initial rate (µM/min) vs. mol % hydrocinnamaldehyde relative to formaldehyde. Observed increase in initial rate with increasing hydrocinnamaldehyde to 100 mol % (1:1 hydrocinnamaldehyde:formaldehyde), followed by a plateau in rate. Catalyst **13** was used for each reaction.
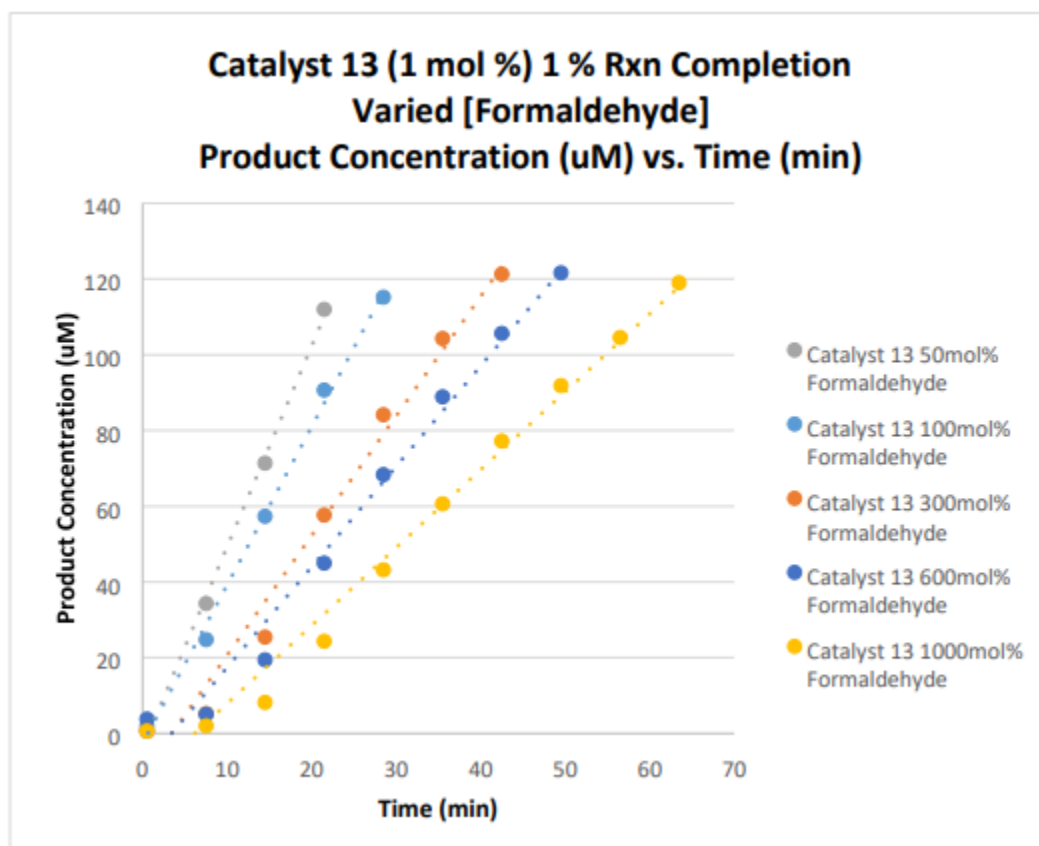
Figure 55. Reaction progress data for the crossed aldol reaction in the presence of 1:2 α/β-peptide **13** to 1 % product formation. Formaldehyde was varied from 50 mol % to 1000 mol %, relative to hydrocinnamaldehyde, which was held constant.

Mol% Formaldehyde	Rate (µM/minutes)
50	5.067
100	4.1784
300	3.4441
600	2.889
1000	2.217

Figure 56. Initial rate (µM/minutes) vs. mol % formaldehyde. The data reveal an inhibitory effect on initial rate of high formaldehyde concentrations. Catalyst **13** was used for each reaction.

2.5.5 General Procedure for Circular Dichroism Measurements

All CD measurements were performed on an Aviv Biomedical model 420 CD spectrometer in 1

mm quartz strain-free cuvettes (Helma). CD measurements were obtained for catalysts **13** and **17**

at 120 µM and 600 µM in isopropanol. 370 µL total volume was used. These concentrations of

peptide correspond to the concentrations used for initial rate measurements (120 µM) and the

reaction used to evaluate preparative capability (600 µM). Prior to each measurement an

isopropanol blank was recorded, which was linear across all wavelengths (185-260 nm).

Wavelength scans were collected from 260 nm to 190 nm with a 1 nm bandwidth and 10 second

averaging time. All values for which the dynode reached >600 V were excluded during data work

up. Data were converted to ellipticity (deg cm^2 $dmol^{-1}$) according to the equation: $[\Theta]$ =

$\psi(1000/nlc)$ where ψ is the CD signal in degrees, n is the number of amides, l is the path length in

centimeters, and c is the peptide concentration in decimoles per cm^3.
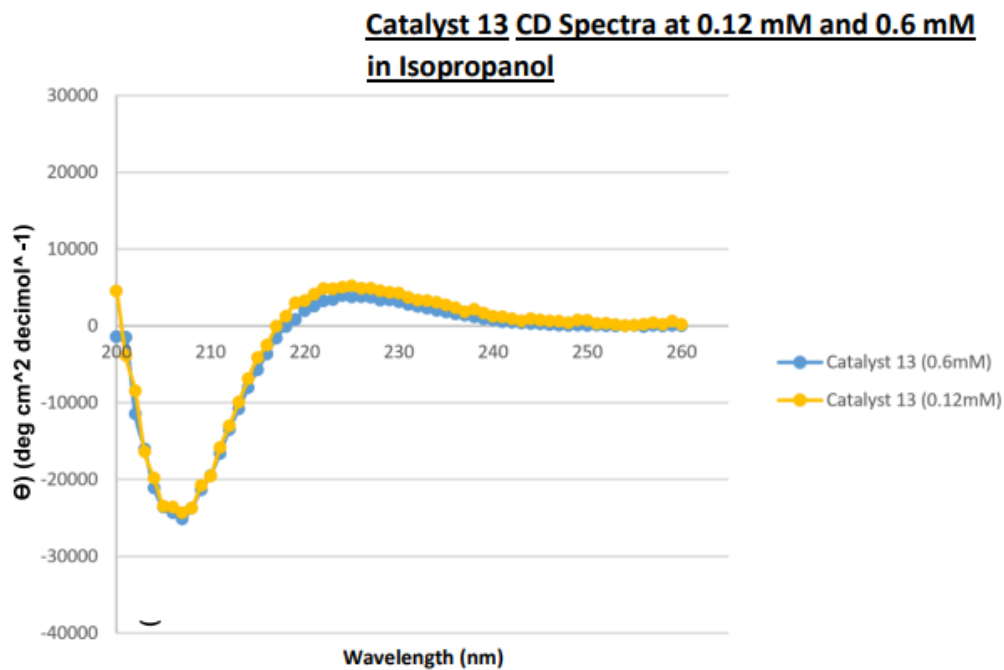
Figure 57. CD spectra is of catalyst **13** at 0.12 mM and 0.6 mM, normalized for concentration and the number of amide groups.
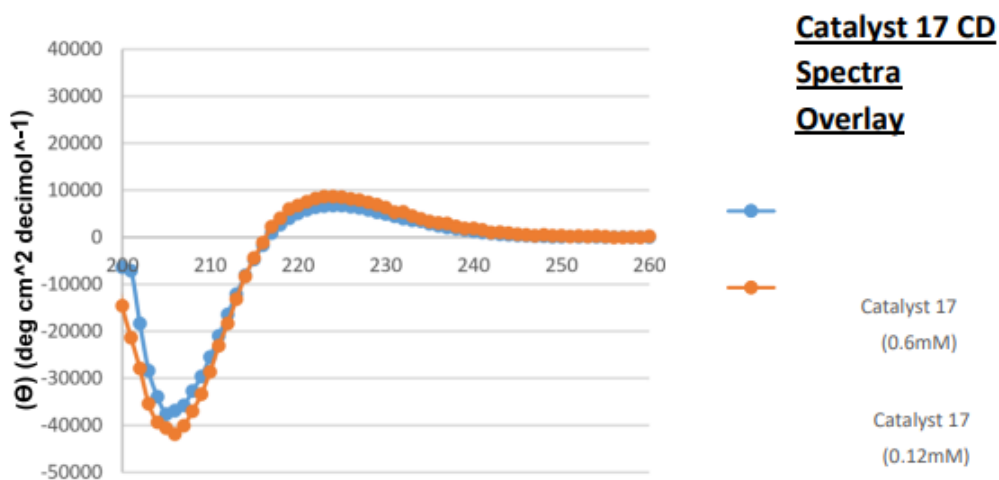
Figure 58. CD spectra of catalyst **17** at 0.12 mM and 0.6 mM, normalized for concentration and the number of amide groups.

2.5.6 Calibration Curves for Initial Rate Measurements and Percent Yield Determination
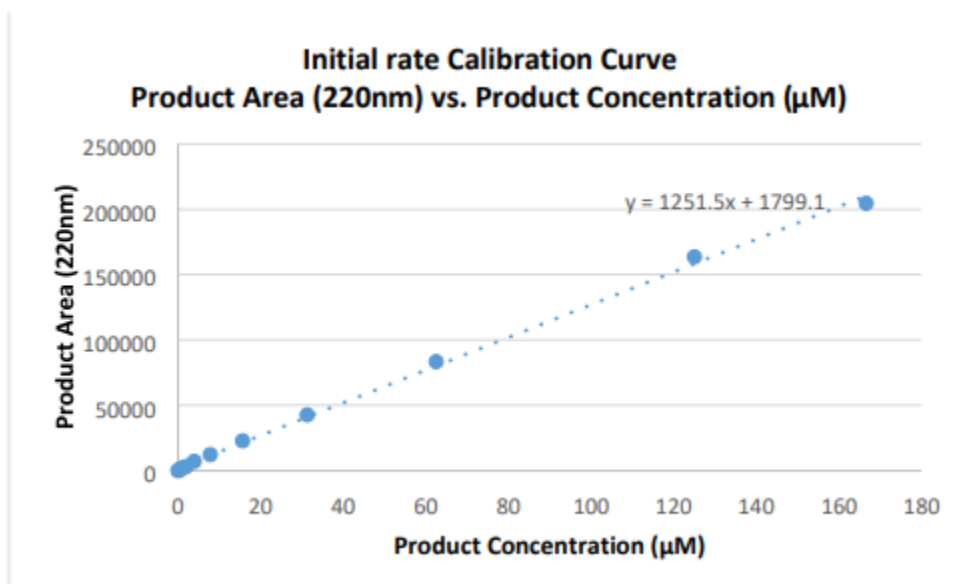
Figure 59. Calibration curve for UPLC-based concentration determination of 2-benzylacrylaldehyde, for reactions used to determine initial rate.
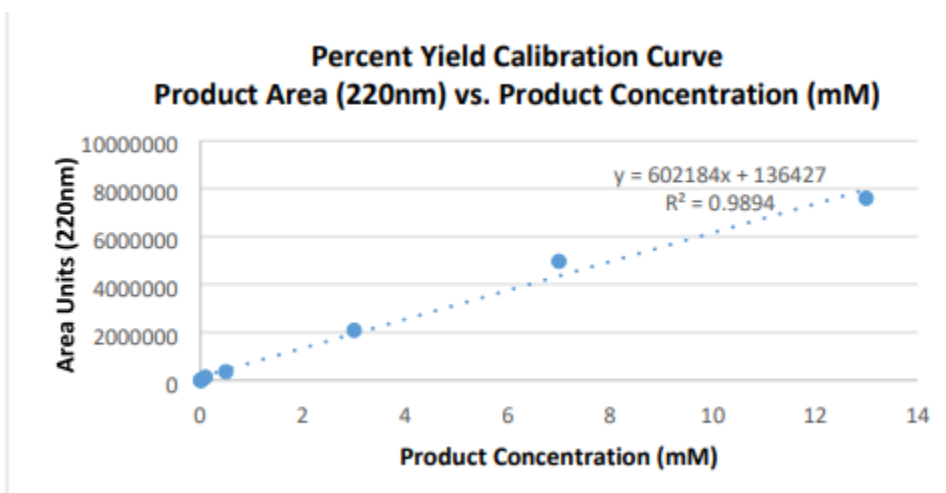
Figure 60. Calibration curve for UPLC-based concentration determination of 2-benztlacrylaldehyde, for reactions used to follow a catalytic crossed aldol reaction that proceeds to completion.
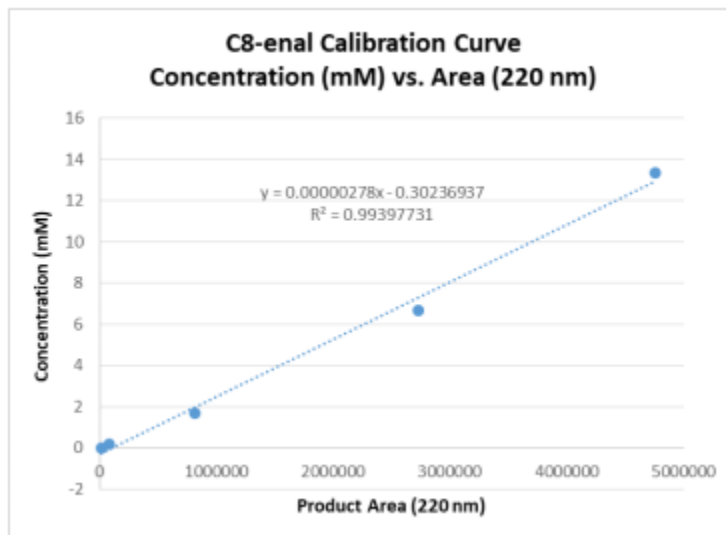
Figure 61. Calibration curve for UPLC-based concentration determination of (E)-cyclohept-1-enecarbaldehyde, for reactions used to follow a catalytic foldamer catalyzed aldol cyclization. Synthetic standard of (E)-cyclohept-1-enecarbaldehyde matches literature values.[48]
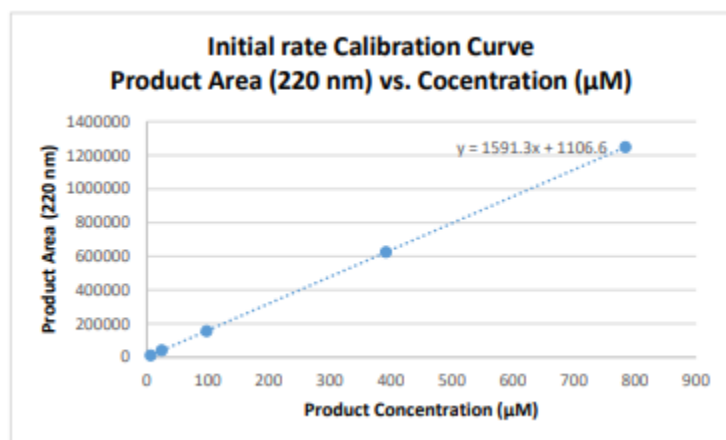
Figure 62. Calibration curve for UPLC-based concentration determination of 2-methylenehexanal for reactions used to determine initial rate.

2.5.7 UPLC evidence for build-up of catalyst –derived intermediate(s) under crossed aldol reaction conditions.
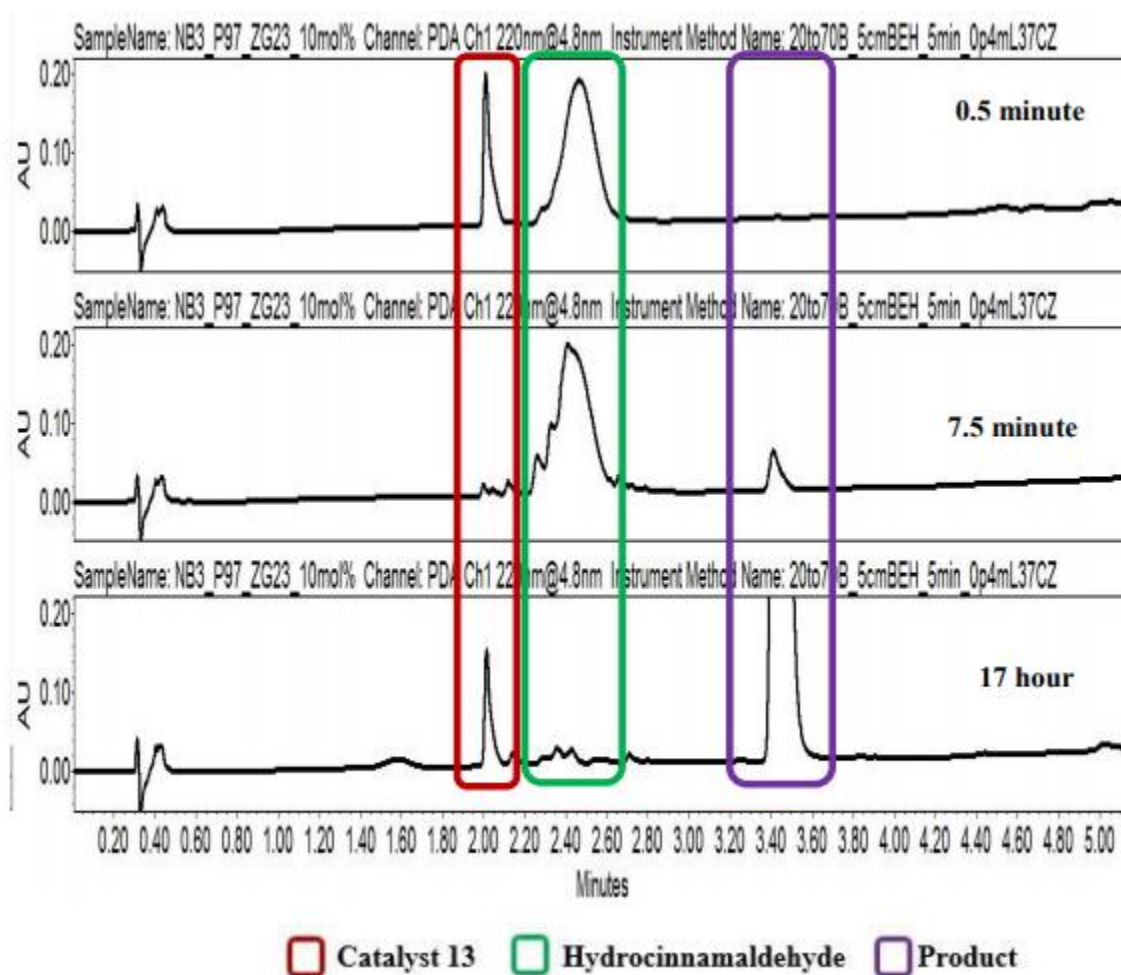
Figure 63. UPLC chromatograms at 0.5 minute, 7.5 minute and 17 hour reaction times for the crossed aldol reaction catalyzed by 10 mol % **13**; quantitative yield is ultimately achieved. The peak corresponding to catalyst **13** is highlighted in red. The peaks highlighted in green include hydrocinnamaldehyde and unidentified intermediates. The peak highlighted in purple is the α-methylenated product. Each chromatogram has been scaled to the same y-axis value, which causes the product peak in the final trace to be off-scale. The peak for **13** quickly disappears after exposure to the mixture of formaldehyde and hydrocinnamaldehyde. As product formation nears completion, the peak corresponding to **13** reappears. We believe that transiently functionalized derivatives of **13** elute in the region within the green square.
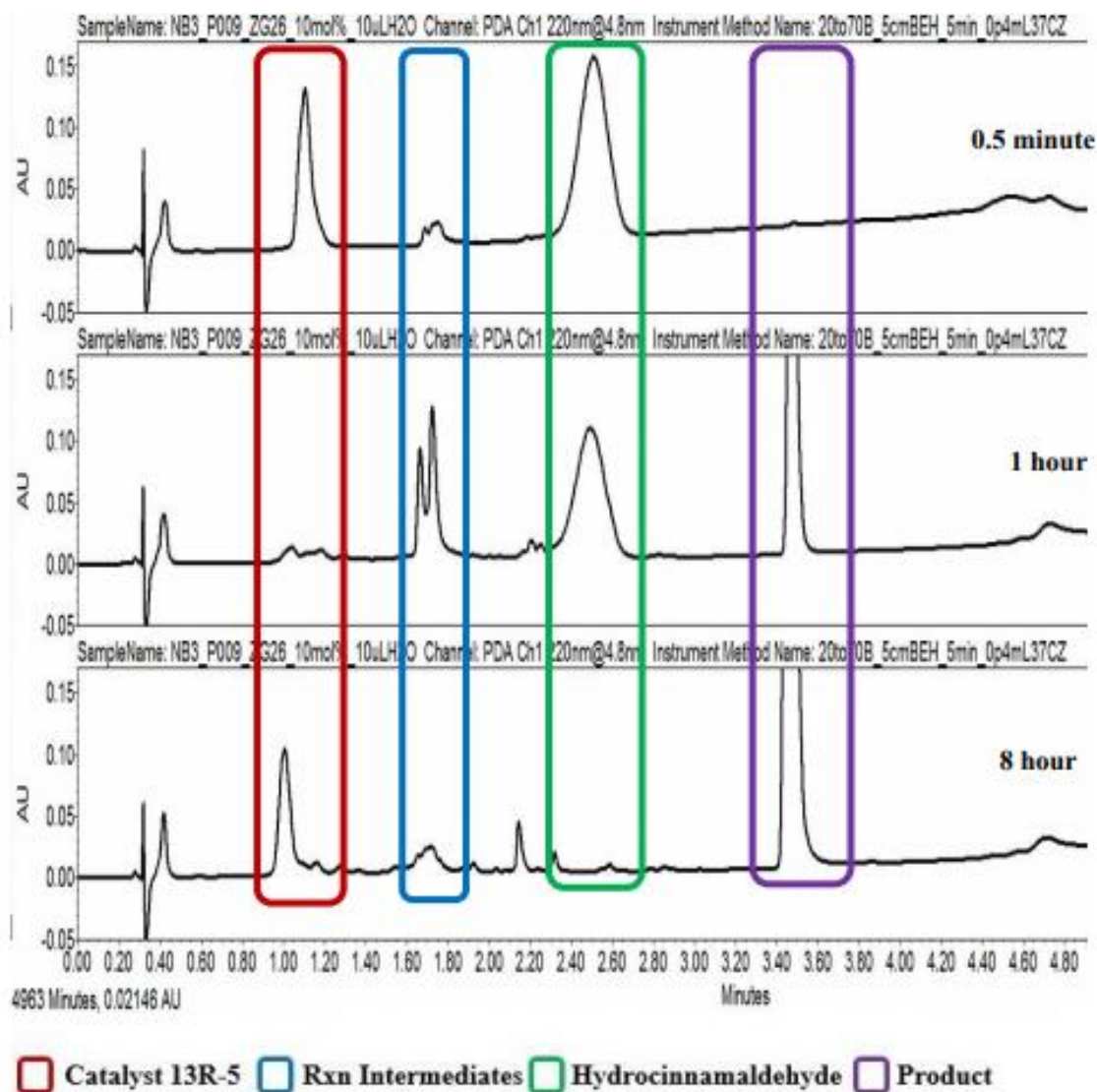
Figure 64. UPLC chromatograms at 0.5 minute, 1 hour and 8 hour reaction times for the crossed aldol reaction catalyzed by 10 mol % **13R-5**; quantitative yield is ultimately achieved. Highlighted in red is the peak corresponding to **13R-5**. Highlighted in blue are transient intermediates, presumably derived from **13R-5**. Highlighted in green is hydrocinnamaldehyde. Highlighted in purple is the alpha methylenated product. Each chromatogram has been scaled to the same y-axis value, which causes the product peak to be off scale. The peak for **13R-5** quickly disappears after exposure to the mixture of formaldehyde and hydrocinnamaldehyde. As product formation nears completion, the peak corresponding to **13R-5** reappears. We believe that transiently functionalized derivatives of **13R-5** elute in the region within the blue square.
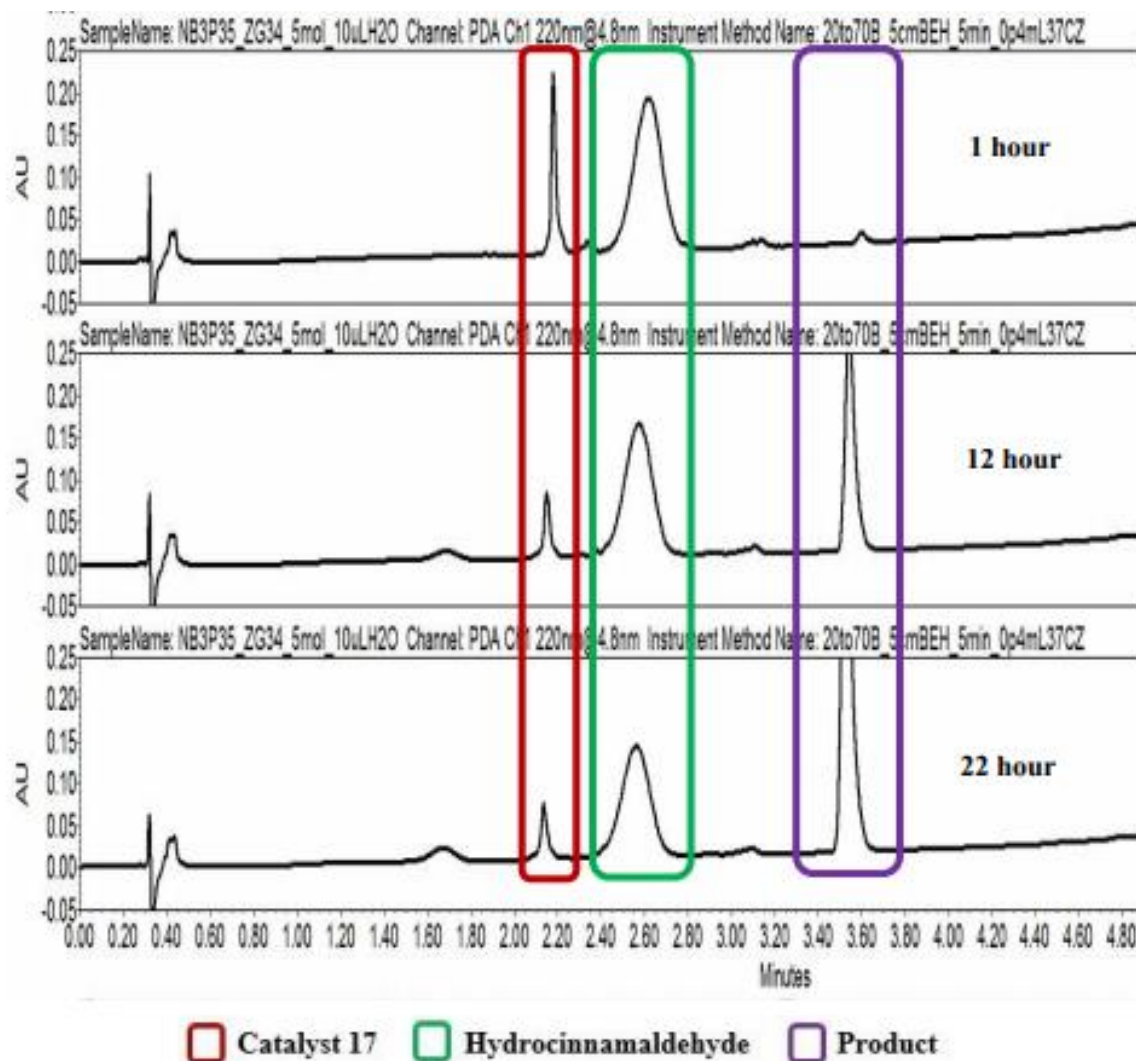
Figure 65. UPLC chromatograms at 1 hour, 12 hour and 22 hour reaction times for the crossed aldol reaction catalyzed by 5 mol % **17**. Highlighted in red is the peak corresponding to **17**. Highlighted in green is hydrocinnamaldehyde. Highlighted in purple is the alpha methylenated product. Each chromatogram has been scaled to the same y-axis value, which causes the product peak to be off scale. The peak for **17** slowly disappears after exposure to the mixture of formaldehyde and hydrocinnamaldehyde, and some still remains after 22 hours. We believe that this is evidence for the lack of transiently functionalized derivatives of **17** due to precluded catalytic action.
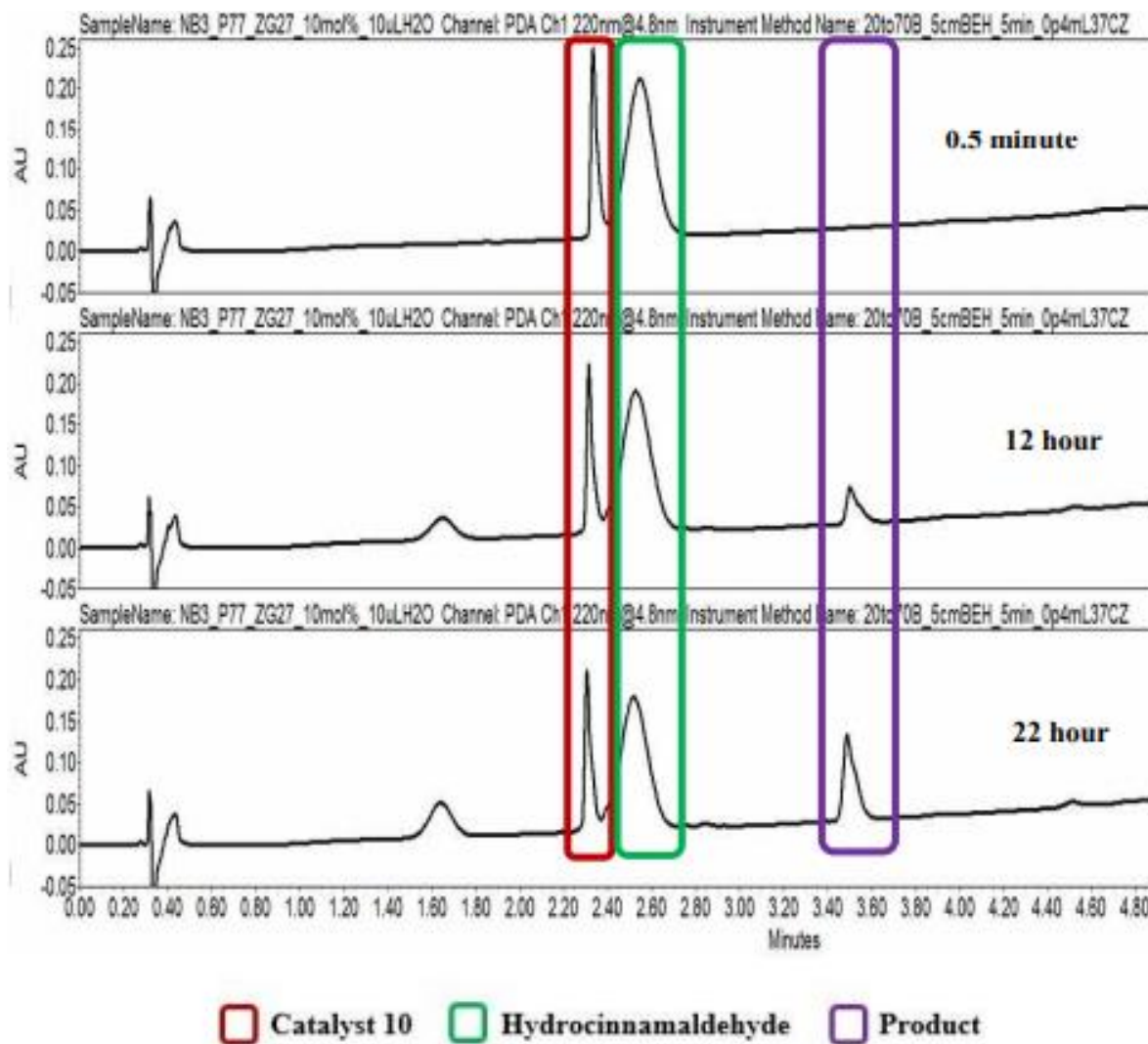
Figure 66. UPLC chromatograms at 0.5 minutes, 12 hour and 22 hour reaction times for the crossed aldol reaction catalyzed by 10 mol % **10**. Highlighted in red is the peak corresponding to **10**. Highlighted in green is hydrocinnamaldehyde. Highlighted in purple is the alpha methylenated product. Each chromatogram has been scaled to the same y-axis value. The peak for **10** remains after exposure to the mixture of formaldehyde and hydrocinnamaldehyde after 22 hours. We believe that this is evidence for the lack of transiently functionalized derivatives of **10**, which cannot form an intramolecular macrocycle due to the lack of a catalytic diad.
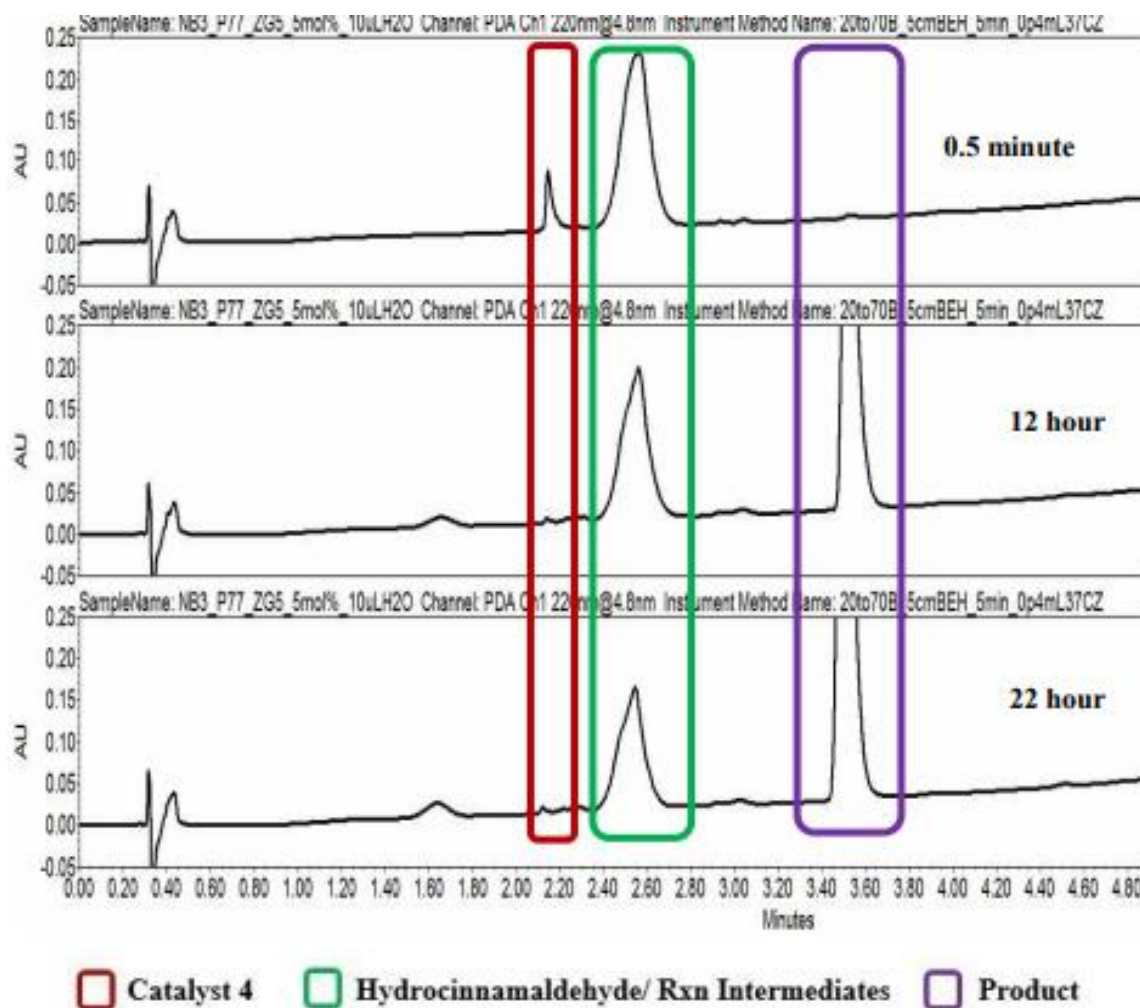
Figure 67. UPLC chromatograms at 0.5 minute, 12 hour and 22 hour reaction times for the crossed aldol reaction catalyzed by 5 mol % **4**. The peak corresponding to catalyst **4** is highlighted in red. The peaks highlighted in green include hydrocinnamaldehyde and unidentified intermediates. The peak highlighted in purple is the α-methylenated product. Each chromatogram has been scaled to the same y-axis value, which causes the product peak in the final trace to be off-scale. The peak for **4** quickly disappears after exposure to the mixture of formaldehyde and hydrocinnamaldehyde. We believe that transiently functionalized derivatives of **4** elute in the region within the green square.
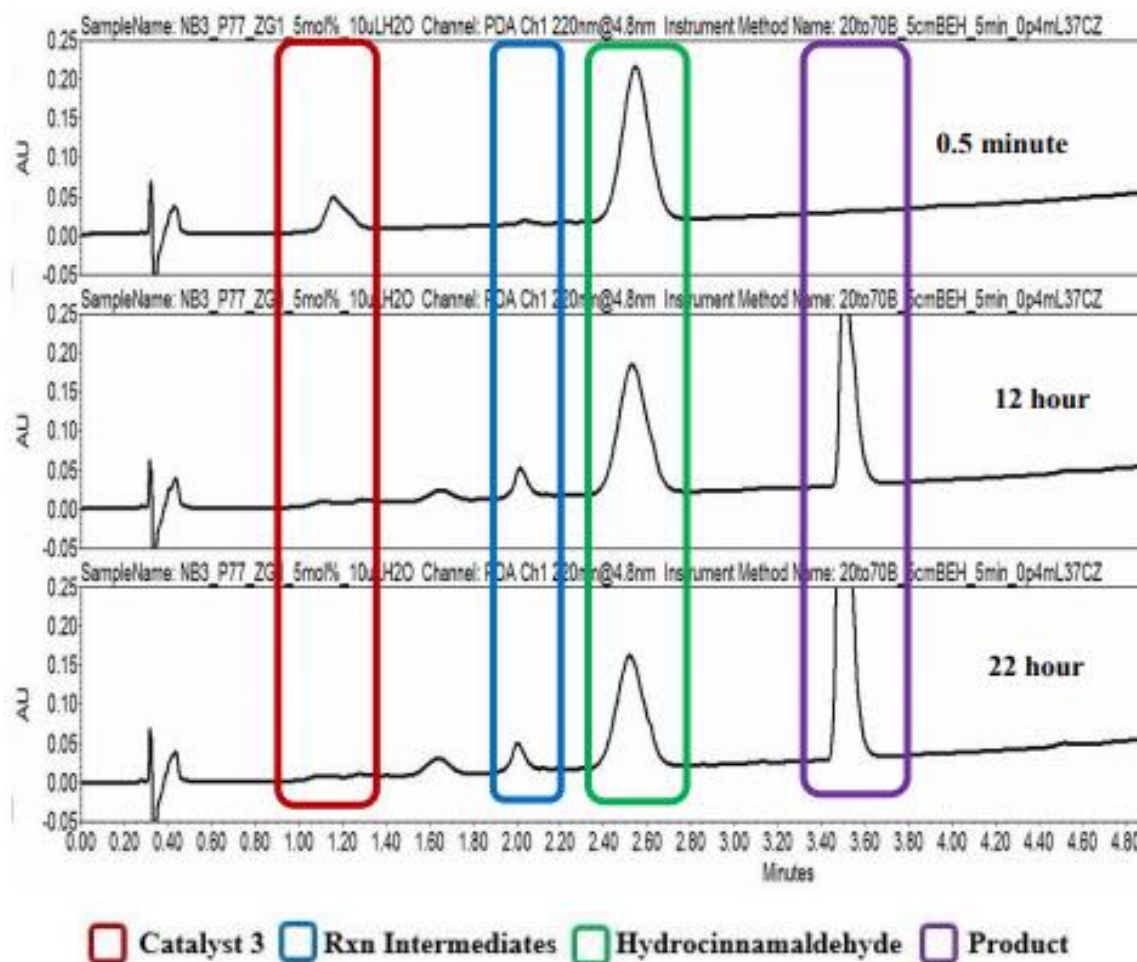
Figure 68. UPLC chromatograms at 0.5 minute, 12 hour and 22 hour reaction times for the crossed aldol reaction catalyzed by 5 mol % **3**. Highlighted in red is the peak corresponding to **3**. Highlighted in blue are reaction intermediates, presumably derived from **3**. Highlighted in green is hydrocinnamaldehyde. Highlighted in purple is the alpha methylenated product. Each chromatogram has been scaled to the same y-axis value, which causes the product peak to be off scale. The peak for **3** quickly disappears after exposure to the mixture of formaldehyde and hydrocinnamaldehyde. We believe that transiently functionalized derivatives of **3** elute in the region within the blue square.
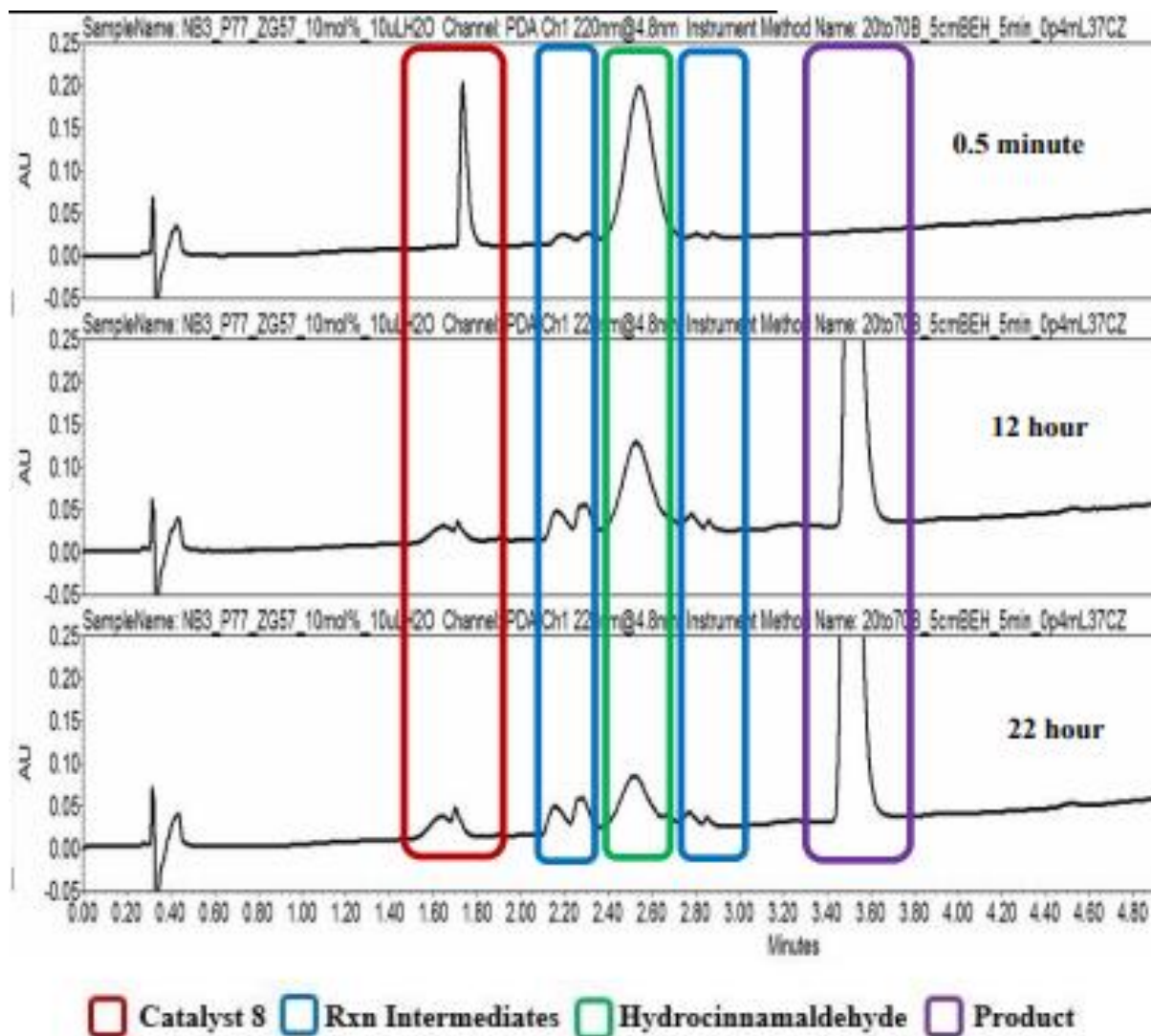
Figure 69. UPLC chromatograms at 0.5 minute, 12 hour and 22 hour reaction times for the crossed aldol reaction catalyzed by 10 mol % **8**. Highlighted in red is the peak corresponding to **8**. Highlighted in blue are reaction intermediates, presumably derived from **8**. Highlighted in green is hydrocinnamaldehyde. Highlighted in purple is the alpha methylenated product. Each chromatogram has been scaled to the same y-axis value, which causes the product peak to be off scale. The peak for **8** quickly disappears after exposure to the mixture of formaldehyde and hydrocinnamaldehyde. We believe that transiently functionalized derivatives of **8** elute in the region within the blue squares.
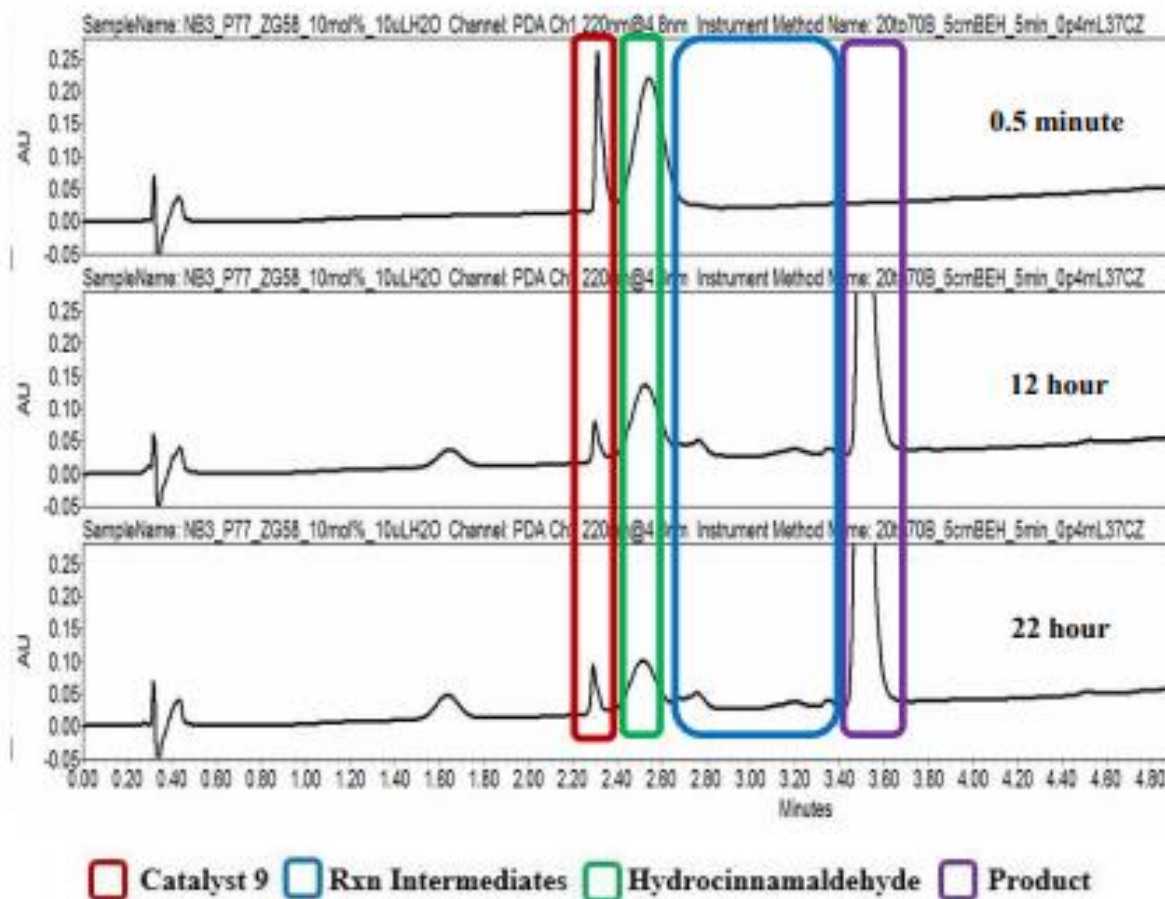
Figure 70. UPLC chromatograms at 0.5 minute, 12 hour and 22 hour reaction times for the crossed aldol reaction catalyzed by 10 mol % **9**. Highlighted in red is the peak corresponding to **9**. Highlighted in blue are reaction intermediates, presumably derived from **9**. Highlighted in green is hydrocinnamaldehyde. Highlighted in purple is the alpha methylenated product. Each chromatogram has been scaled to the same y-axis value, which causes the product peak to be off scale. The peak for **9** slowly disappears after exposure to the mixture of formaldehyde and hydrocinnamaldehyde, with some remaining after 22 hour.
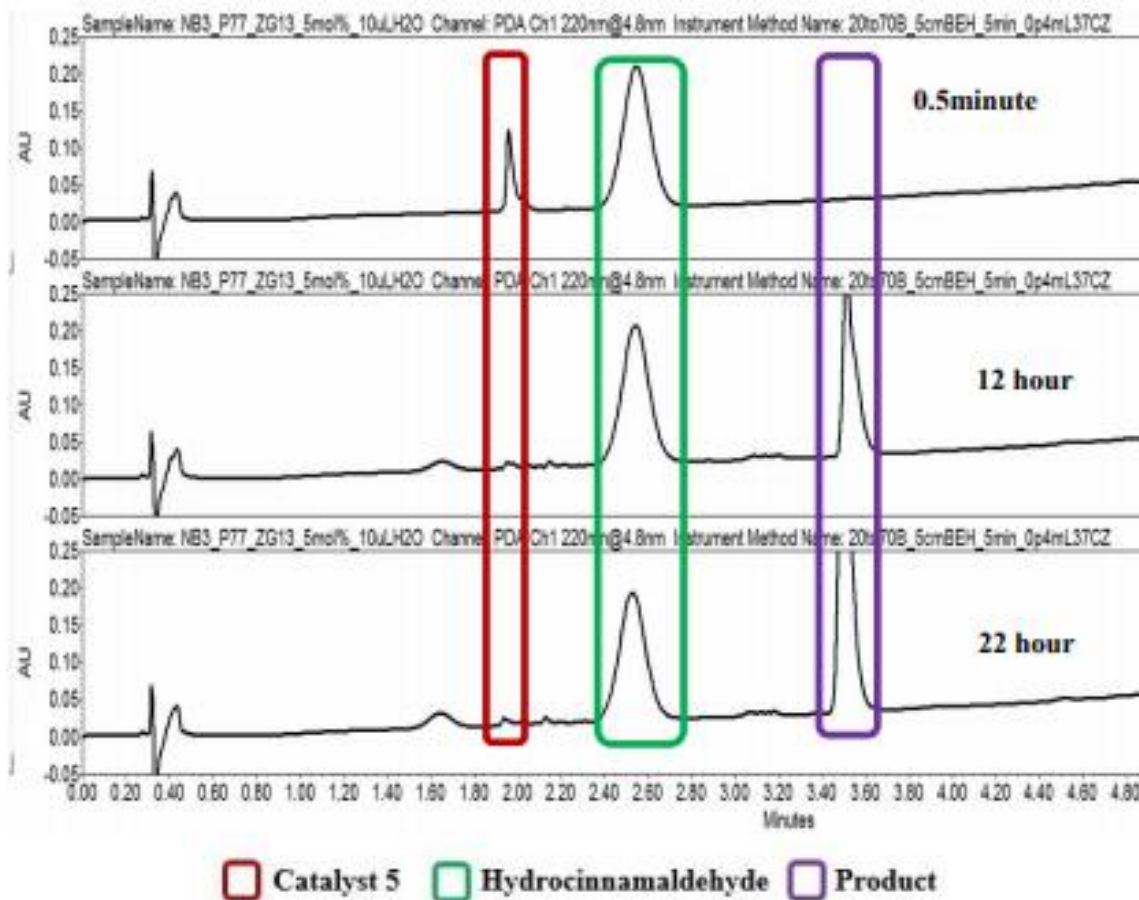
Figure 71. UPLC chromatograms at 0.5 minute, 12 hour and 22 hour reaction times for the crossed aldol reaction catalyzed by 5 mol % **5**. Highlighted in red is the peak corresponding to **5**. Highlighted in green is hydrocinnamaldehyde. Highlighted in purple is the alpha methylenated product. Each chromatogram has been scaled to the same y-axis value, which causes the product peak to be off scale. The peak for **5** disappears after exposure to the mixture of formaldehyde and hydrocinnamaldehyde.
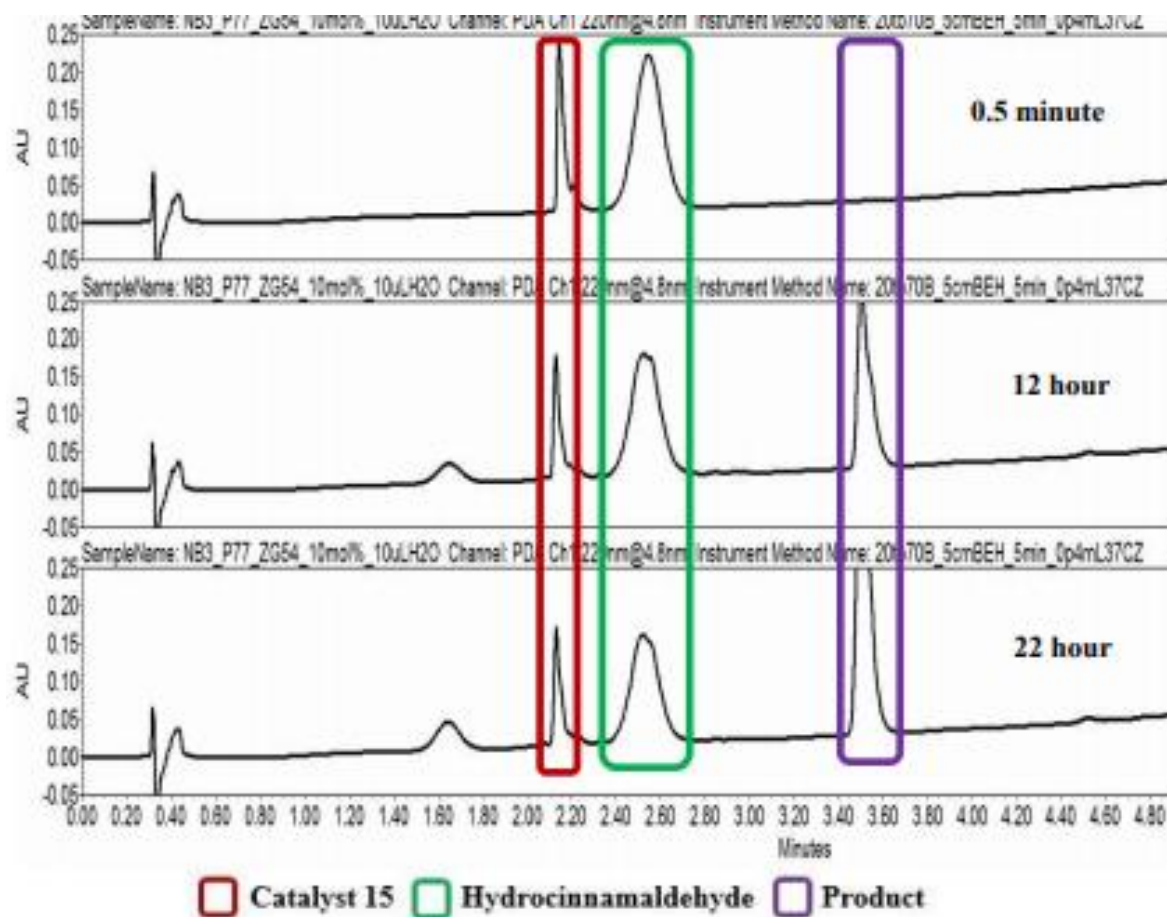
Figure 72. UPLC chromatograms at 0.5 minute, 12 hour and 22 hour reaction times for the crossed aldol reaction catalyzed by 10 mol % **15**. Highlighted in red is the peak corresponding to **15**. Highlighted in green is hydrocinnamaldehyde. Highlighted in purple is the alpha methylenated product. Each chromatogram has been scaled to the same y-axis value, which causes the product peak to be off scale. The peak for **15** remains after exposure to the mixture of formaldehyde and hydrocinnamaldehyde, suggesting the lack of macrocyle formation. This agrees with the fact that **15** cannot undergo dual covalent activation.

2.5.8 General Procedure for Measurement of Distances and Angles Reported in Figure 3
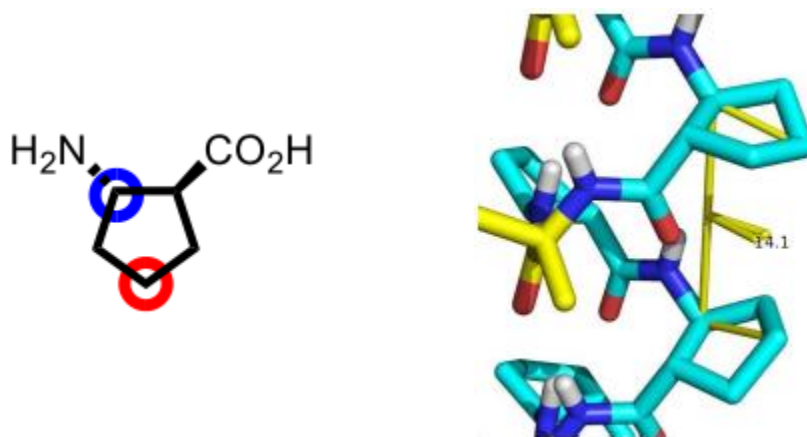
Figure 73. Data from the file PUCDEX in the Cambridge Structural Database, corresponding to the 1:2 α/β-peptide shown in **Figure 3C**., were exported to Pymol. The following procedure was used to generate the angles reported in **Figure 3**. A pair of ACPC residues in PUCDEX was selected, based on the spacing of an APC pair in one of the bis-APC 1:2 α/β-peptides for which crossed aldol reactivity was assessed. For each of the selected ACPC residues, a vector was defined based on the positions of the two ring atoms highlighted above. The angle between these two vectors was determined. For each possible APC diad arrangement in the structures shown in **Figure 3A-C**, all possible vector angle measurements were made, and the average angle was determined. ACPC residue with carbons used to define vector highlighted (red and blue). To measure the dihedral angle, the dihedral angle option in the measurement tool under the wizard window in Pymol was selected. The selection mode was changed to "atoms." First the carbon circled in red was selected, followed by the carbon circled in blue within the same five membered ring. Next, the carbon circled in blue within the other ACPC representing the diad was selected, followed by the carbon circled in red. Thus, each ACPC residue contributed two atoms each (one vector), and the dihedral angle between the two vectors was measured. A close-up of 1:2 α/β-peptide crystal structure shown in **Figure 3C** of the main text, showing the dihedral angle measured for one possible i,i+3 diad.
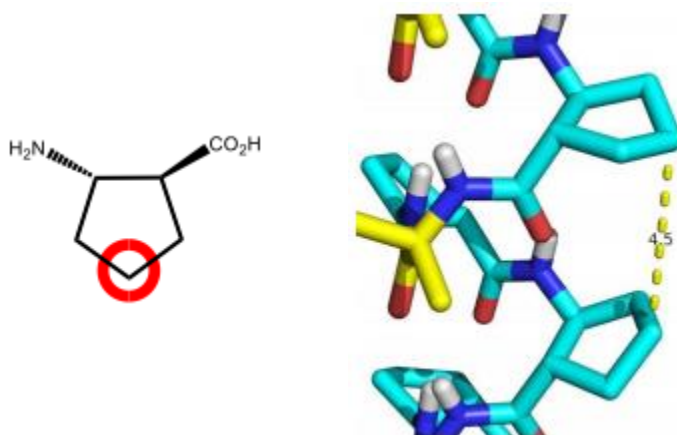
Figure 74. Data from the file PUCDEX in the Cambridge Structural Database, corresponding to the 1:2 α/βpeptide shown in **Figure 3C**., were exported to Pymol. The following procedure was used to generate the distances reported in **Figure 3**. A pair of ACPC residues in PUCDEX was selected, based on the spacing of an APC pair in one of the

bis-APC 1:2 α/βpeptides for which crossed aldol reactivity was assessed. For each of the selected ACPC residues, the ring atom circled in red was selected. The distance between these two atoms, from each of the ACPC residues was measured. For each possible APC diad arrangement in the structures shown in **Figures 3A-C**, all possible distance measurements were made, and the average distance was determined. To measure the distance, the distance option in the measurement tool under the wizard window in Pymol was selected. The selection mode was changed to "atoms." First the carbon circled in red was selected. Next, the carbon circled in red within the other ACPC representing the diad was selected. A close-up of 1:2 α/β-peptide crystal structure shown in **Figure XC** of the main text, showing the distance measured for one possible i,i+3 diad.

	(i,i+1)	**(i,i+2)**	**(i,i+3)**	**(i,i+4)**	**(i,i+6)**
β-peptide	(8.2 ± 0.1 Å, 142 ± 10°)	(7.6 ± 0.2 Å, 99 ± 6°)	(6.6 ± 0.4 Å, 33 ± 6°)	(11.9 ± 0.3 Å, 163 ± 4°)	—
1:2 αβ-peptide	(8.3 ± 0.1 Å, 146 ± 7°)	(9.0 ± 0.5 Å, 148 ± 15°)	(5.5 ± 0.4 Å, 10 ± 2°)	(10.8 ± 0.2 Å, 141 ± 9°)	(10.5 ± 0.4 Å, 5 ± 2°)
1:1 αβ-peptide	—	(8.1 ± 0.1 Å, 134 ± 11°)	—	(11.3 ± 0.6 Å, 106 ± 0.4°)	(13.6 Å, 6°)

Figure 75. Distances and angles for ACPC diads in crystal structures measured as described above. A similar table is found in **Figure 3D**; however, this version provides standard deviations in all distance and angle measurements.

2.5.9 Aldol-based Cyclization
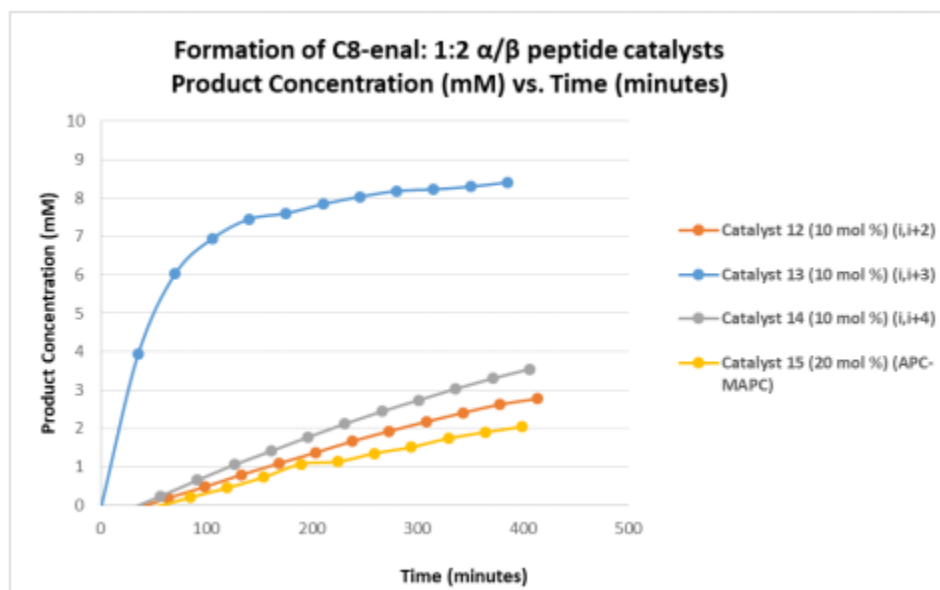
Figure 76. Reaction progress data for the intramolecular aldol cyclization reaction in the presence of 1:2 α/β-peptides **12**, **13**, **14**, and **15**. Reaction progress was monitored up to 400 minutes. Catalyst **15**, which contains an i,i+3 APC-MAPC diad was loaded at 20 mol %, while bis-APC catalysts **12**, **13**, and **14** were loaded at 10 mol %. Therefore, the total concentration of APC residues was constant across these reactions. 10 mM product corresponds to quantitative yield.

Catalyst, mol %	% Yield @ 180 minutes	% Yield @ 400 minutes
12	11	28
13	76	84
14	18	35
15	11	20

Figure 77. Percent yields measured for various catalysts based on the UPLC data shown in **Figure X** using the calibration curve shown in **Figure X**.

2.5.10 Hexanal Methylenation

1:2 α/β-peptides: Hexanal Methylenation
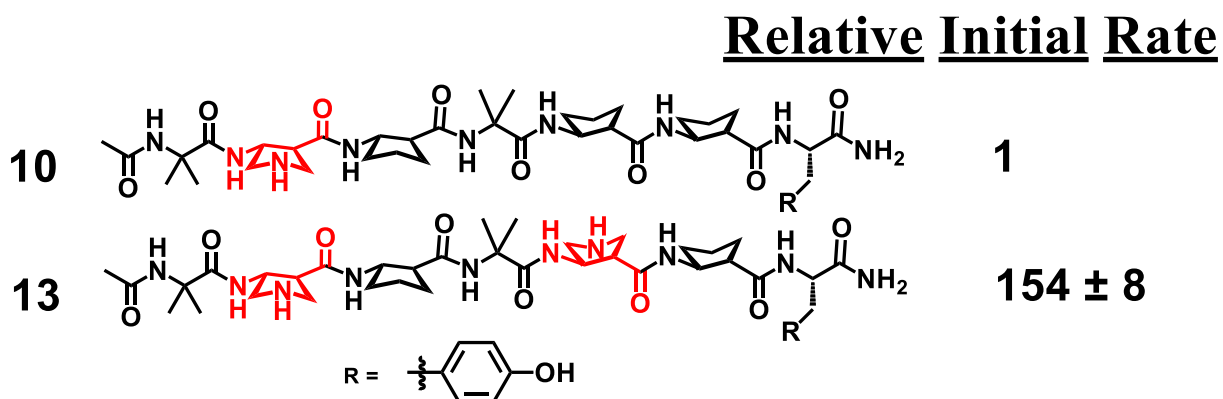
Relative Initial Rate

10	**1**
13	**154 ± 8**

R =

Figure 78. 1:2 α/β-Peptide catalysts **10**, and **13**. For the bis-APC peptide **13**, initial rate (vREL) values relative to mono-APC catalyst **10** are shown.
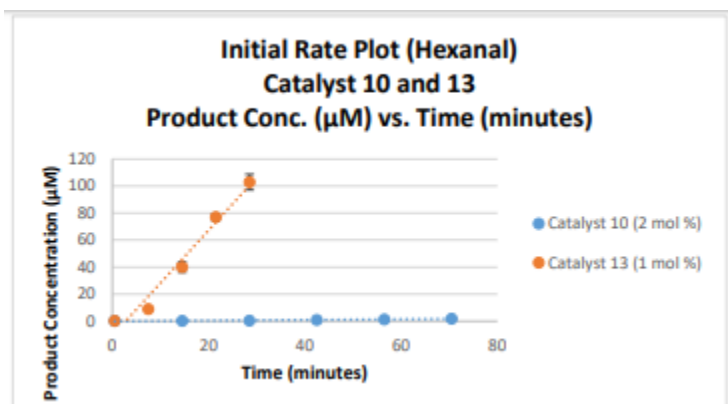
Figure 79. Reaction progress data for the crossed aldol reaction of hexanal and formaldehyde in the presence of 1:2 α/β-peptide **10** and **13** (respectively at 2 and 1 mol % relative to aldehyde starting materials), between 0.5 and 70.5 minutes after catalyst addition. The reaction employing catalyst **10** was run in triplicate, the reaction employing catalyst **13** was run in duplicate, and error bars denote standard deviation among product concentration measurements at a given time point. Reaction conditions are described above. The maximum amount of product detected, 112 μM, corresponds to 1 % yield.

Peptide	Rate (1)	Rate (2)	Rate (3)	Avg Rate (µM/min)	StDev (µM/min)
10	0.0186	0.0246	0.0328	0.0253	0.004
13	4.1	3.71		3.91	0.20

Peptide	vREL (1)	vREL (2)		Avg vREL	StDev vREL
10	n/a	n/a		Control Peptide	n/a
13	162	147		154	8

Figure 80. Initial rates measured for each reaction with catalysts **10**, and **13**, along with the average vREL and standard deviation for **13** (1 mol %) relative to mono-APC catalyst **10** (2 mol %).

2.5.11 Spectra

Highest peak is labeled. Other peaks correspond to [M+H], [M+Na], [M+K], or [M-NH$_3$]

Catalyst 1: [M+H] Calculated = 792.98
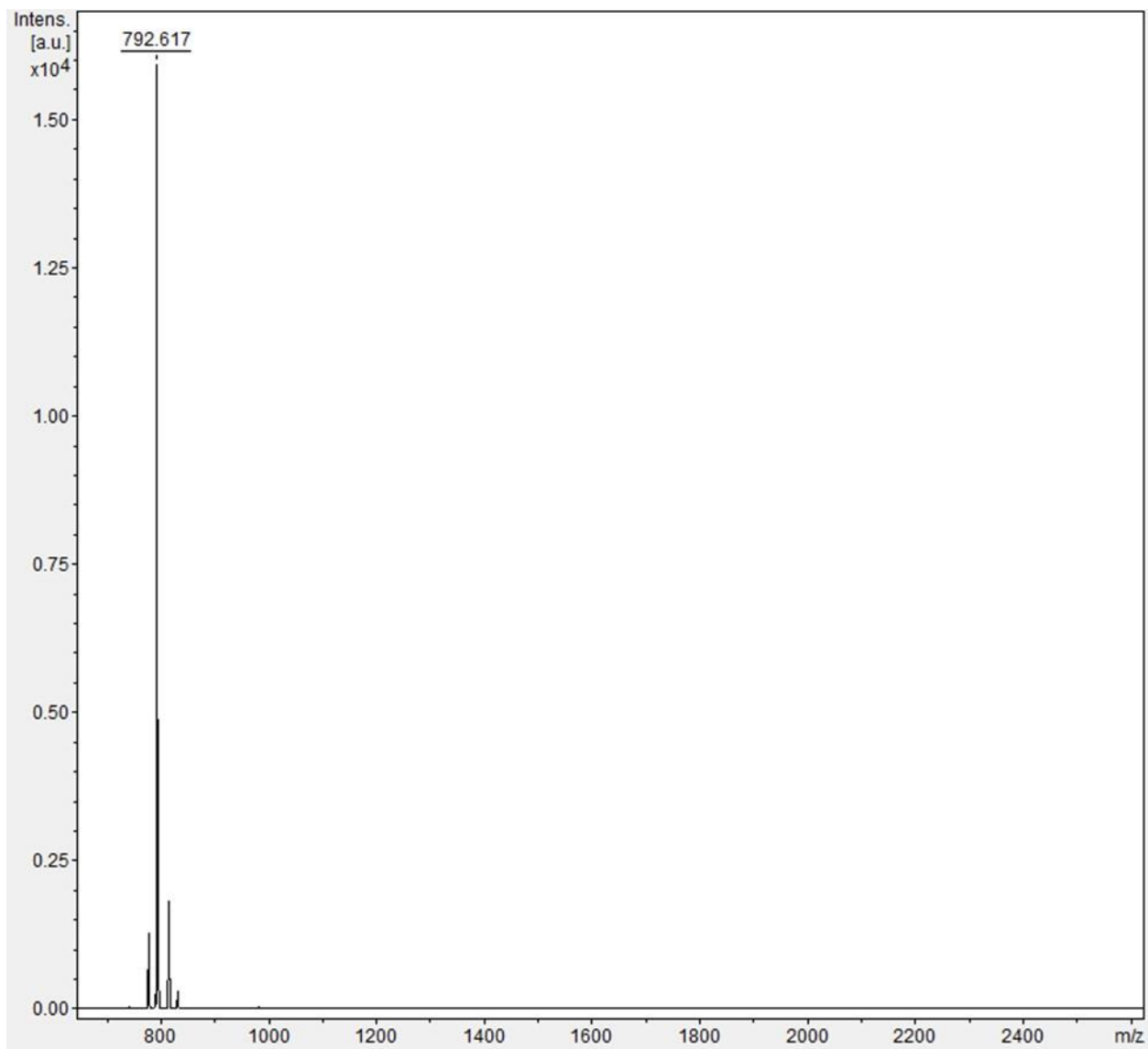
Catalyst 2: [M+H] Calculated = 793.98
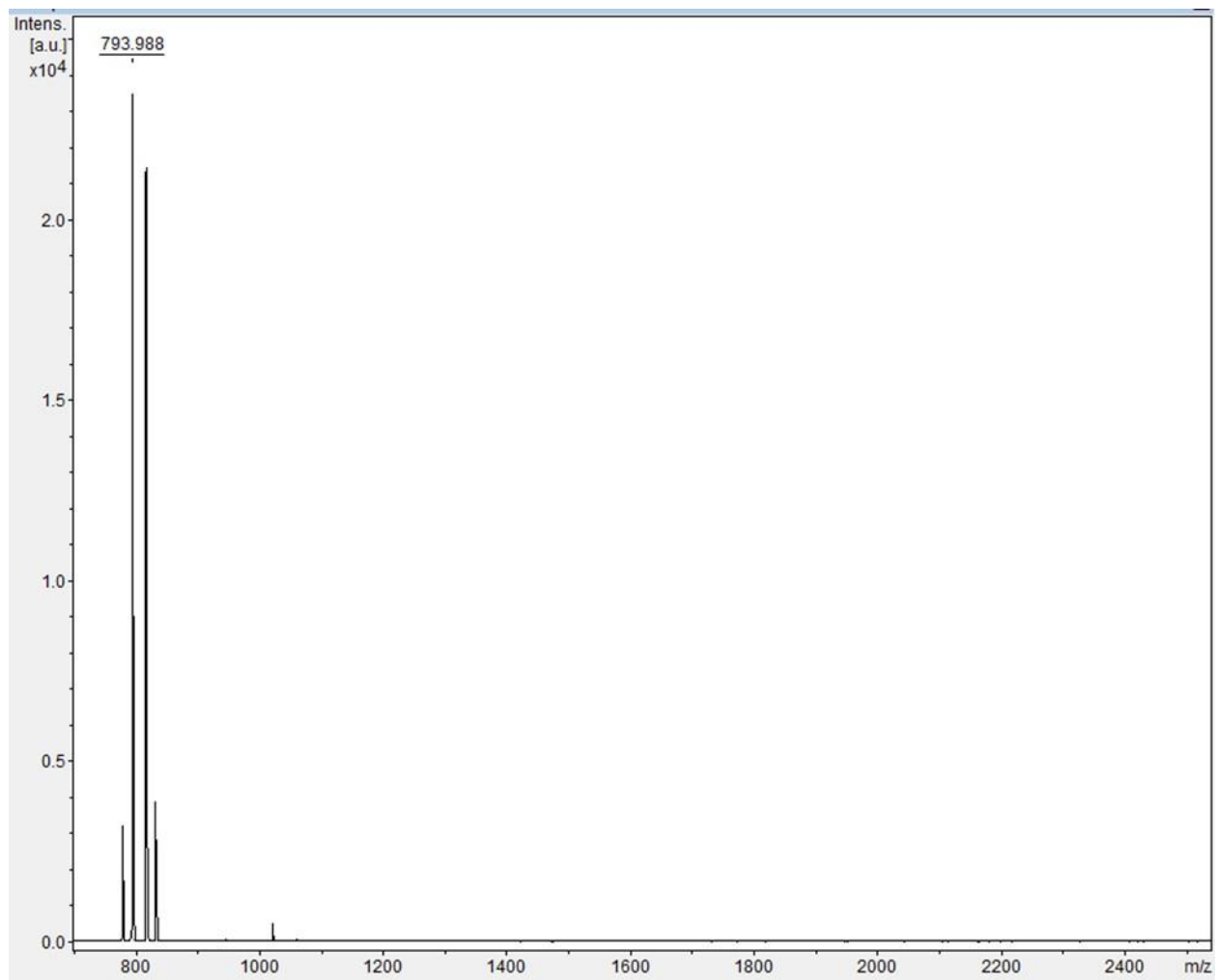
Catalyst 3: [M+H] Calculated = 793.98
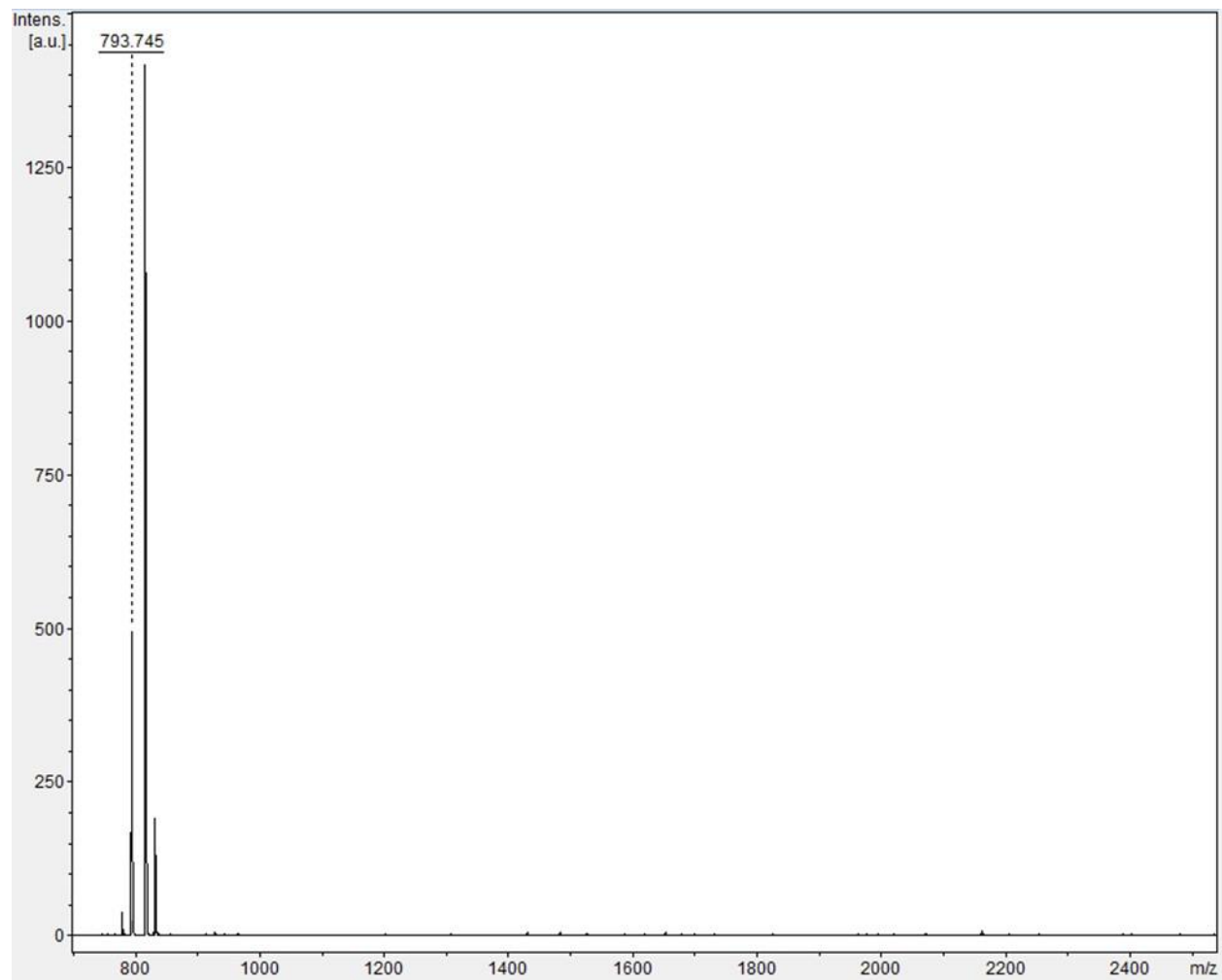
Catalyst 3R-1: [M+H] Calculated = 810.01
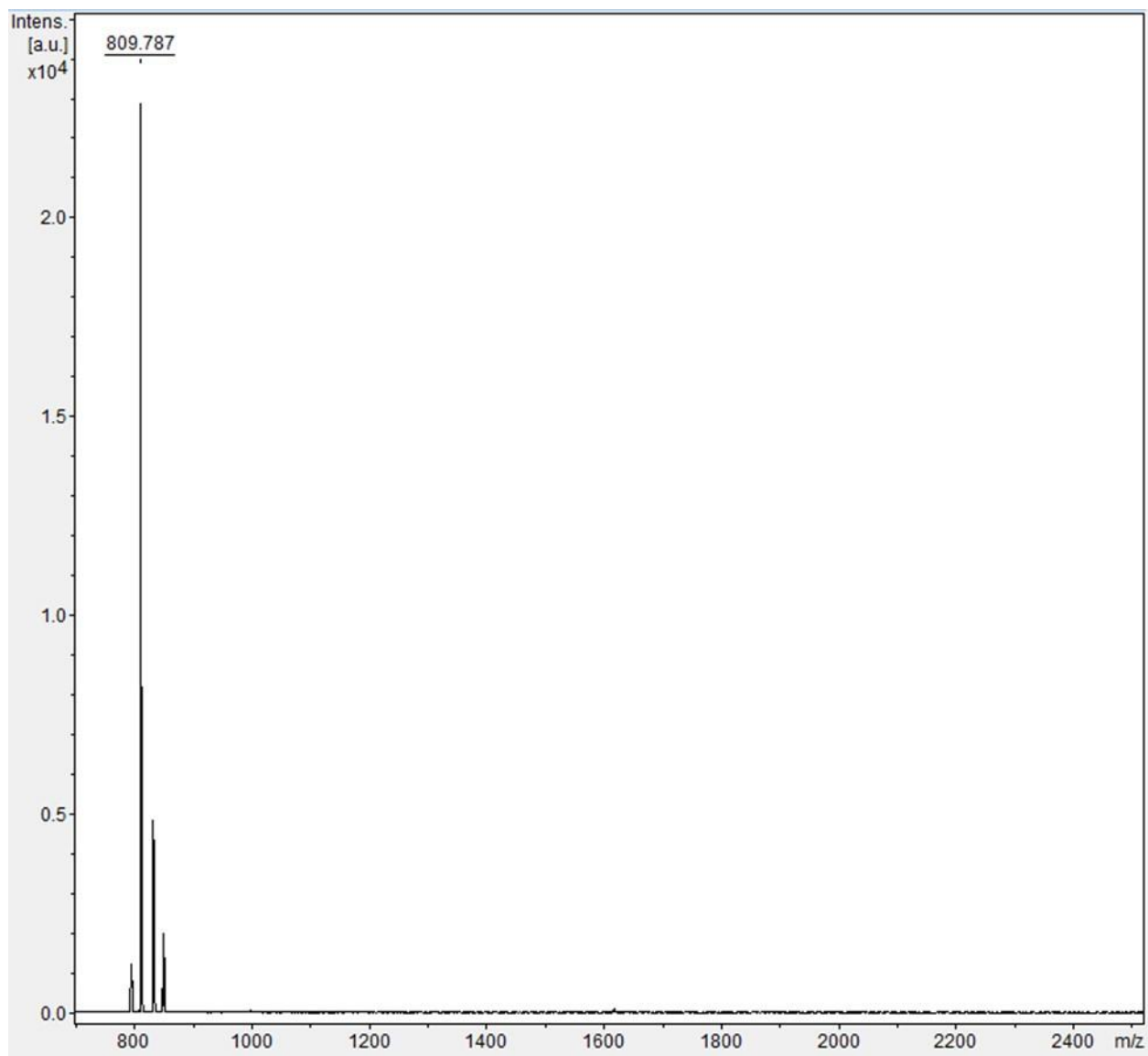
Catalyst 4: [M+H] Calculated = 793.98
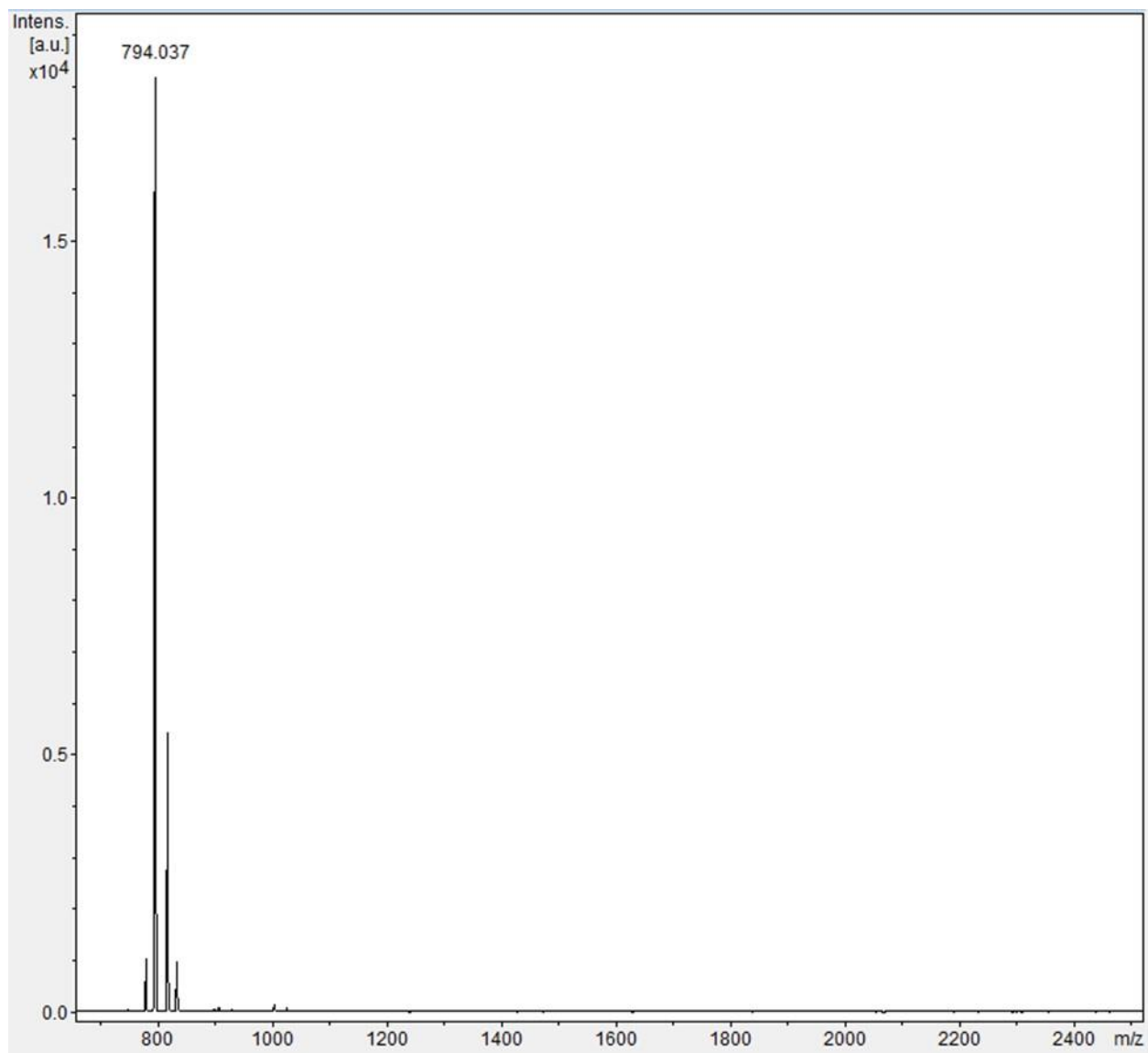
Catalyst 4R-1: [M+H] Calculated = 767.93
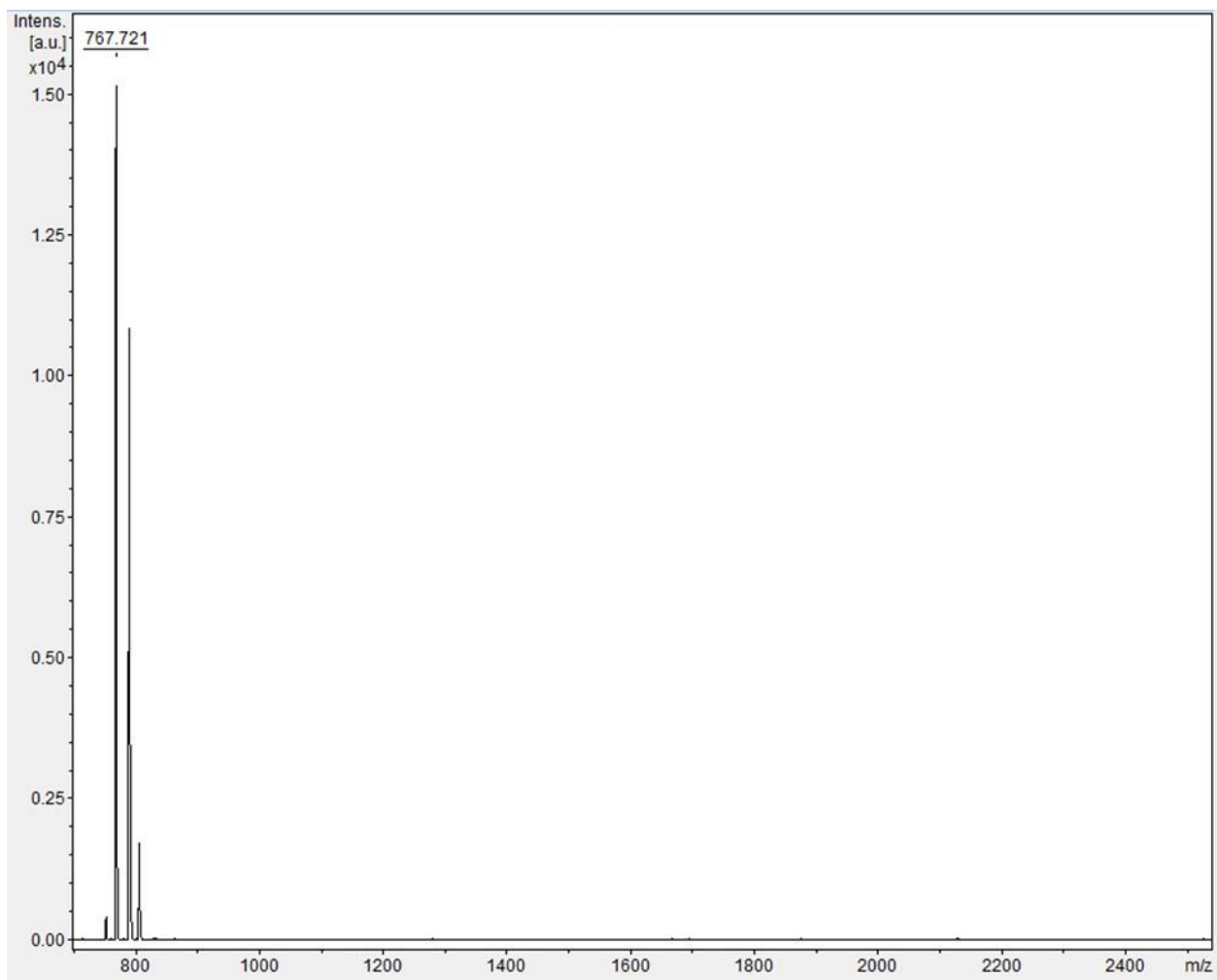
Catalyst 4R-4: [M+H] Calculated = 735.84
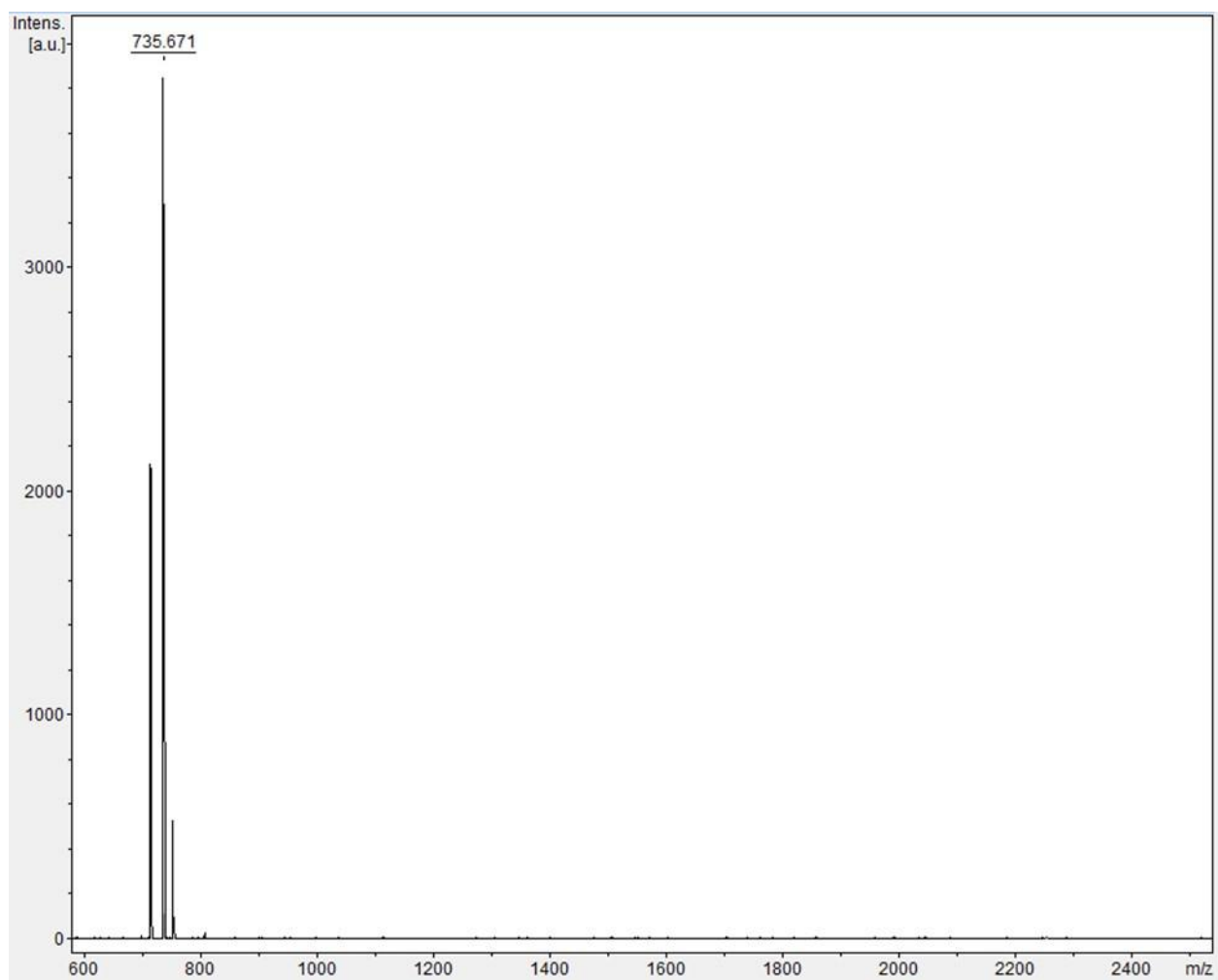
Catalyst 5: [M+H] Calculated = 1016.26
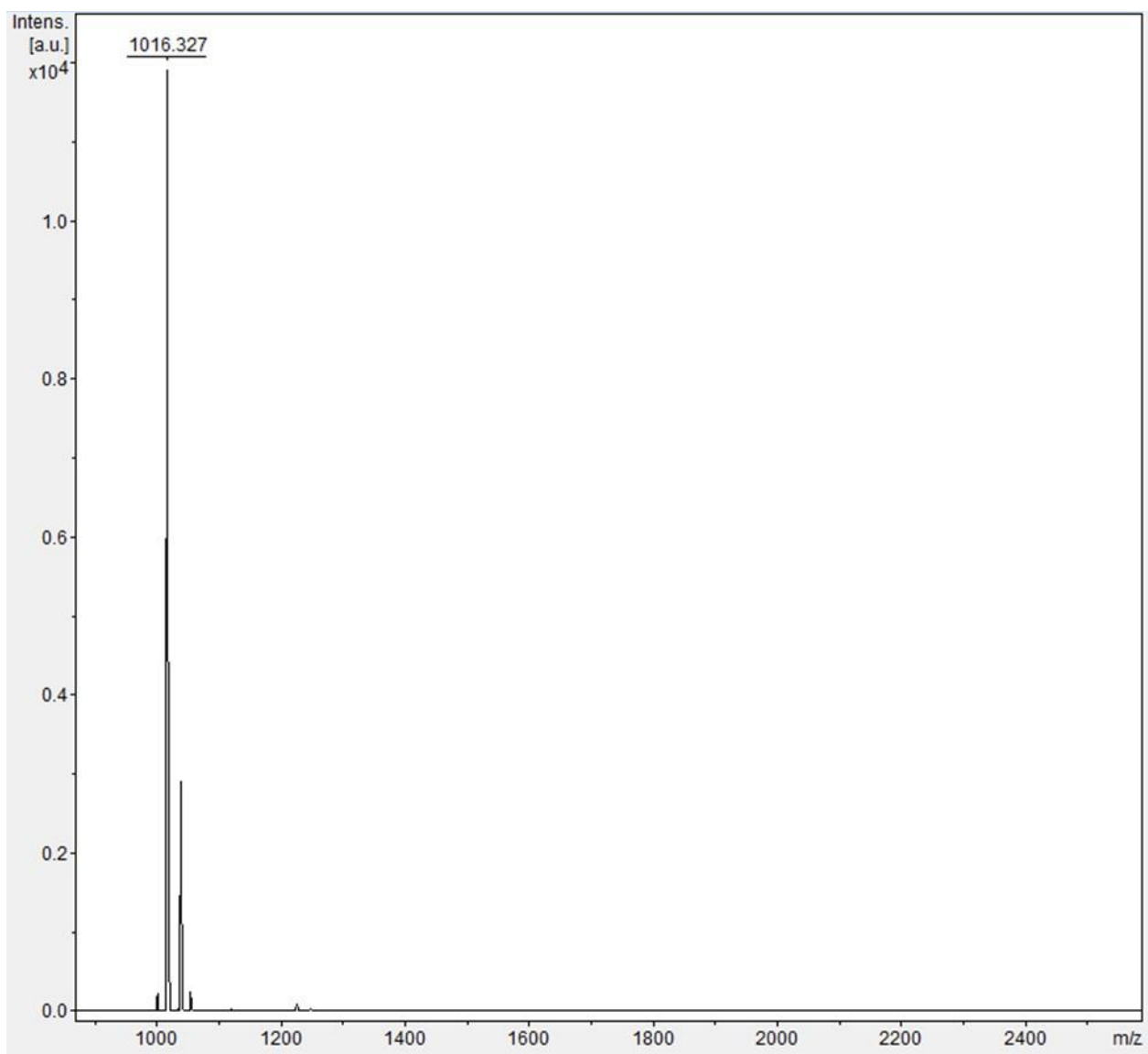
Catalyst 6: [M+Na] Calculated = 834.45
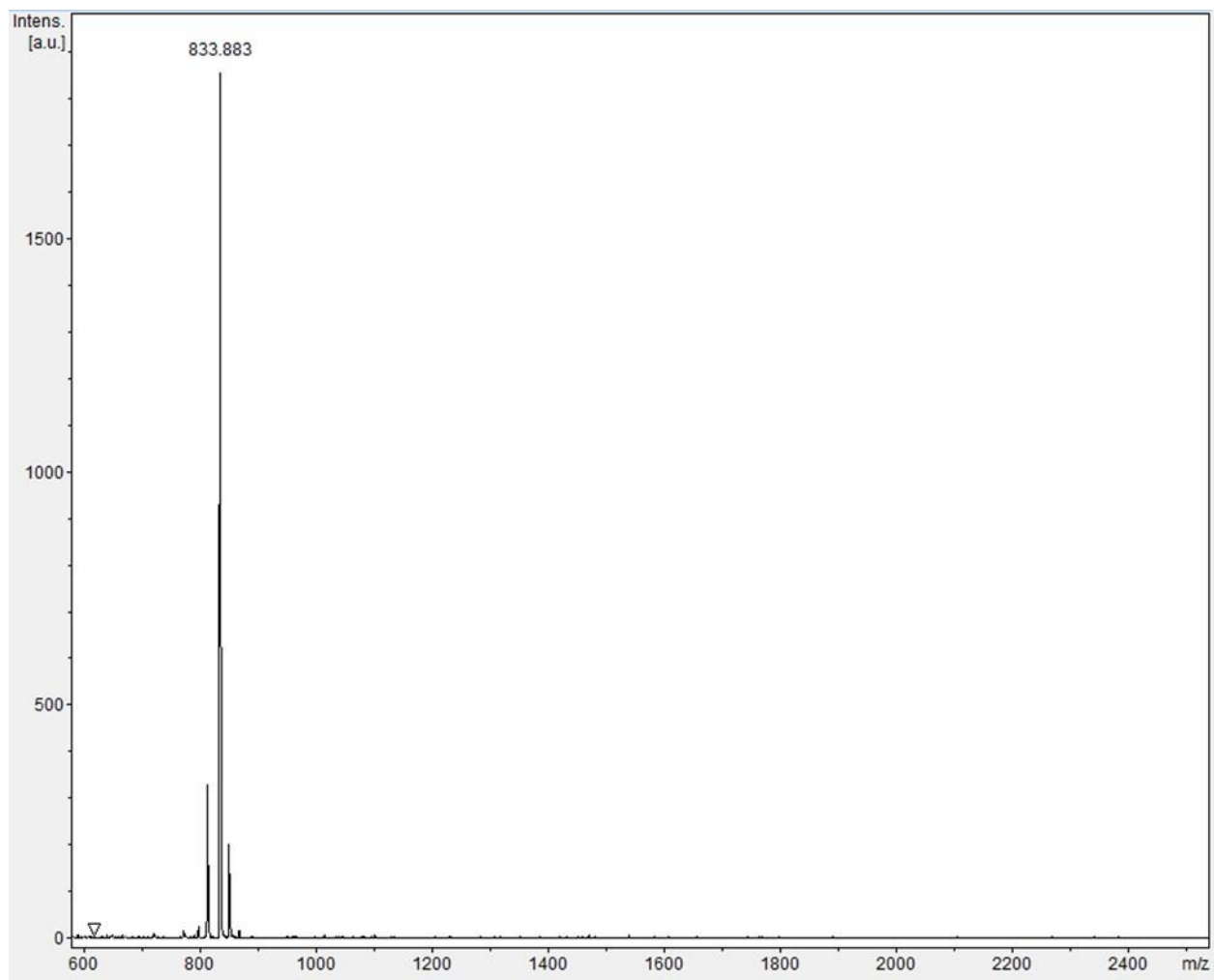
Catalyst 7: [M+Na] Calculated = 835.44

122
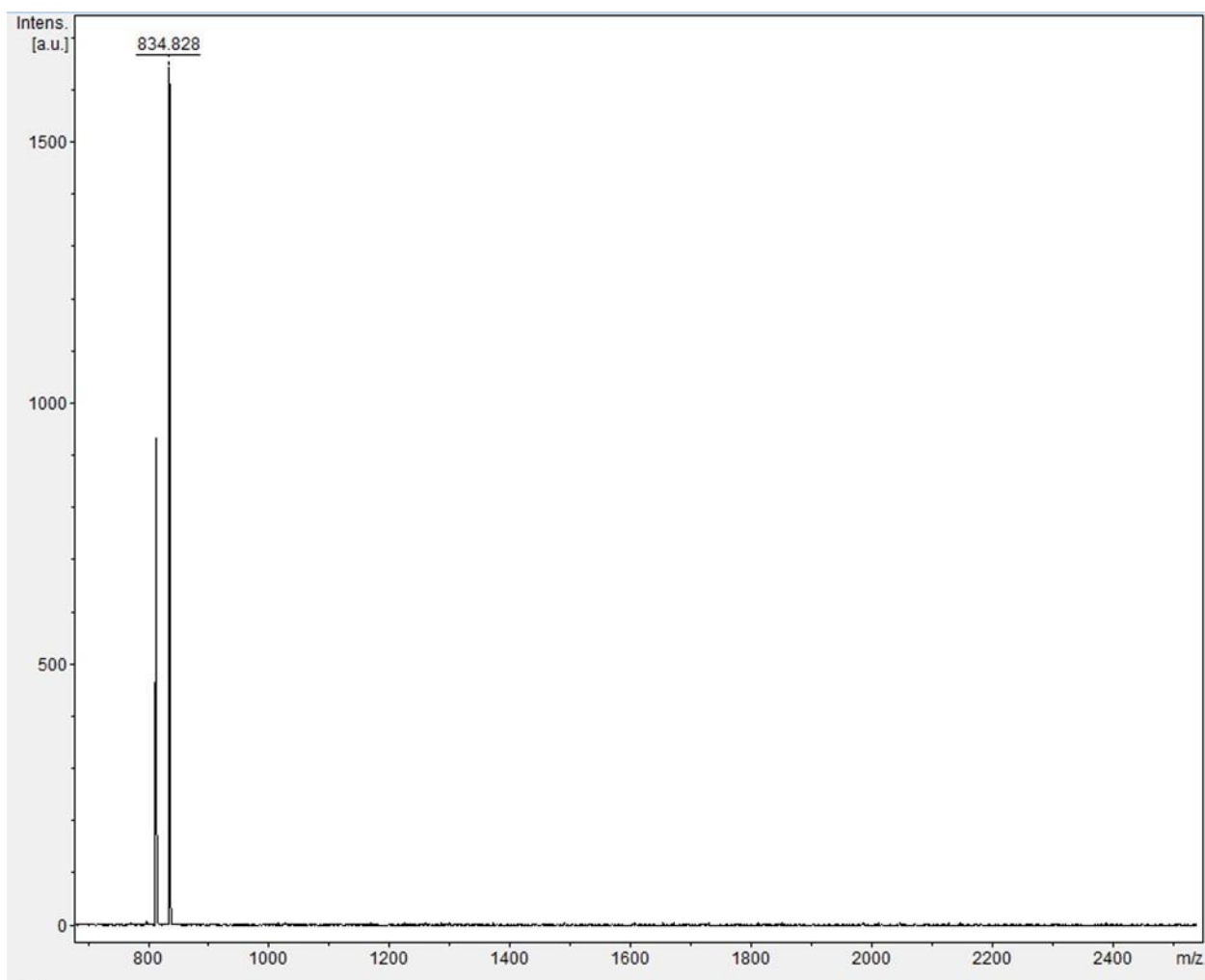
Catalyst 8: [M+H] Calculated = 812.97
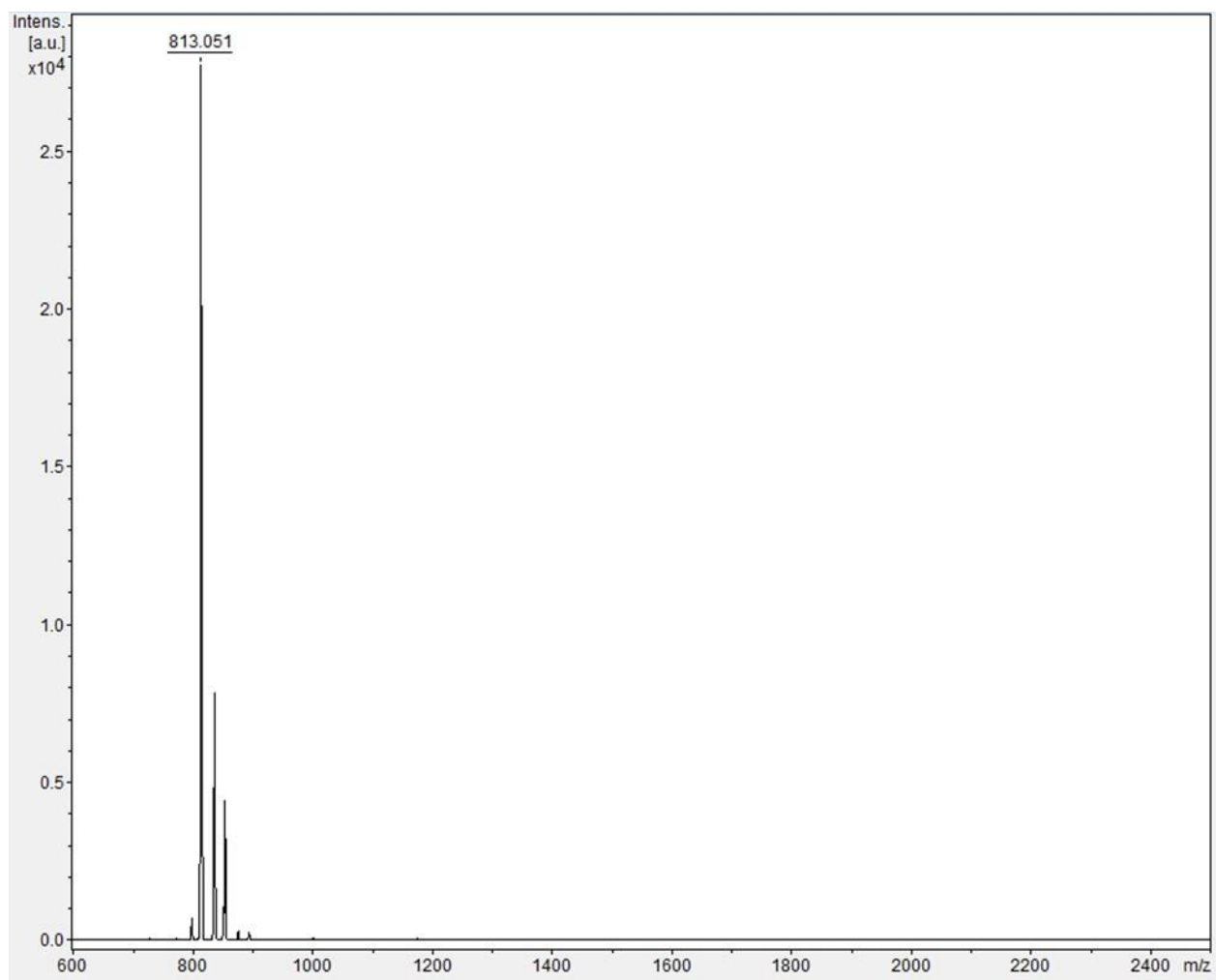
Catalyst 9: [M+H] Calculated = 1009.22
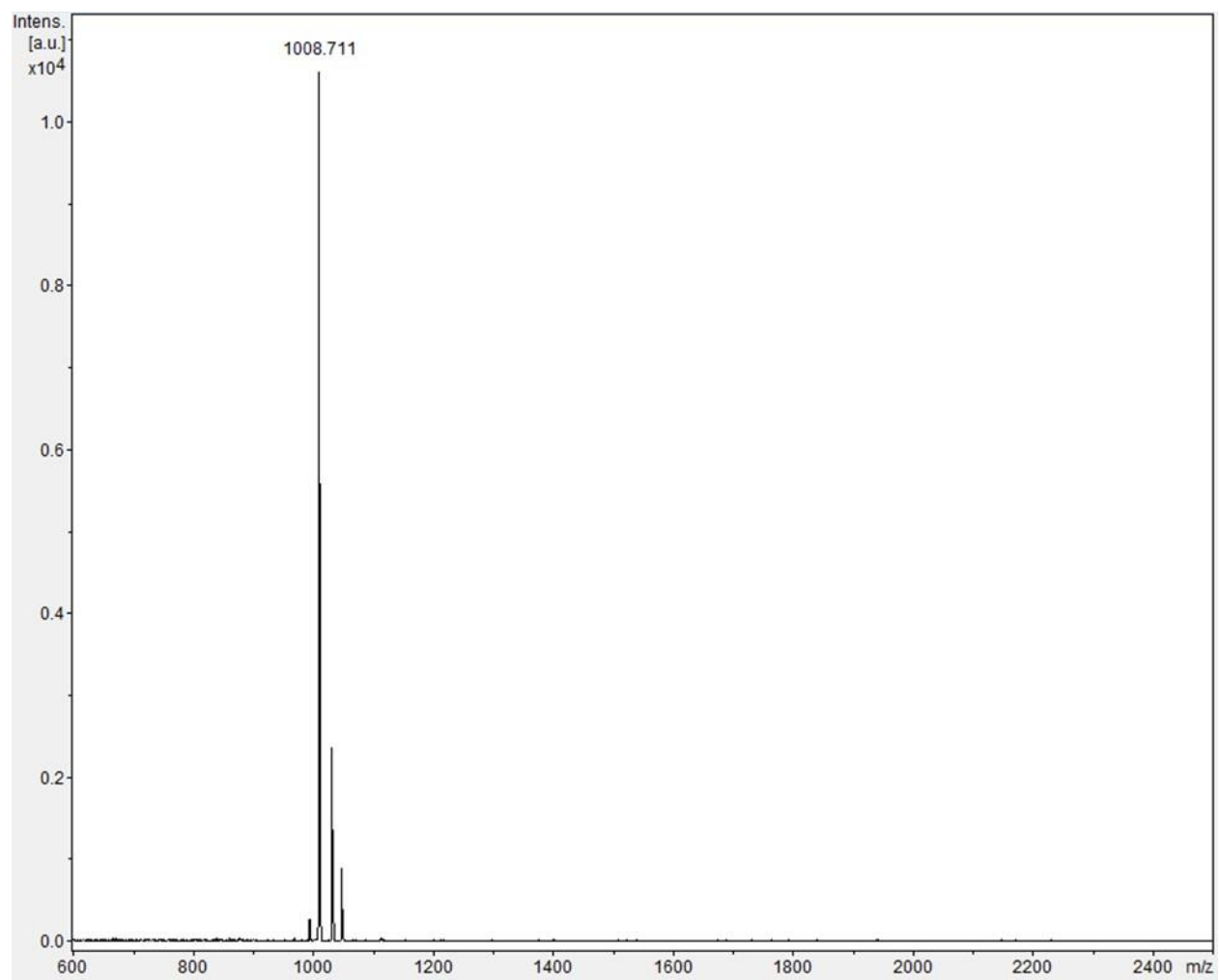
Catalyst 10: [M+Na] Calculated = 860.46
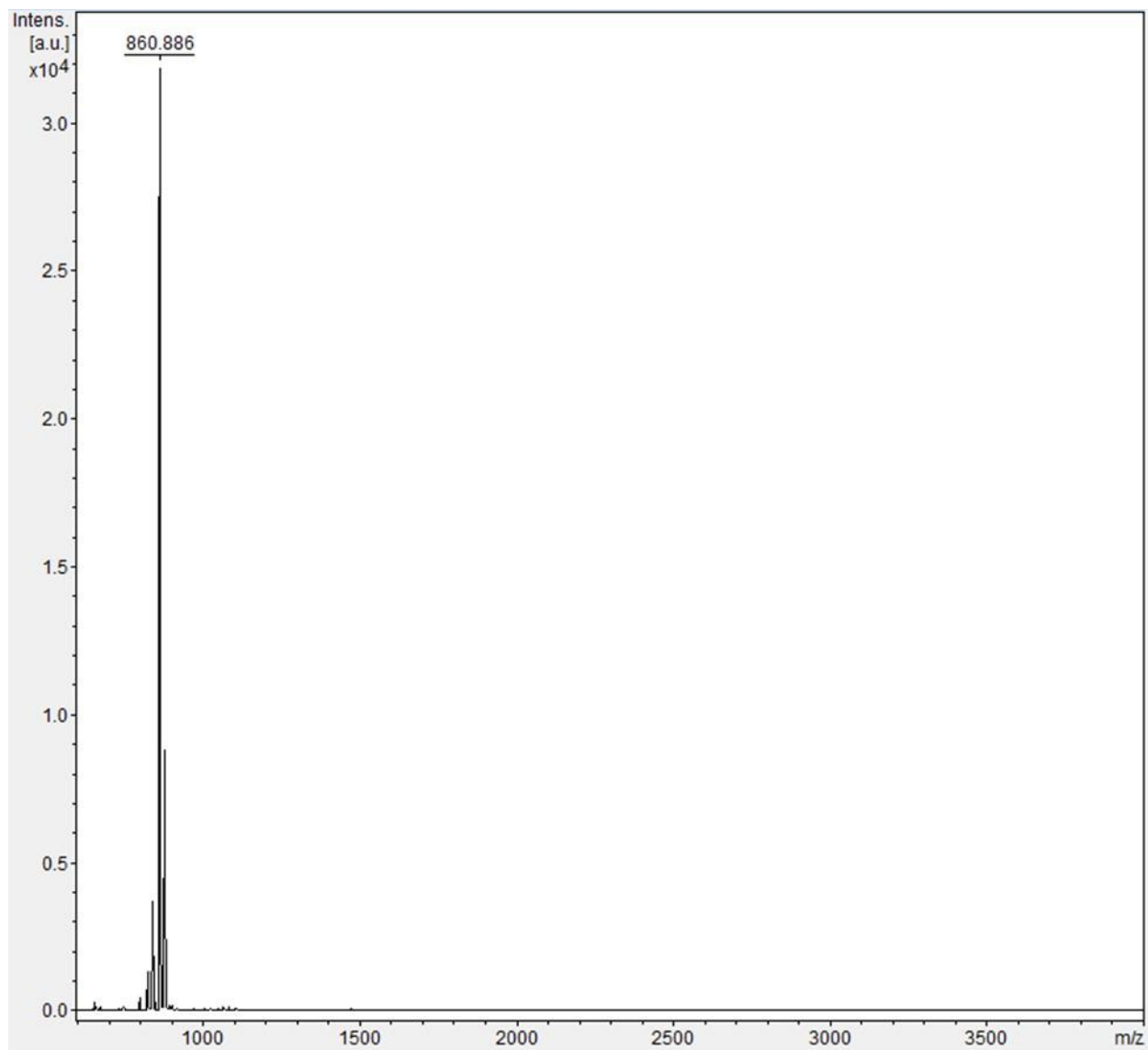
Catalyst 11: [M+H] Calculated = 839.01
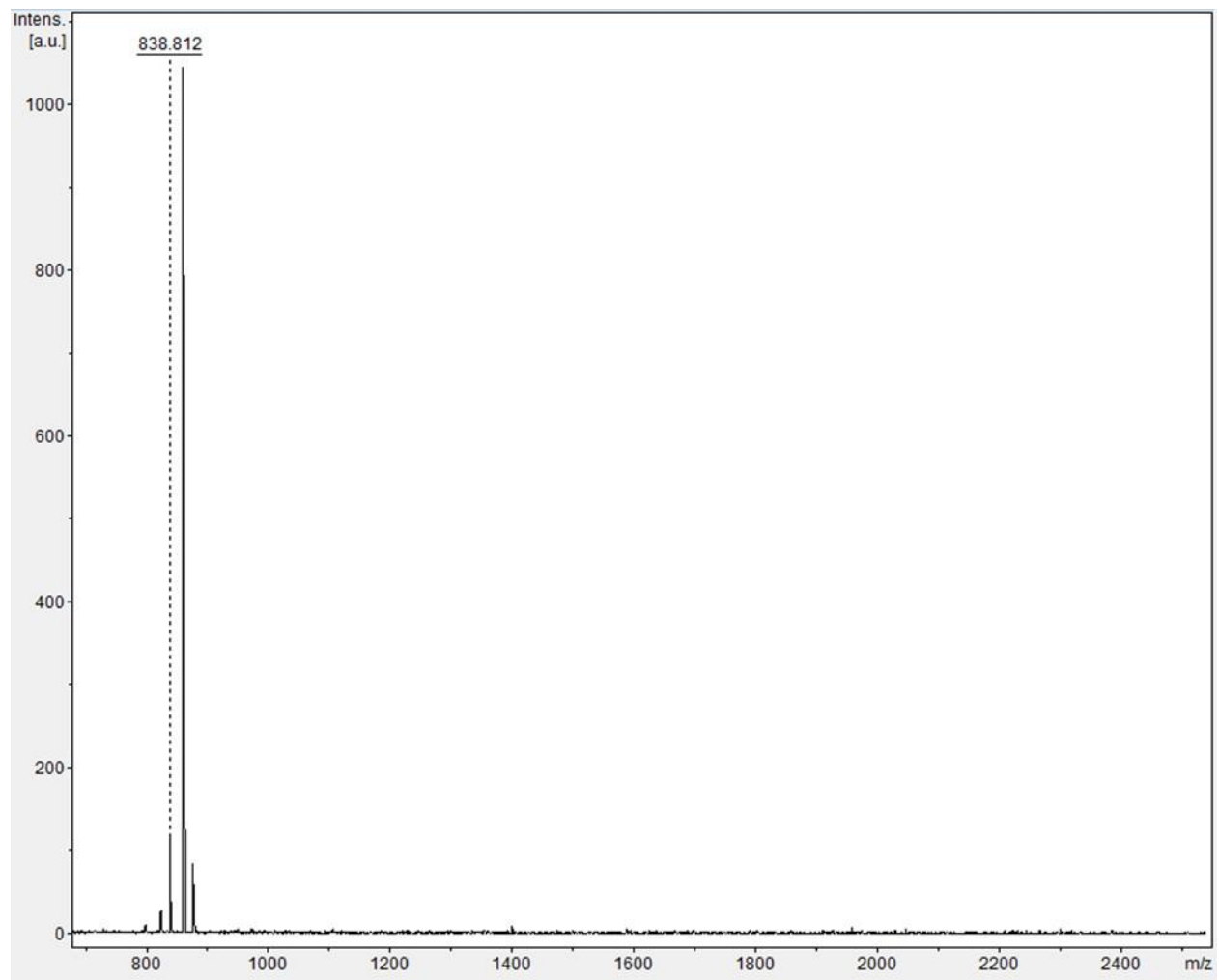
Catalyst 12: [M+Na] Calculated = 861.46
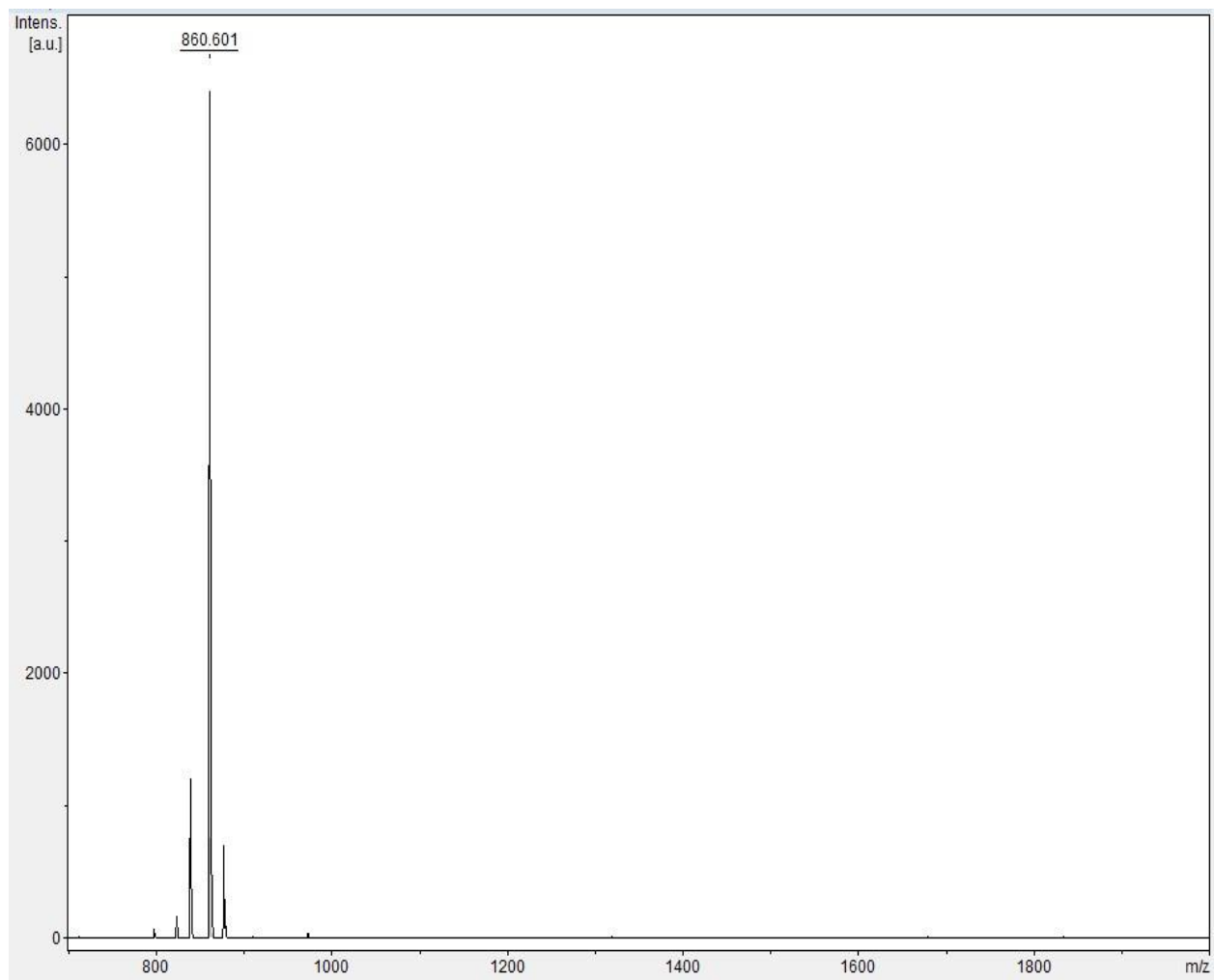
Catalyst 13: [M+Na] Calculated = 861.46
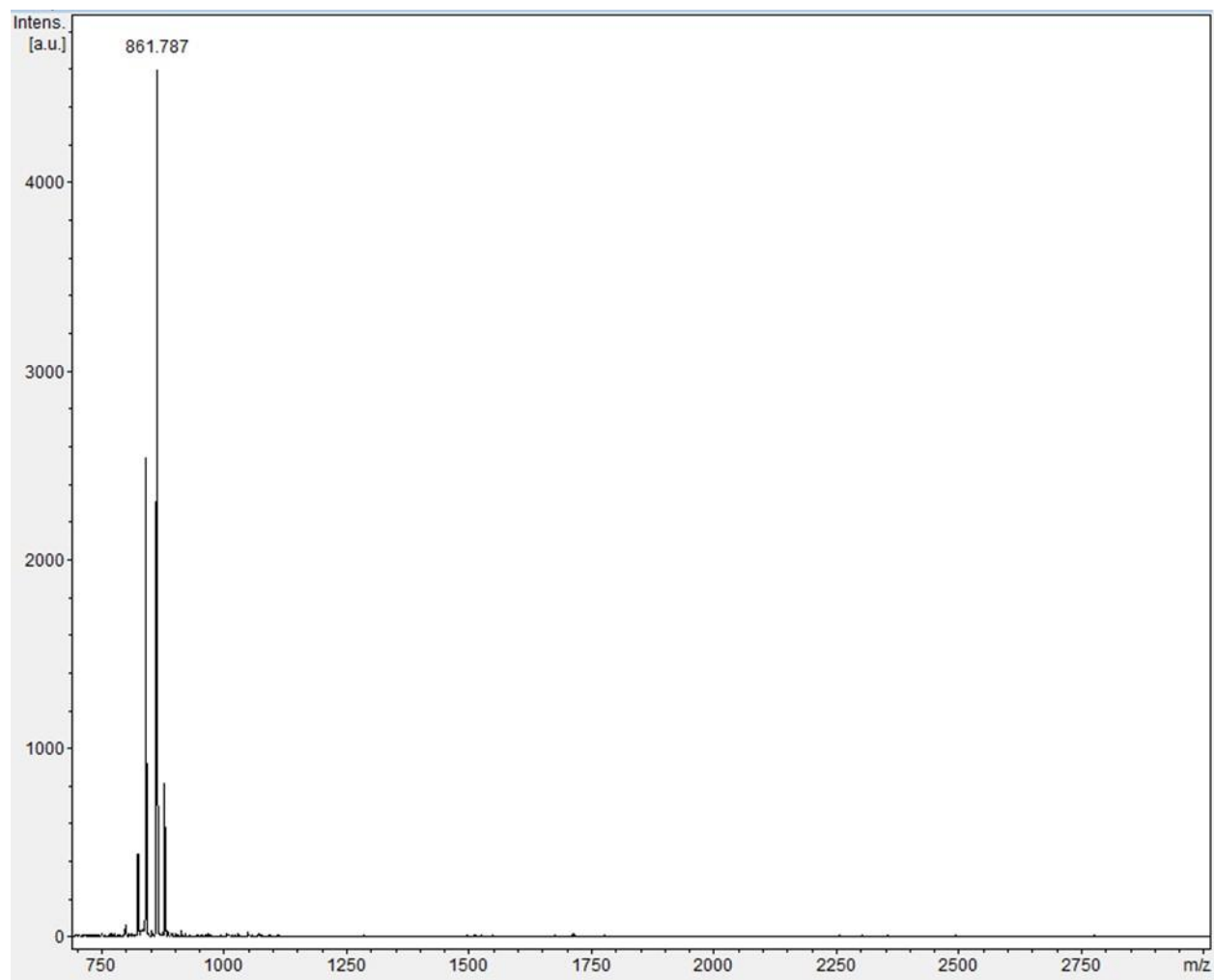
Catalyst 13: [M+Na] Calculated = 861.46
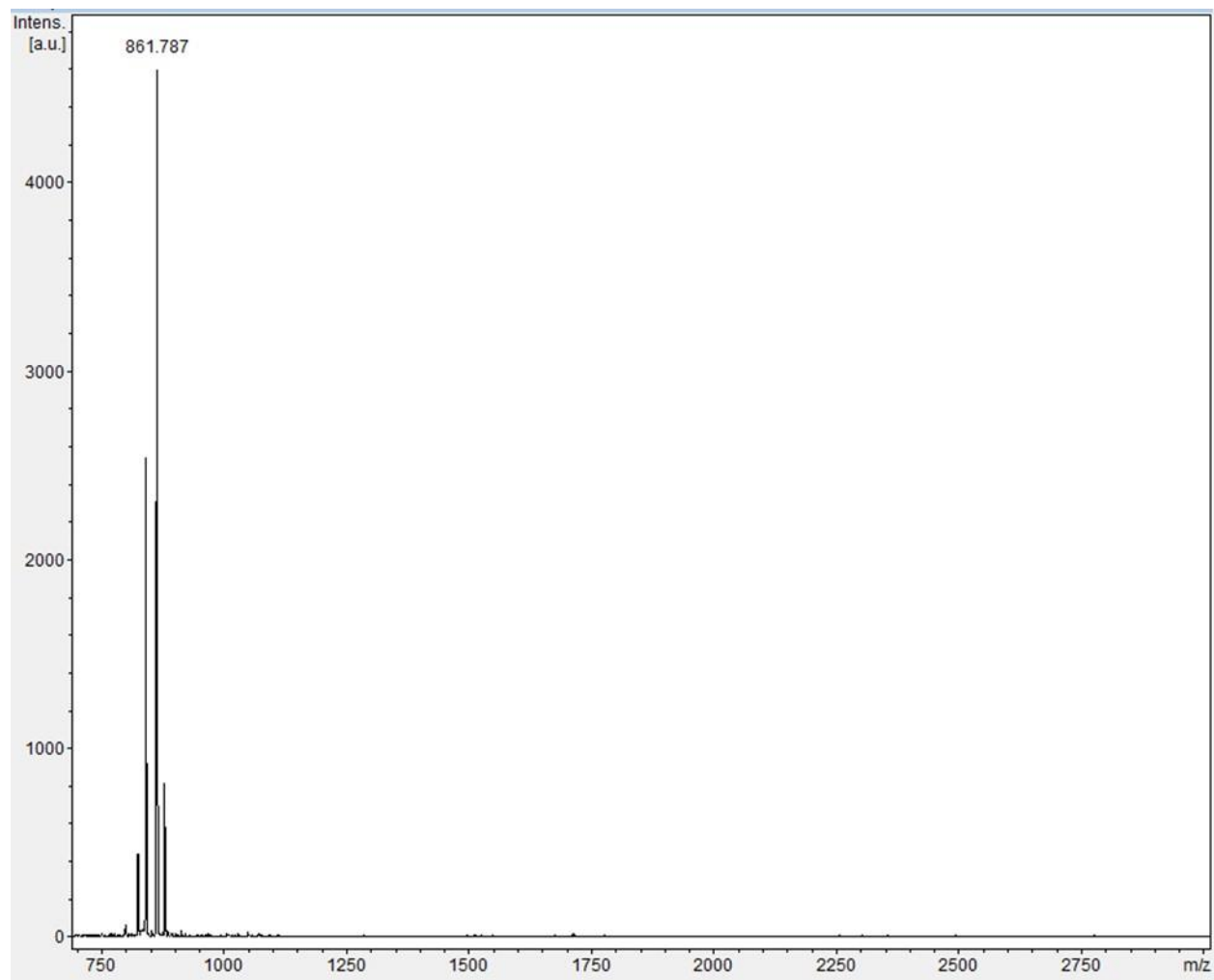
Catalyst 13R-1: [M+H] Calculated = 855.05
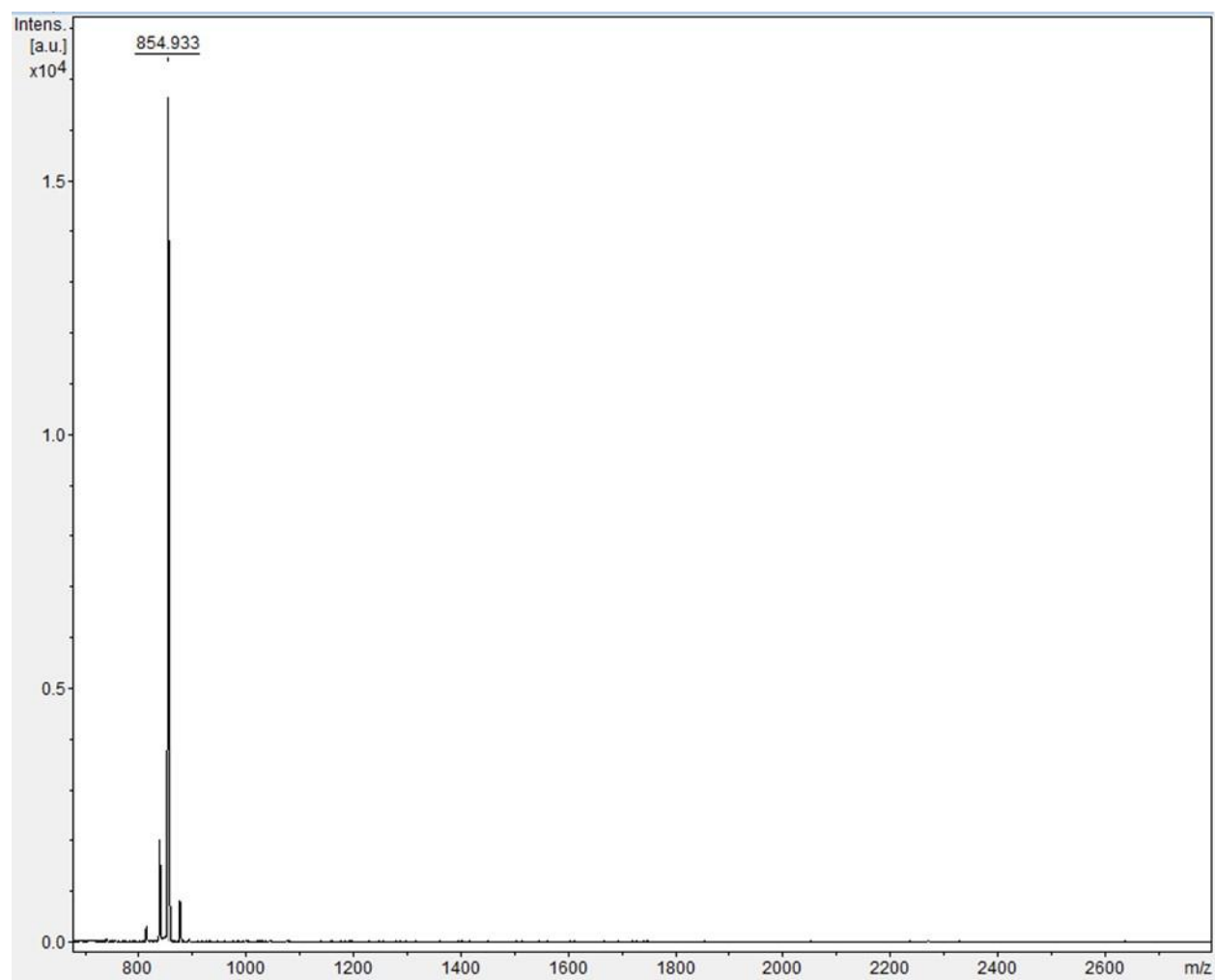
Catalyst 13R-2: [M+H] Calculated = 824.98
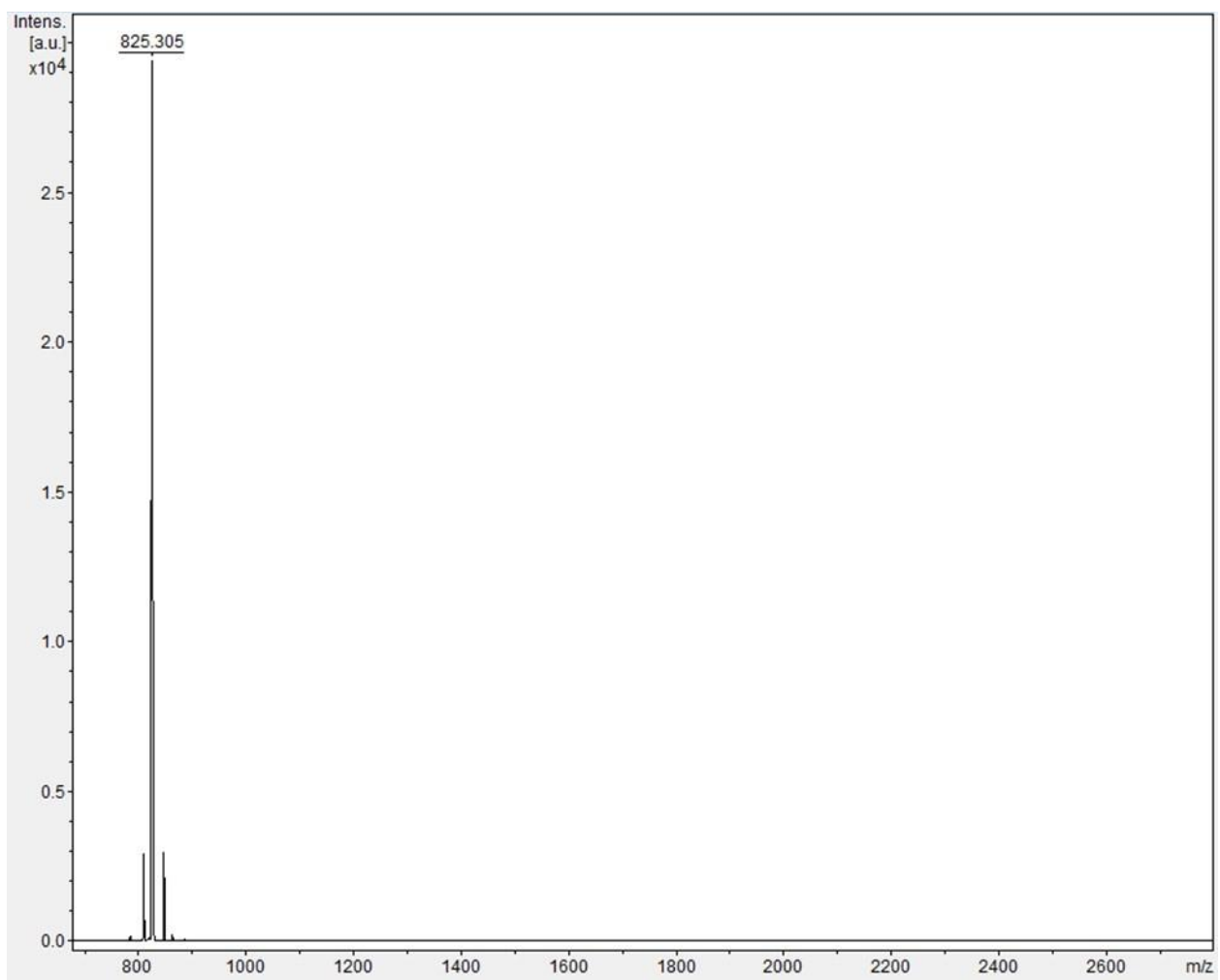
Catalyst 13R-3: [M+H] Calculated = 841.02
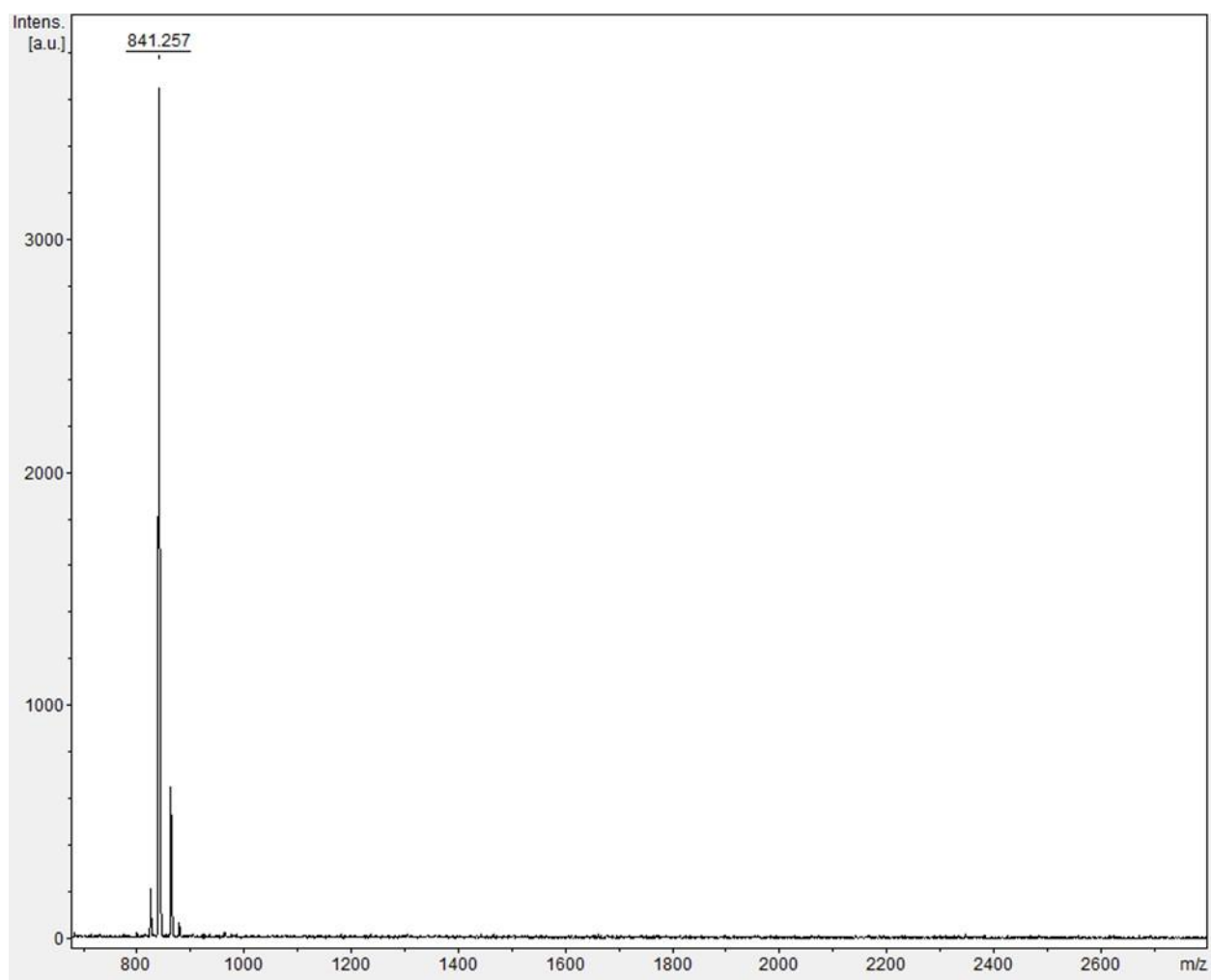
Catalyst 13R-4: [M+Na] Calculated = 793.4
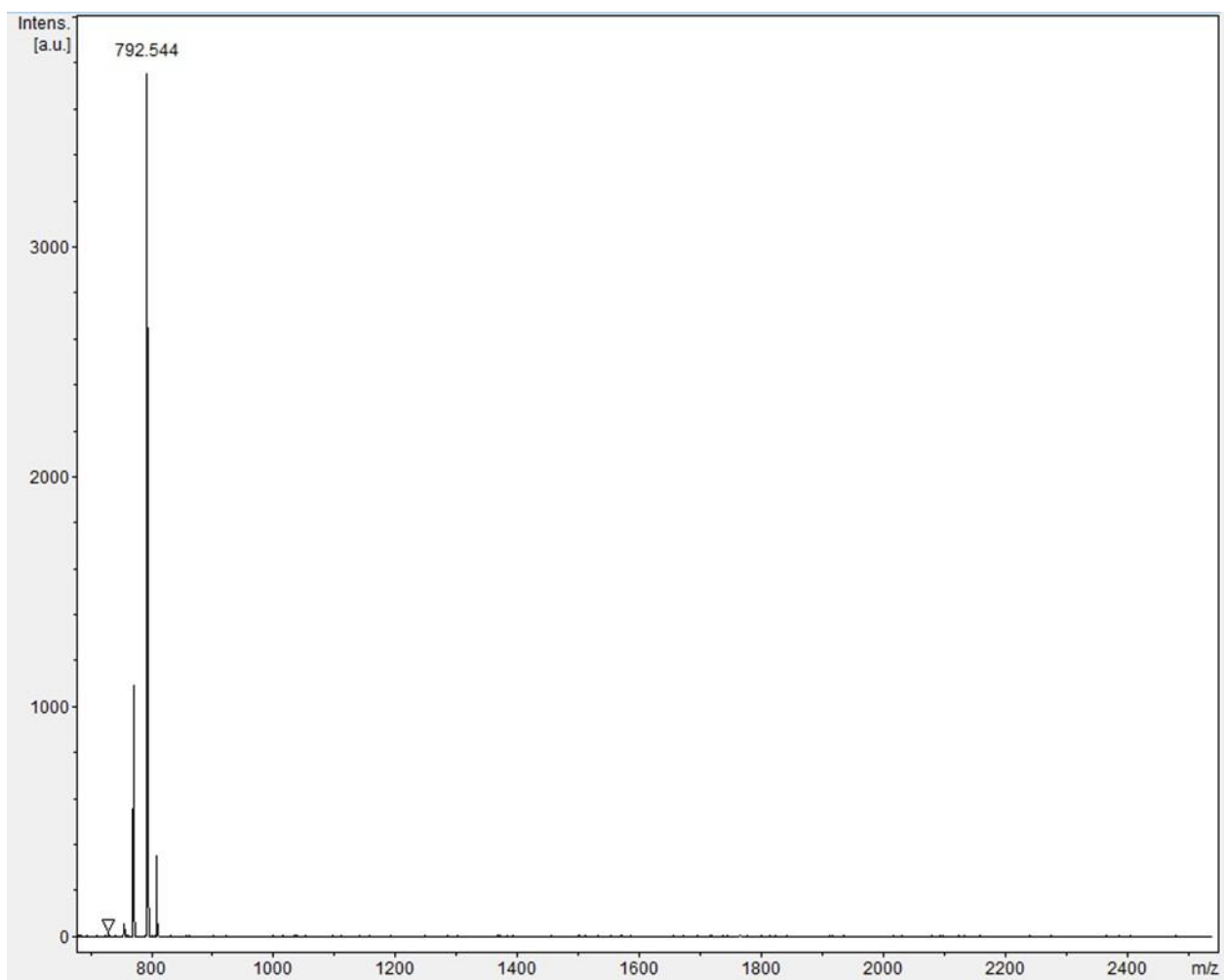
Catalyst 13R-5: [M+Na] Calculated = 833.43
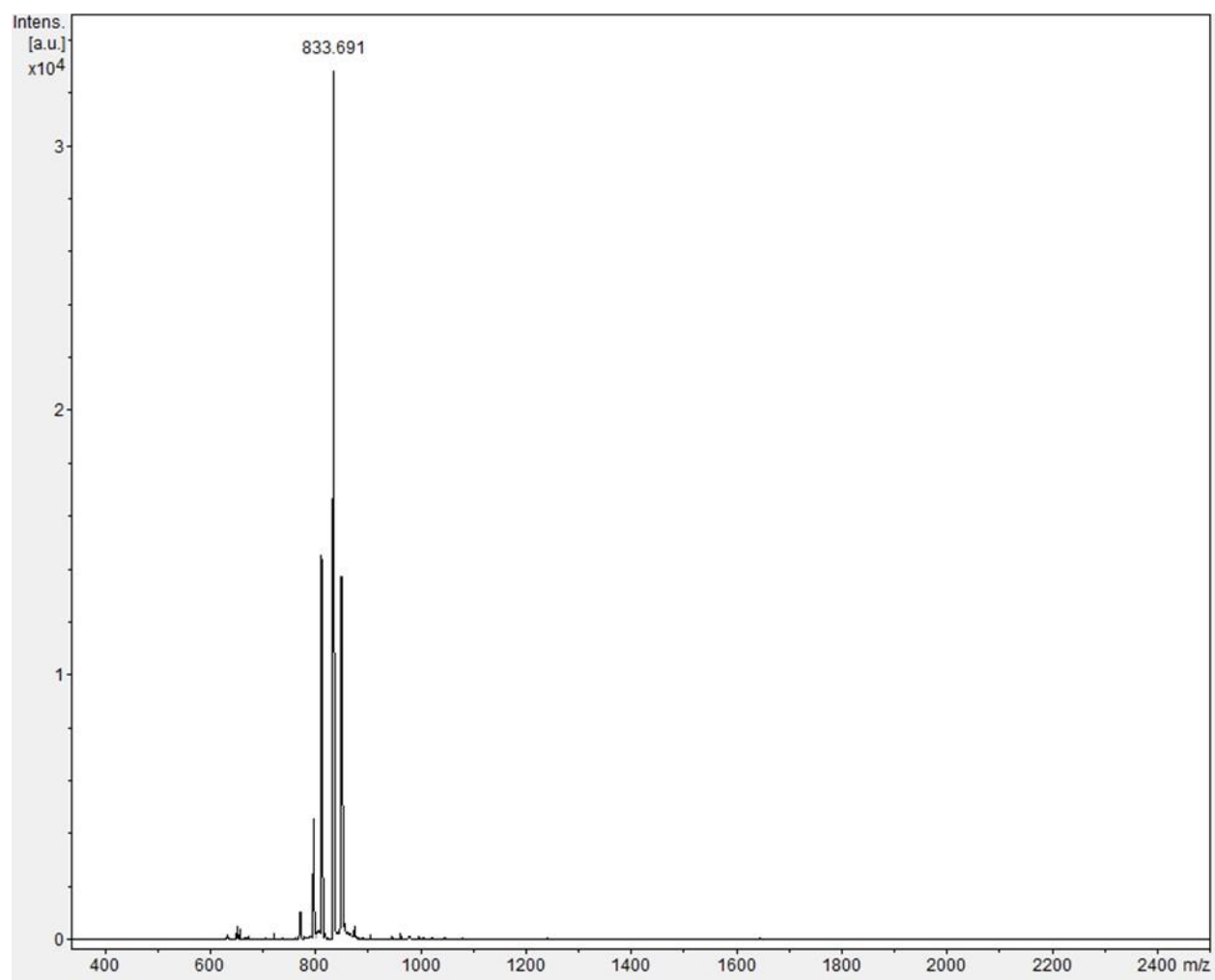
13R-5(D-Ala): [M+Na] Calculated = 833.43
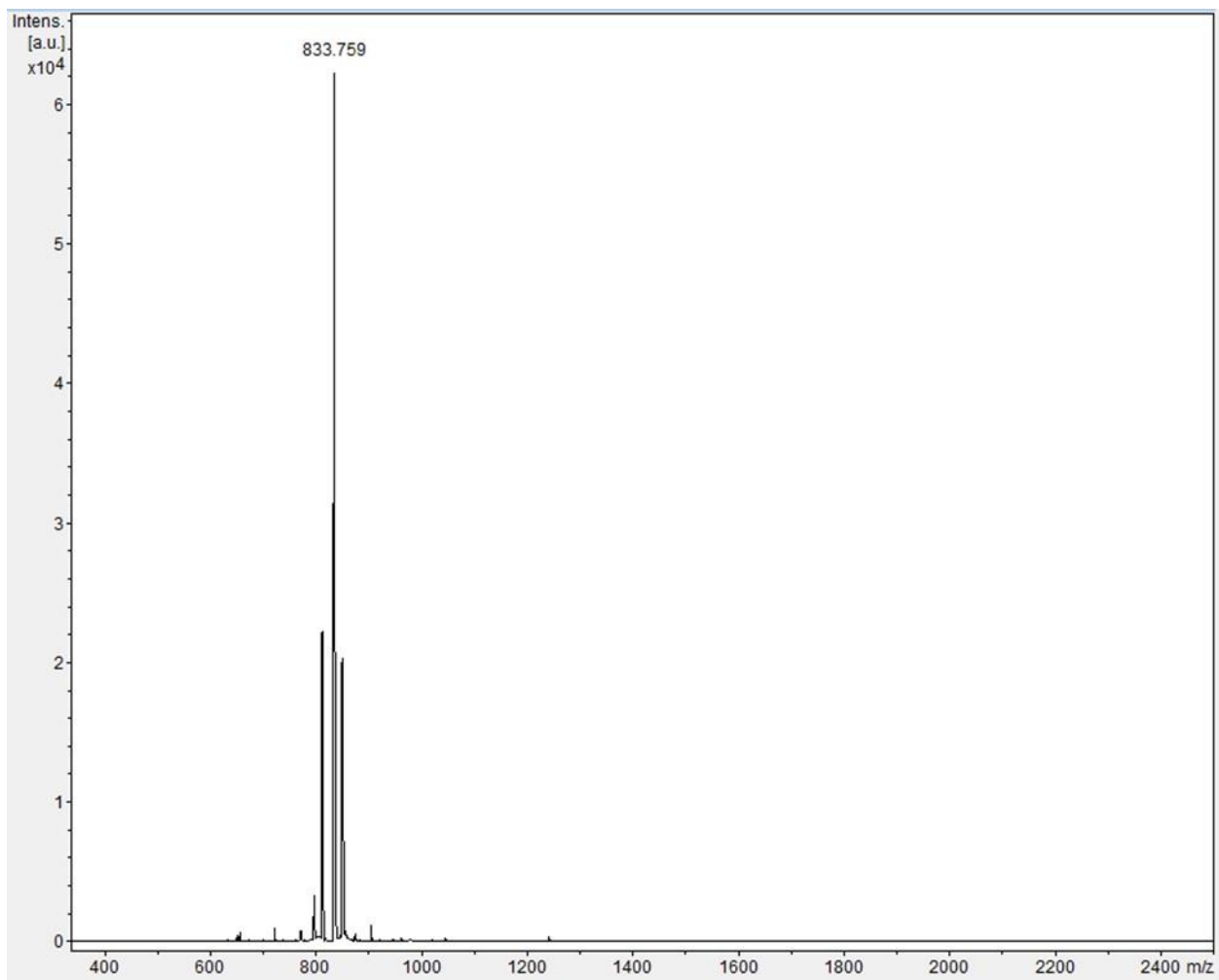
Catalyst 14: [M+H] Calculated = 839.01
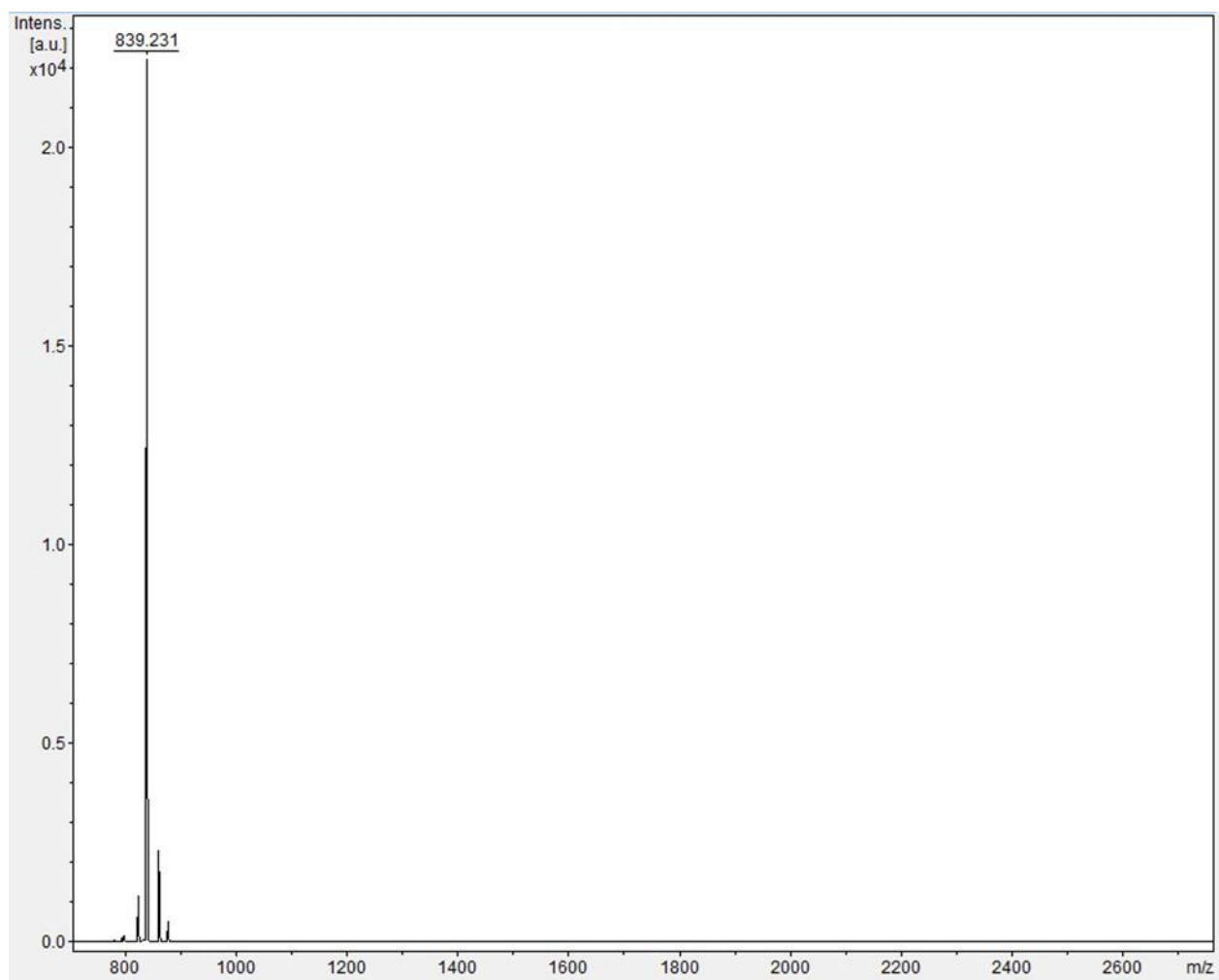
Catalyst 15: [M+H] Calculated = 853.04
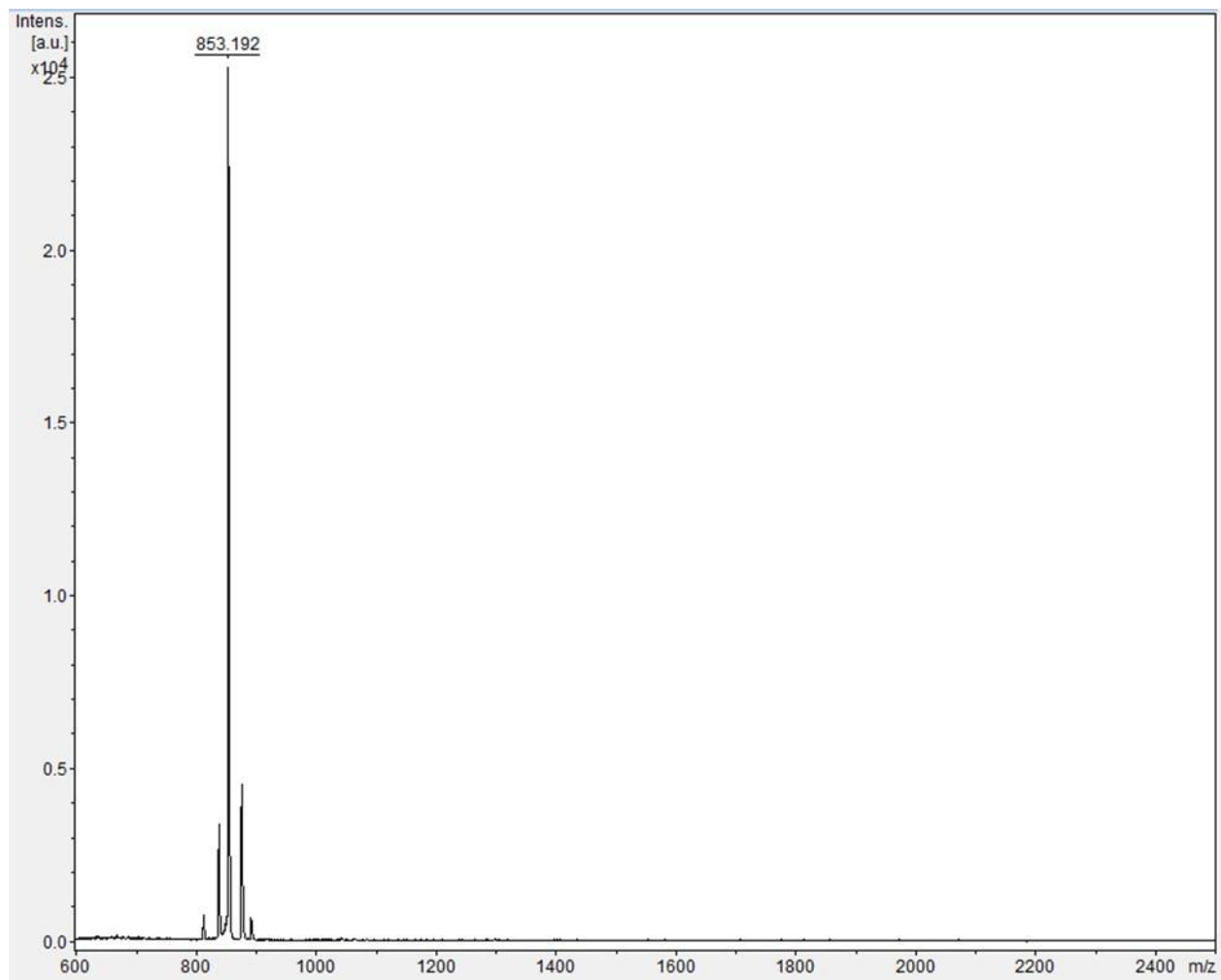
Catalyst 16: [M+H] Calculated = 853.04
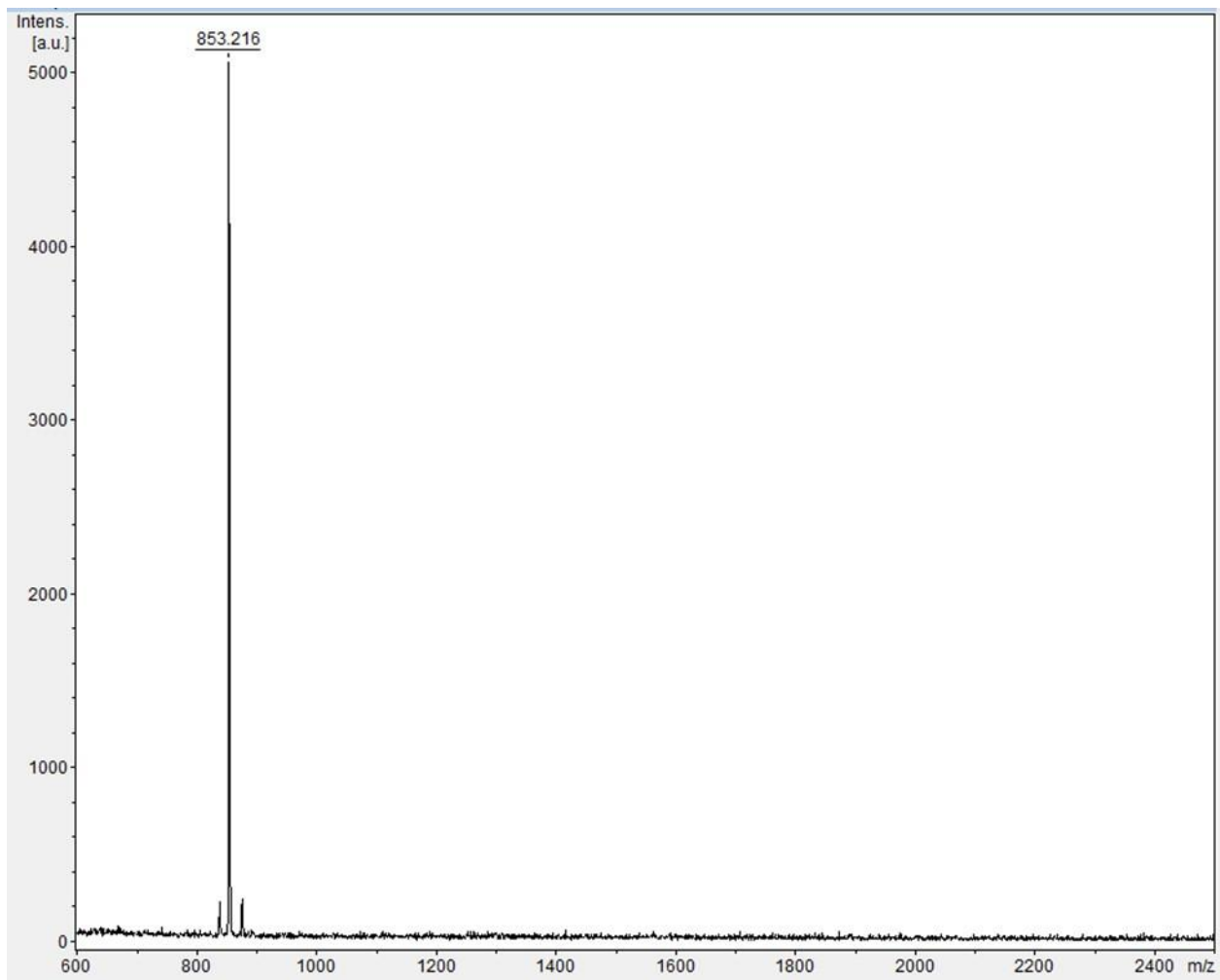
Catalyst 17: [M+Na] Calculated = 1056.23
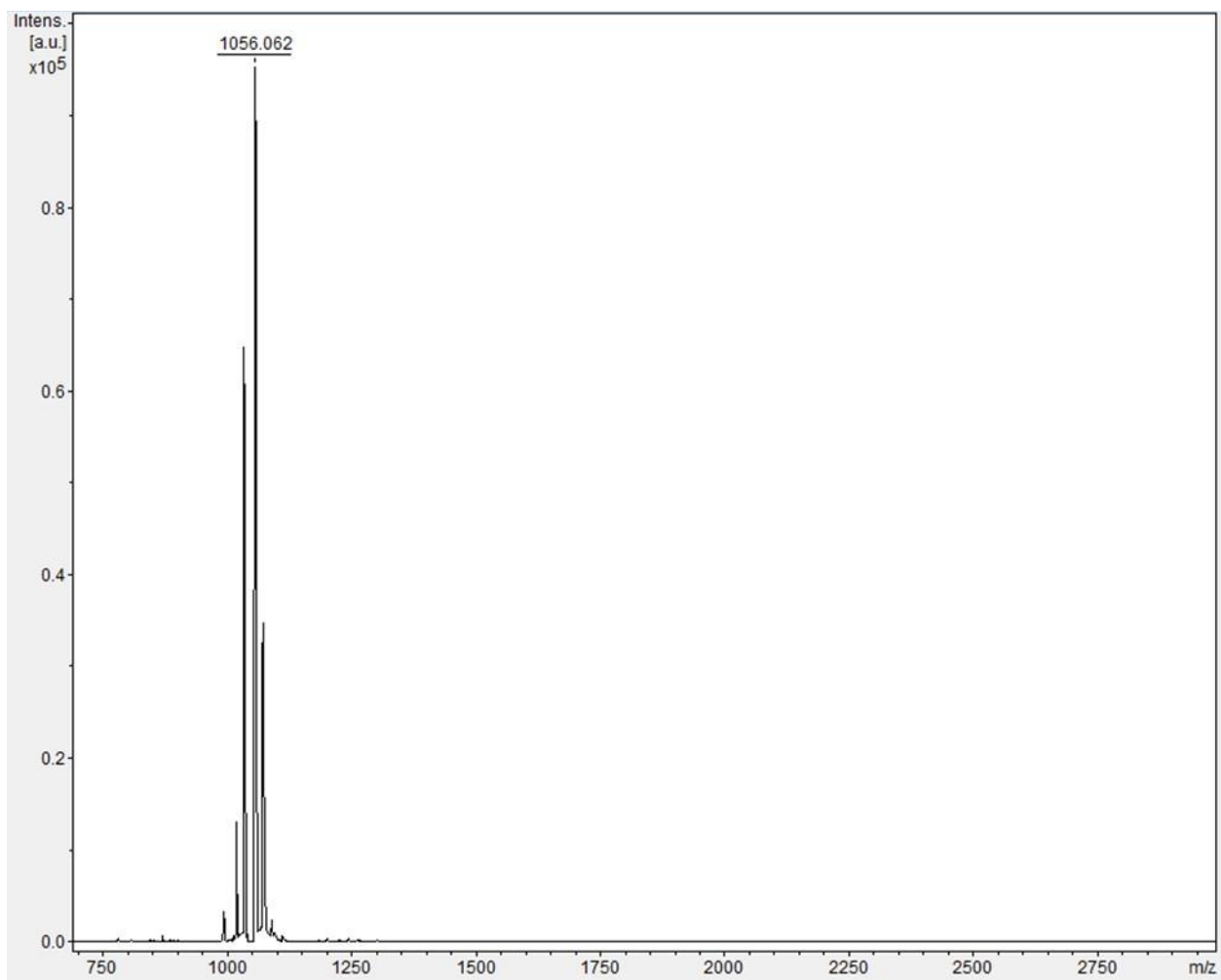
Catalyst 17(D-Ala): [M+Na] Calculated = 1055.57
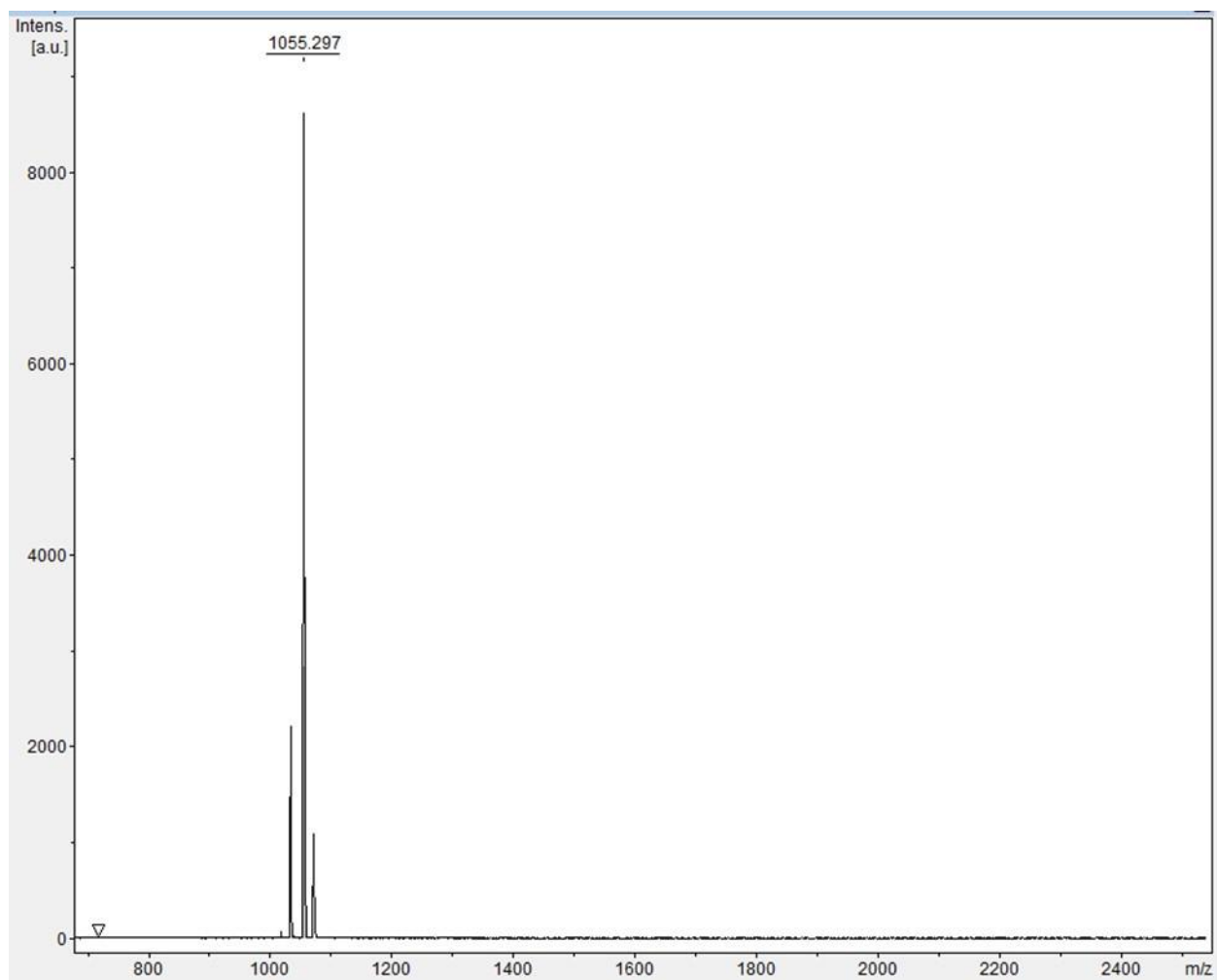
Catalyst 17(D-Ala)(D-Ala): [M+H] Calculated = 1033.24
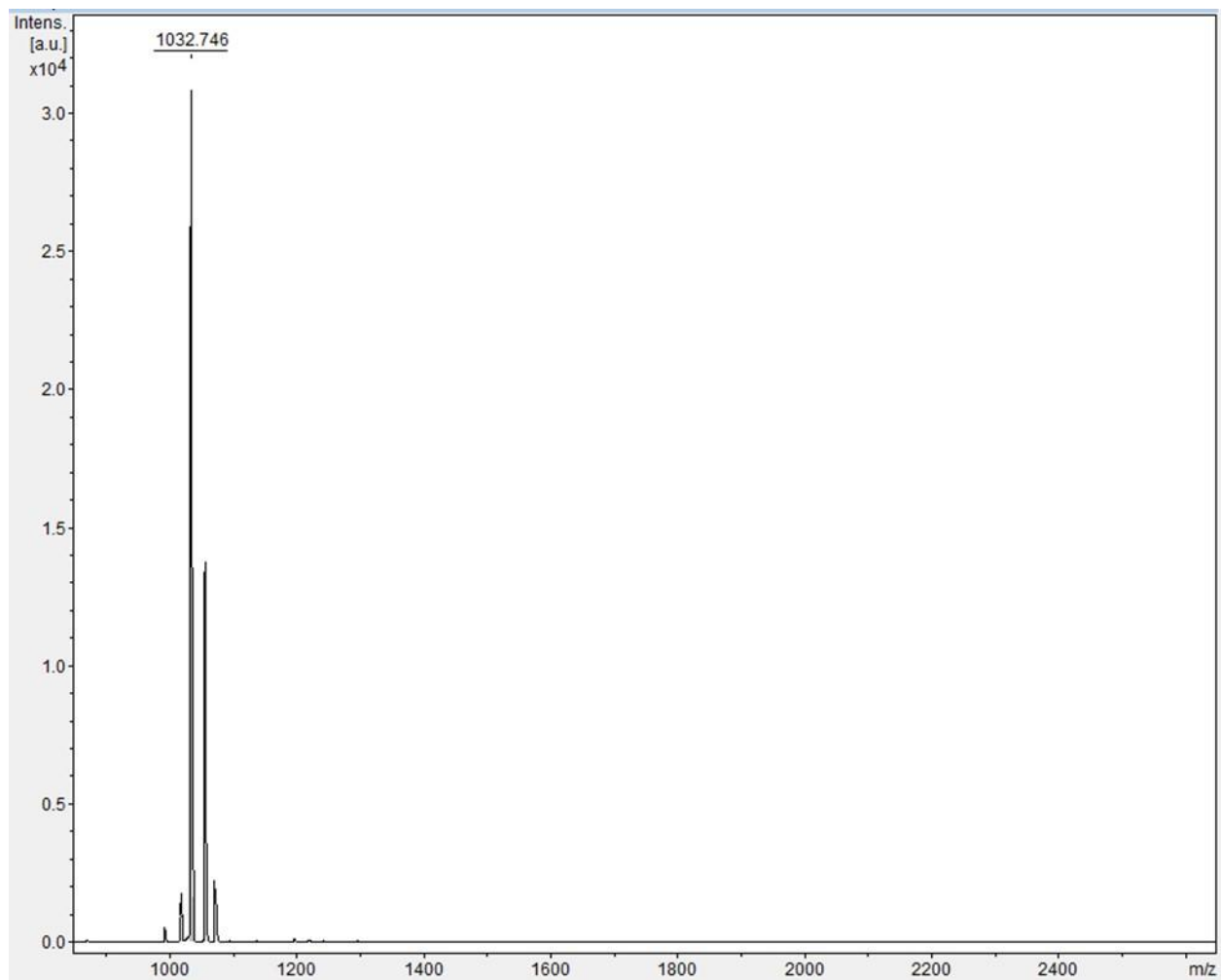
¹H NMR: Fmoc-MAPC-OH TFA salt
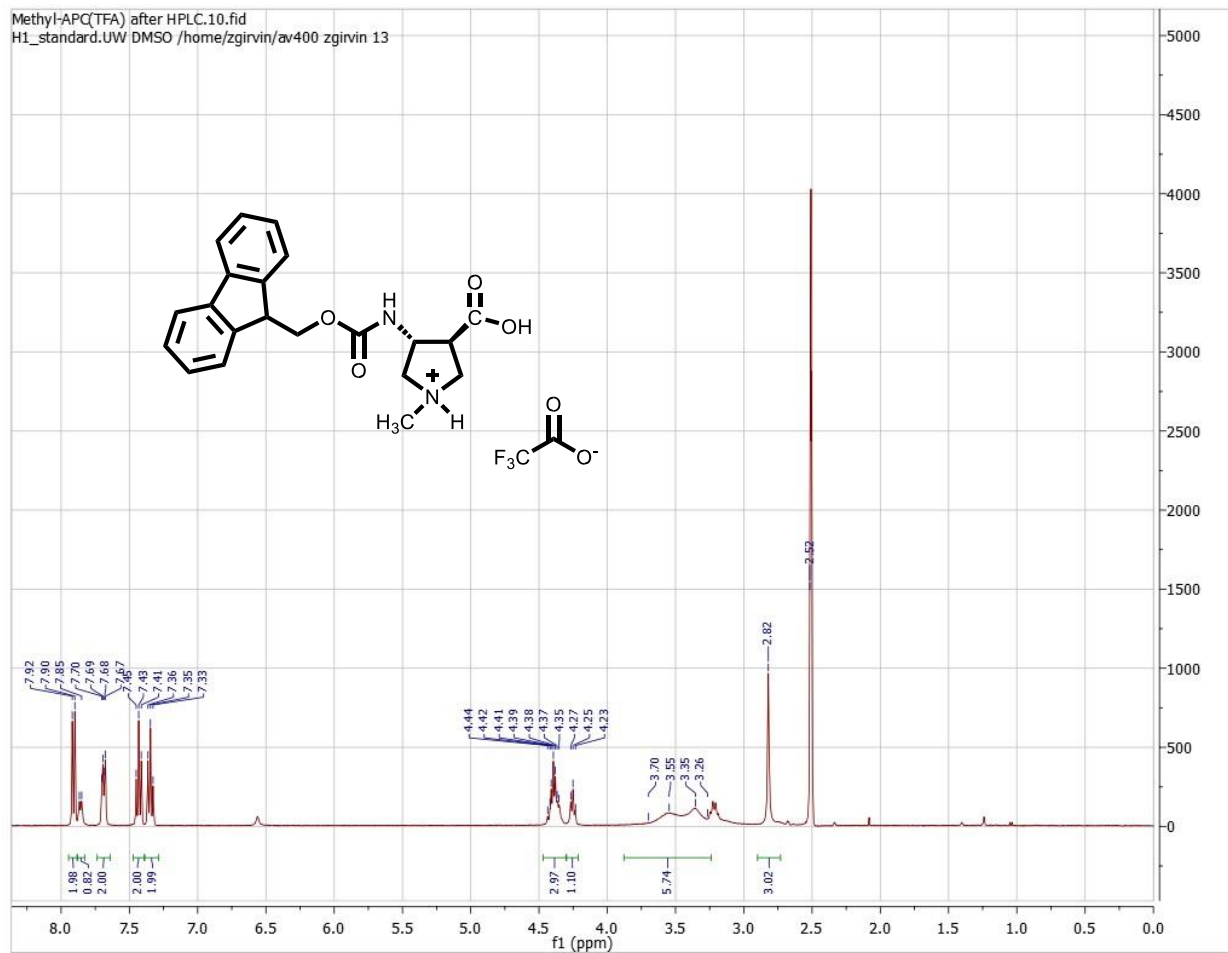
^{13}C NMR: Fmoc-MAPC-OH TFA salt
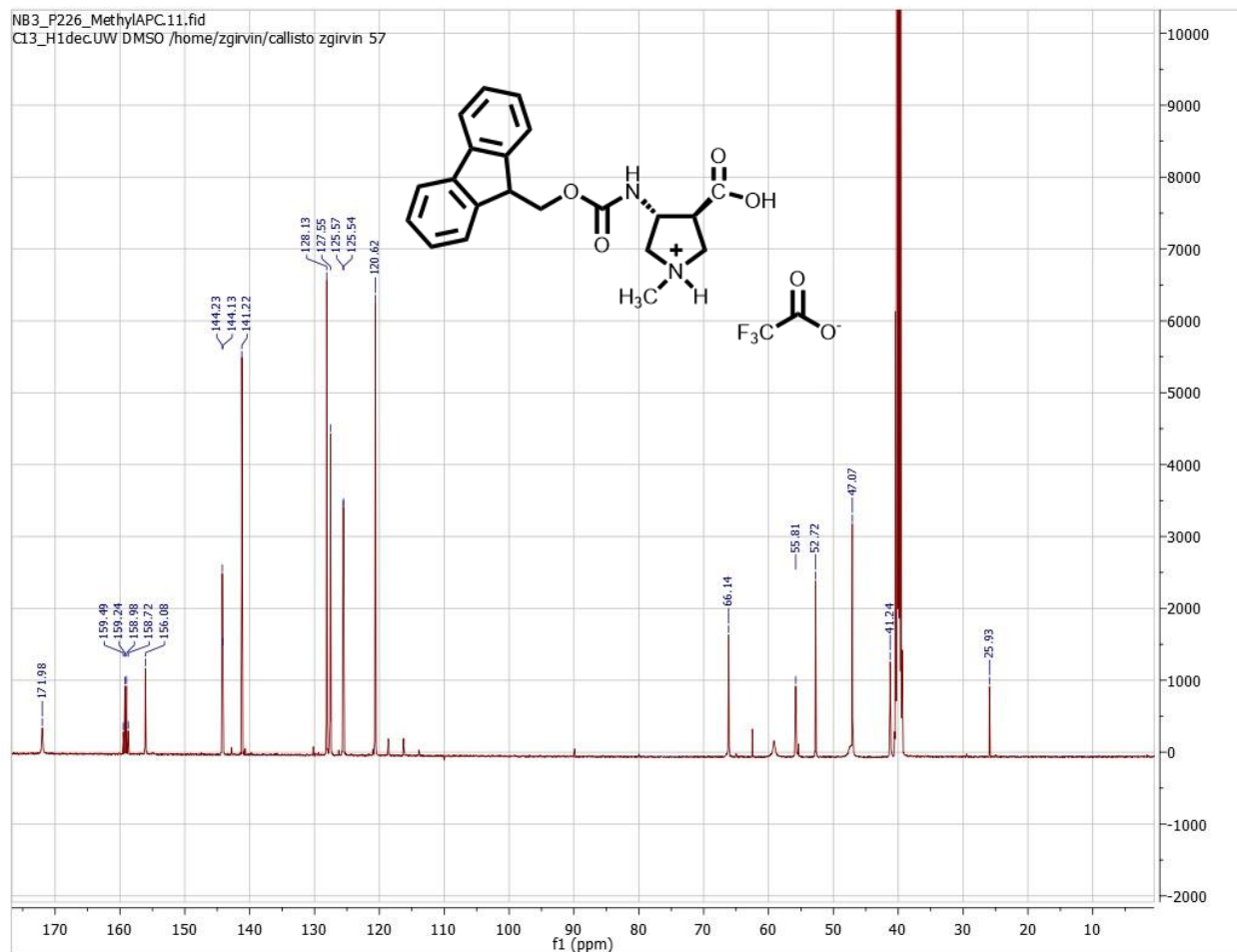
Note: ^{13}C spectrum obtained for sample dissolved in D$_6$-DMSO. δ 159.49, 159.24, 158.98, 158.72 signals correspond to the carbonyl of the trifluoroacetate counter ion, with splitting due to the three F atoms. ^{1}H-NMR spectrum obtained for sample dissolved in D$_6$-DMSO. UPLC Trace of Fmoc-MAPC-OH TFA salt (254 nm channel): 98.9 % purity
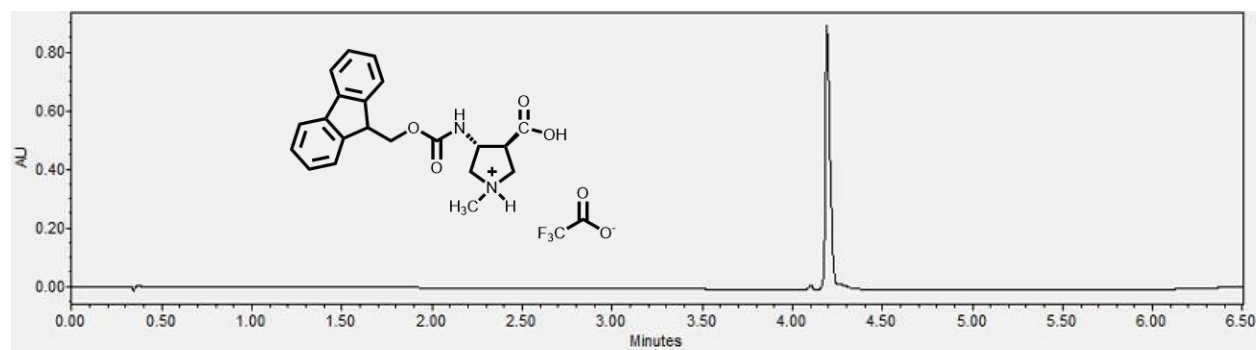
UPLC Purity Analyses

UPLC Method used for every purity check: 10-50%B solvent over 5 minutes (A = H_2O, 0.1 % TFA, B = acetonitrile, 0.1% TFA). Flow rate of 0.4 mL/min, using a Waters Acquity BEH C18 column 1.7μm, 2.1mm x 50mm. Every catalyst was > 95% pure. Detection at 220 nm (corresponding to amide bond absorbance).

Catalyst 1:
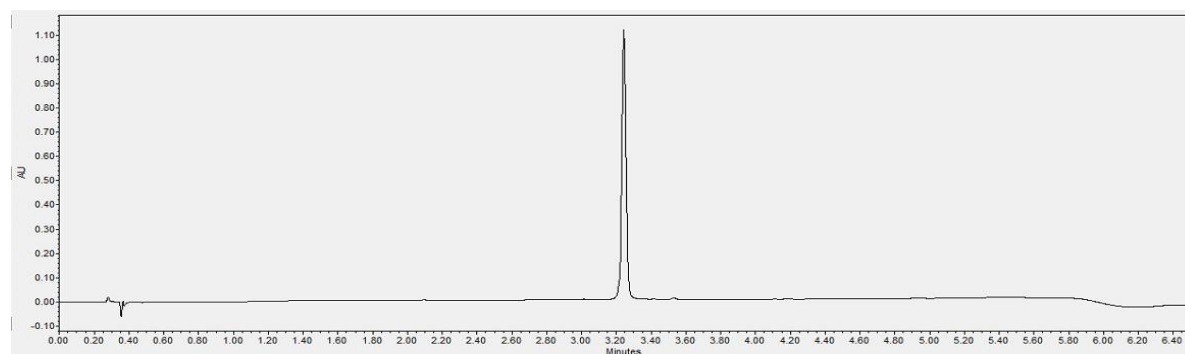
Catalyst 2:
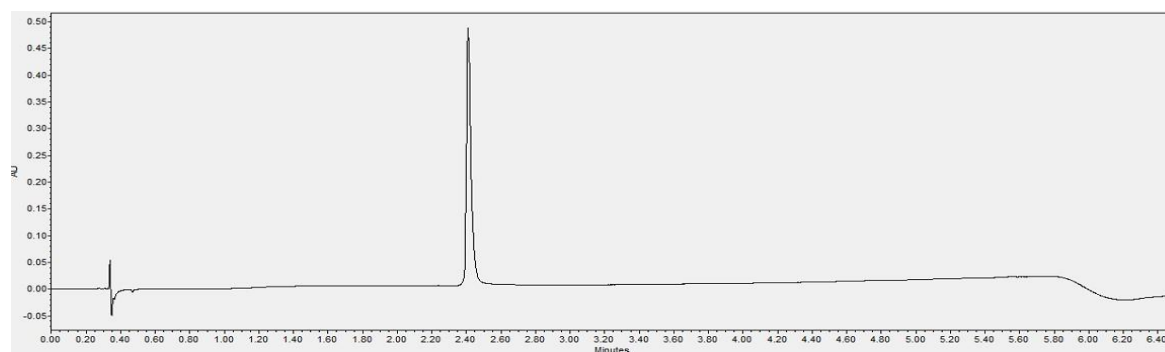
Catalyst 3:
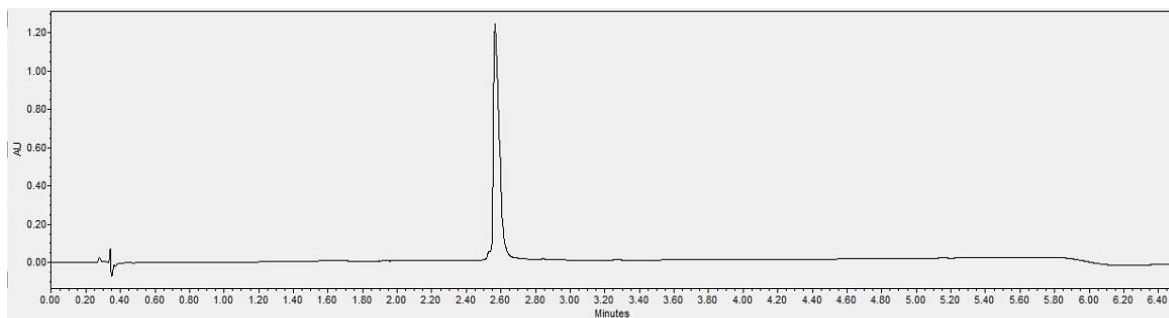
Catalyst 3R-1:
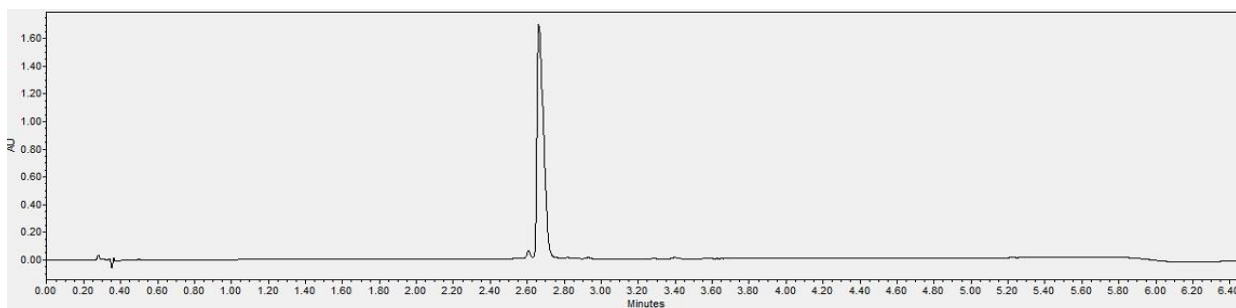
Catalyst 4:
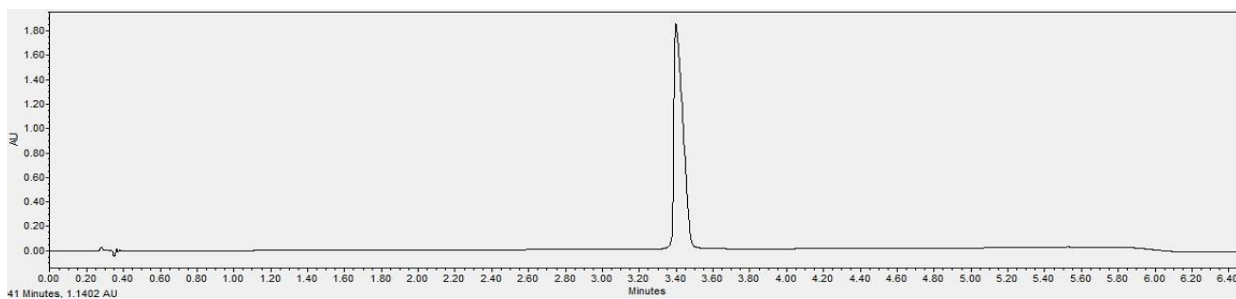
Catalyst 4R-1:
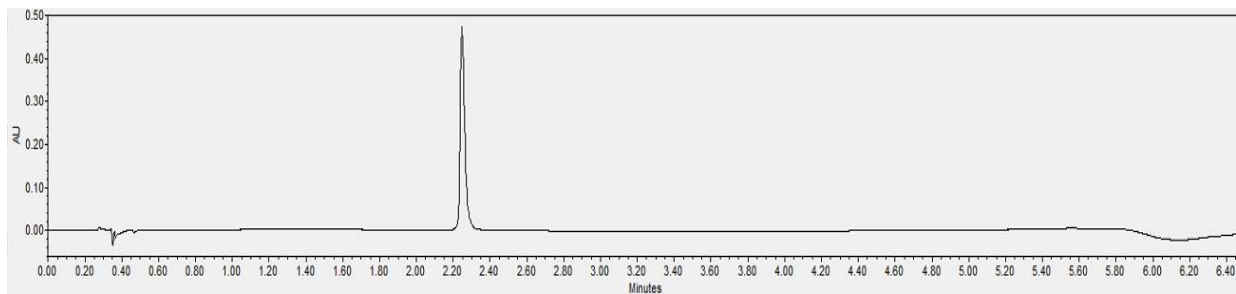
Catalyst 4R-2: Forms gel in isopropanol; unable to obtain purity spectra or test for reactivity.

Catalyst 4R-3: Insoluble in isopropanol; unable to obtain purity spectra or test for reactivity.

Catalyst 4R-4:
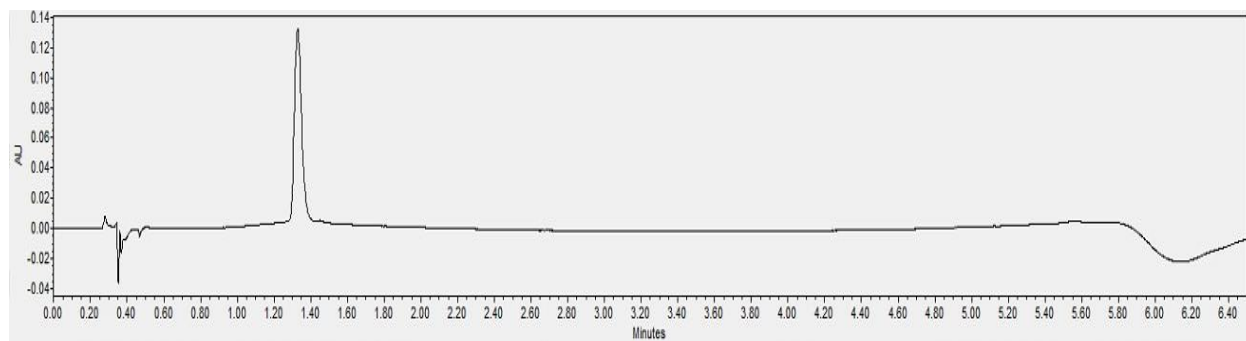
Catalyst 5:
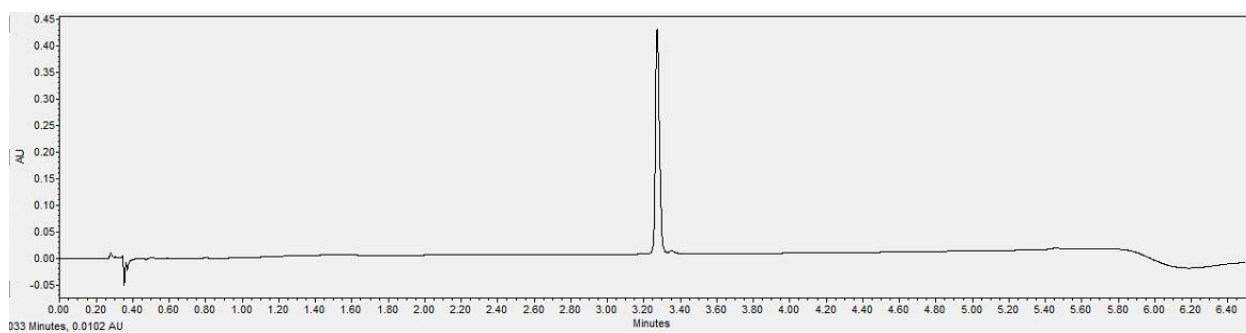
Catalyst 6:
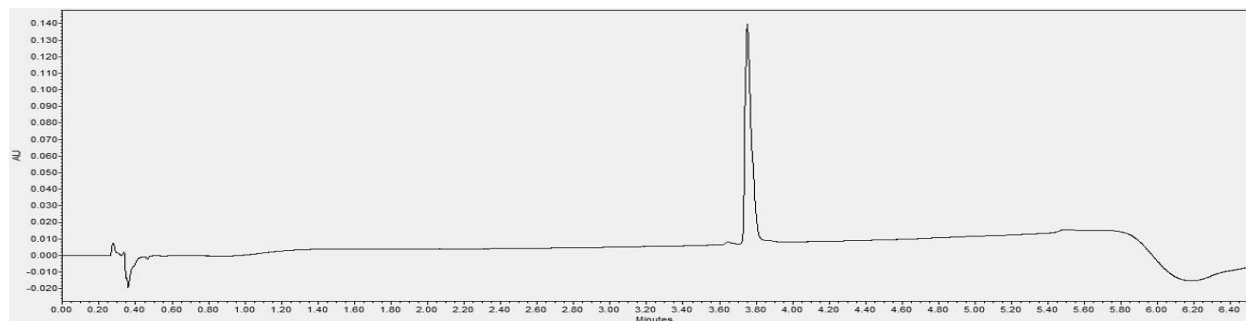
Catalyst 7:
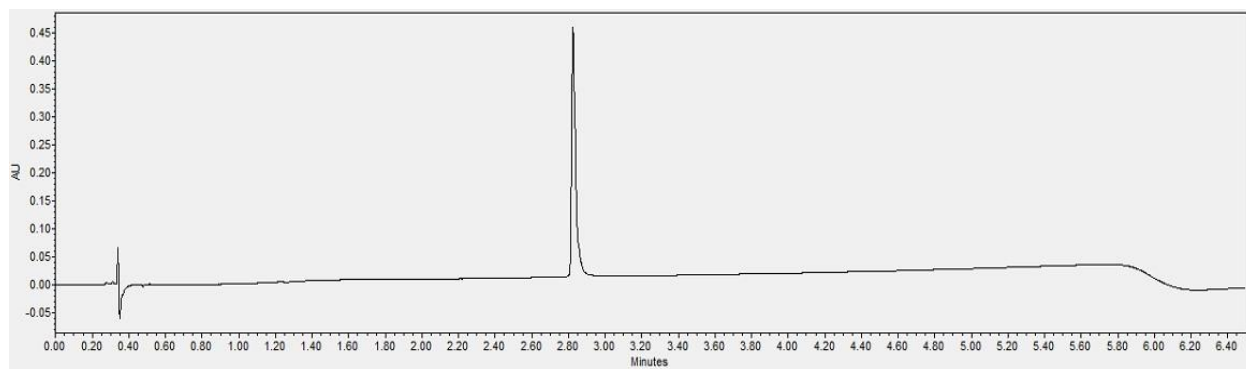
Catalyst 8:
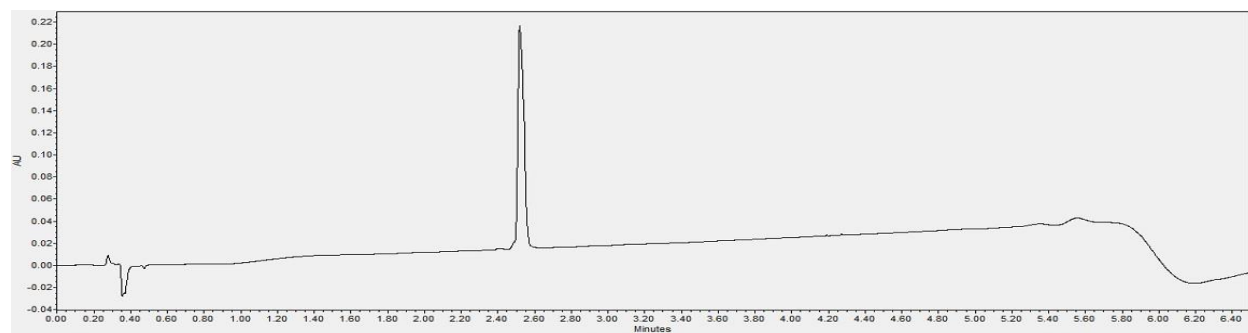
Catalyst 9:
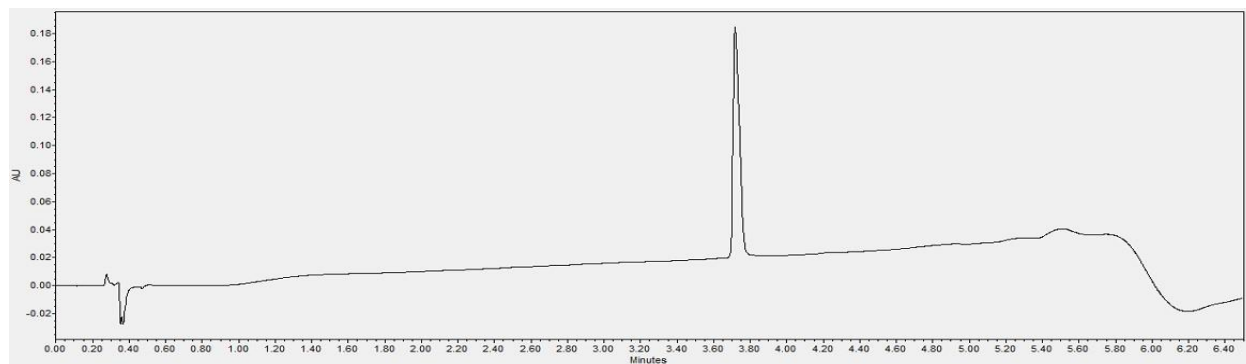
Catalyst 10:
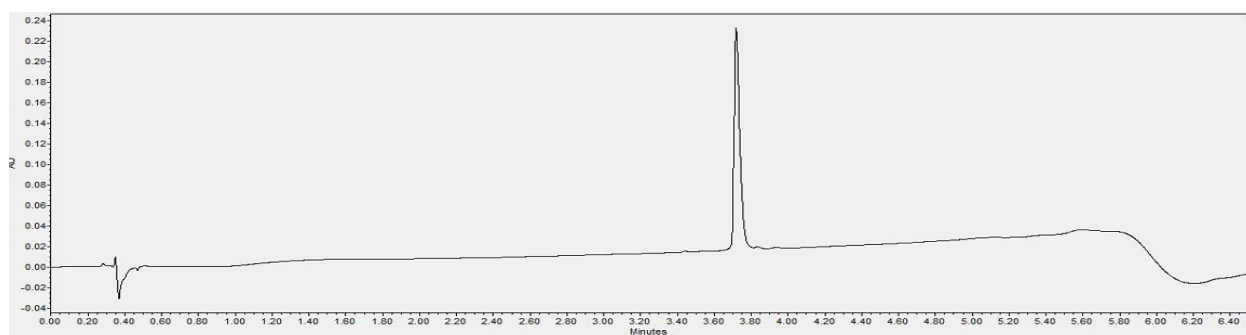
Catalyst 11:
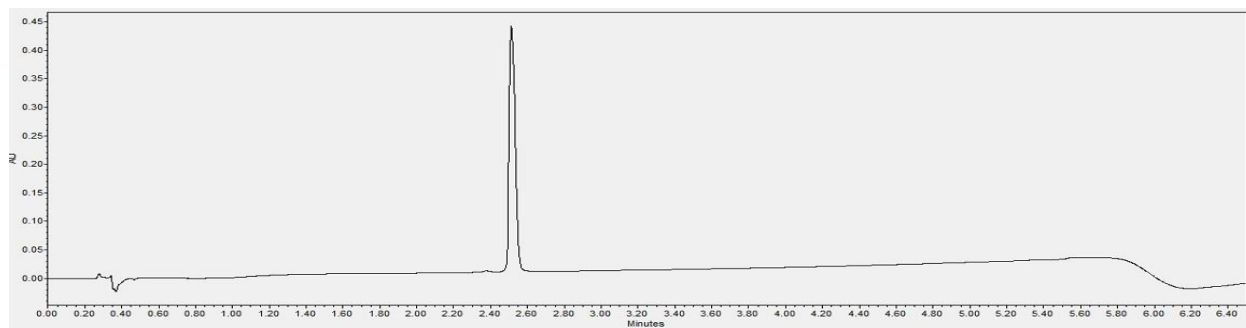
Catalyst 12:
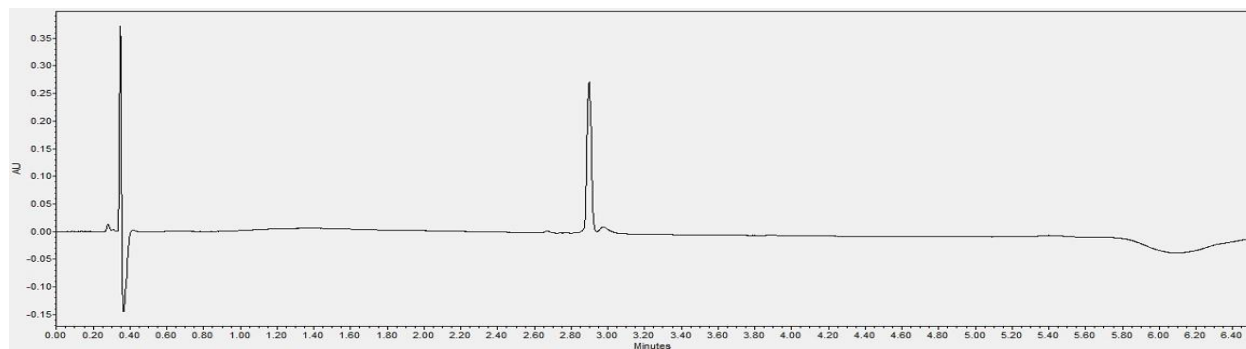
Catalyst 13:
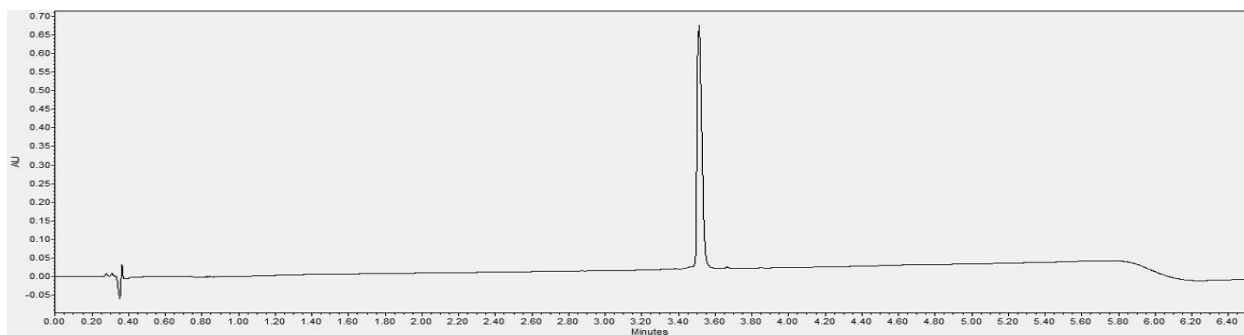
Catalyst 13R-1:
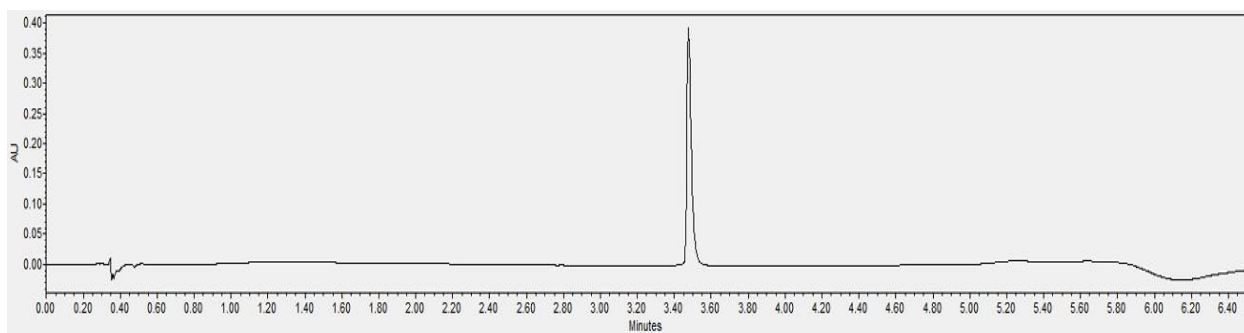
Catalyst 13R-2:
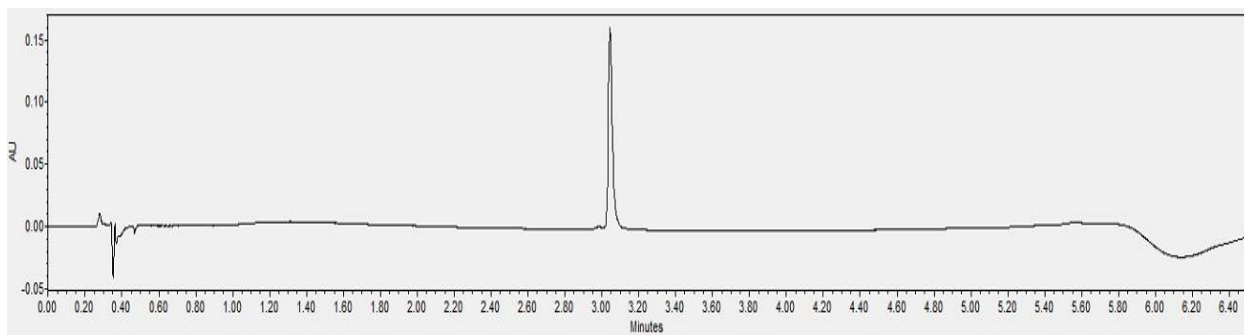
Catalyst 13R-3:
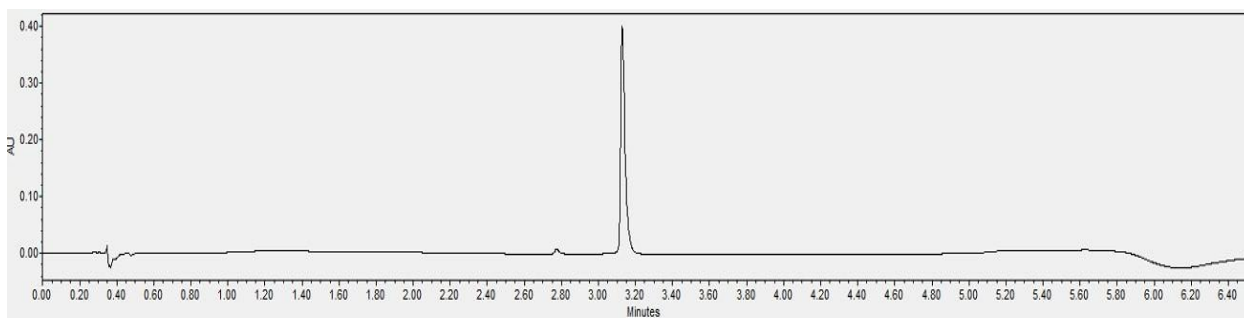
13R-4:
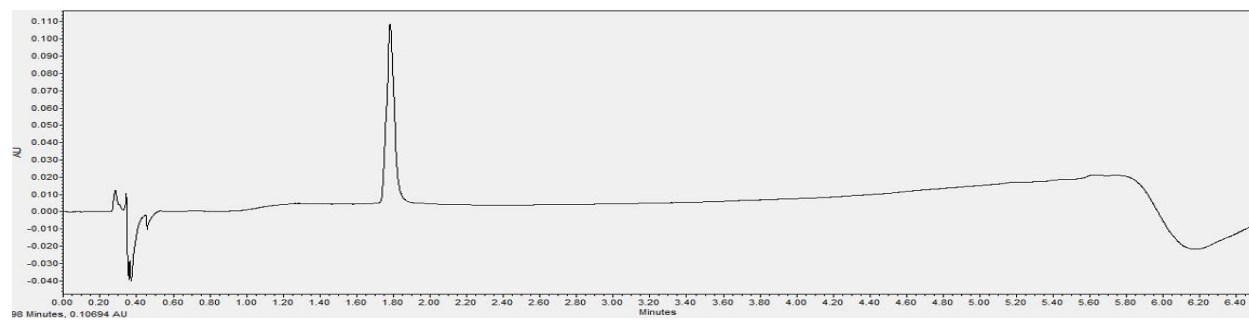
Catalyst 13R-5:
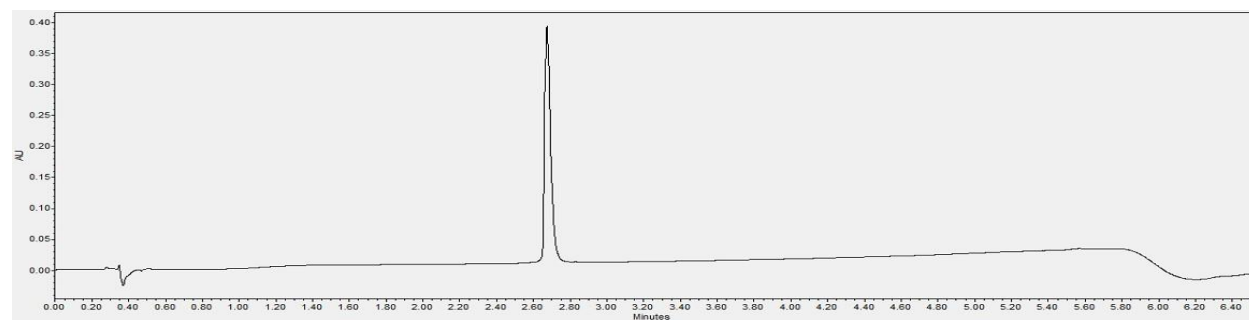
Catalyst 13R-5(d)-Ala:
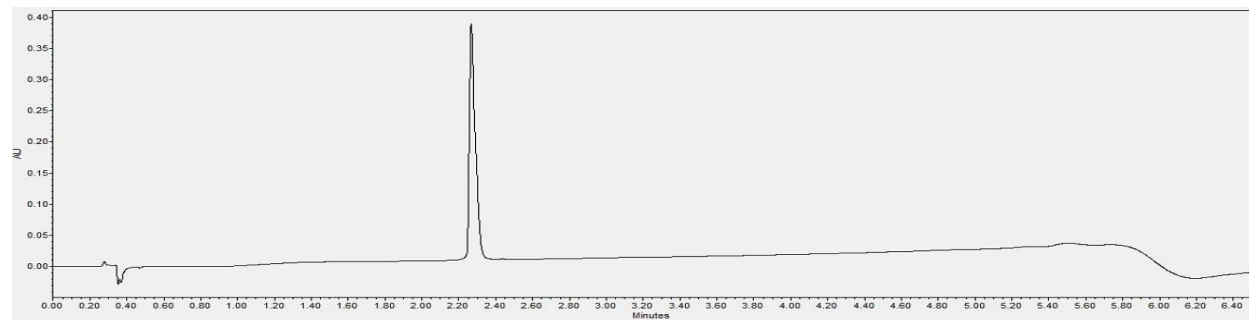
Catalyst 14:
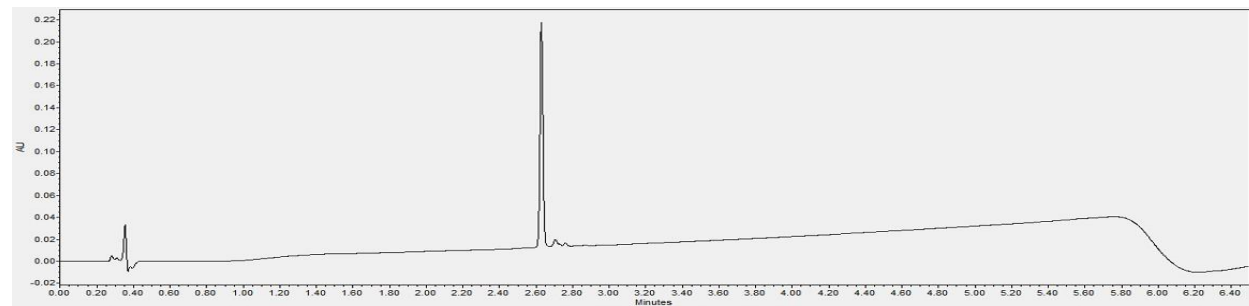
Catalyst 15:
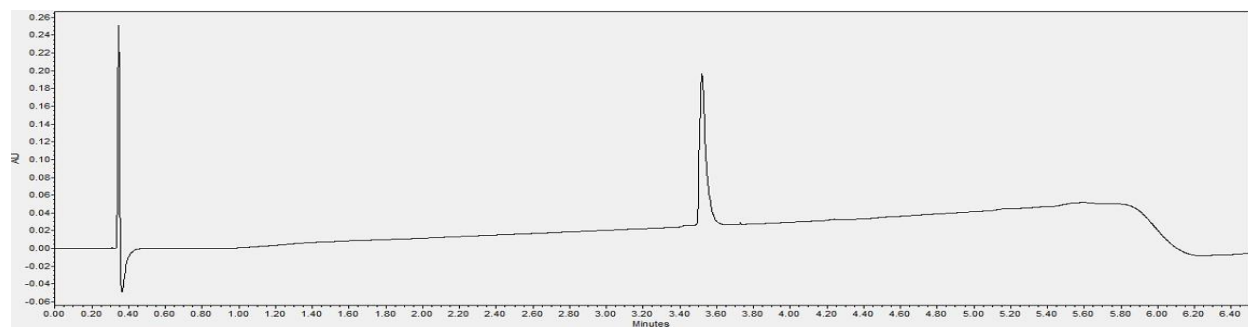
Catalyst 16:
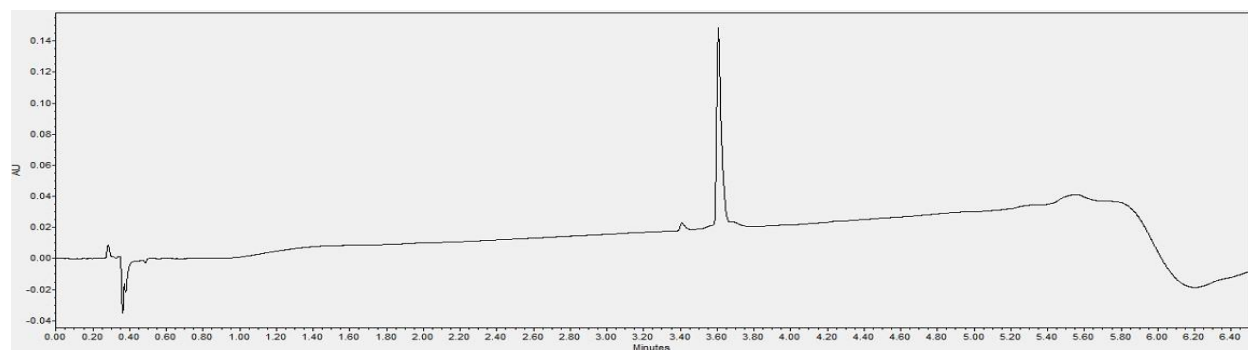
Catalyst 17:
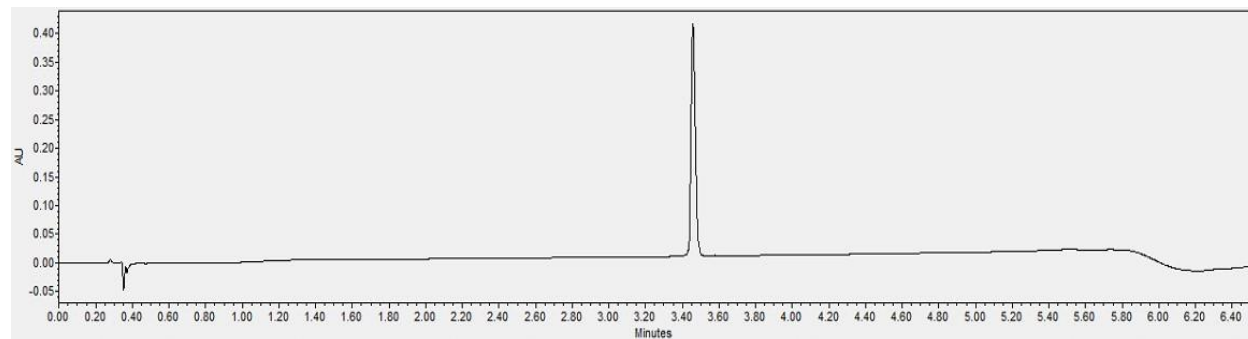
Catalyst 17-(d)Ala:
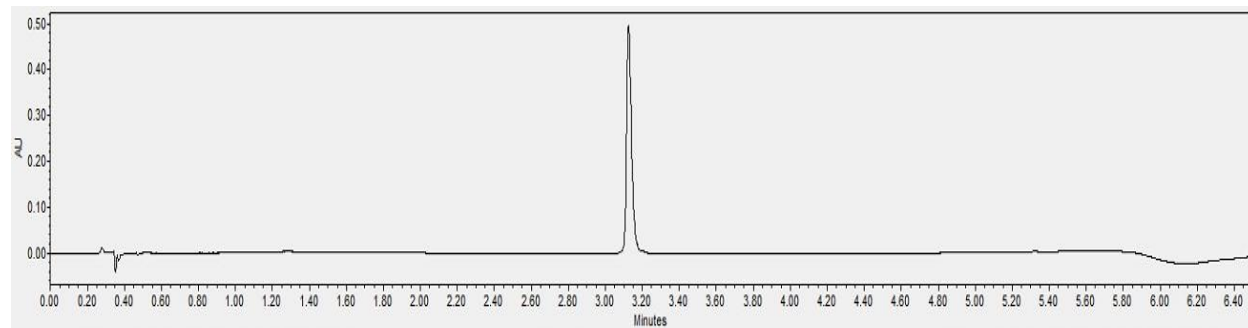
17-(d)Ala-(d)Ala:
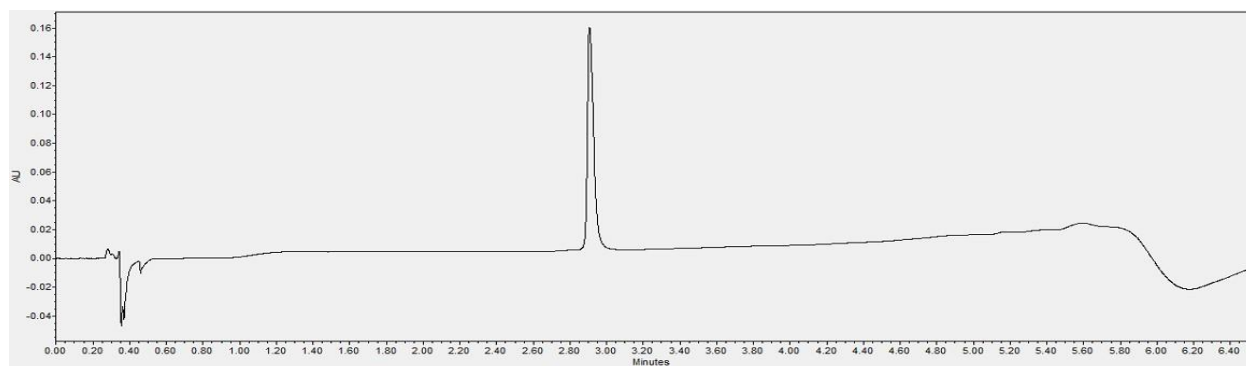
2.6 References

(1) Wolfenden, R. *Annu. Rev. Biochem*. 2011, 80, 645−667.

(2) Herschlag, D.; Natarajan, A. *Biochemistry* 2013, 52, 2050−2067.

(3) Khersonsky, O.; Tawfik, D. S. *Annu. Rev. Biochem*. 2010, 79, 471−505.

(4) Desper, J. M.; Breslow, R. *J. Am. Chem. Soc*. 1994, 116, 12081−12082.

(5) Cramer, K. D.; Zimmerman, S. C. *J. Am. Chem. Soc*. 1990, 112, 3680−3682.

(6) Zhao, Q.; Lam, Y.; Kheirabadi, M.; Xu, C.; Houk, K. N.; Schafmeister, C. E. *J. Org. Chem*. 2012, 77, 4784−4792.

(7) Miller, S. J. *Acc. Chem. Res*. 2004, 37, 601−610.

(8) Doyle, A. G.; Jacobsen, E. N. *Chem. Rev*. 2007, 107, 5713−5743.

(9) Park, Y.; Harper, K. C.; Kuhl, N.; Kwan, E. E.; Liu, R. Y.; Jacobsen, E. N. *Science* 2017, 355, 162−166.

(10) DiRocco, D. A.; Ji, Y.; Sherer, E. C.; Klapars, A.; Reibarkh, M.; Dropinski, J.; Mathew, R.; Maligres, P.; Hyde, A. M.; Limanto, J.; Brunskill, A.; Ruck, R. T.; Campeau, L.; Davies, I. W. *Science* 2017, 356, 426−430.

(11) Wiesner, M.; Revell, J. D.; Wennemers, H. *Angew. Chem., Int. Ed.* 2008, 47, 1871−1874.

(12) Liu, L.; Cotelle, Y.; Avestro, A.; Sakai, N.; Matile, S. J. *Am. Chem. Soc.* 2016, 138, 7876−7879.

(13) Gellman, S. H. *Acc. Chem. Res.* 1998, 31, 173−180.

(14) Hill, D. J.; Mio, M. J.; Prince, R. B.; Hughes, T. S.; Moore, J. S. *Chem. Rev.* 2001, 101, 3893−4012.

(15) Guichard, G.; Huc, I. *Chem. Commun.* 2011, 47, 5933−5941.

(16) Erkkila, A.; Pihko, P. M.¨*Eur. J. Org. Chem.* 2007, 2007, 4205−4216.

(17) Cheng, R. P.; Gellman, S. H.; DeGrado, W. F. *Chem. Rev.* 2001, 101, 3219−3232.

(18) Fernandes, C.; Faure, S.; Pereira, E.; Thery, V.; Declerck, V.; Guillot, R.; Aitken, D. J. *Org. Lett.* 2010, 12, 3606−3609.

(19) Winkler, J. D.; Piatnitski, E. L.; Mehlmann, J.; Kasparec, J.; Axelsen, P. H. *Angew. Chem., Int. Ed.* 2001, 40, 743−745.

(20) Martinek, T. A.; Fülöp, F. *Chem. Soc. Rev.* 2012, 41, 687−702.

(21) Appella, D. H.; Christianson, L. A.; Klein, D.; Powell, D. R.;

Huang, X.; Barchi, J. J.; Gellman, S. H. *Nature* 1997, 387, 381−384.

(22) Schmitt, M. A.; Choi, S. H.; Guzei, I. A.; Gellman, S. H. *J. Am. Chem. Soc.* 2006, 128, 4538−4539.

(23) Choi, S. H.; Guzei, I. A.; Spencer, L.; Gellman, S. H. *J. Am. Chem. Soc*. 2008, 130, 6544−6550.

(24) Choi, S. H.; Guzei, I. A.; Spencer, L.; Gellman, S. H. *J. Am. Chem. Soc.* 2008, 130, 6544−6550.

(25) Johnson, L. M.; Gellman, S. H. *Methods Enzymol*. 2013, 523, 407−429.

(26) Erkkila, A.; Pihko, P. M.¨*J. Org. Chem*. 2006, 71, 2538−2541.

(27) Price, J. L.; Hadley, E. B.; Steinkruger, J. D.; Gellman, S. H. *Angew. Chem., Int. Ed*. 2010, 49, 368−371.

(28) Miller, S. A.; Bobbitt, J. A.; Leadbeater, N. E. *Org. Biomol. Chem*. 2017, 15, 2817−2822.

(29) Alford, J. S.; Abascal, N. C.; Shugrue, C. R.; Colvin, S. M.; Romney, D. K.; Miller, S. J. *ACS Cent. Sci*. 2016, 2, 733.

(30) Giuliano, M. W.; Miller, S. J. *Top. Curr. Chem*. 2015, 372, 157.

(31) Metrano, A. J.; Abascal, N. C.; Mercado, B. Q.; Paulson, E. K.;

Hurtley, A. E.; Miller, S. J. *J. Am. Chem. Soc*. 2017, 139, 492−516.

(32) Schnitzer, T.; Wennemers, H. *J. Am. Chem. Soc*. 2017, 139, 15356−15362.

(33) Coffey, P. L.; Drauz, K. H.; Roberts, S. M.; Skidmore, J.; Smith, J. A. *Chem. Commun*. 2001, 2330−2331.

(34) Maayan, G.; Ward, M. D.; Kirshenbaum, K. *Proc. Natl. Acad. Sci. U. S. A*. 2009, 106, 13679−13684.

(35) Müller, M. M.; Windsor, M. A.; Pomerantz, W. C.; Gellman, S. H.; Hilvert, D. *Angew. Chem., Int. Ed*. 2009, 48, 922−925.

(36) Wang, P. S. P.; Nguyen, J. B.; Schepartz, A. *J. Am. Chem. Soc*. 2014, 136, 6810−6813.

(37) Becart, D.; Diemer, V.; Salaun, A.; Oiarbide, M.; Nelli, Y. R.; Kauffmann, B.; Fischer, L.; Palomo, C.; Guichard, G. *J. Am. Chem. Soc.* 2017, 139, 12524−12532.

(38) Taylor, A. I.; Pinheiro, V. B.; Smola, M. J.; Morgunov, A. S.; Peak-Chew, S.; Cozens, C.; Weeks, K. M.; Herdewijn, P.; Holliger, P. *Nature* 2015, 518, 427−430.

(39) Akagawa, K.; Kudo, K. *Acc. Chem. Res*. 2017, 50, 2429−2439.

(40) Kinghorn, M. J.; Valdivia-Berroeta, G. A.; Chantry, D. R.;

Smith, M. S.; Ence, C. C.; Draper, S. R. E.; Duval, J. S.; Masino, B. M.;

Cahoon, S. B.; Flansburg, R. R.; Conder, C. J.; Price, J. L.; Michaelis,

D. J. *ACS Catal*. 2017, 7, 7704−7708.

(41) Lewis, C. A.; Gustafson, J. L.; Chiu, A.; Balsells, J.; Pollard, D.;

Murry, J.; Reamer, R. A.; Hansen, K. B.; Miller, S. J. *J. Am. Chem. Soc*.

2008, 130, 16358−16365.

(42) Narlikar, G.; Gopalakrishnan, V.; McConnell, T. S.; Usman, N.;

Herschlag, D. *Proc. Natl. Acad. Sci. U. S. A*. 1995, 92, 3668−3672.

(43) Warshel, A. *J.* Biol. Chem. 1998, 273, 27035−27038.

(44) Jiang, L.; Althoff, E. A.; Clemente, F. R.; Doyle, L.;

Rothlisberger, D.; Zanghellini, A.; Gallaher, J. L.; Betker, J. L.;

Tanaka, F.; Barbas, C. F., III; Hilvert, D.; Houk, K. N.; Stoddard, B.

L.; Baker, D. *Science* 2008, 319, 1387−1391.

(45) Romero, M. L.; Rabin, A.; Tawfik, D. S. *Angew. Chem., Int. Ed*.

2016, 55, 15966−15971.

(46) HS. Lee, P.R. LePlae, E.A. Porter, S.H. Gellman,. *J. Org. Chem.* 66, 35973599 (2001).

(47) X. Ariza, G. Asins, J. Garcia, F.G. Hegardt, K. Makowski, D. Serra, J. Velasco, *Journal of Labeled Compounds and Radiopharmaceuticals.* 53, 556-558 (2010).

(48) Molnar, I. G., Tanzer, E., Daniliuc, C., Gilmour, R.,. *Chem. Eur. J.* 2014, 20, 794-800.

Chapter 3

Foldamer-templated Catalysis of Macrocycle Formation

Portions of this chapter are published in:

Isolation and characterization of E,E-diene **B** were performed by Mark Katherine Andrews.

2D NMR studies on Catalyst **1** were performed by Xinyu Liu.

3.1 Abstract

Macrocycles, compounds containing a ring of 12 or more atoms, find use in human medicine, fragrances, and biological ion sensing. The efficient preparation of macrocycles is a fundamental challenge in synthetic organic chemistry because the high entropic cost of large-ring closure allows undesired intermolecular reactions to compete. Here, we present a bioinspired strategy for macrocycle formation through carbon–carbon bond formation. The process relies on a catalytic oligomer containing α- and β-amino acid residues to template the ring-closing process. The α/β-peptide foldamer adopts a helical conformation that displays a catalytic primary amine–secondary amine diad in a specific three-dimensional arrangement. This catalyst promotes aldol reactions that form rings containing 14 to 22 atoms. Utility is demonstrated in the synthesis of the natural product robustol.

3.2 Introduction

Macrocyclic compounds, containing a ring of 12 or more atoms, play important roles in biology and medicine.[1-3] Engineered macrocycles have engendered new technologies[4] and new therapeutic strategies.[5] Efficient synthesis of macrocycles is challenging because the entropic penalty associated with ring closure allows competition from intermolecular side-reactions, reducing yields of the desired products.[6-10] Preorganization of linear precursors through multipoint coordination of a metal cation, an anion, or a neutral partner can facilitate synthesis of specific macrocycle classes (**Figure 1A**), but this strategy depends on noncovalent interaction sites in the linear precursor.[9-12] Intramolecular alkene metathesis can be very effective for formation of large rings.[9, 13-15] This process features catalytic metal-based activation of terminal alkenes in a linear precursor, but additional coordination between internal functionality and the metal center is necessary.[9, 13-16] Biosynthetic machinery overcomes the entropic cost of

macrocycle formation by holding linear precursors in appropriate conformations, catalyzing the

ring-closure reaction, and inhibiting competing intermolecular processes.[17,18] We took inspiration

from biological catalysts to develop a macrocyclization catalyst in which a well folded oligomer

activates both ends of a linear precursor and orients the termini for reaction, thereby serving as a

template for ring closure through carbon–carbon bond formation.

A *Macrocyclization Strategies*

Guest-mediated cyclization | Ring-closing metathesis | *This Work*: Foldamer catalysis
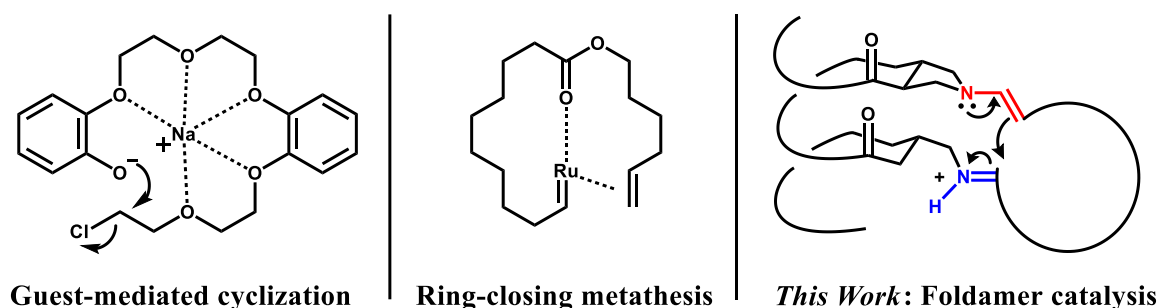
B *Foldamer vs. Small Molecule Catalysis*
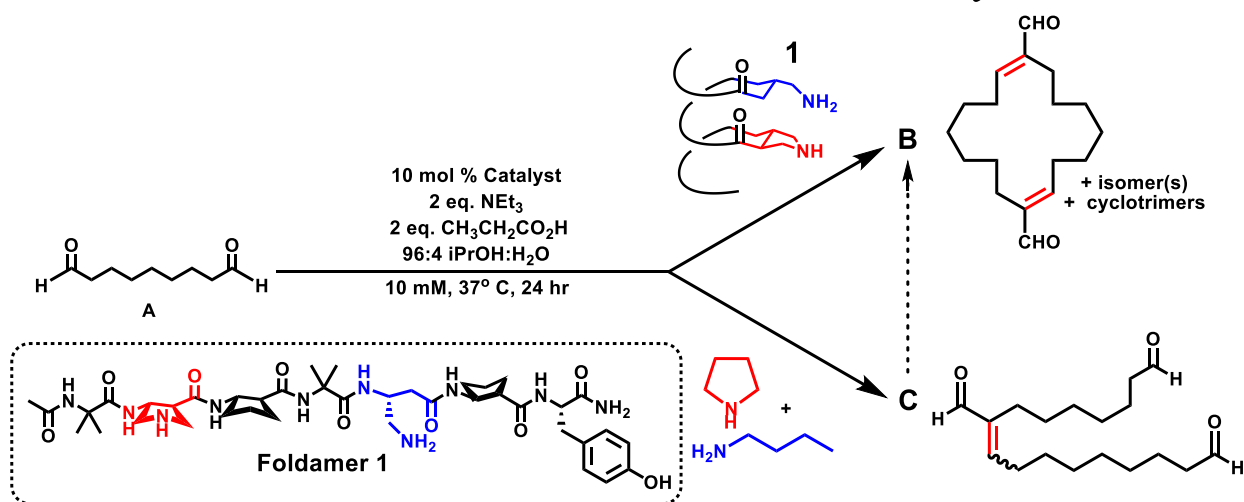
Figure 1. (A) Prior approaches and foldamer approach to macrocyclization. (B) Divergent reactivity: Foldamer versus small molecule catalysis. eq., equivalent(s). Image rights belong to AAAS.

Our approach uses a foldamer designed to facilitate macrocyclization through aldol condensation by proper orientation of two catalytic groups. We build on pioneering work by Miller et al., who employed related design principles to achieve site-specific catalytic functionalization of complex substrates.[19] Our work complements the development of small molecules that serve as bifunctional catalysts, such as the recent mimicry of glycotransferase enzymes with cyclic bis-thioureas[20] and the recent stereoselective formation of nucleoside phosphoramidates with bisimidazoles.[21] Neither of these cases, however, involved macrocycle formation.

3.3 Results

Oligomer **1** (**Figure 1B**) contains both α- and β-amino acid residues and features an αββ backbone repeat pattern, which favors a helical conformation that has approximately three residues per turn.[22,23] Use of β residues with a five-membered ring constraint, such as the cyclopentane- and pyrrolidine-based residues in **1**, enhances helix stability.[22] A related α/β-peptide containing two pyrrolidine-based residues catalyzes intermolecular crossed aldol condensations involving formaldehyde as the electrophile.[24] Optimal catalysis required i,i+3 spacing of the pyrrolidine residues, which causes alignment of these two catalytic units upon helical folding. α/β-Peptide **1** is distinct from the earlier example in that one of the catalytic units is a primary amine, a difference that proved to be consequential.

The current study began with an unexpected observation. We asked whether α/β-peptide **1** would promote cyclization of C9 dialdehyde **A** to form cyclooctene-1-aldehyde (**Figure 1B**). The reaction conditions, based on precedents from Pihko et al. and studies described in chapter 2,[24,25] included propionic acid and triethylamine as additives and aqueous isopropanol as solvent. The cyclooctene derivative, however, was not observed when 10 mM **A**

was allowed to react in the presence of 10 mole % (mol %) **1**, although **A** appeared to be fully consumed within 24 hours. Instead, the foldamer catalyzed formation of a product mixture in which the principal components were cyclodimers. Mary Katherine Andrews isolated the major cyclodimer and identified it by two-dimensional (2D) nuclear magnetic resonance (NMR) spectroscopy to be the 16-membered ring E,E diene **B**. Liquid chromatography–mass spectrometry (LC-MS) revealed initial formation of intermolecular aldol adduct **C**, but the amount of this intermediate remained low throughout the reaction, suggesting rapid cyclization (**Figure 2, 3**). By contrast, a 1:1 mixture of pyrrolidine and n-butylamine (10 mol % each) catalyzed slow formation of the linear dimer **C**, with only trace levels of cyclodimer detected after 24 hours. We hypothesized that the foldamer acts by a bifunctional mechanism, serving as a template to overcome the entropic cost of large-ring closure.
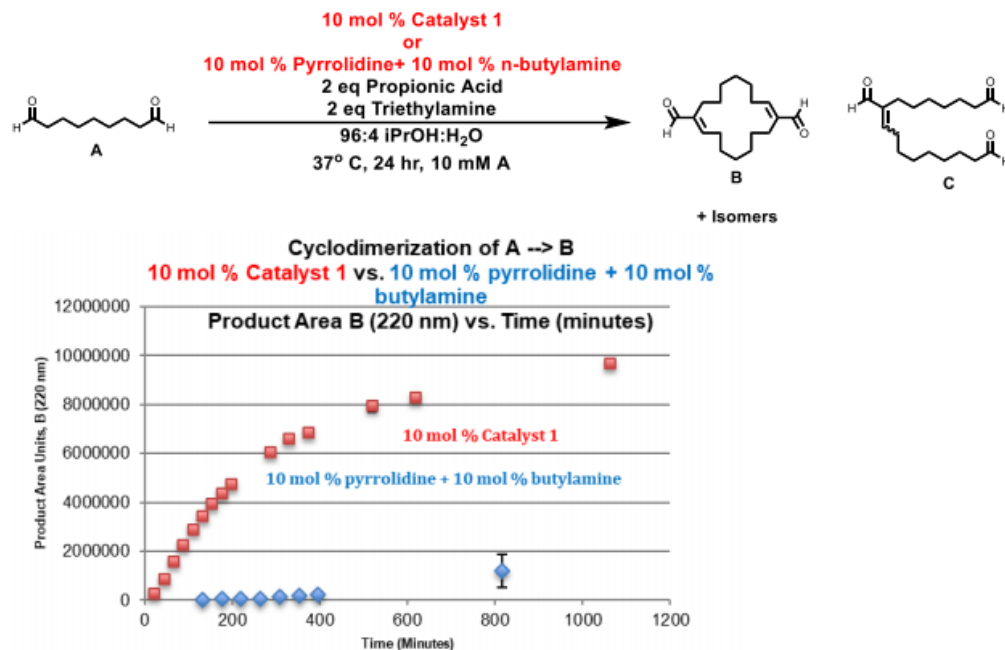
Figure 2. Plot of area units (220 nm) vs. time (minutes) of reaction progress data for the cyclodimerization of **A** → **B** in the presence of either 10 mol % catalyst **1** or 10 mol % pyrrolidine + 10 mol % butylamine. Error bars correspond to the standard deviation over two reactions. Units = arbitrary units.
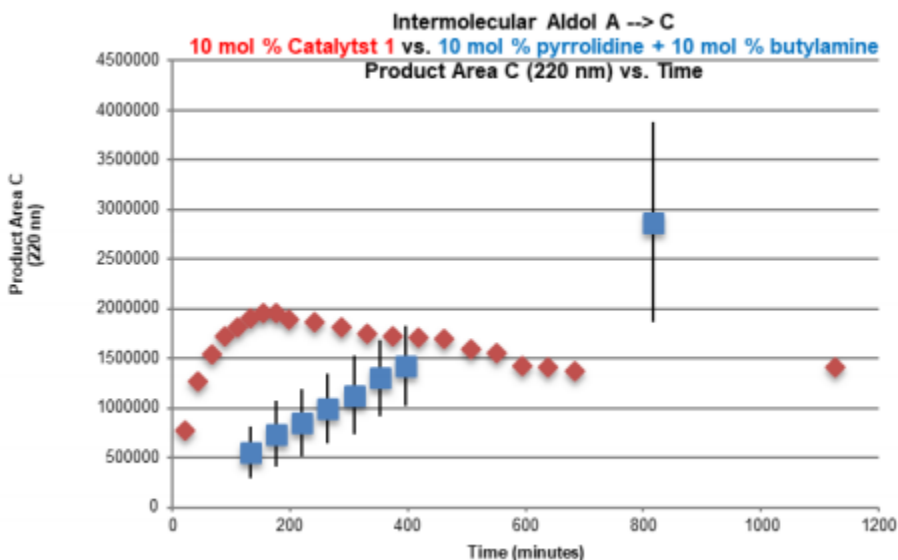
Figure 3. Amount of intermolecular aldol adduct detected as a function of time for reactions of the C9 dialdehyde catalyzed by 10 mol % foldamer **1** or by a mixture of 10 mol % pyrrolidine and 10 mol % butylamine. The vertical scale is the area of the peak in an LC-MS chromatogram that has a mass corresponding to the linear aldol adduct **C** (possibly a mixture of geometric isomers), based on absorbance at 220 nm. Error bars correspond to the standard deviation over two reactions.

To gain further insight on the capabilities of foldamer **1**, we prepared symmetrical

dialdehydes **D1** to **D4** (**Figure 4A**), each containing a central methoxyphenyl ring that allowed

us to monitor starting material, products, and transient intermediates through ultraviolet

absorbance. Initial studies focused on **D3**, which can form a 16-membered ring enal, matching

the ring size of cyclodimer **B**. When we reacted **D3** with **1**, we observed nearly full conversion to

macrocyclic E-enal **E3**. By contrast, the control reaction with pyrrolidine and n-butylamine

produced only a trace amount of **E3** after 24 hours (**Figure 4**).

α/β-Peptide **1** proved to be versatile in terms of product ring size (**Figure 4A**). We

observed efficient conversion of **D4** to 18-membered ring E-enal **E4** and of **D2** to 14-membered

ring E-enal **E2**. The foldamer-catalyzed reaction of **D1** took longer to reach completion and led

to a mixture of E-enal **E1** and cyclodimers. Precedents suggest that this outcome arises because of strain that develops upon 12-membered ring formation.[7,8] However, efficient and stereospecific synthesis of the 14-, 16-, and 18-membered ring enals suggests that catalyst **1** is broadly competent for formation of larger rings.

A *Scope: Ring Size*
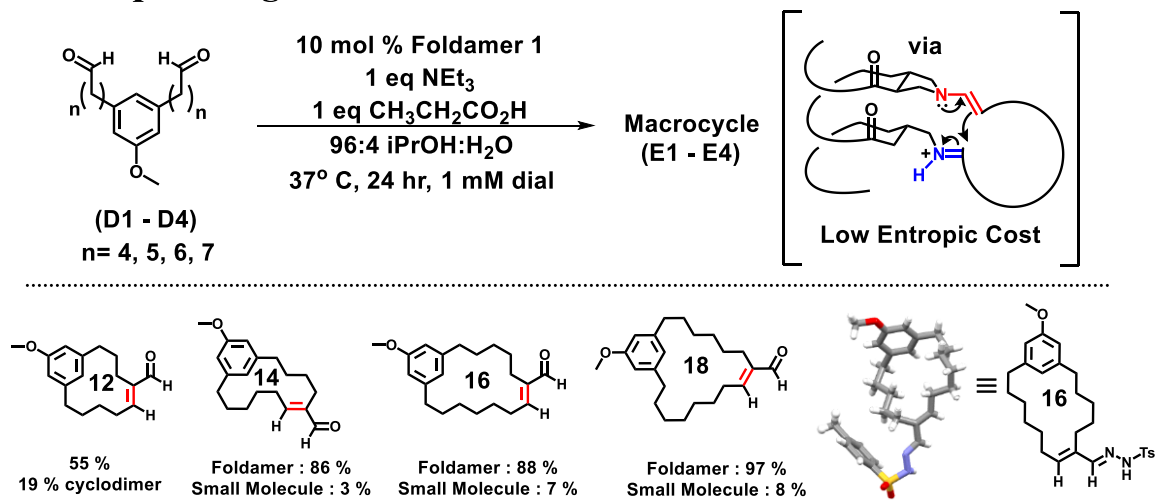
B *Mechanism*
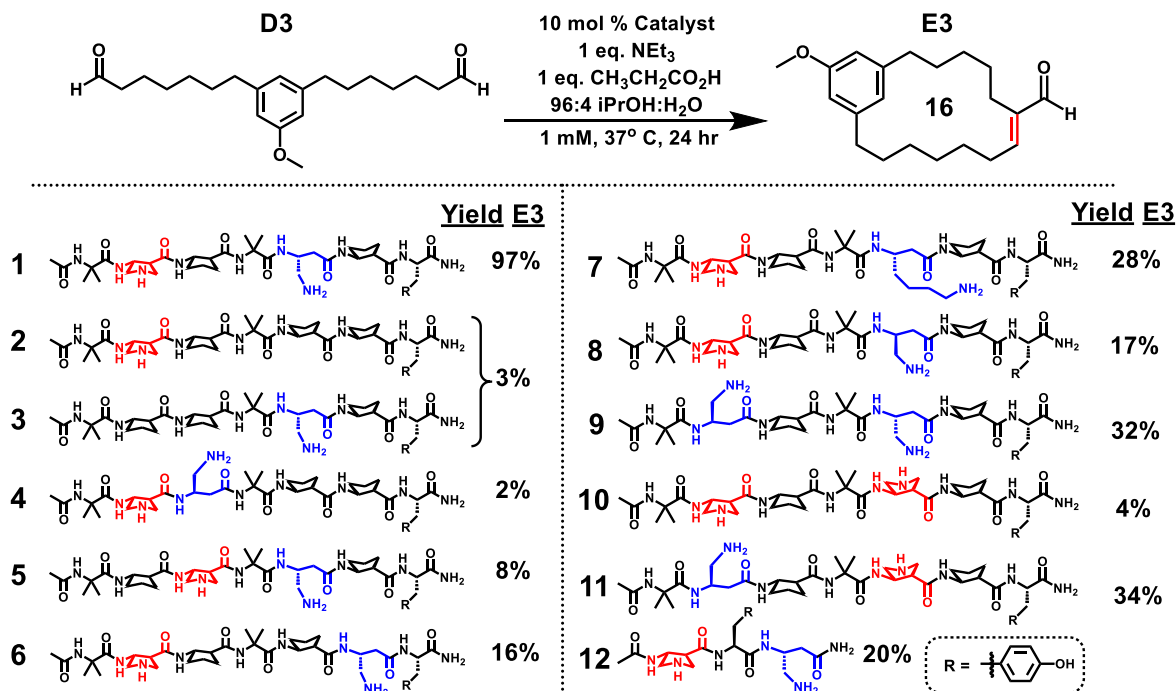
Figure 4. (A) Foldamer-catalyzed macrocyclization: Ring size variation. Isolated yields are reported for foldamer-catalyzed reactions; however, yields for the pyrrolidine/n-butylamine catalyst pair ("small molecule") are estimated on the basis of LC-MS data. Ts, p-toluenesulfonyl. (B) Identification of features critical for foldamer catalysis of macrocyclization. Image rights belong to AAAS.
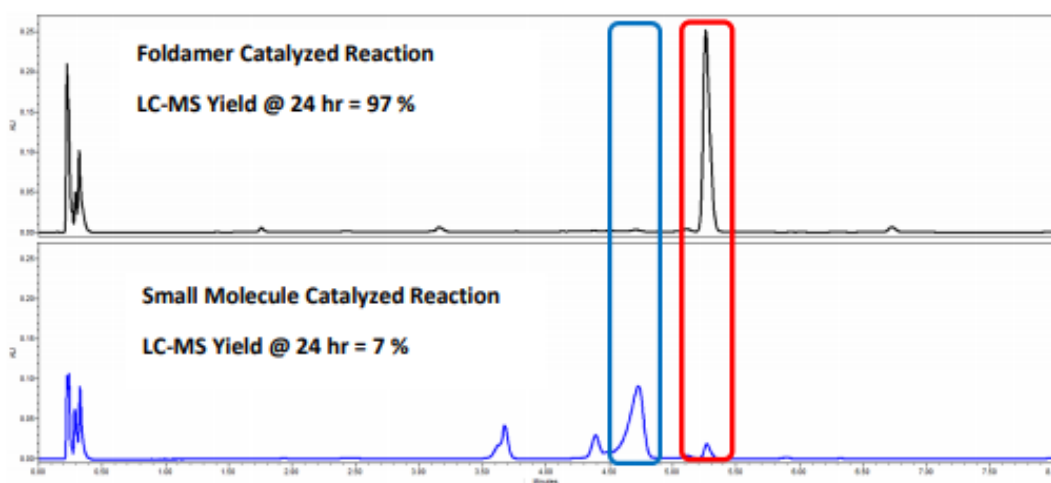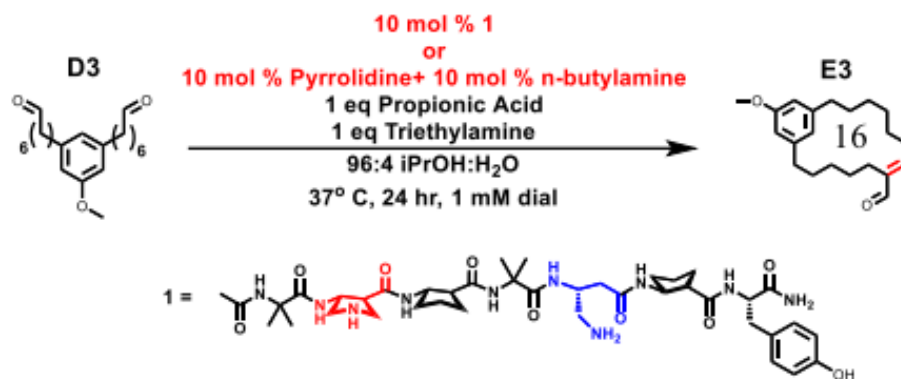
Figure 5. LC-MS chromatograms (275 nm) at 24 hours reaction time for the macrocyclization reaction of dialdehyde **D3** catalyzed by either **1** or pyrrolidine + n-butylamine. Highlighted in blue is starting material **D3**. Highlighted in red is product **E3**.

Comparing formation of enal **E3** with α/β-peptide **1** and a set of related oligomers

reveals that catalytic efficacy is very sensitive to specific features of foldamer structure (**Figure**

4B). As noted above, a control mixture of pyrrolidine and n-butylamine was much less effective

than α/β-peptide **1** at promoting macrocycle formation. Similarly low reactivity was observed for

a pair of monofunctional α/β peptides (**2** + **3**) that provide the secondary and primary amine

groups as β-residue side chains in separate molecules. These results are consistent with a

bifunctional mechanism involving activation of the two aldehyde groups in a substrate on a

single catalyst molecule. A bifunctional mechanism is further supported by the observation that

macrocyclization to form **E3** displayed first-order dependence on α/β-peptide **1** (**Figure 6**).
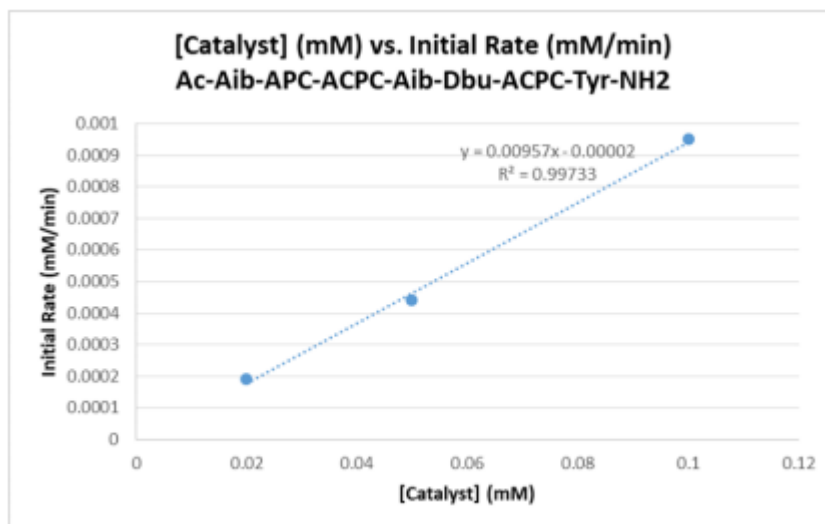
Figure 6. Initial rate (mM/minute) vs. [Catalyst **1**] (mM) for the macrocyclization of **D3** to form **E3**. The linear relationship observed is consistent with the hypothesis that the catalytic reaction is first order in catalyst **1**, i.e., that only one molecule of **1** is involved in the rate-determining transition state. Each reaction was run in duplicate, with different stock solutions of catalyst **1** and **D3**, and error bars denote standard deviation among product concentration measurement at a given time point. Reaction conditions are described above.

2D NMR studies of **1** conducted by Xinyu Liu, in either d_7-isopropanol or d_3-methanol, revealed

numerous nuclear Overhauser effects consistent with the expected helical conformation (**Figure**

7, 8) and the alignment of the primary and secondary amine side chains, which is essential for

bifunctional   catalysis.
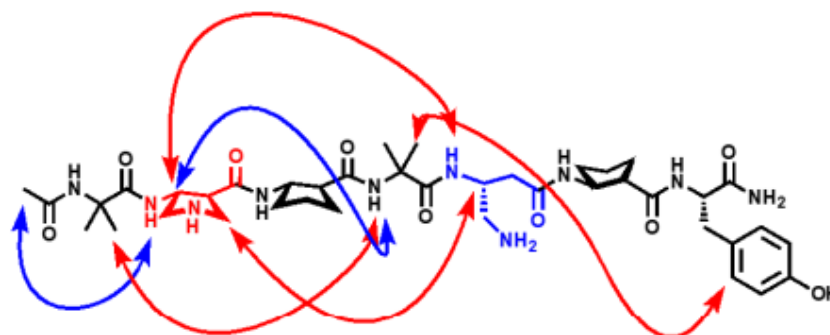
Figure 7. Graphical representation of ROEs observed for catalyst **1** between protons on residues that are not adjacent in sequence in CD_3OH. Blue lines indicate i,i+2 ROEs. Red lines indicate i,i+3 ROEs.
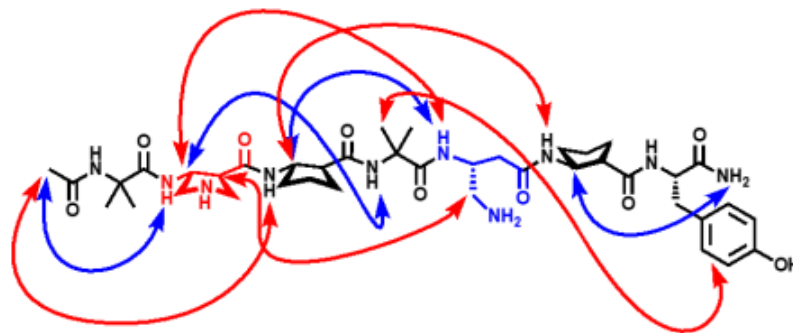
Figure 8. Graphical representation of ROEs observed for catalyst **1** between protons on residues that are not adjacent in sequence in iPrOH-d7. Blue lines indicate i,i+2 ROEs. Red lines indicate i,i+3 ROEs.

The spacing between reactive side chains along the foldamer backbone is crucial for catalytic efficacy, as shown by the low yields obtained with α/β-peptides **4** to **6**, which are sequence isomers of **1**. When the β residues bearing the reactive amine groups were adjacent in primary sequence (i,i+1 spacing; **4**), macrocyclization was barely detectable. The isomers with i,i+2 and i,i+4 spacing, **5** and **6**, were poor catalysts as well. Because the helical conformation favored by the αββ backbone has three residues per turn,[22] differences among **1** and sequence isomers **4** to **6** support the conclusion that optimal catalysis requires alignment of the primary and secondary amine groups along the helix axis. When the β residues that provide the reactive groups were properly spaced (i,i+3) but the linker between the primary amino group and the backbone was lengthened, as in **7**, catalytic activity suffered. Thus, even if the primary and secondary amines are aligned along the helix axis, increased flexibility of the segment between the two amino groups appears to be deleterious. α/β-Peptide **8** is the diastereomer of **1** that differs only in the configuration at the backbone carbon bearing the primary amine side chain, a change expected to diminish helix stability.[26] We observed only a low yield of enal **E3** with **8**, consistent with high sensitivity of the reaction to the spatial positioning of the amino groups provided by the foldamer scaffold. Overall, this set of comparisons shows that catalytic activity depends on

the ability of the α/β-peptide backbone to achieve a specific arrangement of the primary amine–

secondary amine diad (**Figure 9**).
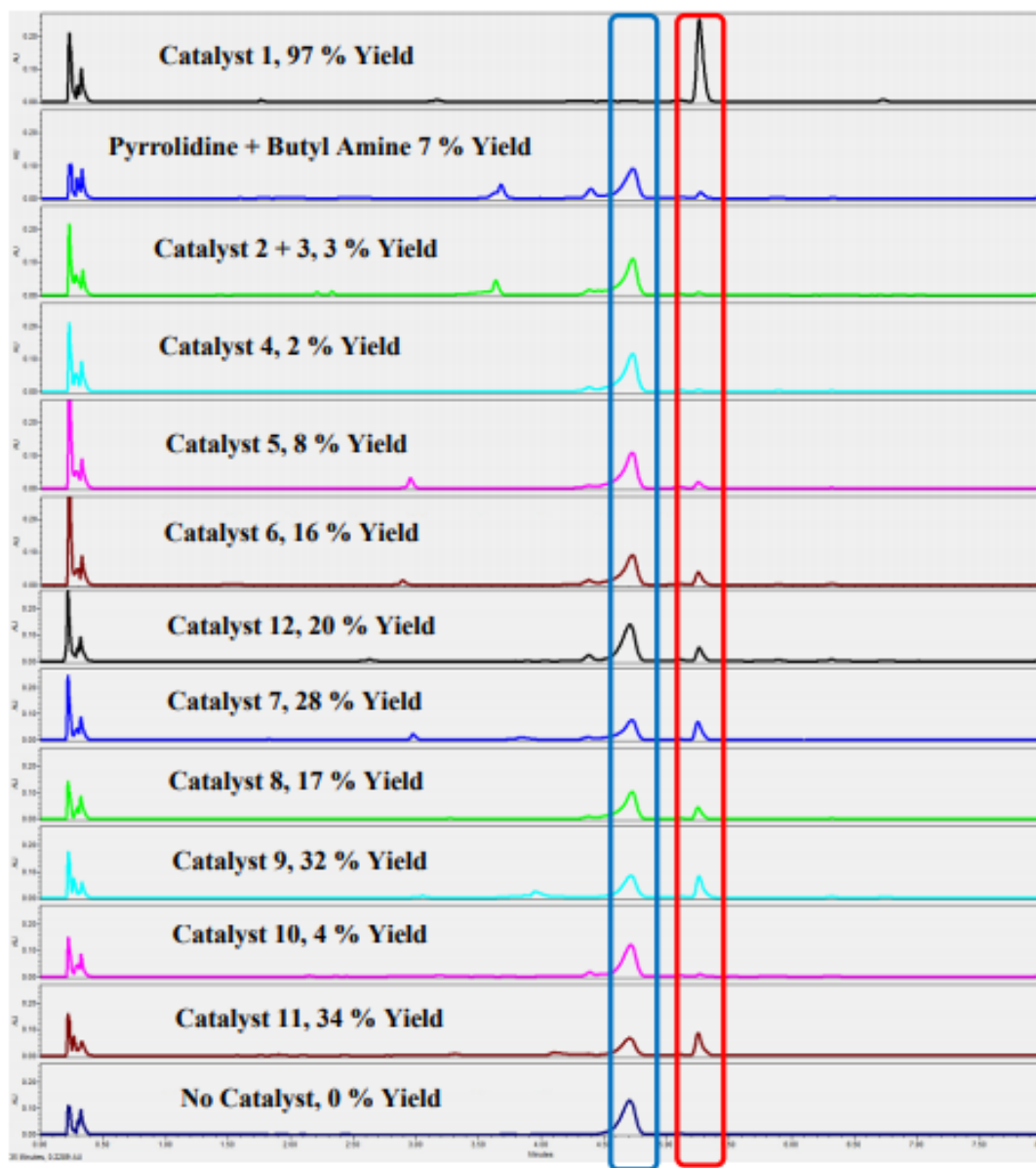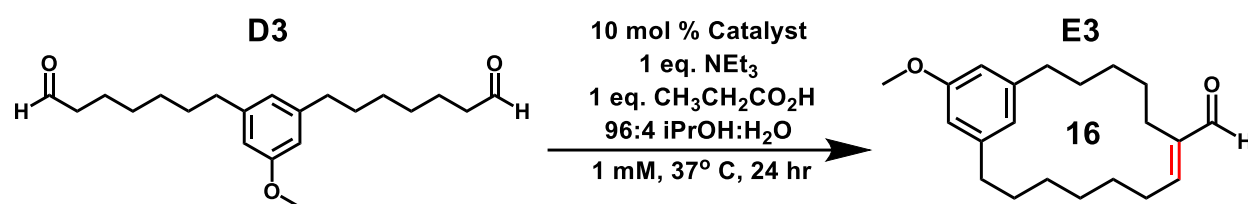
Figure 9. LC-MS chromatograms (275 nm) at 24 hours reaction time for the macrocyclization of dialdehyde **D3** catalyzed by 10 mol % indicated catalyst(s). Highlighted in blue id dialdehyde **D3**. Highlighted in red is product **E3**. Percent yield determined by calibration curve in experimental section of this chapter.

The chemical nature of the amine groups is critical for intramolecular aldol condensation (**Figure 10**, **13**, **16**). **Figure 10** depicts our proposed catalytic cycle for the macrocyclization of **D3** to 16-membered enal **E3**, catalyzed by **1**. We hypothesize that the primary amine of **1** condenses with one aldehyde group of **D3**, to generate an electrophilic imine, which under the acidic reaction conditions can be protonated to the iminium. The secondary amine can condense with the other aldehyde of **D3** to form a nucleophilic enamine.
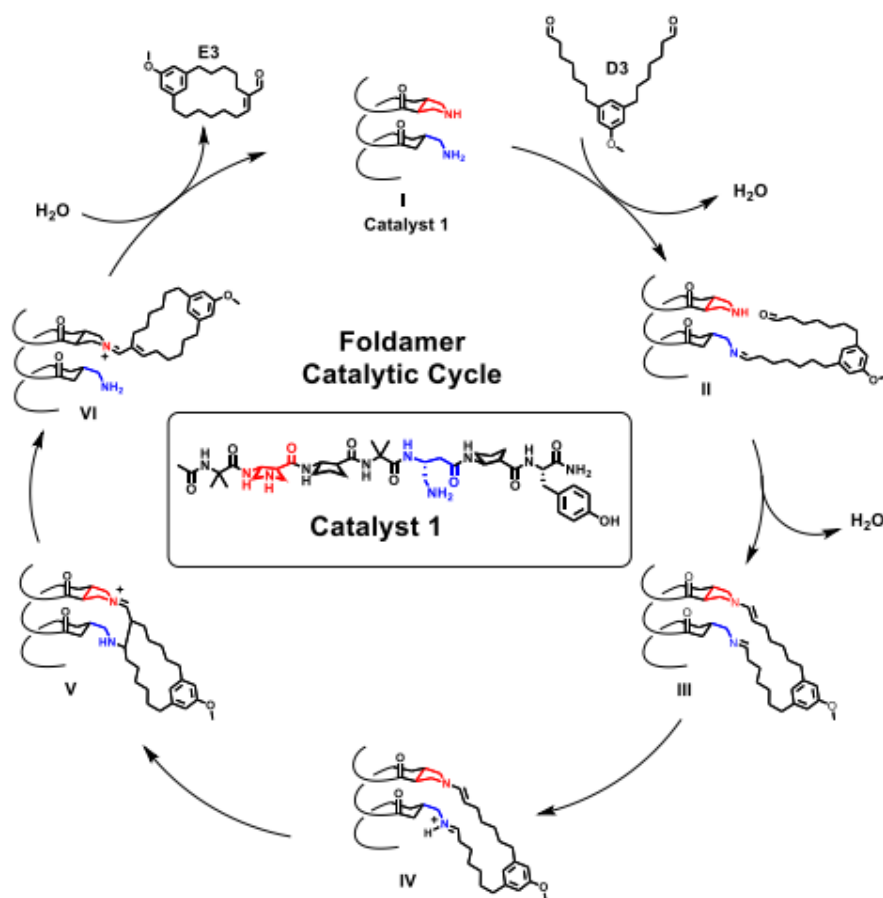
Figure 10. Proposed catalytic cycle for the cyclization of dial **D3** to 16-membered enal **E3**, catalyzed by **1**.

These two events generate **IV**, a bis-covalent catalyst-substrate intermediate that preorganizes a nucleophilic enamine and electrophilic iminium. Cyclization via carbon-carbon bond formation to **V**, followed by elimination and hydrolysis generates macrocyclic enal **E3**, and catalyst **1**. We believe catalyst **1** contains the optimal amine diad for catalysis based on prior work on amine

catalysis, which highlights the predominant use of secondary amines over primary amines for nucleophilic enamine catalysis.[27,28] Secondary amines are known to form enamines readily, while enamine formation from primary amines is often sluggish. Support for this mechanism was obtained by monitoring the macrocyclization of dial **D3** to **E3** catalyzed by 30 mol % **1** by LC-MS. **Figure 11** shows potential intermediates that were observed by LC-MS.
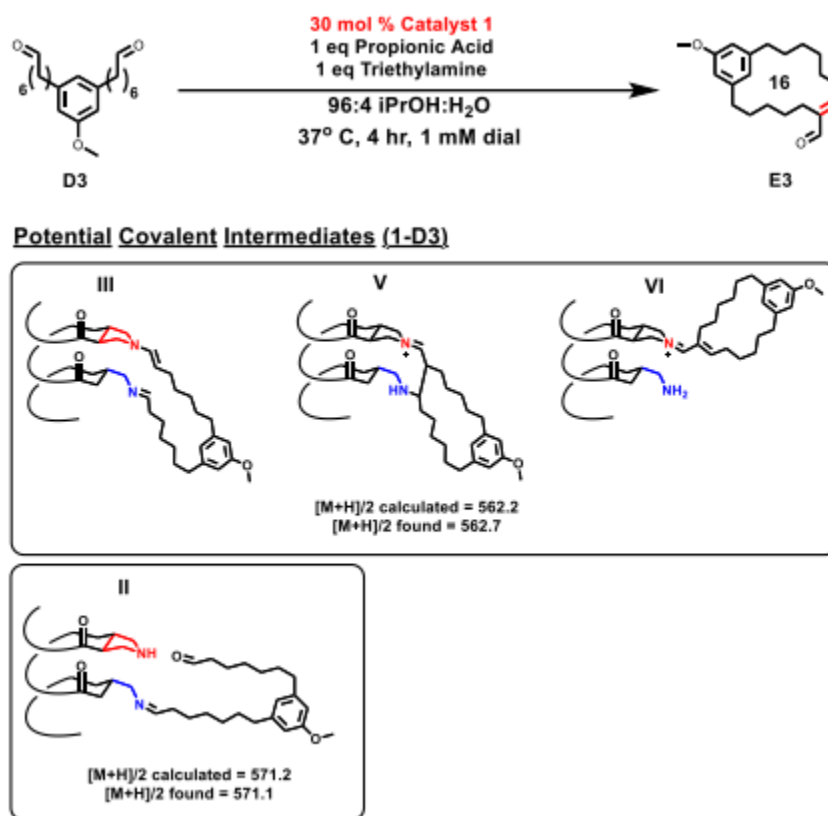
Figure 11. Macrocyclization of dial **D3** to 16-membered enal **E3**, in the presence of 30 mol % **1**. Structures of possible covalent intermediates are drawn, along with their calculated m/z values. Proposed intermediates are named according to the proposed catalytic cycle depicted in **figure 10**. The proposed intermediates are depicted with the enamine formed on the secondary amine and iminium formed on the primary amine residue, though the respective species could form on either amine. Mass spectrometry alone cannot identify the exact intermediate structures since a single m/z value can correspond to multiple potential structures. Other intermediates are possible; we depict only those involved in the proposed catalytic cycle.

LC-MS also allowed for monitoring the buildup of catalyst-substrate covalent intermediates and plotting their formation vs. reaction time. In the presence of catalyst **1**, we observed rapid

formation of catalyst-substrate intermediates over the first 40 minutes of the reaction, followed by dissipation over the remaining time, while product **E3** is formed.
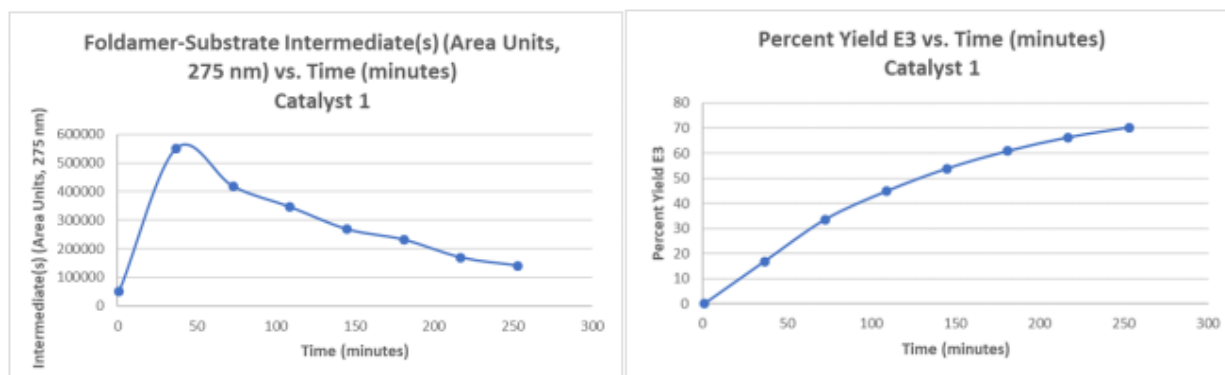
Figure 12. (Left) Plot of foldamer-substrate intermediate(s) (Area Units, 275 nm) vs. time (minutes) for the macrocyclization reaction **D3** → **E3**, in the presence of 30 mol % catalyst **1**. (Right) Plot of percent yield (**E3**) vs. Time (minutes). We interpret the buildup in intermediate peak area over the first 40 minutes to correspond to the formation of **II-VI** of **figure 11**. Breakdown of these intermediates over the remaining time results in decreases peak area, which can be seen in the above plot (left). This hypothesis is supported by the consumption of **D3** and the production of **E3**. A plot of percent yield vs. time shows that **E3** is formed in 70 % yield over the first 4 hours of the reaction.

α/β-Peptide **9** presents a diad of primary amino groups with the optimal sequence spacing, but the yield of 16-membered ring enal **E3** was substantially lower for this catalyst relative to α/β-peptide **1**. α/β-Peptide **10** presents a secondary amine diad, and in this case, the macrocyclic product was barely detectable. The variations in catalytic efficacy among **1**, **9**, and **10** may arise because primary amines favor imine adducts with aldehydes (**Figure 10**),[27] whereas secondary amines favor enamine adducts (**Figure 10**).[28] **Figure 13** depicts the proposed catalytic cycle for the macrocyclization of **D3** to **E3** in the presence of catalyst **10**. Monitoring this reaction by LC-MS resulted in the formation of fewer catalyst-substrate intermediates which was supported by the low yield of **E3** in the presence of **10** (**Figure 14**, **15**).
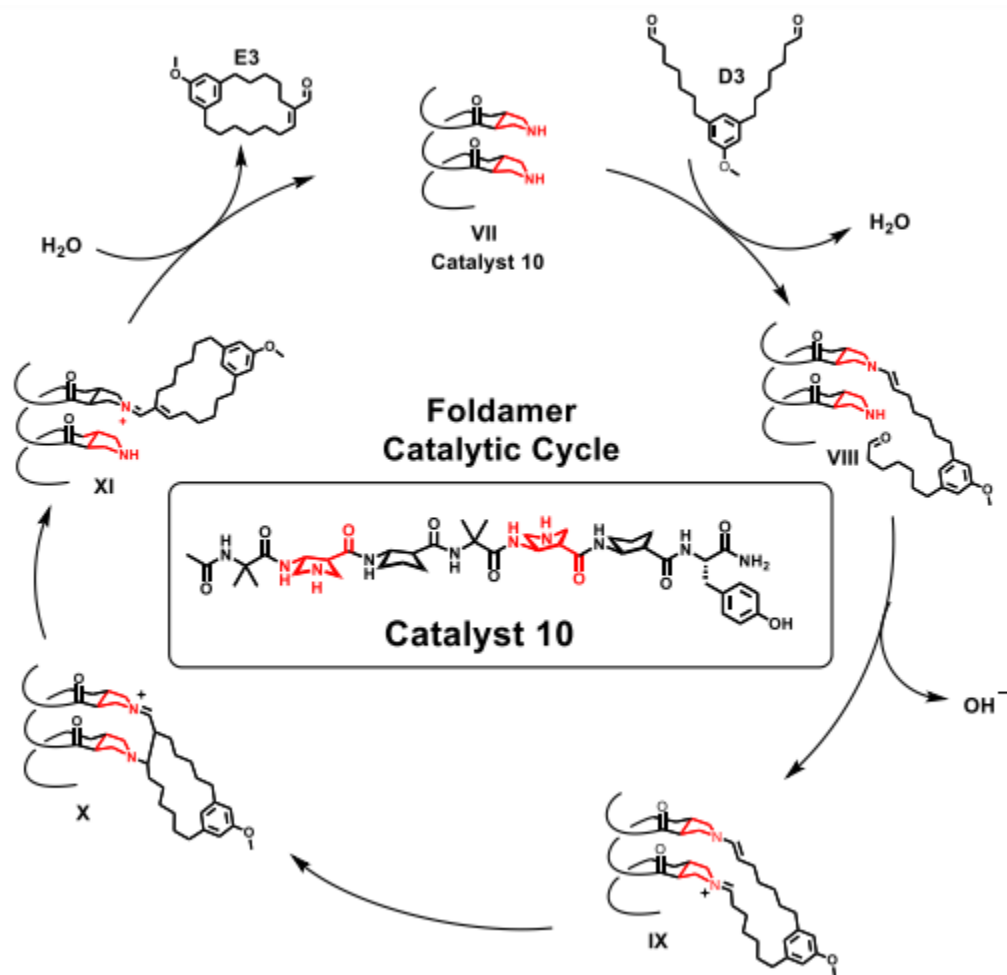
Figure 13. Proposed catalytic cycle for the macrocyclization of dial **D3** to 16-membered enal **E3**, in the presence of 30 mol % catalyst **10**.
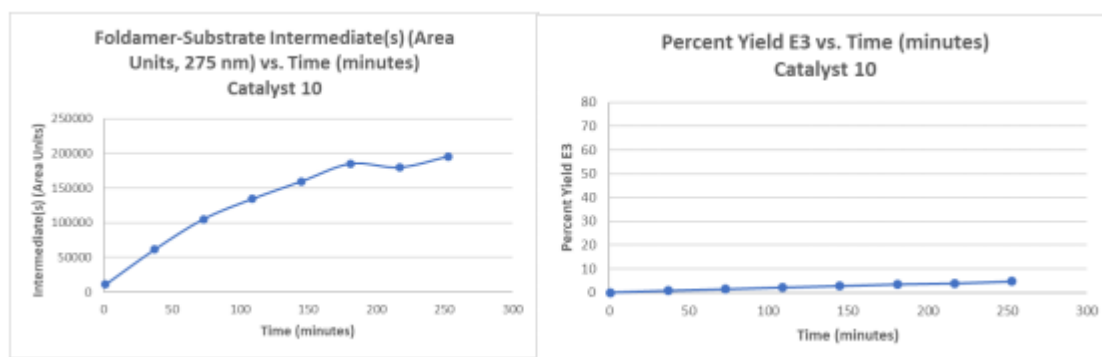
Figure 14. (Left) Plot of foldamer-substrate intermediate(s) (Area Units, 275 nm) vs. time (minutes) for the macrocyclization reaction **D3** → **E3**, in the presence of 30 mol % catalyst **10**. (Right) Plot of percent yield (**E3**) vs.

Time (minutes). In the presence of **1** , it appears that a much smaller population of covalent intermediates is formed, compared to the reaction catalyzed by **1**. We interpret these data to suggest that a primary amino group (as in **1** or **9**) captures aldehyde much more rapidly than a secondary amino group.
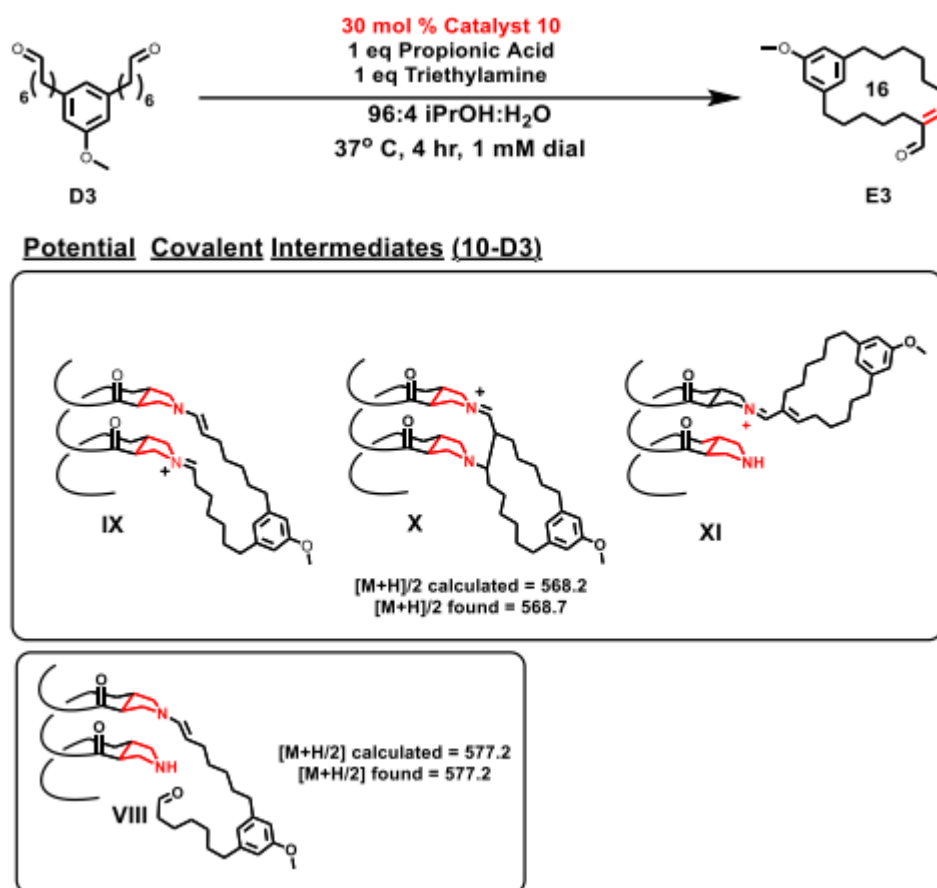
Figure 15. Macrocyclization of dial **D3** to 16-membered enal **E3**, in the presence of 30 mol % **10**. Structures of possible covalent intermediates are drawn, along with their calculated m/z values. Proposed intermediates are named according to the proposed catalytic cycle depicted in **figure X**. Mass spectrometry alone cannot identify the exact intermediate structures since a single m/z value can correspond to multiple potential structures. Other intermediates are possible; we depict only those involved in the proposed catalytic cycle.

Macrocycle formation presumably requires the generation of an electrophilic iminium and nucleophilic enamine on a single catalyst scaffold, a combination that is favored by the reactive diad of **1**. Previously, we found that α/β-peptide **10** was an excellent catalyst for intermolecular crossed aldol reactions.[24] The distinct catalytic profiles of α/β-peptides **1** and **10** show that once a favorable foldamer scaffold is identified, reaction selectivity can be achieved by modifying the catalytic groups.
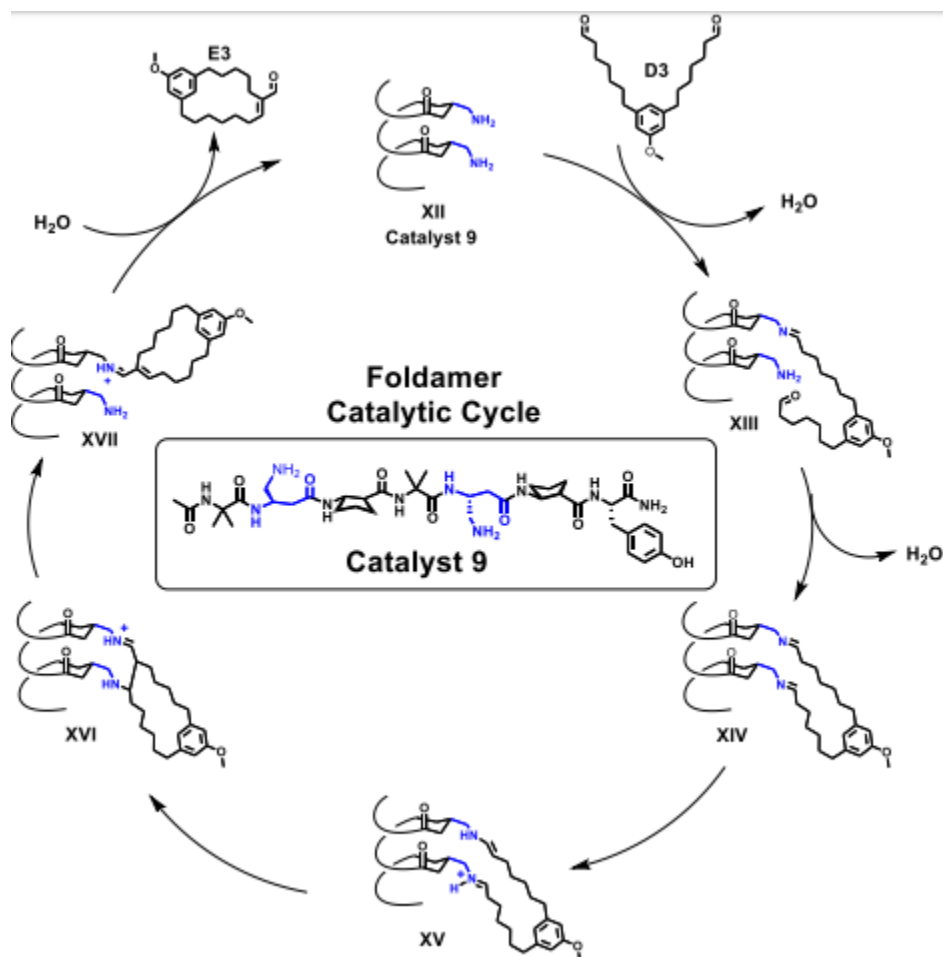
Figure 16. Proposed catalytic cycle for the macrocyclization of dial **D3** to 16-membered enal **E3**, catalyzed by **9**.

Our proposed catalytic cycle for the macrocyclization of dial **D3** to 16-membered enal **E3**, catalyzed by **9**, we hypothesized that the bis-primary amine diad predominately forms the thermodynamically favorable bis-imine species, **XIV**. This hypothesis is supported by the following considerations. 1) Primary amines have not been employed in enamine catalysis as frequently as secondary amines, since primary amines prefer to form imines, which readily form iminium ions under acidic conditions.[27,28,65] 2) Formation of an enamine from a primary amine-based iminium ion is often sluggish since deprotonation of the α carbon competes with deprotonation of the iminium nitrogen. Based on these considerations, we hypothesize that

catalyst **9** forms a smaller population of the reactive enamine-iminium species **XV** relative to the extent of enamine-iminium species **IV** formed by catalyst **1**, and this difference leads to slower product formation in the presence of **9** relative to **1**. Monitoring the formation of catalyst-substrate covalent intermediates via LC-MS (**Figure 17**, **18**) shows rapid detection of
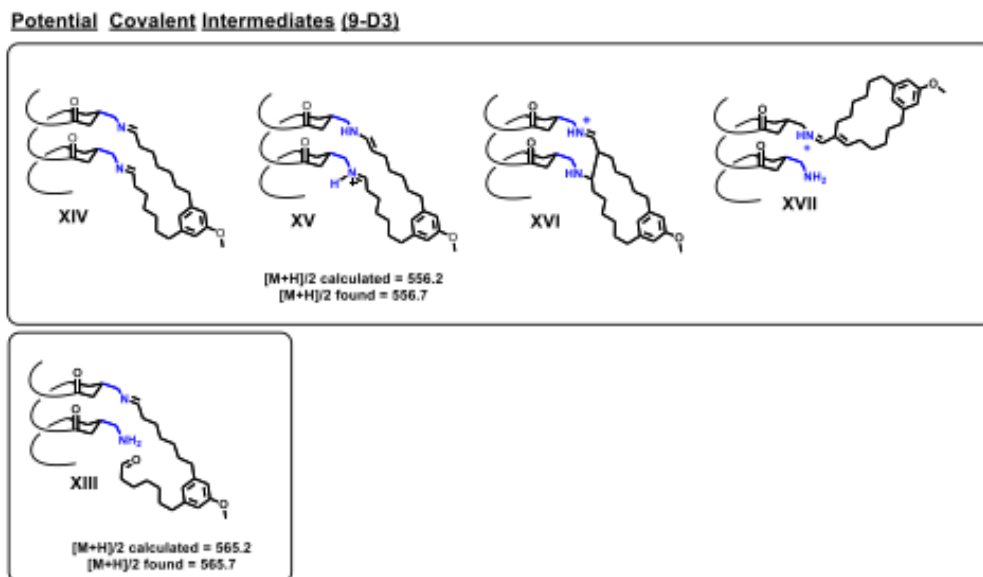
Figure 17. Macrocyclization of dial **D3** to 16-membered enal **E3**, in the presence of 30 mol % **9**. Possible covalent intermediates formed, along with their calculated m/z values. Proposed intermediates are named according to the proposed catalytic cycle depicted in **figure 16**. Mass spectrometry alone cannot be used to identify the exact intermediate structures since a single m/z value can correspond to multiple potential structures. Other intermediates are possible; we depict only those involved in the proposed catalytic cycle.
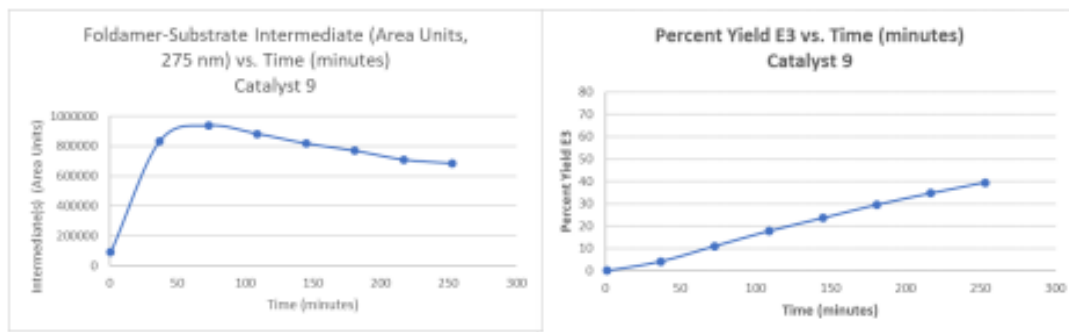
Figure 18. (Left) Plot of foldamer-substrate intermediate(s) (Area Units, 275 nm) vs. time (minutes) for the macrocyclization reaction **D3 → E3**, in the presence of 30 mol % catalyst **9**. (Right) Plot of percent yield (E3) vs. Time (minutes).

intermediates. These intermediates seem to be consumed more slowly than the intermediates in the presence of catalyst **1**. This observed slower consumption of intermediates correlates well

with the final product yield, as catalyst **9** only produces 39 % **E3** in the first 4 hours, compared to 70 % **E3** produced by catalyst **1**. We hypothesize that the slower breakdown rate of intermediates and lower yield of **E3** after 4 hours (39 %), as compared to catalyst **1**, suggests that a high population of bis-imine **XIV** is formed rapidly in the presence of bis-primary amine catalyst **9**. As described in **Figure 16**, formation of the requisite enamine species, which is necessary for formation of **E3**, could be slower than in the case of catalyst **1**, which bears both a primary and secondary amine. The slow breakdown of intermediates observed in the reaction catalyzed by **9** could be representative of the slowed formation of reactive enamine-iminium **XV**.

The modest macrocycle yield obtained with **11** shows that swapping the primary and secondary amine group positions in the α/β-peptide backbone causes erosion of catalytic efficacy. This observation highlights the ability to explore diverse spatial arrangements of reactive groups that is provided by a foldamer scaffold, which is inherently modular. Tripeptide **12** features i,i+2 spacing but is too small to adopt a stable helical conformation. This tripeptide was slightly more effective than the longer α/β-peptide with i,i+2 spacing,[5] which raises the possibility that a stable folded conformation can cause a modest diminution of intrinsic amine reactivity, perhaps because of steric hindrance.

The efficient foldamer-catalyzed macrocyclization introduced here may be useful for the synthesis of large-ring natural products, analogs of these natural products, and macrocycles of potential therapeutic utility. We could produce the 18-membered ring core of nostocyclyne A (**Figure 19**)[29] from dialdehyde **F** with 10 mol % **1**. Because the substrate is unsymmetrical, two macrocyclic E-enals are possible. Both were formed in 75% total yield, with a 2.8:1 ratio. The identity of the major isomer was established by a crystal structure of the tosylhydrazone derivative.
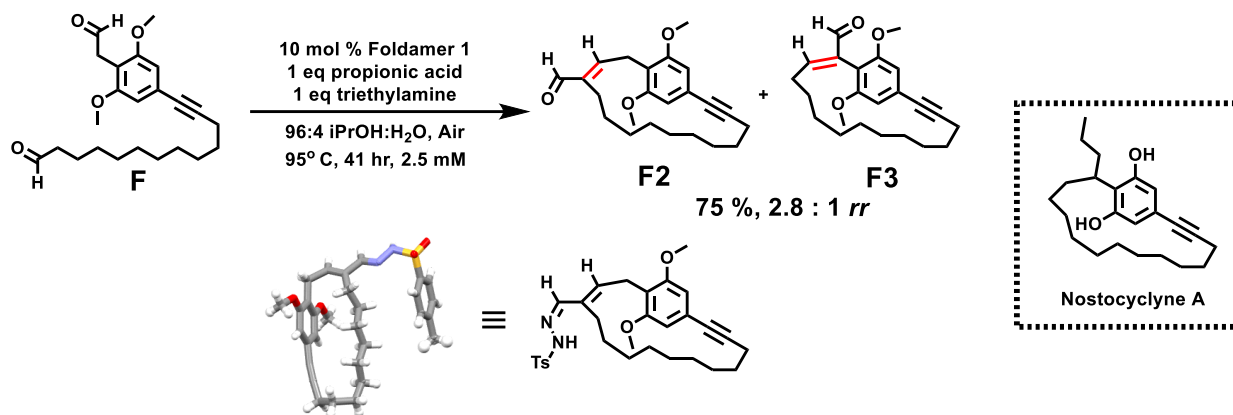
Figure 19. Foldamer-catalyzed formation of the macrocyclic core of nostocyclyne A. Identity of product **F2** was established by measns of the crystal structure of the tosylhydrazone derivative. *rr*, regioisomer ratio.

We further demonstrated the utility of foldamer-catalyzed macrocyclization by achieving total synthesis of the natural product robustol,[30] which contains a 22-membered ring (**Figure 20**). This compound is related to the turriane family of natural products, several of which have been prepared by application of macrocycle closing alkene or alkyne metathesis.[31] Our route to an appropriate dialdehyde substrate began with two nickel-catalyzed reductive crosscoupling reactions, pioneered by Weix et al.,[32] to prepare boronate ester **R1** and phenol **R3**. Copper-catalyzed Chan-Lam-Evans coupling of these two compounds generated diester **R4**,[33,34] and redox manipulations provided dialdehyde **R5**. The foldamer-catalyzed reaction efficiently generated the desired 22-membered ring skeleton as a mixture of isomers (**R6**). Heating with Wilkinson's catalyst induced decarbonylation,[35] and the resulting alkene mixture was hydrogenated to produce **R7**. The methyl groups were removed by treatment with excess BBr$_3$ to yield a single product with an ^{1}H NMR spectrum matching that of natural robustol.[30]
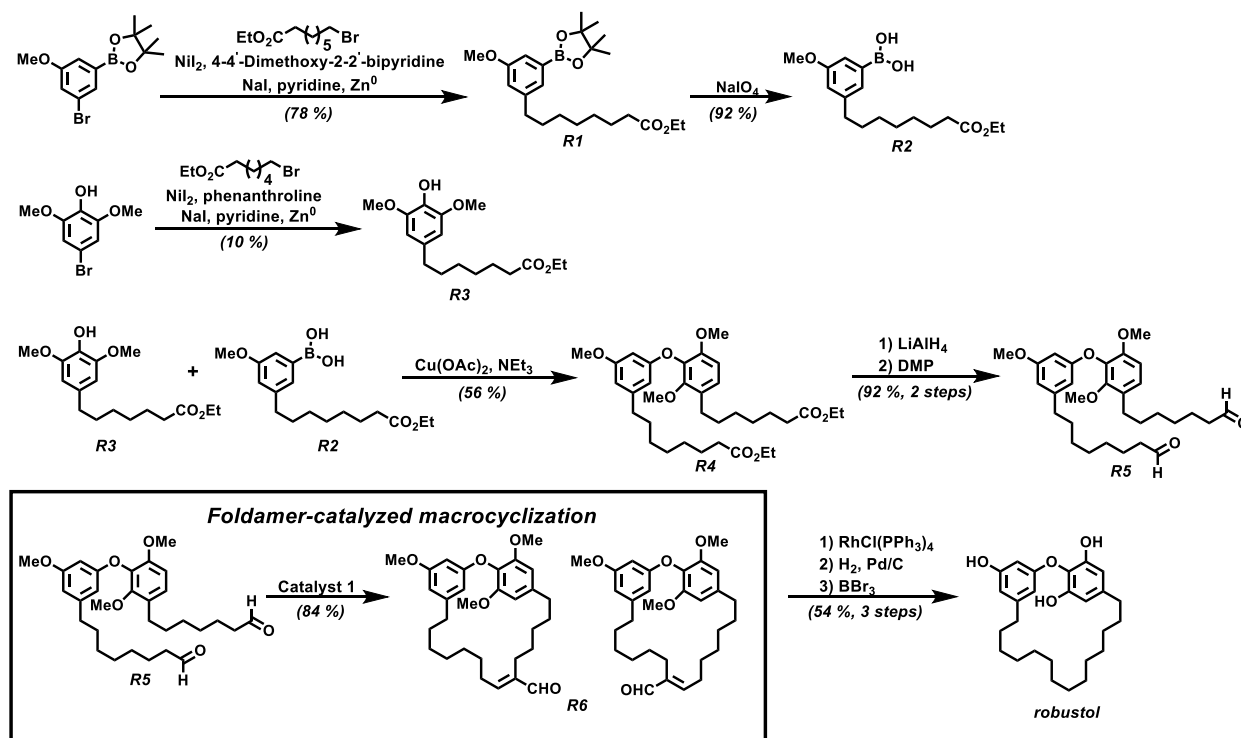
Figure 20. Total synthesis of robustol. The key step, foldamer-catalyzed closure of the 22-membered ring, is highlighted. See experimental section of this chapter for full reaction protocols and product characterization.

Our results suggest that a broad range of macrocycles will be accessible through intramolecular aldol condensations catalyzed by foldamer **1**, with limitations arising when ring closure causes significant internal strain.[7,8] Because polar groups (amine, carboxylic acid, hydroxyl) are abundant in the reaction medium, aldol macrocyclizations catalyzed by α/β-peptide **1** will likely display considerable functional group tolerance. Macrocyclic compounds are of interest for pharmaceutical development, as exemplified by the hepatitis C drug vaniprevir,[36] and our method should enable synthesis of diverse structures to support discovery of therapeutic agents (**Figure 21**).
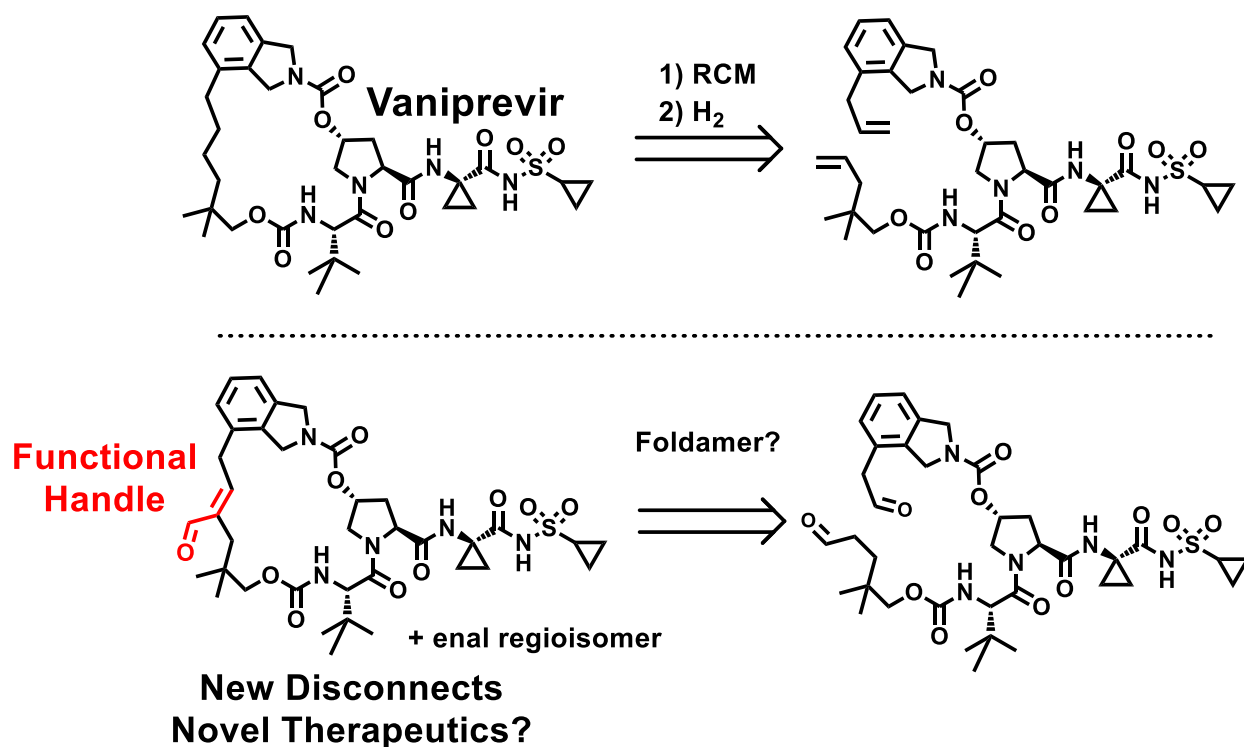
Figure 21. Macrocyclic hepatitis C drug, vaniprevir, is currently prepared by olefin ring closing metathesis (RCM), followed by the hydrogenation of the double bond. Foldamer-catalyzed macrocyclization offers a novel disconnection strategy that provides a functional enal handle.

3.4 Conclusions

Our use of a foldamer scaffold to achieve optimal arrangement of the primary amine–secondary amine diad was inspired by the role of protein scaffolds in positioning catalytic groups in enzyme active sites.[37] The prevalence of β-amino acid residues in our foldamer backbone allows us to use residue-based strategies for conformational preorganization,[23] an opportunity that is not available for catalyst designs based entirely on α-amino acid residues. Well-characterized foldamer scaffolds allow systematic variation of the arrangement of a reactive group set, such as the primary amine–secondary amine diad in **1**, which is useful for catalyst optimization.[24] Small molecule scaffolds for bifunctional catalysis[38-40] may be less amenable to exploration of alternative geometries for a given functional group diad relative to

foldamer-based skeletons because small molecules lack the modularity of foldamers. We speculate that the αββ backbone of **1**, and related backbones containing preorganized β- and/or γ-amino acid residues, will provide scaffolds that can be harnessed to enable bifunctional or polyfunctional catalysis of other useful reactions.

3.5 Experimental

3.5.1 Materials and Instrumentation

a. Materials and Reagents

All solvents and most reagents were obtained from Sigma-Aldrich. 6-Heptyn-1-ol, 7-octyn-1-ol

1,3-dibromo-5-methoxybenzene were obtained from TCI America. All commercial reagents and

solvents were used without purification. Filtered Millipore water was used as an additive for all

macrocyclization reactions. Chromatography was performed on silica gel (200-425 mesh) using

standard techniques. Products were visualized by UV or KMnO$_4$ stain. Protected amino acids

and coupling reagents were obtained from Chem-Impex International, Inc. Solid phase peptide

synthesis (SPPS) resins were obtained from EMD Millipore. ACS-grade DMF from Sigma-

Aldrich was used as a washing solvent during SPPS, and biotech-grade DMF from Sigma-

Aldrich was used during amino acid coupling.

b. Instrumentation

Solid-phase peptide synthesis was performed using a CEM MARS microwave system in Torviq

polypropylene syringes fitted with a porous polypropylene disc at the bottom. Preparative HPLC

was performed using a Shimadzu HPLC system (SCL-10VP system controller, LC-6AD pumps,

SIL-10ADVP autosampler, SPD-10VP UV-vis detector, FRC-10A fraction collector), equipped

with a Waters XSelect CSH Prep C18 column (5 µm particle size, 19 mm x 250 mm), operating

at 12 mL/min. Peptide purity measurements, crude reaction yield determination, reaction

monitoring, and reaction order experiments were performed on a Waters Acquity Arc® LC-MS

instrument. Peptide concentration measurements were performed on a Thermo Scientific

NanoDrop One[C]. ^{1}H and ^{13}C NMR spectra were acquired on 400, 500 and 600 MHz Bruker

NMR instruments. NMR chemical shifts are reported in ppm and are referenced to tetramethylsilane (TMS; 0.00 ppm) for ^{1}H NMR. For ^{13}C NMR, chemical shifts are reported in ppm and are referenced to the residual solvent peak for CDCl$_3$ (77.16 ppm). Coupling constants (*J*) are reported in Hz. Mass spectrometry data were collected on a Thermo Q Exactive Plus instrument via flow injection with electrospray ionization or via an ASAP-MS (asap-ms.com), both located in the Chemistry Instrumentation Center at the University of Wisconsin – Madison. Peptide identity was determined via MALDI-TOF-MS analysis on a Bruker microflex LRF.

c. Instrument acknowledgements

Instrument Name, Instrument Type, Grant Award Year

Bruker microflex LRF, MALDI-TOF-MS, Generous gift from the Bender Fund

Thermo Q Extractive Plus, Mass Spectrometer, NIH 1S10 OD020022, 2015

Bruker Advance III-400, NMR Spectrometer, NSF CHE-1048642 2010

Bruker Advance III-500, NMR Spectrometer, Generous gift from Paul J. Bender 2012

Bruker Advance III-HD-600, NMR Spectrometer, NIH S10 OD012245 2013

3.5.2 General Procedures

a. Peptide Synthesis and Purification

NovaPEG Rink Amide resin (150 μmol by amine loading [0.49 mmol/g], 306 mg) is added to a Torviq solid-phase peptide synthesis vessel along with a micro stir bar. Resin is swelled in DCM for 30 minutes before beginning synthesis. Fmoc amino acid (3.5 eq., 525 μmol) and HATU (3.45 eq., 517.5 μmol) are weighed into 10 mL glass vials. Amino acid and coupling reagent are pre-activated by adding 3 mL biotech grade DMF and DIEA (8 eq., 210 μL, 1200 μmol), and

vortexing. The pre-activated amino acid sits at room temperature for 5 minutes. DCM used to swell the resin is aspirated from the vessel, the resin is washed 5X with DMF, and the vessel is then capped at the bottom. The pre-activated amino acid solution is added to the vessel.

Coupling of amino acids (α,α-disubstituted-α-amino acids, and β-amino acids): The reaction vessel containing the resin and pre-activated amino acid is transferred to the microwave reactor, and the temperature sensor is placed in the vessel. The microwave coupling program is initiated which ramps to 70° C over two minutes and holds at 70° C for thirteen minutes. After the coupling, the vessel is taken out of the microwave reactor and the liquid is removed by aspiration. The resin is then washed 5X with ACS grade DMF. The vessel is then capped.

Deprotection of amino acids (α,α-disubstituted-α-amino-acids, and β-amino acids): To the reaction vessel is added 6 mL of 20 %v/v piperidine in ACS DMF, and the vessel is moved to the microwave reactor. The temperature probe is placed in the vessel. The microwave deprotection program is initiated, which ramps to 80° C over two minutes and holds at 80° C for four minutes. After deprotection, the liquid is removed by aspiration, and the resin is washed 5X with ACS DMF. Subsequent coupling and deprotection steps are carried out until the final residue has been coupled.

N-terminal acetylation of peptides: To the reaction vessel, containing resin bearing the peptide with the terminal residue deprotected, is added 3 mL Biotech grade DMF, 50 eq. DIEA and 50 eq acetic anhydride. The mixture is allowed to stir for 45 minutes at room temperature. The solution is then aspirated, and the resin is washed 3X with DMF, followed by 5X with DCM, and 5X with MeOH. The resin is dried by leaving it on the aspirator for 15 minutes.

Cleavage of peptides from resin: Cleavage is performed by drawing 3 mL of 2.5 % TIPS, 2.5 % water, 95% TFA into the reaction vessel using the syringe plunger and rocking the vessel for 3 hour at room temperature. Crude peptide solution is expunged into a 50-mL centrifuge tube, resin is washed 3× with TFA, and TFA is blown off from the combined filtrate under a stream of N_2. Once most of the TFA is removed, the crude peptide is precipitated by addition of 40 mL cold diethyl ether and pelleted using a centrifuge at 4,300 rpm for 5 minutes. The ether supernatant is decanted, and the crude peptide solid is dried under a stream of N_2. Crude peptide is prepared for HPLC purification by dissolving the solid in about 4 mL of 1:1 H_2O-MeCN and transferring to an HPLC vial. HPLC solvent A is 0.1 % TFA in filtered and degassed Millipore H_2O, and solvent B is 0.1 % TFA in acetonitrile. A linear gradient of 10-60 % B is used to identify product peaks (via MALDI-TOF MS analysis of collected fractions). A flow rate of 35 mL/min was used. The column used for HPLC purification was an XBridge® Prep C8 5µm OBD™ 30 x 150 mm.

   b. **General procedure: determination of concentration and purity of stock solutions**

Collected peptide HPLC fractions are frozen over dry ice and lyophilized. The lyophilized powder is dissolved in about 1.5 mL of isopropanol, and the solution is sonicated for 30 minutes. 10 µL of peptide stock solution is added to 290 µL of a 6 M aqueous guanidinium chloride solution. The solution is sonicated for 50 minutes and then placed in a quartz cuvette. A UV-Vis spectrum is acquired of the solution, and the peptide concentration is calculated using the absorbance at 280 nm and the molar absorptivity of tyrosine at 280 nm[1] (Extinction coefficient used: 1280 $M^{-1}cm^{-1}$).[41] Catalyst loadings for all reactions are based on concentration determined in this way. Stock solutions of catalysts in isopropanol are stored in a 20° C freezer. Purity analyses over several months showed no degradation of any peptide catalyst. For purity analysis,

5 µL of the peptide stock solution is added to a LC-MS vial containing 45 µL isopropanol (10-fold dilution) and mixed. A 3 µL injection is run on a LC-MS equipped with a 5 cm XBridge® C18 column with 3.5 µm pore size at a flow rate of 0.75 mL/min. The method used is 10-50 %B over 5 minutes. LC-MS Solvent A is 0.1 % formic acid in filtered/degassed Millipore H_2O, and Solvent B is 0.1 % formic acid in acetonitrile. Purity is assessed by LC-MS via integration of the 220 nm and 275 nm channels.

c. General procedure: foldamer-catalyzed preparative macrocyclization

To a 250 mL round bottom flask equipped with a magnetic stir bar was added 17.3 mg (0.052 mmol) dialdehyde **D3**, followed by 49.6 mL isopropanol, 2.1 mL water (4 vol % overall), propionic acid (1 eq, 0.052 mmol, 3.88 µL), and triethylamine (1 eq, 0.052 mmol, 7.25 µL). Added last was catalyst **1** (10 mol %, 0.0052 mmol, 344.2 µL of a 15.12 mM stock solution of **1** in isopropanol). The round bottom flask was capped, submerged in a pre-heated oil bath at 37° C, and stirred for 24 hours. There is no need for the exclusion of air; the flask is capped to prevent evaporation of solvent.

After stirring for 24 hours, 25 µL of the reaction mixture was analyzed via LC-MS. For analysis of crude reaction mixtures, a 10 µL injection volume was injected onto a XBridge C18 3.5 µm 2.1 mm x 50 mm column. The LC-MS method employed was a gradient of 10-90 % B over 5 minutes, followed by a 2 minute 95 % B flush and 1 minute re-equilibration to 10 % B. Solvent A is 0.1 % formic acid in filtered/degassed Millipore water, and solvent B is 0.1 % formic acid in acetonitrile. The sample manager was maintained at the reaction temperature (37° C). A 10 µL injection volume was used. The product peak (275 nm) was integrated and converted to concentration in mM using a calibration curve generated with a pure synthetic standard of macrocyclic enal **E3** in order to determine a crude LC-MS yield.

The solvent was then removed via rotary evaporation. Chloroform (3 mL) is added to the crude reaction mixture in order to separate the desired product from peptide catalyst **1**, which precipitated to form a white solid. The chloroform is filtered through a cotton plug in a Pasteur pipette to give a clear light-yellow solution. Chloroform (3 mL) is added to the crude reaction mixture again to ensure complete transfer of the crude reaction mixture and filtered through a cotton pipette. The chloroform layers are concentrated via rotary evaporation to provide the crude product. The crude product is purified by silica column chromatography eluting with 8:2 pentanes:diethyl ether (fractions analyzed via UV or $KMnO_4$ stain) to yield 14.4 mg of **E3** as a clear oil (88 % yield).

d. General procedure: Percent yield measurements

For dialdehyde substrates **D2-D4**, crude reaction yield was determined for both foldamer- and small molecule-catalyzed reactions to compare catalytic activities. After the reaction mixture had stirred for 24 hours, the reaction mixture is analyzed via LC-MS. For analysis of crude reaction mixtures, a 10 µL aliquot is injected onto a XBridge C18 3.5 µm 2.1 mm x 50 mm column. The LC-MS method employed is a gradient of 10-90 % B over 5 minutes, followed by a 2-minute 95 % B flush and 1 minute re-equilibration to 10 % B. The flow rate is 0.75 mL/min. Solvent A is 0.1 % formic acid in filtered/degassed Millipore water, and solvent B is 0.1 % formic acid in acetonitrile. The sample manager is maintained at the reaction temperature (37° C). The product peak (275 nm) is integrated and converted to concentration in mM using a calibration curve generated with a pure synthetic standard of **E3** in order to determine a crude LC-MS yield.

3.5.3 Substrate Synthesis and Product Characterization

Synthesis of dialdehyde substrates D1-D4

Sonogashira Coupling

6 mol % PdCl$_2$(PPh$_3$)$_3$
12 mol % CuI
18 mol % PPh$_3$
0.1 M, NEt$_3$, 100° C, N$_2$, 20 hr

3 eq
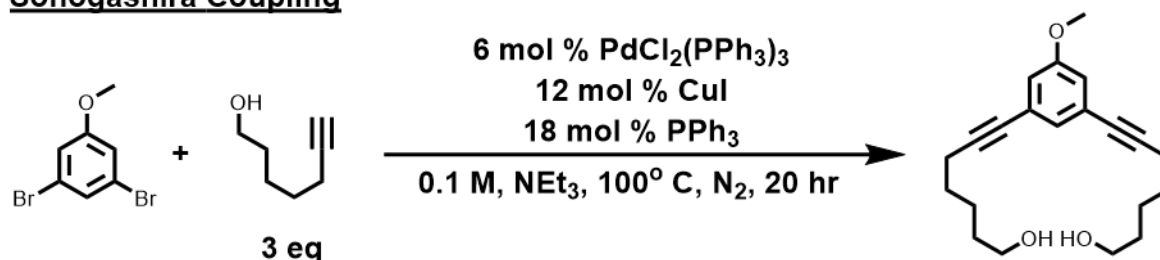
Sonogashira coupling general procedure.[42]

To a 1 L round bottom flask equipped with a stir bar were added 5 g (0.0188 mol) 1,3-dibromo-5-methoxybenzene and 6.38 g (0.057 mol, 3 eq) hept-6-yn-1-ol. The following chemicals were then added: PdCl$_2$(PPh$_3$)$_3$ (0.0011 mol, 0.792 mg, 6 mol %), CuI (0.0023 mol, 0.430 mg, 12 mol %), and PPh$_3$ (0.0034 mol, 0.888 mg, 18 mol %). Triethylamine (188 mL) was then added. The round bottom flask was fitted with a reflux condenser and purged with nitrogen for two minutes. The round bottom flask was lowered into a pre-heated oil bath (100^0 C). The reaction mixture was stirred vigorously and allowed to reflux for 20 hr.

After 20 hours the flask was removed from the oil bath and allowed to cool to room temperature. Volatiles were removed under vacuum. The crude reaction mixture was then loaded onto a silica plug. Triphenylphosphine, and other non-polar impurities were eluted with 6:4 pentanes: diethyl ether. Subsequently, 97:3 DCM:MeOH was used to elute the diol product as an orange oil. This mobile phase will elute the diol product prior to triethylamine. Any fractions containing triethylamine should not be subjected to subsequent hydrogenation reaction as the triethylamine will poison the Pd/C.

Note: Purification is necessary to remove metal salts, triethylamine, and triphenylphosphine. Triethylamine and triphenylphosphine will inhibit the Pd/C catalyst employed in the subsequent hydrogenation. Any other impurities could be carried forward.

<u>High-Pressure Hydrogenation</u>
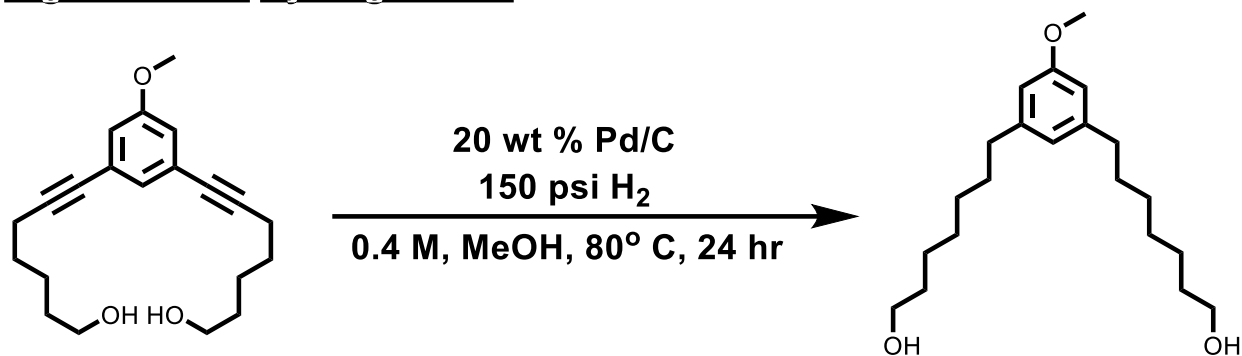
To a 1 L pressure tube equipped with a stir bar was added 1.18 g of 10 wt % Pd/C (20 wt % relative to the diol starting material). The pressure tube was then capped with a rubber septum. The pressure vessel was stringently purged with nitrogen while venting through a needle for five minutes. 5.9 g (0.018 mol) crude diol was dissolved in 45 mL anhydrous methanol (0.1 M) and N_2 was bubbled through the solution to remove any oxygen. The diol solution was then added via syringe into the pressure tube while purging with N_2 continued. The rubber septum was then replaced with a pressure head, and the tube was filled to 150 psi with H_2. The pressure tube was vented and refilled with H_2. This process was repeated 3 times. The pressure tube was filled to 150 psi with H_2 and submerged in a pre-heated oil bath at 80^0 C. The reaction mixture was stirred for 24 hours. At 12 hours the pressure vessel was cooled to room temperature and refilled to 150 psi with H_2 (H_2 consumption can cause the pressure to drop too low for hydrogenation to occur). The pressure tube was re-submerged in the oil bath.

Note: If full hydrogenation does not occur, the problem most likely arises because the pressure dropped is too low. Refilling tube as described ensures that this problem does not occur.

After 24 hours, the pressure vessel was cooled to room temperature and vented in the fume hood. The reaction mixture was filtered through a plug of celite, eluting with methanol. The filtration was done under N_2 pressue to ensure exclusion of atmospheric O_2. The filtrate was concentrated under vacuum to obtain the crude hydrogenated product, which was carried forward without purification.

Dess-Martin periodinane Oxidation
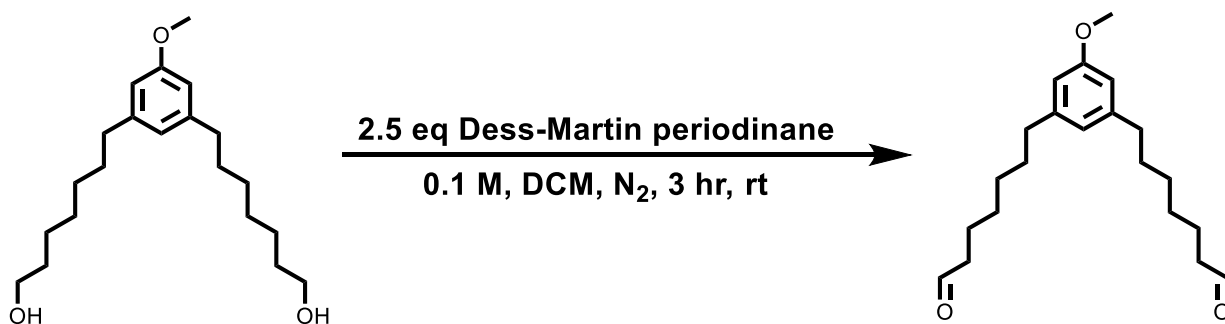
To a 1 L flask equipped with a stir bar was added crude diol (0.018 mol, 6.1 g), followed by 180 mL dichloromethane (0.1 M). Dess-Martin periodinane (0.045 mol, 19 g, 2.5 eq) was then added all at once. The reaction mixture was stirred under N_2 for 3 hours, at which point 200 mL diethyl ether was then added. The entire contents of the flask were combined with 300 mL saturated aqueous sodium bicarbonate containing 75 g sodium thiosulfate pentahydrate. The mixture was stirred vigorously for 1 hour at room temperature. The mixture was transferred to a separatory funnel and the organic layer was removed. The aqueous layer was extracted 2 X with 100 mL diethyl ether. All the organic layers were then combined and washed with 100 mL saturated aqueous sodium bicarbonate (2X), and brine (1X). The organic layers were then dried with magnesium sulfate, filtered, and concentrated under vacuum. The light orange oil obtained was purified via column chromatography, eluting with 7:3 pentanes: diethyl ether to yield 4.9 g of dialdehyde **D3** as a clear oil (79 % yield over three steps).

Dialdehyde D3: ^{1}**H NMR** (400 MHz, CDCl$_3$) δ 9.76 (t, J = 1.81 Hz, 1 H),

D3

6.58 (broad signal, 1 H), 6.54 (m, 2 H), 3.79 (s, 3 H), 2.54 (t, J = 7.56

Hz, 4 H), 2.42 (td, J = 7.35, 1.72 Hz, 4 H), 1.57-1.69 (m, 8 H), 1.31-1.42

(m, 8 H). ^{13}**C** (125 MHz, CDCl$_3$) δ 203.00, 159.74, 144.18, 121.21,

111.37, 55.25, 44.03, 36.09, 31.31, 29.20, 29.16, 22.14. **HRMS** *m/z*

(ESI): calculated for [C$_{21}$H$_{32}$O$_3$ + NH$_4$]$^+$ 350.2690, found 350.2685.
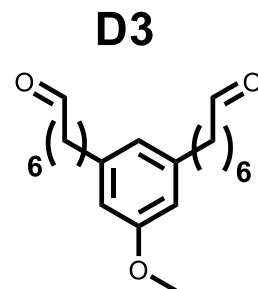
Substrate Synthesis
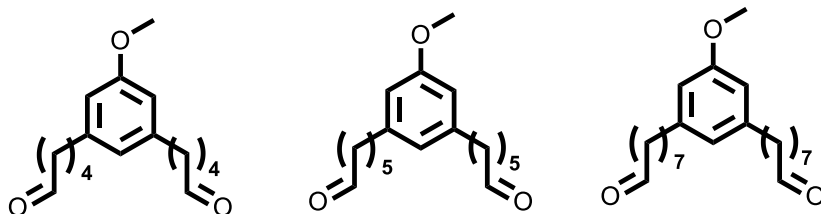
The three substrates shown above (**D1**, **D2**, and **D4**) were prepared via the same reaction

sequence as described above.

Dialdehyde D1: ^{1}**H NMR** (500 MHz, CDCl$_3$) δ 9.75 (t, J = 1.72 Hz, 2H),

D1

6.58 (broad signal, 1 H), 6.55 (broad signal, 2H), 3.78 (s, 3 H), 2.58 (t, J

= 7.45 Hz, 4 H), 2.46 (td, J = 7.29, 1.72, 4 H), 1.61-1.71 (m, 8 H). ^{13}**C**

NMR (125 MHz, CDCl$_3$) δ 202.71, 159.56, 143.6, 121.60, 111.55,

55.27, 43.89, 35.85, 30.90, 21.86. **HRMS** *m/z* (ESI): calculated for [C$_{17}$H$_{24}$O$_3$ + NH$_4$]$^+$

294.2064, 294.2059 found.
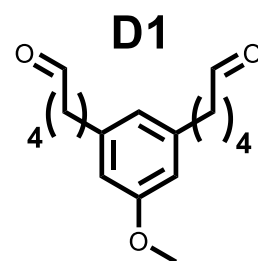
Dialdehyde D2: **^{1}H NMR** (500 MHz, CDCl$_3$) δ 9.76 (t, J = 1.79 Hz, 2 H), 6.58 (broad signal, 1 H), 6.52-6.56 (m, 2 H), 3.78 (s, 3 H), 2.56 (t, J = 7.75 Hz, 4 H), 2.43 (td, J = 7.32, 1.79 Hz, 4 H), 1.58-1.70 (m, 8 H), 1.32-1.42 (m, 4 H). **^{13}C NMR** (125 MHz, CDCl$_3$) δ 202.66, 159.66, 143.87, 121.05, 111.31, 55.13, 43.86, 35.79, 31.12, 28.83, 21.94. **HRMS** *m/z* (ESI): calculated for [C$_{19}$H$_{28}$O$_3$ + NH$_4$]$^+$ 322.2377, 322.2371 found.
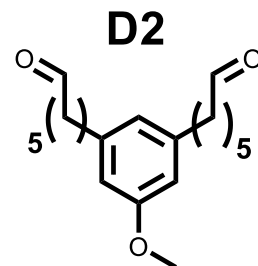
Dialdehyde D4: **^{1}H NMR** (500 MHz, CDCl$_3$) δ 9.76 (t, J = 1.80 Hz, 2 H), 6.58, (broad signal, 1 H), 6.54 (broad signal, 2 H), 3.79 (s, 3 H), 2.54 (t, J = 7.57 Hz, 4 H), 2.41 (td, J = 7.34, 1.8 Hz, 4H), 1.57-1.67 (m, 8 H), 1.29-1.37 (m, 12 H). **^{13}C NMR** (125 MHz, CDCl$_3$) δ 203.06, 159.72, 144.29, 121.23, 111.33, 55.25, 44.04, 36.16, 31.48, 29.37, 29.28, 29.23, 22.2. **HRMS** *m/z* (ESI): calculated for [C$_{22}$H$_{36}$O$_3$ + NH$_4$]$^+$ 378.3003, 378.2997 found.
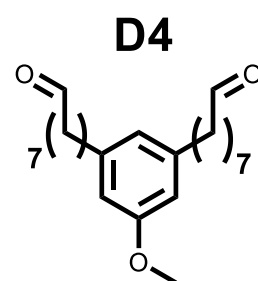
Product E3: **^{1}H NMR** (500 MHz, CDCl$_3$) δ 9.30 (s, 1H), 6.55 (broad signal, 1H), 6.53 (m, 2H), 6.37 (t, J = 6.83 Hz, 1 H), 3.79 (s, 3H), 2.56-2.64 (m, 4H), 2.19 (q, J = 7.25 Hz, 2 H), 2.15 (t, J = 7.03 Hz, 2 H), 1.60-1.67 (m, 4 H), 1.48-1.55 (m, 2 H), 1.32-1.39 (m, 4 H), 1.18-1.26 (m, 2 H), 1.03-1.10 (m, 2H). **^{13}C NMR** (125 MHz, CDCl$_3$) δ 195.31, 159.79, 155.79, 143.62, 143.22, 143.21, 122.06, 112.15, 110.87, 55.08, 35.13, 35.08, 30.16, 29.50, 28.08, 27.57, 27.55, 27.48, 27.28, 26.09, 24.44. **HRMS** *m/z* (ESI): calculated for [C$_{21}$H$_{30}$O$_2$ + NH$_4$]$^+$ 332.2584, 332.2579 found.
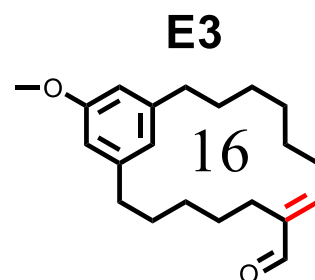
Product E1: **¹H NMR** (500 MHz, CDCl₃) δ 9.35 (s, 1 H), 6.65 (broad signal, 1 H), 6.59 (broad signal, 1 H), 6.27 (t, J = 7.32 Hz, 1 H), 3.81 (s, 3 H), 2.67 (t, J = 5.80 Hz, 2 H), 2.58 (t, J = 6.26 HZ, 2 H), 1.92-1.99 (m, 2 H), 1.86 (t, J = 6.92 Hz, 2 H), 1.70-1.76 (m, 2 H), 1.60-1.68 (m, 2 H), 1.5-1.56 (m, 2 H). **¹³C NMR** (125 MHz, CDCl₃) δ 195.99, 160.14, 155.79, 143.44, 143.31, 142.93, 121.91, 112.22, 111.54, 55.18, 36.83, 33.78, 28.69, 28.39, 27.90, 27.45, 21.08. **HRMS** *m/z* (ESI): calculated for [C₁₇H₂₂O₂ +H]⁺ 259.1693, 259.1689 found.
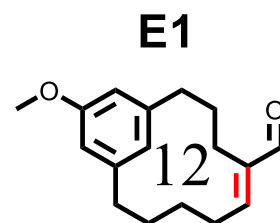
Product E2: **¹H NMR** (500 MHz, CDCl₃) δ 9.31 (s, 1 H), 6.59 (broad signal, 1 H), 6.52 (broad signal, 1 H), 6.50 (broad signal, 1 H), 6.36 (t, J = 8.22 Hz, 1 H), 3.78 (s, 3 H), 2.62-2.67 (m, 2 H), 2.58-2.62 (m, 2H), 2.12-2.18 (m, 4 H), 1.65-1.71 (m, 2 H), 1.58-1.64 (m, 2 H), 1.13-1.25 (m, 6 H). **¹³C NMR** (125 MHz, CDCl₃) δ 195.50, 159.95, 155.5, 144.19, 143.00, 142.75, 122.37, 111.91, 111.38, 55.09, 35.22, 34.43, 29.67, 29.66, 28.75, 28.52, 27.41, 27.34, 22.99. **HRMS** *m/z* (ESI): calculated for [C₁₉H₂₉O₃ + NH₄]⁺ 304.2271, found 304.2267.
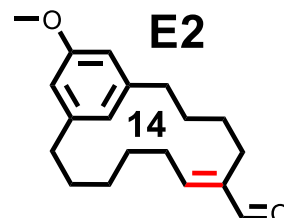
Product E4: **¹H NMR** (500 MHz, CDCl₃) δ 9.35 (s, 1 H), 6.56 (broad signal, 1 H), 6.50-6.53 (m, 2 H), 6.42 (t, J = 8.07, 1 H), 3.77 (s, 3 H), 2.54-2.62 (m, 4 H), 2.28 (q, 7.50 Hz, 2 H), 2.20 (t, J = 7.29 Hz, 2 H), 1.56-1.61 (m, 4 H), 1.40-1.46 (m, 2 H), 1.26-1.32 (m, 10 H), 1.15-1.18 (m, 2 H). **¹³C NMR** (125 MHz, CDCl₃), δ 195.45, 159.65, 155.40, 144.11, 143.69, 143.45, 121.71, 111.47, 111.45, 55.08, 35.31, 30.55,
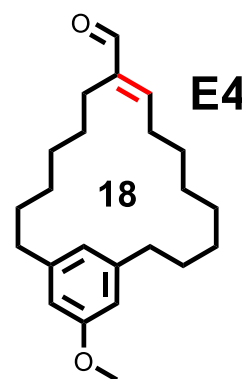
30.50, 29.71, 29.59, 29.40, 29.15, 28.83, 28.65, 28.22, 27.90, 27.64, 23.44. **HRMS** *m/z* (ESI): calculated for $[C_{23}H_{34}O_2 + H]^+$ 343.2632, found 343.2626.

Nostocyclyne A core

Synthesis of dialdehyde G
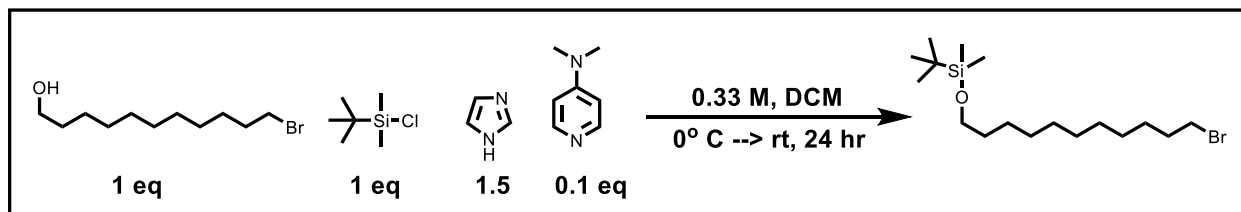
To an oven-dried 250 mL round bottom flask equipped with a stir bar was added 11-bromo-1-undecanol (5 g, 0.02 mol). 60 mL dry dichloromethane was then added, and the reaction solution was cooled to 0° C under nitrogen. The following reagents were then added: tert-butyldimethylsilyl chloride (3 g, 1 eq, 0.02 mol), imidazole (2.04 g, 1.5 eq, 0.03 mol), and 4-dimethylaminopyridine (0.224 g, 0.1 eq, 0.002 mol). The reaction mixture was allowed to warm to room temperature over 24 hours. After 24 hours, the reaction solution was diluted with water and diethyl ether. The water layer was back-extracted two times with diethyl ether. The combined ether layers were washed with brine, dried over $MgSO_4$, and concentrated via rotatory evaporation to yield the crude product as a light brown oil. Crude product was purified by a silica plug eluting with diethyl ether, to yield 6.5 g of a clear oil (89 %). ^1H and ^{13}C NMR spectra matched those reported. (Gegenhuber, T., Schenzel, A.M., Zetterlund, P. B., Barner-Kowollik, C.; A facile route to segmented copolymers by fusing ambient temperature step-growth and RAFT polymerization, *Chem. Commun.* **53**, 10648-10651 (2017).
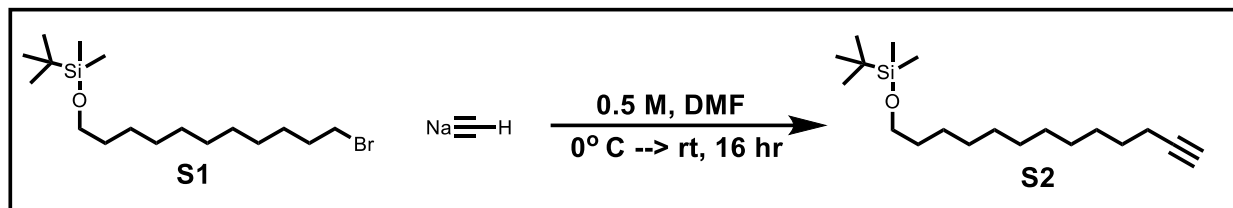
To an oven-dried 50 mL round bottom flask equipped with a stir bar was added **S1** (3 g, 0.0082 mol, 1 eq). 16 mL anhydrous dimethylformamide was then added under nitrogen, and the reaction solution was cooled to 0° C under nitrogen. 2.36 g (1.1 eq) of a 18 % wt solution of sodium acetylide in xylenes was added dropwise over two minutes. After addition of sodium acetylide, the ice bath was removed and the reaction mixture was stirred under nitrogen for 16 hours. After 16 hours, the reaction was quenched by the addition of 5 mL water. A saturated solution of aqueous LiCl was then added, followed by diethyl ether. The ether layer was washed five times with sat. aq. LiCl, dried over MgSO$_4$, and concentrated via rotary evaporation to yield 1.54 g **S2** as a light orange oil (60 %). **S2** was used without further purification.
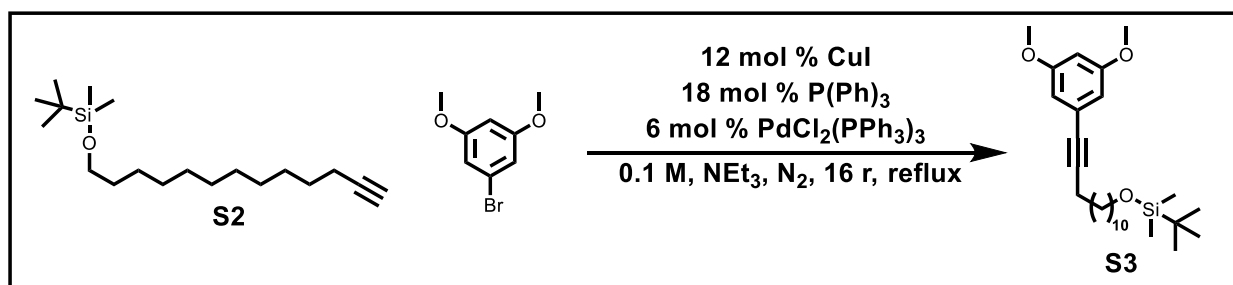
S2 (0.00451 mol, 1.41 g) and 1-bromo-3,5-dimethoxybenzene (0.984 g, 0.00451 mol, 1 eq) were added to an oven-dried 250 mL round bottom flask. The following reagents were then added: copper iodide (0.104 g, 0.00054 mol, 12 mol %), triphenylphosphine (0.213 g, 0.00081 mol, 18 mol %), and bis(triphenylphosphine)palladium(II) dichloride (0.190 g, 0.00027 mol, 6 mol %). 45 mL triethylamine was then added to the round bottom flask, which was then fitted with a

condenser and purged under nitrogen for five minutes. The round bottom flask was submerged

in a preheated oil bath at 100° C, and the reaction mixture stirred at reflux for 16 hours. After

the flask had cooled, the solvent was removed via rotary evaporation. The residue was purified

via silica column chromatography eluting with 7:3 pentane: diethyl ether, followed by a flush

with diethyl ether, to yield 0.752 g **S3** as a dark orange oil (53 %). **S3** was used without further

purification.
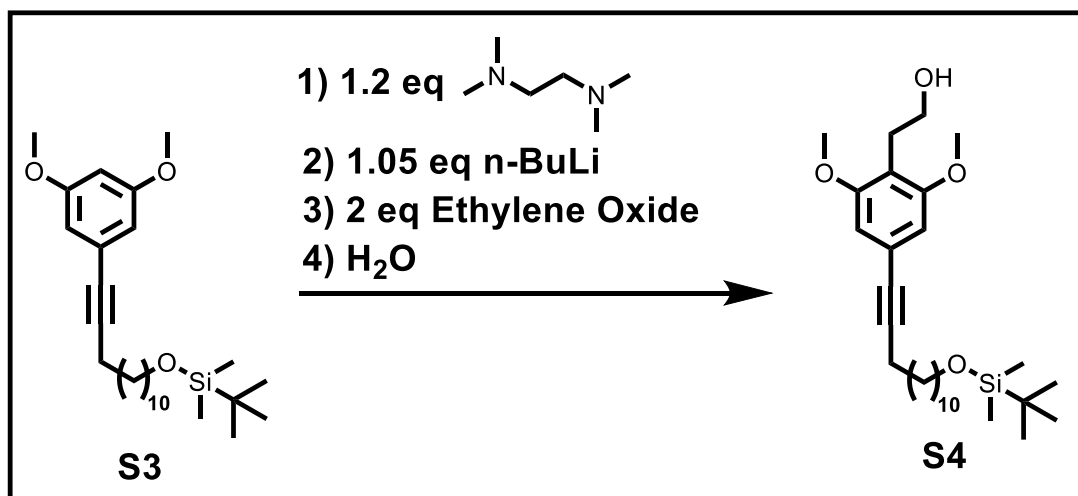
To a flask equipped with a stir bar was added **S3** (0.712 g, 0.0016 mol), followed by 2 mL

anhydrous THF. The mixture was put under nitrogen and cooled to 0° C.

Tetramethylethylenediamine (TMEDA) (289 μL, 0.00192 mol, 1.2 eq) was then added, and the

reaction mixture was stirred at 0° C for 30 minutes. After 30 minutes, n-butytllithium (1.05 eq,

672 μL of a 2.5 M stock solution in hexanes) was added dropwise, and the reaction mixture was

stirred at 0° C for 3 hours. A solution of ethylene oxide (2 eq, 0.0032 mol; 1 mL of a 2.5-3.3 M

solution in THF) was added dropwise over 10 minutes. The reaction mixture warmed to room

temperature overnight. The next day, the reaction was cooled to 0° C, and 5 mL of ice-cold

water was added dropwise, and the reaction mixture was allowed to stir for 30 minutes at room

temperature. The THF was then removed via rotary evaporation. Water and diethyl ether were

then added. The ether layer was separated. The aqueous layer was extracted two times with

diethyl ether. The combined organic layers were washed with brine, dried over MgSO$_4$, and

concentrated by rotary evaporation to yield the crude product. The crude product was purified

via silica column chromatography, eluting with 7:3 pentanes:diethyl ether, to yield 190 mg **S4** as

a clear oil (24 %). This material was carried on without characterization.
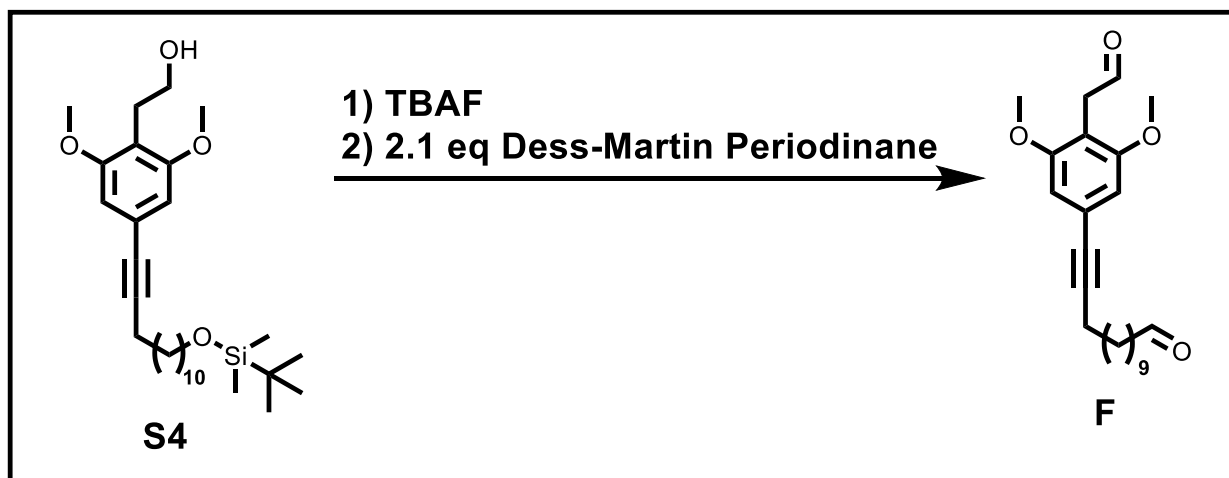
S4 (0.190 g, 0.00039 mol) was dissolved in 3.85 mL dry THF, and the solution was cooled to 0°

C under nitrogen. Tetrabutylammonium fluoride (1 eq, 390 µL, 1 M solution in THF) was added

dropwise. The reaction mixture was allowed to warm to room temperature over 16 hours and

then concentrated via rotary evaporation. The residue was dissolved in ethyl acetate, and this

solution was washed with 4 X with saturated aqueous ammonium chloride. The ethyl acetate

layer was dried over MgSO$_4$ and concentrated via rotary evaporation. The crude product was

carried forward without purification. The crude product was dissolved in 4 mL of dry

dichloromethane. Dess-martin periodinane (2.1 eq, 0.00081 mol, 0.346 g) was then added all at

once. The reaction mixture was stirred at room temperature for 2 hours. After 2 hours, the

mixture was diluted with ether, and the resulting solution was poured into 25 mL of saturated

aqueous sodium bicarbonate containing 25 g/100 mL of sodium thiosulfate pentahydrate. The

mixture was allowed to stir at room temperature for 1 hour, at which time the ether layer was separated. The aqueous layer was extracted two times with diethyl ether. The combined organic layers were washed successively with saturated aqueous sodium bicarbonate and brine, dried over MgSO$_4$, and concentrated via rotary evaporation. The crude product was purified via silica column chromatography, eluting with 7:3 pentanes: diethyl ether to yield 53.1 mg **F**, as a waxy solid (37 % over two steps).

^{1}H NMR (400 MHz, CDCl$_3$) δ 9.76 (t, J = 1.86 Hz, 1 H), 9.56 (t, J = 1.94 Hz, 1 H), 6.62 (s, 2 H), 3.79 (s, 6 H), 3.66 (d, J = 1.94 Hz, 2 H), 2.37-2.45 (m, 4 H), 1.56-1.68 (m, 4 H), 1.40-1.49 (m, 2 H), 1.27-1.33 (m, 10 H). **^{13}C NMR** (125 MHz, CDCl$_3$) δ 202.95, 200.58, 158.11, 124.21, 109.64, 107.02, 90.34, 80.06, 55.78, 43.02, 38.15, 29.44, 29.39, 29.35, 29.16, 29.14, 28.98, 28.74, 22.07, 19.42. **HRMS** *m/z* (ESI): calculated for [C$_{23}$H$_{32}$O$_4$ + NH$_4$]$^+$ 390.2639, 390.2629 found.

Foldamer catalyzed cyclization to nostocyclyne A core
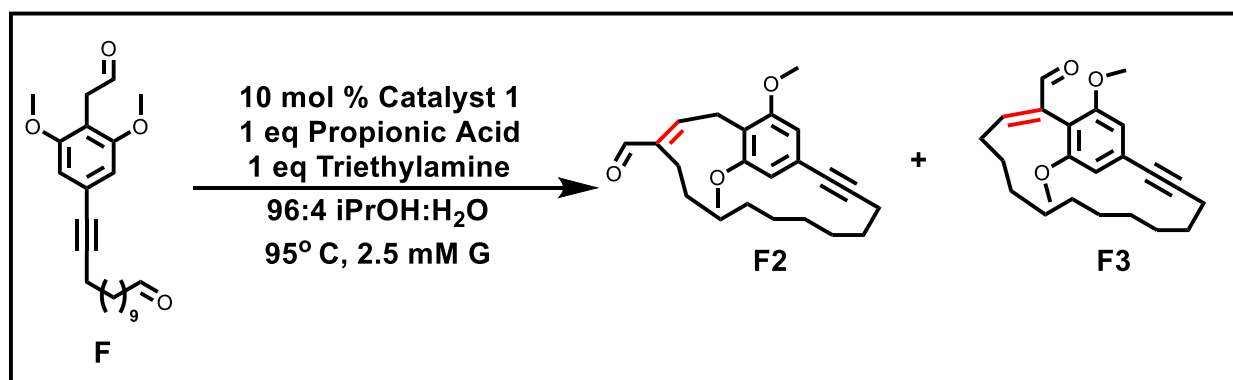
To a oven-dried 250 mL round bottom flask equipped with a stir bar was added **G** (0.000118 mol, 43.9 mg). 43.1 mL isopropanol and 1.89 mL water were then added. The mixture was vortexed for 5 minutes to get **F** completely dissolved. Next, propionic acid (0.000118 mol, 1 eq, 8.83 µL) and triethylamine (0.000118 mol, 1 eq, 16.64 µL) were added. Added last was catalyst

1 (10 mol %, 0.0000118 mol; 2.14 mL of a 5.51 mM stock solution in isopropanol). The round bottom flask was then submerged in a preheated oil bath at 95° C, and the reaction mixture was stirred for 41 hours (at which point LC-MS analysis showed that the reaction had stopped) open to air. After 41 hours the reaction mixture was concentrated via rotary evaporation. 5 mL of chloroform was added to the residue in order to separate the desired product from peptide catalyst **1**, which precipitates to form a white solid upon addition of chloroform. The chloroform was filtered through a cotton plug in a Pasteur pipette to give a clear light-yellow solution. The process was repeated once more. The chloroform layers were concentrated via rotary evaporation to provide the crude product. The crude product was purified by silica column chromatography eluting with 7:3 pentane:ether to yield 23.1 mg **F2** (55 %), and 8.4 mg **F3** (20 %), indicating that **F2** and **F3** were formed as a 2.8:1 mixture of regio-isomers in 75 % total yield.

F2 **^{1}H NMR** (500 MHz, CDCl$_3$) δ 9.29 (s, 1 H), 6.81 (t, J = 5.82 Hz, 1 H), 6.59 (s, 2 H), 3.81 (s, 6 H), 3.66 (d, J = 5.71 Hz, 2 H), 2.35 (m, 2 H), 1.72-1.78 (m, 2 H), 1.59-1.66 (m, 2 H), 1.47-1.54 (m, 2 H), 1.32-1.39 (m, 2 H), 1.13-1.21 (m, 2 H), 0.8-0.97 (m, 2 H), 0.70-0.79 (m, 2 H), 0.36-0.45 (m, 2 H). **^{13}C NMR** (125 MHz, CDCl$_3$) δ 196.28, 157.59, 154.21, 144.79, 123.76, 116.33, 107.05, 92.61, 82.47, 55.71, 31.44, 29.85, 29.36, 28.22, 28.01, 27.15, 26.29, 24.80, 23.13, 19.55. **HRMS** *m/z* (ESI): calculated for [C$_{23}$H$_{30}$O$_3$ + H]$^+$ 355.2268, 355.2259 found.

F3 **^{1}H NMR** (500 MHz, CDCl$_3$) δ 9.61 (s, 1 H), 6.98 (t, J = 8.13 Hz, 1 H), 6.64 (s, 2 H), 3.74 (s, 6 H), 2.38-2.41 (m, 2 H), 1.96-2.02 (m, 2 H), 1.66-1.67 (m, 2 H), 1.48-1.49 (m, 4 H), 1.08-1.21 (m, 4 H), 1.00-1.08 (m, 2 H), 0.82-0.92 (m, 2 H), 0.62-0.72 (m, 2 H). **^{13}C NMR** (125 MHz, CDCl$_3$) δ 193.13, 157.46, 156.33, 139.32, 125.71, 111.05, 107.50, 93.60, 82.83,

55.91, 30.47, 30.35, 29.70, 29.56, 28.72, 28.25, 28.19, 26.51, 26.35, 19.97. **HRMS** *m/z*

(ESI): calculated for $[C_{23}H_{30}O_3 + H]^+$ 355.2268, 355.2261 found.

Total synthesis of robustol
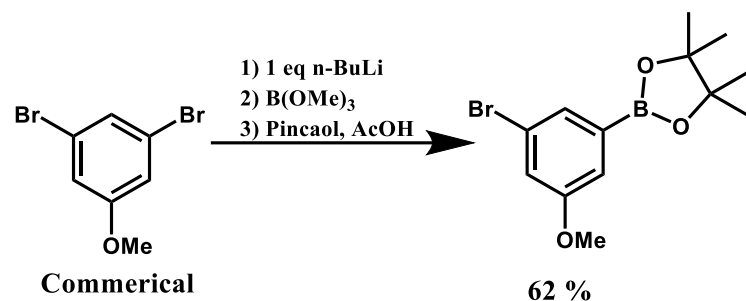
2-(3-bromo-5-methoxyphenyl)-4,4,5,5-tetramethyl-1,3,2-dioxaborolane was synthesized via the

reported method and matched the reported ^{1}H and ^{13}C spectra.[51]
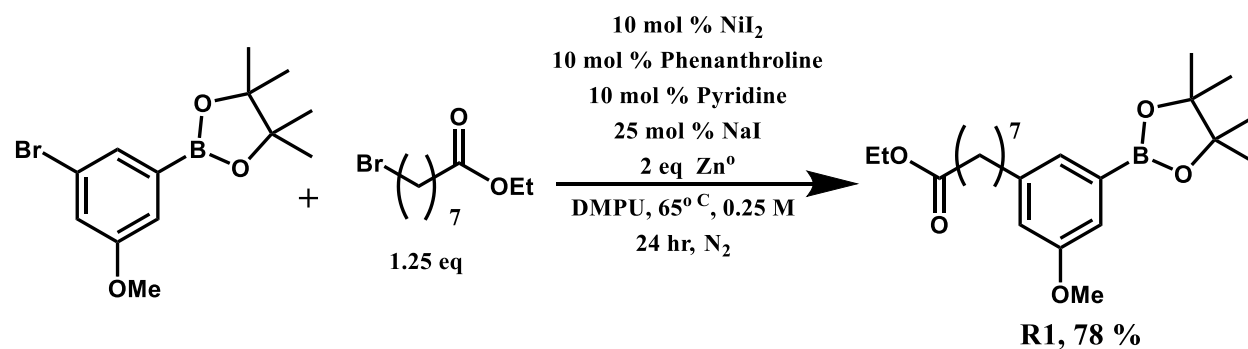
To an oven dried round bottom flask equipped with a stir bar was added NiI$_2$ (250 mg, 0.8

mmol), 1,10-phenanthroline (144 mg, 0.8 mmol), and NaI (300 mg, 2 mmol). 2-(3-Bromo-5-

methoxyphenyl)-4,4,5,5-tetramethyl-1,3,2-dioxaborolane (2.5 g, 8 mmol) and ethyl 8-

bromooctanoate (2.3 g, 9.1 mmol) were dissolved in 32 mL of DMPU and added to the round

bottom flask, followed by pyridine (64 µL, 0.8 mmol), and zinc dust (16 mmol, 1.1 g). The flask

was then capped with a septum and sparged with nitrogen for one minute at room temperature.

The reaction vessel was then submerged in a preheated 65° C oil bath and allowed to stir for 24 hours.

After 24 hours, the reaction mixture was allowed to cool to room temperature, and 30 mL of 1 M aqueous sodium bisulfate was added. The mixture was rapidly stirred for 15 minutes at room temperature, and then extracted with ethyl acetate three times. The combined ethyl acetate layers were washed with brine, dried over magnesium sulfate, filtered, and concentrated via rotary evaporation. The crude oil was purified via column chromatography, eluting with 9:1 pentanes:diethyl ether → 8:2 pentanes:diethyl ether → 100 % diethyl ether, to yield 2.7 g of **R1** as a clear oil (78 %).

^{1}H NMR (400 MHz, CDCl$_3$) δ 7.23 (broad singlet, 1 H), 7.14 (d, J = 2.43 HZ, 1 H), (t, J = 2.00 Hz, 1 H), 4.12 (q, J = 7.10 Hz, 2 H), 3.82 (s, 3 H), 2.56 (t, J = 7.60 Hz, 2 H), (t, J = 7.43 Hz, 2 H), 1.55 – 1.66 (m, 4 H), 1.3 – 1.36 (m, 18 H). **^{13}C NMR** (125 MHz, CDCl$_3$) δ 173.90, 159.12, 143.95, 127.45, 118.25, 115.63, 83.76, 60.15, 55.25, 35.80, 34.37, 31.41, 29.22, 29.12, 29.06, 24.97, 24.85, 14.25. **^{11}B** (128 MHz) δ 30.53. **HRMS** *m/z* (ESI): calculated for [C$_{23}$H$_{37}$BO$_5$ + NH$_4$]$^+$ 421.3109, found 422.3073.
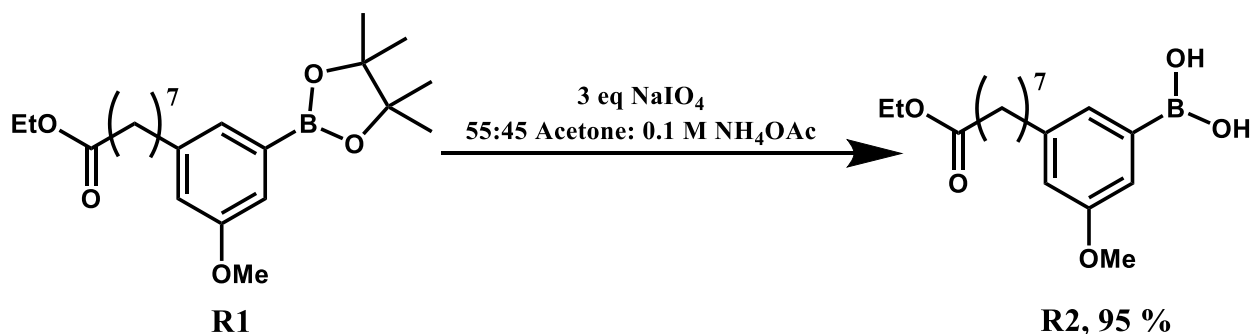
To an oven dried round bottom flask equipped with a stir bar was added **R1** (1.22 g, 3 mmol). **R1** was then dissolved in 83 mL acetone and 68 mL of a 0.1 M aqueous solution of ammonium

acetate. Once all solids had dissolved, sodium periodate (1.93 g, 9 mmol) was added, and the reaction mixture was stirred at room temperature for 48 hours.

After 48 hours, the acetone was removed via rotary evaporation. A 1:1 mixture of ethyl acetate and brine was then added to the crude reaction mixture. The aqueous layer was extracted two more times with ethyl acetate. The combined ethyl acetate layers were dried over magnesium sulfate, and concentrated via rotary evaporation to yield **R2** as a light yellow oil (0.920 g, 95 %). **R2** was used without further purification.

The ^{1}H NMR of unpurified **R2** in d_6-DMSO is provided below.
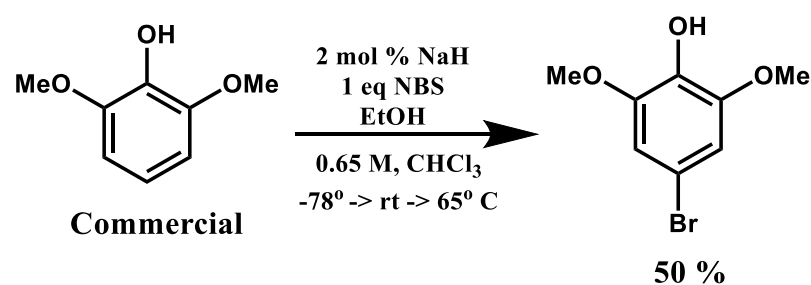
4-bromo-2,6-dimethoxyphenol was synthesized via the reported method and matched the reported 1H and 13C spectra.[52]
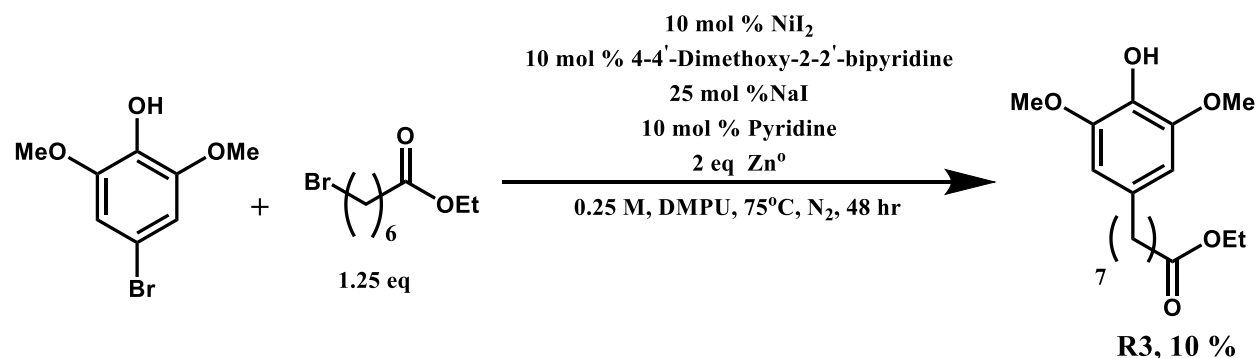
To an oven dried round bottom flask equipped with a stir bar was added NiI$_2$ (259 mg, 0.83 mmol), 4-4-dimethoxy-2-2-bipyridine (179 mg, 0.83 mmol), and NaI (311 mg, 2.1 mmol). 4-

bromo-2,6-dimethoxyphenol (1.93 g, 8.3 mmol) and ethyl 7-bromoheptanoate (2.45 g, 10.3 mmol) were dissolved in 33 mL of DMPU and added to the round bottom flask, followed by pyridine (67 μL, 0.83 mmol), and zinc dust (16.6 mmol, 1.1 g). The flask was then capped with a septum and sparged with nitrogen for one minute at room temperature. The reaction vessel was then submerged in a preheated 75° C oil bath and allowed to stir for 48 hours.

After 48 hours, the reaction mixture was allowed to cool to room temperature, and 30 mL of 1 M aqueous sodium bisulfate was added. The mixture was rapidly stirred for 15 minutes at room temperature, and then extracted with ethyl acetate three times. The combined ethyl acetate layers were washed with brine, dried over magnesium sulfate, filtered, and concentrated via rotary evaporation. The crude oil was purified via column chromatography, eluting with 1:1 pentanes:diethyl ether to yield 200 mg of **R3** (10 %).

¹H NMR (400 MHz, CDCl₃) δ 6.39 (s, 2 H), 5.35 (s, 1 H), 4.12 (q, J = 7.10 Hz, 2 H), 3.88 (s, 3 H), 2.52 (t, J = 7.75 Hz, 2 H), 2.30 (t, J = 7.75 Hz, 2 H), 1.58 – 1.67 (m, 4 H), 1.32 – 1.39 (m, 4 H), 1.25 (t, J = 7.10 Hz, 3 H). **¹³C NMR** (125 MHz, CDCl₃) δ 173.85, 146.82, 133.85, 132.60, 104.86, 60.19, 56.23, 36.11, 34.34, 31.57, 28.99, 28.92, 24.90, 14.25. **HRMS** *m/z* (ESI): calculated for [C₁₇H₂₆O₅ - H]⁻ 309.1708, found 309.1707.
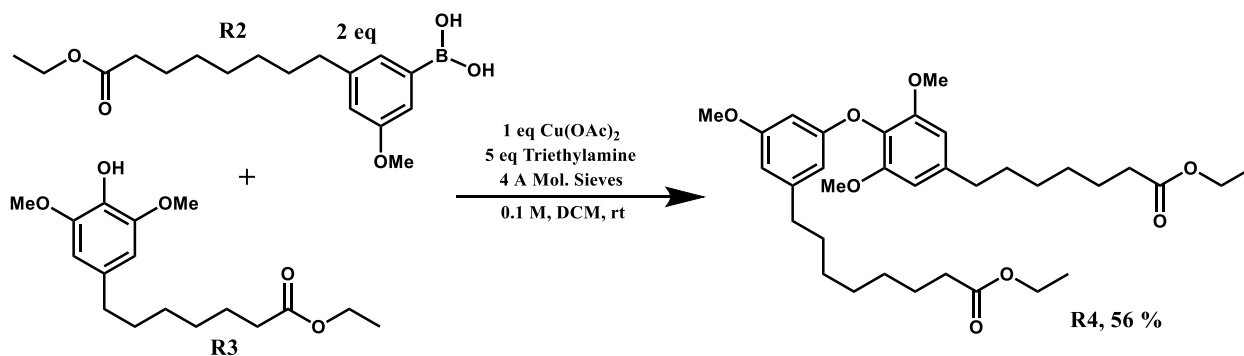
To an oven dried vial equipped with a stir bar was added **R3** (200 mg, 0.644 mmol) and **R2** (415 mg, 1.2 mmol). Cu(OAc)$_2$ (175 mg, 9.67 mmol, 1 eq relative to the average mole amount of **R2** and **R3**), 4 Å molecular sieves, and triethylamine (0.673 mL, 4.84 mmol) were then added. Added last was 6.4 mL of anhydrous dichloromethane. The reaction vessel was capped with a septum, and the mixture was stirred at room temperature for 36 hours. The reaction mixture was then concentrated via rotary evaporation, and the residue was purified via column chromatography, eluting with 7:3 diethyl ether:pentanes to give **R4** (207 mg, 56 %) as a light-yellow oil.

^{1}H NMR (400 MHz, CDCl$_3$) δ 6.45 (s, 2 H), 6.34 (m, 1 H), 6.32 (m, 1 H), 6.24 (t, J = 2.36 Hz, 1 H), 4.1 – 4.15 (m, 4 H), 3.76 (s, 6 H), 3.73 (s, 3 H), 2.59 – 2.61 (m, 2 H), 2.48 – 2.51 (m, 2 H), 2.26 – 2.32 (m, 4 H), 1.57 – 1.67 (m, 8 H), 1.39 – 1.41 (m, 4 H), 1.24 – 1.30 (m, 12 H).

^{13}C NMR (125 MHz, CDCl$_3$) δ 173.89, 173.84, 160.44, 159.67, 153.10, 144.95, 140.24, 129.94, 107.53, 107.07, 105.43, 98.32, 60.22, 60.17, 56.23, 55.20, 36.51, 36.14, 34.39, 34.36, 31.29, 31.03, 29.15, 29.12, 29.10, 29.07, 29.01, 25.01, 24.99, 24.92, 14.28. **HRMS** *m/z* (ESI): calculated for [C$_{34}$H$_{50}$O$_8$ + NH$_4$]$^+$ 604.3844, found 604.3845.
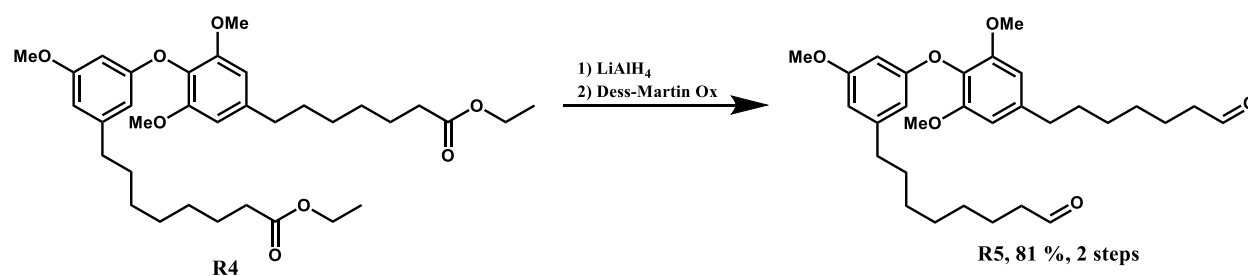
To an oven-dried vial equipped with a stir bar was added LiAlH$_4$ (45 mg, 1.1 mmol, 43 mg). While purging with nitrogen at 0° C, 1 mL of anhydrous THF was added via syringe. **R4** (163 mg, 0.28 mmol) was dissolved in 2 mL of anhydrous THF and added dropwise to the slurry of

LiAlH$_4$. The reaction mixture was stirred at 0° C for 10 minutes and then warmed to room temperature over one hour.

The reaction mixture was then cooled to 0° C, and 50 µL of water was carefully added dropwise. Then 50 µL of 15 % aqueous NaOH solution was added, followed by 150 µL of water. The slurry was warmed to room temperature and rapidly stirred for 20 minutes. MgSO$_4$ was then added, and the slurry was stirred for an additional 20 minutes at room temperature. The slurry was then filtered. The filtrate was then concentrated via rotary evaporation to give the crude diol as a clear oil. ^{1}H NMR spectra of the unpurified diol is provided below. The diol was not purified prior to Dess-Martin oxidation.

To the crude diol was added 2 mL of anhydrous DCM, and Dess-Martin periodinane (257 mg, 0.6 mmol, 2.4 eq). The reaction mixture was stirred for 3 hours at room temperature. The mixture was then diluted with ether, and the resulting solution was poured into 25 mL of saturated aqueous sodium bicarbonate containing 25 g/100 mL of sodium thiosulfate pentahydrate. The mixture was allowed to stir at room temperature for 1 hour, at which time the ether layer was separated. The aqueous layer was extracted two times with diethyl ether. The combined organic layers were washed successively with saturated aqueous sodium bicarbonate and brine, dried over MgSO$_4$, and concentrated via rotary evaporation. The crude product was purified via silica column chromatography, eluting with 7:3 diethyl ether:pentanes to yield **R7** as a light yellow oil (110 mg, 81 % over two steps).

^{1}H NMR (400 MHz, CDCl$_3$) δ 9.78 (t, J = 1.76 Hz, 1 H), 9.76 (t, J = 1.86 Hz, 1 H), 6.45 (s, 2 H), 6.32 – 6.36 (m, 2 H), 6.23 (t, J = 2.29 Hz, 1 H), 3.76 (s, 6 H), (s, 3 H), 2.60 (t, J = 7.70 Hz, 2 H), 2.50 (t, J = 7.75 Hz, 2 H), 2.45 (td, J = 7.37, 1.73 Hz, 2 H), 2.41 (td, J = 7.41, 1.87 Hz, 2 H), 1.55 – 1.71 (m, 8 H), 1.37 – 1.42 (m, 4 H), 1.29 – 1.33 (m, 6 H). **^{13}C NMR** (125

MHz, CDCl₃) δ 202.29, 202.75, 160.45, 159.67, 153.11, 144.89, 140.26, 129.26, 107.58, 107.03, 105.48, 105.46, 98.33, 56.24, 55.20, 43.90, 43.89, 36.48, 36.11, 31.26, 30.98, 29.22, 29.13, 29.09, 29.04, 29.03, 22.07, 22.01. The expected product structure contains 29 non-equivalent carbons, but only 28 ^{13}C NMR resonances were observed. We speculate that resonances for two non-equivalent carbons are overlapped. **HRMS** *m/z* (ESI): calculated for $[C_{30}H_{42}O_6 + NH_4]^+$ 516.3320, found 516.3318.
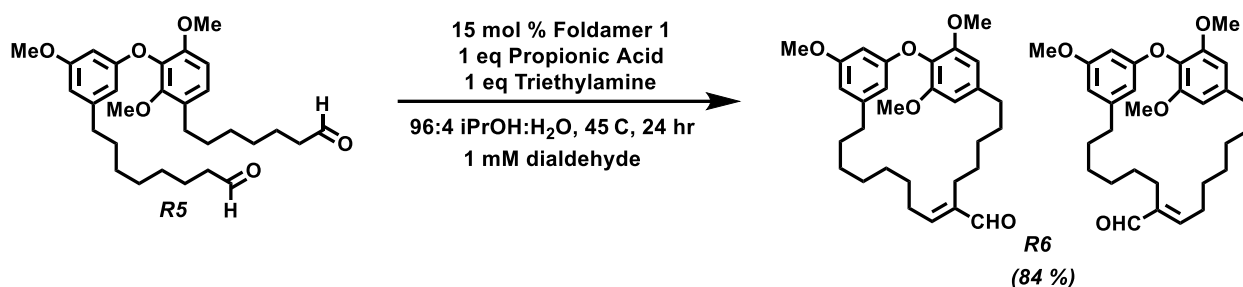
To an oven-dried round-bottom flask equipped with a stir bar was added **R5** (34 mg, 0.0682 mmol) and 62.8 mL of isopropanol. Subsequently added were water (2.72 mL), propionic acid (5.1 µL, 0.0682 mol), and triethylamine (9.5 µL, 0.0682 mol). Added last was catalyst **1** (15 mol %, 2.57 mL of a 3.98 mM stock solution in isopropanol). The reaction vessel was capped with a septum (to prevent evaporation) and submerged in a preheated oil bath at 50° C for 24 hours.

The solvent was then removed via rotary evaporation. Chloroform (3 mL) was added to the residue in order to separate the desired product from peptide catalyst **1**, which precipitated to form a white solid. The chloroform was filtered through a cotton plug in a Pasteur pipette to give a clear light-yellow solution. Chloroform (3 mL) was added to the residue again to ensure complete transfer of the desired product. This solution was filtered through a cotton plug. The combined chloroform solutions were concentrated via rotary evaporation to provide the crude product. The crude product was purified by silica column chromatography eluting with 1:1

pentanes:diethyl ether to obtain **R6** as a mixture of two regioisomers as a clear oil (29 mg, 84 %).

The regioisomers were not separated prior to the next reaction.

¹H NMR, and **¹³C NMR** are provided below. **HRMS** *m/z* (ESI): calculated for $[C_{30}H_{40}O_5 + NH_4]^+$ 498.3214, found 498.3211.

1) 1.25 eq RhCl(PPh₃)₄
165° C, 0.05 M, Benzonitrile, N₂
2) 30 % Pd/C, 1 atm H₂
30 mM, 3:1 EtOAc:MeOH, rt, 24 hr

R6

R7
(85 %, 2 steps)
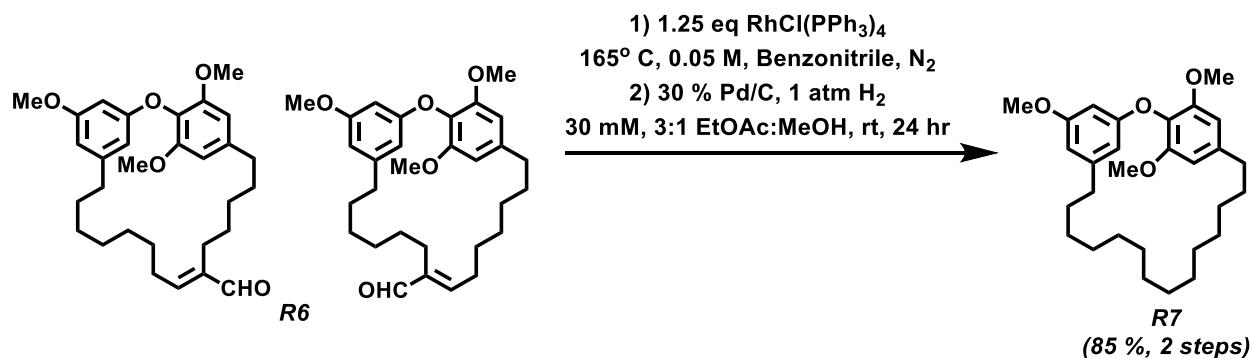
To an oven-dried 10 mL round-bottom flask equipped with a stir bar was added **R6** (38 mg,

0.079 mmol). **R6** was dissolved in 1.6 mL of anhydrous benzonitrile, and nitrogen gas was

bubbled through the solution for 20 minutes. RhCl(PPh₃)₄ (92 mg, 0.099 mmol, 1.25 eq) was

added to the solution, and nitrogen gas was bubbled through the solution for 10 minutes. The

round bottom was fitted with a reflux condenser and submerged in a preheated oil bath at 165° C.

The reaction mixture was stirred for 3 hours, and then allowed to cool to room temperature. The

reaction mixture was frozen on dry ice and placed on a lyophilizer so that benzonitrile could

sublime overnight. The crude oily-solid product was purified via silica column chromatography,

eluting with 9:1 pentanes:diethyl ether → 8:2 pentanes:diethyl ether → 7:3 pentanes:diethyl

ether to yield 35.7 mg of a clear oil (quantitative yield). NMR analysis of the clear oil suggests

the presence of one major alkene along with minor alkene isomers. (¹H NMR spectra of the

decarbonylation product mixture is shown in the experimental spectrum section below.)

The decarbonylation product was then hydrogenated. To an oven-dried 10 mL round-bottom flask equipped with a stir bar was added 10.7 mg of 10 wt. % Pd/C (30 wt. % relative to decarbonylation product). The round-bottom flask was then capped with a rubber septum. The vessel was stringently purged with nitrogen while venting through a needle for five minutes. The decarbonylation product (52 mg, 0.115 mmol) was dissolved in 3.8 mL of 3:1 ethyl acetate:methanol (30 mM) and N_2 was bubbled through the solution to remove oxygen. The decarbonylation product solution was then added via syringe into the round bottom flask while purging with N_2 continued. The round-bottom flask was put under one atmosphere of hydrogen (hydrogen balloon). The reaction mixture was stirred for 24 hours at room temperature. After 24 hours the reaction mixture was filtered over celite, eluting with ethyl acetate. The filtrate was concentrated via rotary evaporation to yield **robustol trimethyl ether** as a white solid (44 mg, 85 %). The hydrogen NMR spectrum matches that reported[53].

^{1}H NMR (400 MHz, CDCl$_3$) δ 6.67 (t, J = 2.23, 1 H), 6.47 (s, 2 H), 6.36 – 6.37 (m, 1 H), 5.80 – 5.82 (m, 1 H), 3.80 (s, 3 H), 3.77 (s, 6 H), 2.62 (t, J = 6.42 Hz, 2 H), 2.40 (t, 8.10 Hz, 2 H), 1.62 – 1.70 (m, 2 H), 1.42 – 1.49 (m, 2 H), 1.23 – 1.30 (m, 20 H). **^{13}C NMR** (125 MHz, CDCl$_3$) δ 160.61, 159.66, 152.98, 144.79, 140.35, 129.88, 108.33, 105.75, 104.72, 99.17, 56.25, 36.18, 35.78, 30.99, 30.71, 29.70, 28.58, 28.32, 28.03, 27.95, 27.94, 27.92, 27.81, 27.73, 27.48, 27.26. **HRMS** *m/z* (ESI) (**R7**): calculated for [C$_{29}$H$_{42}$O$_4$ + H])$^+$ 455.3156, found 455.3153. **HRMS** *m/z* (ESI) for decarbonylated mixture prior to hydrogenation: calculated for [C$_{29}$H$_{42}$O$_4$ + H]$^+$ 453.2999, found 453.2998.
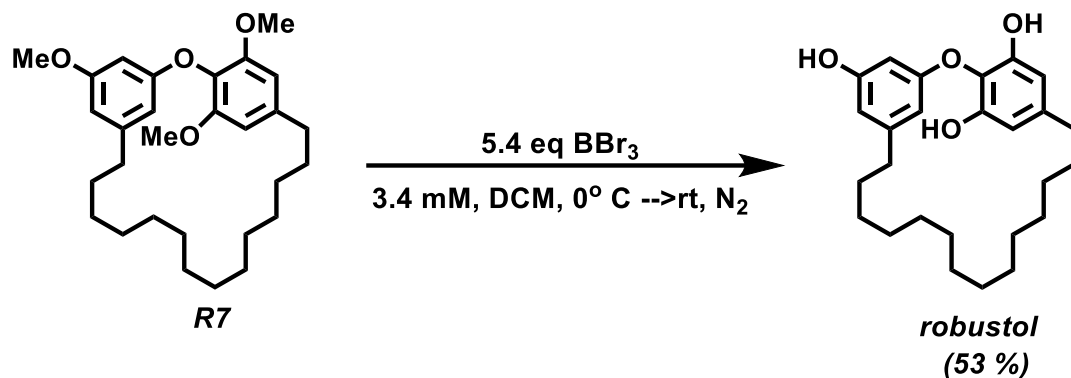
To an oven-dried vial equipped with a stir bar was added **R7** (23.5 mg, 0.0516 mmol). 1.5 mL of anhydrous DCM was then added, and the mixture was cooled to 0° C and put under a nitrogen atmosphere. A 1 M solution of boron tribromide in DCM (5.4 eq, 0.28 mmol, 279 µL) was then added to the reaction mixture dropwise over 20 minutes. The reaction mixture was allowed to warm to room temperature over 2 hours, and stirred for 4 hours at room temperature.

The reaction mixture was then diluted with 10 mL of anhydrous DCM. 2.5 mL of water was then added, and the mixture was stirred for 15 minutes at room temperature. The DCM layer was removed, and the aqueous layer was extracted two times with DCM. The combined DCM layers were dried over $MgSO_4$. The DCM was then removed via rotary evaporation to yield a clear oil. Purification via column chromatography yielded Robustol as an oily-solid (11.1 mg, 53 %). The hydrogen NMR spectrum matches that reported for the original isolation of robustol[53]. No ^{13}C NMR spectrum was reported in the original publication[53].

^{1}H NMR (400 MHz, CDCl$_3$) δ 6.59 (t, J = 2.41 Hz, 1 H), 6.44 (s, 2 H), 6.39 (broad singlet, 1 H), 5.99 (broad singlet, 1 H), 5.02 (broad singlet, 1 H), 4.87 (broad singlet, 1 H), 2.54 (t, 6.45 Hz, 2 H), 2.38 – 2.43 (m, 2 H), 1.58 – 1.65 (m, 2 H), 1.40 – 1.48 (m, 2 H), 1.22 – 1.32 (m, 20 H). **^{13}C NMR** (125 MHz, CDCl$_3$) δ 157.78, 156.87, 148.47, 146.80, 126.66, 110.69, 108.63, 104.88, 101.45, 35.70, 30.87, 30.65, 28.86, 28.33, 28.30, 28.23, 27.87, 27.83, 27.80,

27.80 (two carbon signals overlap) 27.55, 27.03. **^{13}C dept135 NMR** (125 MHz, CDCl$_3$)

Positive peaks: 110.69, 108.63, 104.88, 101.45, 77.21. Negative peaks: 35.70, 35.67, 30.87,

30.65, 28.86, 28.33, 28.30, 28.23, 27.87, 27.83, 27.80, 27.80 (two carbon signals overlap),

27.55, 27.03. **HRMS** *m/z* (ESI): calculated for [C$_{26}$H$_{36}$O$_4$ – H]$^-$ 411.2535, found 411.2539. LC-

MS trace of robustol showed > 99 % purity via the 275 nm channel (see spectra section).

3.5.4 2D NMR of Catalyst 1

Peptide samples were analyzed on a Bruker Avance 600 MHz spectrometer equipped with a 5

mm, z-axis gradient, triple resonance, cryogenic probe. Catalyst **1** was dissolved in 600 μL of

CD$_3$OH or iPrOH-d7 at a concentration of 2 mM or 0.2 mM with trace amounts of 2,2-dimethyl-

2-silapentane-5-sulfonate (DSS) as internal reference. All the spectra were taken at 24°C. The

following standard Avance pulse programs were employed: 1D with solvent suppression using

excitation sculpting (zgesgp), 2D TOCSY with excitation sculpting (mlevesgpph), and 2D

ROESY with excitation sculpting (roesyesgpph). TOCSY experiments used a mixing time of 100

ms. ROESY experiments used a mixing time of 300 ms.

Data were processed using TopSpin 3.6.1. Data were analyzed using NMRFAM Sparky,[64] with

employment of sequential assignment procedures to assign chemical shifts of protons.
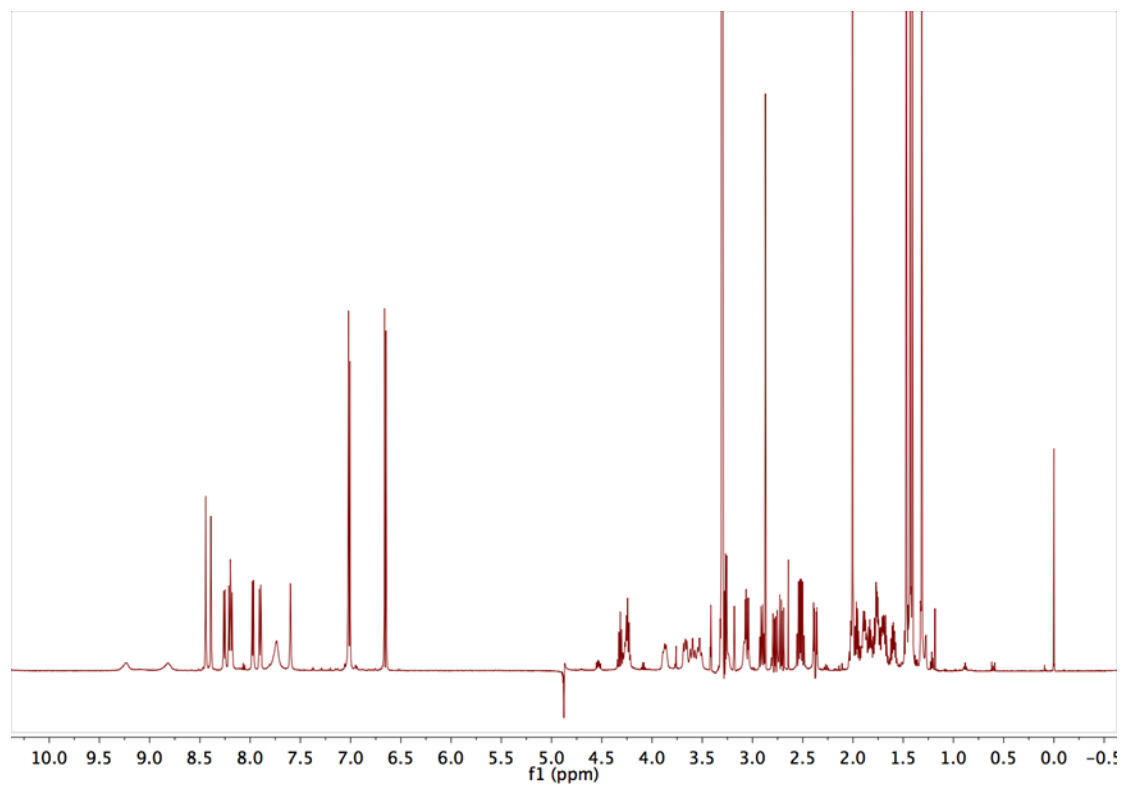
Figure 22. Solvent suppressed ^{1}H-NMR of 2 mM catalyst **1** in CD$_3$OH.
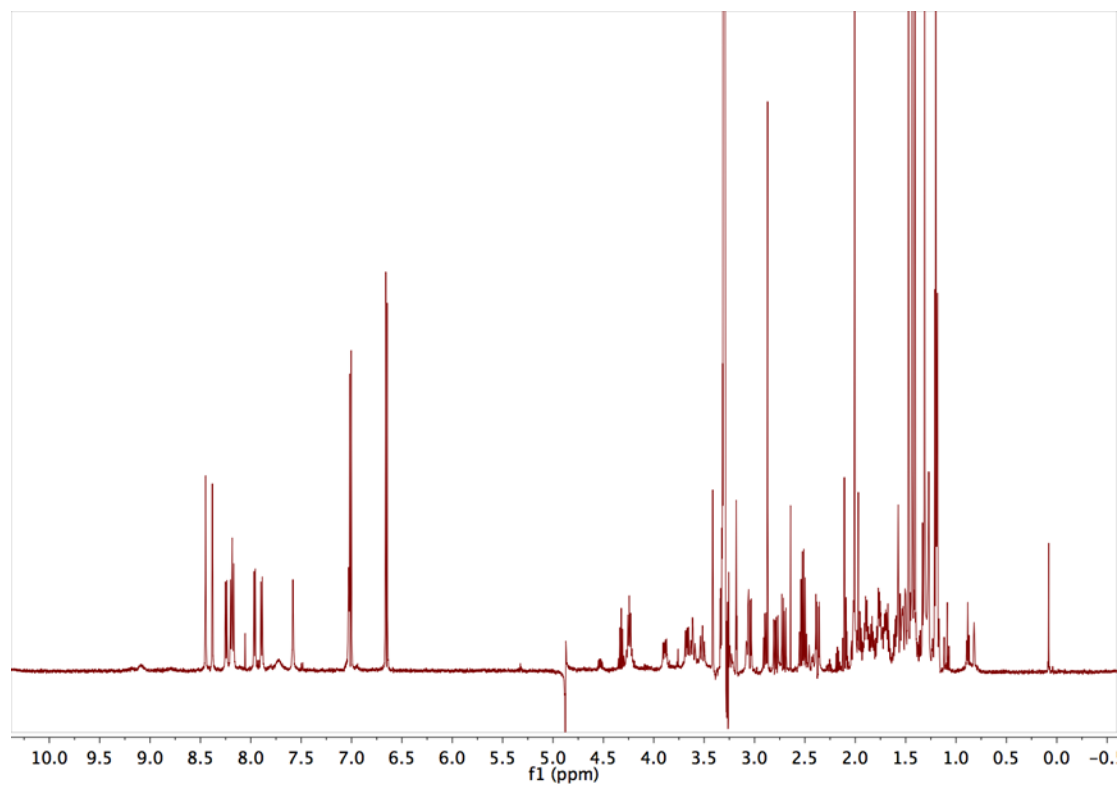
Figure 23 Solvent suppressed ^{1}H-NMR of 0.2 mM catalyst **1** in CD$_3$OH.
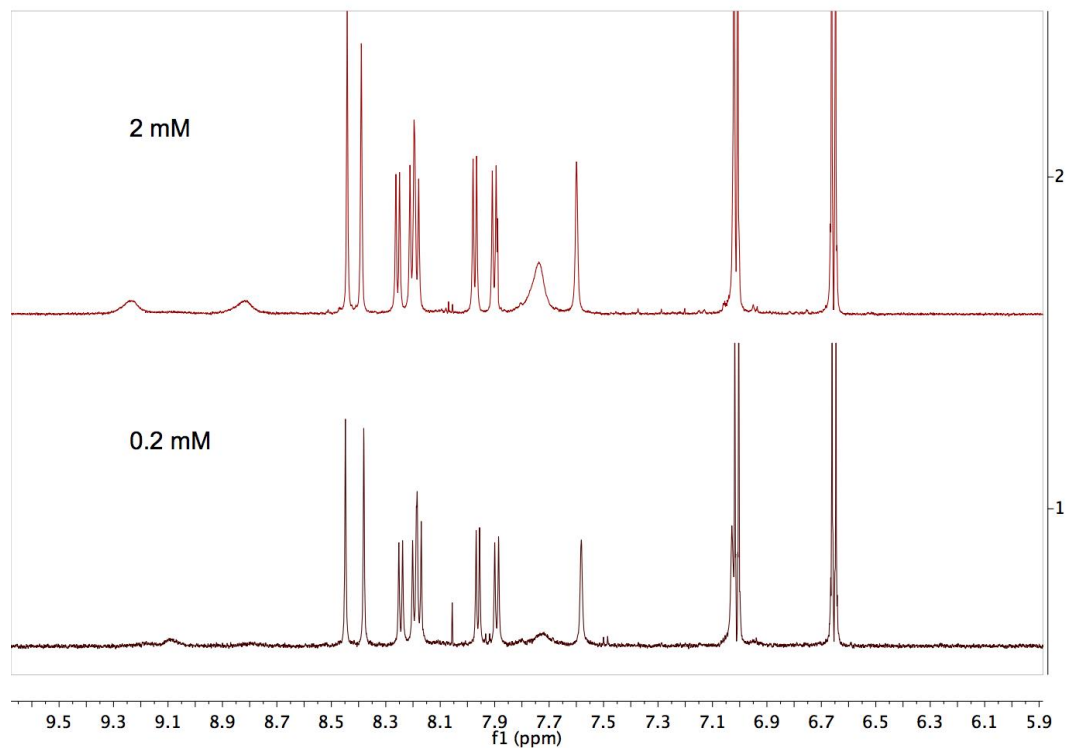
Figure 24. Comparison of the solvent-suppressed ^{1}H-NMR amide region of catalyst **1** in CD$_3$OH at 2 mM and 0.2 mM.
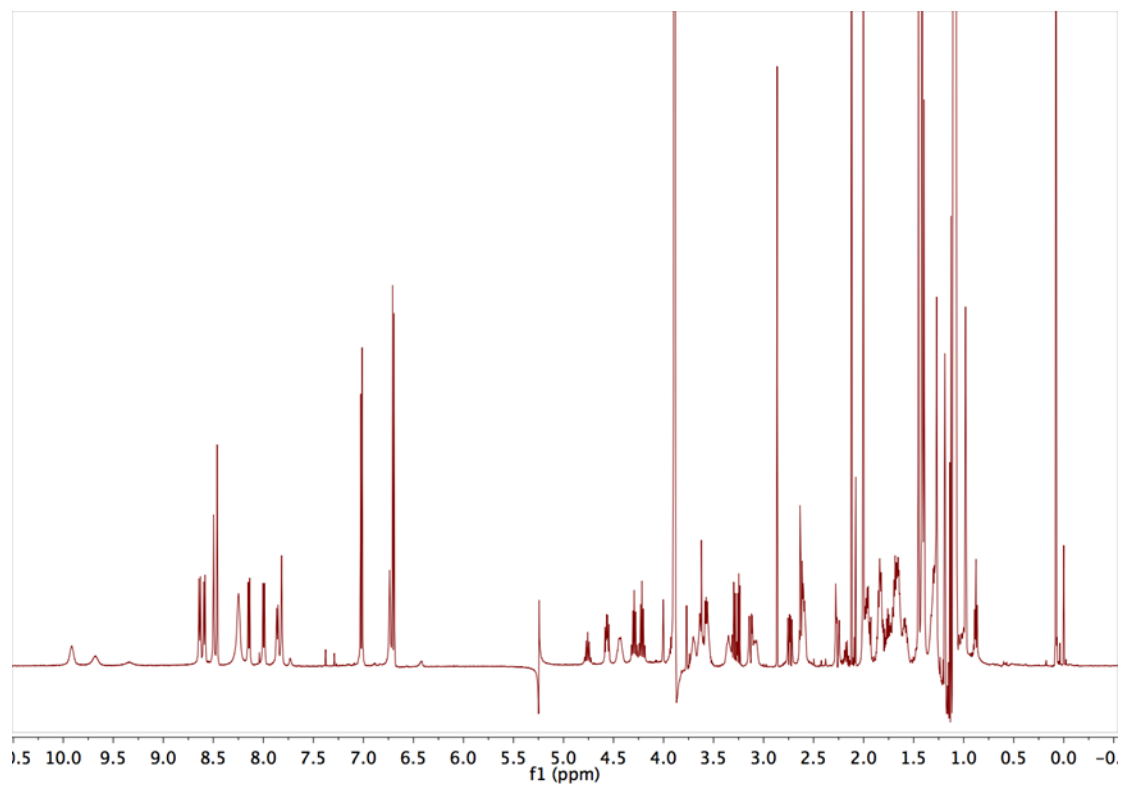
Figure 25. Solvent-suppressed ^{1}H-NMR spectrum of catalyst **1** in iPrOH-d$_7$. Strong signals at 1.09 and 3.89 ppm arise from the solvent. The signal at 0.08 ppm is attributed to silicone grease.
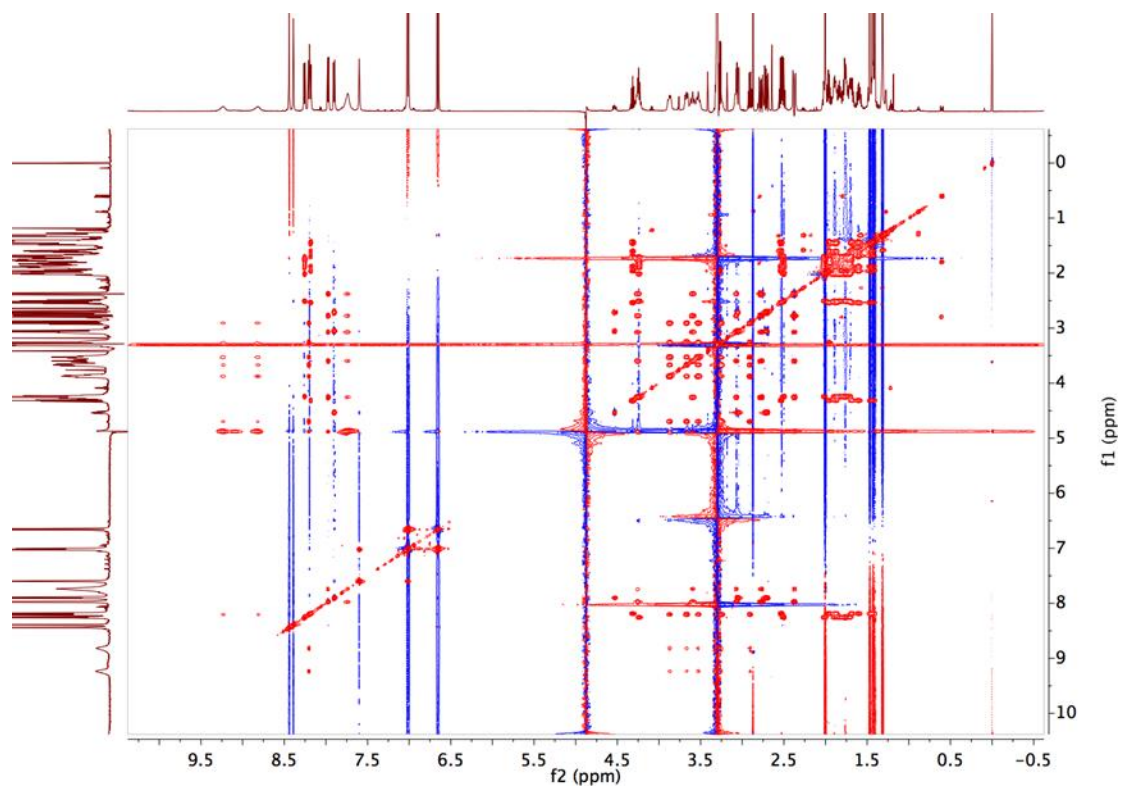
Figure 26. Solvent-suppressed 2D TOCSY NMR of 2 mM catalyst **1** in CD$_3$OH.
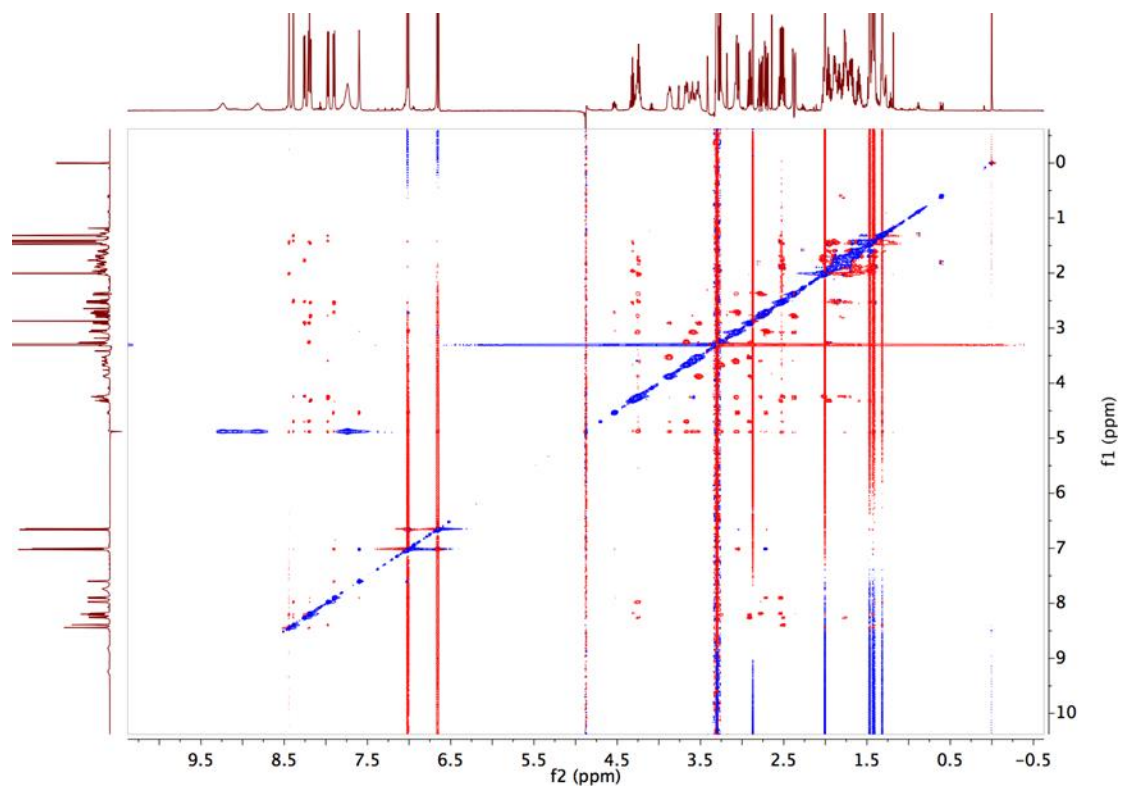
Figure 27. Solvent-suppressed 2D ROESY NMR of 2 mM catalyst **1** in CD$_3$OH.

Peptide	HN	Hα	Hβ	Hγ	Hδ	Hε	Other
N-terminus							CH3: 2.00
Aib1	8.44	-	1.47, 1.43	-	-	-	
APC2	8.20	2.91	4.70	3.67, 3.25	9.23, 8.82	3.87, 3.52	
ACPC3	8.26	2.51	4.24	2.01, 1.76	1.76, 1.73	1.89, 1.83	
Aib4	8.39	-	1.41, 1.31	-	-	-	
DBU5	7.97	2.77, 2.38	4.26	3.59, 3.07	7.74	-	
ACPC6	8.19	2.53	4.31	1.96, 1.45	1.68, 1.60	1.88, 1.45	
Tyr7	7.90	4.53	3.05, 2.71	-	7.02	6.66	
C-terminus	7.60, 7.02						

Figure 28. Proton resonances (ppm) for catalyst **1** in CD_3OH.

ROE Assignment	CS1(ppm)	CS2(ppm)
NtermAc-APC2HN	2.00	8.20
Aib1HB-Aib4HN	1.47	8.39
APC2HB-Aib4HN	4.70	8.39
APC2HB-DBU5HN	4.70	7.97
APC2HE-DBU5HB	3.87	4.26
Aib4HB-Tyr7HD	1.31	7.02

Figure 29. Non-sequential ROE's observed for catalyst **1** in CD_3OH.
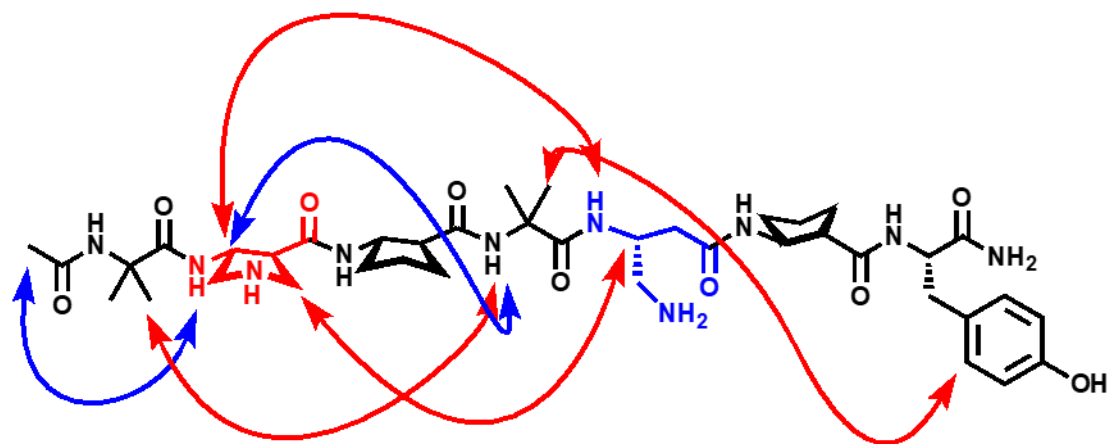
Figure 30. Graphical representation of ROEs observed for catalyst **1** between protons on residues that are not adjacent in sequence in CD₃OH. Blue lines indicate i,i+2 ROEs. Red lines indicate i,i+3 ROEs.
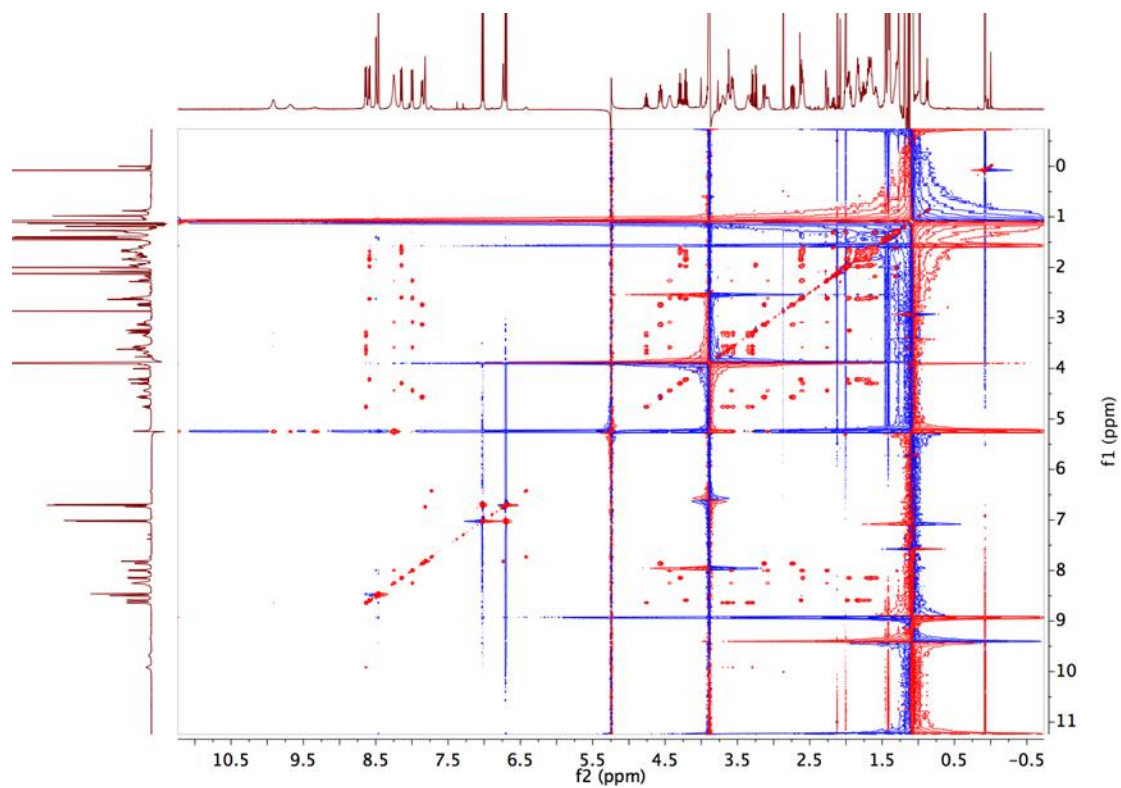
Figure 31. Solvent-suppressed 2D TOCSY NMR of catalyst **1** in iPrOH-d7 at 2mM.
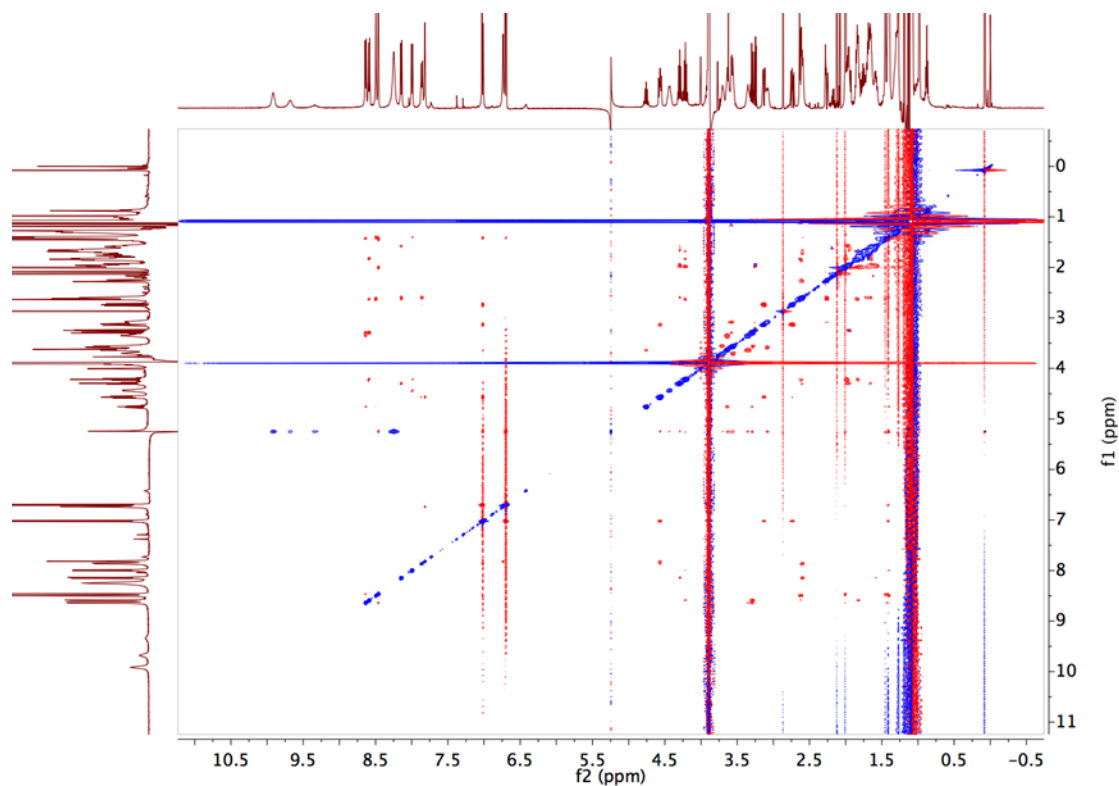
Figure 32. Solvent-suppressed 2D ROESY NMR of catalyst **1** in iPrOH-d7 at 2mM.

Peptide	HN	Hα	Hβ	Hγ	Hδ	Hε	Other
N-terminus							CH3: 2.01
Aib1	8.46	-	1.46, 1.42	-	-	-	
APC2	8.64	3.30	4.76	3.64, 3.35	9.92, 9.68	3.70, 3.56	
ACPC3	8.59	2.62	4.22	1.98, 1.84	1.76, 1.68	1.84	
Aib4	8.50	-	1.41, 1.40	-	-	-	
DBU5	8.00	2.61, 2.26	4.44	3.58, 3.08	8.25	-	
ACPC6	8.14	2.60	4.30	1.96, 1.59	1.66	1.71, 1.66	
Tyr7	7.86	4.57	3.13, 2.74	-	7.02	6.70	
C-terminus	7.82, 6.74						

Figure 33. Proton resonances (ppm) for catalyst **1** in iPrOH-d7.

ROE Assignment	CS1(ppm)	CS2(ppm)
NtermAc-APC2HN	2.01	8.64
NtermAc-ACPC3HN	2.01	8.59
APC2HB-Aib4HN	4.76	8.50
APC2HB-DBU5HN	4.76	8.00
APC2HA-DBU5HG	3.30	3.58
ACPC3HB-DBU5HN	4.22	8.00
ACPC3HB-ACPC6HN	4.22	8.14
Aib4HB-Tyr7HD,HE	1.41	7.02, 6.70
ACPC6HB-CtermHN	4.30	7.82, 6.74

Figure 34. Non-sequential ROEs observed for catalyst **1** in iPrOH-d7.
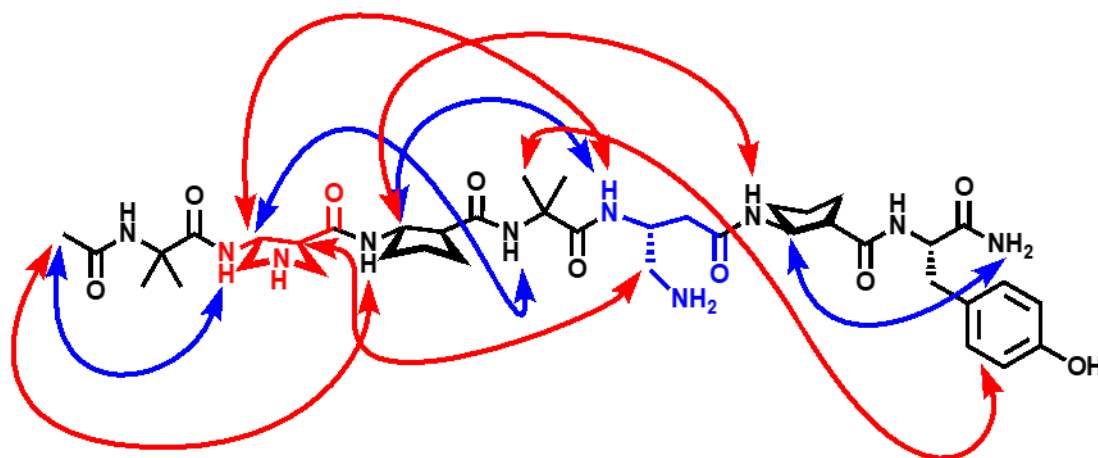
Figure 35. Graphical representation of ROEs observed for catalyst **1** between protons on residues that are not adjacent in sequence in iPrOH-d7. Blue lines indicate i,i+2 ROEs. Red lines indicate i,i+3 ROEs.

3.5.5 Cyclodimerization of nonanedial

a. **Divergent Reactivity: Foldamer vs. small molecule catalyzed control (LC-MS evidence)**
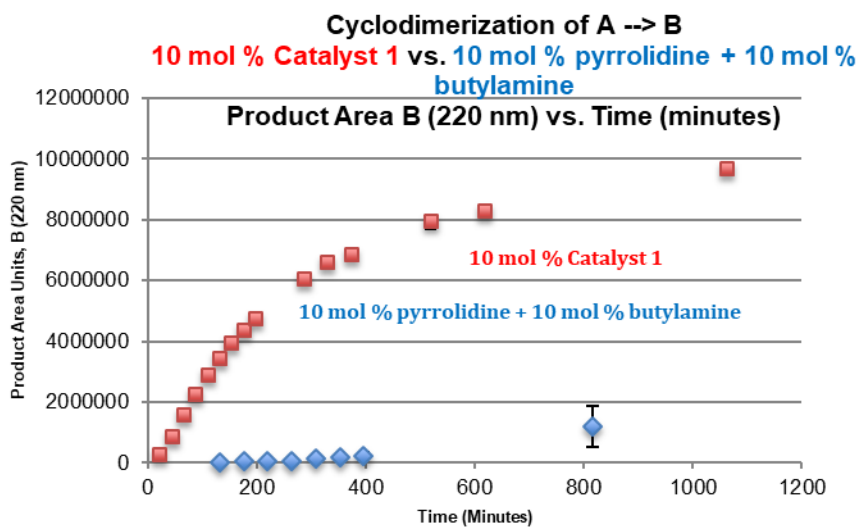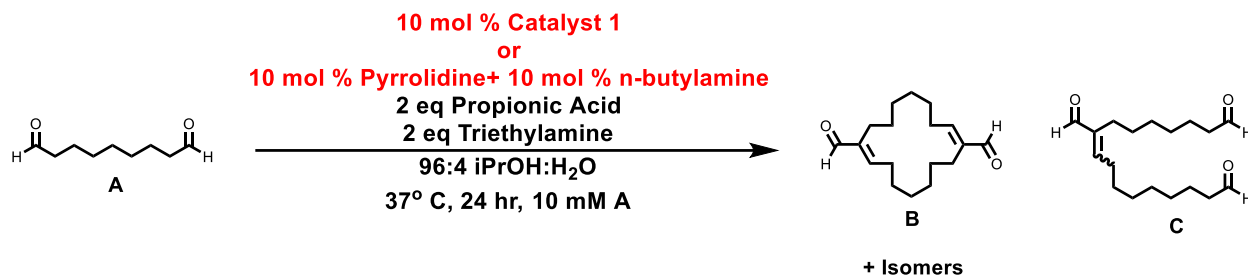
Figure 36. Plot of area units (220 nm) vs. time (minutes) of reaction progress data for the cyclodimerization of **A** → **B** in the presence of either 10 mol % catalyst **1** or 10 mol % pyrrolidine + 10 mol % butylamine. Error bars correspond to the standard deviation over two reactions.
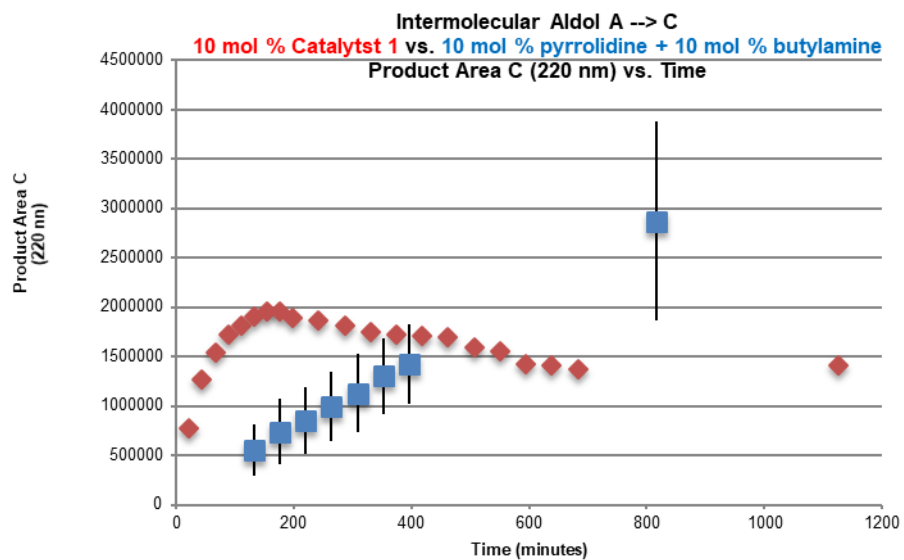
Figure 37. Amount of intermolecular aldol adduct detected as a function of time for reactions of the C9 dialdehyde catalyzed by 10 mol % foldamer **1** or by a mixture of 10 mol % pyrrolidine and 10 mol % butylamine. The vertical scale is the area of the peak in an LC-MS chromatogram that has a mass corresponding to the linear aldol adduct C (possibly a mixture of geometric isomers), based on absorbance at 220 nm. Error bars correspond to the standard deviation over two reactions.
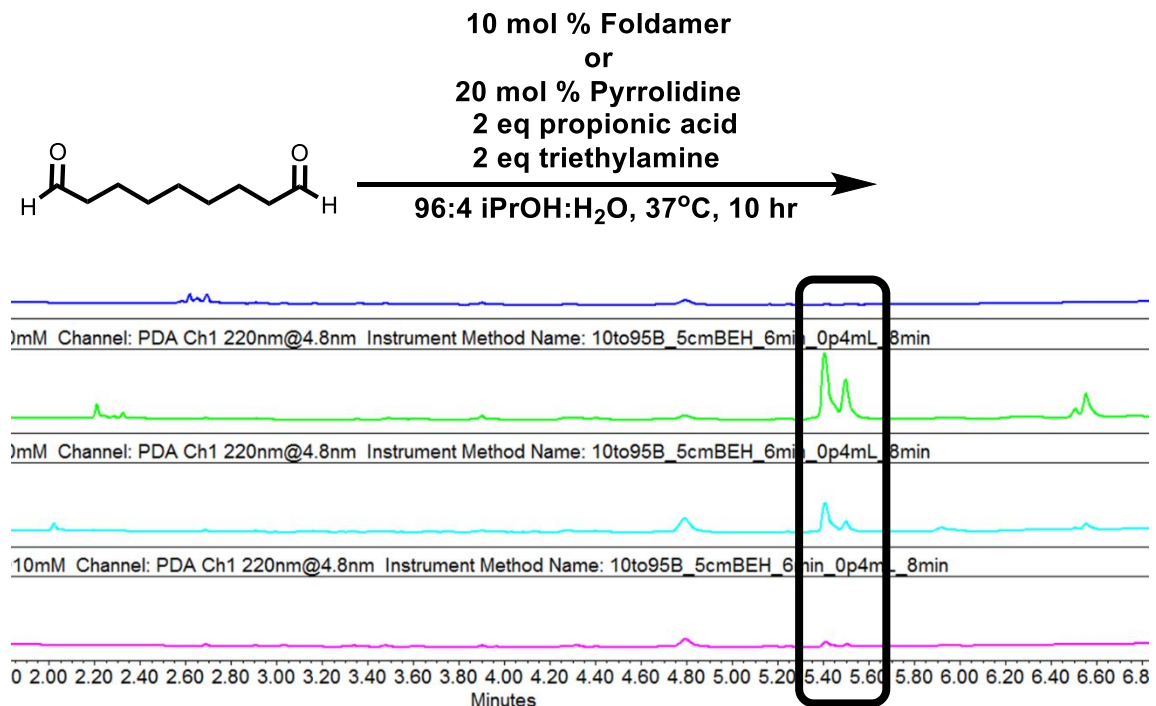
Figure 38. Cyclization of 1,9-nonanedialdehyde in the presence of either 10 mol % foldamer **10** (blue trace), 10 mol % foldamer **1** (green trace), 10 mol % foldamer **9** (cyan trace), or 20 mol % pyrrolidine (pink trace). UPLC traces (220 nm) of the crude reaction mixtures after 10 hours. Product cyclodimers are circles in black.

b. Purification and structure determination of E,E diene B
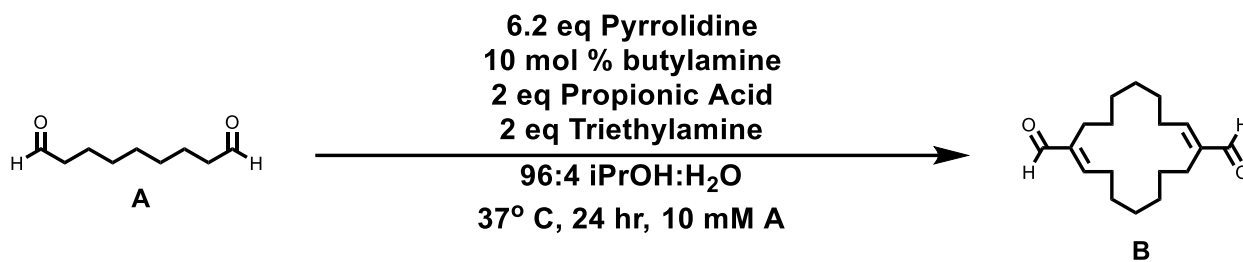
To a 250 mL flask equipped with a stir bar were added 128 mL isopropanol, 5.12 mL H_2O, and 0.2 g **A** (1.28 mmol). Propionic acid (2.56 mmol, 190.98 µL, 2 eq) and triethylamine (2.56 mmol, 356.8 µL, 2 eq) were then added. Added last were pyrrolidine (7.9 mmol, 662.5 µL, 6.2 eq) and butylamine (0.128 mmol, 12.6 µL, 10 mol %). The flask was fitted with a rubber septum and lowered into a preheated oil bath (37°C). The reaction mixture was stirred for 24 hours.

After 24 hours, the volatiles were removed via rotary evaporation to obtain a crude oil. The oil was dissolved in 6 mL of hexafluoroisopropanol. The crude oil was purified via preparative HPLC to obtain < 2 mg of a white solid (< 1.1 % yield). HPLC purification conditions: HPLC solvent A is 0.1 % TFA in filtered and degassed Millipore H_2O, and solvent B is 0.1 % TFA in acetonitrile. An XBridge® Prep C8 5µm 30 X 150 mm column operating at a flow rate of 35 mL/min was used. A linear gradient of 45-75 % B over 45 minutes was employed.

^{1}H NMR (500 MHz, d^2-HFIP): δ 9.28 (s, 1H), 6.88 (t, J = 8.0 Hz, 1H), 2.56 (q, J = 8.0 Hz, 2H), 2.46 (d, J = 6.9 Hz, 2H), 1.69 (dq, J = 10.5, 6.2, 5.7 Hz, 2H), 1.66 – 1.58 (m, 2H), 1.55 (m, 4H).

^{13}C NMR (125 MHz, $(CF_3)_2CDOD$) δ 200.35, 162.15, 143.10, 28.59, 27.79, 27.32, 27.18, 26.75, 22.53. **HRMS** *m/z* (ESI) Calculated for $[C_{18}H_{28}O_2 + Na]^+$ 299.1982, 299.1979 found.
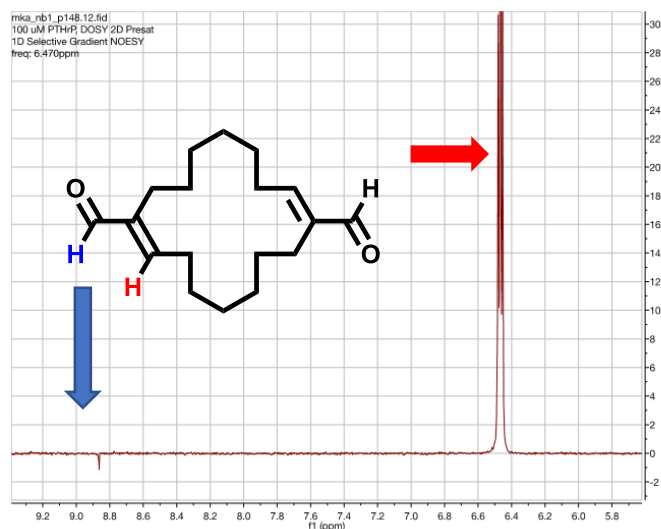
Figure 39. 1 D NOE spectrum of **B**. The alkene hydrogen was irradiated with a d8 time of 0.3 sec. The spectrum was acquired at 500 MHz in d_2-HFIP.
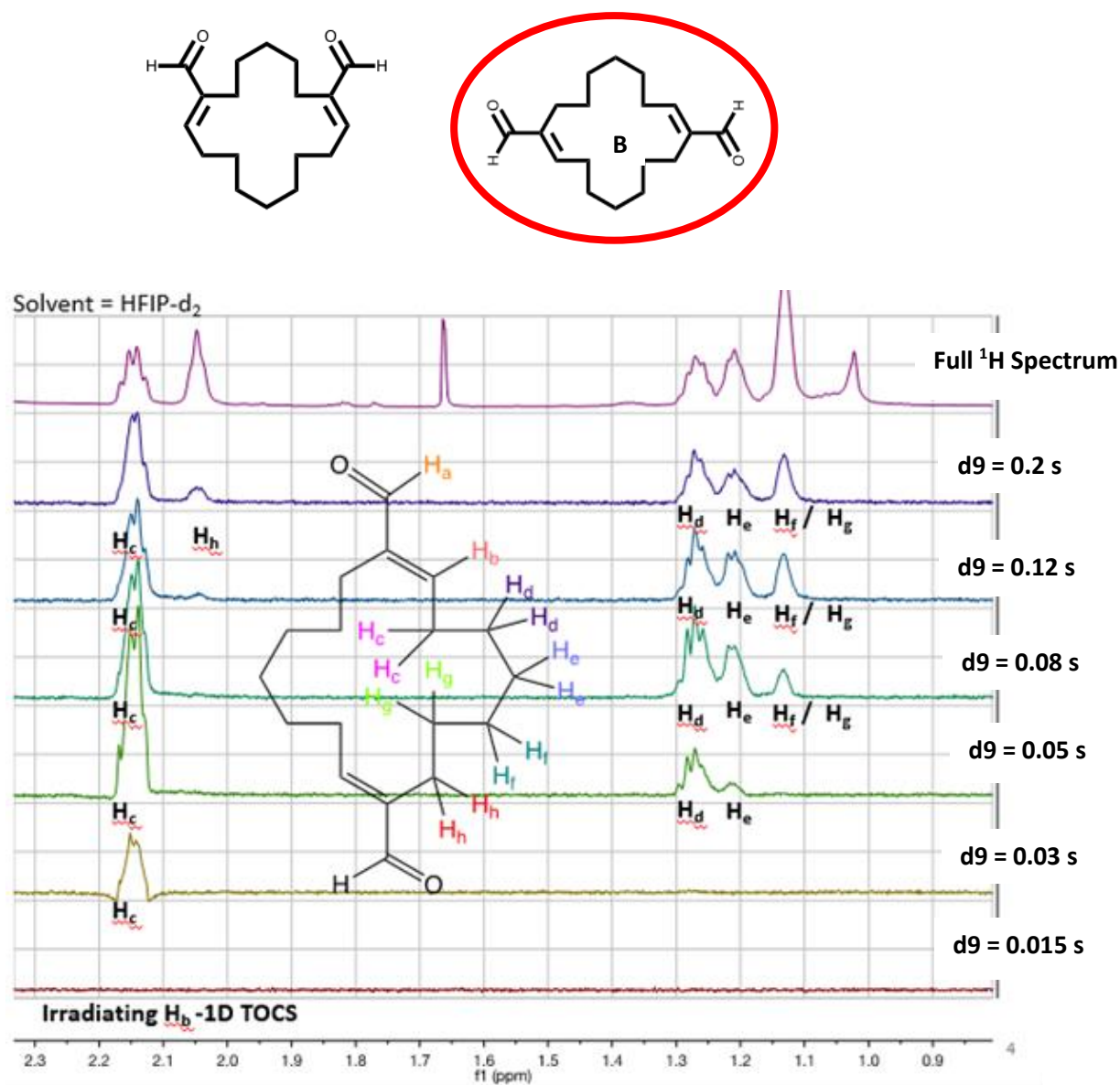
Figure 40. 1D TOCSY spectra acquired with varying mixing times used to differentiate between the two symmetrical cyclodimer structures. When the alkene proton (H_b) is irradiated, six signals should appear as the mixing time is increased to transfer magnetization along the chain for isomer **B**. The mixing time (d9 parameter) was varied from 0.015 to 0.2 sec. At 0.015 sec mixing time, no other signal was observed (bottom trace). The peak assigned to H_c appeared as the mixing time was increased to 0.03 sec. The peaks assigned to H_d and H_e appeared as the mixing time was further increased, suggesting those were the next two methylene protons along the ring. As d9 was increased to 0.05 sec, a signal integrating to 4H appeared; this signal was assigned to overlapping resonances for H_f and H_g. The signal assigned to H_h appeared with the longest mixing time; H_h is the furthest proton from H_b along the array of CH_2 units. These 1D TOCSY data allowed us to differentiate between the two geometric isomers because only four sets of CH_2 protons would be expected upon irradiating the alkene proton of the alternative isomer. The spectra were acquired at 500 MHz in d_2-HFIP.
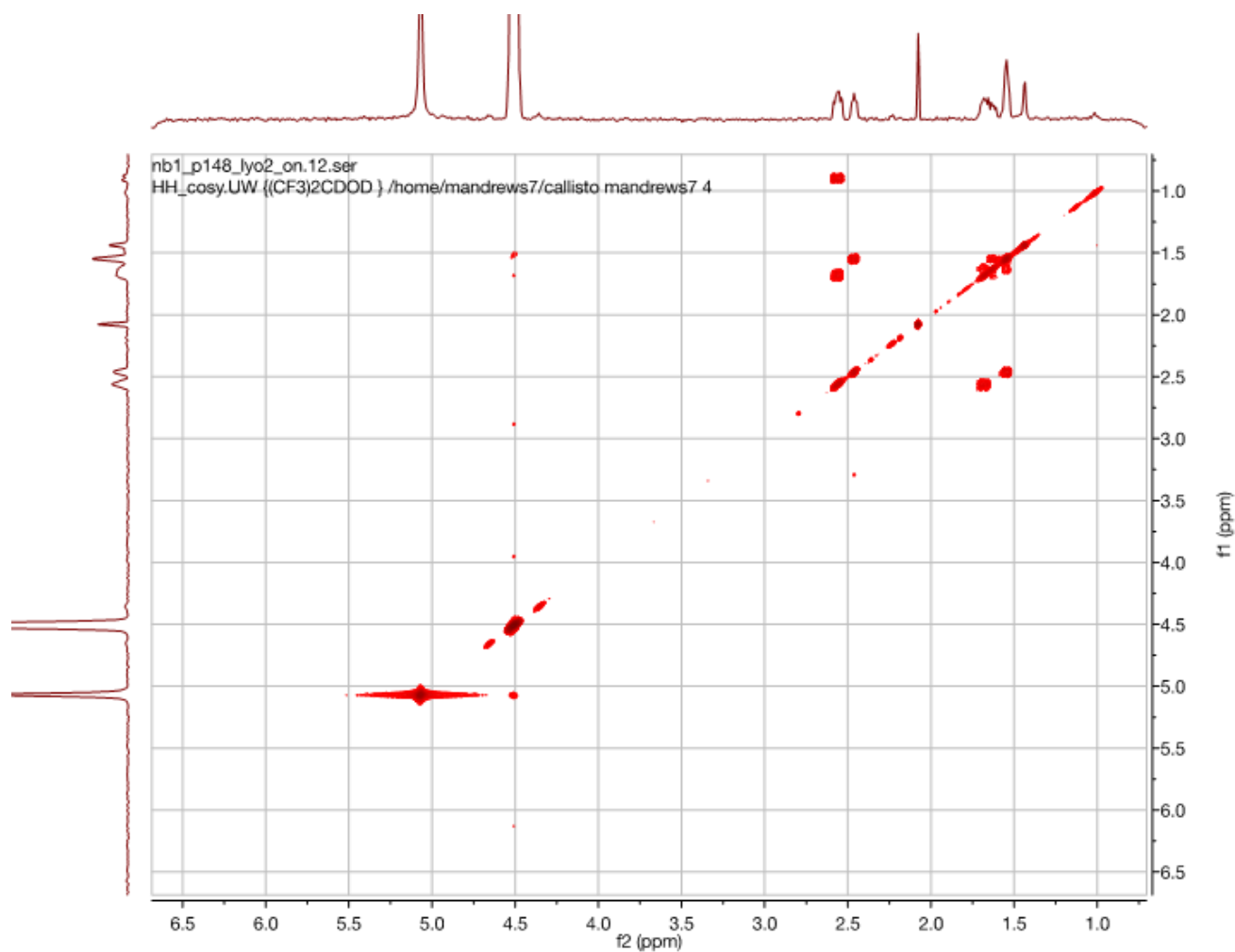
Figure 41. 2D COSY spectrum of **B**. The spectrum was acquired at 500 MHz in d_2-HFIP (4 scans, TD = 1024). The spectrum shows the correlation between the proton peaks in isomer **B**. The signals assigned to overlapping resonances for H_f and H_g, at ~1.55 ppm, show two COSY correlations, one for H_e (~1.75 ppm), the third set of CH_2 protons from the alkene proton, and one for H_h (~2.5 ppm), the CH_2 protons adjacent to the aldehyde. These two correlations are consistent with our assignment of the peak at 1.55 ppm to overlapping resonances from H_f and H_g. Other correlations include the two CH_2 protons closest to the double bond (H_d/H_c) as well as the second closest set of protons to the double bond and the third closest (H_e/H_d). These correlations are consistent with the structure we have assigned to cyclodimer **B.**
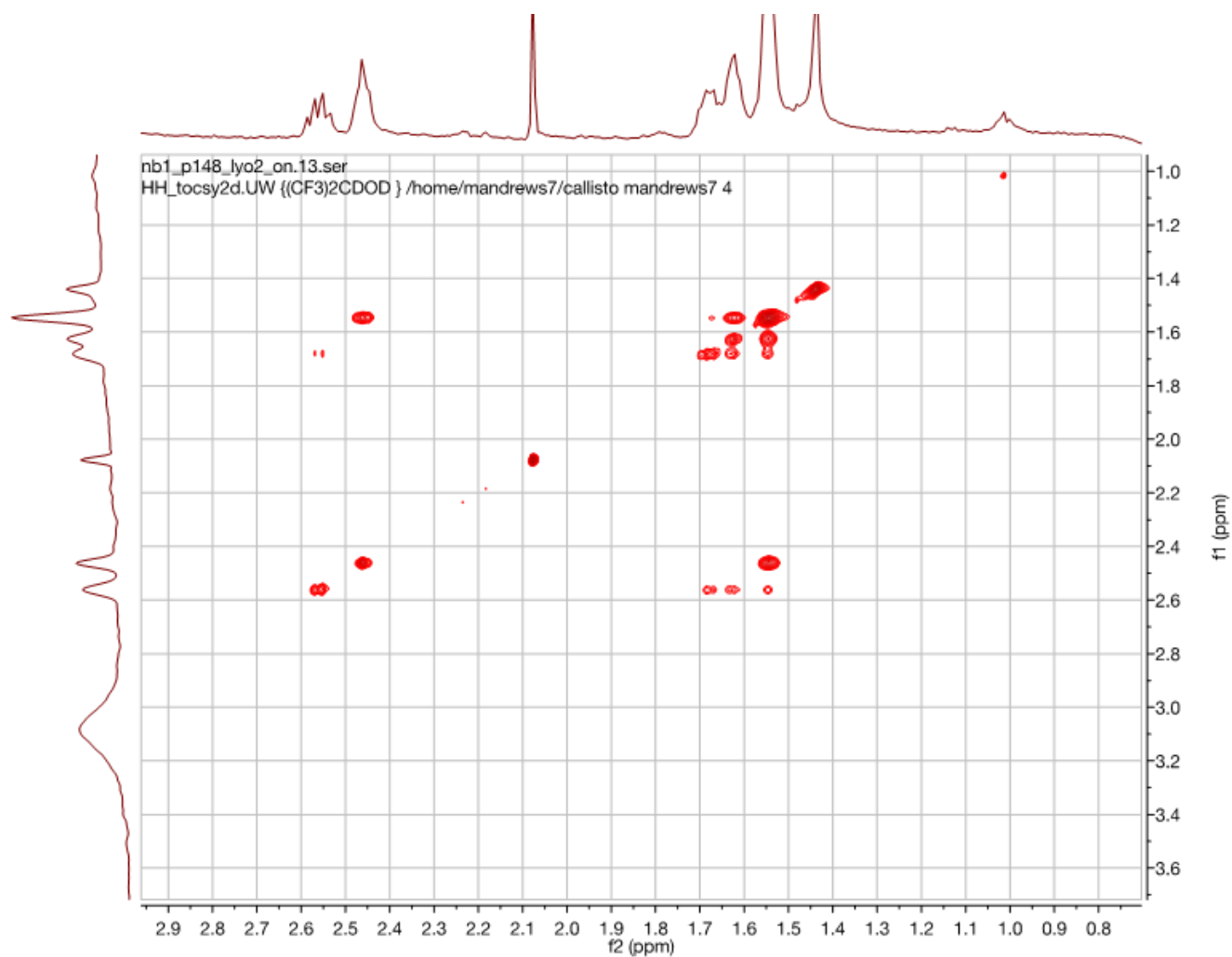
Figure 42. 2D TOCSY spectra of B, showing one spin system. The spectrum was acquired at 500 MHz in d_2-HFIP (4 scans, TD=1024). These data support our assignment of the cyclodimer structure as that labelled **B** above, rather than the alternative shown. For the alternative isomer, two separate spin systems are expected; one involving three non-equivalent CH_2 groups between the two aldehydes, and another for four non-equivalent CH_2 groups between the two double bonds. However, the TOCSY spectrum shows that there are six CH_2 resonances, and that all are encompassed within a single spin system, which argues against the alternative structure but is consistent with structure assignment **B**.

3.5.6 LC-MS Traces of Foldamer Catalyzed Macrocyclizations

a. LC-MS overlays: foldamer vs. small molecule catalyzed macrocyclizations
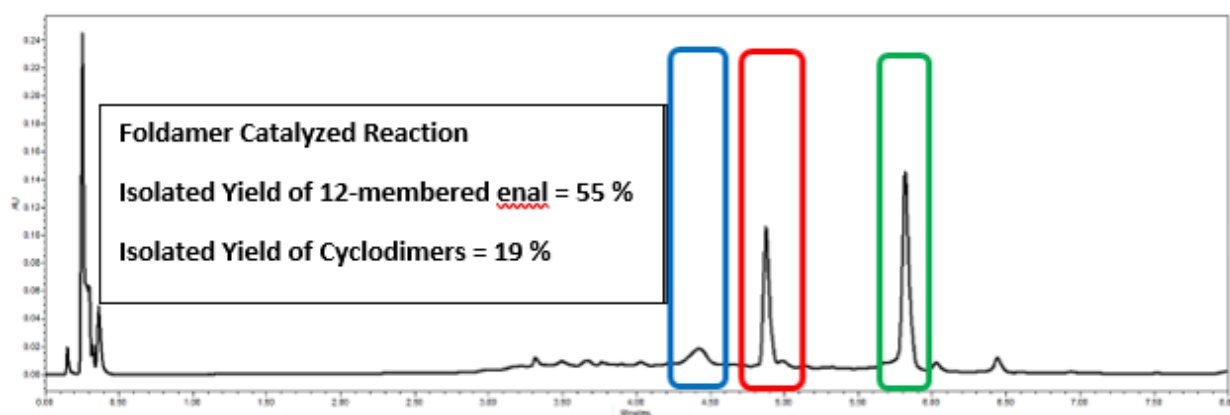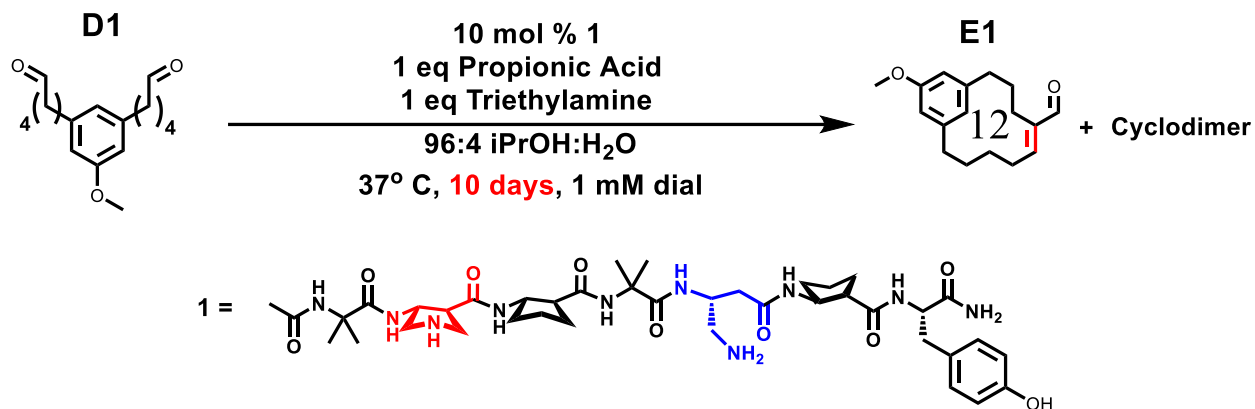
Figure 43. LC-MS chromatogram (275 nm) at ten days reaction time for the macrocyclization reaction starting from dialdehyde **D1** catalyzed by **1**. Isolated yields based on the mass of **E1** and cyclodimer byproducts after column chromatography are reported. Highlighted in blue is remaining dialdehyde starting material **D1**. Highlighted in red is product **E1**. Highlighted in green are cyclodimers, which presumably contain a 24-membered ring.
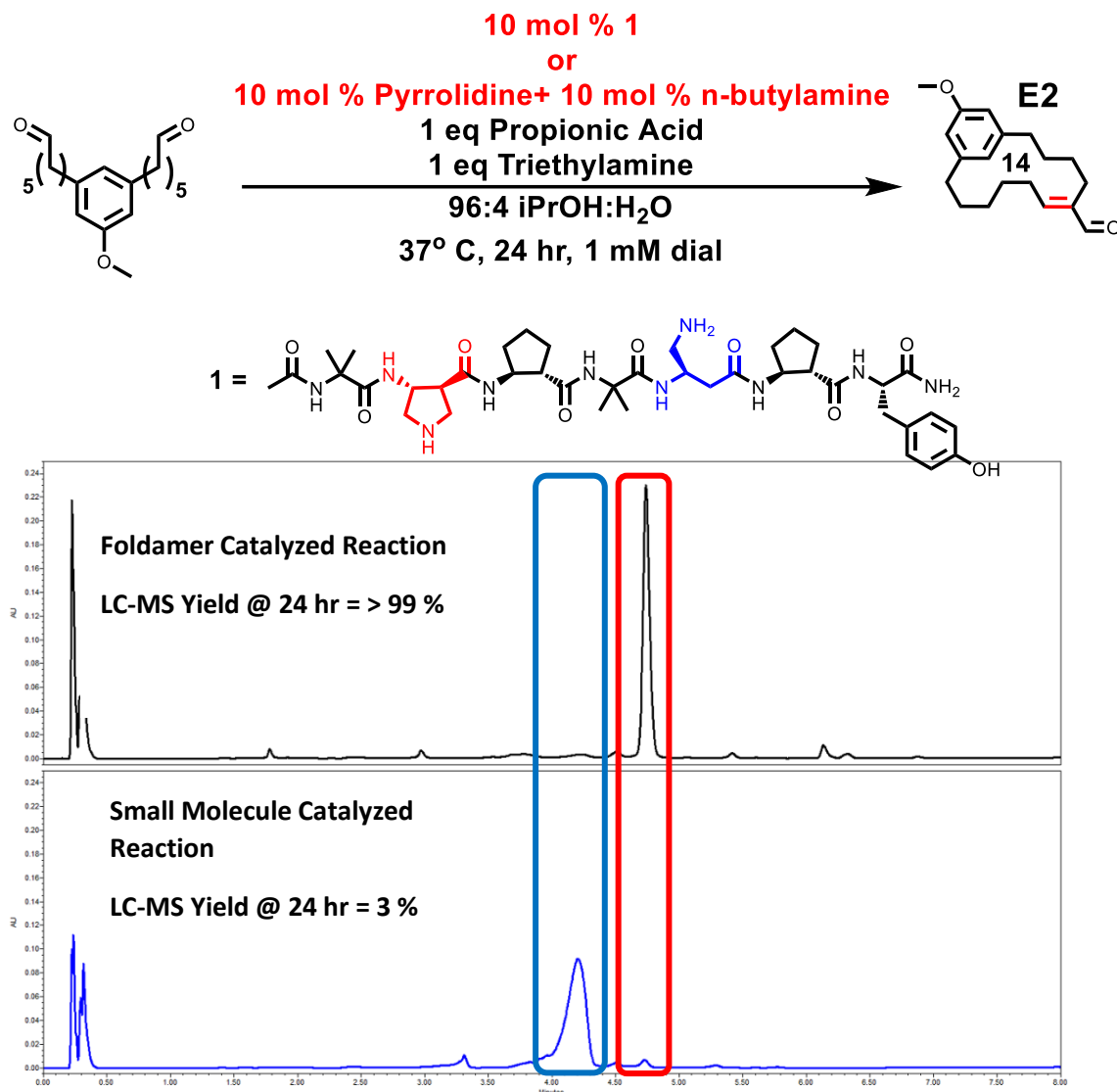
Figure 44. LC-MS chromatograms (275 nm) at 24 hours reaction time for the macrocyclization reaction of dialdehyde **D2** catalyzed by either **1** or pyrrolidine + butylamine. Highlighted in blue is starting material **D2**. Highlighted in red is product **E2**.
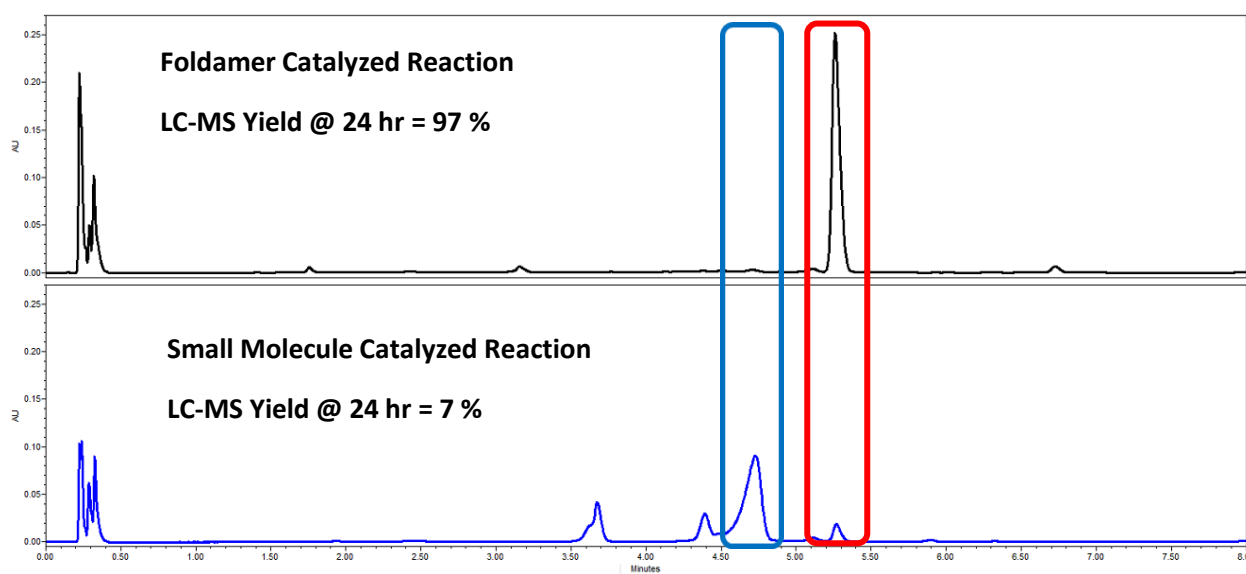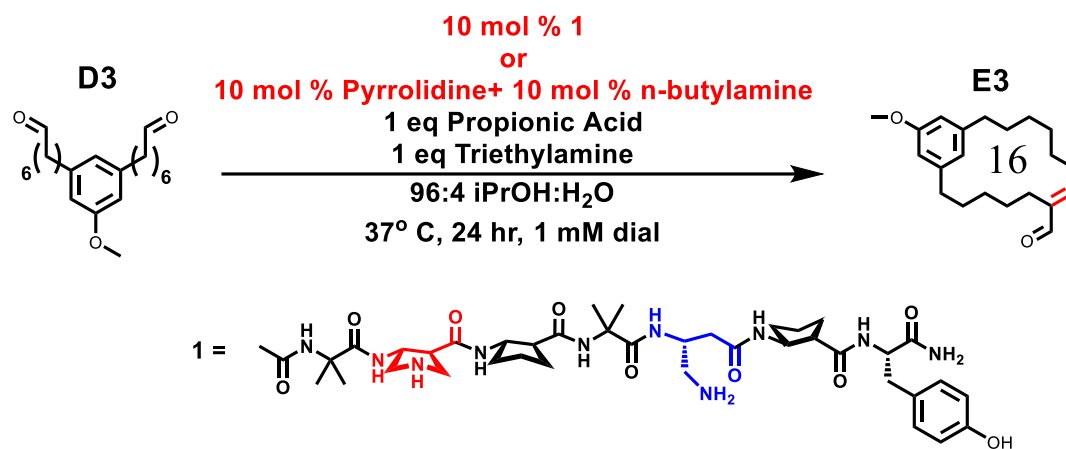
Figure 45. LC-MS chromatograms (275 nm) at 24 hours reaction time for the macrocyclization reaction of dialdehyde **D3** catalyzed by either **1** or pyrrolidine + butylamine. Highlighted in blue is starting material **D3**. Highlighted in red is product **E3**.
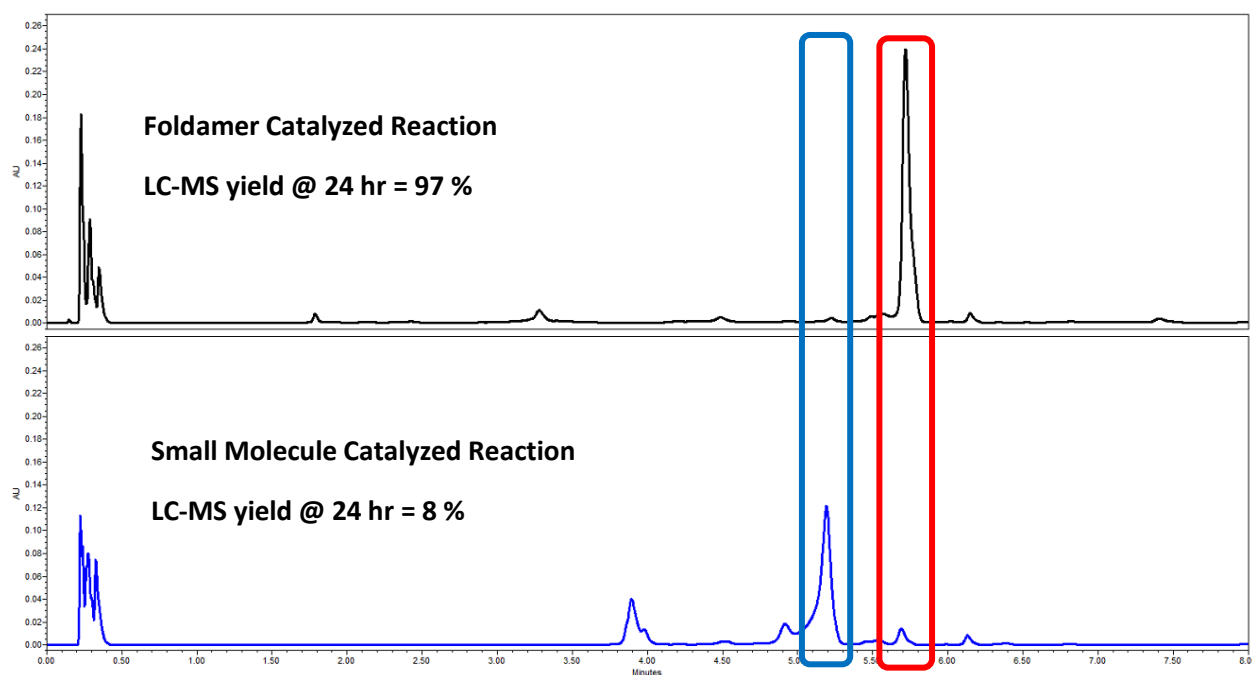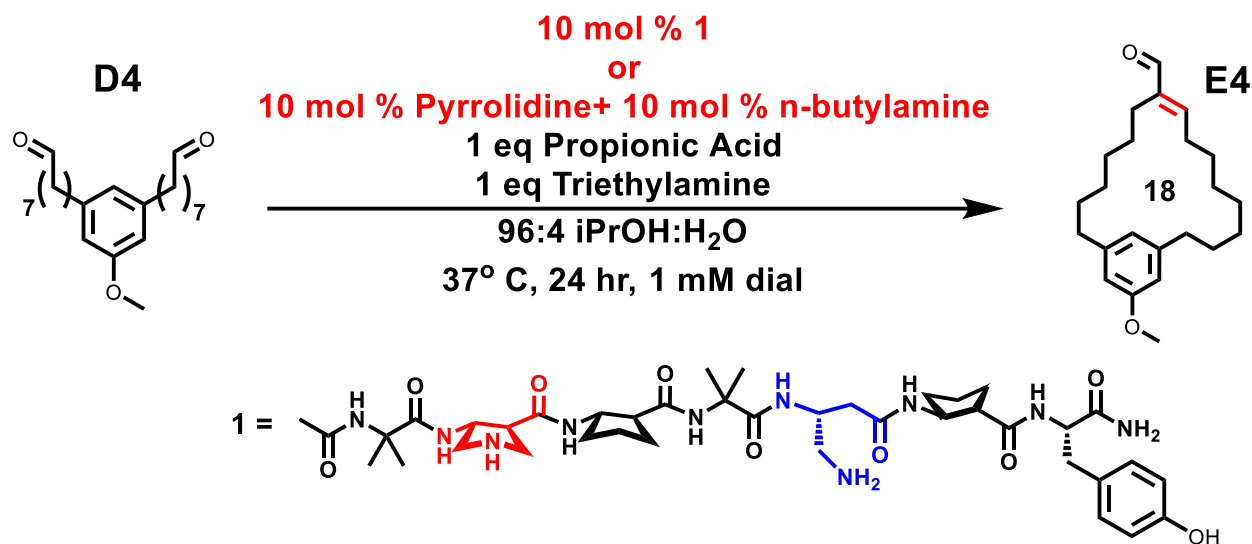
Figure 46. LC-MS chromatograms (275 nm) at 24 hours reaction time for the macrocyclization reaction of dialdehyde **D4** catalyzed by either **1** or pyrrolidine + butylamine. Highlighted in blue is dialdehyde starting material **D4**. Highlighted in red is product **E4**.

b. Foldamer/small molecule catalyzed control reactions: Macrocyclization of D3 to E3
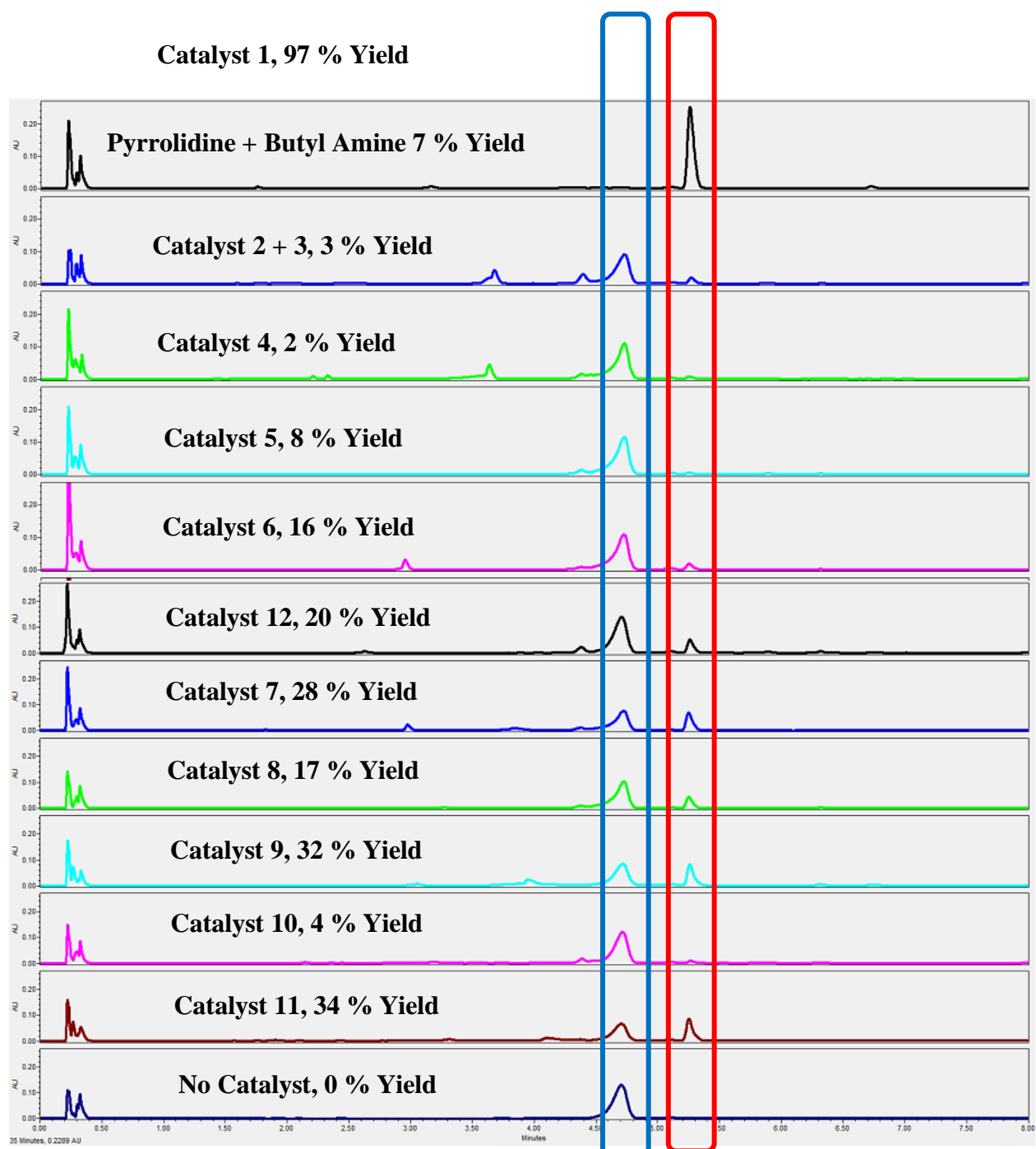
Figure 47. LC-MS chromatograms (275 nm) at 24 hours reaction time for the macrocyclization reaction of **D3** to form **E3**, catalyzed by foldamers **1-12**. Highlighted in blue is starting dialdehyde **D3**. Highlighted in red is macrocyclic product **E3**. Reactions conducted following the general procedure described above. LC-MS yield was determined based on a calibration curve for **E3** (external standard).

c. Order of reaction with respect to catalyst 1
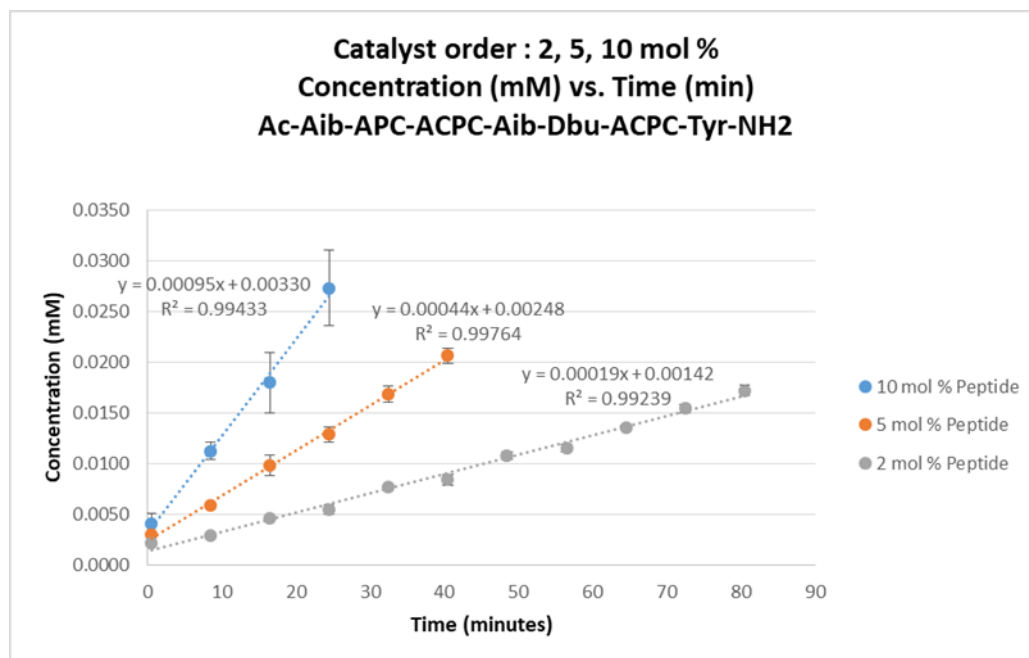
Figure 48. Reaction progress data for the macrocyclization reaction of dialdehyde **D3** to form enal **E3** in the presence of varying mol % of catalyst **1** between 0.5 and 80 minutes after catalyst addition. The mol % loading of **1** was varied between 2 and 10 mol %. Each reaction was monitored to no greater than 2.5 % completion (initial rate regime). Each reaction was run in duplicate, using different stock solutions of catalyst **1** and dialdehyde **D3**. Error bars denote standard deviation for product concentration measurements at a given time point. Reaction conditions are described above.
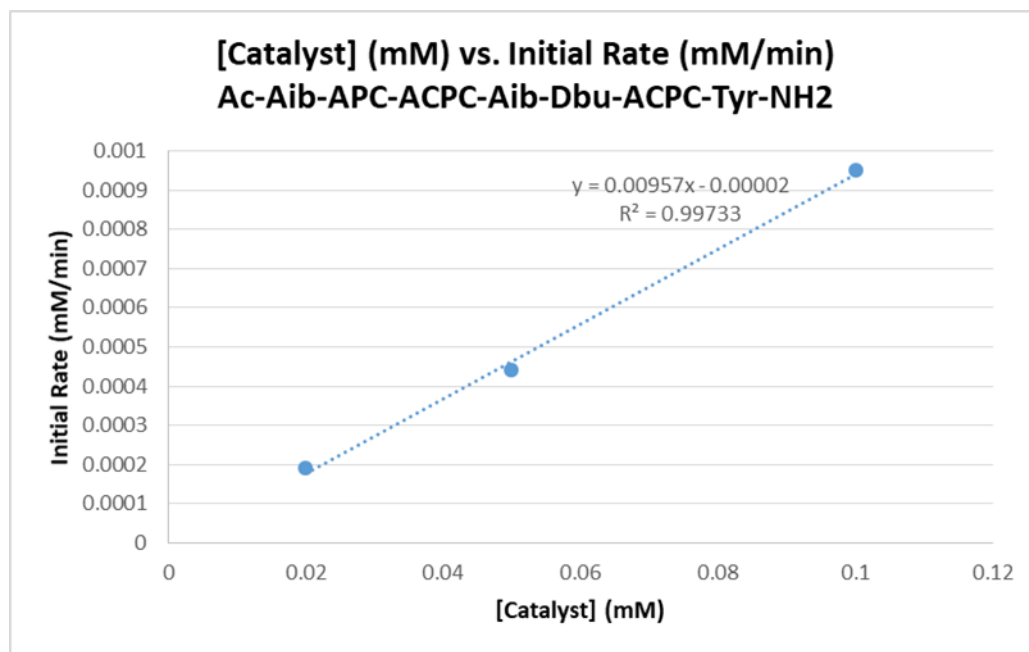
Figure 49. Initial rate (mM/minute) vs. [Catalyst **1**] (mM) for the macrocyclization of **D3** to form **E3**. Initial rate(s) (mM/minute) are from supplementary figure **6**. The linear relationship observed is consistent with the hypothesis that the catalytic reaction is first order in catalyst **1**, i.e., that only one molecule of **1** is involved in the rate-

determining transition state. Each reaction was run in duplicate, with different stock solutions of catalyst **1** and **D3**, and error bars denote standard deviation among product concentration measurement at a given time point. Reaction conditions are described above.

d. LC-MS monitoring of transient reaction intermediates
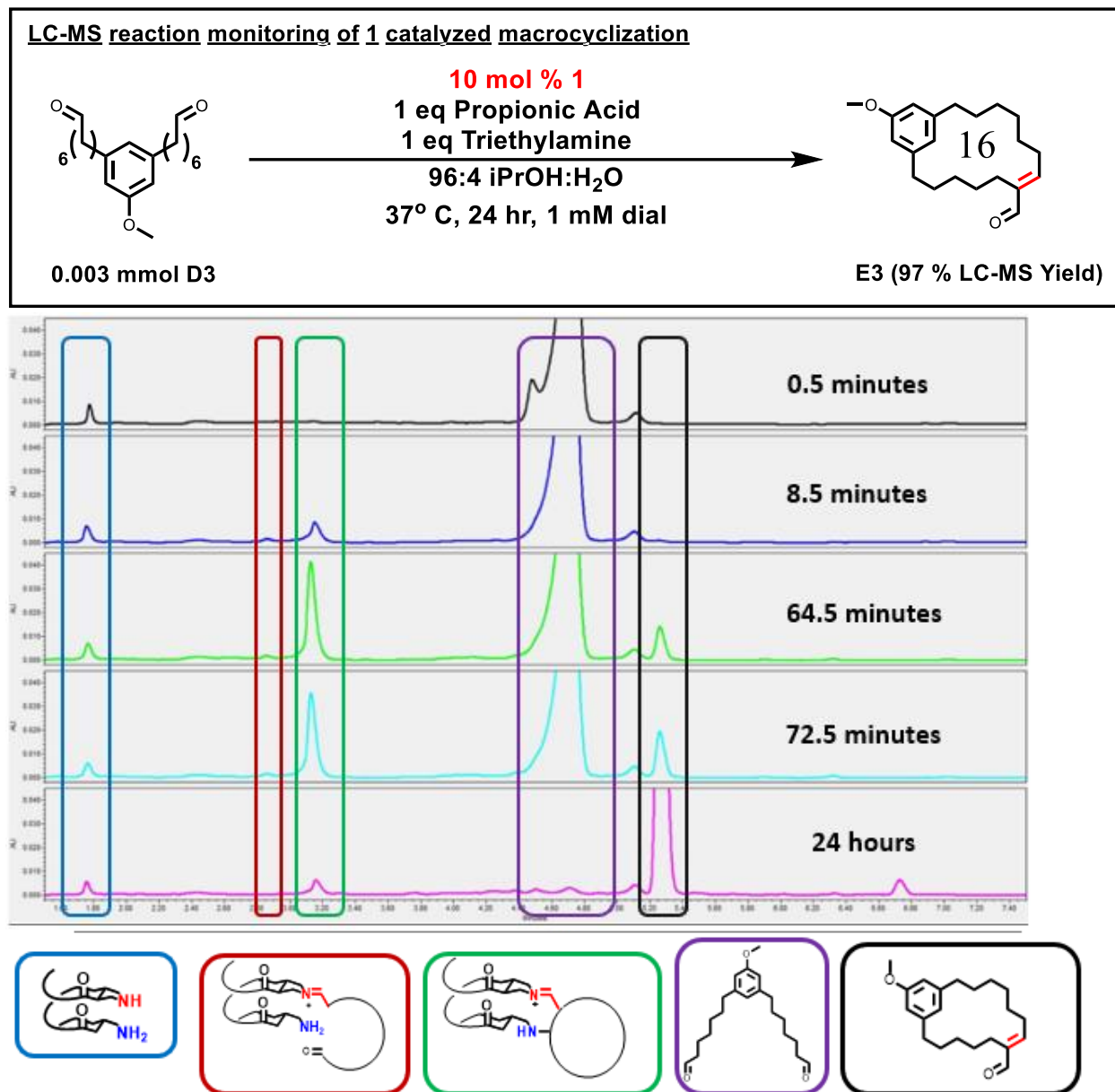
Figure 50. LC-MS chromatograms at 0.5 minute, 8.5 minute, 64.5 minute, 72.5 minute, and 24 hours for the macrocyclization of **D3** → **E3** catalyzed by 10 mol % **1**. The peak highlighted in blue corresponds to catalyst **1**. Highlighted in red is the mono-covalent intermediate shown above (or an isomer), based on the mass spectra. The peak highlighted in green corresponds to the bicyclic intermediate shown above (or an isomer), based on the mass spectra. This potential bicyclic intermediate grows in during the first 64 minutes and then slowly diminishes throughout the remaining 23 hours. The peak highlighted in purple corresponds to **D3**. The peak highlighted in black is **E3**. Each chromatogram has been scaled to the same y-axis value, which causes the product peak in the final trace to be off-scale.

e. Concentration optimization
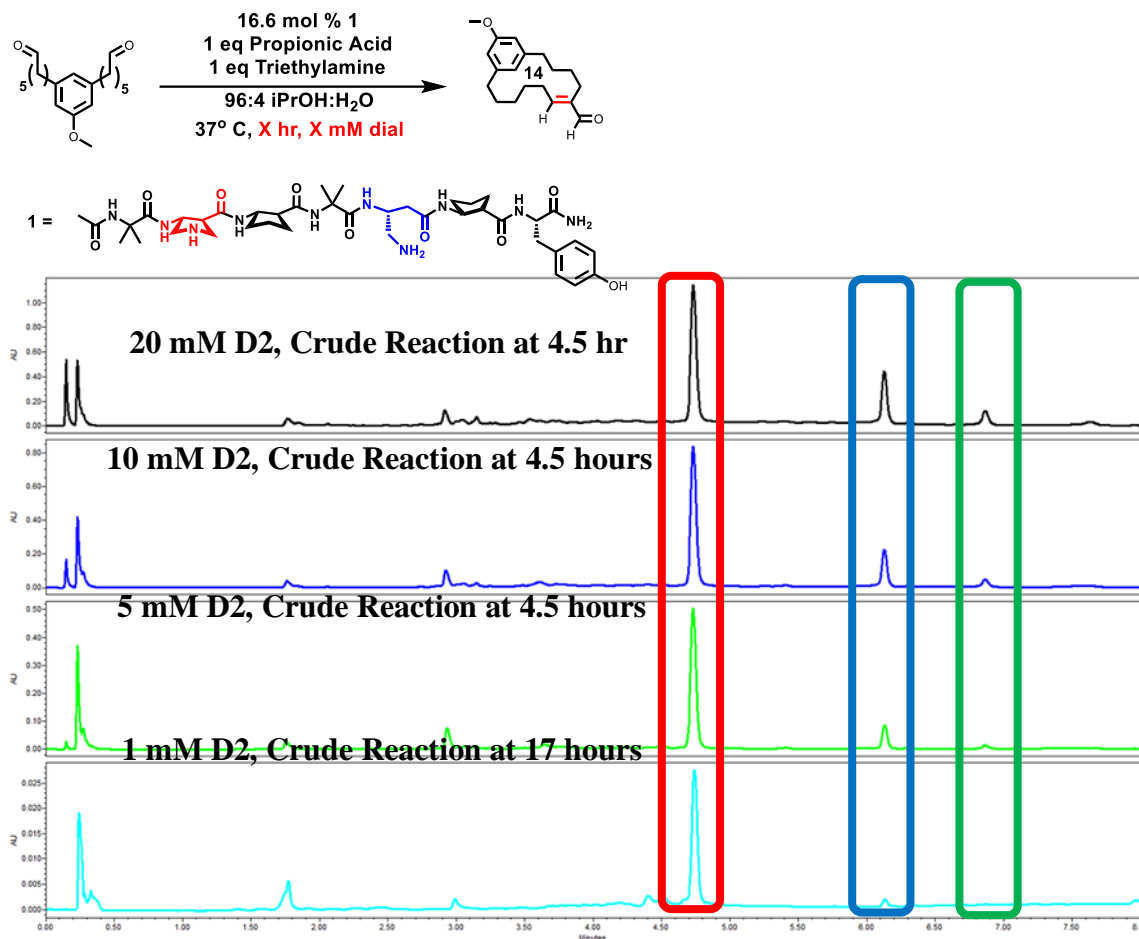
Figure 51. Optimization of dialdehyde concentration **D2** to promote macrocyclization over competing oligomerization. LC-MS chromatograms are shown at the time of reaction completion. Initial dialdehyde concentrations of 20 mM, 10 mM, 5 mM, and 1 mM were tested. Highlighted in red is the product **E2**. Highlighted in blue and green are peaks whose mass spectra correspond to dimeric and trimeric products. At 1 mM **D2**, the formation of dimeric and trimeric byproducts is suppressed.

f. Macrocyclization scale up and lowered catalyst loading
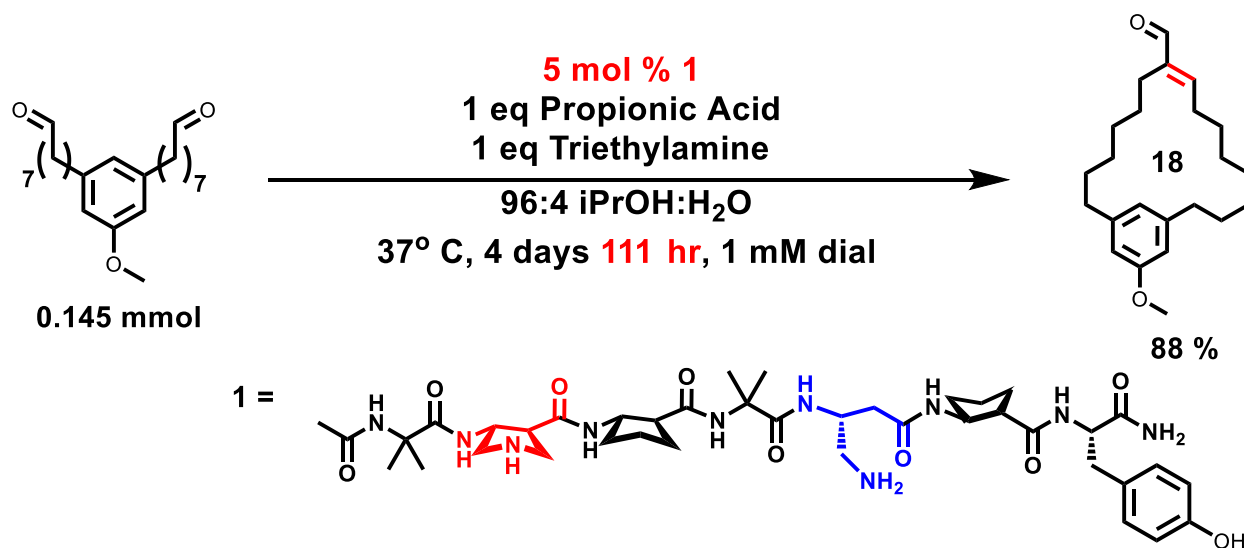
Figure 52. Macrocyclization of **D4** to **E4**, catalyzed by 5 mol % **1**. **E4** was obtained in 88 % isolated yield on 0.145 mmol scale using 5 mol % catalyst **1**. Lowering the catalyst loading of **1** from 10 mol % to 5 mol % required an extended reaction time of 111 hours (4 days 15 hours).

3.5.7 X-ray Crystallography

X-ray crystallography: Structure of tosylhydrazone derivative of E3
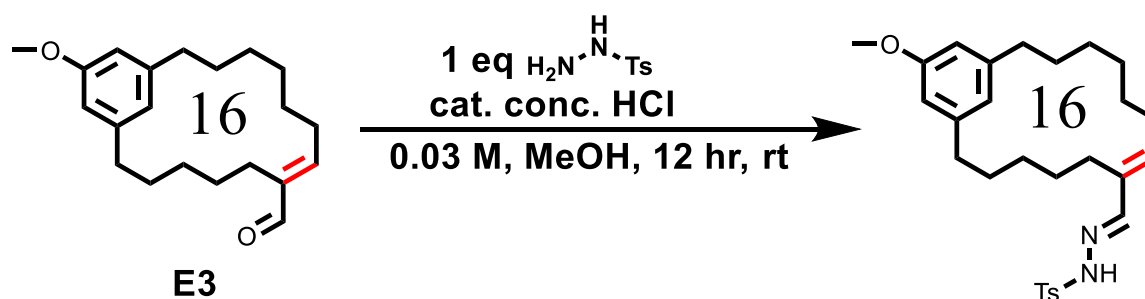
Figure 53. Derivatization of **E3** to a p-tosylhydrazone. The p-tosylhydrazone derivative (white solid) was added to a 10 mL glass vial and dissolved in a minimal amount of boiling diethyl ether and a few drops of methanol. The vial was placed, uncapped, inside a 250 mL glass vial with an inch of diethyl ether inside. The 250 mL vial was capped and allowed to stand at room temperature. Needle-like crystals that were suitable for diffraction grew within 24 hours.

Crystallographic Experimental Section

Data Collection

A colorless crystal with approximate dimensions $0.252 \times 0.11 \times 0.02$ mm^3 was selected under oil under ambient conditions and attached to the tip of a MiTeGen MicroMount©. The crystal was mounted in a stream of cold nitrogen at 100(1) K and centered in the X-ray beam by using a video camera.

The crystal evaluation and data collection were performed on a Bruker Quazar SMART APEXII diffractometer with Mo K$_\alpha$ ($\lambda = 0.71073$ Å) radiation and the diffractometer to crystal distance of 4.96 cm^3.

The initial cell constants were obtained from three series of ω scans at different starting angles. Each series consisted of 12 frames collected at intervals of 0.5° in a 6° range about ω with the exposure time of 10 seconds per frame. The reflections were successfully indexed by an automated indexing routine built in the APEX3 program suite. The final cell constants were calculated from a set of 9067 strong reflections from the actual data collection.

The data were collected by using the full sphere data collection routine to survey the reciprocal space to the extent of a full sphere to a resolution of 0.64 Å. A total of 63635 data were harvested by collecting 5 sets of frames with 0.5° scans in ω and φ with exposure times of 36 sec per frame. These highly redundant datasets were corrected for Lorentz and polarization effects. The absorption correction was based on fitting a function to the empirical transmission surface as sampled by multiple equivalent measurements.[44]

Structure Solution and Refinement

The systematic absences in the diffraction data were uniquely consistent for the space group $P2_1/c$ that yielded chemically reasonable and computationally stable results of refinement.[45-50]

A successful solution by the direct methods provided most non-hydrogen atoms from the E-map. The remaining non-hydrogen atoms were located in an alternating series of least-squares cycles and difference Fourier maps. All non-hydrogen atoms were refined with anisotropic displacement coefficients. All hydrogen atoms except H2(N2) were included in the structure factor calculation at idealized positions and were allowed to ride on the neighboring atoms with relative isotropic displacement coefficients.

The final least-squares refinement of 313 parameters against 9693 data resulted in residuals R (based on F^2 for $I \geq 2\sigma$) and wR (based on F^2 for all data) of 0.0437 and 0.1120, respectively. The final difference Fourier map was featureless.

Summary

Crystal Data for $C_{28}H_{38}N_2O_3S$ (M =482.66 g/mol): monoclinic, space group P2$_1$/c (no. 14), a = 25.166(4) Å, b = 5.3969(8) Å, c = 20.643(3) Å, β = 113.312(4)°, V = 2574.8(6) Å^3, Z = 4, T = 99.99 K, μ(MoKα) = 0.158 mm^{-1},$Dcalc$ = 1.245 g/cm^3, 63635 reflections measured (1.762° ≤ 2Θ ≤ 67.002°), 9693 unique (R_{int} = 0.0636, R$_{sigma}$ = 0.0492) which were used in all calculations. The final R_1 was 0.0437 (I > 2σ(I)) and wR_2 was 0.1120 (all data).
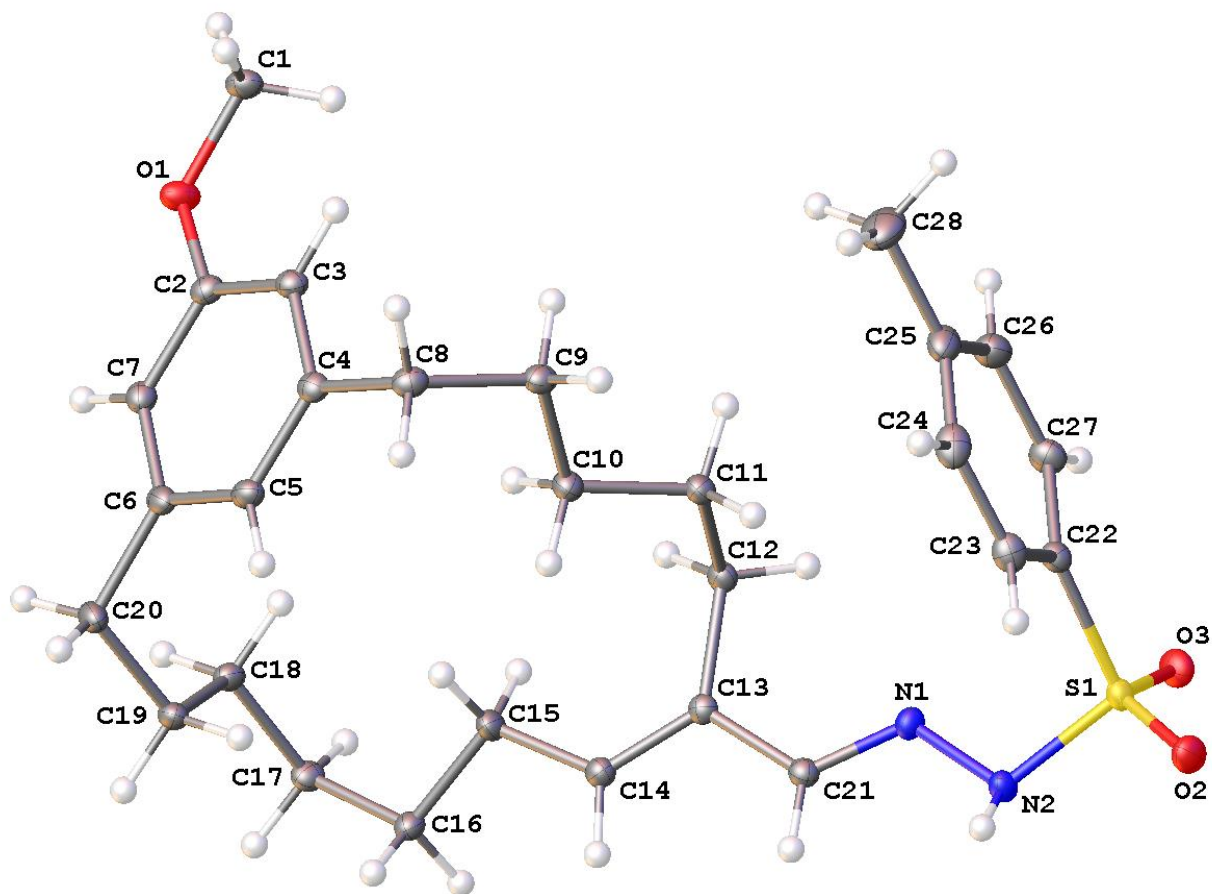
Figure 54. A molecular drawing of tosylhydrazone derivative of **E3** shown with 50% probability ellipsoids.

Figure 55. Crystal data and structure refinement for tosylhydrazone derivative of **E3**.

Identification code	Gellman180
Empirical formula	$C_{28}H_{38}N_2O_3S$
Formula weight	482.66
Temperature/K	99.99
Crystal system	monoclinic
Space group	$P2_1/c$
a/Å	25.166(4)
b/Å	5.3969(8)
c/Å	20.643(3)
$\alpha/°$	90
$\beta/°$	113.312(4)
$\gamma/°$	90
Volume/Å^3	2574.8(6)
Z	4
$\rho_{calc}g/cm^3$	1.245
μ/mm^{-1}	0.158
F(000)	1040.0
Crystal size/mm^3	$0.252 \times 0.11 \times 0.02$
Radiation	MoKα ($\lambda = 0.71073$)
2Θ range for data collection/°	1.762 to 67.002
Index ranges	$-38 \leq h \leq 38, -8 \leq k \leq 8, -31 \leq l \leq 31$
Reflections collected	63635
Independent reflections	9693 [$R_{int} = 0.0636$, $R_{sigma} = 0.0492$]
Data/restraints/parameters	9693/0/313
Goodness-of-fit on F^2	1.024
Final R indexes [I>=2σ (I)]	$R_1 = 0.0437$, $wR_2 = 0.1028$

Final R indexes [all data] $R_1 = 0.0670$, $wR_2 = 0.1120$

Largest diff. peak/hole / e Å^{-3} 0.45/-0.41

Figure 56. Fractional atomic coordinates ($\times 10^4$) and equivalent isotropic displacement parameters (Å$^2 \times 10^3$) for tosylhydrazone derivative of **E3**. U_{eq} is defined as 1/3 of of the trace of the orthogonalised U_{IJ} tensor.

Atom	x	y	z	U(eq)
S1	8967.1(2)	9077.8(5)	933.5(2)	12.58(6)
O1	6030.1(4)	5393.7(16)	4176.2(4)	17.37(17)
O2	9449.1(4)	8195.8(17)	796.6(5)	18.68(17)
O3	8709.1(4)	11425.8(15)	652.6(5)	17.67(17)
N1	8042.7(4)	7146.9(18)	886.5(5)	13.35(18)
N2	8463.4(4)	6924.6(18)	604.3(5)	14.03(18)
C1	6374.3(5)	7214(2)	4659.9(6)	15.9(2)
C2	6305.6(5)	3805(2)	3895.9(6)	13.2(2)
C3	6894.8(5)	3836(2)	4050.2(6)	13.1(2)
C4	7126.8(5)	2134(2)	3718.6(6)	12.94(19)
C5	6760.4(5)	427(2)	3244.1(6)	14.3(2)
C6	6166.7(5)	382(2)	3091.3(6)	13.9(2)
C7	5943.7(5)	2076(2)	3422.6(6)	14.0(2)
C8	7763.7(5)	2255(2)	3862.2(6)	14.5(2)
C9	7921.4(5)	4536(2)	3527.0(6)	14.4(2)
C10	7570.6(5)	4728(2)	2732.7(6)	14.7(2)
C11	7763.3(5)	6855(2)	2387.8(6)	14.0(2)
C12	7330.2(5)	7458.1(19)	1634.3(6)	12.8(2)
C13	7273.3(5)	5400.3(19)	1117.0(6)	11.50(19)
C14	6846.8(5)	3704(2)	909.6(6)	13.1(2)
C15	6343.9(5)	3620(2)	1124.9(6)	15.7(2)
C16	5829.0(5)	2132(2)	622.4(6)	13.9(2)

C17	5294.5(5)	2351(2)	798.6(6)	14.4(2)
C18	5402.0(5)	1738(2)	1564.1(6)	13.4(2)
C19	5670.6(5)	-806(2)	1799.5(6)	14.4(2)
C20	5771.1(5)	-1439(2)	2563.8(6)	17.3(2)
C21	7711.8(5)	5272(2)	818.1(6)	12.39(19)
C22	9131.9(5)	9129(2)	1846.4(6)	12.86(19)
C23	9453.7(5)	7205(2)	2267.0(6)	16.5(2)
C24	9555.0(5)	7179(2)	2979.5(7)	19.5(2)
C25	9345.8(5)	9050(2)	3279.5(6)	19.5(2)
C26	9027.1(5)	10966(2)	2844.6(7)	19.9(2)
C27	8914.6(5)	11007(2)	2132.2(6)	16.7(2)
C28	9460.2(7)	9011(3)	4051.7(7)	30.5(3)

Figure 57. Anisotropic displacement parameters ($\mathring{A}^2 \times 10^3$) for tosylhydrazone derivative of **E3**. The anisotropic displacement factor exponent takes the form: $-2\pi^2[h^2a^{*2}U_{11}+2hka^*b^*U_{12}+\ldots]$.

Atom	U_{11}	U_{22}	U_{33}	U_{23}	U_{13}	U_{12}
S1	11.98(12)	11.70(11)	14.69(13)	-0.46(9)	5.97(10)	-1.50(9)
O1	14.8(4)	19.9(4)	17.0(4)	-5.9(3)	5.9(3)	0.1(3)
O2	15.3(4)	21.0(4)	23.0(4)	-3.3(3)	11.0(3)	-2.1(3)
O3	21.4(4)	13.3(4)	17.5(4)	3.3(3)	6.9(3)	0.1(3)
N1	12.0(4)	15.4(4)	14.0(4)	0.0(3)	6.5(3)	-0.7(3)
N2	13.7(4)	13.6(4)	16.9(5)	-2.8(3)	8.3(4)	-2.7(3)
C1	19.6(5)	14.2(5)	14.2(5)	-2.4(4)	6.8(4)	0.7(4)
C2	15.3(5)	14.2(5)	10.3(5)	0.9(4)	5.2(4)	1.3(4)
C3	14.5(5)	13.6(5)	10.7(5)	-0.6(4)	4.4(4)	-0.3(4)
C4	15.0(5)	12.4(4)	10.6(5)	1.5(4)	4.2(4)	0.5(4)
C5	19.1(5)	11.9(4)	13.3(5)	-0.9(4)	7.8(4)	-0.1(4)
C6	19.3(5)	12.2(4)	10.4(5)	0.3(4)	6.0(4)	-3.1(4)

C7	13.5(5)	16.4(5)	11.4(5)	0.6(4)	4.0(4)	-2.0(4)
C8	14.1(5)	16.0(5)	12.4(5)	-0.2(4)	4.1(4)	2.1(4)
C9	13.4(5)	16.6(5)	12.5(5)	-2.4(4)	4.4(4)	-1.5(4)
C10	15.5(5)	15.2(5)	13.0(5)	-1.4(4)	5.1(4)	-3.3(4)
C11	14.1(5)	14.0(5)	14.0(5)	-2.4(4)	5.7(4)	-3.1(4)
C12	14.3(5)	10.4(4)	14.3(5)	-0.3(4)	6.2(4)	-0.5(4)
C13	12.1(5)	10.9(4)	11.2(5)	1.1(3)	4.3(4)	0.8(3)
C14	14.6(5)	12.2(4)	13.2(5)	-0.5(4)	6.3(4)	-0.9(4)
C15	15.5(5)	17.2(5)	16.2(5)	-4.4(4)	7.9(4)	-6.0(4)
C16	14.7(5)	16.4(5)	11.4(5)	-1.6(4)	5.9(4)	-2.7(4)
C17	12.3(5)	17.3(5)	12.4(5)	-1.9(4)	3.6(4)	-1.3(4)
C18	13.3(5)	15.2(5)	12.6(5)	-2.9(4)	6.2(4)	-1.5(4)
C19	18.0(5)	13.0(5)	13.2(5)	-3.2(4)	7.4(4)	-3.6(4)
C20	23.0(6)	15.6(5)	13.8(5)	-1.9(4)	7.8(4)	-7.6(4)
C21	12.3(5)	12.8(4)	11.5(5)	-0.5(4)	4.0(4)	-0.7(4)
C22	11.4(5)	12.8(4)	13.3(5)	-0.6(4)	3.7(4)	-1.2(4)
C23	13.1(5)	15.1(5)	20.3(6)	2.0(4)	5.5(4)	1.7(4)
C24	13.9(5)	22.4(6)	18.9(6)	6.2(4)	2.8(4)	0.6(4)
C25	17.1(5)	25.0(6)	14.8(5)	-0.8(4)	4.6(4)	-6.8(5)
C26	21.8(6)	19.2(5)	19.8(6)	-4.2(4)	9.5(5)	-2.6(5)
C27	18.2(5)	12.9(5)	18.6(5)	-0.6(4)	6.9(4)	1.6(4)
C28	31.1(7)	43.4(8)	15.3(6)	-0.1(6)	7.5(5)	-7.9(6)

Figure 58. Bond lengths for tosylhdrazone derivative of **E3**.

Atom	Atom	Length/Å	Atom	Atom	Length/Å
S1	O2	1.4315(9)	C10	C11	1.5274(16)
S1	O3	1.4372(9)	C11	C12	1.5400(16)

S1	N2	1.6544(10)		C12	C13	1.5076(15)
S1	C22	1.7621(12)		C13	C14	1.3451(15)
O1	C1	1.4240(14)		C13	C21	1.4637(15)
O1	C2	1.3667(13)		C14	C15	1.4990(16)
N1	N2	1.4009(13)		C15	C16	1.5284(15)
N1	C21	1.2824(14)		C16	C17	1.5307(15)
C2	C3	1.3880(16)		C17	C18	1.5301(16)
C2	C7	1.3969(15)		C18	C19	1.5226(16)
C3	C4	1.4036(15)		C19	C20	1.5342(16)
C4	C5	1.3938(15)		C22	C23	1.3896(15)
C4	C8	1.5119(16)		C22	C27	1.3893(16)
C5	C6	1.3998(16)		C23	C24	1.3899(17)
C6	C7	1.3863(16)		C24	C25	1.3923(19)
C6	C20	1.5114(15)		C25	C26	1.3959(18)
C8	C9	1.5391(16)		C25	C28	1.5035(18)
C9	C10	1.5274(16)		C26	C27	1.3834(17)

Figure 59. Bond angles for tosylhydrazone derivative of **E3**.

Atom	Atom	Atom	Angle/°		Atom	Atom	Atom	Angle/°
O2	S1	O3	119.76(5)		C10	C11	C12	113.66(9)
O2	S1	N2	104.87(5)		C13	C12	C11	112.99(9)
O2	S1	C22	110.92(5)		C14	C13	C12	124.54(10)
O3	S1	N2	107.65(5)		C14	C13	C21	118.24(10)
O3	S1	C22	107.18(5)		C21	C13	C12	117.21(9)
N2	S1	C22	105.55(5)		C13	C14	C15	125.96(10)
C2	O1	C1	117.38(9)		C14	C15	C16	113.79(9)
C21	N1	N2	116.83(9)		C15	C16	C17	112.76(9)

N1	N2	S1	110.57(7)	C18	C17	C16	114.58(9)
O1	C2	C3	124.76(10)	C19	C18	C17	113.53(9)
O1	C2	C7	114.57(10)	C18	C19	C20	113.62(9)
C3	C2	C7	120.67(10)	C6	C20	C19	112.93(9)
C2	C3	C4	119.54(10)	N1	C21	C13	118.77(10)
C3	C4	C8	119.30(10)	C23	C22	S1	119.27(9)
C5	C4	C3	119.21(10)	C27	C22	S1	119.98(9)
C5	C4	C8	121.45(10)	C27	C22	C23	120.66(11)
C4	C5	C6	121.35(10)	C22	C23	C24	119.08(11)
C5	C6	C20	120.91(10)	C23	C24	C25	121.35(11)
C7	C6	C5	118.79(10)	C24	C25	C26	118.24(11)
C7	C6	C20	120.29(11)	C24	C25	C28	120.91(12)
C6	C7	C2	120.44(11)	C26	C25	C28	120.85(12)
C4	C8	C9	112.87(9)	C27	C26	C25	121.29(11)
C10	C9	C8	113.23(9)	C26	C27	C22	119.36(11)
C9	C10	C11	113.33(9)				

Figure 60. Hydrogen bonds for tosylhydrazone derivative of **E3**.

D	H	A	d(D-H)/Å	d(H-A)/Å	d(D-A)/Å	D-H-A/°
N2	H2	O3[1]	0.866(16)	2.190(16)	3.0250(14)	161.6(14)

[1]+X,-1+Y,+Z

Figure 61. Torsion angles for tosylhydrazone derivative of **E3**.

A	B	C	D	Angle/°	A	B	C	D	Angle/°
S1	C22	C23	C24	-176.39(9)	C8	C4	C5	C6	-177.47(10)
S1	C22	C27	C26	177.27(9)	C8	C9	C10	C11	-174.80(9)
O1	C2	C3	C4	-178.88(10)	C9	C10	C11	C12	-166.29(9)
O1	C2	C7	C6	178.92(10)	C10	C11	C12	C13	-66.29(13)

O2	S1	N2	N1	161.72(8)
O2	S1	C22	C23	-39.42(11)
O2	S1	C22	C27	144.02(9)
O3	S1	N2	N1	-69.71(9)
O3	S1	C22	C23	-171.82(9)
O3	S1	C22	C27	11.62(11)
N2	S1	C22	C23	73.64(10)
N2	S1	C22	C27	-102.93(10)
N2	N1	C21	C13	178.80(9)
C1	O1	C2	C3	0.20(16)
C1	O1	C2	C7	-179.64(10)
C2	C3	C4	C5	-0.55(16)
C2	C3	C4	C8	177.09(10)
C3	C2	C7	C6	-0.92(17)
C3	C4	C5	C6	0.12(16)
C3	C4	C8	C9	-70.85(13)
C4	C5	C6	C7	-0.08(16)
C4	C5	C6	C20	178.64(10)
C4	C8	C9	C10	-55.61(13)
C5	C4	C8	C9	106.74(12)
C5	C6	C7	C2	0.48(16)
C5	C6	C20	C19	-71.91(14)
C7	C2	C3	C4	0.95(16)
C7	C6	C20	C19	106.79(12)
C11	C12	C13	C14	98.56(13)
C11	C12	C13	C21	-82.05(12)
C12	C13	C14	C15	2.97(18)
C12	C13	C21	N1	-14.44(15)
C13	C14	C15	C16	159.13(11)
C14	C13	C21	N1	164.99(10)
C14	C15	C16	C17	-172.54(10)
C15	C16	C17	C18	-53.04(13)
C16	C17	C18	C19	-54.79(13)
C17	C18	C19	C20	-179.21(9)
C18	C19	C20	C6	-59.37(13)
C20	C6	C7	C2	-178.25(10)
C21	N1	N2	S1	-163.13(8)
C21	C13	C14	C15	-176.42(10)
C22	S1	N2	N1	44.51(9)
C22	C23	C24	C25	-0.65(18)
C23	C22	C27	C26	0.75(17)
C23	C24	C25	C26	0.25(18)
C23	C24	C25	C28	-179.71(12)
C24	C25	C26	C27	0.67(18)
C25	C26	C27	C22	-1.17(18)
C27	C22	C23	C24	0.15(17)
C28	C25	C26	C27	-179.37(12)

Figure 62. Hydrogen atom coordinates ($Å×10^4$) and isotropic displacement parameters ($Å^2×10^3$) for tosylhydrazone derivative of **E3**.

Atom	x	y	z	U(eq)

H2	8608(6)	5460(30)	615(8)	19(4)
H1A	6572.33	8232.91	4431.04	24
H1B	6661.74	6392.32	5073.7	24
H1C	6125.72	8269.31	4807.93	24
H3	7139.29	5001.28	4378.03	16
H5	6916.76	-728.5	3019.82	17
H7	5542.13	2059.69	3327.07	17
H8A	7873.78	737.21	3675.86	17
H8B	7990.12	2294.54	4378.4	17
H9A	7857.17	6050.32	3757.11	17
H9B	8337.87	4461.34	3617.56	17
H10A	7157.49	4959.11	2644.88	18
H10B	7605.73	3150.85	2507.91	18
H11A	8140.65	6423.34	2373.1	17
H11B	7820.73	8355.42	2683.89	17
H12A	6946.06	7787.27	1643.02	15
H12B	7456.92	8985.59	1470.95	15
H14	6866.18	2444.52	598.13	16
H15A	6215.44	5335.45	1152.83	19
H15B	6473.75	2884.5	1602.17	19
H16A	5940.93	365.96	642.84	17
H16B	5729.93	2721.84	134.21	17
H17A	5143.84	4064.17	695.95	17
H17B	4991.16	1225.74	484.48	17
H18A	5661.27	3011.22	1876.04	16
H18B	5029.57	1818.06	1620.5	16
H19A	6045.53	-877.74	1749.25	17

H19B 5413.95	-2077.11	1483.24	17
H20A 5393.75	-1467.79	2608.54	21
H20B 5941.29	-3118.45	2676.53	21
H21 7750.66	3825.74	578.03	15
H23 9602.47	5925.27	2070.25	20
H24 9771.39	5858.2	3267.73	23
H26 8884.58	12267.17	3041.61	24
H27 8690.97	12307.41	1841.17	20
H28A 9663.52	7478.32	4264.03	46
H28B 9092.11	9088.53	4108.79	46
H28C 9699.66	10439.52	4285.42	46

X-ray Crystallography: tosylhydrazone derivative of the G2
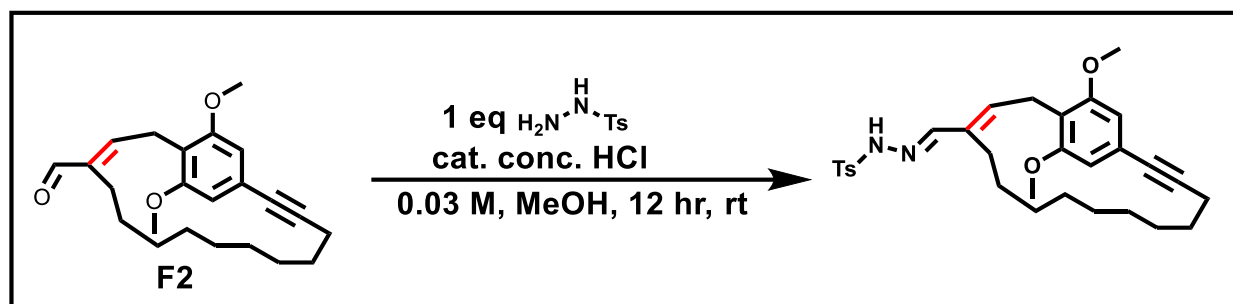
F2 (15 mg, 0.0000423 mol) was put in a 10 mL glass vial, and 0.9 mL methanol was added to produce a slurry. 1 eq p-toluenesulfonyl hydrazide (0.0000453 mol, 8.4 mg) was added, along with 15 µL of concentrated hydrochloric acid. Within 1 hour the slurry became a clear solution. The reaction mixture was stirred overnight at room temperature, at which time a white solid precipitated out of solution. The white solid was filtered, added to a 10 mL glass vial, and dissolved in minimal boiling diethyl ether. A few drops of methanol were then added. The vial was placed, uncapped, in a 250 mL glass vial with about one inch of diethyl ether in the 250 mL vial. The 250 mL glass vial was capped, and allowed to sit at room temperature. After two days, cubic crystals had appeared, which were suitable for diffraction.

Crystallographic Experimental Section

Data Collection

A colorless crystal with approximate dimensions $0.201 \times 0.121 \times 0.057$ mm^3 was selected under oil under ambient conditions and attached to the tip of a MiTeGen MicroMount©. The crystal was mounted in a stream of cold nitrogen at 100(1) K and centered in the X-ray beam by using a video camera.

The crystal evaluation and data collection were performed on a Bruker Quazar SMART APEXII diffractometer with Mo K$_\alpha$ ($\lambda = 0.71073$ Å) radiation and the diffractometer to crystal distance of 4.96 cm.[43]

The initial cell constants were obtained from three series of ω scans at different starting angles. Each series consisted of 12 frames collected at intervals of 0.5° in a 6° range about ω with the exposure time of 10 seconds per frame. The reflections were successfully indexed by an automated indexing routine built in the APEX3 program suite. The final cell constants were calculated from a set of 9868 strong reflections from the actual data collection.

The data were collected by using the full sphere data collection routine to survey the reciprocal space to the extent of a full sphere to a resolution of 0.70 Å. A total of 39986 data were harvested by collecting 6 sets of frames with 0.5° scans in ω and φ with exposure times of 20 sec per frame. These highly redundant datasets were corrected for Lorentz and polarization effects. The absorption correction was based on fitting a function to the empirical transmission surface as sampled by multiple equivalent measurements.[44]

Structure Solution and Refinement

The systematic absences in the diffraction data were consistent for the space groups $P\bar{1}$ and $P1$. The E-statistics strongly suggested the centrosymmetric space group $P\bar{1}$ that yielded chemically reasonable and computationally stable results of refinement.[45-50]

A successful solution by the direct methods provided most non-hydrogen atoms from the E-map. The remaining non-hydrogen atoms were located in an alternating series of least-squares cycles and difference Fourier maps. All non-hydrogen atoms were refined with anisotropic displacement coefficients. All hydrogen atoms except H1(N1) were included in the structure

factor calculation at idealized positions and were allowed to ride on the neighboring atoms with relative isotropic displacement coefficients.

Atoms C23–C29 are equally disordered over two positions. The disorder was refined with restraints and constraints.

The final least-squares refinement of 392 parameters against 8366 data resulted in residuals R (based on F^2 for $I \geq 2\sigma$) and wR (based on F^2 for all data) of 0.0400 and 0.1103, respectively. The final difference Fourier map was featureless.

Crystal Data for $C_{30}H_{38}N_2O_4S$ (M =522.68 g/mol): triclinic, space group P$\bar{1}$ (no. 2), $a =$ 9.065(3) Å, $b = 9.191(2)$ Å, $c = 16.946(4)$ Å, $\alpha = 93.668(12)°$, $\beta = 93.821(9)°$, $\gamma =$ 102.162(11)°, $V = 1372.8(6)$ Å^3, $Z = 2$, $T = 100.0$ K, $\mu(\text{MoK}\alpha) = 0.156$ mm^{-1}, $Dcalc =$ 1.264 g/cm^3, 39986 reflections measured ($2.416° \leq 2\Theta \leq 61.162°$), 8366 unique ($R_{int} = 0.0323$, $R_{sigma}= 0.0256$) which were used in all calculations. The final R_1 was 0.0400 (I > 2σ(I)) and wR_2 was 0.1103 (all data).
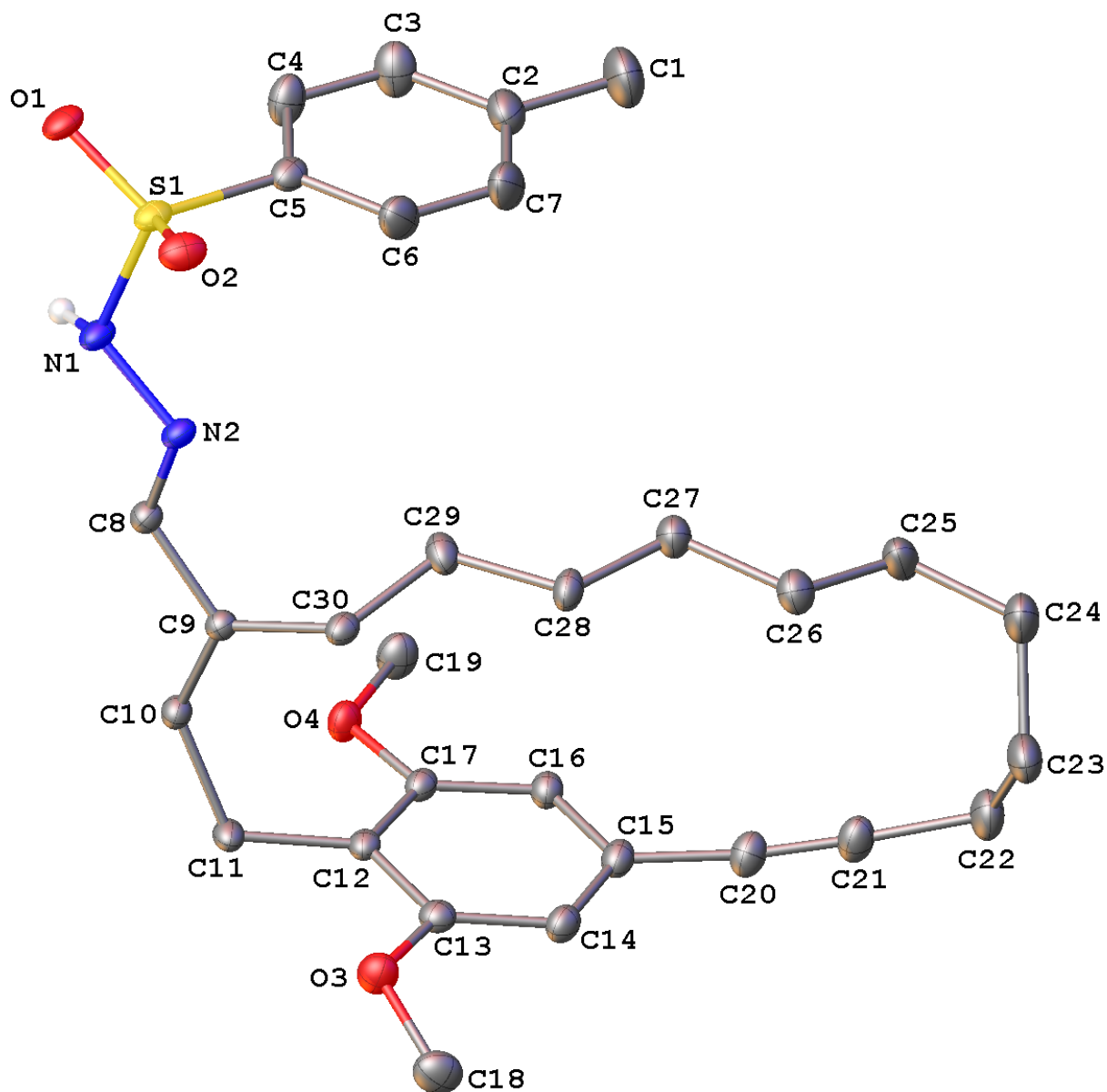
Figure 63. A molecular drawing of tosylhydrazone derivative of **F2** shown with 50% probability ellipsoids. All H atoms attached to C atoms and one disorder component (atoms C23a–C29a) are omitted.
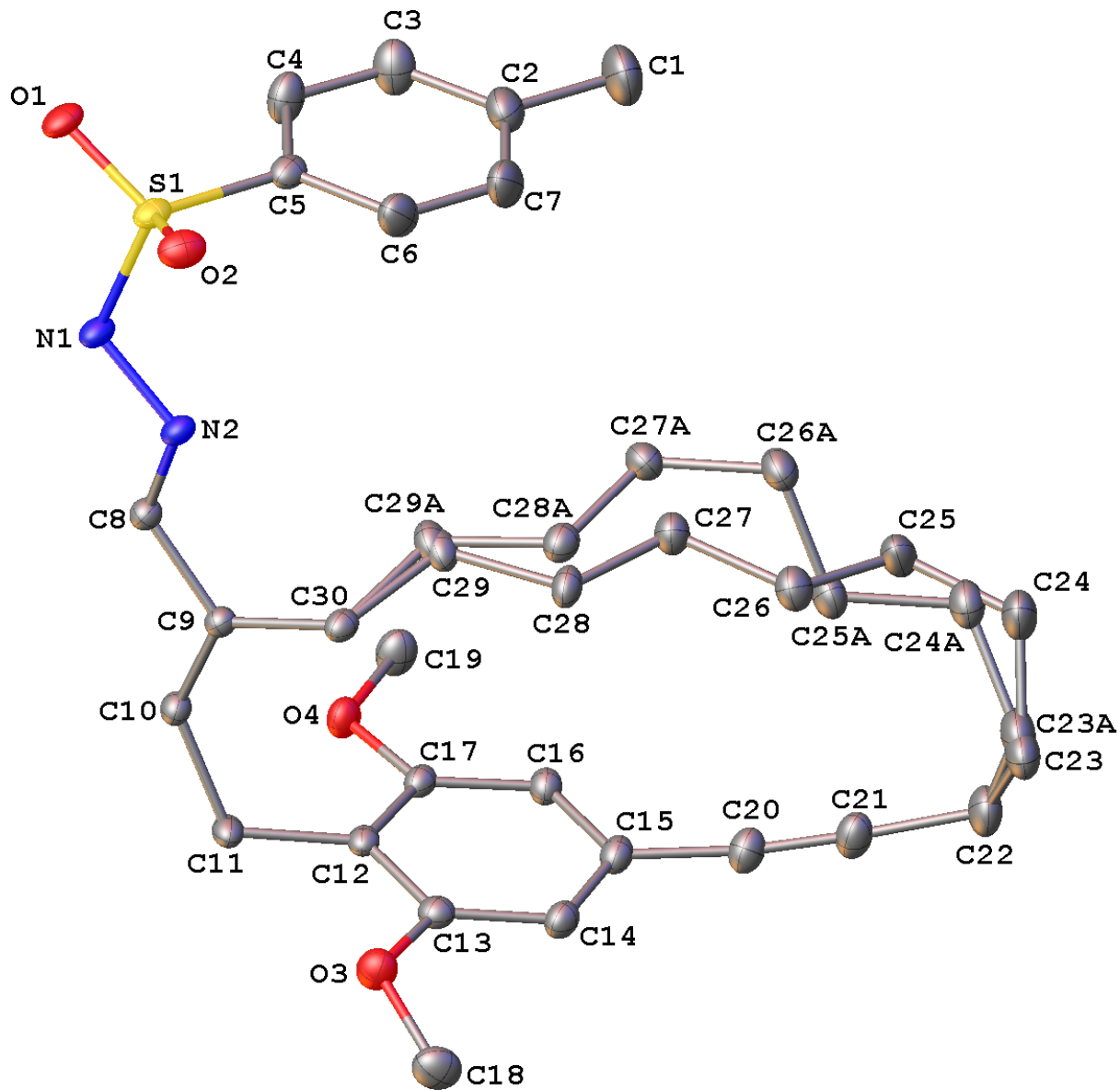
Figure 64. A molecular drawing of tosylhydrazone derivative of **F2** shown with 50% probability ellipsoids. All H atoms are omitted, but both disorder components are shown.

Figure 65. Crystal data and structure refinement for tosylhydrazone derivative of **F2**.

Identification code	gellman181
Empirical formula	$C_{30}H_{38}N_2O_4S$
Formula weight	522.68
Temperature/K	100.0
Crystal system	triclinic
Space group	$P\bar{1}$
a/Å	9.065(3)
b/Å	9.191(2)
c/Å	16.946(4)
α/°	93.668(12)
β/°	93.821(9)
γ/°	102.162(11)
Volume/Å^3	1372.8(6)
Z	2
$\rho_{calc}g/cm^3$	1.264
μ/mm^{-1}	0.156
F(000)	560.0
Crystal size/mm^3	$0.201 \times 0.121 \times 0.057$
Radiation	MoKα (λ = 0.71073)
2Θ range for data collection/°	2.416 to 61.162
Index ranges	$-12 \le h \le 12$, $-13 \le k \le 13$, $-24 \le l \le 24$
Reflections collected	39986
Independent reflections	8366 [R_{int} = 0.0323, R_{sigma} = 0.0256]
Data/restraints/parameters	8366/2/392
Goodness-of-fit on F^2	1.028
Final R indexes [I>=2σ (I)]	R_1 = 0.0400, wR_2 = 0.1050

Final R indexes [all data] $R_1 = 0.0475$, $wR_2 = 0.1103$

Largest diff. peak/hole / e Å^{-3} 0.52/-0.35

Figure 66. Fractional atomic coordinates ($\times 10^4$) and equivalent isotropic displacement parameters (Å$^2 \times 10^3$) for tosylhydrazone derivative of **F2**. U_{eq} is defined as 1/3 of of the trace of the orthogonalised U_{IJ} tensor.

Atom	x	y	z	U(eq)
S1	3417.5(3)	944.7(3)	9185.2(2)	16.06(7)
O1	3172.4(9)	-322.8(9)	9654.5(5)	20.08(16)
O2	2233.4(9)	1716.4(9)	9025.2(5)	22.47(17)
O3	8788.8(10)	9900.6(9)	8634.3(5)	22.50(17)
O4	11338.4(9)	5981.5(9)	8586.5(5)	19.60(16)
N1	4841.4(10)	2116.0(10)	9686.2(5)	17.04(17)
N2	5427.6(10)	3367.0(9)	9279.6(5)	15.50(16)
C1	5560(2)	-814(2)	6029.9(9)	48.0(4)
C2	5026.4(16)	-377.8(15)	6816.0(7)	29.5(3)
C3	5290.7(16)	-1121.9(16)	7482.4(8)	31.3(3)
C4	4805.1(14)	-733.5(15)	8208.4(7)	26.3(2)
C5	4032.8(11)	413.7(12)	8269.4(6)	17.80(19)
C6	3753.7(16)	1173.4(14)	7612.1(7)	29.1(3)
C7	4254.0(19)	768.7(16)	6892.8(8)	35.4(3)
C8	6709.0(11)	4132.8(11)	9591.0(6)	15.23(18)
C9	7477.5(11)	5460.2(11)	9239.5(6)	13.58(17)
C10	8762.2(11)	6253.6(11)	9632.7(6)	15.25(18)
C11	9773.1(12)	7694.8(12)	9444.8(6)	16.83(19)
C12	10034.0(11)	7916.4(11)	8586.2(6)	14.72(18)
C13	9547.9(11)	9049.4(12)	8194.2(6)	17.01(19)
C14	9779.8(12)	9237.8(12)	7399.3(6)	19.0(2)
C15	10513.2(12)	8278.8(12)	6981.6(6)	18.7(2)

C16	11063.9(12)	7177.9(12)	7364.7(6)	17.34(19)
C17	10827.5(11)	7018.8(11)	8162.1(6)	15.45(18)
C18	8637.0(15)	11299.3(14)	8360.3(8)	27.8(2)
C19	12121.0(14)	5008.5(14)	8181.5(7)	25.2(2)
C20	10621.6(13)	8349.9(14)	6141.2(7)	23.5(2)
C21	10569.7(15)	8287.6(14)	5434.2(7)	25.0(2)
C22	10341.1(17)	8172.6(16)	4564.0(7)	30.5(3)
C23	8673(7)	7848(17)	4246(12)	33.6(17)
C24	7893(4)	6198(4)	4104(2)	36.1(7)
C25	7938(4)	5267(3)	4813.1(16)	33.7(6)
C26	7119(3)	5764(3)	5515.4(15)	25.9(5)
C27	7266(3)	4869(3)	6237.3(14)	24.4(4)
C28	6731(4)	5567(4)	6968(2)	20.3(6)
C29	7120(40)	4860(20)	7737(9)	21.2(14)
C23A	8689(7)	7565(17)	4253(12)	33.6(17)
C24A	8023(3)	5963(3)	4431(2)	27.9(6)
C25A	7854(4)	5733(3)	5302.8(15)	26.1(5)
C26A	6887(3)	4239(3)	5472.0(14)	25.8(5)
C27A	7124(3)	3921(3)	6334.3(14)	23.0(4)
C28A	6674(5)	4995(4)	6955(2)	21.2(6)
C29A	7120(40)	4730(20)	7796(9)	21.2(14)
C30	6788.5(11)	5801.4(11)	8459.5(6)	15.91(18)

Figure 67. Anisotropic displacement parameters ($\text{Å}^2 \times 10^3$) for tosylhydrazone derivative of **F2**. The anisotropic displacement factor exponent takes the form: $-2\pi^2[h^2a^{*2}U_{11}+2hka^*b^*U_{12}+\ldots]$.

Atom	U_{11}	U_{22}	U_{33}	U_{23}	U_{13}	U_{12}
S1	12.56(11)	13.84(12)	20.37(13)	4.28(9)	-0.43(8)	-0.67(8)
O1	16.8(3)	17.3(4)	24.5(4)	7.8(3)	1.7(3)	-2.1(3)

O2	15.9(3)	19.9(4)	31.2(4)	3.8(3)	-1.1(3)	3.4(3)
O3	25.5(4)	20.7(4)	22.9(4)	2.2(3)	4.2(3)	7.9(3)
O4	23.5(4)	20.9(4)	16.0(4)	4.9(3)	0.7(3)	7.8(3)
N1	16.0(4)	14.5(4)	18.4(4)	5.3(3)	-0.9(3)	-2.1(3)
N2	16.0(4)	12.7(4)	17.0(4)	4.0(3)	2.1(3)	0.1(3)
C1	71.8(12)	49.3(9)	20.7(7)	-1.6(6)	6.5(7)	8.7(8)
C2	35.0(6)	30.9(6)	18.2(5)	0.2(5)	-2.2(5)	-0.9(5)
C3	34.7(7)	38.8(7)	24.3(6)	4.1(5)	3.3(5)	15.9(6)
C4	28.5(6)	33.2(6)	20.7(5)	8.9(5)	2.3(4)	12.8(5)
C5	15.3(4)	17.5(5)	18.5(5)	3.6(4)	-2.6(3)	-0.6(4)
C6	42.3(7)	23.1(6)	21.9(6)	4.8(4)	-6.3(5)	8.8(5)
C7	57.0(9)	29.1(6)	18.2(6)	5.8(5)	-6.0(6)	6.9(6)
C8	15.9(4)	14.8(4)	14.5(4)	2.2(3)	0.9(3)	1.8(3)
C9	13.9(4)	12.9(4)	13.6(4)	1.7(3)	1.1(3)	1.8(3)
C10	15.4(4)	16.5(4)	13.1(4)	2.5(3)	1.0(3)	1.4(3)
C11	16.5(4)	17.6(5)	13.1(4)	0.7(3)	0.3(3)	-3.1(4)
C12	13.4(4)	15.0(4)	13.6(4)	1.8(3)	0.1(3)	-1.7(3)
C13	15.5(4)	15.8(4)	18.2(5)	1.2(4)	-0.2(3)	0.6(3)
C14	20.1(5)	19.2(5)	17.1(5)	5.4(4)	-0.6(4)	2.6(4)
C15	18.0(4)	21.3(5)	15.4(5)	4.8(4)	0.2(4)	0.3(4)
C16	17.1(4)	19.5(5)	14.4(5)	2.5(4)	1.0(3)	1.6(4)
C17	14.6(4)	15.7(4)	14.6(4)	3.5(3)	-1.0(3)	0.0(3)
C18	31.1(6)	21.9(5)	31.6(6)	0.9(5)	-2.5(5)	10.3(5)
C19	29.8(6)	25.3(6)	24.1(6)	5.7(4)	3.4(4)	12.7(5)
C20	25.3(5)	26.8(6)	19.7(5)	7.1(4)	2.3(4)	6.9(4)
C21	33.3(6)	25.2(5)	19.6(5)	6.2(4)	4.3(4)	11.3(5)
C22	42.9(7)	33.3(6)	16.1(5)	3.6(5)	6.2(5)	8.3(6)

C23	43.4(8)	37(5)	15.9(7)	2(3)	1.7(5)	-0.5(12)
C24	58(2)	32.3(16)	16.8(15)	3.7(13)	2.6(14)	7.1(14)
C25	61.3(19)	21.8(11)	16.8(12)	0.6(11)	-1.1(11)	7.5(12)
C26	30.6(13)	27.6(12)	18.4(11)	1.8(9)	-0.9(10)	5.0(10)
C27	31.9(12)	24.1(12)	16.5(10)	2.4(9)	1.3(8)	4.6(9)
C28	20.7(12)	25.4(16)	13.7(11)	5.8(14)	0.2(8)	1.9(15)
C29	19.6(5)	27(3)	14.1(17)	0.0(19)	-0.3(17)	0(2)
C23A	43.4(8)	37(5)	15.9(7)	2(3)	1.7(5)	-0.5(12)
C24A	33.5(13)	32.4(15)	16.5(14)	1.8(13)	1.5(12)	4.8(11)
C25A	33.9(14)	28.0(12)	16.0(12)	-1.1(9)	2.8(10)	6.4(10)
C26A	29.3(11)	27.9(12)	16.9(10)	-1.4(9)	0.0(8)	-0.1(9)
C27A	27.9(11)	20.8(12)	18.3(10)	-1.1(8)	1.3(8)	1.8(9)
C28A	21.9(12)	22.0(15)	18.7(12)	4.9(14)	-0.6(8)	1.9(15)
C29A	19.6(5)	27(3)	14.1(17)	0.0(19)	-0.3(17)	0(2)
C30	14.2(4)	15.9(4)	16.2(5)	4.0(3)	-1.2(3)	0.2(3)

Figure 68. Bond lengths for tosylhydrazone derivative of **F2**.

Atom	Atom	Length/Å	Atom	Atom	Length/Å
S1	O1	1.4396(8)	C13	C14	1.3932(15)
S1	O2	1.4267(9)	C14	C15	1.3964(16)
S1	N1	1.6424(10)	C15	C16	1.3958(15)
S1	C5	1.7581(12)	C15	C20	1.4387(16)
O3	C13	1.3648(13)	C16	C17	1.3943(15)
O3	C18	1.4247(15)	C20	C21	1.1931(17)
O4	C17	1.3675(12)	C21	C22	1.4693(17)
O4	C19	1.4240(14)	C22	C23	1.532(4)
N1	N2	1.4043(12)	C22	C23A	1.529(4)

N2	C8	1.2844(13)		C23	C24	1.529(14)
C1	C2	1.506(2)		C24	C25	1.523(4)
C2	C3	1.3901(18)		C25	C26	1.539(4)
C2	C7	1.387(2)		C26	C27	1.531(3)
C3	C4	1.3846(18)		C27	C28	1.513(4)
C4	C5	1.3854(16)		C28	C29	1.55(2)
C5	C6	1.3888(16)		C29	C30	1.537(3)
C6	C7	1.384(2)		C23A	C24A	1.527(15)
C8	C9	1.4557(14)		C24A	C25A	1.520(4)
C9	C10	1.3449(14)		C25A	C26A	1.521(4)
C9	C30	1.5037(14)		C26A	C27A	1.519(3)
C10	C11	1.5090(14)		C27A	C28A	1.530(4)
C11	C12	1.5093(14)		C28A	C29A	1.51(2)
C12	C13	1.4010(14)		C29A	C30	1.537(3)
C12	C17	1.3992(14)				

Figure 69. Bond angles for tosylhydrazone derivative of **F2**.

Atom	Atom	Atom	Angle/°		Atom	Atom	Atom	Angle/°
O1	S1	N1	103.35(5)		O3	C13	C14	123.04(10)
O1	S1	C5	108.88(5)		C14	C13	C12	121.49(10)
O2	S1	O1	120.33(5)		C13	C14	C15	119.46(10)
O2	S1	N1	108.34(5)		C14	C15	C20	120.36(10)
O2	S1	C5	107.57(5)		C16	C15	C14	120.33(10)
N1	S1	C5	107.78(5)		C16	C15	C20	119.19(10)
C13	O3	C18	117.93(9)		C17	C16	C15	119.08(10)
C17	O4	C19	117.65(9)		O4	C17	C12	115.03(9)
N2	N1	S1	113.50(7)		O4	C17	C16	123.09(9)

C8	N2	N1	113.86(9)	C16	C17	C12	121.87(9)
C3	C2	C1	120.70(14)	C21	C20	C15	172.77(13)
C7	C2	C1	120.95(13)	C20	C21	C22	174.30(14)
C7	C2	C3	118.35(12)	C21	C22	C23	113.7(8)
C4	C3	C2	121.30(12)	C21	C22	C23A	113.0(8)
C3	C4	C5	119.25(11)	C24	C23	C22	115.7(9)
C4	C5	S1	120.32(9)	C25	C24	C23	116.1(7)
C4	C5	C6	120.54(11)	C24	C25	C26	114.1(2)
C6	C5	S1	119.13(9)	C27	C26	C25	112.9(2)
C7	C6	C5	119.19(12)	C28	C27	C26	111.9(2)
C6	C7	C2	121.36(12)	C27	C28	C29	113.3(4)
N2	C8	C9	120.85(9)	C30	C29	C28	109.6(11)
C8	C9	C30	117.22(9)	C24A	C23A	C22	115.4(9)
C10	C9	C8	117.00(9)	C25A	C24A	C23A	115.0(8)
C10	C9	C30	125.76(9)	C24A	C25A	C26A	115.3(2)
C9	C10	C11	129.75(9)	C27A	C26A	C25A	111.7(2)
C10	C11	C12	117.90(9)	C26A	C27A	C28A	116.7(2)
C13	C12	C11	121.82(9)	C29A	C28A	C27A	113.5(5)
C17	C12	C11	120.49(9)	C28A	C29A	C30	117.2(13)
C17	C12	C13	117.64(9)	C9	C30	C29	114.4(9)
O3	C13	C12	115.43(9)	C9	C30	C29A	109.1(9)

Figure 70. Hydrogen bonds for tosylhydrazone derivative of **F2**.

D	H	A	d(D-H)/Å	d(H-A)/Å	d(D-A)/Å	D-H-A/°
N1	H1	O1[1]	0.868(17)	2.037(17)	2.9025(13)	175.8(16)

[1] 1-X,-Y,2-Z

Figure 71. Torsion angles for tosylhydrazone derivative of **F2.**

A	B	C	D	Angle/°	A	B	C	D	Angle/°
S1	N1	N2	C8	-167.09(8)	C11	C12	C17	O4	-0.83(14)
S1	C5	C6	C7	179.21(11)	C11	C12	C17	C16	178.84(9)
O1	S1	N1	N2	171.42(7)	C12	C13	C14	C15	-0.02(16)
O1	S1	C5	C4	-27.39(11)	C13	C12	C17	O4	176.88(9)
O1	S1	C5	C6	153.54(9)	C13	C12	C17	C16	-3.44(15)
O2	S1	N1	N2	-59.87(9)	C13	C14	C15	C16	-2.55(16)
O2	S1	C5	C4	-159.31(9)	C13	C14	C15	C20	173.35(10)
O2	S1	C5	C6	21.63(11)	C14	C15	C16	C17	2.08(16)
O3	C13	C14	C15	-177.32(10)	C15	C16	C17	O4	-179.37(10)
N1	S1	C5	C4	84.07(10)	C15	C16	C17	C12	0.98(15)
N1	S1	C5	C6	-95.00(10)	C17	C12	C13	O3	-179.56(9)
N1	N2	C8	C9	179.60(9)	C17	C12	C13	C14	2.95(15)
N2	C8	C9	C10	175.58(10)	C18	O3	C13	C12	162.85(10)
N2	C8	C9	C30	-5.95(14)	C18	O3	C13	C14	-19.69(15)
C1	C2	C3	C4	-179.94(14)	C19	O4	C17	C12	178.42(9)
C1	C2	C7	C6	179.73(14)	C19	O4	C17	C16	-1.25(15)
C2	C3	C4	C5	0.4(2)	C20	C15	C16	C17	-173.87(10)
C3	C2	C7	C6	0.0(2)	C21	C22	C23	C24	-89.1(13)
C3	C4	C5	S1	-179.39(10)	C21	C22	C23A	C24A	-64.2(13)
C3	C4	C5	C6	-0.34(19)	C22	C23	C24	C25	56.0(15)
C4	C5	C6	C7	0.14(19)	C22	C23A	C24A	C25A	66.7(14)
C5	S1	N1	N2	56.25(8)	C23	C24	C25	C26	62.8(7)
C5	C6	C7	C2	0.0(2)	C24	C25	C26	C27	-176.5(3)
C7	C2	C3	C4	-0.3(2)	C25	C26	C27	C28	168.6(3)
C8	C9	C10	C11	-177.24(10)	C26	C27	C28	C29	-170.0(13)

C8 C9 C30 C29	-78.5(13)	C27 C28 C29 C30	170.2(12)
C8 C9 C30 C29A	-75.3(12)	C28 C29 C30 C9	-165.3(12)
C9 C10 C11 C12	-38.62(16)	C23A C24A C25A C26A	167.2(4)
C10 C9 C30 C29	99.8(13)	C24A C25A C26A C27A	164.2(2)
C10 C9 C30 C29A	103.1(12)	C25A C26A C27A C28A	63.0(3)
C10 C11 C12 C13	116.01(11)	C26A C27A C28A C29A	-172.7(13)
C10 C11 C12 C17	-66.37(13)	C27A C28A C29A C30	177.0(14)
C11 C12 C13 O3	-1.87(14)	C28A C29A C30 C9	-173.4(16)
C11 C12 C13 C14	-179.37(9)	C30 C9 C10 C11	4.44(17)

Figure 72. Hydrogen atom coordinates ($\text{Å}\times10^4$) and isotropic displacement parameters ($\text{Å}^2\times10^3$) for tosylhydrazone derivative of **F2**.

Atom	x	y	z	U(eq)
H1	5466(19)	1622(18)	9893(10)	30(4)
H1A	6426.64	-1282.1	6119.76	72
H1B	5864.08	78.34	5741.97	72
H1C	4736.79	-1521.42	5716.62	72
H3	5814.78	-1912.51	7438.85	38
H4	4999.4	-1247.75	8659.66	32
H6	3225.85	1961.21	7655.47	35
H7	4064.19	1287.13	6442.51	42
H8	7161.21	3828.88	10056.86	18
H10	9081.49	5845.23	10099.05	18
H11A	10772.4	7782.25	9739.33	20
H11B	9340.28	8528.35	9656.7	20
H14	9441.74	10012.48	7143.53	23
H16	11592.45	6545.85	7086.02	21
H18A	7952.18	11128.64	7875.11	42

H18B 9631.92	11868.81	8248	42
H18C 8222.33	11862.59	8769.23	42
H19A 11443.26	4409.13	7750.55	38
H19B 12452.68	4346.35	8554.07	38
H19C 13005.47	5600.39	7961.17	38
H22A 10810.35	7367.58	4348.94	37
H22B 10868.78	9120.14	4368.19	37
H22C 10969.37	7509.68	4344.07	37
H22D 10690.96	9173.19	4372.99	37
H23A 8108.96	8334.05	4626.59	40
H23B 8599.99	8318.47	3739.51	40
H24A 6820.13	6131.56	3918.96	43
H24B 8368.48	5745.32	3668.92	43
H25A 9008.42	5317.05	4997.01	40
H25B 7470.91	4211.8	4639.39	40
H26A 7542.21	6835.42	5671.07	31
H26B 6032.52	5651.31	5343.74	31
H27A 6661.78	3839.09	6117.52	29
H27B 8338.2	4812.18	6345.11	29
H28A 5620.02	5462.29	6891.85	24
H28B 7200.49	6646.56	7028.27	24
H29A 6502.83	3828.84	7726.26	25
H29B 8199.84	4807.58	7775.59	25
H23C 8067.19	8222.95	4483.79	40
H23D 8605.42	7621.71	3670.55	40
H24C 7013.68	5635.59	4136.08	33
H24D 8676.98	5311.28	4226.85	33

H25C 7405.7	6538.64	5536.35	31
H25D 8875.07	5837.6	5575.63	31
H26C 5806.38	4240.41	5343	31
H26D 7147.09	3434.32	5127.03	31
H27C 8208.96	3922.19	6451.91	28
H27D 6542.69	2901.67	6398.1	28
H28C 7155.03	6031.42	6856.1	25
H28D 5563.48	4897.45	6890.24	25
H29C 8224.02	4759.36	7842.63	25
H29D 6601.96	3700.49	7893.19	25
H30C 7220.97	6845.6	8353.42	19
H30D 5680.72	5683.53	8478.49	19
H30A 7173.74	6869.64	8383.78	19
H30B 5677.99	5639.98	8482.88	19

Figure 73. Atomic occupancy for tosylhydrazone derivative of **F2**.

Atom	*Occupancy*	Atom	*Occupancy*	Atom	*Occupancy*
H22A	0.5	H22B	0.5	H22C	0.5
H22D	0.5	C23	0.5	H23A	0.5
H23B	0.5	C24	0.5	H24A	0.5
H24B	0.5	C25	0.5	H25A	0.5
H25B	0.5	C26	0.5	H26A	0.5
H26B	0.5	C27	0.5	H27A	0.5
H27B	0.5	C28	0.5	H28A	0.5
H28B	0.5	C29	0.5	H29A	0.5
H29B	0.5	C23A	0.5	H23C	0.5
H23D	0.5	C24A	0.5	H24C	0.5

H24D 0.5	C25A 0.5	H25C 0.5
H25D 0.5	C26A 0.5	H26C 0.5
H26D 0.5	C27A 0.5	H27C 0.5
H27D 0.5	C28A 0.5	H28C 0.5
H28D 0.5	C29A 0.5	H29C 0.5
H29D 0.5	H30C 0.5	H30D 0.5
H30A 0.5	H30B 0.5	

3.4.7 Calibration Curves

LC-MS Calibration Curves: E1, E2, and E3
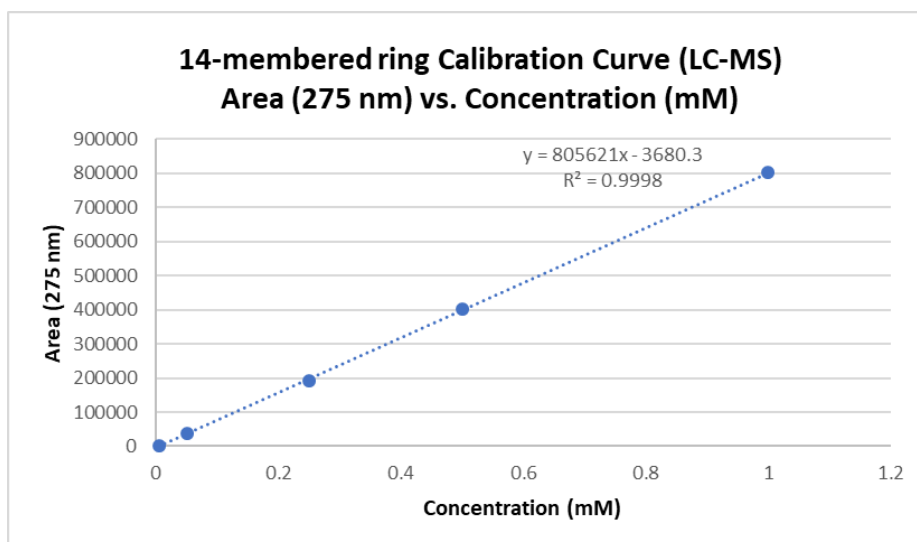
Figure 74. Calibration curve of **E2** for LCMS-based determination of crude reaction yield for small molecule- and foldamer-catalyzed macrocyclization.
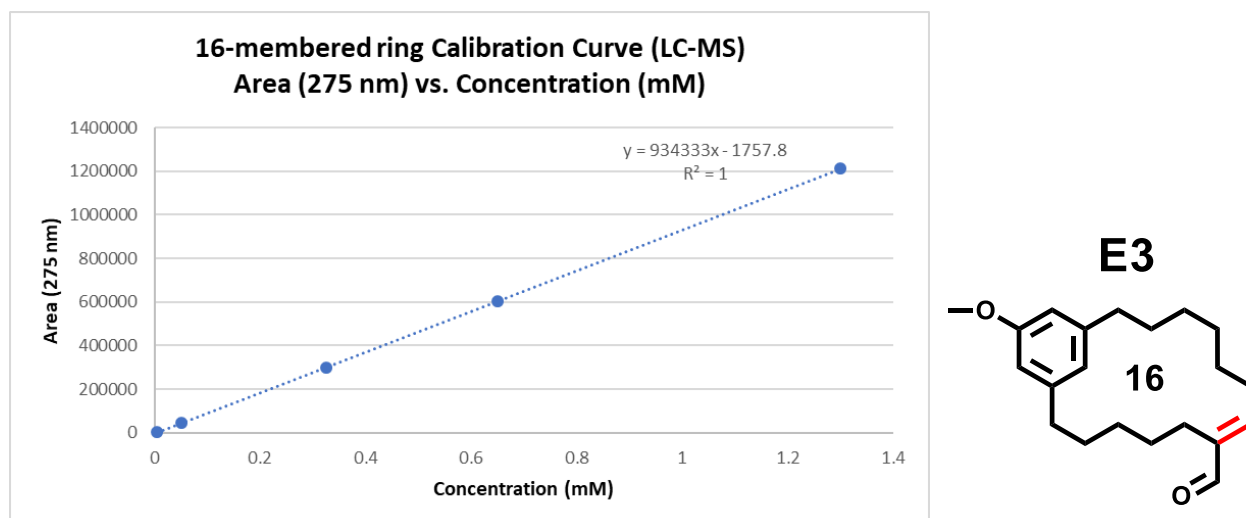
Figure 75. Calibration curve of **E3** for LCMS-based determination of crude reaction yield for small molecule- and foldamer-catalyzed macrocyclization.
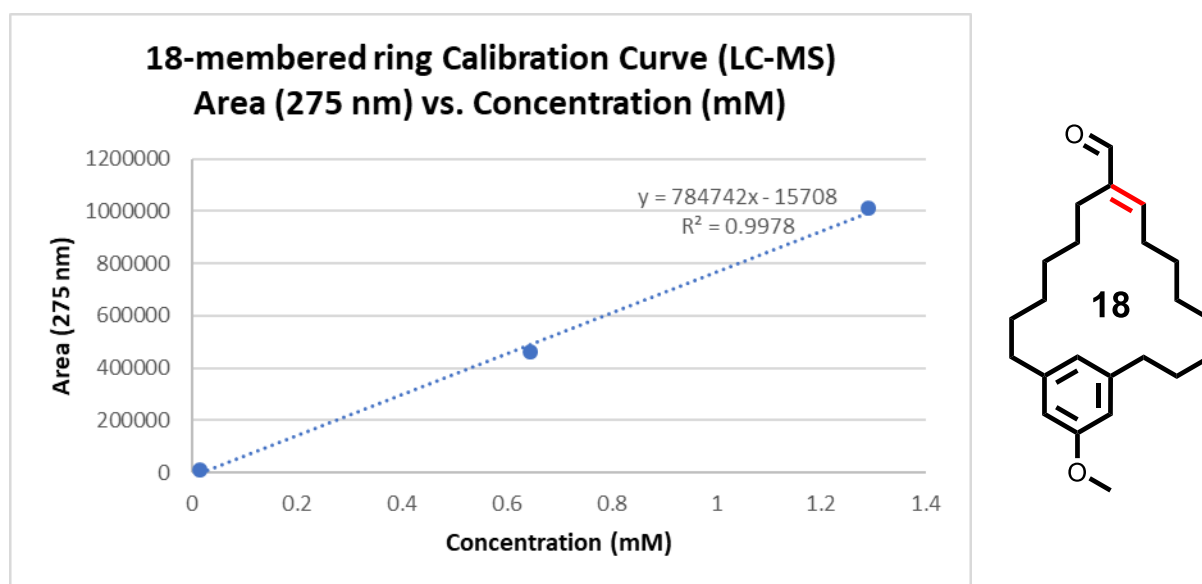
Figure 76. Calibration curve of **E4** for LCMS-based determination of crude reaction yield for small molecule- and foldamer-catalyzed macrocyclization.

3.6 Spectra: ^{1}H-NMR, NOE, ^{13}C-NMR, Mass Spec, LC-MS traces
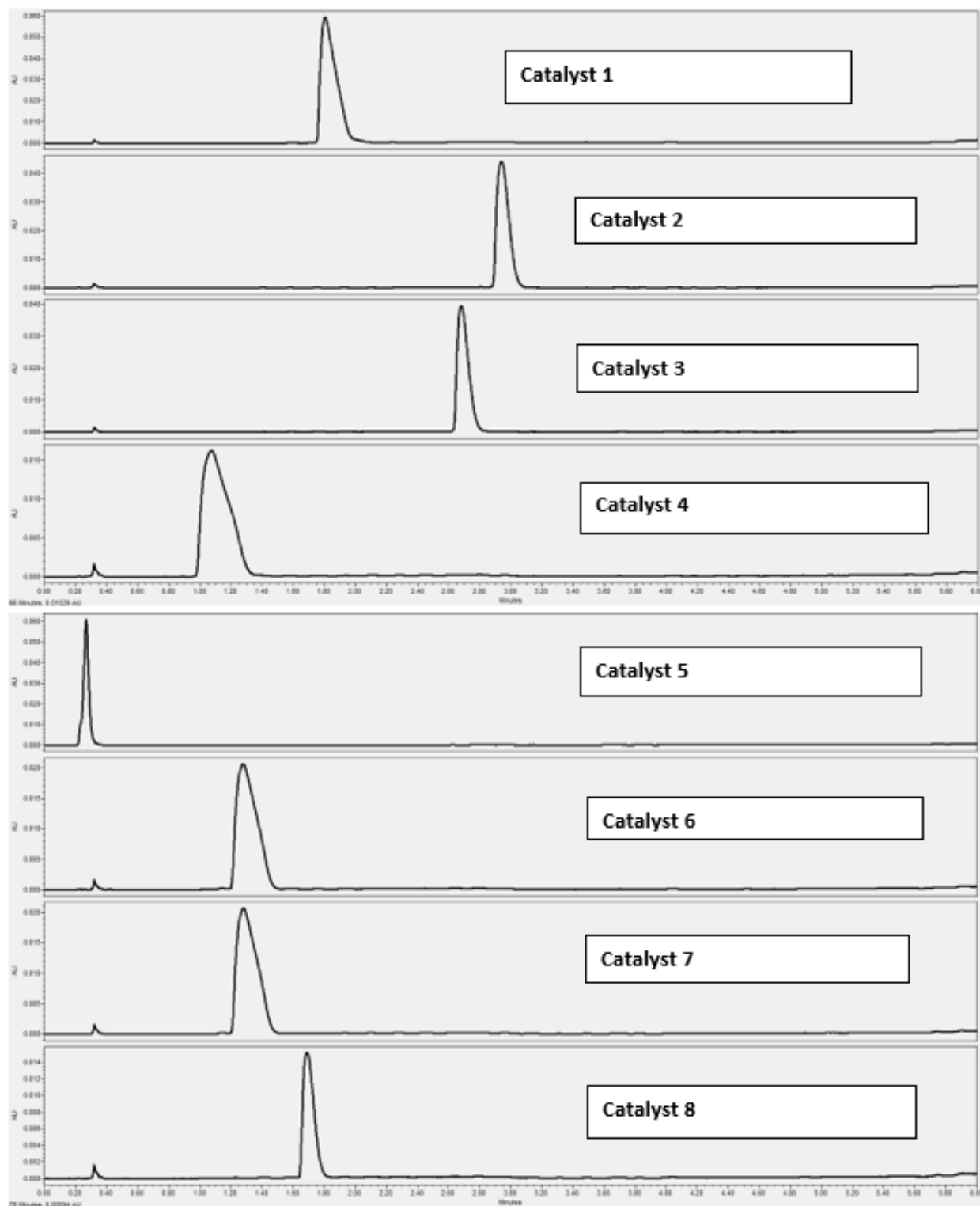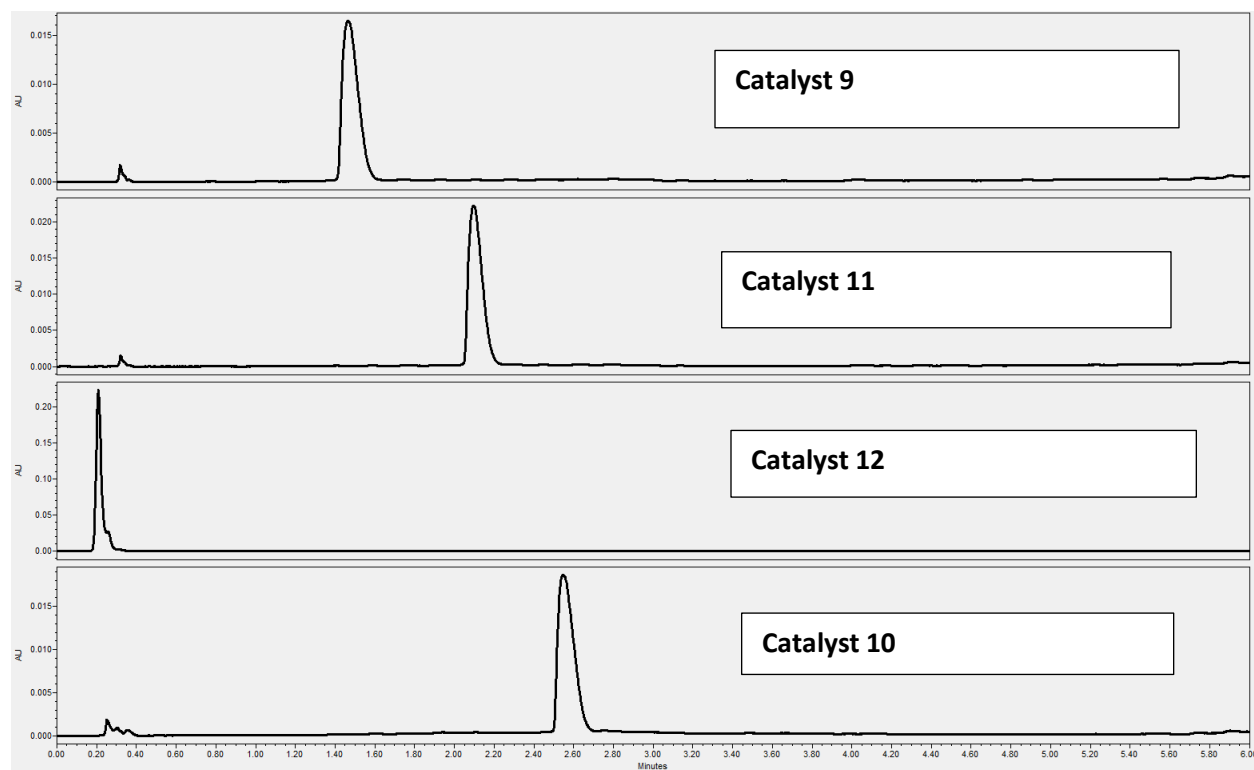
LC-MS traces for catalysts. Every catalyst was > 95 % pure. Detection at 220 nm (corresponding to amide bond absorbance).

NB5_P158_Fr 10-18 C5 Substrate.10.fid
H1_standard.UW CDCl3 /home/zgirvin/callisto zgirvin 59

NB5_P158_Fr 10-18 C5 Substrate.11.fid
C13_H1dec.UW CDCl3 /home/zgirvin/callisto zgirvin 59
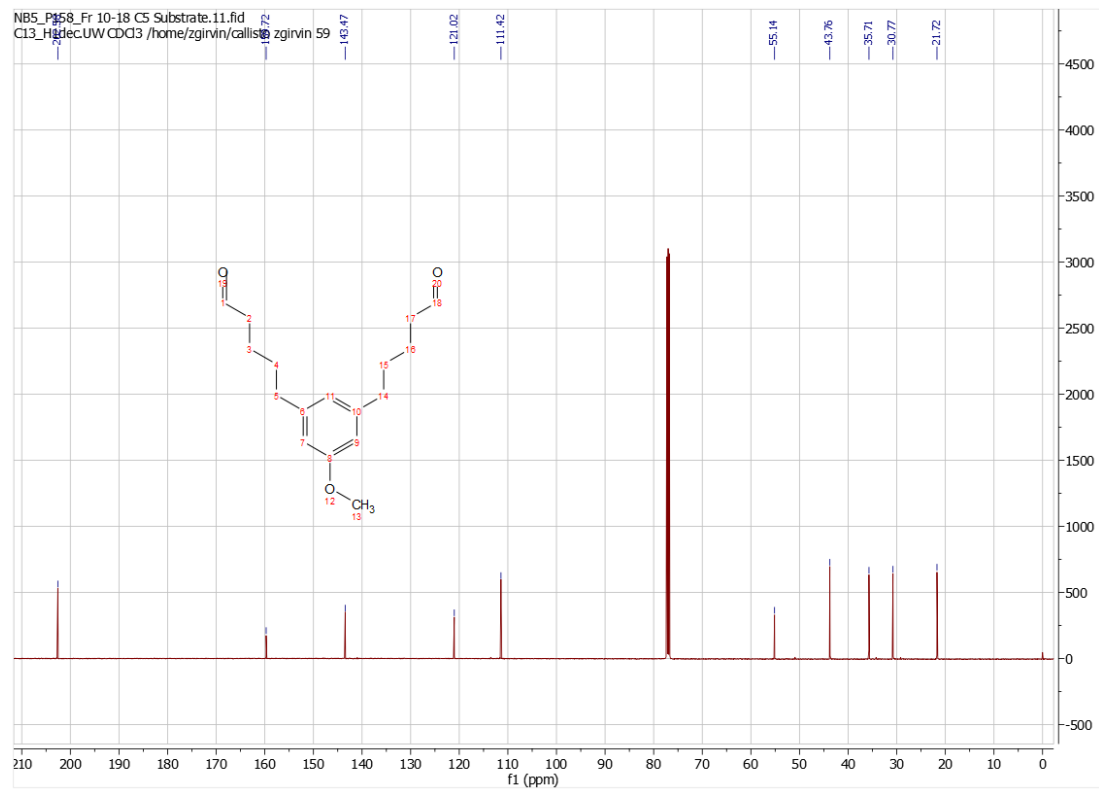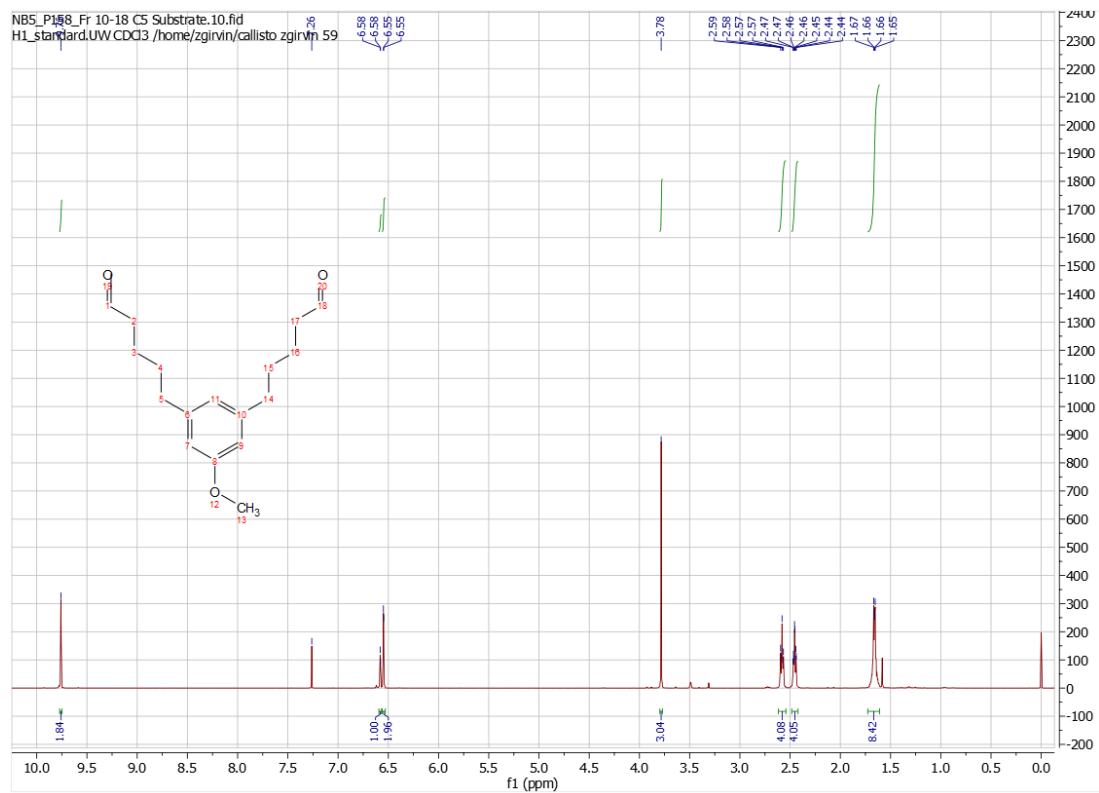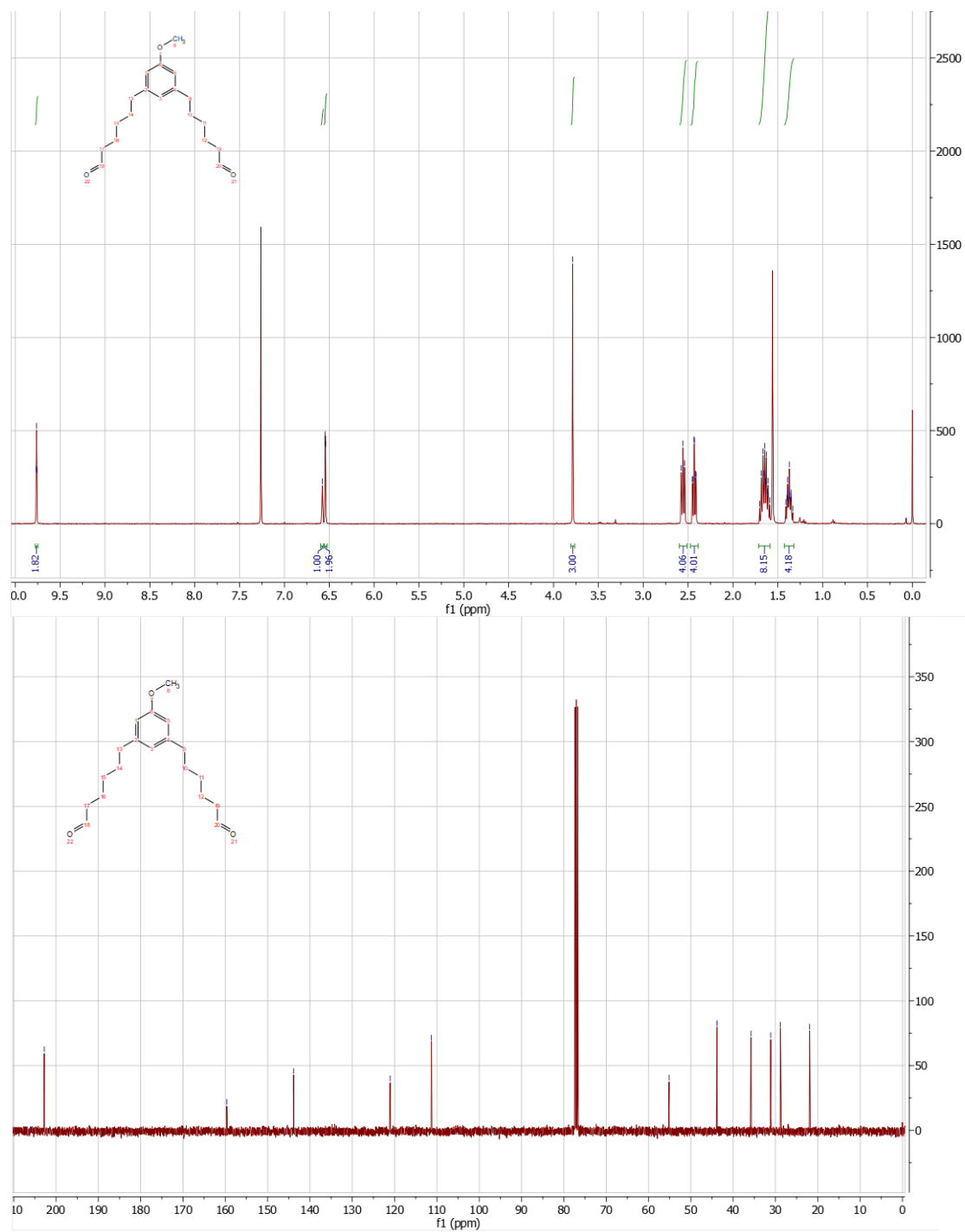
Spectra for **D1**

Spectra for **D2**
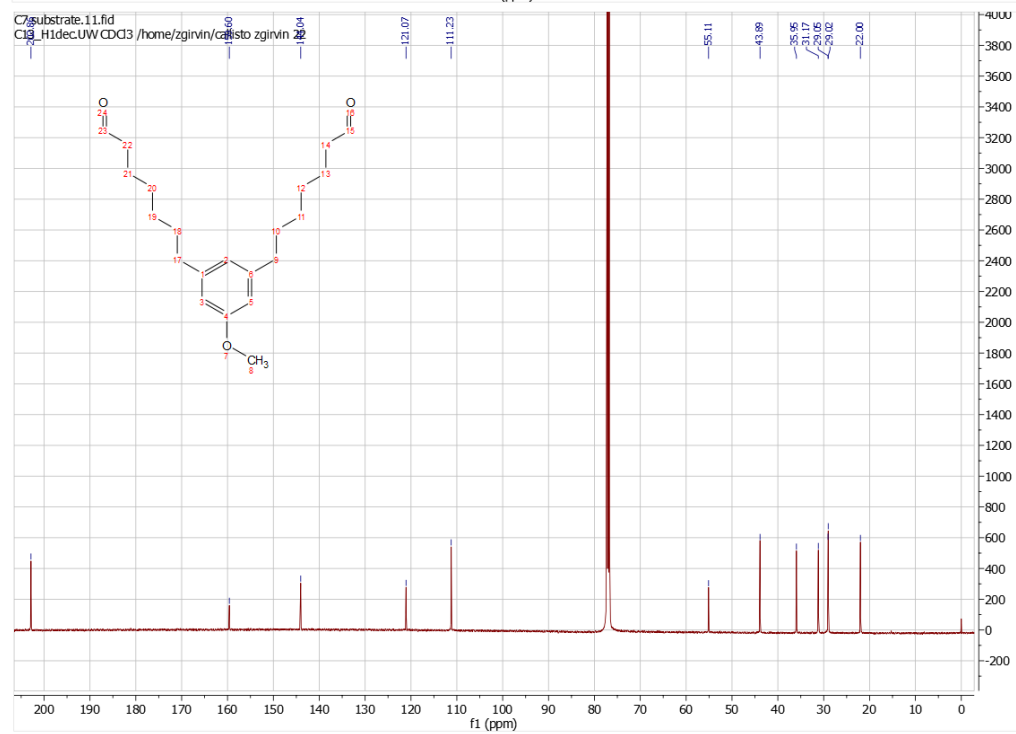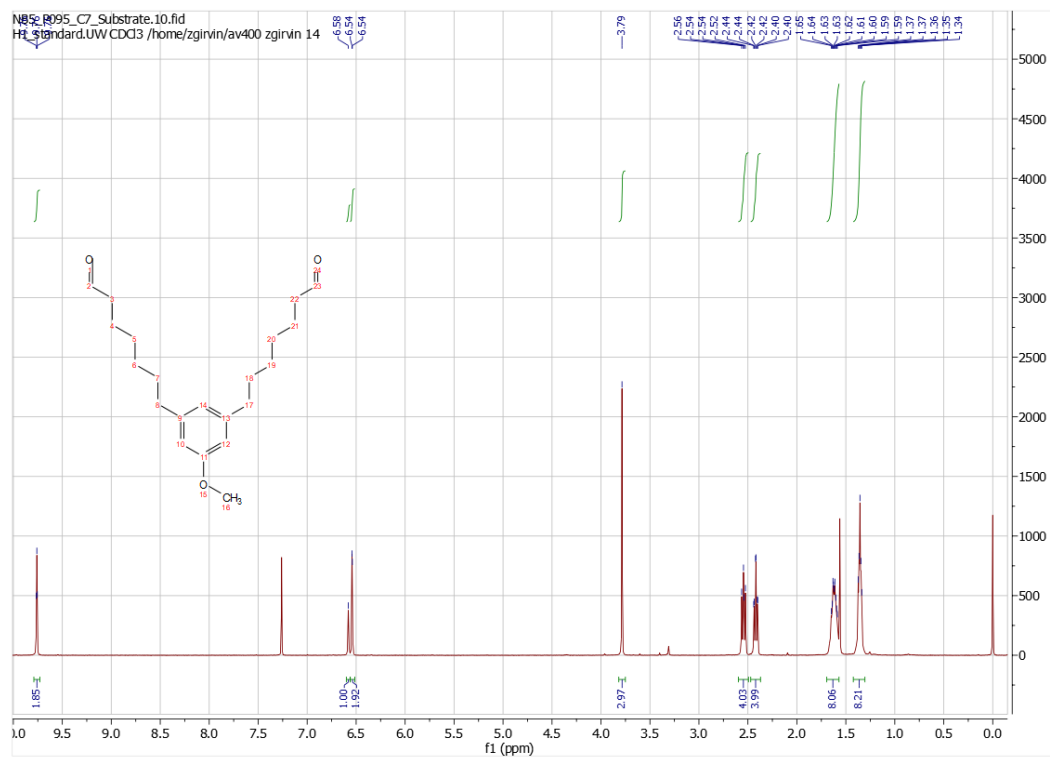
Spectra for **D3**

Spectra for **D4**

12-enal_Paper.10.fid
H1_standard.UW CDCl3 /home/zgirvin/callisto zgirvin 42

12-enal_Paper.11.fid
C13_H1decoUW CDCl3 /home/zgirvin/callisto zgirvin 42
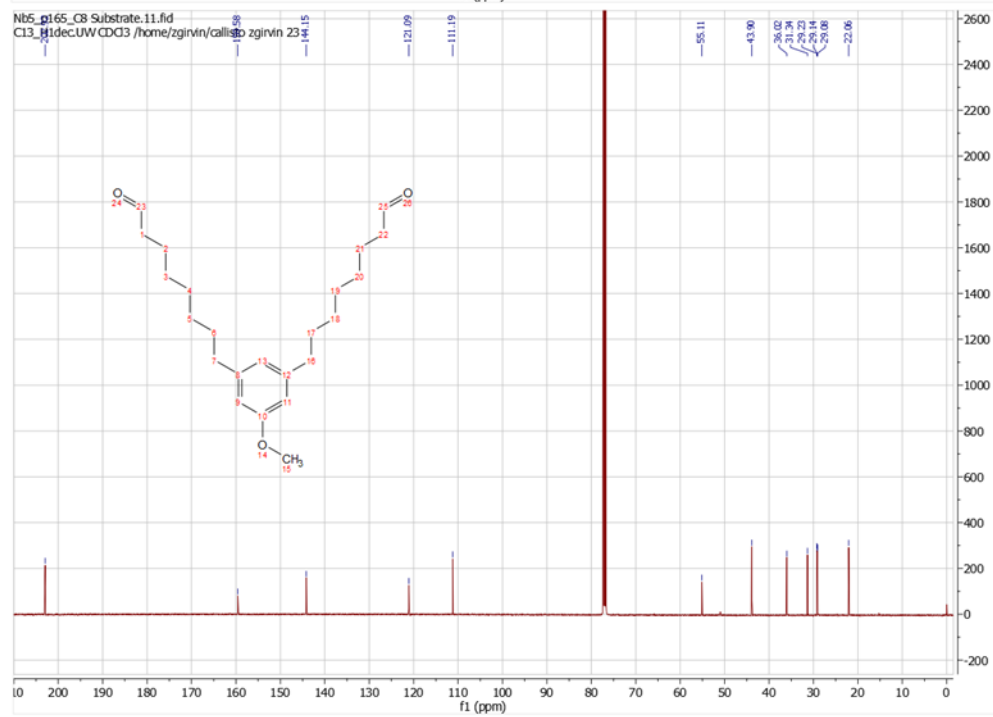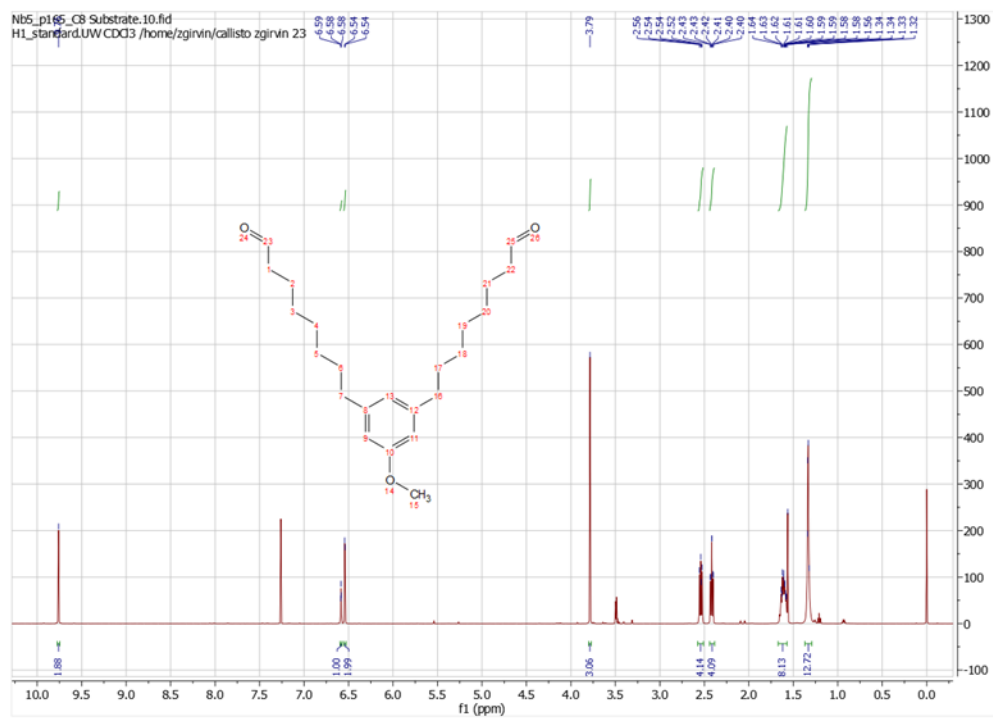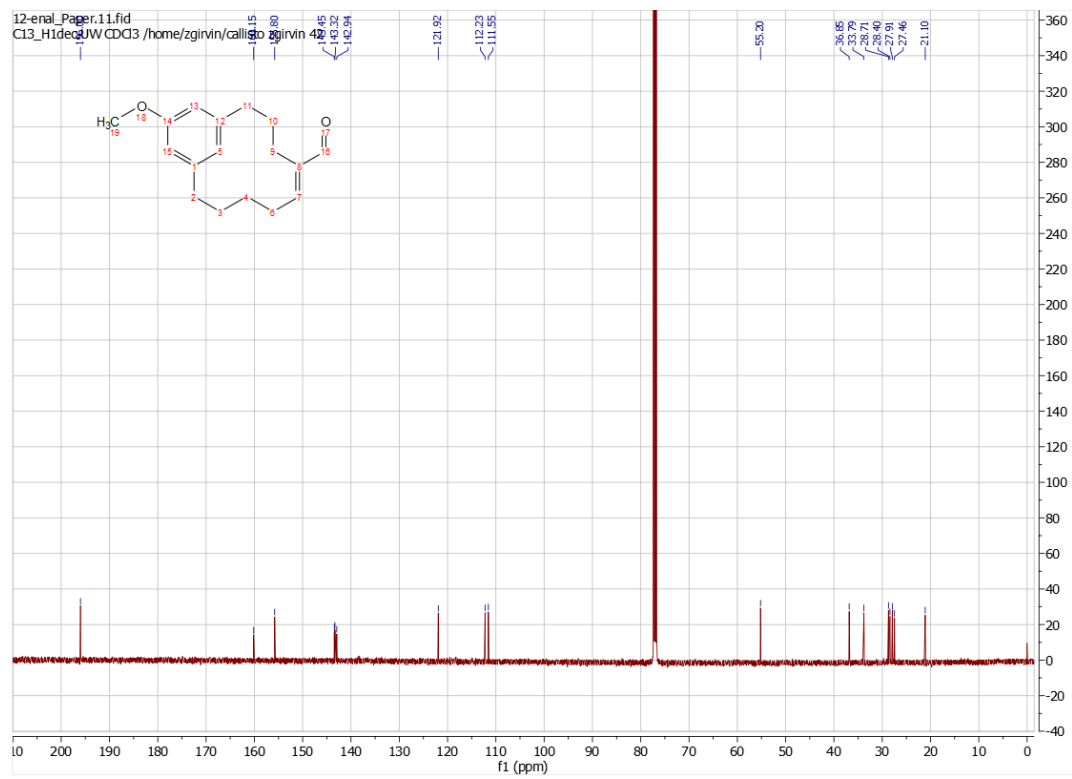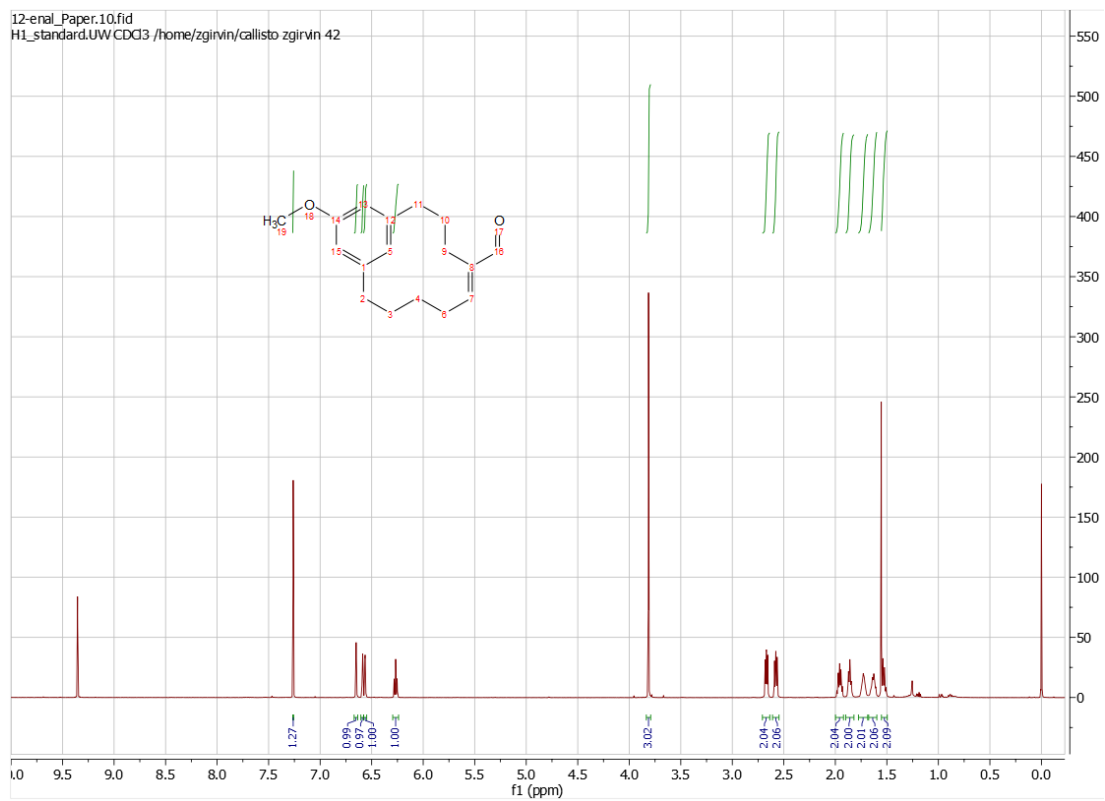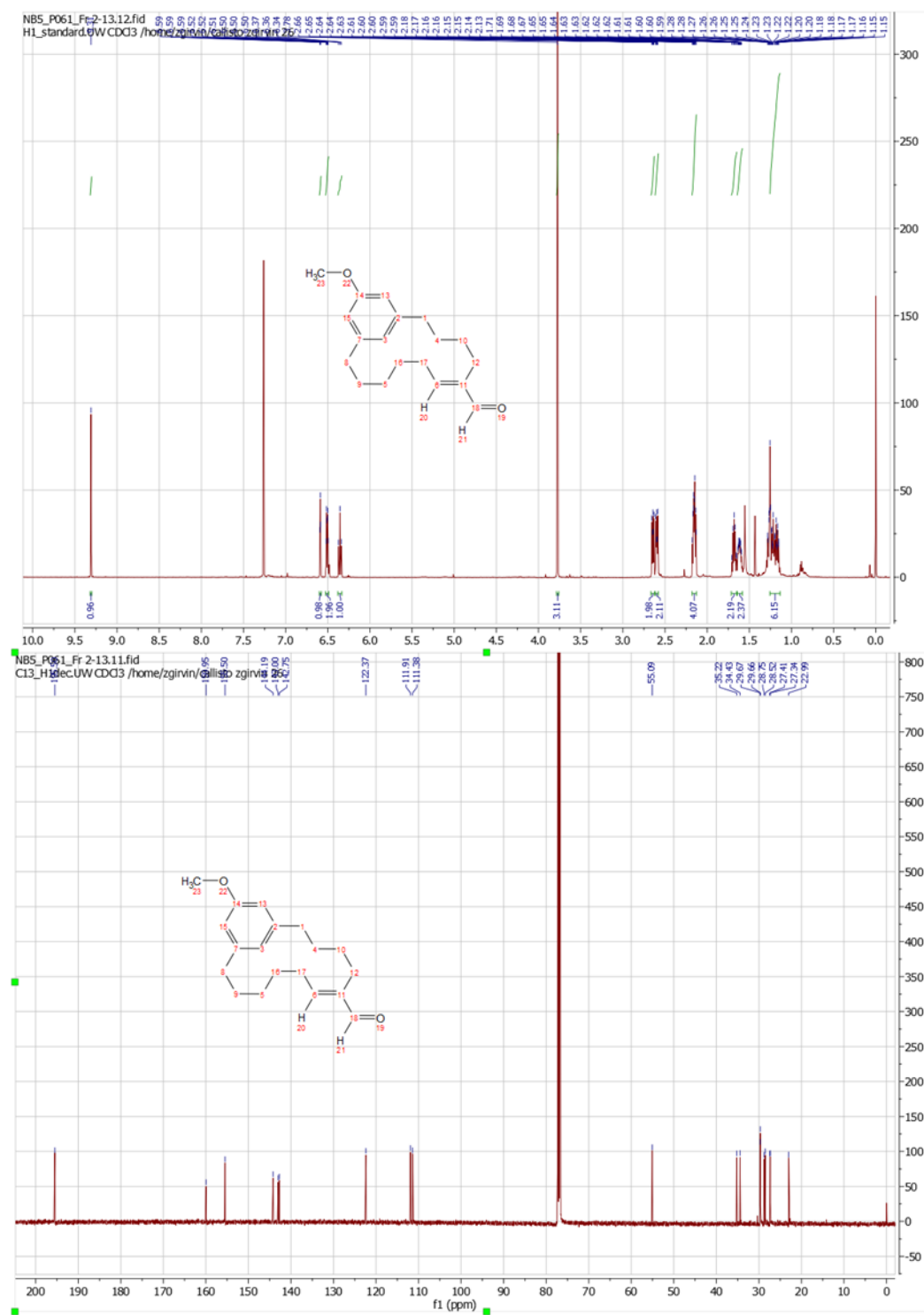
Spectra for **E1**

Spectra for **E2**
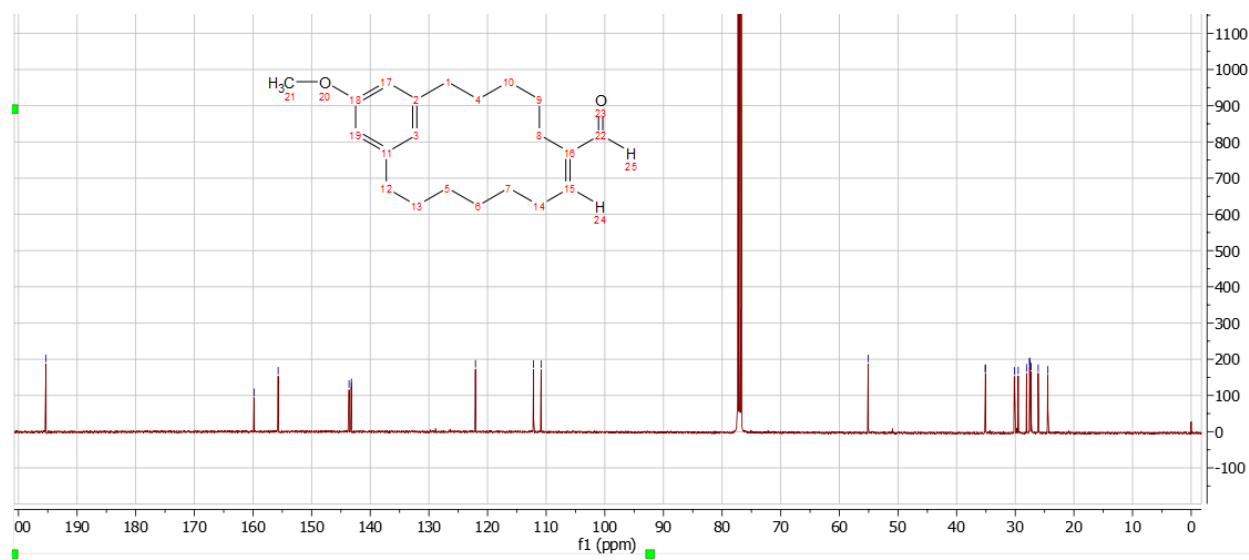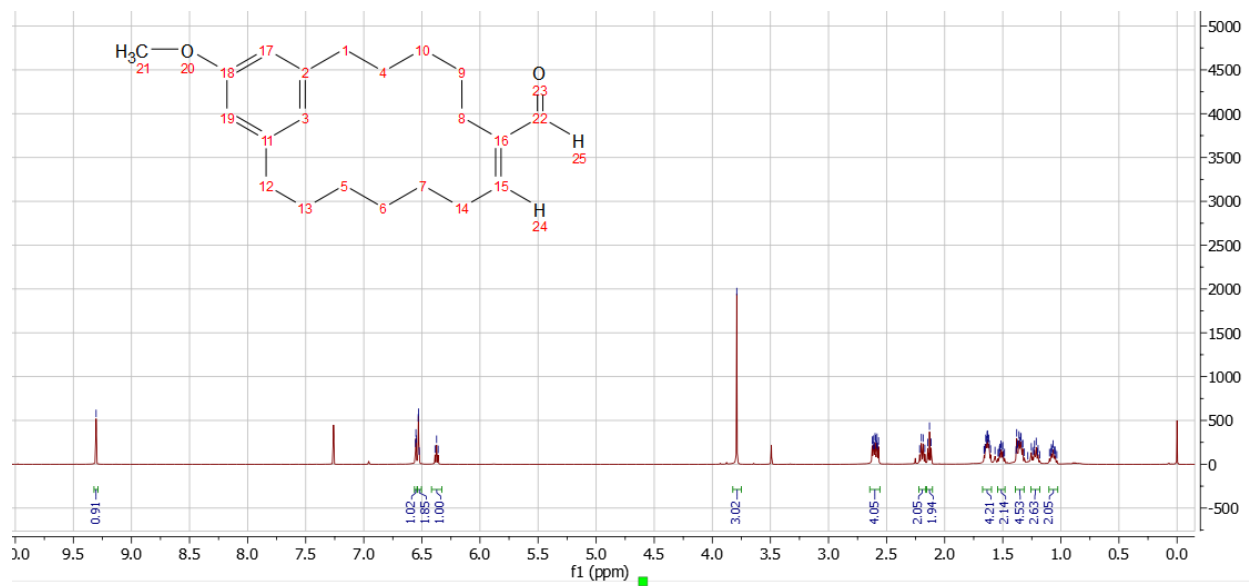
Spectra for **E3**
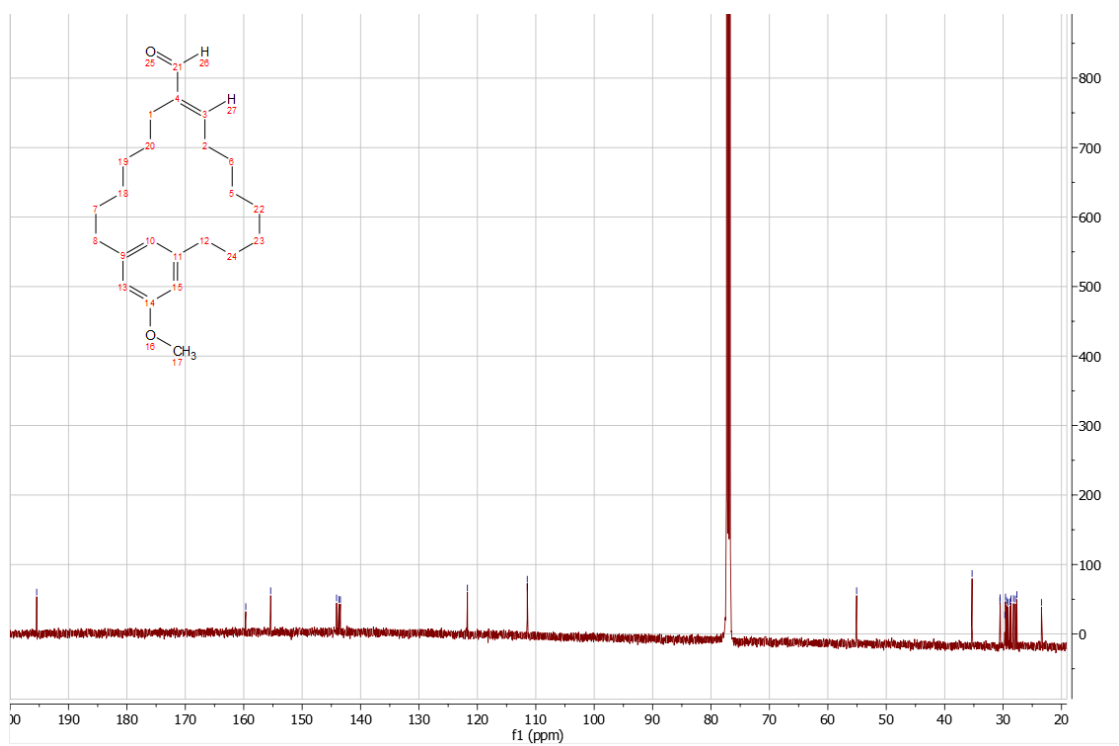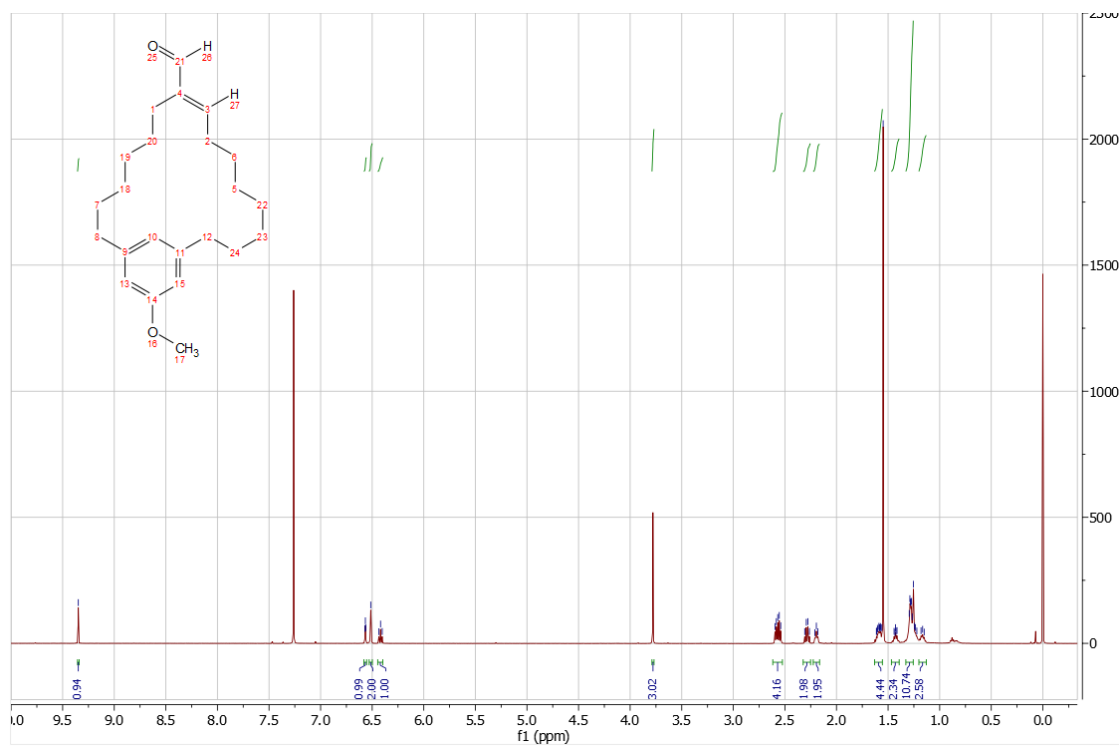
Spectra for **E4**
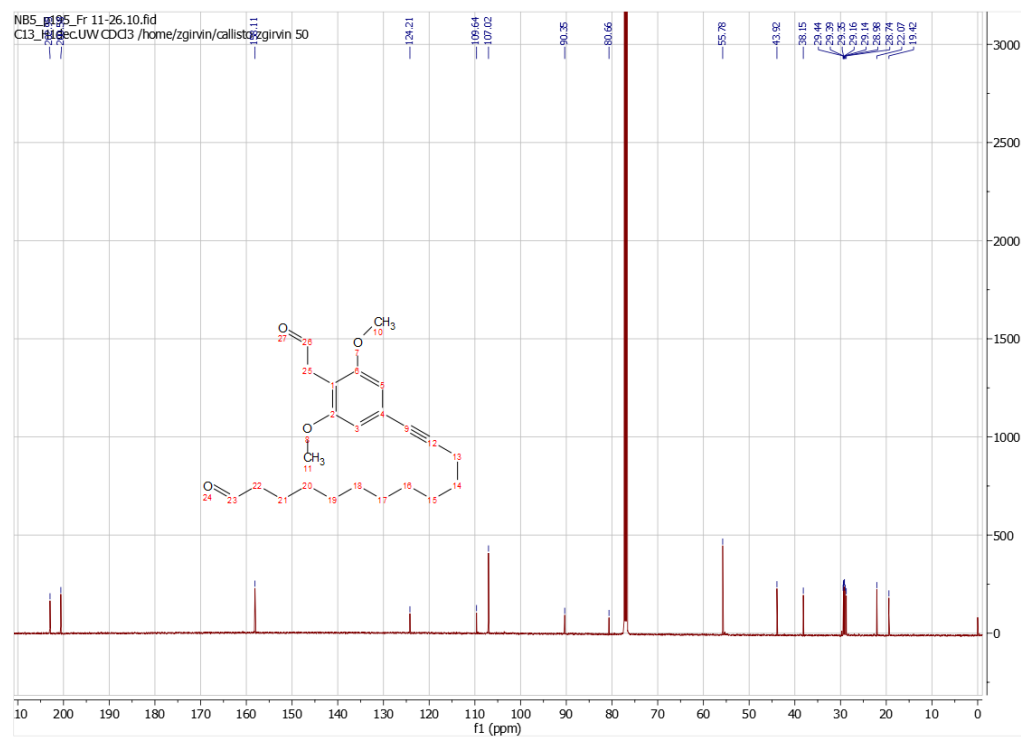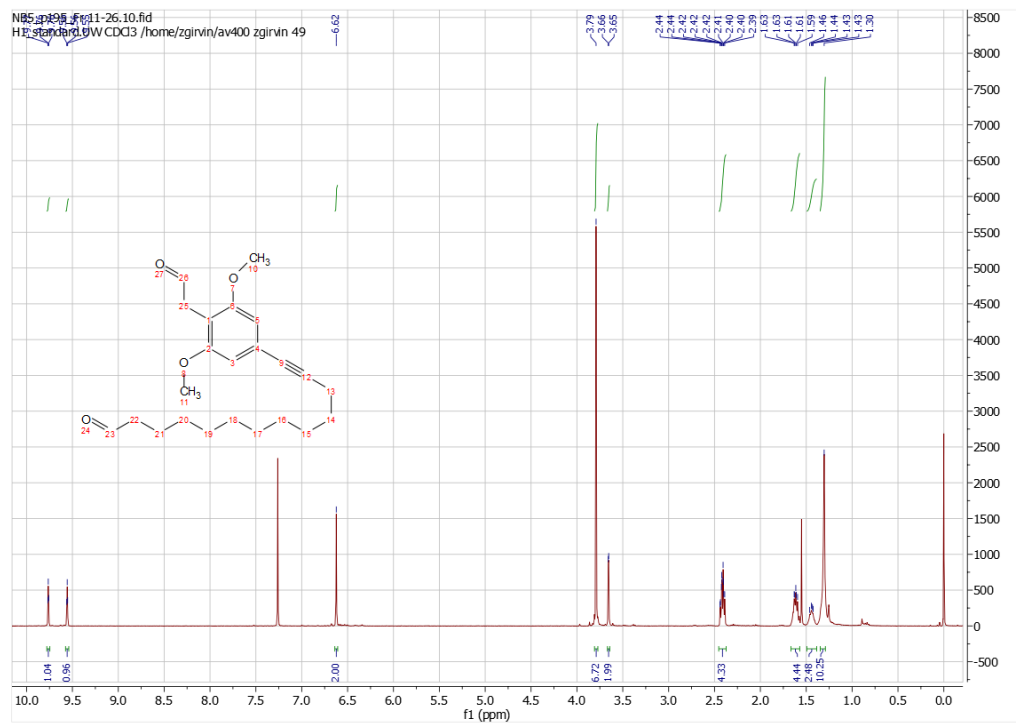
Spectra for **F**
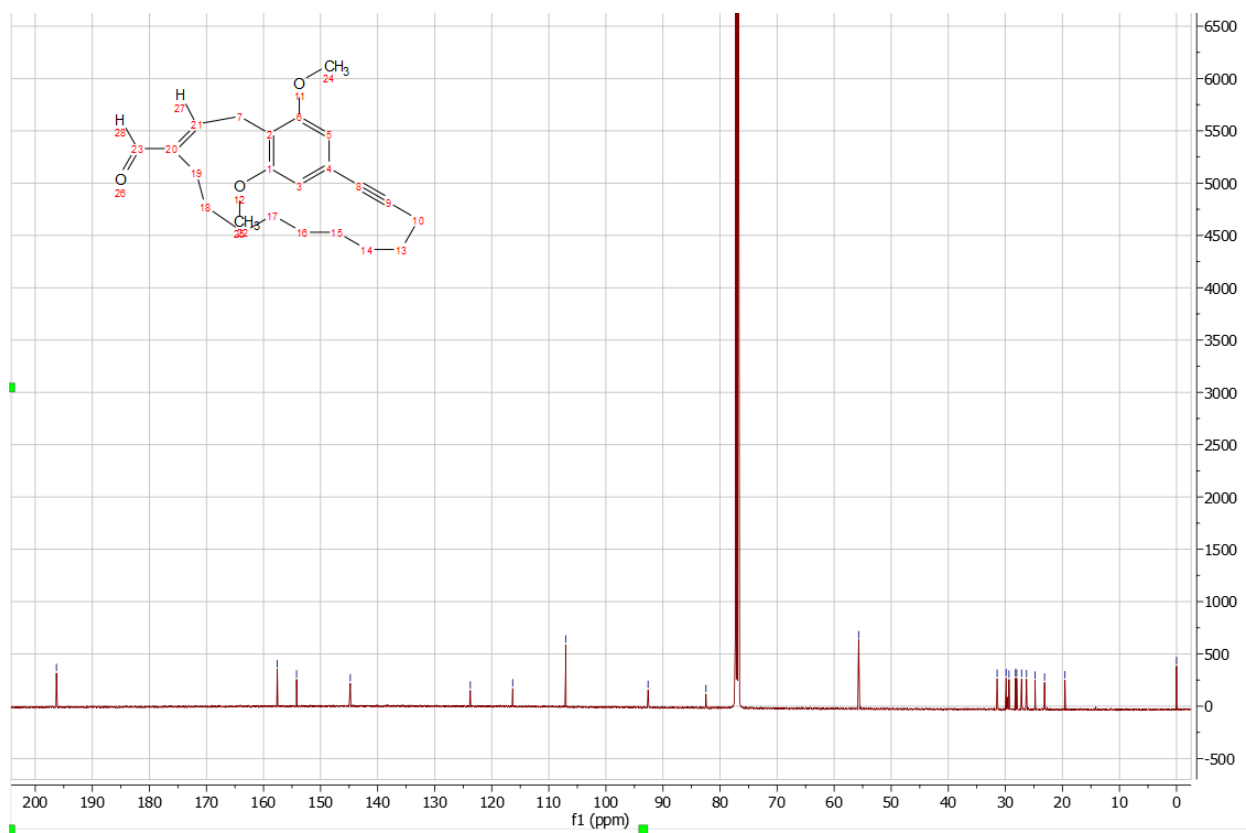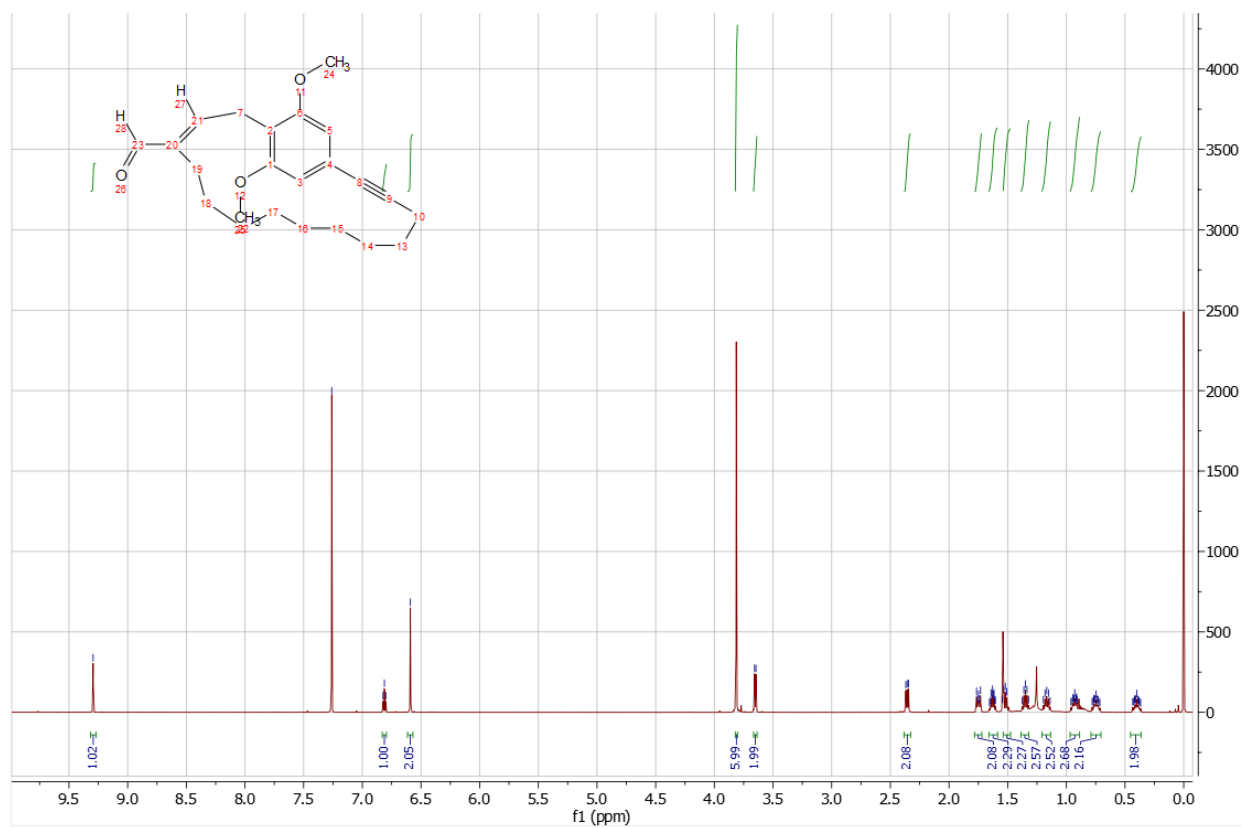
Spectra for **F2**
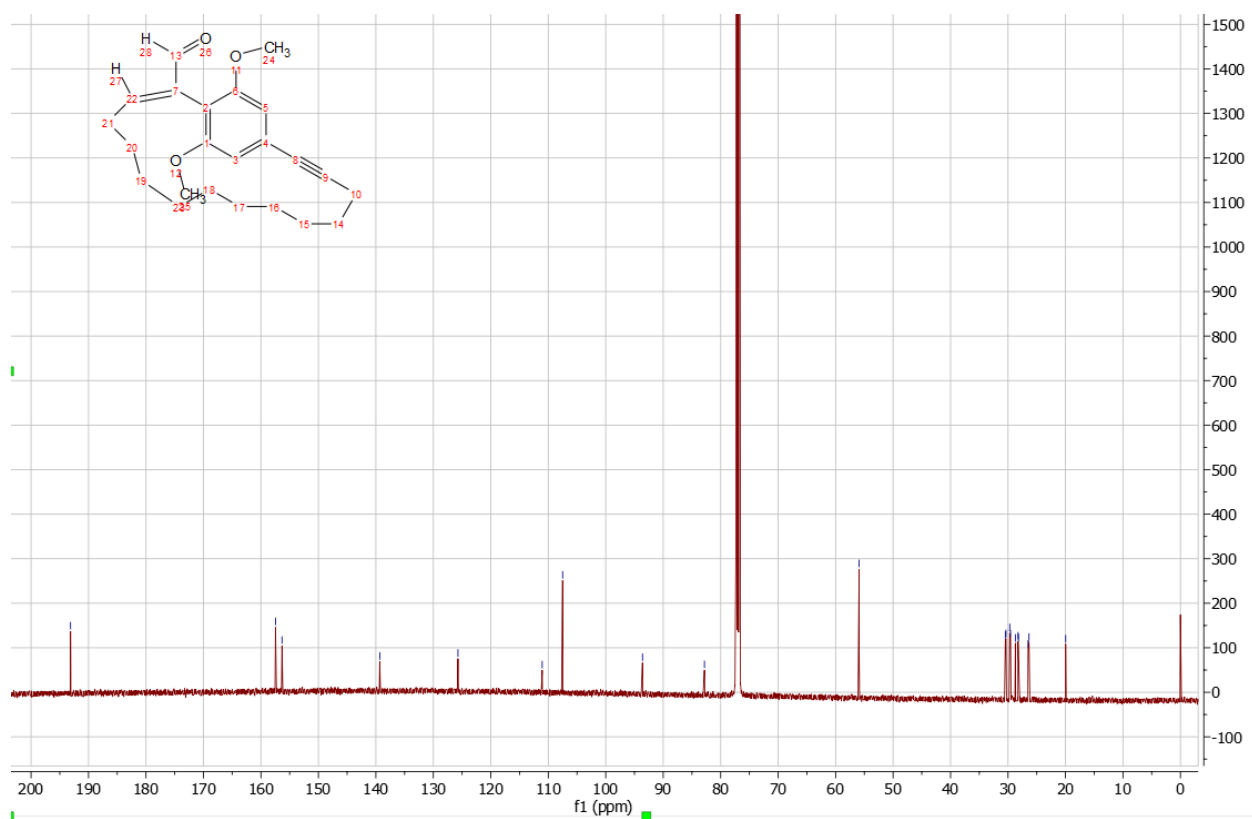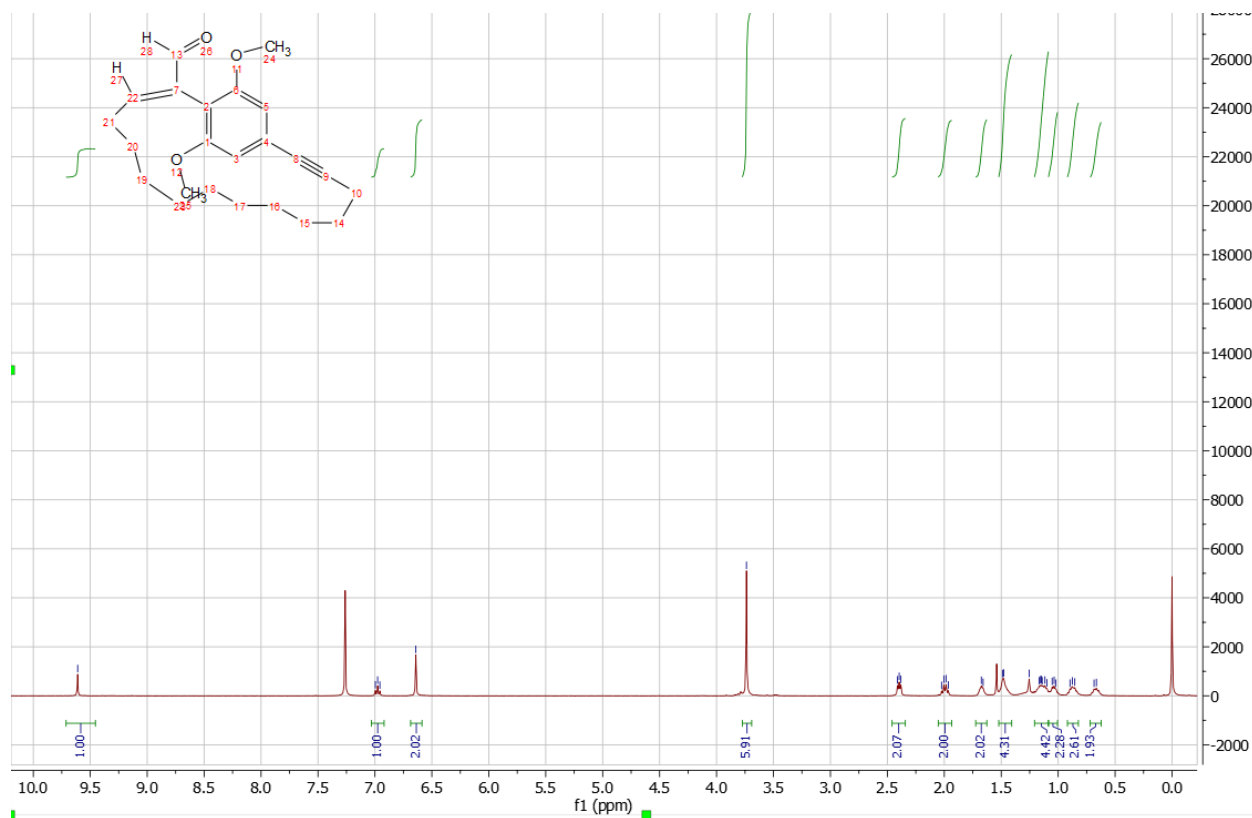
Spectra for **F3**

NMR studies on enal configuration.

The configuration of the enal was established via 1D NOE. The alkene peak of each respective enal was selectively irradiated with a d8 time of 0.3 s. Spectra were acquired at 500 MHz in CDCl$_3$.

1D NOE spectrum for **E1**.

1D NOE spectra for **E2**

1D NOE spectrum for **E3**
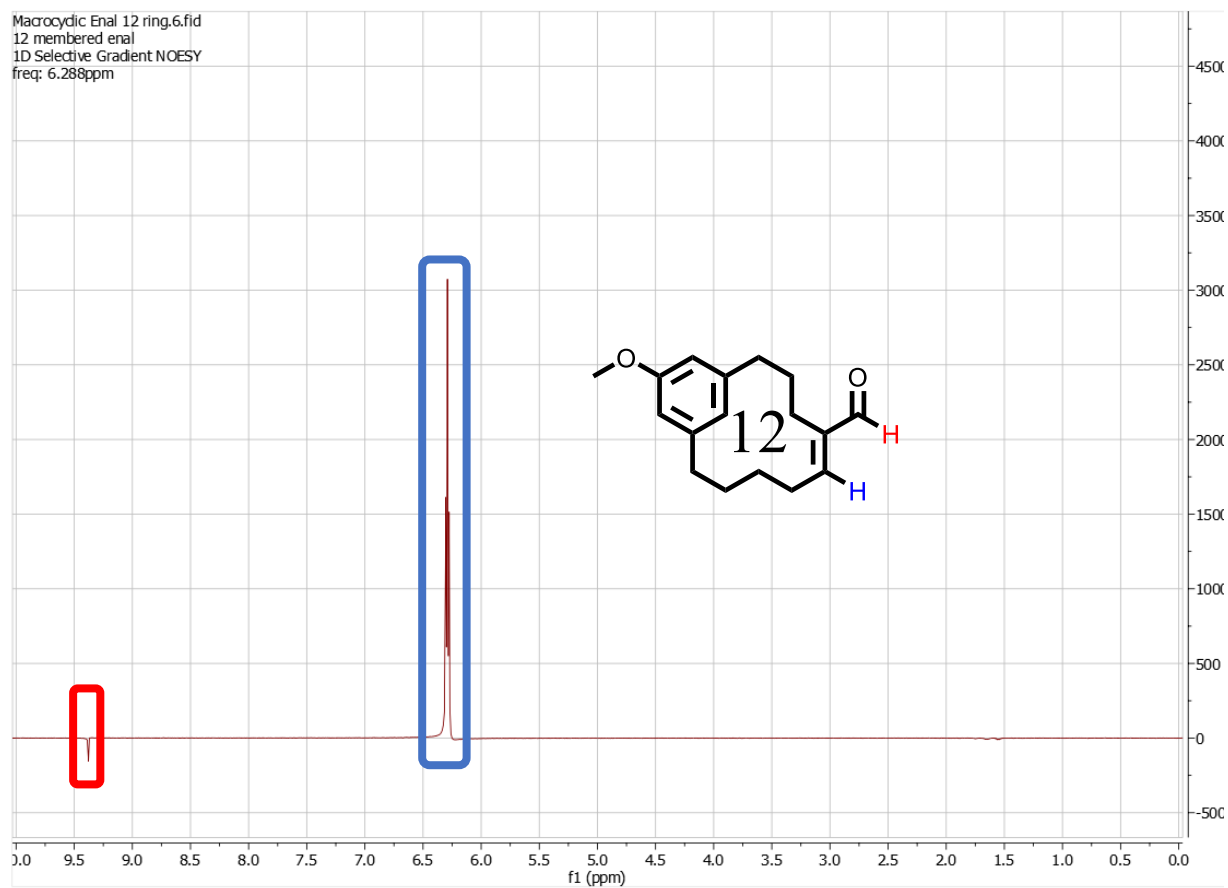
1D NOE spectrum for **E4**
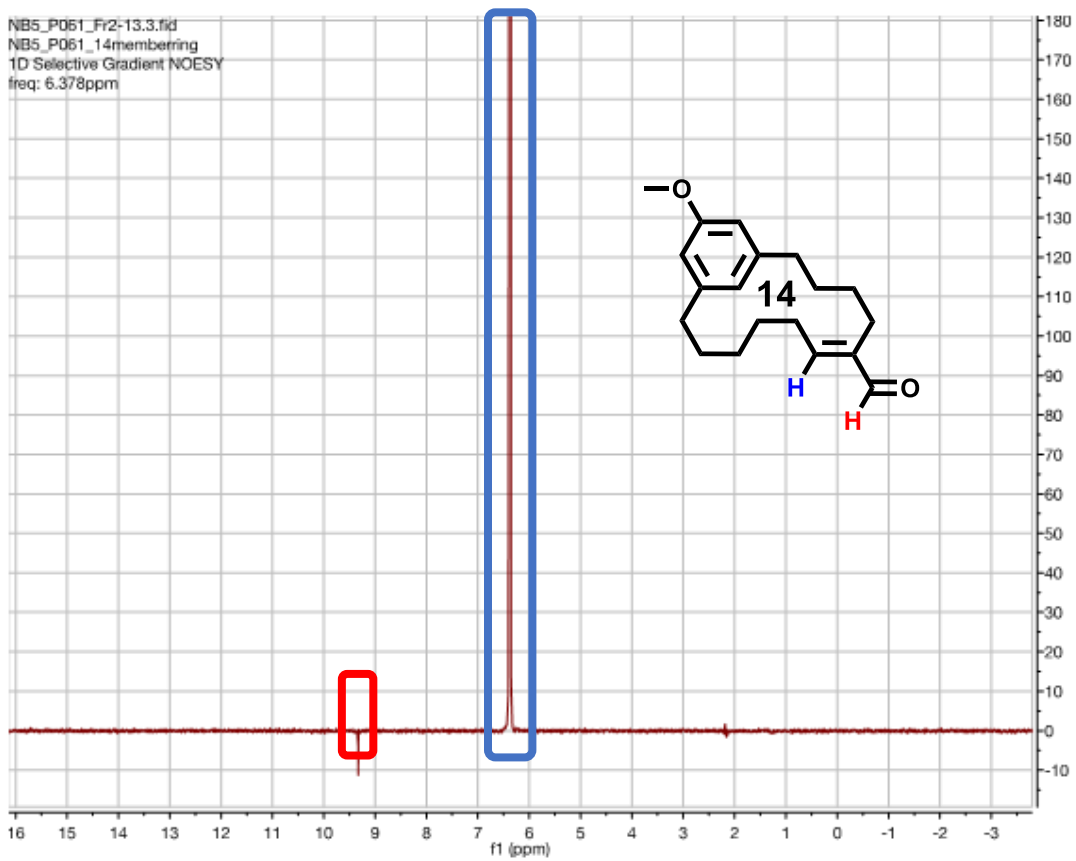
1D NOE spectrum for **G3**
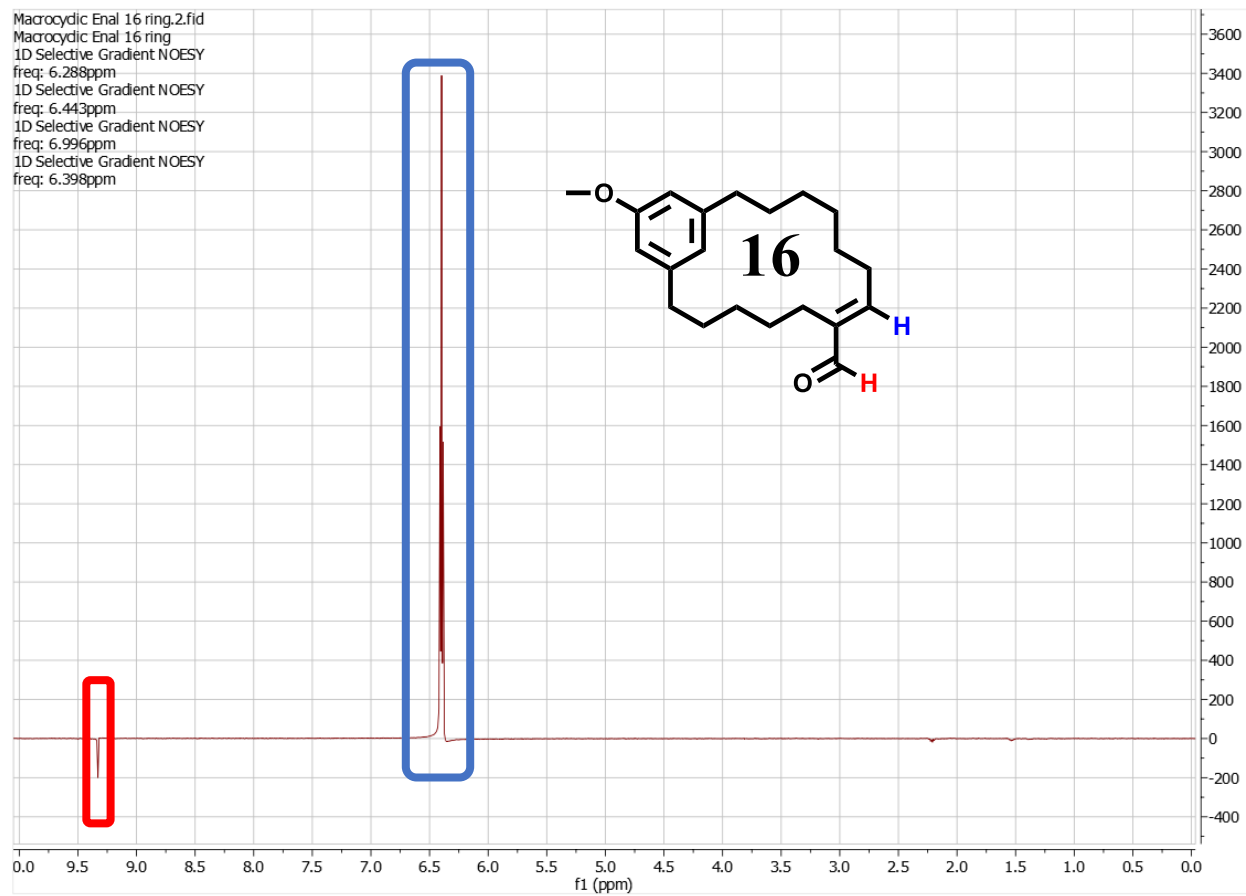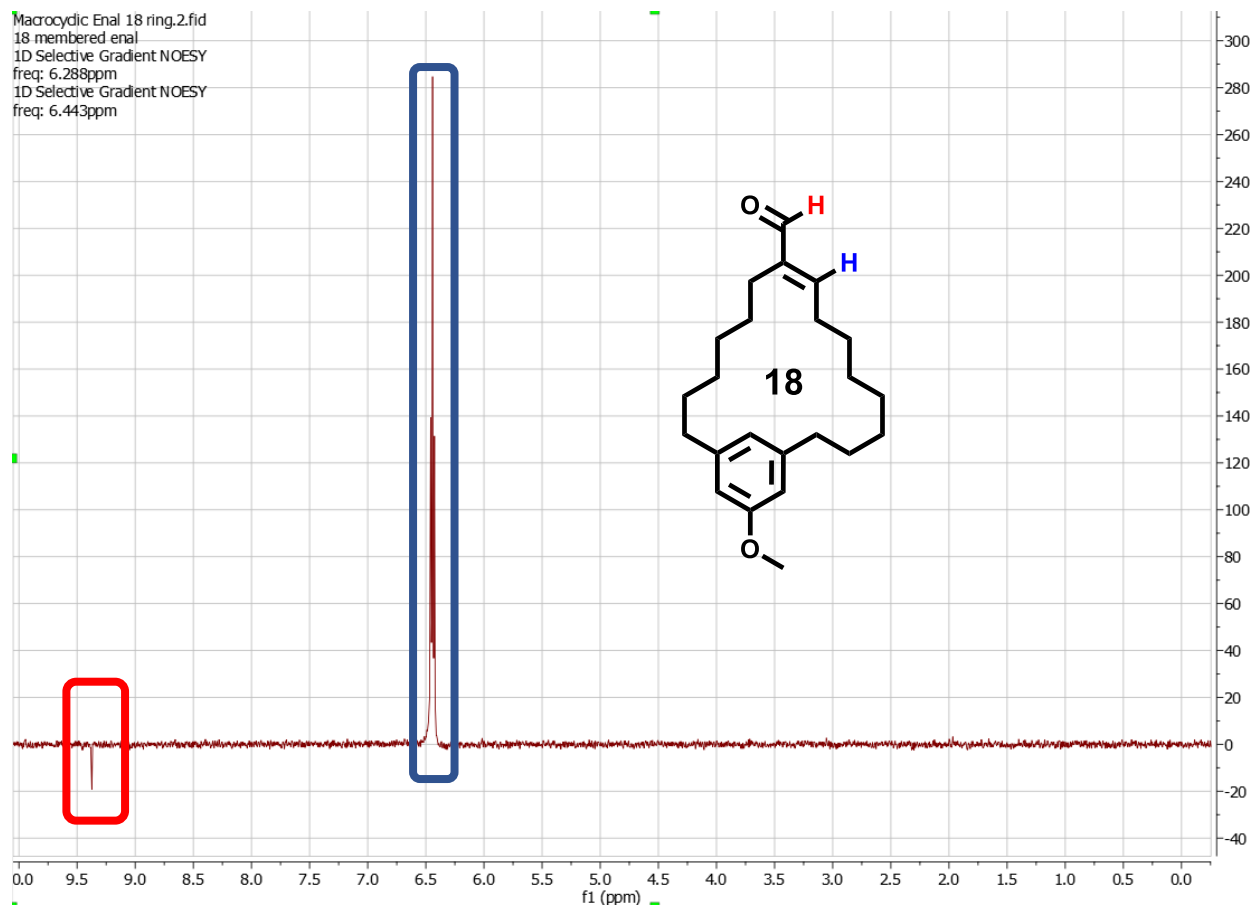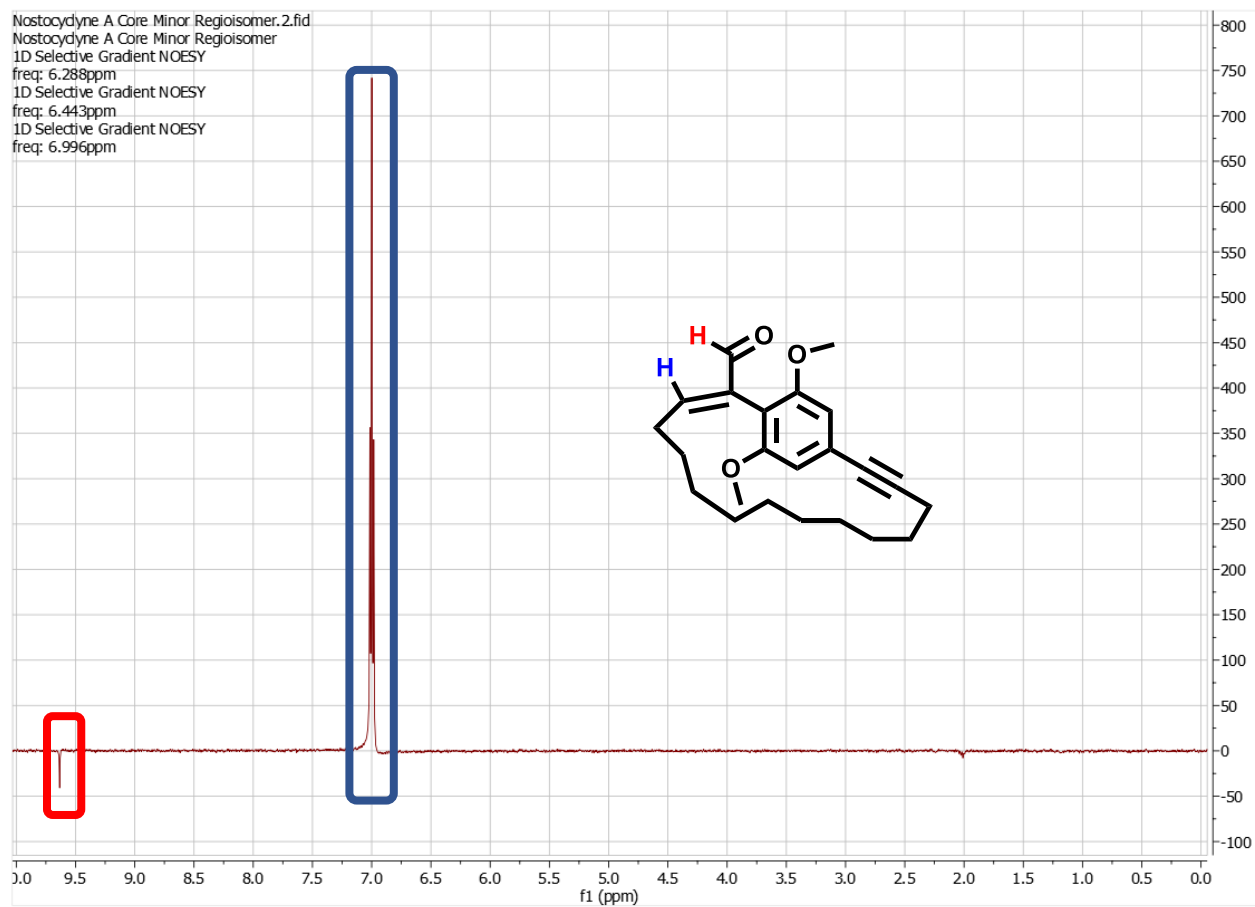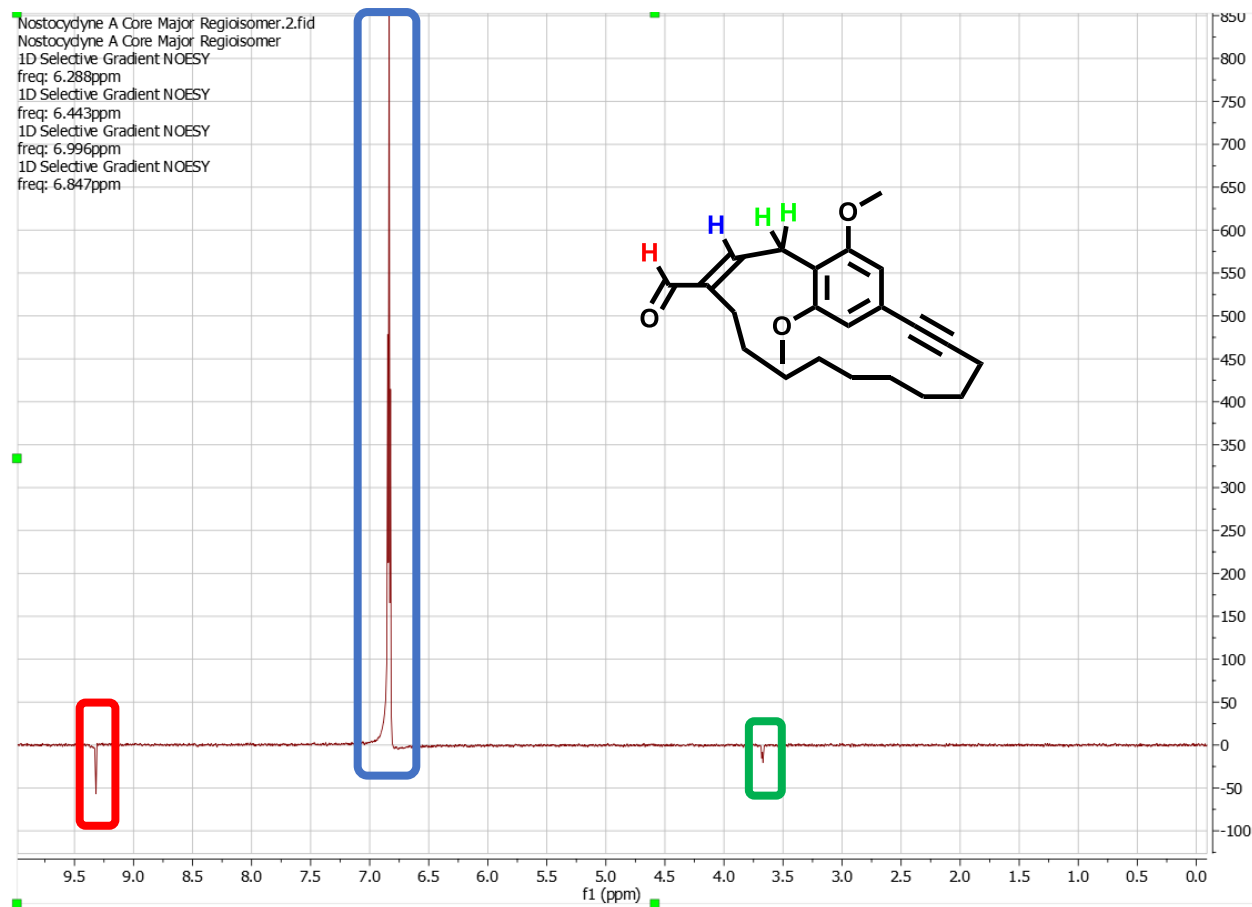
1D NOE spectrum for **G2**
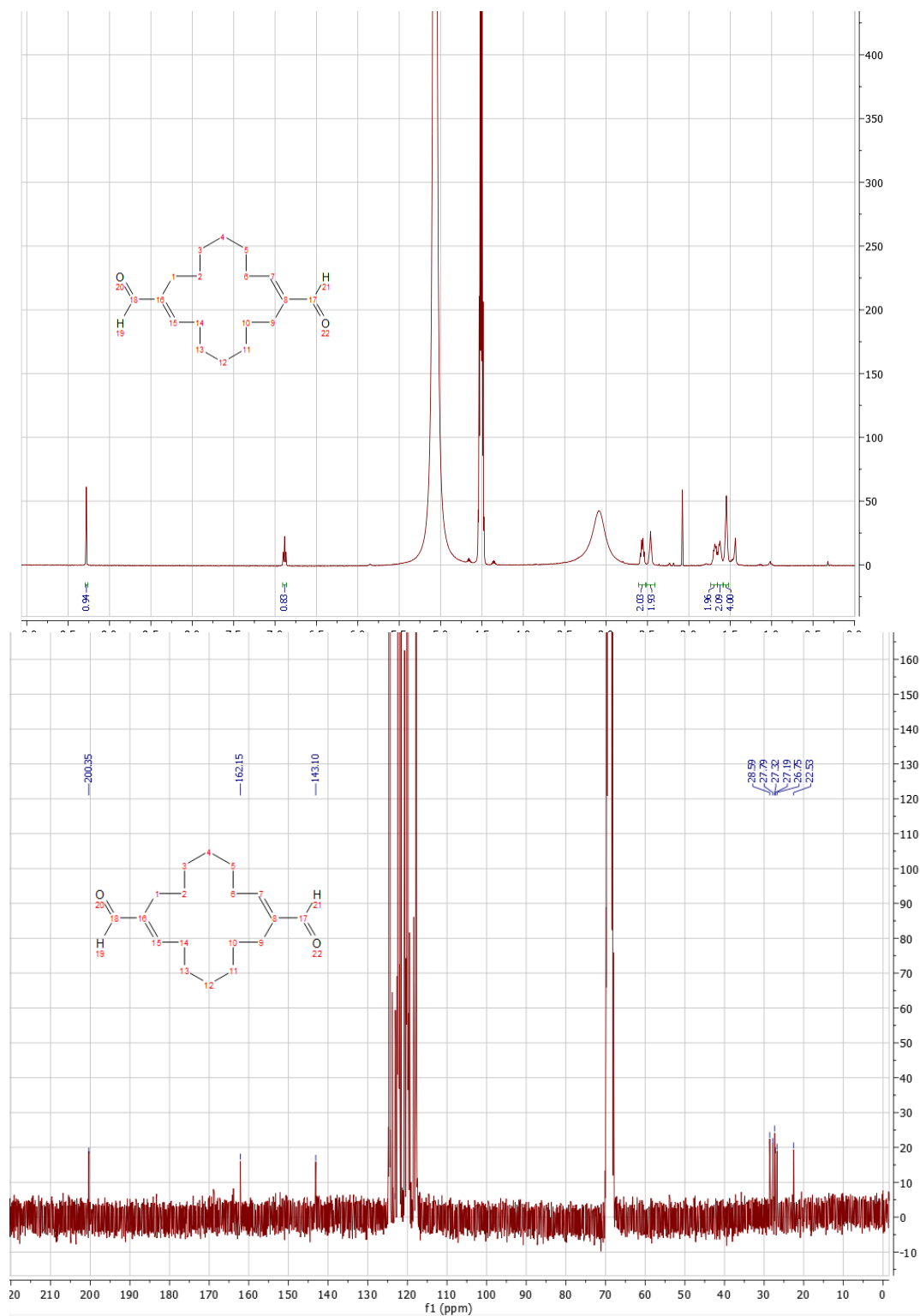
Spectra for **B**. Acquired in d₂-HFIP. Solvent signals appear at 5.18 ppm, 4.51 ppm, and 3.12 ppm in the ^{1}H NMR. Solvent signals appear at 120.27 ppm and 68.02 ppm in the fluorine coupled ^{13}C NMR.

Hydrogen NMR of crude product, which was used as is.

Hydrogen NMR of product used as is.

Hydrogen NMR of product used as is.
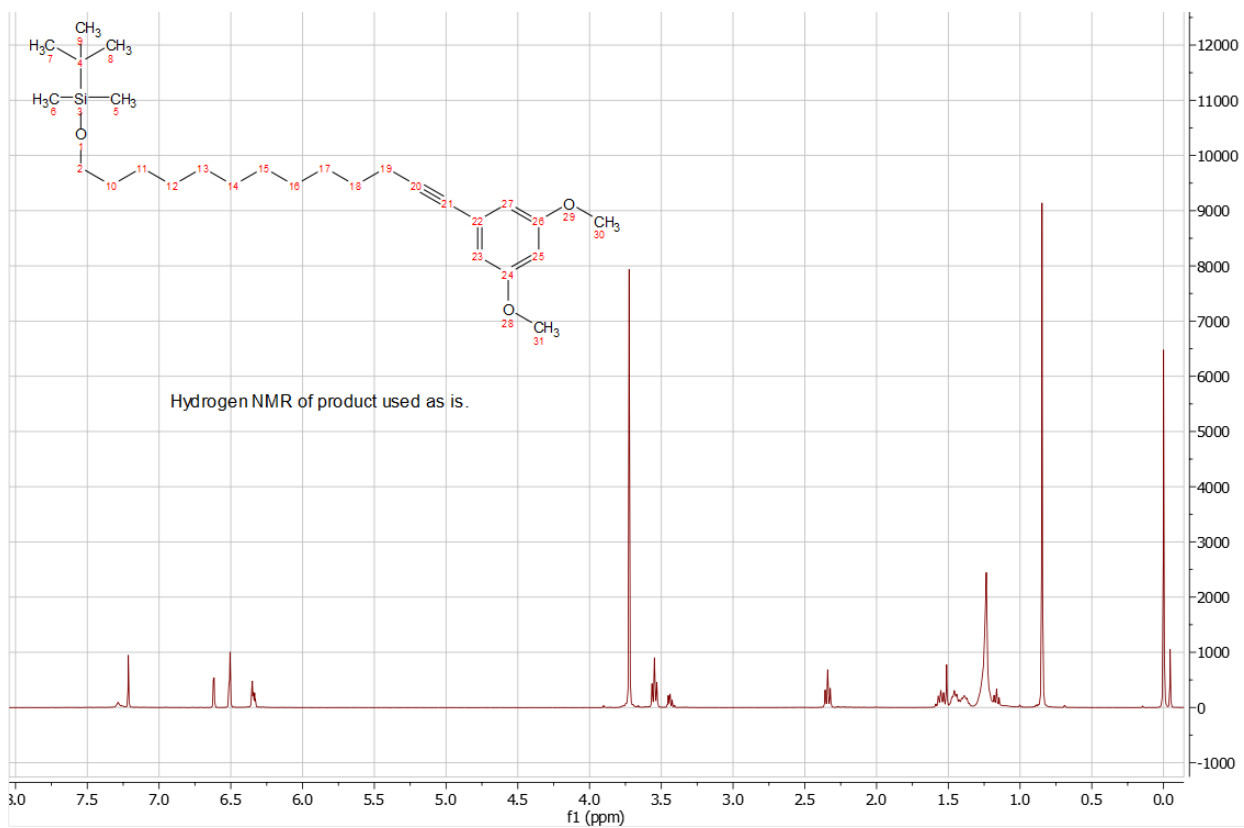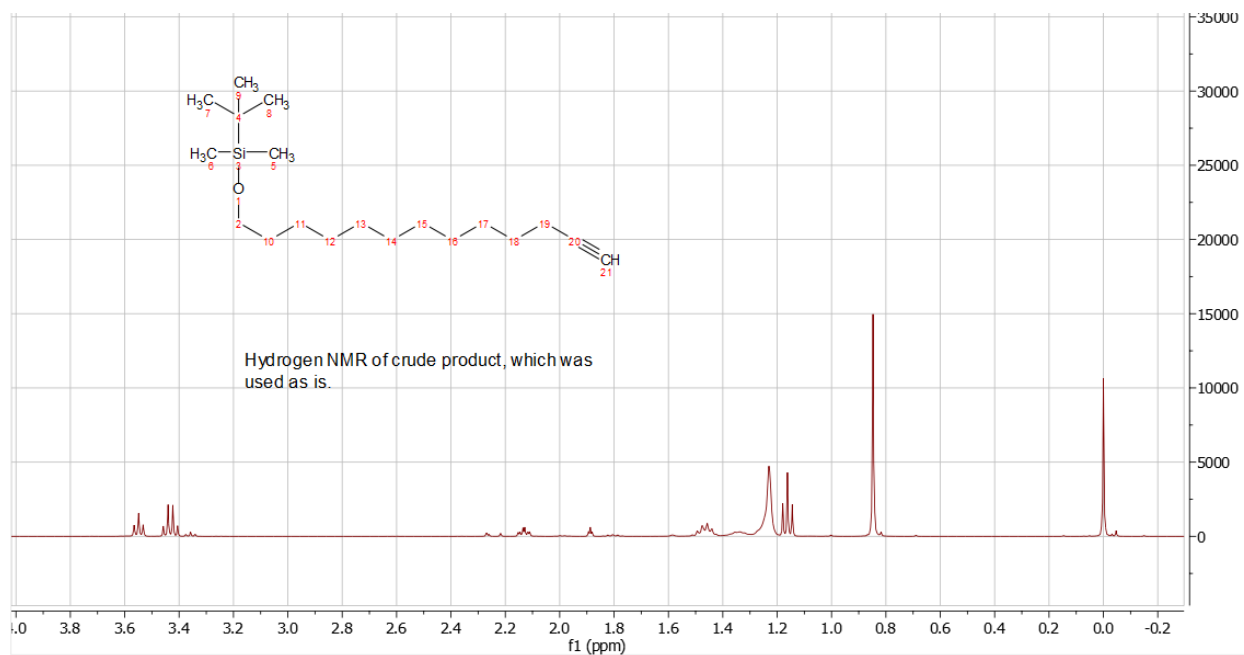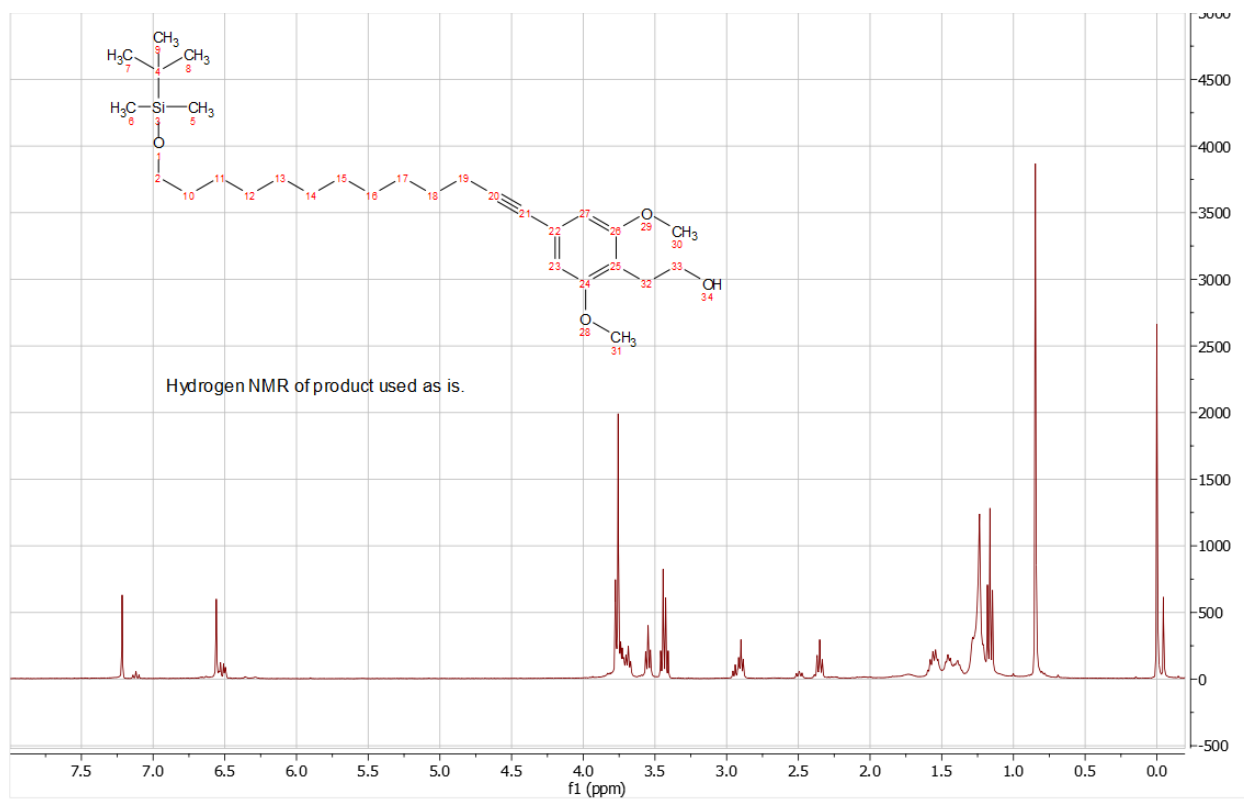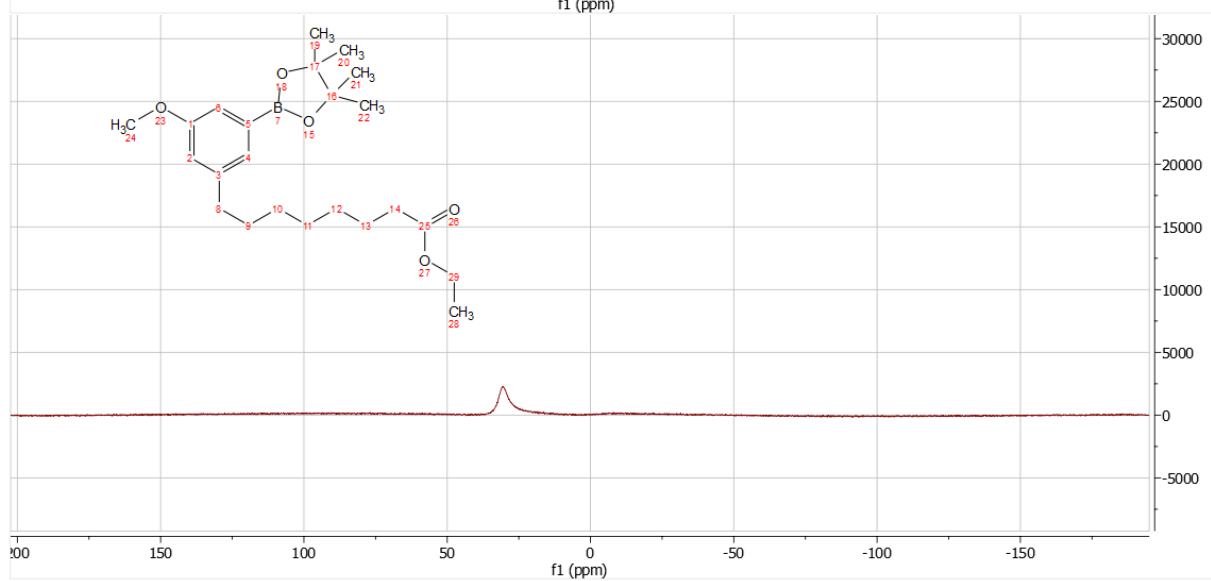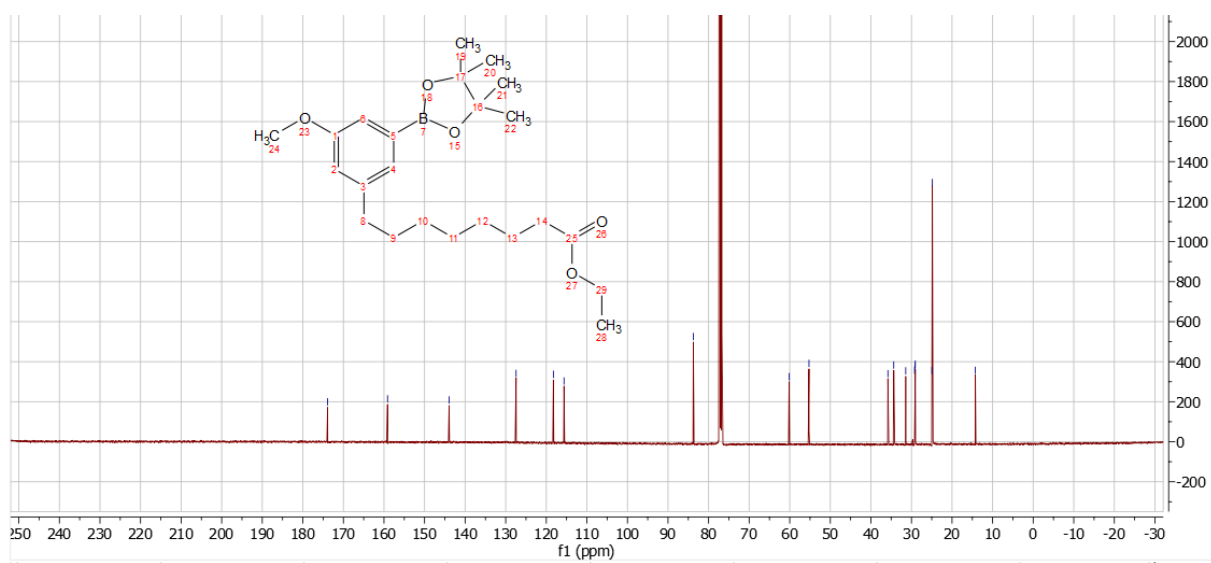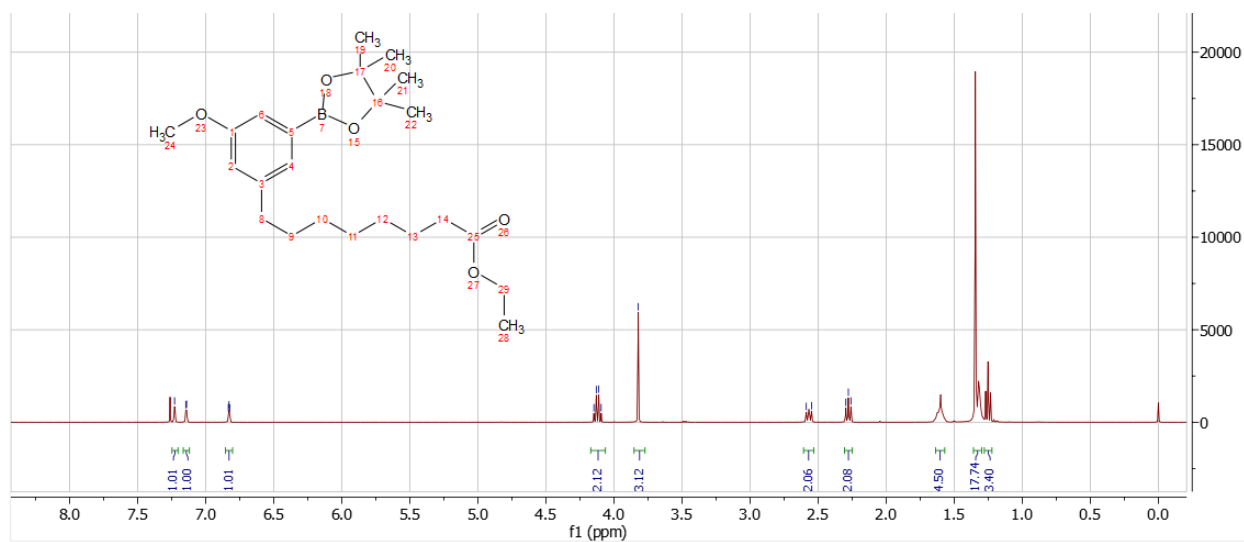
Spectra for **R2**. ¹H, ¹³C, ¹¹B spectra (top to bottom).
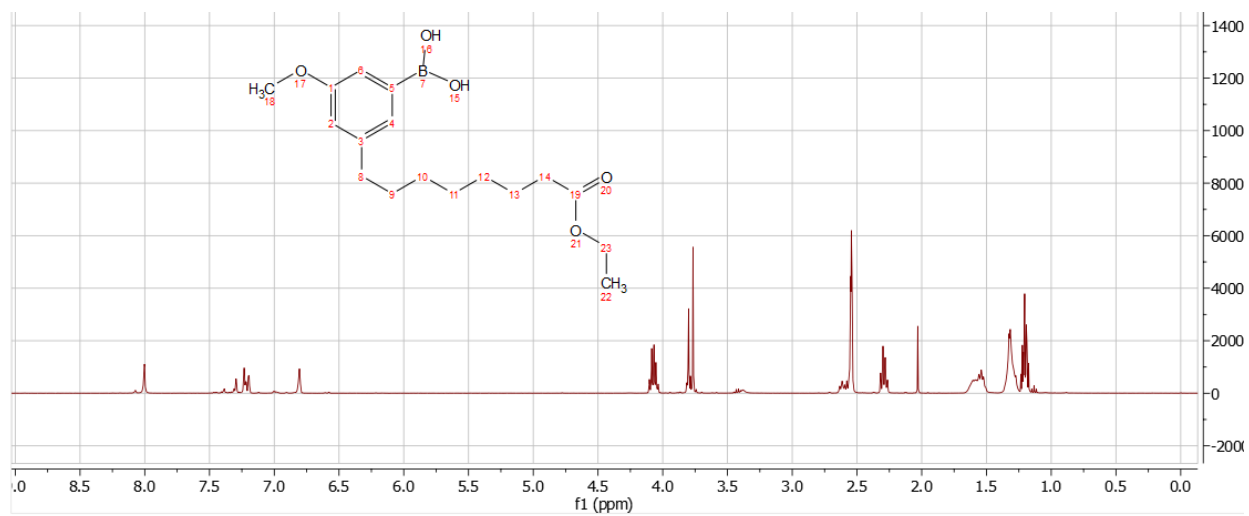
^{1}H spectrum of **R3**. **R3** was carried forward without purification.
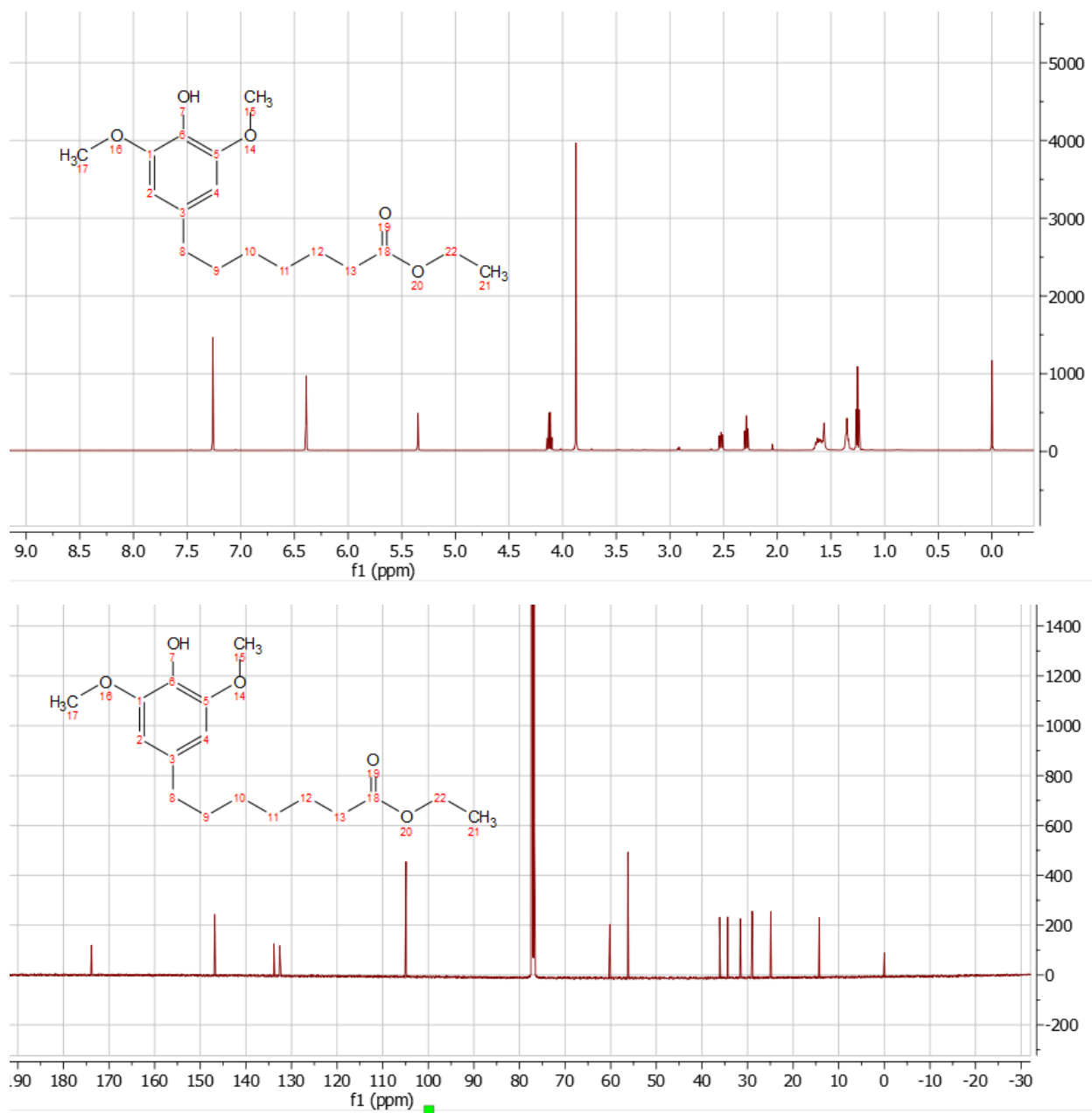
^{1}H and ^{13}C NMR spectra for **R5**.
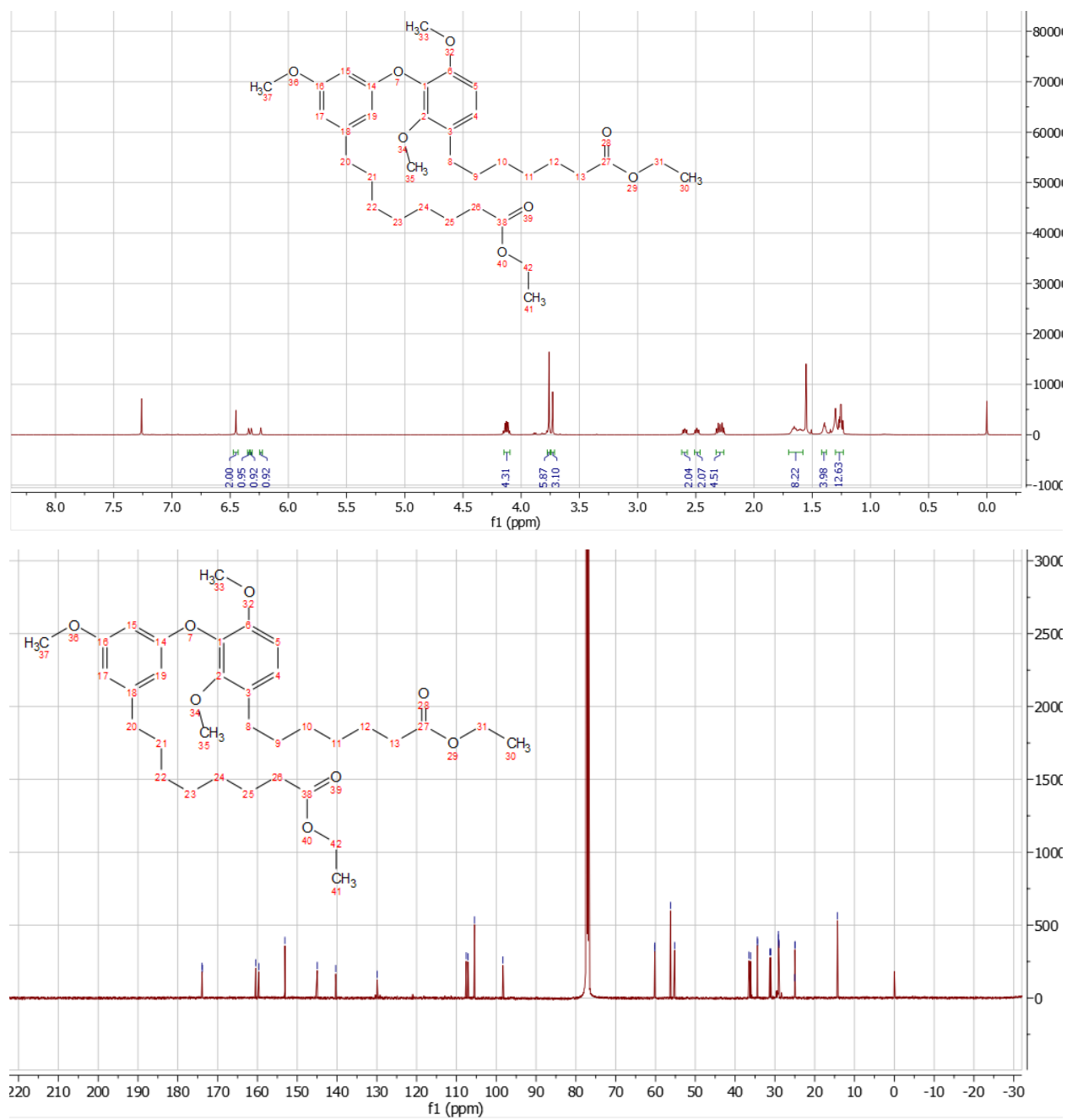
^{1}H and ^{13}C NMR spectra of **R6**.
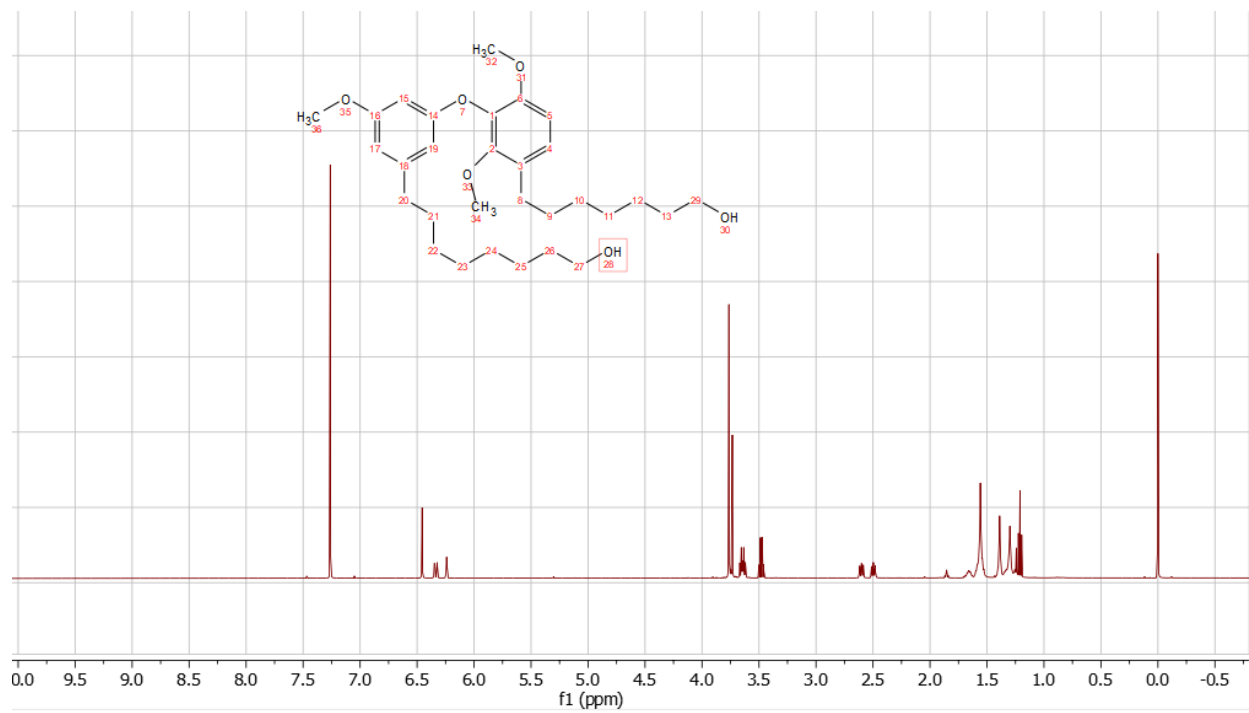
¹H NMR of the crude diol following LiAlH₄ reduction of **R6**. Diethyl ether is present in the ¹H NMR spectrum. The diol was carried forward without further purification.
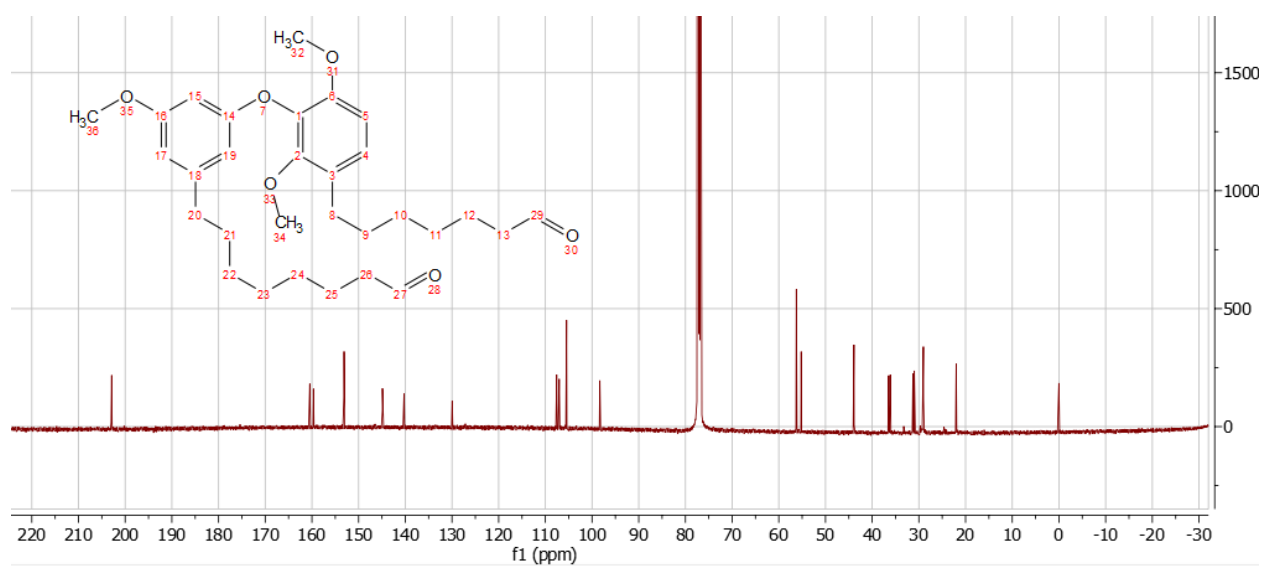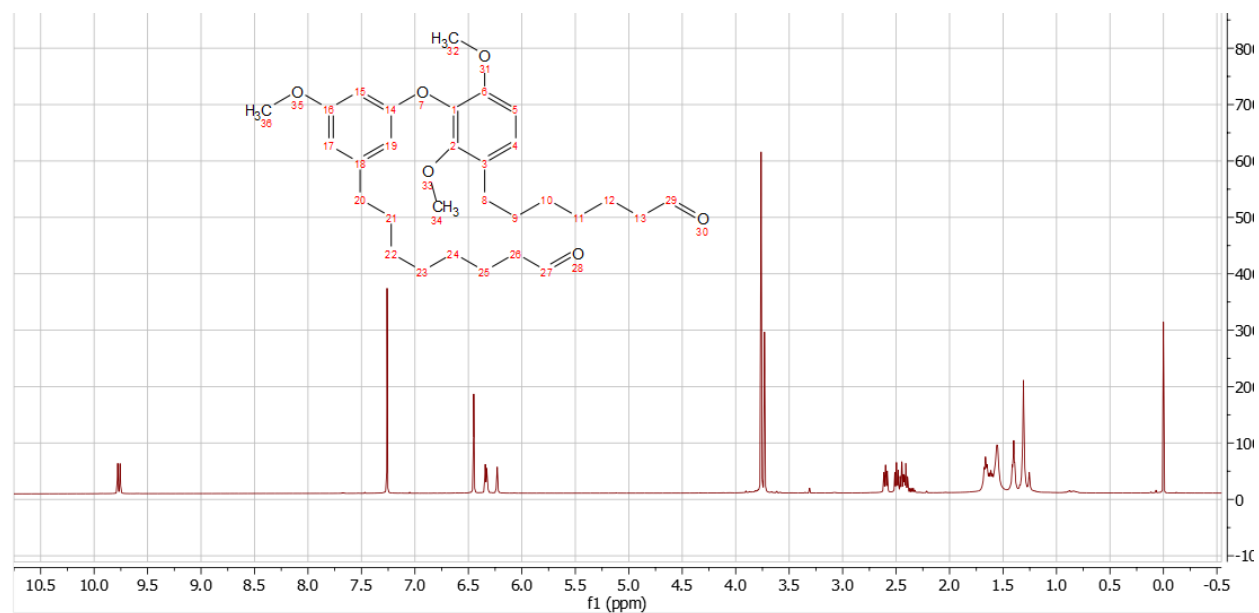
¹H and ¹³C NMR spectra of **R7.**
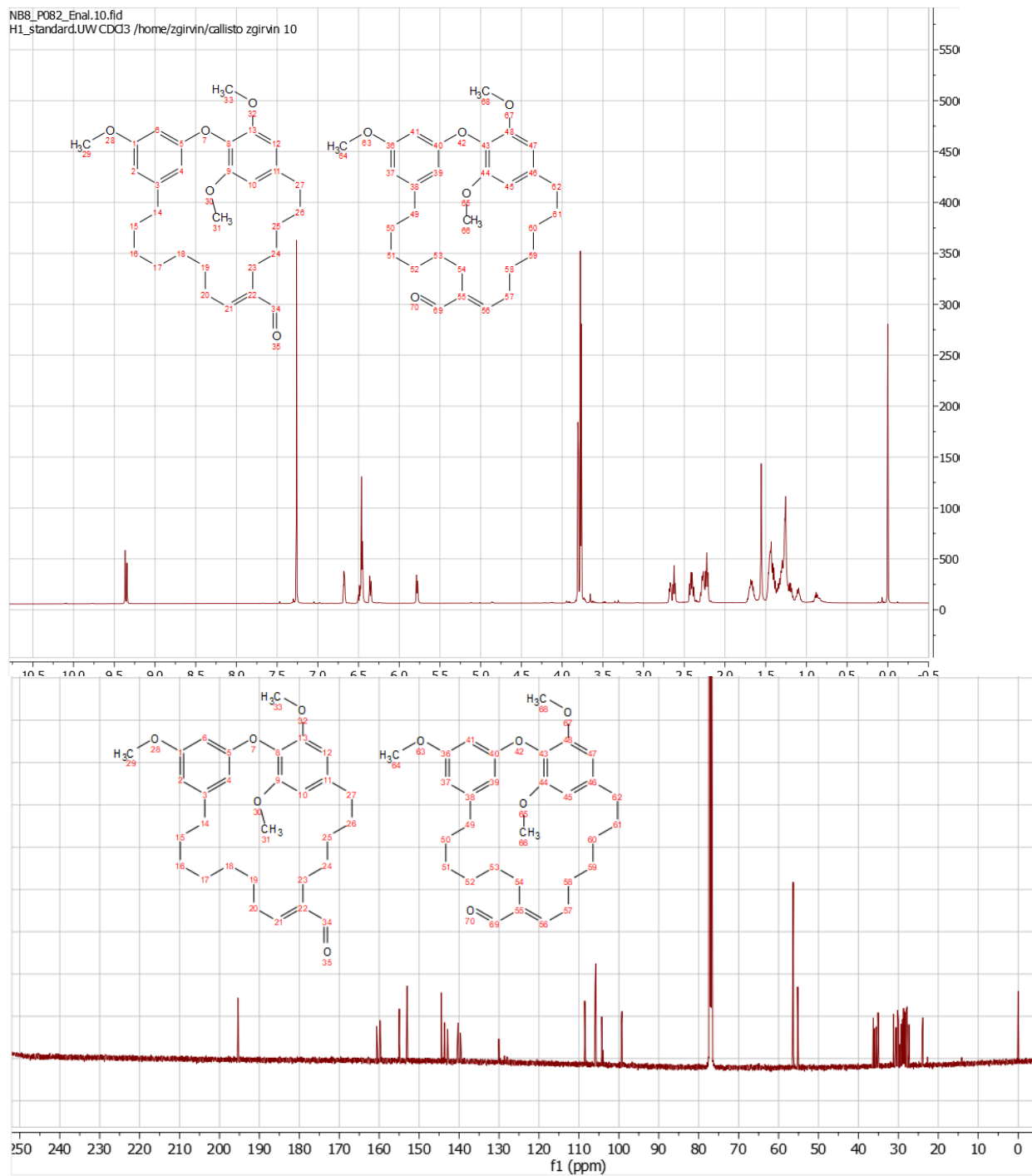
¹H and ¹³C NMR spectra of **R6** as a 1.3 : 1 mixture of regiosiomers. The ratio of regioisomers was determined via integration of each respective aldehyde singlet present in the ¹H spectrum. The mixture was carried forward and decarbonylated.
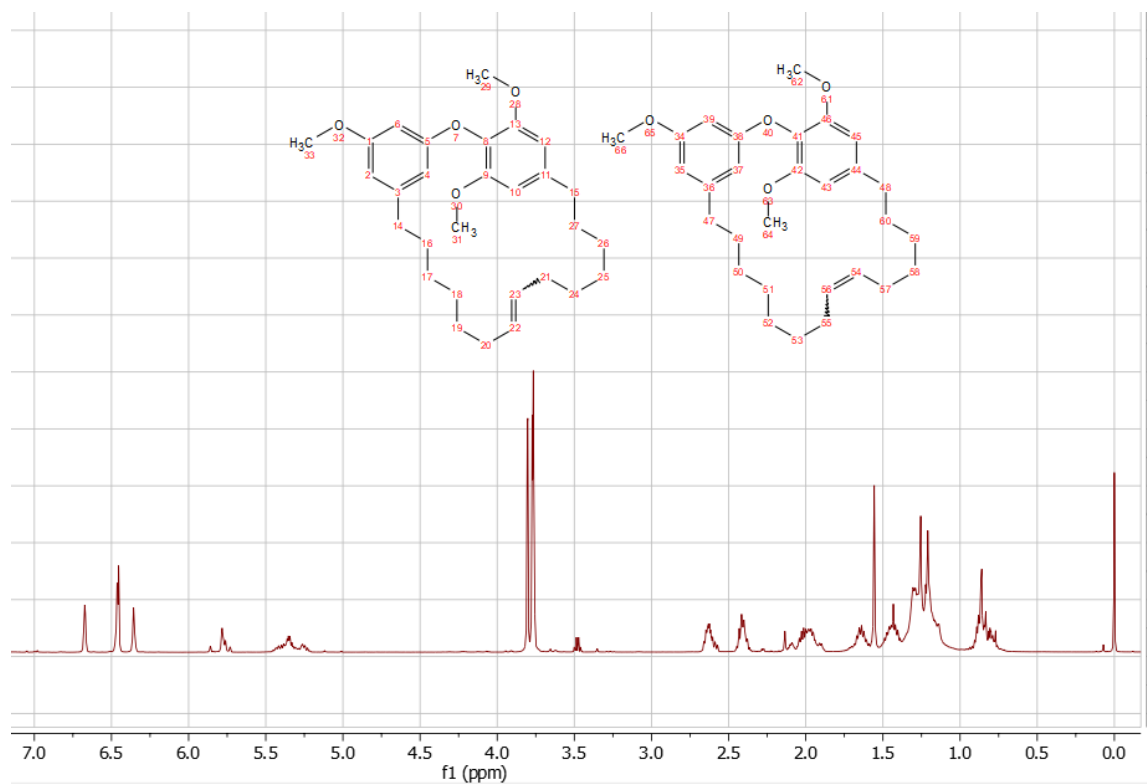
^{1}H and ^{13}C spectra of the clear oil obtained after **R6** were subjected to decarbonylation conditions. There appears to be a mixture of alkene isomers. High resolution mass spectrometry showed a single mass, suggesting a mixture of geometric and/or regio-isomers. Subjecting the alkene mixture to hydrogenation resulted in a single pure compound, **R7**. Alkene geometries for the mixture of compounds is not known.
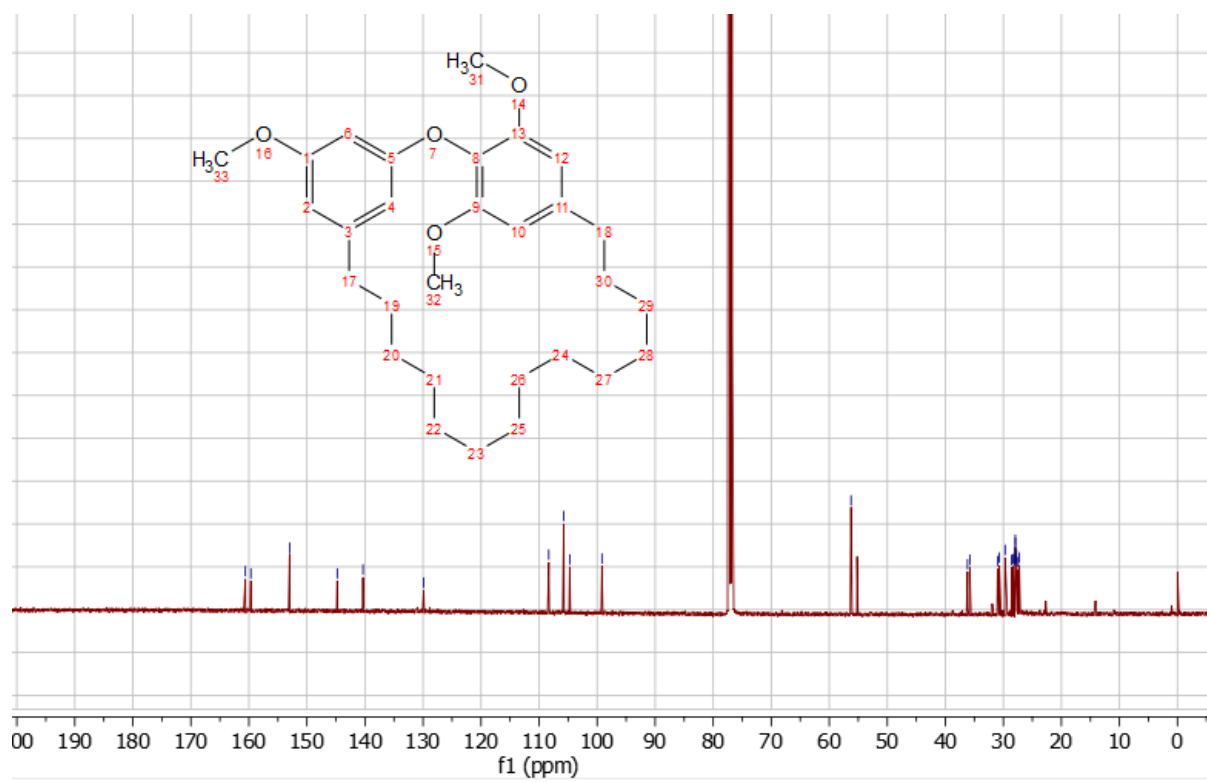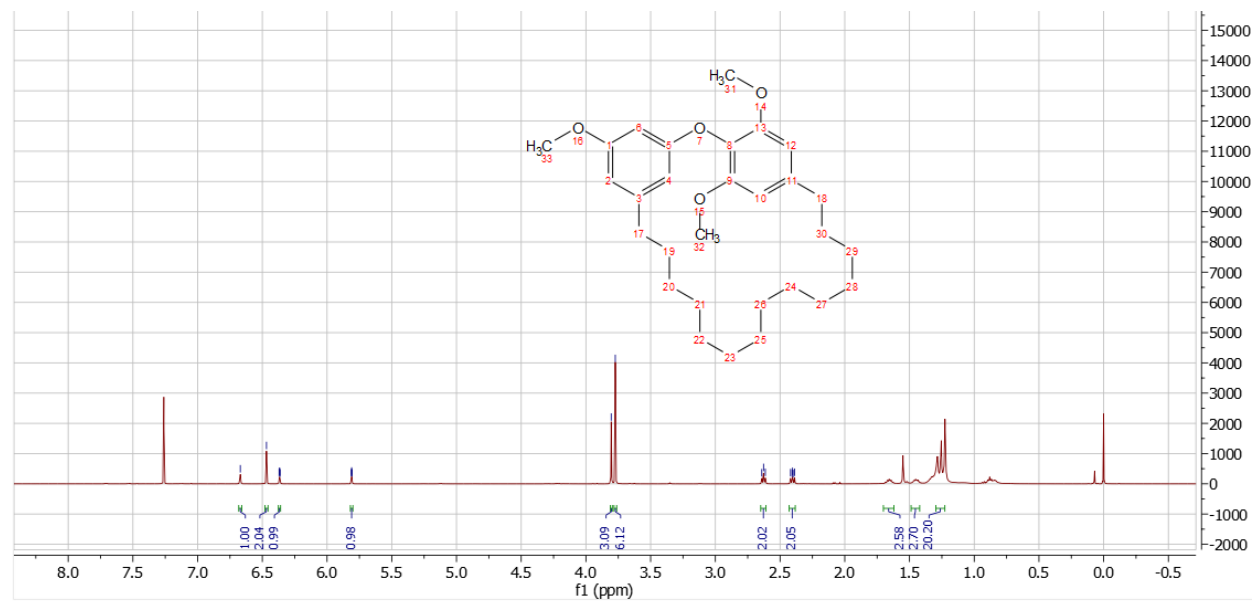
^{1}H and ^{13}C NMR spectra of **R7**.
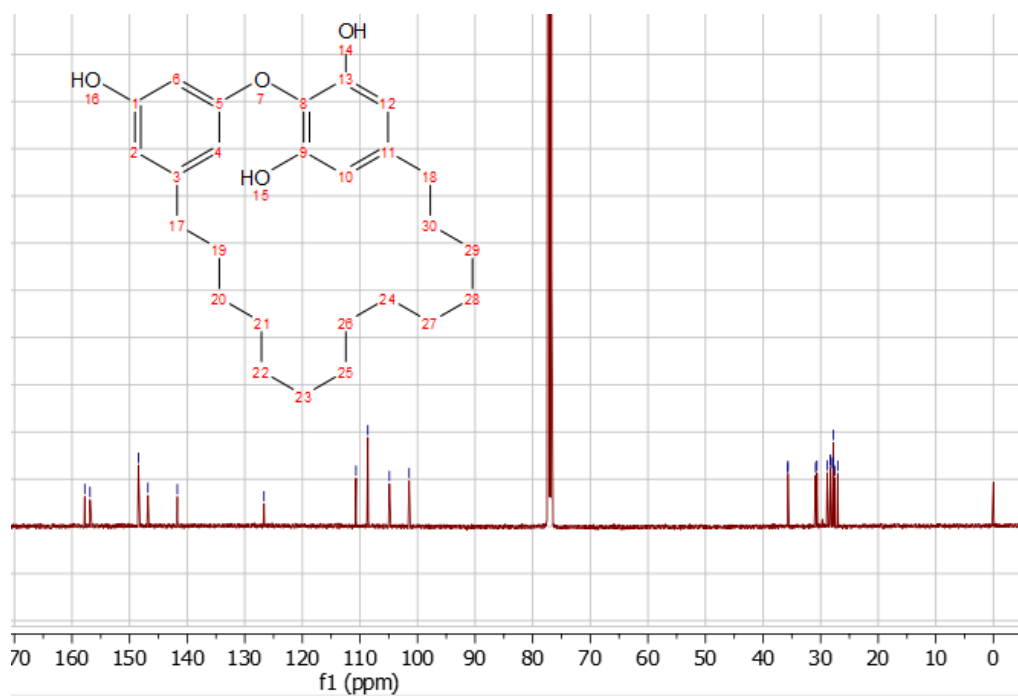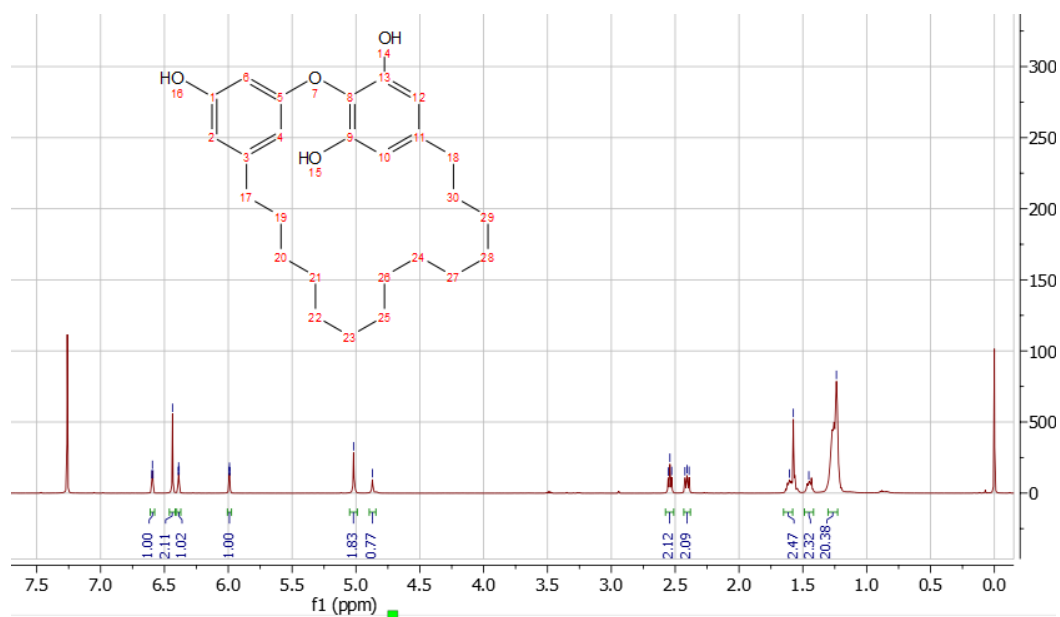
^{1}H and ^{13}C NMR spectra for robustol.
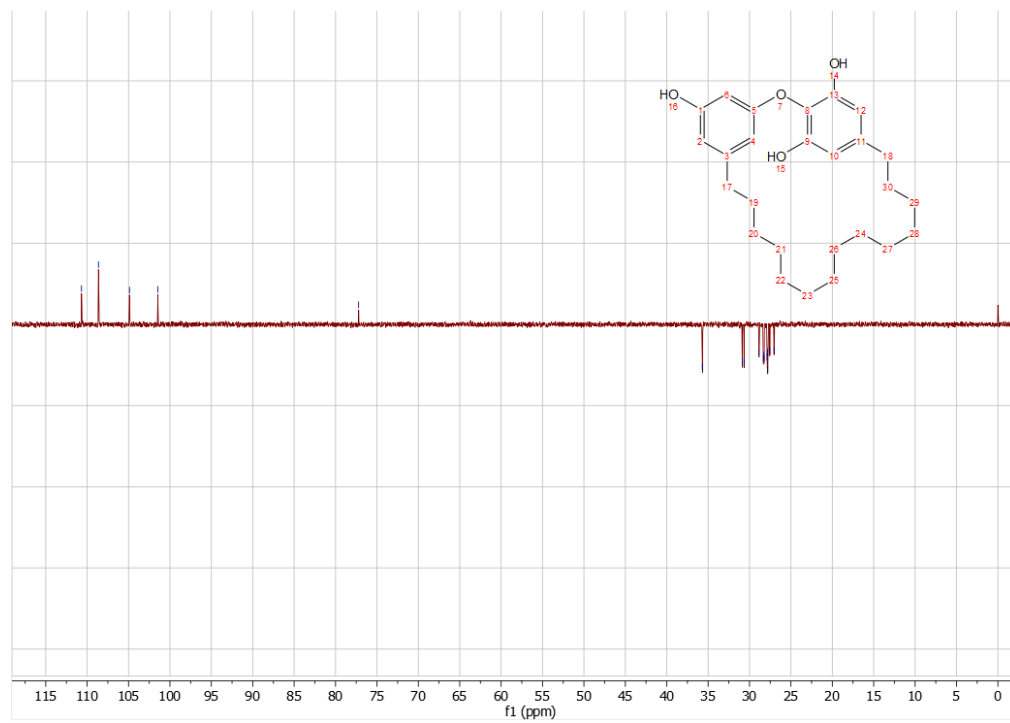
^{13}C dept135 spectra for robustol.

Foldamer-catalyzed reaction of D1 --> Cyclodimers

D1

10 mol % Catalyst 1
1 eq Propionic Acid
1 eq Triethylamine

96:4 iPrOH:H_2O, 1 mM D1
37° C, 10 days

Unsymmetrical Enal formed after intermolecular aldol reaction between two molecules of D1.

Potential cyclodimers formed (can also have geometric isomers based on alkene configuration)
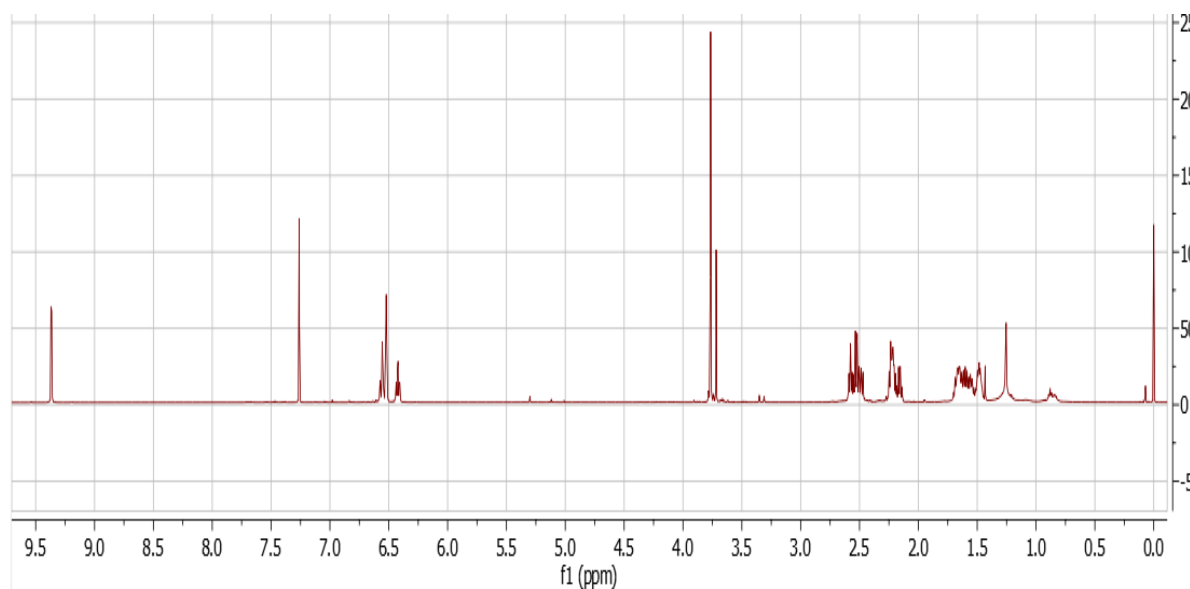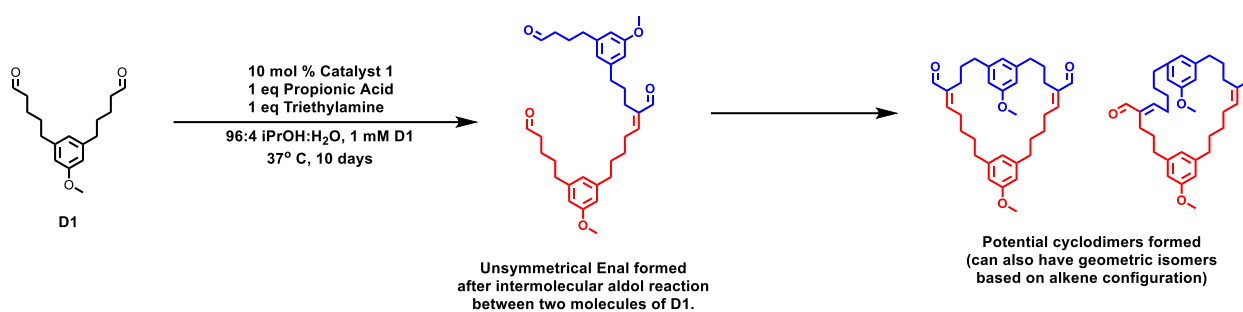
^{1}H NMR spectrum of the mixture of cyclodimers generated from the foldamer-catalyzed reaction of dialdehyde **D1**.
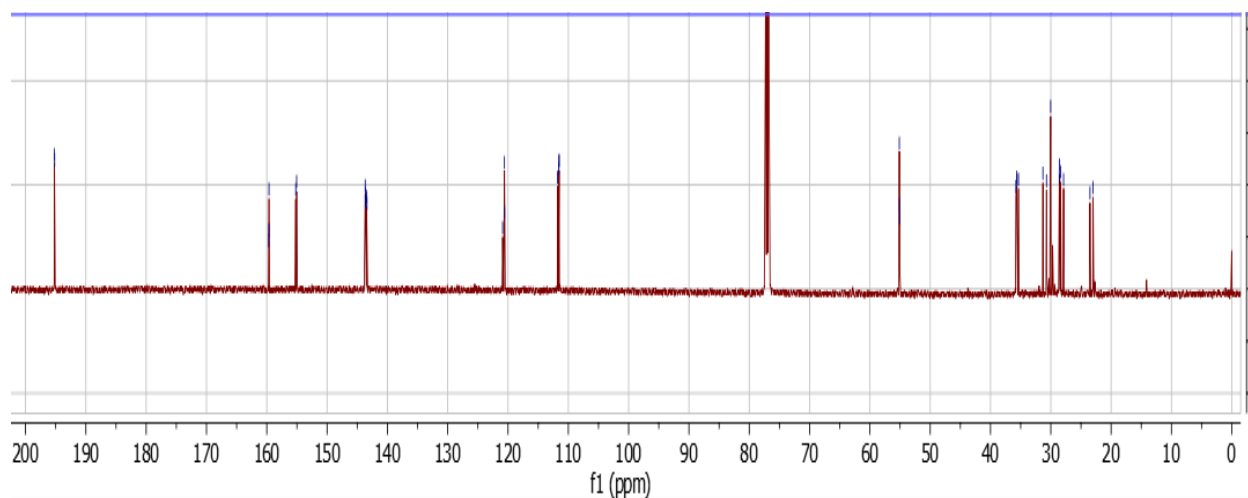
^{13}C NMR spectrum for the mixture of cyclodimers generated from the foldamer-catalyzed reaction of dialdehyde **D1**.
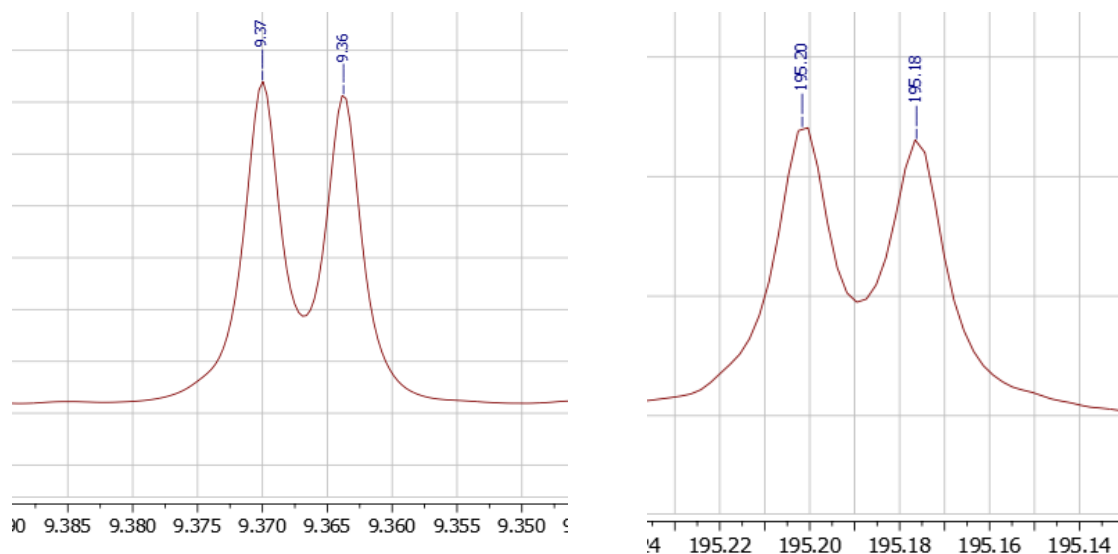
Zoom-in on the ^{1}H NMR (above left) and ^{13}C NMR spectrum (above right) of the cyclodimers formed by foldamer-catalyzed cyclization of D1. The ^{1}H NMR region from 9.35 – 9.385 ppm is depicted, which shows two resolved aldehyde singlet signals. The ^{13}C NMR region from 195.14 – 195.22 ppm is depicted, which shows two resolved aldehyde signals.

HRMS *m/z* (ESI): calculated for $[C_{34}H_{44}O_4 + NH_4]^+$ 534.3578, found 534.3573.

MALDI-TOF MS spectra reported below contain multiple peaks, which correspond to [M+H], [M+Na], and [M+K] ions. The labeled peak is identified under the spectrum according to which ion it pertains to.
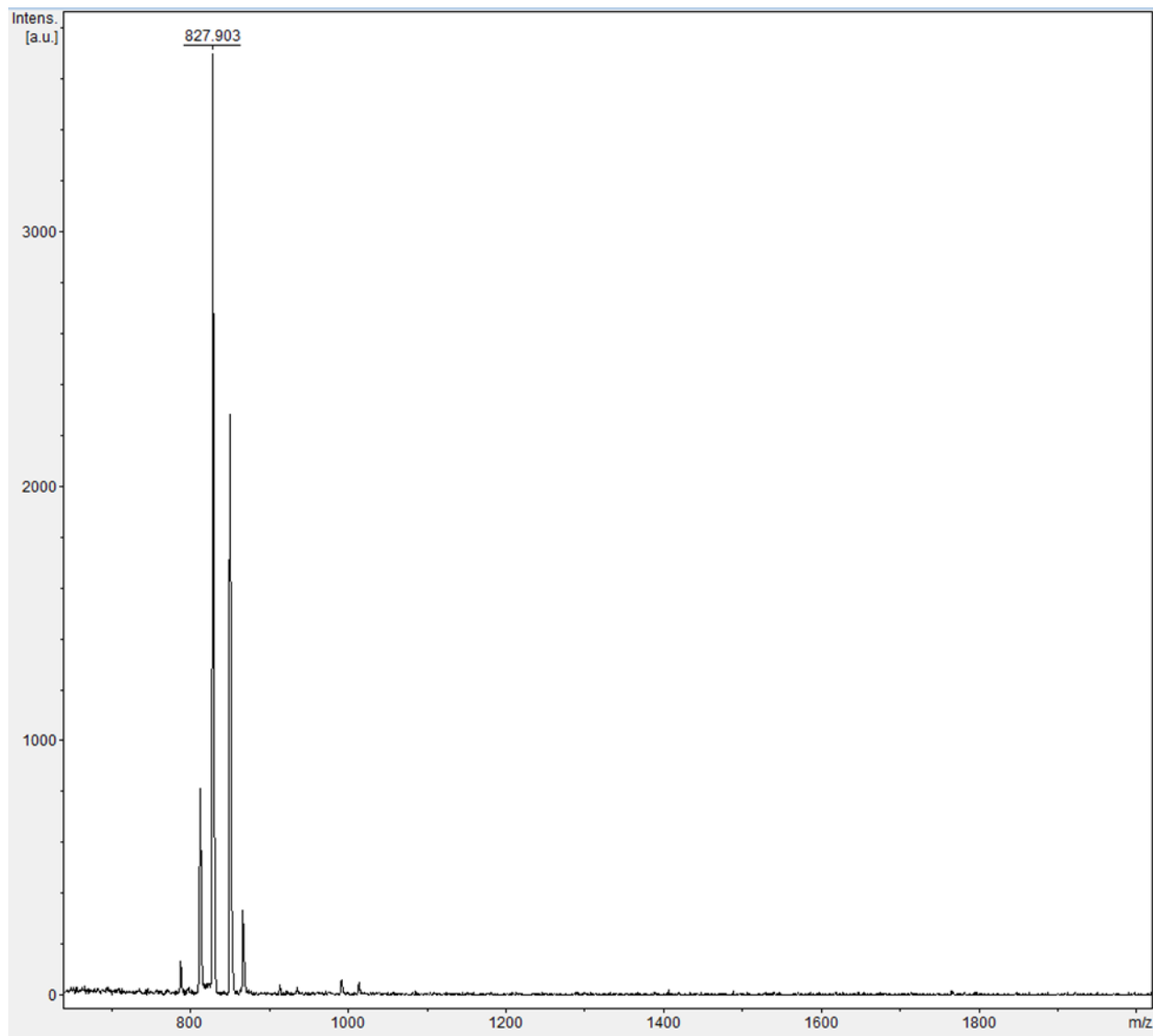
Catalyst **1** M + H calculated = 828.001, 827.903 found.
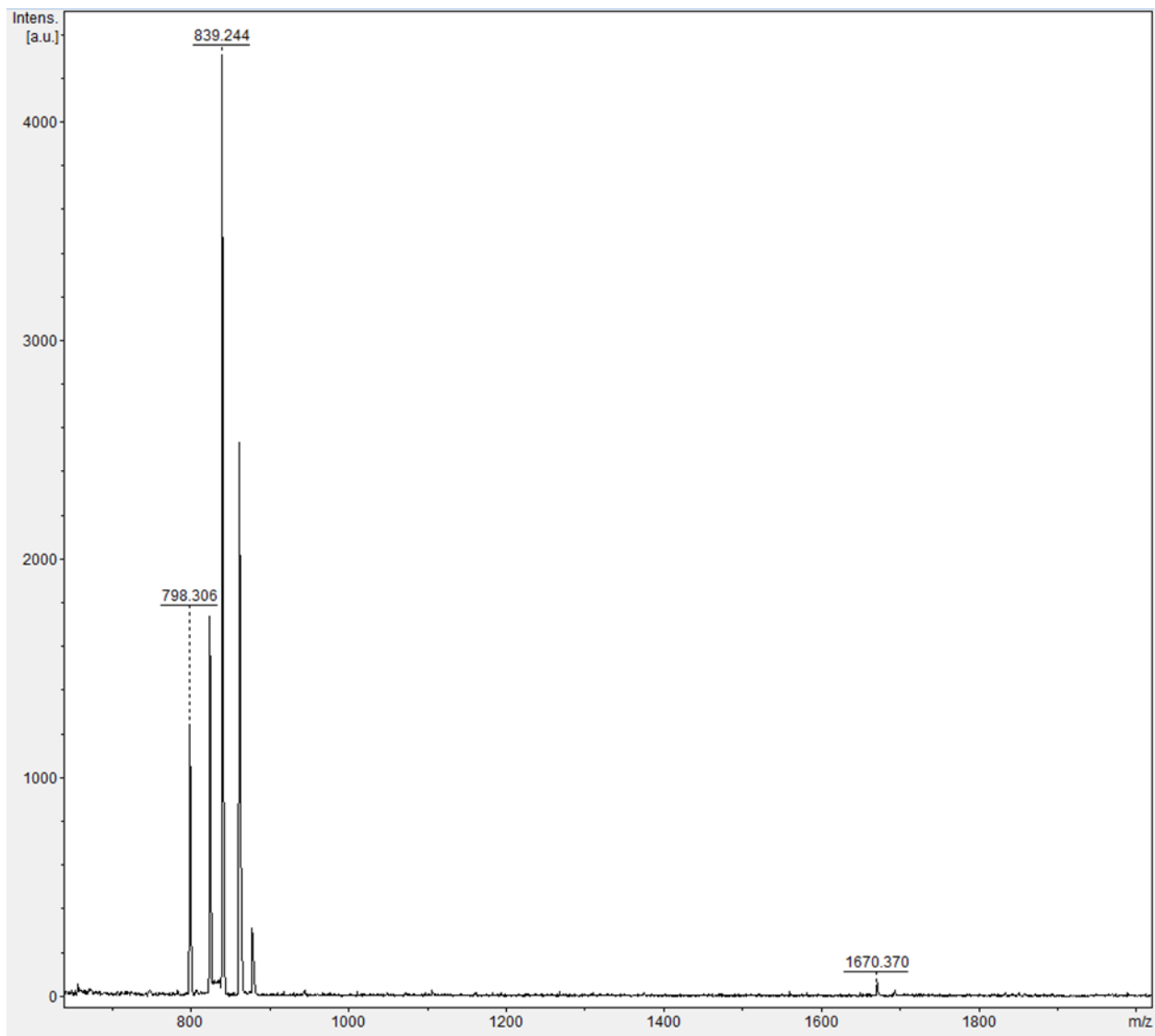
Catalyst **2** M + H calculated 839.023, 839.244 found.
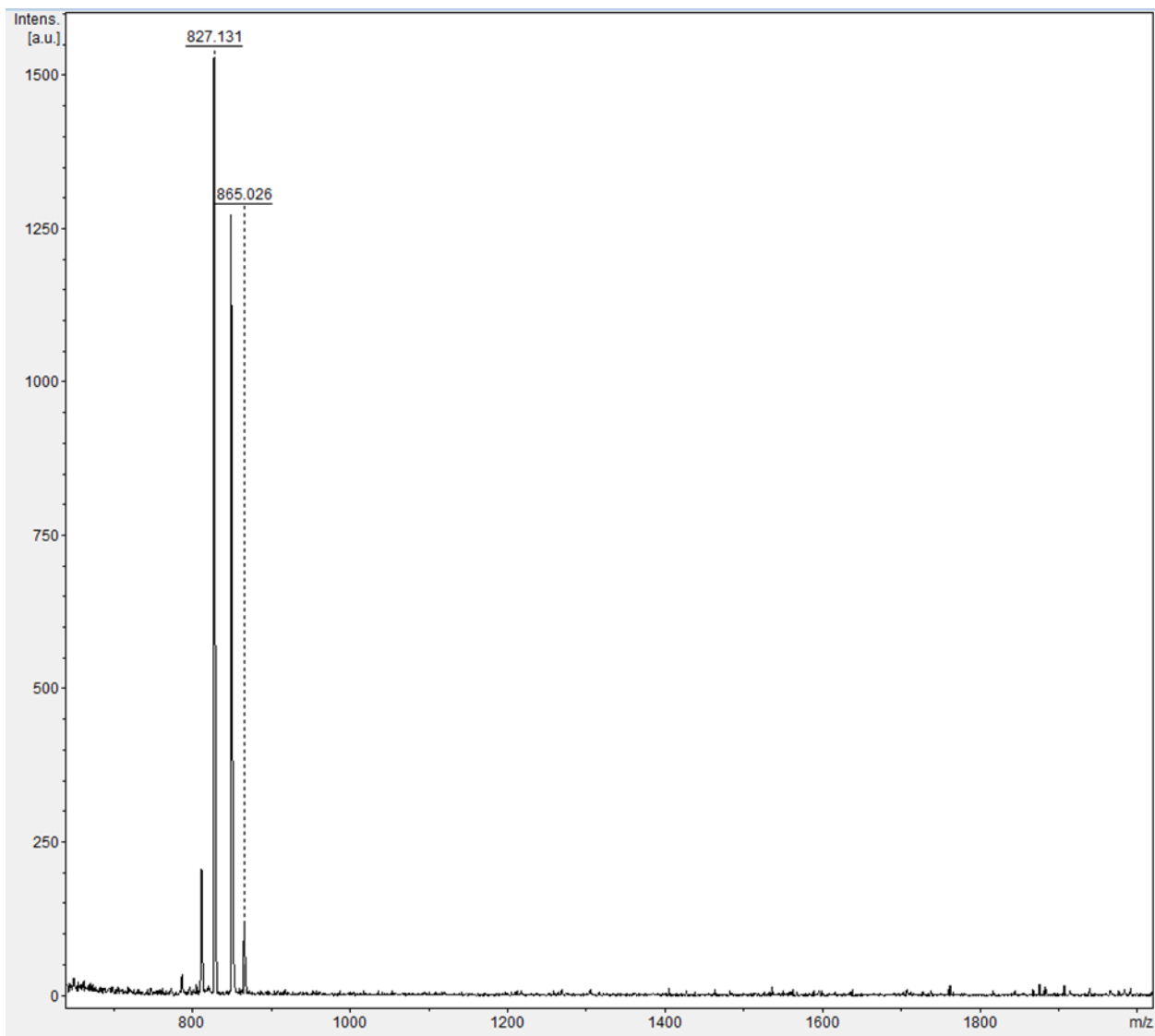
Catalyst **3** M + H calculated 827.014, 827.131 found.
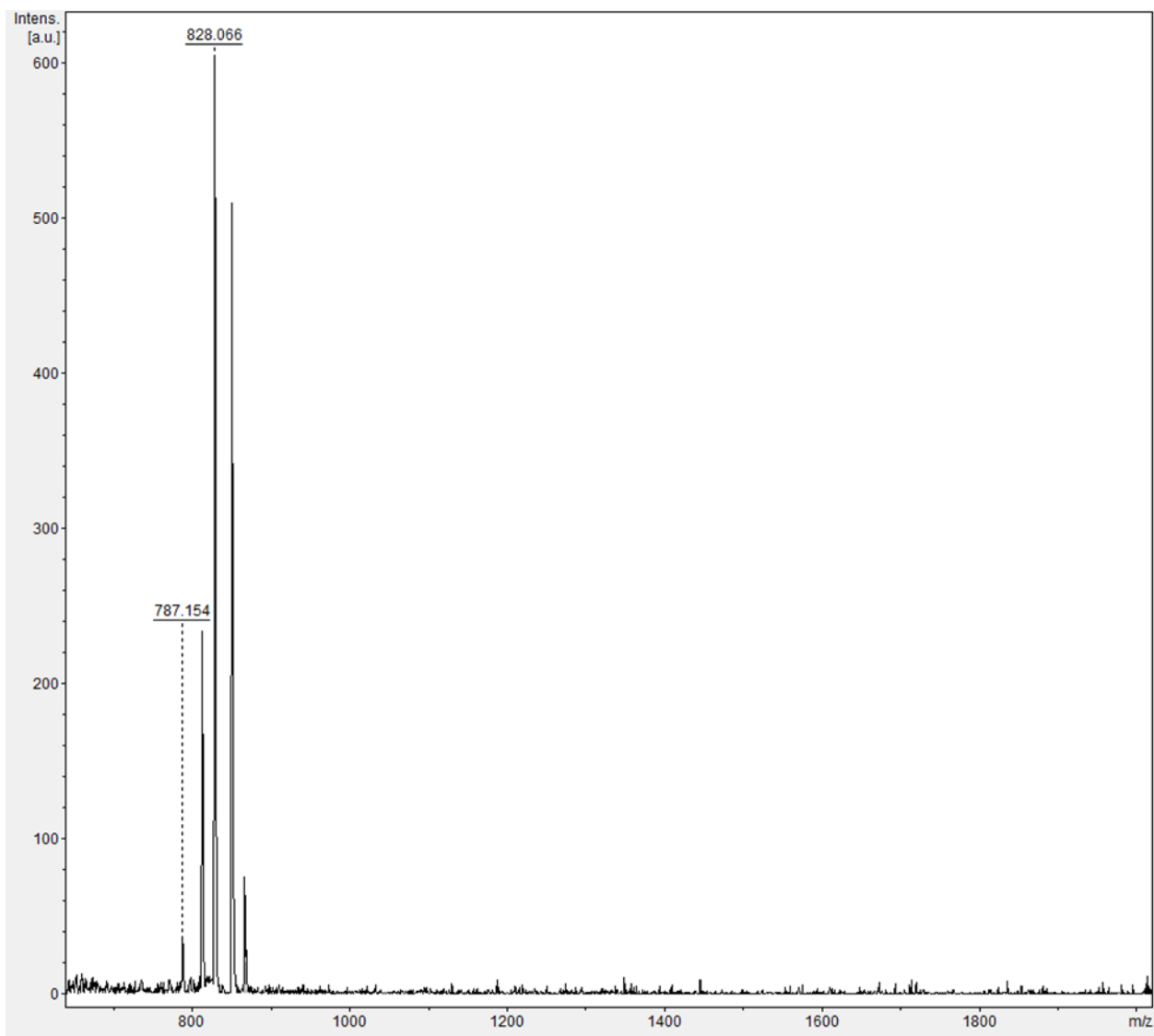
Catalyst **4** M + H calculated = 828.001, 828.066 found.
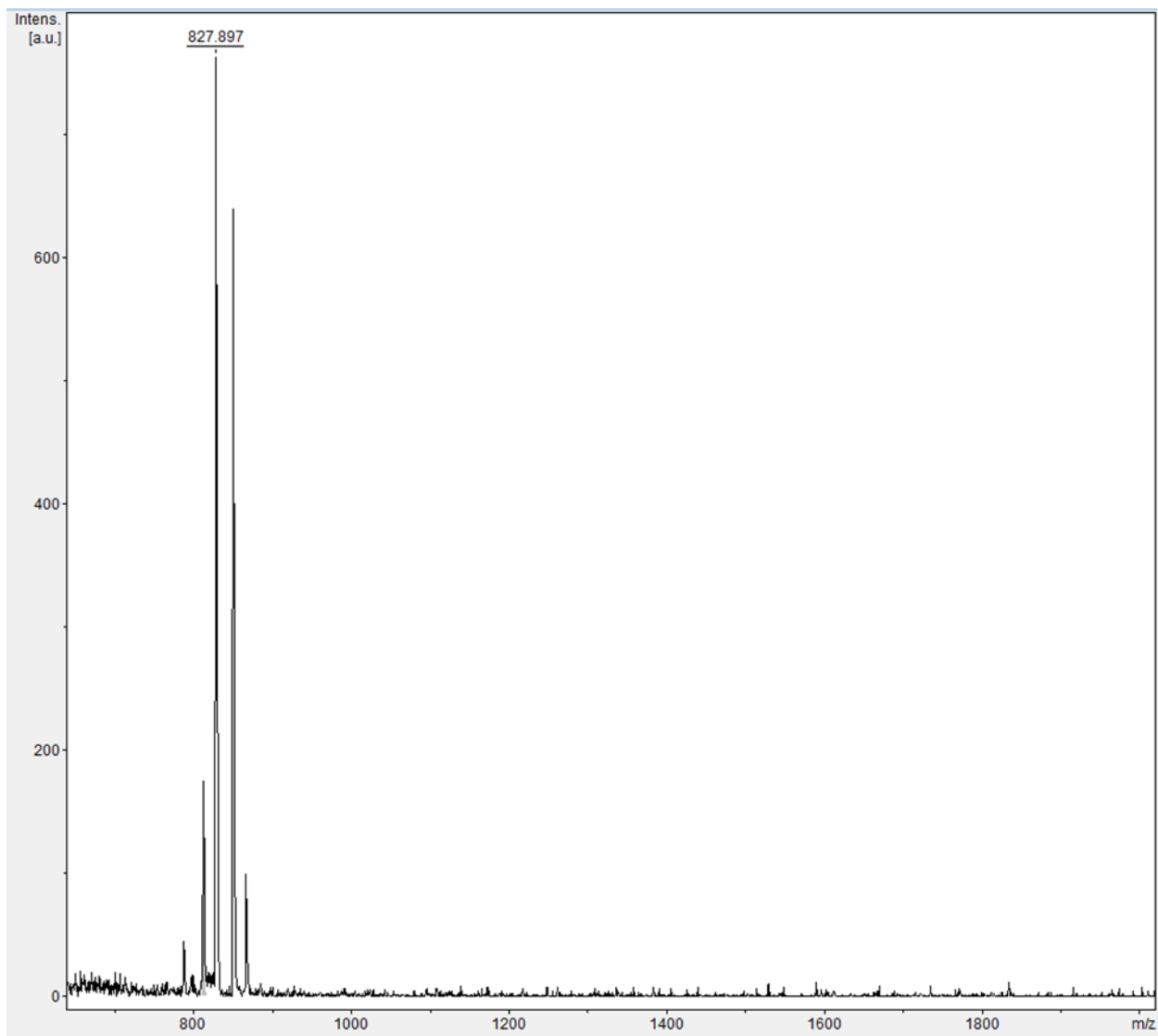
Catalyst **5** M + H calculated 828.001, 827.897 found.
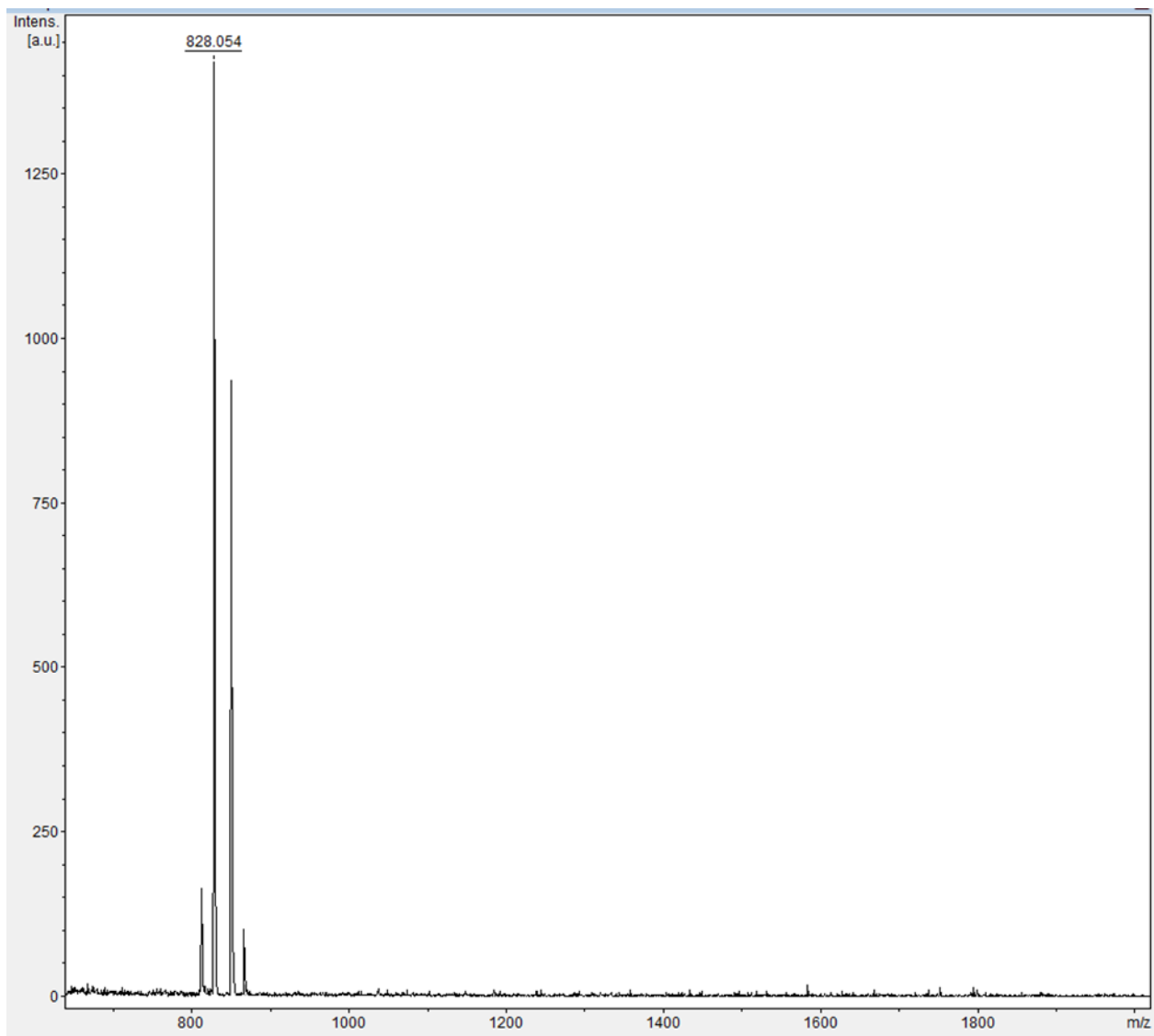
Catalyst **6** M + H calculated 828.001, 828.054 found

Catalyst 12

A high-resolution mass spectrum was acquired of catalyst **12** instead of a MALDI-TOF MS spectrum since catalyst **12** is a trimer, whose mass is too small to be accurately measured by MALDI-TOF MS.

HRMS *m/z* (ESI): $[C_{20}H_{30}N_6O_5 + NH_4]^+$ calculated 452.2603, 452.2612 found.
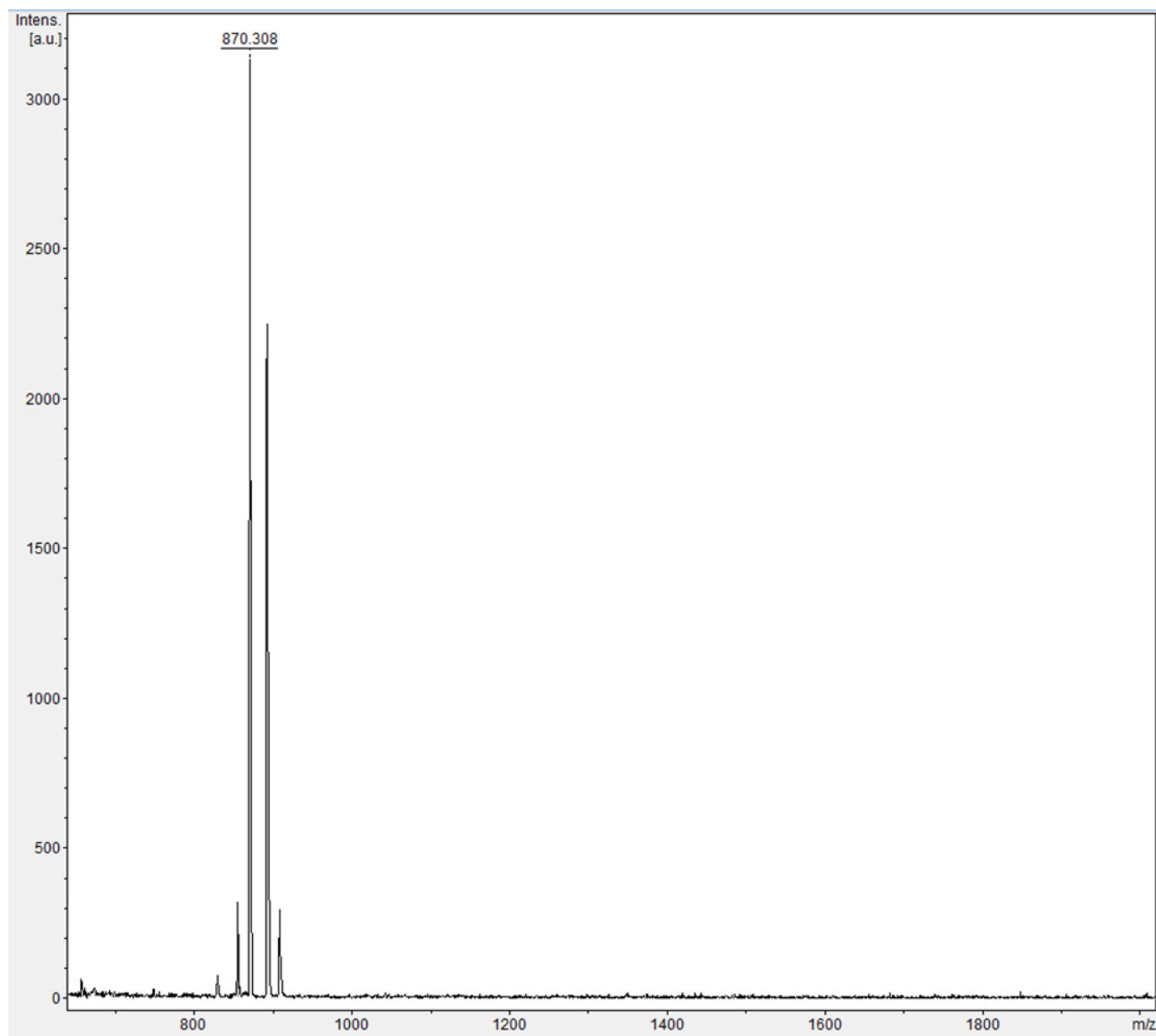
Catalyst **7** M + H calculated 870.083, 870.308 found.
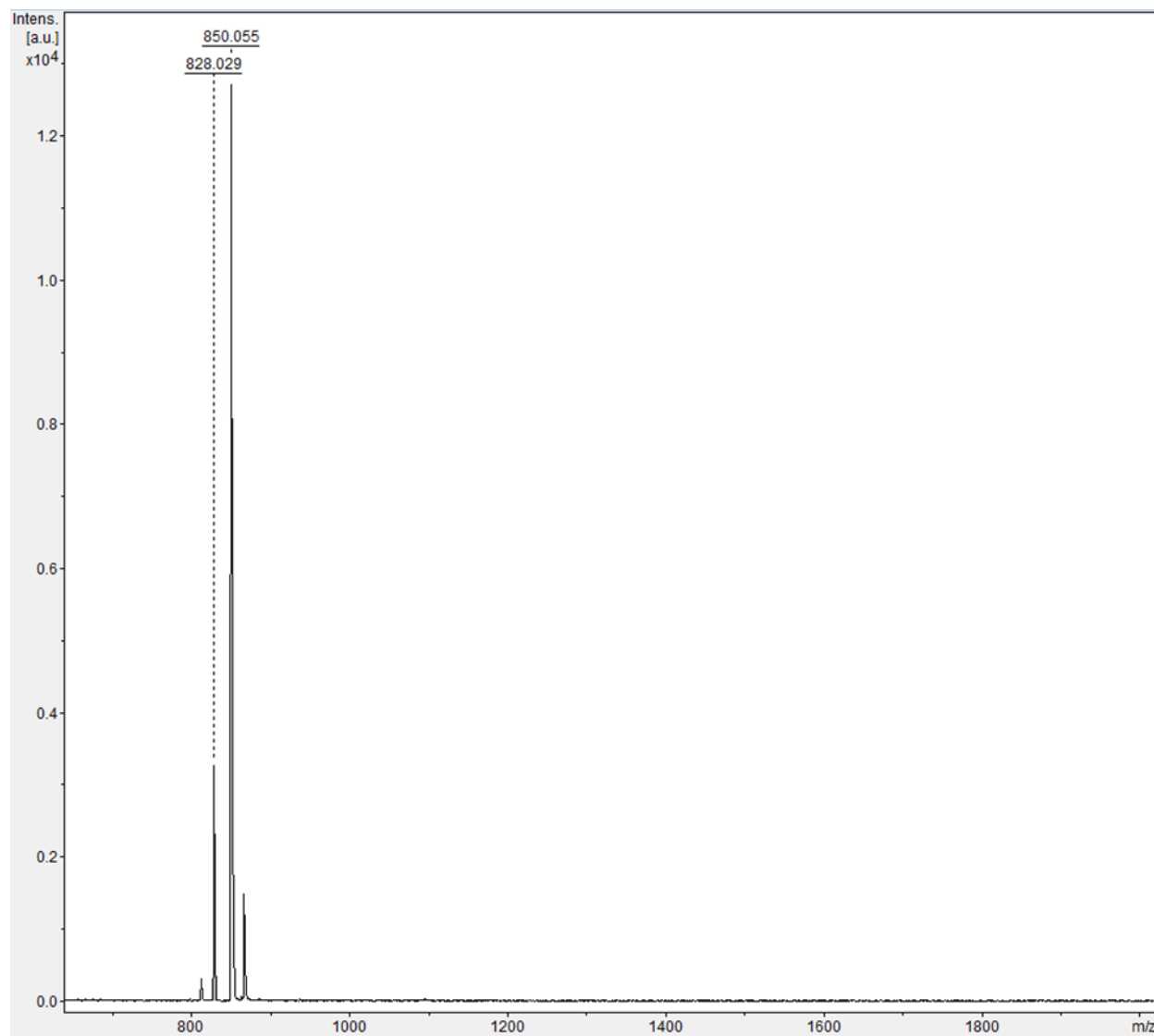
Catalyst **8** M + H calculated 828.001, 828.029 found.
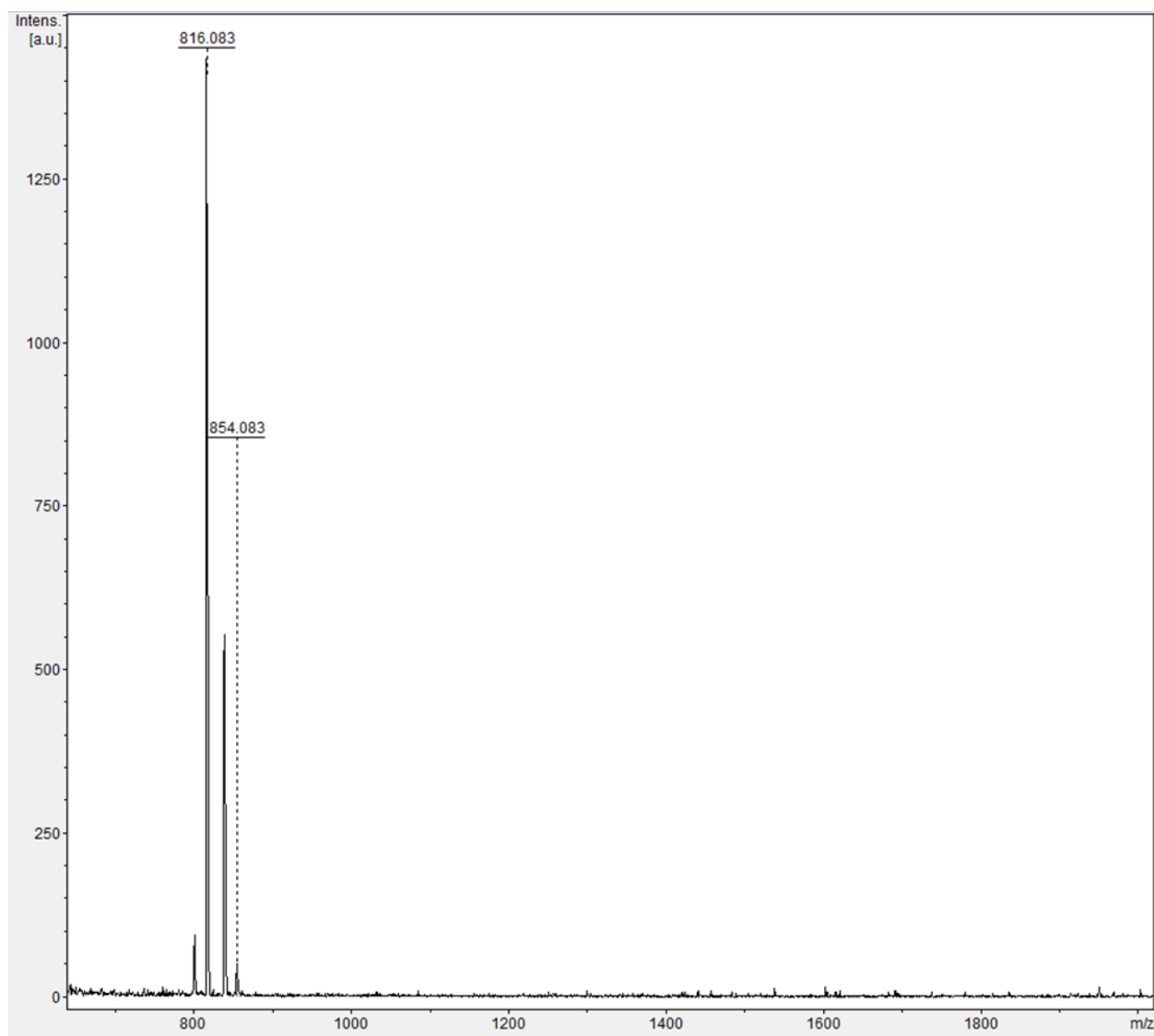
Catalyst **9** M + H calculated 815.993, 816.083 found.
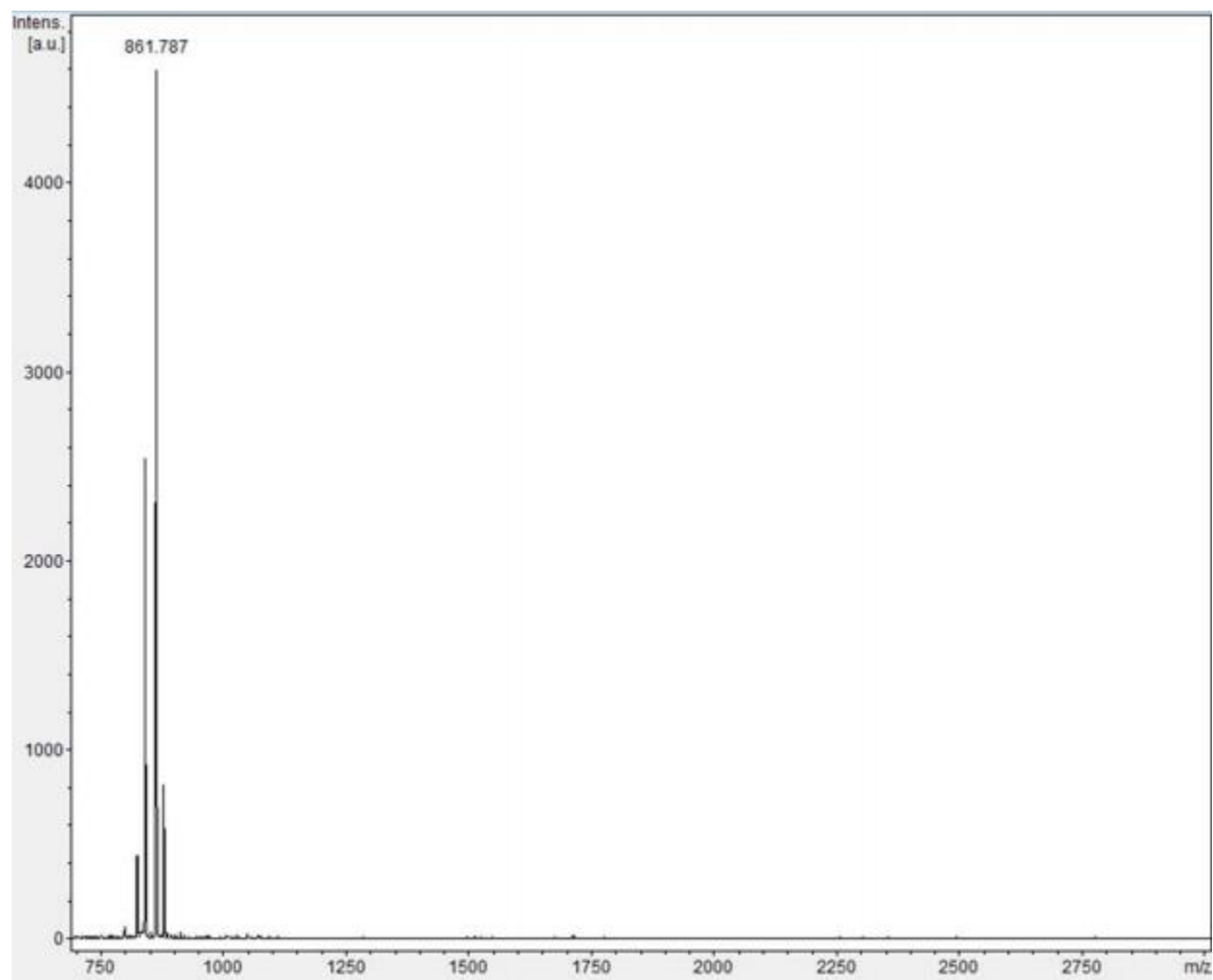
Catalyst **10** M + Na calculated 861.467, 861.787 found.
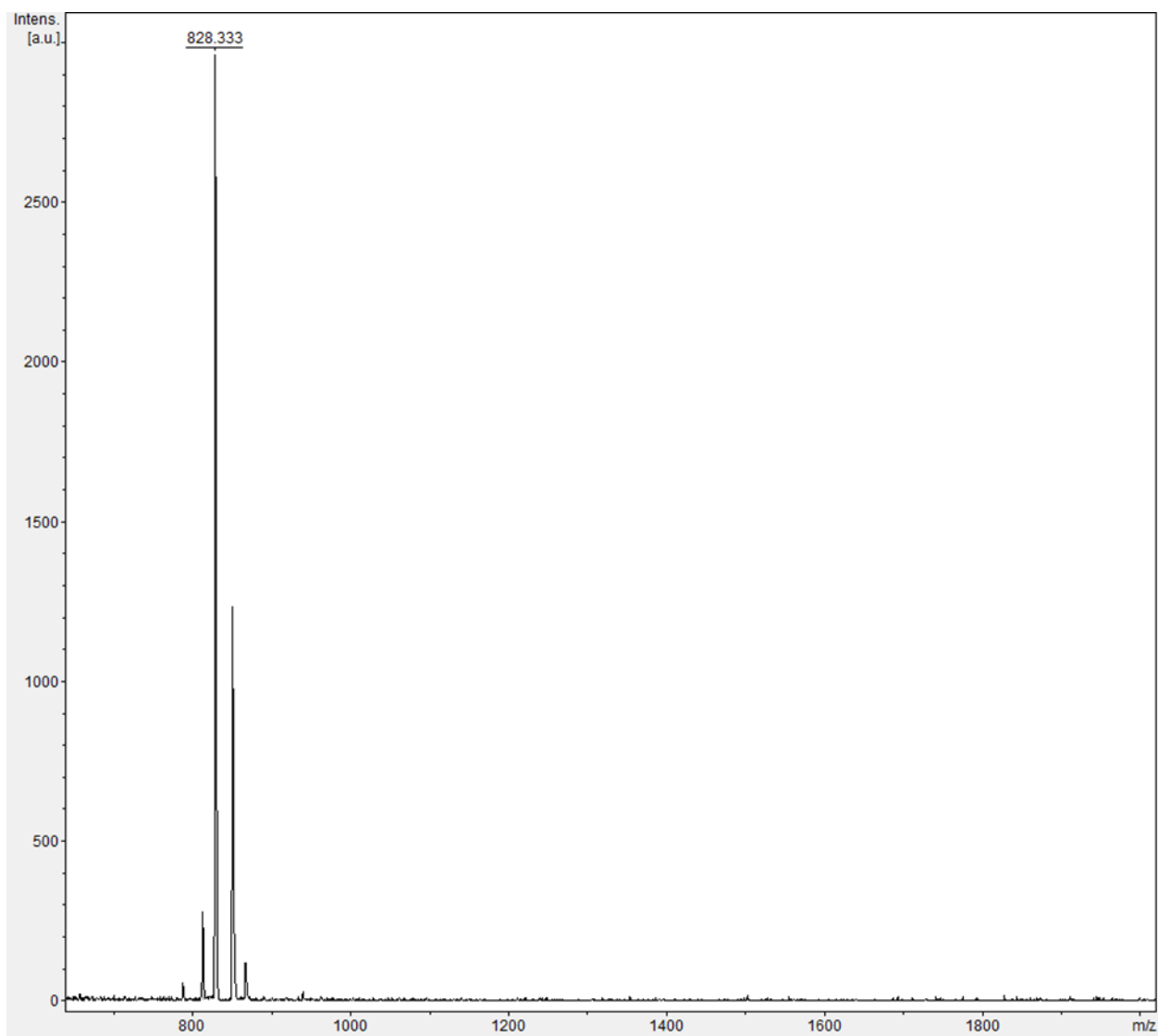
Catalyst **11** M + H calculated 828.001, 828.333 found.

3.7 References

1. E. A. Villar, D. Beglov, S. Chennamadhavuni, J. A. Porco Jr., D. Kozakov, S.Vajda, A. Whitty, How proteins bind macrocycles. *Nature Chemical Biology* **10**, 723-732 (2014).

2. K. R. Campos, P. J. Coleman, J. C. Alvarez, S. D. Dreher, R. M. Garbaccio, N. K. Terrett, R. D. Tillyer, M. D. Truppo, E. R. Parmee, The importance of synthetic chemistry in the pharmaceutical industry. *Science* **363**, 6424 (2019).

3. D. J. Newman, G. M. Cragg, *Macrocycles in Drug Discovery* 1-499 (2014).

4. M. Iyoda, J. Yamakawa, M. J. Rahman, Conjugated macrocycles: Concepts and applications. *Angew. Chem. Int. Ed.* **50**, 10522-10553 (2011).

5. A. Rosenquist, B. Samuelsson, P-O Johansson, M. D. Cummings, O. Lenz, P. Raboisson, K. Simmen, S. Vendeville, H. de Kock, M. Nilsson, A. Horvath, R. Kalmeijer, G. de las Rosa, M. Beumont-Mauviel, Discovery and development of Simeprevir (TMC435), a HCV NS3/4A protease inhibitor. *J. Med. Chem.* **57**, 1673-1693 (2014).

6. T. Gulder, P. S. Baran, Strained cyclophane natural products: Macrocyclization at its limits. *Nat. Prod. Reports.* **29**, 899-934 (2012).

7. C. Galli, L. Mandolini, The role of ring strain on the ease of ring closure of bifunctional chain molecules. *Eur. J. Org. Chem.* 3117-3125 (2000).

8. M. A. Casadei, C. Galli, L. Mandolini, Ring-closure reactions. 22. Kinetics of cyclization of diethyl (.omega.-bromoalkyl)malonates in the range of 4- to 21-membered rings. Role of ring strain., *J. Am. Chem. Soc.*, **106**, 1051-1056 (1984).

9. A. Furstner, Recent advancements in ring closing olefin metathesis. *Topics in Catalysis* **4**, 285-299 (1997).

10. V. Marti-Centelles, M. D. Pandey, M. I. Burguete, S. V. Luis, Macrocyclization reactions: The importance of conformational, configurational, and template-induced preorganization. *Chem. Rev.* **115**, 8736-8834 (2015).

11. C. J. Pedersen, Cyclic polyethers and their complexes with metal salts. *J. Am. Chem. Soc.* **89**, 2495-2496 (1967).

12. S. J. Rowan, S. J. Cantrill, G. R. L. Cousins, J. K. M. Sanders, J. F. Stoddart, Dynamic covalent chemistry, *Angew. Chem. Int. Ed.*, **41**, 898-952 (2002).

13. H. E. Blackwell, J. D. Sadowsky, R. J. Howard, J. N. Sampson, J. A. Chao, W. E. Steinmetz, D. J. O'Leary, R. H. Grubbs, Ring-closing metathesis of olefinic peptides: design, synthesis, and structural characterization of macrocyclic helical peptides. *J. Org. Chem.* **66**, 5291-5302 (2001).

14. X. Shen, T. T. Nguyen, M. J. Koh, D. Xu, A. W. H. Speed, R. R. Schrock, A. H. Hoveyda, Kinetically E-selective macrocyclic ring-closing metathesis. *Nature*, **541**, 380-385 (2017).

15. A. Sytniczuk, M. Dabrowski, L. Banach, M. Urban, S. Czarnocka-Sniadala, M. Milewski, A. Kajetanowicz, K. Grela, At long last: Olefin metathesis macrocyclization at high concentration. *J. Am. Chem. Soc.* **140**, 8895-8901 (2018).

16. J. R. Ludwig, P. M. Zimmerman, J. B. Gianino, C. S. Schindler, Iron(III)-catalyzed carbonyl-olefin metathesis, *Nature,* **533** 374-379 (2016).

17. D. L. Akey, J. D. Kittendorf, J. W. Giraldes, R. A. Fecik, D. H. Sherman, J. L. Smith, Structural basis for macrolactonization by the pikromycin thioesterase. *Nature Chemical Biology* **2**, 537-542 (2006).

18. F. Kopp, M. A. Marahiel, Macrocyclization strategies in polyketide and nonribosomal biosynthesis. *Nat. Prod. Rep.* **24**, 735-749 (2007).

19. C. A. Lewis, S. J. Miller, Site-selective derivatization and remodeling of erythromycin A by using simple peptide-based chiral catalysts. *Angew. Chem. Int. Ed.* **45**, 5616-5619 (2006).

20. Y. Park, K. C. Harper, N. Kuhl, E. U. Kwan, R. Y. Liu, E. N. Jacobsen, Macrocyclic bis-thioureas catalyze stereospecific glycosylation reactions. *Science* **355**, 162-166 (2017).

21. D. A. DiRocco, Y. Ji, E. C. Sherer, A. Klapars, M. Reibarkh, J. Dropiniski, R. Mathew, P. Maligres, A. M. Hyde, J. Limanto, A. Brunskill, R. T. Ruck, L-C. Campeau, I. W. Davies, A multifunctional catalyst that stereoselectively assembles prodrugs. *Science* **356**, 426-430 (2017).

22. S. H. Choi, I. Guzei, L. Spencer, S. H. Gellman, Crystallographic characterization of helical secondary structures in 2:1 and 1:2 α/β-peptides. *J. Am. Chem. Soc.* **131**, 2917-2924 (2009).

23. J. L. Price, E. B. Hadley, J. D. Steingkruger, S. H. Gellman, Detection and analysis of chimeric tertiary structure via backbone thioester exchange: packing of an α-helix against an α/β-helix, *Angew. Chem. Int. Ed.* **49**, 368-371 (2010).

24. Z. C. Girvin, S. H. Gellman, Exploration of diverse reactive diad geometries for bifunctional catalysis via foldamer backbone variation. *J. Am. Chem. Soc.* **140**, 12476-12483 (2018).

25. A. Erkkila, P. M. Pihko, Mild organocatalytic α-methylenation of aldehydes. *J. Org. Chem.* **71**, 2538-2541 (2006).

26. E. Krause, M. Bienert, P. Schmieder, H. Wenschuh, The helix-destabilizing propensity scale of D-amino acids: the influence of side chain steric effects, *J. Am. Chem. Soc.* **122**, 4865-4870 (2000).

27. A. Erkkila, I. Majander, P. Pihko, Iminium catalysis, *Chem. Rev.* **107**, 5416-5470 (2007).

28. S. Mukherjee, J. W. Yang, S. Hoffmann, B. List, Asymmetric enamine catalysis, *Chem. Rev.* **107**, 5471-5569 (2007).

29. A. Ploutno, S. Carmeli, Nostocyclyne A, a novel antimicrobial cyclophane from the cyanobacterium *Nostoc* sp. *J. Nat. Prod.* **63**, 1524-1526 (2000).

30. J. R. Cannon, P. W. Chow, M. W. fuller, B. H. Hamilton, B. W. Metcalf, A. J. Power, Phenolic constituents of Grevillea Robusta (Proteaceaf). The structure of robustol, a novel macrocyclic phenol, *Aust. J. Chem.*, **26** 2257-2275 (1973).

31. A. Furstner, F. Stelzer, A. Rumbo, H. Krause, Total synthesis of the turrianes and evaluation of their DNA-cleaving properties. *Chem. Eur. J.*, **8** 1856-1871 (2002).

32. D. A. Everson, B. A. Jones, D. J. Weix, Replacing conventional carbon nucleophiles with electrophiles: Nickel-catalyzed reductive alkylation of aryl bromides and chlorides. *J. Am. Chem. Soc.* **134**, 6146-6159 (2012).

33. D. A. Evans, J. L. Katz, T. R. West, Synthesis of diaryl ethers through the copper-promoted arylation of phenols with arylboronic acids. An expedient synthesis of thyrozine. *Tetrahedron Letters,* **39**, 2937-2940 (1998).

34. P. Y. S. Lam, C. G. Clark, S. Saubern, J. Adams, M. P. Winters, D. M. T. Chan, A. Combs, New aryl/heteroaryl C-N bond cross-coupling via arylboronic acid/cuprate acetate arylation, *Tetrahedron Letters,* **39**, 2941-2944 (1998).

35. K. Ohno, J. Tsuji, Organic synthesis by means of noble metal compounds. XXXV. Novel decarbonylation reactions of aldehydes and acyl halides using rhodium complexes. *J. Am. Chem. Soc.* **90**, 99-107 (1968).

36. J. A. McCauley, et. al., Discovery of MK-1220: A macrocyclic inhibitor of hepatitis C virus NS3/4A protease with improved preclinical plasma exposure. *J. Med. Chem.* **53**, 2443-2463 (2010).

37. S. J. Benkovic, S. Hammes-Schiffer, A perspective on enzyme catalysis. *Science* **301**, 1196-1202 (2003).

38. C. E. Song, *Cinchona Alkaloids in Synthesis and Catalysis, Ligands, Immobilization and Organocatalysis* Wiley-VCH: Weinheim, Germany (2008).

39. S-K. Tian, Y. Chen, J. Hang, L. Tang, P. McDaid, L. Deng, Asymmetric organic catalysis with modified cinchona alkaloids. *Acc. Chem. Res.* **37**, 621-631 (2004).

40. M. S. Taylor, E. N. Jacobsen, Asymmetric catalysis by chiral hydrogen-bond donors. *Angew. Chem. Int. Ed.* **45**, 1520-1543 (2006).

41. C. Gill, P. H. von Hippel, Calculation of protein extinction coefficients from amino acid sequence data. *Analytical Biochemistry* **182**, 319-326 (1989).

42. M. P. Wiesenfeldt, T. Knecht, C. Schlepphorst, F. Glorius, Silyarene hydrogenation: A strategic approach that enables direct access to versatile silylated saturated carbo- and heterocycles. *Angew. Chem. Int. Ed.* **57**, 8297-8300 (2018).

43. Bruker-AXS, Version 2018.1-0. Madison, Wisconsin, USA, (2018).

44. L. Krause, R. Herbst-Irmer, G. M. Sheldrick, D. Stalke, Comparison of silver and molybdenum microfocus x-ray sources for single-crystal structure determination, *J. Appl. Cryst.* **48**, 3-10 (2015).

45. G. M., Sheldrick, *XPREP*, *Version 1*, Georg-August-Universitate Gottingen, Gottingen, Germany (2013).

46. G. M. Sheldrick, The *SHELX* homepage: http://shelx.uni-ac.gwdg.de/SHELX/. (2013).

47. G. M. Sheldrick, *SHELXT* – Integrated space-group and crystal-structure determination, *Acta Cryst. A*, **71**, 3-8 (2015).

48. G, M. Sheldrick, Crystal structure refinement with *SHELXL Acta Cryst. C*, 3-8 (2015).

49. O. V., Dolomanov, L. J. Bourhis, R. J. Gildea, J. A. K. Howard, H. Puschmann, *OLEX2*: a complete structure solution, refinement and analysis program

J. Appl. Crystallogr., 42, 339-341 (2009).

50. I. Guzei, *Programs Gn.*, University of Wisconsin-Madison, Madison, Wisconsin, USA, (2007-2013)

51. L. Catti, K. Tiefenbacher, Intramolecular hydroalkoxylation catalyzed inside a self-assembled cavity of an enzyme-like host structure. *Chem. Commun*. **51**, 892-894 (2015).

52. K. Hagiwara, M. Akita, M. Yoshizawa, An aqueous molecular tube with polyaromatic frameworks capable of binding fluorescent dyes. *Chem. Sci.*, **6**, 259-263 (2015).

Additional examples of transition metal catalyzed macrocyclizations Ref 53-64

53. M. Yu, C. Wang, A. F. Kyle, P. Jakubec, D. J. Dixon, R. R. Schrock, A. H. Hoveyda, Synthesis of macrocyclic natural products by catalyst-controlled stereoselective ring-closing methathesis, *Nature* **479**, 88-93 (2011).

54. S. J. Meek, R. V. O'Brien, J. Llaveria, R. R. Schrock, A. H. Hoveyda, Catalytic Z-selective olefin cross-metathesis for natural product synthesis, *Nature*, **471**, 461-466 (2011).

55. V. M. Marx, M. B. Herbert, B. Keitz, R. H. Grubbs, Stereoselective access to *Z* and *E* macrocycles by ruthenium-catalyzed *Z*-selective ring-closing metathesis and ethenolysis, *J. Am. Chem. Soc.*, **135**, 94-97 (2012).

56. C. W. Lee, R. H. Grubbs, Formation of macrocycles *via* ring-closing metathesis, *J. Org. Chem.*, **66**, 7155-7158 (2001).

57. S. R. Chemler, S. J. Danishefsky, Transannular macrocyclization via intramolecular B-alkyl suzuki reaction, *Org. Lett.*, **2**, 2695-2698 (2000).

58. P. Li, J. Li, F. Arikan, W. Ahlbrecht, M. Dieckmann, D. Menche, Total synthesis of etnangien, *J. Am. Chem. Soc.*, **131**, 11678-11679 (2009).

59. L. Peng, F. Zhang, T. Mei, T. Zhang, Y. Li, Studies on novel macrocyclization methods of cembrane-type diterpenoids: a Stille cyclization approach to (±)-isocembrane, *Tett. Lett.*, **44**, 5921-5923 (2003).

60. M. A. Casadei, C. Galli, L. Mandolini, Ring-closure reactions. 22. Kinetics of cyclization of diethyl (.omega.-bromoalkyl)malonates in the range of 4- to 21-membered rings. Role of ring strain. *J. Am. Chem. Soc.*, **106**, 1051-1056 (1984).

61. A. Furstner, F. Stelzer, A. Rumbo, H. Krause, Total synthesis of the turrianes and evaluation of their DNA-cleaving properties, *Chem. Eur. J.*, **8**, 1856-1871 (2002).

62. H. Deng, J. Jung, T. Liu, K. Kuntz, M. Snapper, A. Hoveyda, Total synthesis of anti-HIV agent Chloropeptin I, *J. Am. Chem. Soc.*, **125**, 9032-9034 (2003).

64. W. Lee, M. Tonelli, J. Markley, NMRFAM-SPARKY: enhanced software for biomolecular NMR spectroscopy, *Bioinformatics*, **31**, 1325-1327 (2015).

65. L. Xu, J. Luo, Y. Lu, Asymmetric catalysis with chiral primary amine-based organocatalysts, *Chem. Commun.*, 1807-1821 (2009).

3.7 Acknowledgements

Chapter 4

Catalytic Intramolecular Conjugate Additions of Aldehyde-Derived Enamines to α,β-Unsaturated Esters

2 steps

95 % ee

(-)-yohimbane
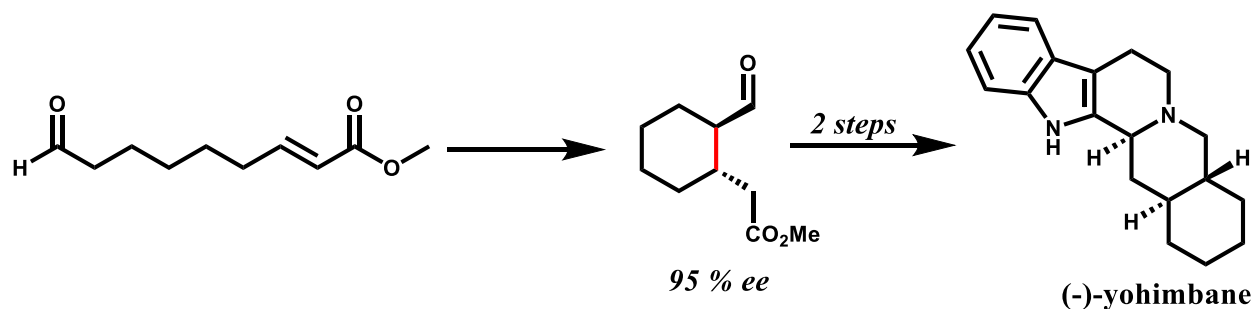
Portions of this chapter are published in:

Xinyu Liu performed all 2D NMR studies.

Philip Lampkin synthesized compound **S9** and performed various screens and purifications.

4.1 Abstract

We report a pairing of known catalysts that enables intramolecular conjugate additions of aldehyde-derived enamines to α,β-unsaturated esters. Despite extensive prior exploration of conjugate additions of aldehyde-derived enamines, catalytic conjugate additions to unactivated enoate esters are unprecedented. Achieving enantioselective and diastereoselective six-membered ring formation requires the coordinated action of a chiral pyrrolidine, for nucleophilic activation of the aldehyde via enamine formation, and a hydrogen bond donor, for electrophilic activation of the enoate ester. Proper selection of the hydrogen bond donor is essential for chemoselectivity, which requires minimizing competition from homoaldol reaction. Utility is demonstrated in a six-step synthesis of (−)-yohimbane from cycloheptene.

4.2 Introduction

Discrimination among competing reaction pathways to favor desired transformations is a central challenge in preparative organic chemistry. Enzymes often exert strict regulation of chemical reactivity because of the highly controlled environment provided to substrates by active sites. Discovering strategies to select among competing reaction pathways via small-molecule catalysts, which cannot envelop substrates, is a driving force for development of new synthetic methods.[1-7]

Prior examples of aldehyde-derived enamines reacting with unactivated α,β-unsaturated esters have involved preformed enamines generated with excess achiral amine.[8] Catalytic addition of aldehydes to unactivated α,β-unsaturated esters, via transient enamine formation, was apparently unknown when we began this work.[9] This reactivity lacuna is surprising because conjugate additions have been explored for over 130 years.[10] Many examples of catalytic

conjugate additions of enamine-based nucleophiles to electron-deficient alkenes are known

(**Figure 1A**).[11] The absence of catalytic aldehyde enamine conjugate additions to conventional

enoate esters likely stems from the low electrophilicity of these enoate esters, as established by

Mayr et al.,[12,13] along with the high electrophilicity of aldehydes, which leads to preference for

homoaldol products.[14] The synthetic value of this unknown transformation arises from the

potential utility of the products.[9,15-18]
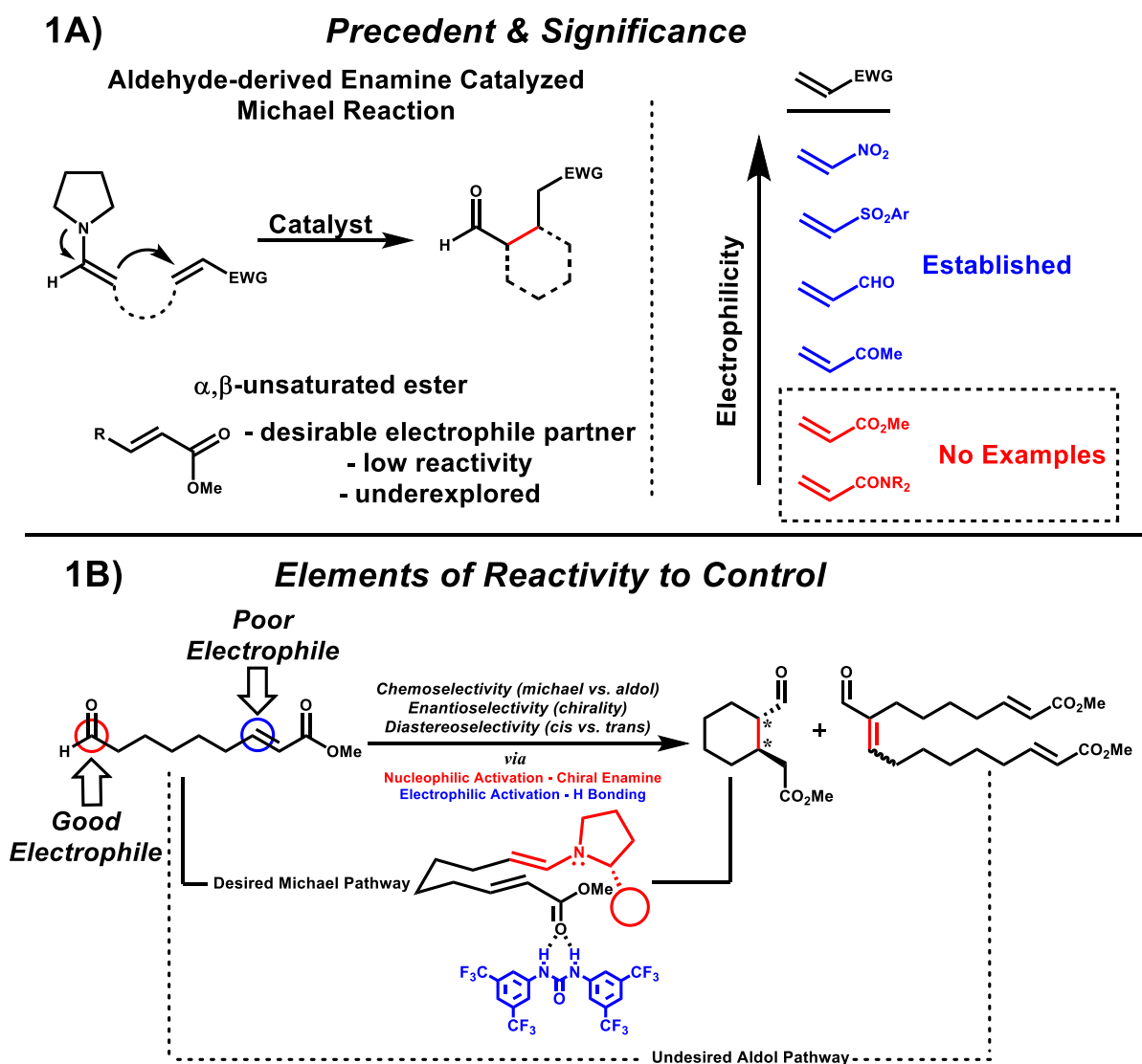
Figure 1. (A) Conjugate addition of aldehyde-derived enamines to electron-deficient olefins is widely practiced but limited by electrophilic reactivity (scale on right adapted from ref 18). (B) For the desired cyclization, conjugate

addition to a weak electrophile (α,βunsaturated ester) must be favored over the competing homoaldol pathway reaction, which is achieved with a specific cocatalyst pairing.

A few examples of intramolecular conjugate additions of ketone-derived enamines to an enoate ester have been reported. These reactions rely upon use of stoichiometric amine and extended reaction times,[19] or on a carefully chosen bifunctional catalyst.[16,17,20] The diminished electrophilicity of a ketone relative to an aldehyde curtails formation of homoaldol byproducts in these cases.[13,14] Therefore, achieving chemoselective conjugate addition of a ketone-derived enamine to an enoate ester does not involve the challenges inherent in comparable aldehyde reactions (**Figure 2**).
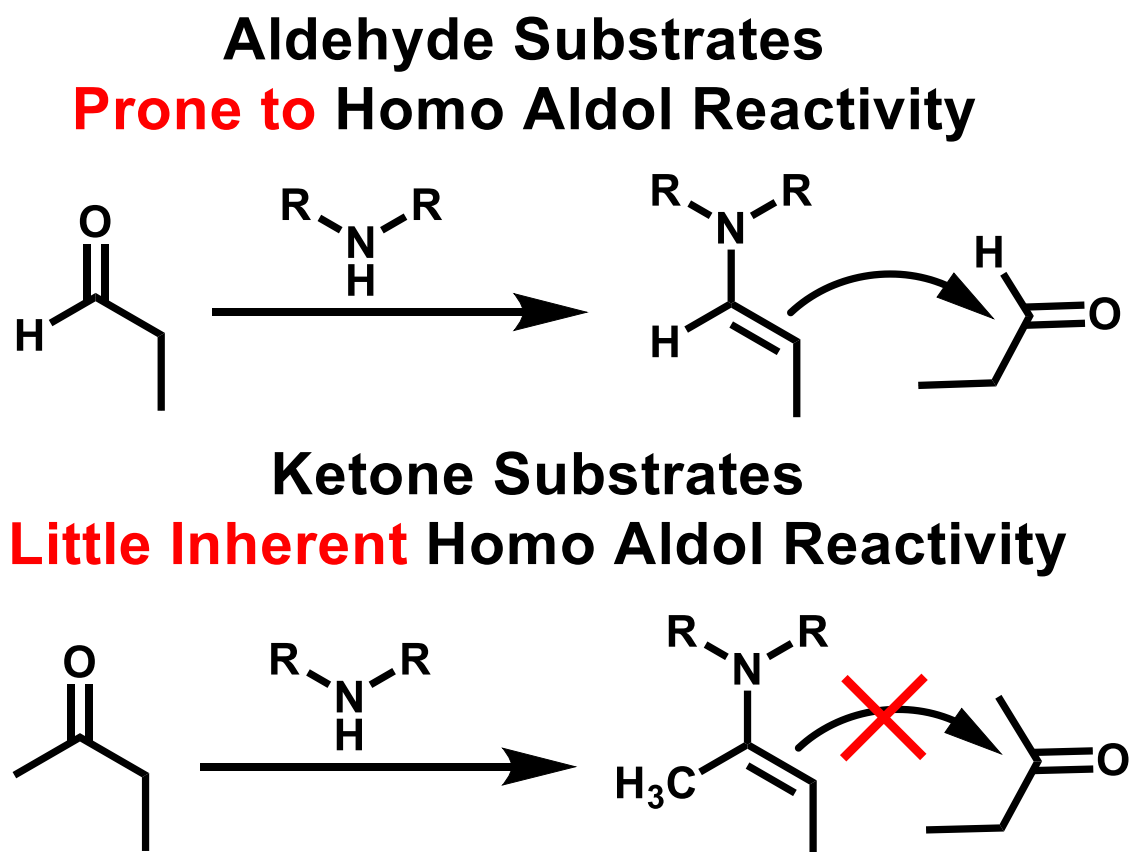
Figure 2. Homo-aldol reactivity poses a challenge of controlling chemoselectivity in aldehyde-derived enamine reactions, while not in ketone-derived enamine reactions.

4.3 Results

We discovered an amine−urea catalyst pair that enables efficient and stereoselective six-membered ring formation via intramolecular conjugate addition of an aldehyde-derived enamine to an α,β-unsaturated ester. Many reaction conditions we examined led to substantial homoaldol product or no reaction at all. Proper choice of the two catalysts, however, enabled useful control over chemo-, diastereo-, and enantioselectivity. The reactivity demonstrated here fills a long-standing void in conjugate additions, extending this reaction mode to the poorest electrophile yet employed with an aldehyde-derived enamine nucleophile.

Our initial studies focused on the cyclization of aldehyde-enoate substrate **1**, which allowed us to evaluate secondary amines for the ability to catalyze the desired cyclization via transient enamine formation.[21] Pyrrolidine cleanly provided racemic **3**, but only a trace of **3** was detected with the widely used Hayashi-Jørgensen catalyst, **2** (**Figure 3**).[22,23] Compound **2** and related 2-substituted pyrrolidines have enabled a wide range of enantioselective conjugate additions of aldehydes to electrophiles more reactive than enoate esters.[24,25] However, the increased steric hindrance arising from the bulky substituent adjacent to nitrogen, relative to pyrrolidine itself, apparently inhibits reaction with an enoate ester, a weak electrophile.[12,13]

We hypothesized that the desired conjugate addition would require electrophilic activation of the enoate ester in conjunction with enamine-based (nucleophilic) activation of the aldehyde. Brønsted acid and hydrogen bond donor additives have been employed to enhance carbonyl electrophilicity,[26,27] but use of such of such catalysts in our case could create a chemoselectivity problem. The ideal catalyst should activate the ester in preference to the aldehyde to favor cyclization over the intermolecular homoaldol pathway. Yamamoto et al. were able to activate aldehydes relative to ketones with exotic Lewis acids,[28] but we are not aware that

Brønsted acids or hydrogen bond donors have demonstrated this type of chemoselectivity. We surveyed candidate cocatalysts under a consistent set of conditions (**Figure 3**).

Reaction scheme: Reaction Conditions (See Table Below) → + Cis diastereomer → 1) Silica Plug 2) 1 eq H₂N–NH–Ts, MeOH, rt, 10 min → Enantiomers of Major Diastereomer / Enantiomers of Minor Diastereomer

Amine	Co-Catalyst	% Conversion	% Homo-Aldol	d.r.	% ee	[Substrate], M	Temperature (°C)
20 mol % (pyrrolidine)	None	> 99	< 1 %	14 : 1	–	0.1 (CHCl₃)	rt
15 mol %	None	3	7	–	–	0.05	rt
15 mol %	15 mol %	> 99	1.6	8.8 : 1	95	0.05	rt
15 mol %	15 mol %	> 79	3	18 : 1	95	0.05	4
15 mol %	15 mol %	0	–	–	–	0.05	rt
15 mol %	15 mol %	> 99	1.6	6.3 : 1	91	0.05	rt
15 mol %	15 mol %	88	2	7.1 : 1	95	0.05	4
15 mol %	15 mol %	96	2	8.1 : 1	98	0.05	rt
15 mol %	15 mol %	> 99	< 1 %	2.8 : 1	94	0.05	rt
15 mol %	15 mol %	83	7	3.6 : 1	91	0.05	rt
15 mol %	15 mol %	15	37	0.7 : 1	–	0.05	rt
15 mol %	15 mol %	2	100	–	–	0.05	rt
15 mol %	15 mol %	0	–	–	–	0.05	rt
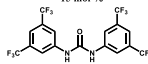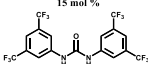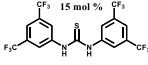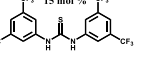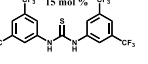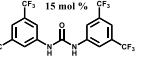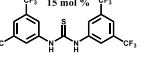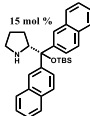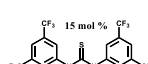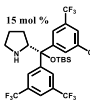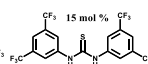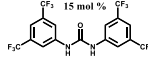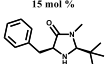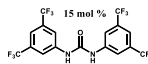
Figure 3. Optimization experiments: Amine screen. See general procedures section of this chapter for details.

2A)

2B)

(5)
5.6:1 d.r.
18 % conv.
76 % HA

(6)
1.7:1 d.r.
29 % conv.
75 % HA

(7)
2.6:1 d.r.
7 % conv.
69 % HA

(8)
7:1 d.r.
96 % conv.
96 % HA

(9)
1.8:1 d.r.
71 % conv.
79 % HA

(10)
6.9:1 d.r.
92 % conv.
25 % HA

(11)
16.2:1 d.r., 95 % ee
87 % conv.
20 % HA

(12)
9.9:1 d.r., 92 % ee
93 % conv.
34 % HA

(13)
2:1 d.r.
29 % conv.
24 % HA

(14)
1.8:1 d.r.
25 % conv.
19 % HA

(15)
16.5:1 d.r., 92 % ee
95 % conv.
8 % HA

(16)
6.3 d.r., 91 % ee
> 99 % conv.
1.6 % HA

(17)
8.8:1 d.r., 95 % ee
> 99 % conv.
1.6 % HA

(18)
10.2:1 d.r., 70 % ee
47 % conv.
3 % HA

(19)
2.4:1 d.r.
14 % conv.
12 % HA

Classes of Additives Evaluated
Urea
Thiourea
Phenols
Diols
Chiral Phosphoric Acids
Triflamides
Benzoic Acid/Weak Acids
Strong Bronsted Acids

Figure 4. Effect of acidic/hydrogen bond donor additives on reaction pathway. Reactions run on 0.05 mmol scale. Percent conversion of **1** (conv.), d.r. (diastereomeric ratio) of **3**, and percent of crude product that corresponds to the homoaldol product (**4**), as determined by 1 H NMR analysis. Percent enantiomeric excess (ee) determined by chiral HPLC. For calculation of percent conversion, see the experimental section of this chapter.

Brønsted acids were not effective as cocatalysts. The strongest acids we examined, trifluoroacetic acid (**5**), squaric acid (**6**), and BINOL phosphoric acid (**7**), gave low conversions and mostly homoaldol product. Weaker acids, benzoic acid (**8**) and propionic acid (**9**), gave high conversions but again mostly the undesired homoaldol product. Among simple phenolic compounds, which may be considered as hydrogen bond donors rather than Brønsted acids under these conditions, better outcomes were observed. Thus, p-nitrophenol (**10**), catechol (**11**) and ethyl protocatechuate (**12**) supported formation of cyclized product **3** with high diastereo- and enantioselectivity, but in each case, a substantial fraction of the starting material was directed along the undesired homoaldol pathway. BINOL (**13**) and TADDOL (**14**) were poor cocatalysts, each providing relatively low yields of **3**, with little diastereoselectivity and significant homoaldol byproduct.

Placing our observations in the context of related reports highlights the chemoselectivity challenge inherent in cyclizing aldehyde-enoate ester **1**. Dixon et al. reported enantioselective formation of a six-membered ring via addition of a ketone-derived enamine to an enoate ester with benzoic acid as a cocatalyst.[17] Scheidt et al. used catechol as a cocatalyst for six-membered ring formation in a comparable process.[16] Chemoselectivity was not a major concern in these systems because homoaldol reactions of ketones are generally unfavorable. Ethyl protocatechuate was an effective cocatalyst for intermolecular conjugate additions of aldehydes to enones,[29] which are more electrophilic than enoate esters.[12,13] 4-Nitrophenol has been used for conjugate additions of enamines derived from **2** to nitro-alkenes,[11i] which are strong electrophiles.[12,13]

We identified three hydrogen bond donor cocatalysts that, in combination with chiral amine **2**, displayed favorable chemo-, enantio-, and diastereoselectivity profiles. Chiral 1,2-

bistriflamide (**15**) provided high conversion to **3** with excellent enantio- and diastereoselectivity. Only a modest amount of homoaldol product (8%) was formed. Compound **15** was reported to catalyze aza-conjugate additions to enoate esters,[30] which suggests that the 1,2-bistriflamide unit may be generally effective for electrophilic activation of this substrate class. Schreiner's thiourea (**16**)[31] and the corresponding urea (**17**) both resulted in total conversion of **1**, with near-complete selectivity for the cyclization product (98%).

The electron-deficient aromatic rings in thiourea **16** are critical because replacing one with an alkyl group (**18**) or replacing both with phenyl rings (**19**) led to much poorer outcomes relative to **16** as cocatalyst. Urea **17** and thiourea **19** are expected to have very similar pKa values,[32] but they perform very differently as cocatalysts for cyclization of **1**. In contrast, thiourea **16** is considerably more acidic than urea **17**, but they perform similarly as cocatalysts. Thus, pKa is not a principal determinant of enoate ester activation in this reaction. These results suggest that the factors determining the efficacy of catalysis via hydrogen bond donation are complex and deserve further attention. The substantial variation in proportion of homoaldol versus intramolecular conjugate addition products observed across the cocatalysts we surveyed raises the possibility that site-selective carbonyl activation might offer a strategy for late-stage functionalization of complex substrates.[33]

We examined a few variants of pyrrolidine **2** (**Figure 3**). Replacing the trimethylsilyl group with t-butyldimethylsilyl led to slight increases in enantioselectivity. Further increases in steric bulk on the pyrrolidine ring substituent, however, caused an erosion in reactivity. The pyrrolidine could not be replaced with an imidazolidinone, which is consistent with earlier studies involving intramolecular conjugate additions of aldehydes.[11d] Trace conversion of starting material **1** was observed in the presence of S-methylbenzylamine, which highlights an

important distinction between aldehyde-enoate ester and ketone-enoate ester cyclizations. All known ketone-enoate ester cyclizations have relied on primary amine catalysts,[16,17,19,20] presumably because primary amines are more effective than secondary amines at forming ketone-derived enamines.[21,34]

Toluene and chlorinated solvents were optimal for the cyclization of **1** (**Figure 4**).
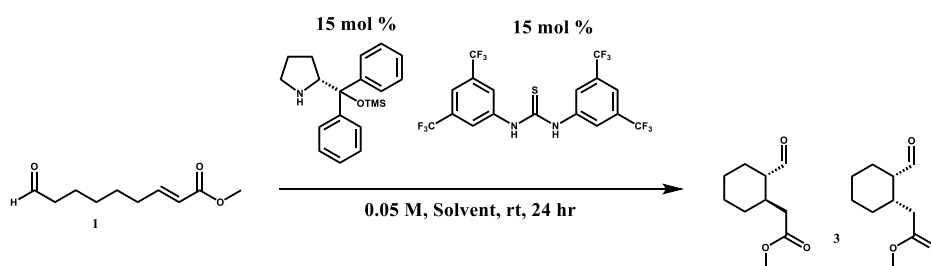
Entry	Solvent	% conversion	d.r. (24 hr)	% HomoAldol (24 hr)	% ee (major diastereomer)
1	toluene	> 99	6.3 : 1	1.6	91
2	o-xylene	98	6.5 : 1	2	92
3	CPME	29	4.3 : 1	14	—
4	THF	7	2 : 1	6	—
5	Acetonitrile	17	2.2 : 1	18	—
6	Diethyl Ether	33	2.7 : 1	21	—
7	DCM	78	5.2 : 1	1	89
8	CHCl$_3$	78	6.2 : 1	4	89
9	Trifluorotoluene	97	6.5 : 1	2	92
10	iPrOH	n/a	—	n/a	—
11	d$_7$-DMF	7	n/a	< 1	—
12	d$_6$-DMSO	6	n/a	< 1	—
13	1,2-DCE	74	6.2 : 1	6	90
14	EtOAc	6	2.4 : 1	4	—

Figure 4. Solvent Screen. Reactions performed and analyzed as outlined in experimental section.

Polar solvents, including alcohols, ethers, nitriles, and amides, gave poor overall conversion, which may indicate that Lewis basic groups in the solvent molecules compete with the enoate ester as hydrogen bond acceptors.

The catalyst loading was examined to try to identify an optimum relative stoichiometry of the two catalytic components (**Figure 5, 6**).

Catalyst Loading Optimization

Entry	Amine Loading	Thiourea Loading	% conversion	d.r.	% HomoAldol (24 hr)	% ee
1	20	20	99 %	5.3 :1	< 1 %	—
2	15	15	99 %	6.3 : 1	1 %	91
3	10	10	92 %	5 : 1	1 %	—
4	5	5	35 %	4.8 : 1	6 %	—
5	10	5	58 %	5.3 : 1	5 %	—
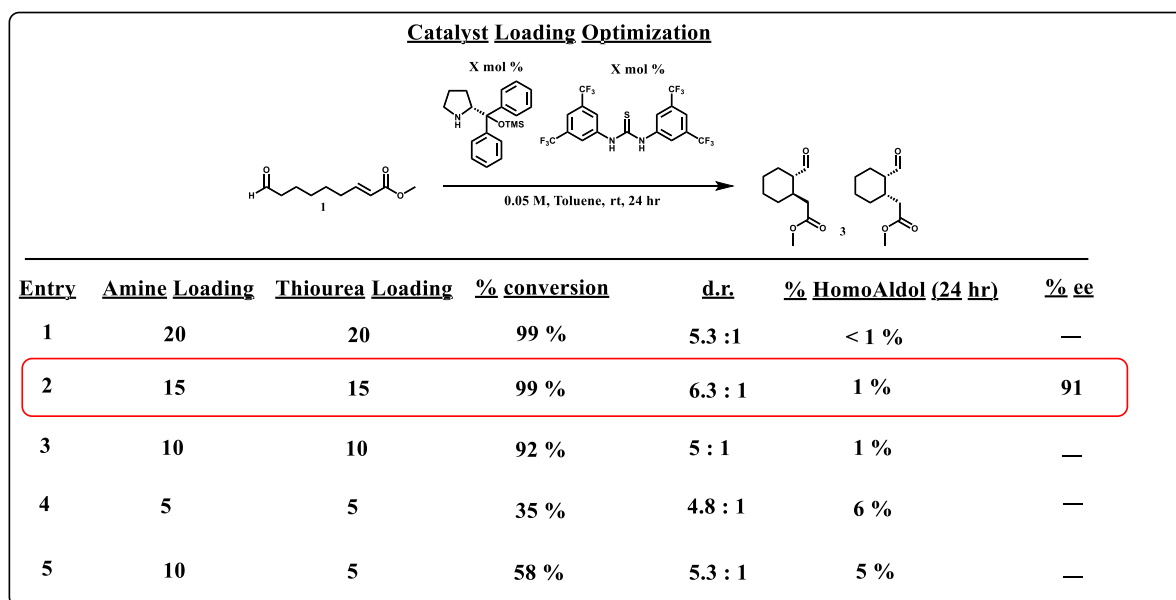
Figure 5. Catalyst loading experiments. Reaction performed and analyzed as described in the experimental section.

Additional studies were carried out to determine whether useful chemoselectivity could be maintained at higher substrate concentrations. The reactions described above were conducted with 0.05 M **1**; **Figure 7** summarizes results obtained with 0.5 M **1**. In each case, 15 mol % pyrrolidine **2** and cocatalyst were used. Although competition from the undesired homoaldol pathway was more apparent with the 10-fold increase in substate concentration, as would be expected, these conditions highlight the superiority of urea cocatalyst **17**, with which the homoaldol product was formed in only 13% yield. This byproduct was formed in slightly higher yield with thiourea **16**, and in much higher yield with bis-triflamide **15** or with catechol (**11**).

Retention of selectivity for cyclization at this substrate concentration suggests that urea **17** is highly selective for electrophilic activation of the enoate ester relative to the aldehyde.
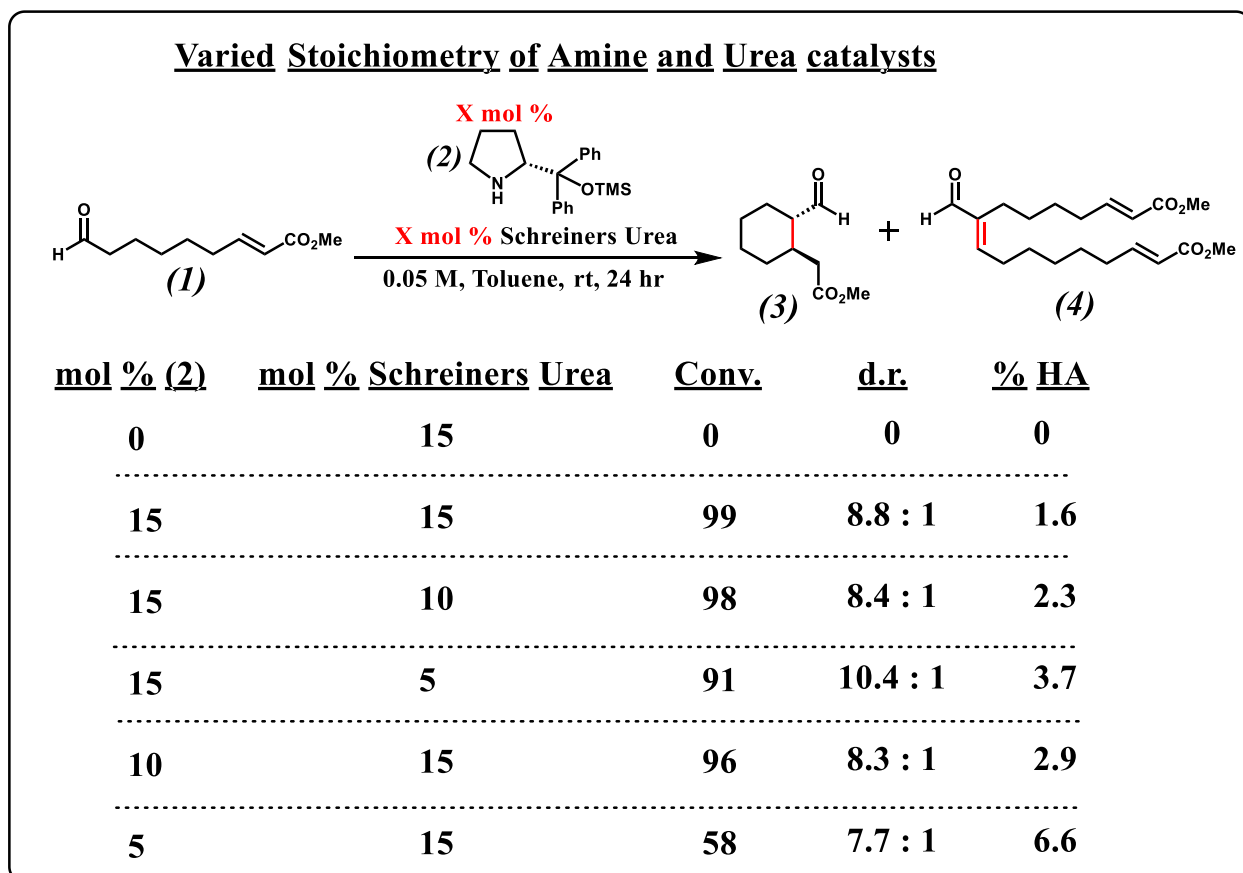
Figure 6. Effect on reaction outcome employing varied stoichiometry of amine and Schreiners urea.

mol % (2)	mol % Schreiners Urea	Conv.	d.r.	% HA
0	15	0	0	0
15	15	99	8.8 : 1	1.6
15	10	98	8.4 : 1	2.3
15	5	91	10.4 : 1	3.7
10	15	96	8.3 : 1	2.9
5	15	58	7.7 : 1	6.6

We explored substrate scope with catalyst pair **2** + **17** (**Figure 8**). Methyl (**3**), ethyl (**20**), and benzyl (**21**) ester cyclization products were formed in similar yields, but enantioselectivity diminished as the ester group became bulkier. Cis versus trans configurations of the products were assigned via NMR analysis. Absolute configuration was determined by X-ray diffraction for derivatives **3A** and **21A** (**Figures 8**); other absolute configurations were assigned by analogy.

3)
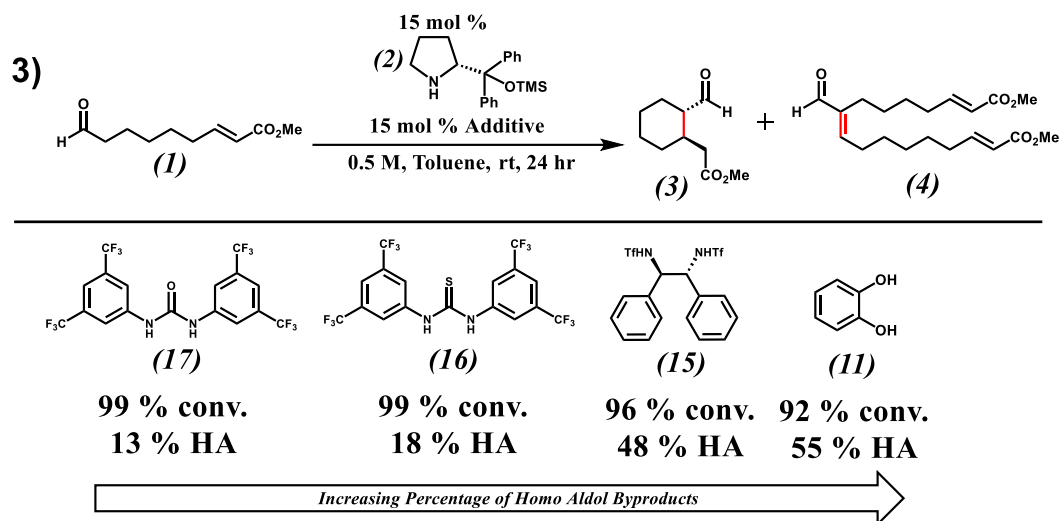
Figure 7. Effect of high substrate concentration on reaction pathway in the presence of lead cocatalysts from Reactions run on 0.05 mmol scale (0.5 M substrate concentration).

Tetrahydropyran product **22** was obtained with high enantioselectivity, although higher

catalyst loadings were required to achieve this outcome. We speculate that the Lewis basic

oxygen in the substrate may compete with the ester carbonyl for hydrogen bonding to urea **17**.

The enoate ester could be replaced with an α,β-unsaturated Weinreb amide (**23**),[35] although the

product was formed with only moderate enantioselectivity. When the length of the substrate was

reduced, cyclopentyl product **24** was obtained in good yield and diasteroselectivity, but without

any enantioselectivity. Compound **24** has been previously used in prostaglandin syntheses.[36,37]

The aldehyde-enoate ester substrate (**25**) that might have formed a seven-membered ring did not

cyclize under our reaction conditions. Enoate ester **26**, too, was unreactive, which is consistent

with Baldwin's ring closure rules.[38] This observation prompted us to evaluate dienoate ester

substrate **27**, which underwent regioselective cyclization to form **28**.

Our new method of generating cyclohexyl aldehyde esters enabled a concise total

synthesis of (−)-yohimbane from cycloheptene (**Figure 9**). (−)-Yohimbane, an indole alkaloid of

the rauwalfia family, displays antipsychotic and antihypertensive activities.[39] The elegant prior

4)
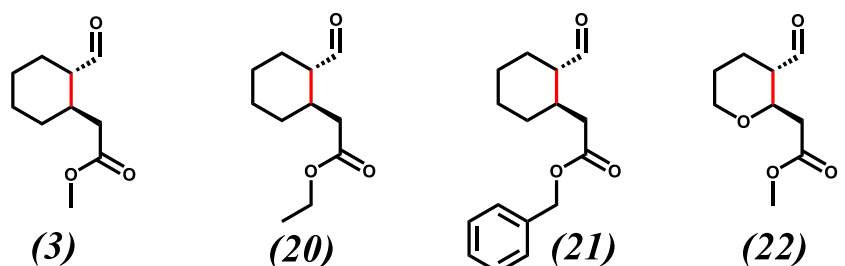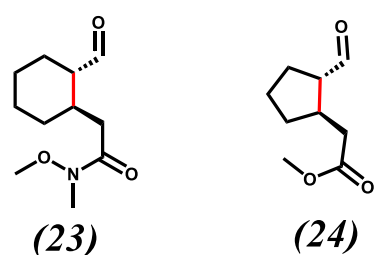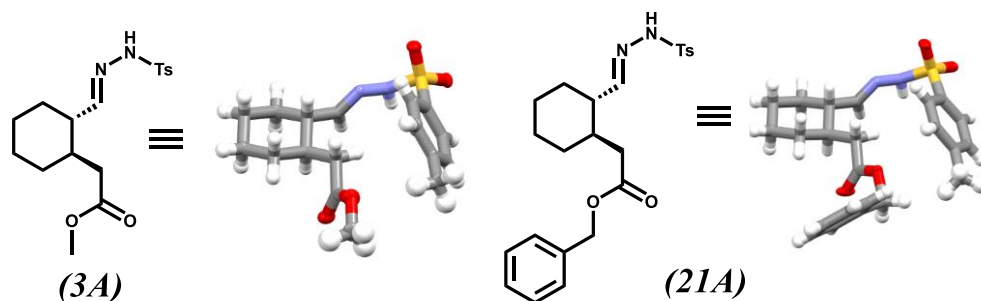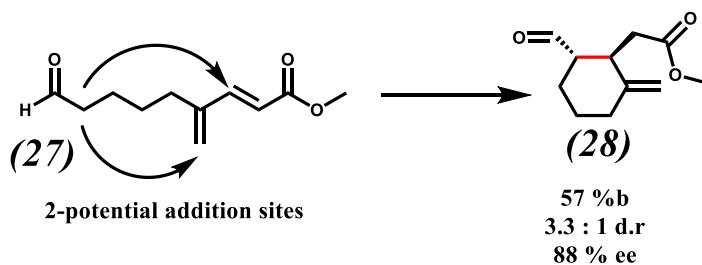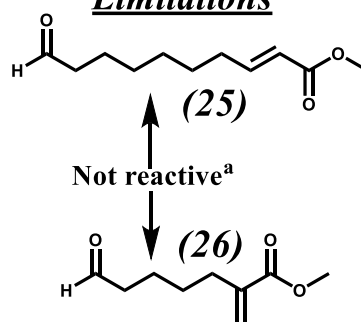
Figure 8. Substrate scope and X-ray structures. Reactions run on 0.5 mmol scale. Yields refer to isolated values. Diastereomeric ratio (d.r.) was determined via 1 H NMR analysis of the crude reaction mixture. (a) 20 mol % **2**, 20 mol % **17**, 0.025 M toluene, 48 h, 0 °C. (b) 30 mol % **2**, 30 mol % **17**, 0.025 M toluene, 72 h, 0 °C. (c) 20 mol % **2**, 20 mol % **16**, 0.05 M toluene, 24 h, rt. Ts = p-toluenesulfonyl. Red indicates bond formed.

enantioselective syntheses of (−)-yohimbane rely on substrate diastereocontrol,[40] enzymatic resolution,[41] or multiple stereodefining steps[42] to control the absolute configuration of the final product. Our cyclization simultaneously sets two adjacent C-sp^3 stereocenters, controlling both relative and absolute configurations, which supports a streamlined route.
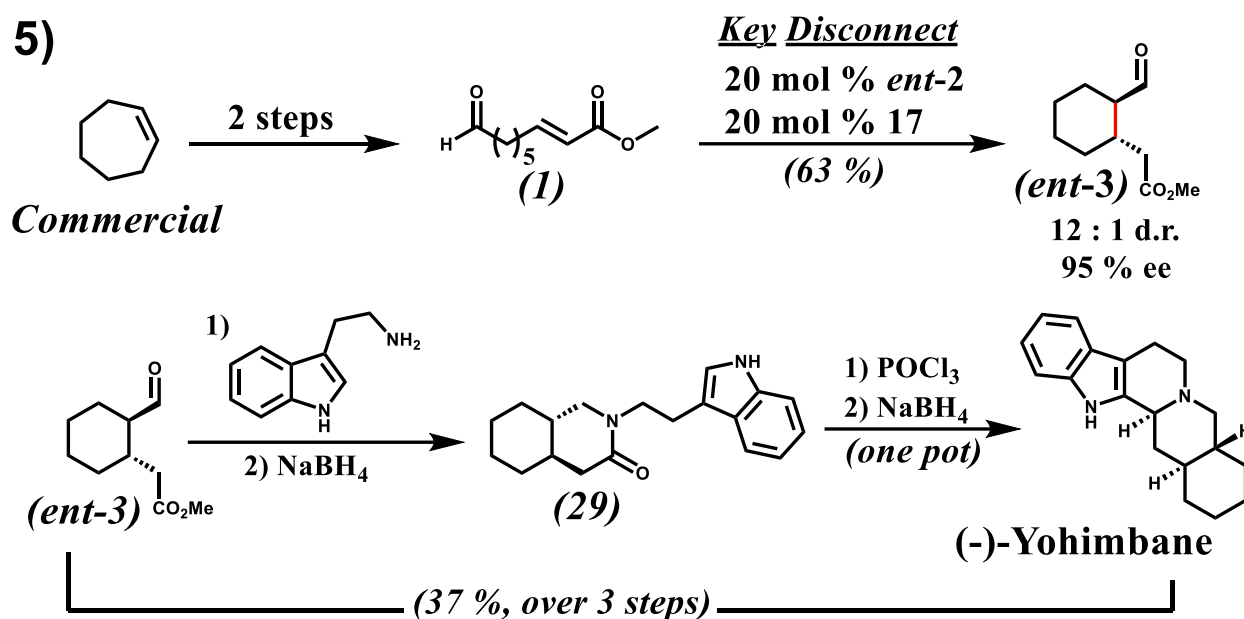
Figure 9. Six-step total synthesis of (-)-yohimbane.

Compound **1** could be prepared in gram quantities from cycloheptene via ozonlysis to generate the monodimethyl acetal,[43] followed by Horner-Wadsworth-Emmons olefination and acetal hydrolysis. Use of pyrrolidine catalyst **ent-2** along with urea cocatalyst **17** produced **ent-3**, which was combined with tryptamine in a one-pot reductive amination-cyclization cascade[44] to form lactam **29**. Bischler-Napieralski reaction[45] of **29** generated (−)-yohimbane in 95% ee.

4.4 Conclusion

Our results demonstrate that the reaction pathway followed by an aldehyde-derived enamine can be controlled through careful choice of the electrophile-activating cocatalyst. These

findings can be seen as part of an increasing communal interest in the development of catalysts that influence selectivity among alternative reaction pathways.[46] Our work reveals surprising variation among diverse Brønsted acid/hydrogen bond donor cocatalysts in terms of the reactivity channel followed by aldehyde-enoate ester **1** in the presence of the widely used Hayashi-Jørgensen catalyst (**2; Figure 4**). Some cocatalysts favor the intramolecular conjugate addition channel to form cyclohexane derivative **3**, while others favor the intermolecular homoaldol condensation channel. A third set of cocatalyst candidates does not promote either reaction. The distinctive ability of urea **17** to provide **3** with superior diastereo- and enantioselectivity could not have been predicted. The enantioselective cyclization mode we have identified represents a new frontier in conjugate additions of aldehyde-derived enamines, which have been extremely widely examined with intrinsically reactive electrophiles such as nitro-alkenes but largely unexplored with the more inert enoate esters.

4.5 Experimental

4.5.1 Materials and Instrumentation

    a. **Materials and reagents**

Solvents and reagents obtained from Sigma-Aldrich included (R)-(+)-α,α-diphenyl-2-pyrrolidinemethanol trimethylsilyl ether, (S)-(-)-α,α-diphenyl-2-pyrrolidinemethanol trimethylsilyl ether, (R)-(+)-α,α-bis[3,5-bis(trifluoromethyl)phenyl]-2-pyrrolidinemethanol, (S)-(-)-α,α-di(2-naphthyl)-2-pyrrolidinemethanol, Schreiner's thiourea catalyst, Schreiner's catalyst, (4R, 5R)-2,2-dimethyl-α, α, α', α'-tetra-phenyldioxolane-4,5-dimethanol, protocatechuic acid ethyl ester, 4-nitrophenol, 3,4-dihydroxy-3-cyclobutene-1,2-dione, 1,1'-bi-2-napthol, (R)-(-)-1,1'-binaphthyl-2-2'diylhydrogenphosphate, catechol, propionic acid, benzoic acid, 1,3-diphenylurea, and trifluoroacetic acid. (R,R)-N-N'-Bis(trifluoromethanesulfonyl)-1,2-diphenylethylenediamine was obtained from TCI America. All commercial reagents were used as received. Chromatography was performed on silica gel (200-425 mesh) using standard techniques. Products were visualized by UV or KMnO$_4$ stain. Solvents used were ACS grade and used as received.

b. Instrument acknowledgements

<ins>**Instrument Name, instrument type, grant, award year**</ins>

Bruker Advance III-400, NMR Spectrometer, NSF CHE-1048642, 2010

Bruker Advance III-500, NMR Spectrometer, Generous gift from Paul J. Bender, 2012

Bruker Advance III-HD-600, NMR Spectrometer, NIH S10 OD012245, 2013

Thermo Q Extractive Plus (Electrospray ionization – quadrupole – ion trap – mass spectrometer), Mass Spectrometer, NIH 1S10 OD020022, 2015

4.5.2 General Procedures

(1)

15 mol %

15 mol %

0.05 M, Toluene, rt, 24 hr

(3)

8.8: 1 d.r.
95 % ee
1.6 % Homo Aldol
> 99 conversion
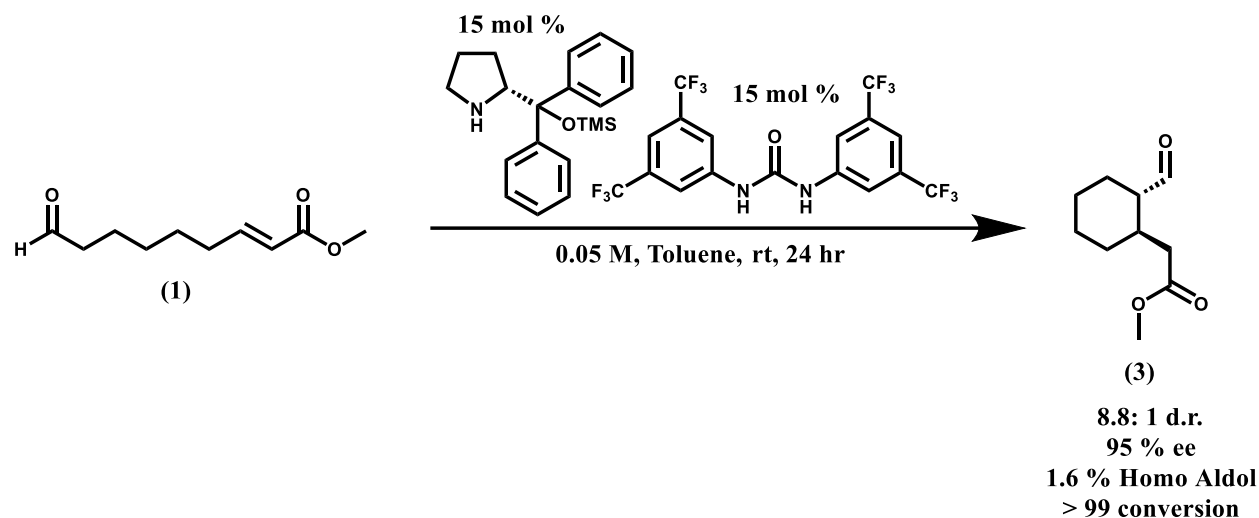
General Procedure: 0.05 mmol cyclization reactions to evaluate hydrogen bond donors, Brønsted acids, solvents, amines, and concentrations.

To a 6 mL glass vial equipped with a magnetic stir were added 710 µL toluene (total volume calculated based on 0.05 M **1**) , 10 mg **1** (0.054 mmol, 300 µL as a 0.181 M stock solution) as a stock solution in toluene, and 3.92 mg Schreiners urea (15 mol %, 0.0081 mmol). Added last was (R)-(+)-α,α-diphenyl-2-pyrrolidinemethanol trimethylsilyl ether (Hayashi-Jørgensen catalyst; 15 mol %, 0.0081 mmol, 75.4 µL of a 0.108 M stock solution) as a stock solution in toluene. The vial was capped, and the reaction mixture was stirred for 24 hours at room temperature. There is no need for exclusion of air.

After stirring for 24 hours, the mixture was diluted with 2 mL of 1:1 water: diethyl ether and shaken vigorously. The organic layer was separated, dried over magnesium sulfate, and concentrated via rotary evaporation. 600 µL of CDCl$_3$ was added to the crude reaction mixture, which was then analyzed by ^{1}H NMR. Percent conversion, percent homo-aldol formation, and the diastereomeric ratio were determined by ^{1}H NMR (integration of the aldehyde signals).

Percent conversion = ((product diastereomer aldehyde resonance integrations + homo aldol aldehyde resonance integration) / (product diastereomer aldehyde resonance integrations + homo aldol aldehyde resonance integration + starting material aldehyde resonance integration)) x 100.

Percent homo aldol = ((homo aldol aldehyde resonance integration) / (product diastereomer aldehyde resonance integrations + homo aldol aldehyde resonance integration)) x 100.

General procedure: Preparative asymmetric cyclization

ent-3

72 %
12 : 1 d.r., 95 % ee
Major diastereomer,
major enantiomer shown
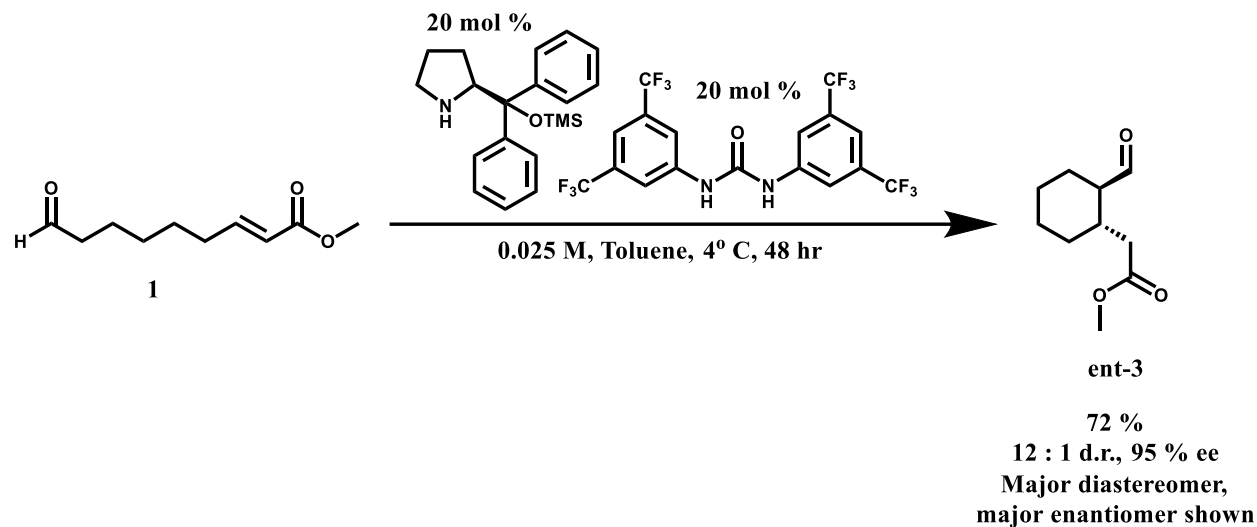
Note: This general procedure uses (*S*)-(-)-α,α-diphenyl-2-pyrrolidinemethanol trimethylsilyl ether. This chiral amine which has the absolute stereochemistry required for the synthesis of (-)-yohimbane. Products **3**, **20-24**, and **27** were synthesized using (*R*)-(+)-α,α-diphenyl-2-pyrrolidinemethanol trimethylsilyl ether, and have the opposite absolute stereochemistry.

To a 22 mL glass vial equipped with a magnetic stir bar was added 9.9 mL toluene (total volume calculated based on 0.025 M **1**) and 49.8 mg **1** (0.27 mmol). The vial was capped and placed at 4° C on a stir plate. After the vial had been cooled for ten minutes, 26.2 mg Schreiners urea (**17**) (20 mol %, 0.054 mmol) and (*S*)-(-)-α,α-diphenyl-2-pyrrolidinemethanol trimethylsilyl ether (20 mol %, 0.054 mmol, 906 μL of a 0.06 M stock solution) as a stock solution in toluene were added. The vial was capped and immediately placed back in a 4° C refrigerator. The reaction mixture was stirred for 48 hours. There is no need for exclusion of air.

After 48 hours, a 100 µL aliquot was concentrated via rotary evaporation. The aliquot was dissolved in 600 µL CDCl$_3$ and analyzed via ^{1}H NMR to obtain: percent conversion (>99 %), diastereomeric ratio (12:1), and percent homo aldol (5 %).

The remaining reaction mixture was concentrated via rotary evaporation. The crude product was purified by silica column chromatography eluting with 7:3 hexanes:diethyl ether (fractions analyzed via KMnO$_4$ stain) to yield 35.7 mg of **ent-3** (95 % ee for the major diastereomer) as a clear oil (35.7 mg, 72 % yield).

Note: We observed minimal amounts of homo aldol products when fresh **1** was used. When **1** was used after weeks or months of storage, higher levels (about 10 %) of homo aldol products were observed. We attribute this to oxidation of the aldehyde to a carboxylic acid after prolonged storage. We speculate that the carboxylic acid impurity serves as a catalyst for homo aldol formation (compare to propionic or benzoic acid, Figure 2). We confirmed this hypothesis by synthesizing new **1**, which provided low levels (1.6 %) of homo aldol products if used immediately after preparation.

General procedure: Preparative racemic cyclization
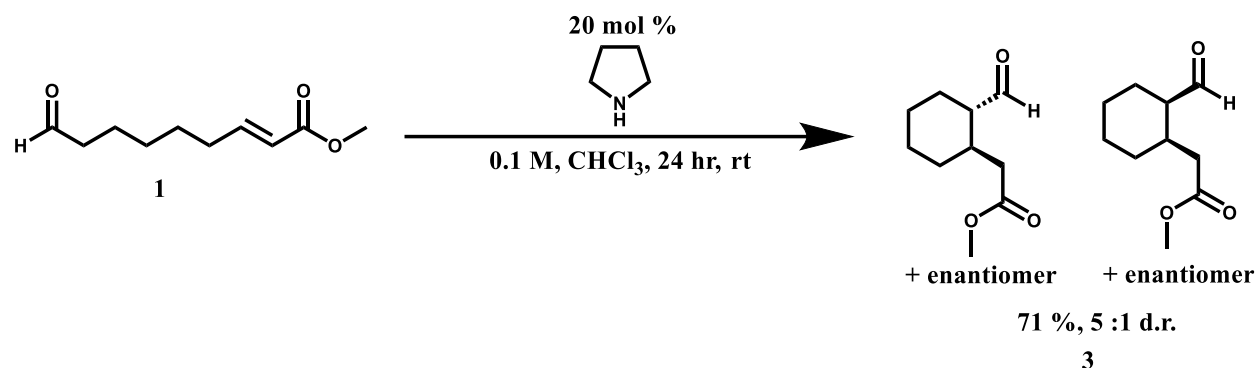
To a 22 mL glass vial equipped with a stir bar were added 86 mg **1** (0.467 mmol) and 4.7 mL of chloroform. Pyrrolidine (0.0934 mmol, 7.7 uL, 20 mol %) was then added. The reaction mixture was stirred vigorously at room temperature for 24 hours, and then the volatiles were removed under vacuum. The crude reaction mixture was purified via column chromatography, eluting with 7:3 pentanes:diethyl ether to yield 61 mg of racemic **3** (61 mg, 71 % yield) as a clear oil.

Note: Some racemic reactions required the addition of Schreiners urea in an equimolar amount relative to pyrrolidine in order to provide sufficient reactivity. Racemic reactions were run in either chloroform or toluene. For detailed reaction conditions of each racemic reaction, refer to the conditions listed in the chiral HPLC traces section.

General procedure: Determination of enantiomeric excess via chiral HPLC

enantiomers of
major diastereomer

p-tosylhyrdrazone derivative
of eantiomers of major diastereomer
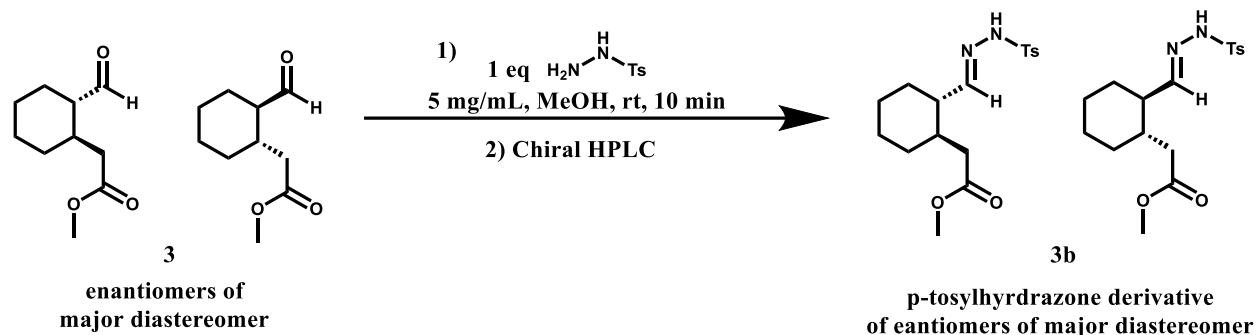
To a 6 mL glass vial equipped with a stir bar were added 5 mg **3** (0.0271 mmol) and 5 mg p-toluenesulfonyl hydrazide (0.0271 mmol, 1 eq). 1 mL of methanol was then added, and the reaction mixture was stirred at room temperature for 10 minutes. The reaction mixture was then transferred to an HPLC vial.

A 5 µL aliquot was injected onto a Daicel ChiralPak IF-3 3µm 4.6 mm x 250 mm column on a Waters Acquit arc LC-MS. The eluent was isocratic, 85 % hexane, 15 % isopropanol + 0.1 % formic acid at a flow rate of 1 mL/min. The tosylhydrazone products were visualized via the 254 nm channel. Enantiomeric excess (% ee) was calculated from the enantiomeric ratio (e.r.) as determined by peak area in the LC-MS trace (254 nm). (Enantiomeric excess = [Peak area of major enantiomer – Peak area of minor enantiomer]). For all conditions used to separate both racemic and enantioenriched products **3**, **20**-**24**, refer to the chiral HPLC trace section. The same procedure was followed for each racemic hydrazone sample.

Note: The major and minor diastereomers of each reaction were inseparable via column chromatography. In most cases, we obtained aldehyde diastereomer mixtures with a diastereomeric ratio of at least 8:1 after column chromatography. This mixture was subjected to hydrazone formation and analyzed via chiral HPLC. We are able to separate each diastereomer

and the corresponding enantiomer via chiral HPLC. The % ee of the major diastereomer is

reported. The graphic above shows the enantiomers of only the major diastereomer and excludes

the enantiomers of the minor diastereomer for the sake of simplicity.

Determination of enantiomeric excess via ^{1}H NMR of 27
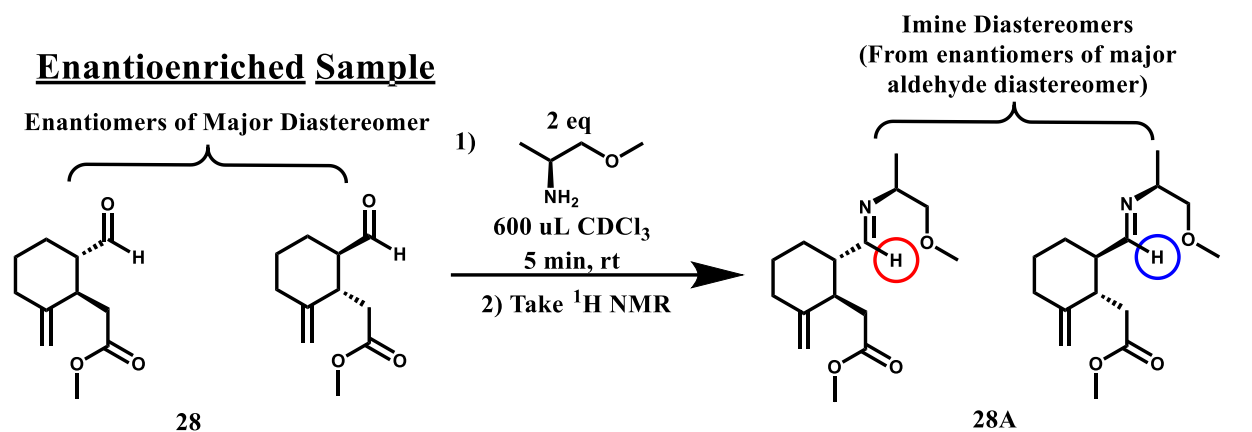
To an NMR tube containing 15 mg **27** (0.0764 mmol) was added 600 µL CDCl$_3$. Next, 13.6 mg

(*S*)-1-methoxy-2-propylamine (0.153 mmol, 2 eq) was added to the NMR tube, and the mixture

was shaken at room temperature for five minutes. After 5 minutes, an ^{1}H NMR spectra was

acquired. Enantiomeric excess was determined via integration of the diastereomeric protons

following the method of Chi and Gellman.[47]

General procedure: Horner-Wadsworth-Emmons Reaction and Acetal Cleavage

30
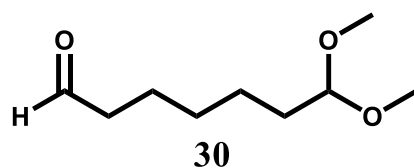
30 was synthesized via a published procedure. ^{1}H and ^{13}C NMR spectra matched those reported.[48]
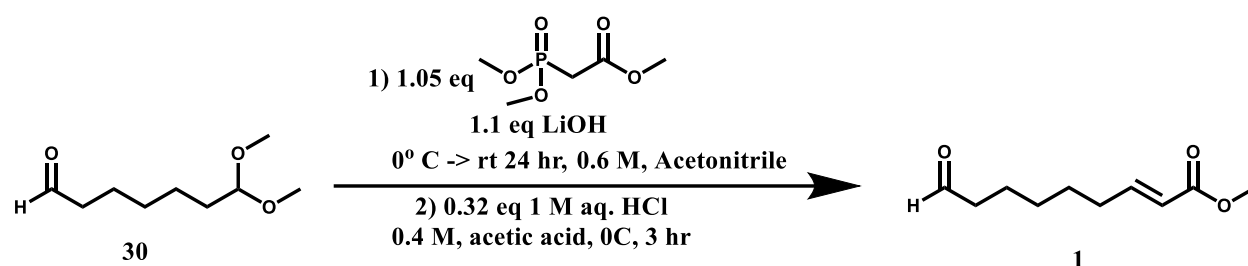
To a 50 mL round bottom flask equipped with a stir bar were added 2.5 g (0.0143 mol) **30**, finely ground lithium hydroxide (0.0157 mol, 378 mg, 1.1 eq), and 23.8 mL acetonitrile. The flask was sealed with a septum, submerged in an ice bath, and allowed to cool to 0° C under a nitrogen atmosphere. Once the solution had cooled, trimethyl phosphonoacetate (0.0150 mol, 2.43 mL, 1.05 eq) was added dropwise via syringe. The reaction mixture was stirred vigorously and allowed to warm to room temperature over 24 hours. The volatiles were then removed under vacuum. The residue was dissolved in 200 mL of 1:1 ethyl acetate:water, which was transferred to a separatory funnel, and the organic layer was removed. The organic layer was then washed with brine. The organic layer was dried with magnesium sulfate, filtered, and concentrated under vacuum to obtain a clear oil. The clear oil was then dissolved in 36 mL of acetic acid and cooled in an ice bath. Before the acetic acid froze, 1 M aqueous hydrogen chloride (0.32 eq, 4.58 mL)

was added. The reaction mixture was allowed to stir for 3 hours at 0° C. After 3 hours, the

mixture was diluted with 200 mL of 1:1 DCM:brine, which was transferred to a separatory

funnel, and the organic layer was removed. The organic layer was dried with magnesium sulfate,

filtered, and concentrated under vacuum to obtain a clear oil. The oil was purified via column

chromatography, eluting with 6:4 pentanes:diethyl ether to yield 1.8 g of **1** as a clear oil (1.8 g,

68 % over two steps).

Substrate 1: **^{1}H NMR** (500 MHz, CDCl$_3$) δ 9.77 (t, *J* = 1.7 Hz, 1H), 6.95 (dt, *J* = 15.6, 7.0 Hz,

1H), 5.82 (dt, *J* = 15.7, 1.6 Hz, 1H), 3.73 (s, 3H), 2.44 (td, *J* = 7.3, 1.7 Hz, 2H), 2.22 (qd, *J* = 7.2,

1.6 Hz, 2H), 1.65 (p, *J* = 7.4 Hz, 2H), 1.49 (p, *J* = 14.6, 7.4 Hz, 2H), 1.40 – 1.32 (m, 2H). **^{13}C**

NMR (125 MHz, CDCl$_3$) δ 202.4, 167.0, 149.1, 121.1, 51.4, 43.7, 31.9, 28.5, 27.7, 21.7. **HRMS**

(ESI-Q-IT) m/z: [M + Na]$^+$ calculated for C$_{10}$H$_{16}$O$_3$Na 207.0992; Found 207.0990.

General procedure: 2.65 mmol scale cyclization of 1.
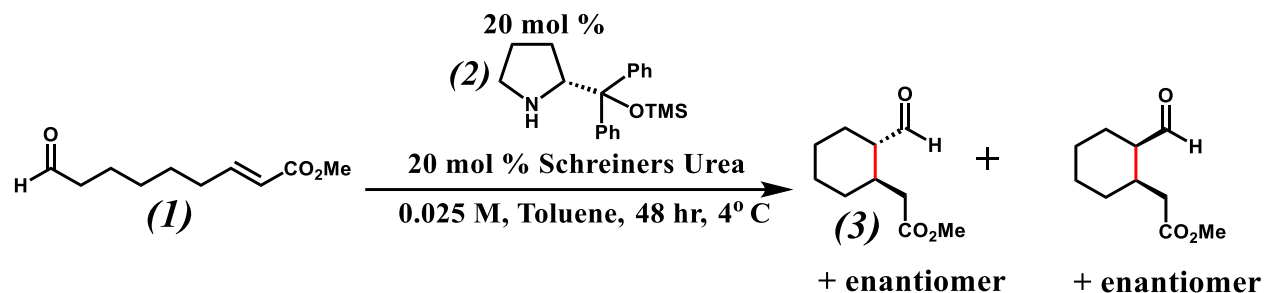
To a 250 mL round bottom flask equipped with a magnetic stir bar was added 106 mL toluene (total volume calculated based on 0.025 M **1**) and 488 mg **1** (2.65 mmol). The round bottom was capped and placed at 4° C on a stir plate. After the vial had been cooled for ten minutes, 193 mg Schreiners urea (**17**) (20 mol %, 0.53 mmol) and (*R*)-(+)-α,α-diphenyl-2-pyrrolidinemethanol trimethylsilyl ether (**2**) (20 mol %, 0.53 mmol, 130 mg) were added. The vial was capped and immediately placed back in a 4° C refrigerator. The reaction mixture was stirred for 48 hours. There is no need for exclusion of air.

After 48 hours, a 100 μL aliquot was concentrated via rotary evaporation. The aliquot was dissolved in 600 μL CDCl$_3$ and analyzed via ^{1}H NMR to obtain: percent conversion (>99 %), diastereomeric ratio (18:1), and percent homo aldol (1.6 %).

The remaining reaction mixture was concentrated via rotary evaporation. The crude product was purified by silica column chromatography eluting with 7:3 hexanes:diethyl ether (fractions analyzed via KMnO$_4$ stain) to yield 307 mg of **3** (95 % ee for the major diastereomer) as a clear oil (307 mg, 63 % yield).

4.5.3 Small Molecule Synthesis, Substrate and Product Characterization.
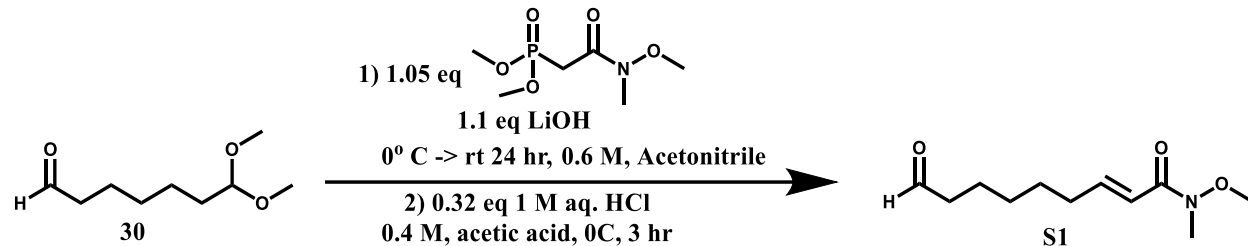
S1 was prepared via the same reaction sequence as described above for **1**. **S1** was purified via column chromatography, eluting with 6:4 hexanes:ethyl acetate to yield 476 mg of **S1** (476 mg, 39 % over two steps) as a clear oil.

Substrate S1: ^{1}H NMR (500 MHz, CDCl$_3$) δ 9.77 (t, J = 1.7 Hz, 1H), 6.96 (dt, J = 15.4, 7.1 Hz, 1H), 6.40 (dt, J = 15.3, 1.6 Hz, 1H), 3.70 (s, 3H), 3.24 (s, 3H), 2.44 (td, J = 7.3, 1.7 Hz, 2H), 2.25 (qd, J = 7.2, 1.5 Hz, 2H), 1.65 (p, J = 7.4 Hz, 2H), 1.51 (p, J = 7.4 Hz, 2H), 1.41 – 1.33 (m, 2H). ^{13}**C NMR** (125 MHz, CDCl$_3$) δ 202.6, 166.9, 147.4, 118.9, 61.6, 43.7, 32.3, 32.2, 28.6, 28.0, 21.8. **HRMS** (ESI-Q-IT) m/z: [M + Na]$^+$ calculated for C$_{11}$H$_{19}$NO$_3$Na 236.1257; Found 236.1254.
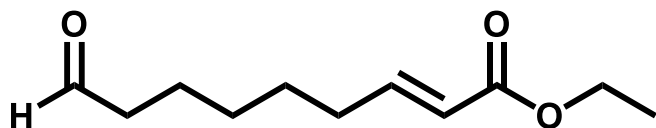
S2 was synthesized via a published procedure. ^{1}H and ^{13}C NMR spectra matched those reported.[49]

S3
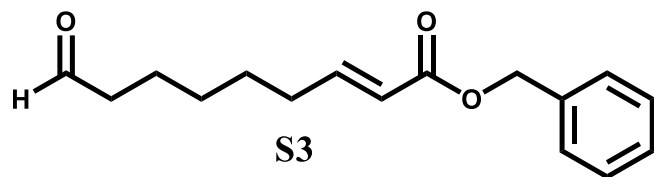
S3 was synthesized via a published procedure. ¹H and ¹³C NMR spectra matched those reported.[50]

S4
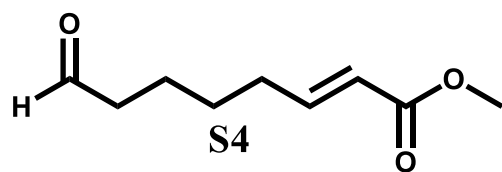
S4 was synthesized via a published procedure. ¹H and ¹³C NMR spectra matched those reported.[51]

S5
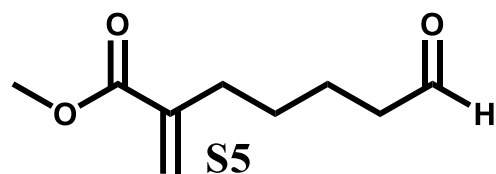
S5 was synthesized via a published procedure. ¹H and ¹³C NMR spectra matched those reported.[52]
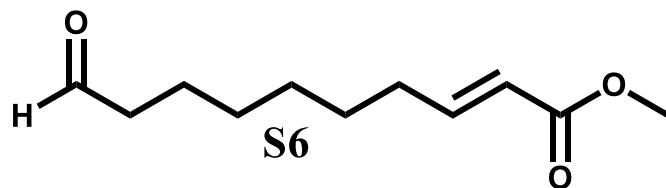
Substrate **S6** was synthesized via a procedure analogous to one published by Schreiber et al. for

the synthesis of **30**.[48] Subsequent Horner-Wadsworth-Emmons olefination and acetal cleavage,

following the general procedure described in section 2f, yielded **S6** as a clear oil (352 mg, 36 %

over two steps).

S6: ^{1}H NMR (500 MHz, CDCl$_3$) δ 9.77 (t, J = 1.8 Hz, 1H), 6.96 (dt, J = 15.5, 7.0 Hz, 1H), 5.82

(dt, J = 15.7, 1.6 Hz, 1H), 3.73 (s, 3H), 2.43 (td, J = 7.3, 1.7 Hz, 2H), 2.20 (qd, J = 7.1, 1.6 Hz,

2H), 1.68 – 1.58 (m, 2H), 1.47 (dq, J = 11.4, 6.9 Hz, 2H), 1.38 – 1.30 (m, 4H). ^{13}**C NMR** (125

MHz, CDCl$_3$) δ 202.7, 167.1, 149.4, 121.0, 51.4, 43.8, 32.0, 28.9, 28.8, 27.7, 21.9. **HRMS** (ESI-

Q-IT) m/z: [M + Na]$^+$ calculated for C$_{11}$H$_{18}$O$_3$Na 221.1148; Found 221.1146.
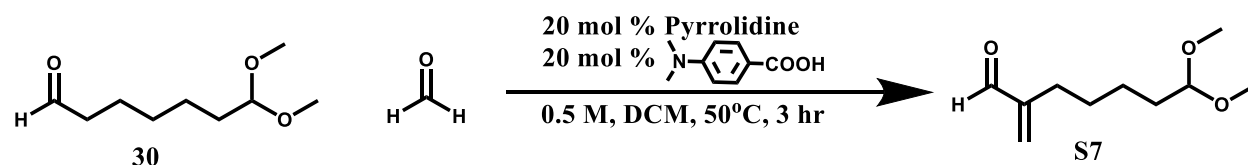
To a 50 mL round bottom flask equipped with a stir bar were added 2.04 g **30** (0.0117 mol), 950

μL of a 37 wt % in water formaldehyde solution (0.0117 mol, 1 eq), 387 mg 4-

(dimethylamino)benzoic acid (2.34 mmol, 20 mol %), and 23.4 mL dichloromethane. To the

resulting slurry was added 192 μL pyrrolidine (2.34 mmol, 20 mol %), resulting in a clear

solution. The reaction vessel was equipped with a condenser, and the mixture was heated to

reflux (oil bath at 50ºC) for 3 hours. The reaction mixture was then cooled and diluted with 100

mL of dichloromethane and washed 2 times with aqueous saturated sodium bicarbonate solution.

The organic layer was separated and washed with brine, then dried over magnesium sulfate, and concentrated via rotary evaporation. The crude oil was purified via column chromatography, eluting with 8:2 hexanes:ethyl acetate, to yield 1.68 g of **S7** as a clear oil (1.68 g, 77 %). ^{1}H and ^{13}C spectra matched those reported.[52]
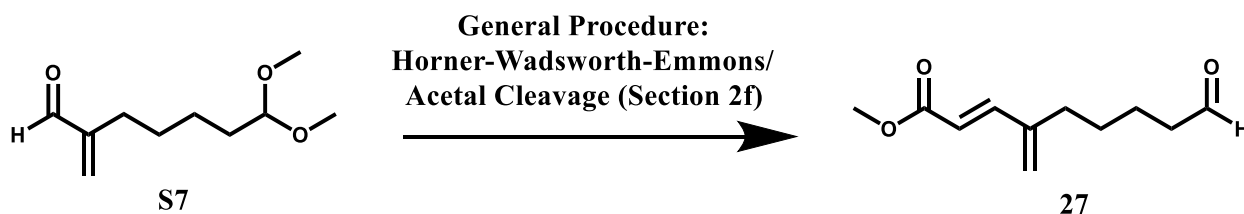
Substrate **S8** was synthesized from **S7** according to the general procedure described in section 2f. Compound **27** was purified via column chromatography, eluting with 6:4 hexanes:diethyl ether to obtain 229 mg **27** as a clear oil (229 mg, 23 % over two steps).

Substrate 27: ^{1}**H NMR** (500 MHz, CDCl$_3$) δ 9.77 (t, J = 1.7 Hz, 1H), 7.31 (dd, J = 16.0, 0.7 Hz, 1H), 5.91 (d, J = 16.0 Hz, 1H), 5.37 (dd, J = 32.7, 1.4 Hz, 2H), 3.77 (s, 3H), 2.47 (td, J = 7.3, 1.7 Hz, 2H), 2.26 (t, J = 7.6 Hz, 2H), 1.67 (dt, J = 15.4, 7.4 Hz, 2H), 1.58 – 1.49 (m, 2H). ^{13}**C NMR** (125 MHz, CDCl$_3$) δ 202.3, 167.5, 146.6, 144.0, 123.6, 117.7, 51.6, 43.6, 31.3, 27.3, 21.7. **HRMS** (ESI-Q-IT) m/z: [M +Na]$^+$ calculated for C$_{11}$H$_{16}$O$_3$Na 219.0992; Found 219.0989.
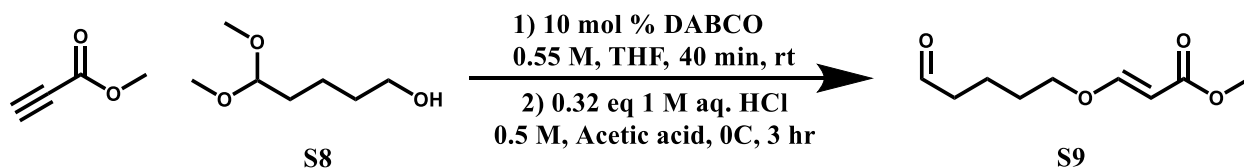
Compound **S8** was synthesized via a published procedure. ^{1}H and ^{13}C spectra matched those reported.[53] The synthesis of **S9** was carried out by Philip Lampkin.

To a 50 mL round bottom flask equipped with a stir bar were added 1.69 g (0.0113 mol, 1.1 eq) **S8,** DABCO (127 mg, 0.00113 mol, 0.1 eq) and 19.0 mL tetrahydrofuran. With stirring, methyl propiolate (0.01035 mol, 0.92 mL, 1 eq) was added dropwise via syringe over 10 minutes. The reaction mixture was then stirred vigorously for 40 minutes at room temperature. The crude reaction mixture was transferred to a separatory funnel and washed with sodium hydroxide (10% solution, 5 mL). The organic layer was removed, and the aqueous layer was extracted with dichloromethane (4 x 15 mL). The organic layers were combined, washed with brine (3 x 20 mL), and dried over magnesium sulfate. The organic solution was concentrated in vacuo to obtain a clear oil. The clear oil was then dissolved in 18 mL of acetic acid and cooled in an ice bath. Before the acetic acid froze, 1 M aqueous hydrogen chloride (0.32 eq, 2.32 mL) was added. The reaction mixture was allowed to stir for 3 hours at 0° C. The reaction was diluted with 100 mL of 1:1 DCM:brine and transferred to a separatory funnel, and the organic layer was removed. The organic layer was dried over magnesium sulfate, filtered, and concentrated under vacuum to obtain a clear oil. The oil was purified via column chromatography, eluting with 4:6 pentanes:diethyl ether to yield 770 mg **S9** as a clear oil (770 mg, 40 % yield over two steps).
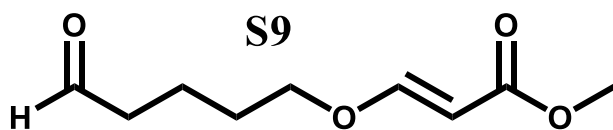
S9: ^{1}**H NMR** (500 MHz, CDCl$_3$) δ 9.79 (s, 1H), 7.58 (d, J = 12.6 Hz, 1H), 5.20 (dd, J = 12.7, 1.2 Hz, 1H), 3.86 (d, J = 4.8 Hz, 2H), 3.70 (s, 3H), 2.51 (td, J = 6.2, 5.5, 2.2 Hz, 2H), 1.82 – 1.66 (m, 4H). ^{13}**C NMR** (125 MHz, CDCl$_3$) δ 201.7, 168.2, 162.3, 96.3, 70.4, 51.1, 43.2, 28.2, 18.4.

HRMS (ESI-Q-IT) m/z: [M + Na]$^+$ calculated for C$_9$H$_{14}$O$_4$Na 209.0784; Found 209.0783. Clear oil.

3
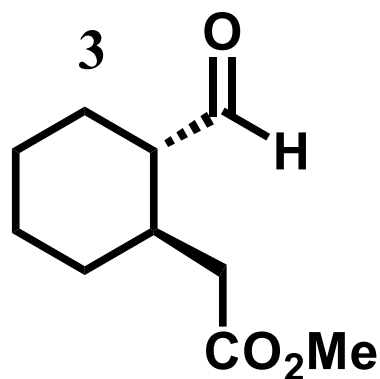
3: ^{1}H NMR (600 MHz, Chloroform-*d*) δ 9.55 (d, *J* = 3.1 Hz, 1H), 3.66 (s, 3H), 2.45 – 2.41 (m, 1H), 2.19 (t, *J* = 7.4 Hz, 1H), 2.11 (ddt, *J* = 21.1, 10.1, 3.7 Hz, 2H), 1.87 – 1.76 (m, 3H), 1.75 – 1.71 (m, 1H), 1.40 – 1.33 (m, 1H), 1.33 – 1.26 (m, 2H), 1.13 – 1.05 (m, 1H). ^{13}**C NMR** (150 MHz, CDCl$_3$) δ 204.1, 172.8, 54.8, 51.5, 39.0, 33.2, 31.1, 25.9, 24.9, 24.5. **HRMS** (ESI-Q-IT) m/z: [M + Na]$^+$ calculated for C$_{10}$H$_{16}$O$_3$Na 207.0992; Found 207.0990. Clear oil. Purified with 7:3 pentanes:diethyl ether (58 mg, 63 %).

20
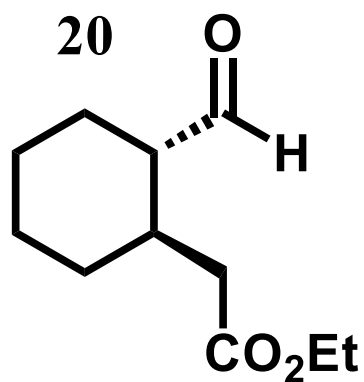
20: ^{1}H NMR (600 MHz, CDCl$_3$) δ 9.56 (d, J = 3.2 Hz, 1H), 4.12 (q, J = 7.1 Hz, 2H), 2.41 (d, J = 10.7 Hz, 1H), 2.19 – 2.16 (m, 1H), 2.16 – 2.12 (m, 1H), 2.10 (tt, J = 10.2, 3.4 Hz, 1H), 1.86 – 1.81 (m, 2H), 1.79 (dddd, J = 10.8, 5.8, 3.6, 1.4 Hz, 1H), 1.73 (dqd, J = 11.3, 4.1, 1.4 Hz, 1H), 1.42 – 1.33 (m, 1H), 1.34 – 1.27 (m, 2H), 1.25 (t, J = 7.1 Hz, 3H), 1.13 – 1.06 (m, 1H). ^{13}C NMR (150 MHz, CDCl$_3$) δ 204.2, 172.3, 60.4, 54.8, 39.3, 33.3, 31.0, 25.9, 24.9, 24.5, 14.2. HRMS (ESI-Q-IT) m/z: [M + H]$^+$ calculated for C$_{11}$H$_{19}$O$_3$ 221.1148; Found 221.1146. Clear oil. Purified with 7:3 pentanes: diethyl ether (74 mg, 67 %).
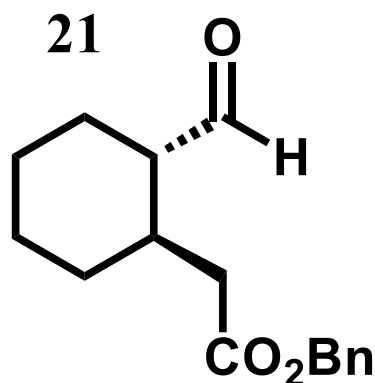
21: ^{1}H NMR (600 MHz, CDCl$_3$) δ 9.54 (d, J = 3.2 Hz, 1H), 7.37 – 7.31 (m, 5H), 5.10 (d, J = 2.2 Hz, 2H), 2.47 (dd, J = 15.3, 4.6 Hz, 1H), 2.23 (dd, J = 15.2, 8.1 Hz, 1H), 2.17 (ddt, J = 14.2, 6.3, 3.8 Hz, 1H), 2.09 (tt, J = 10.1, 3.5 Hz, 1H), 1.85 – 1.79 (m, 2H), 1.77 (dtd, J = 11.2, 3.8, 2.2 Hz, 1H), 1.70 (dtt, J = 9.2, 3.7, 1.7 Hz, 1H), 1.39 – 1.31 (m, 1H), 1.31 – 1.24 (m, 2H), 1.12 – 1.04 (m, 1H). ^{13}C NMR (150 MHz, CDCl$_3$) δ 204.1, 172.1, 135.8, 128.5, 128.2, 66.2, 54.7, 39.1, 33.2, 31.0, 25.8, 24.9, 24.5. HRMS (ESI-Q-IT) m/z: [M + Na]$^+$ calculated for C$_{16}$H$_{20}$O$_3$Na 283.1305; Found 283.1300. Clear oil. Purified with 7:3 pentanes: diethyl ether (83 mg, 64 %).

22

O

H

O

CO₂Me
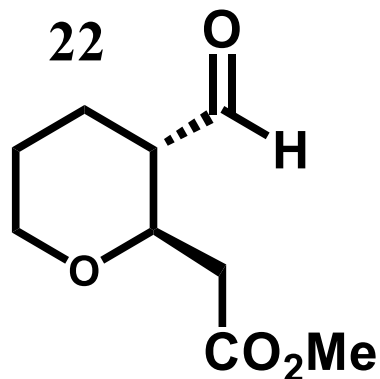
22: ¹H NMR Compound **22** was isolated by Philip Lampkin.

(600 MHz, CDCl₃) δ 9.61 (d, *J* = 2.3 Hz, 1H), 3.99 (m, *J* = 4.1, 1H), 3.96 (ddd, *J* = 9.8, 8.3, 3.5 Hz, 1H), 3.70 (s, 3H), 3.42 (dd, *J* = 14.6, 11.4 Hz, 1H), 2.68 (dd, *J* = 15.3, 3.6 Hz, 1H), 2.51 (dd, *J* = 15.3, 8.4 Hz, 1H), 2.45 (dddd, *J* = 12.1, 9.8, 4.0, 2.3 Hz, 1H), 2.09 (dqd, *J* = 13.0, 3.5, 1.8 Hz, 1H), 1.73 – 1.65 (m, 2H), 1.60 – 1.55 (m, 1H). **¹³C NMR** (150 MHz, CDCl₃) δ 201.9, 171.3, 73.2, 67.6, 52.9, 51.8, 39.2, 24.5, 23.9. **HRMS** (ESI-Q-IT) m/z: [M + Na]⁺ calculated for C₉H₁₄O₄Na 209.0784; Found 209.0783. Clear oil. Purified with 4:6 pentanes:diethyl ether (46 mg, 49 %).

24

O

O

O
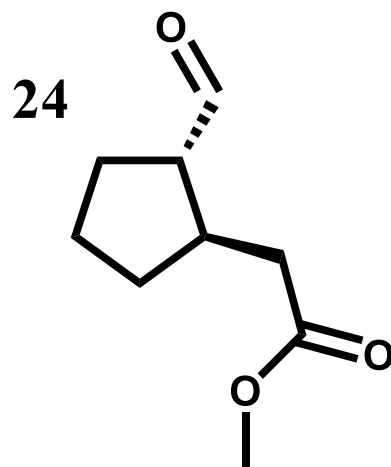
24: ¹H NMR (600 MHz, CDCl₃) δ 9.61 (d, *J* = 3.3 Hz, 1H), 3.66 (s, 3H), 2.58 (h, *J* = 7.7 Hz, 1H), 2.43 – 2.43 (m, 1H), 2.44 – 2.41 (m, 2H), 2.02 – 1.94 (m, 1H), 1.89 (td, *J* = 7.8, 6.6 Hz, 2H), 1.78 – 1.69 (m, 1H), 1.63 (ddt, *J* = 15.7, 13.0, 7.8 Hz, 1H), 1.34 (dq, *J* = 12.7, 8.4 Hz, 1H). **¹³C NMR** (150 MHz, CDCl₃) δ 203.1, 172.8, 57.3, 51.6, 38.9, 37.1, 32.8, 26.7, 24.6. Clear oil. Purified with 7:3 hexanes:diethyl ether (65 mg, 76 %). Trans stereochemistry was assigned based on comparison of spectra to previously published ¹H and ¹³C data.[54,55]
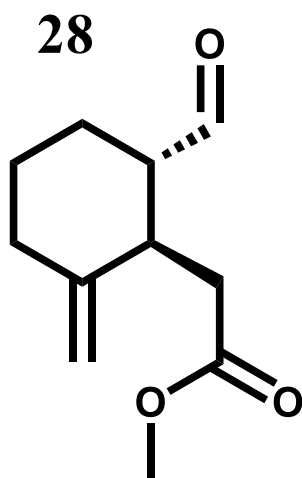
28: ¹H NMR (600 MHz, CDCl₃) δ 9.62 (d, *J* = 1.9 Hz, 1H), 4.78 (p, *J* = 1.1 Hz, 1H), 4.73 (d, *J* = 1.3 Hz, 1H), 3.67 (s, 3H), 3.12 (q, *J* = 7.0 Hz, 1H), 2.60 (dd, *J* = 15.6, 8.2 Hz, 1H), 2.54 (dd, *J* = 15.6, 6.4 Hz, 1H), 2.32 (tdd, *J* = 6.8, 5.0, 1.9 Hz, 1H), 2.26 (ddd, *J* = 13.6, 8.7, 4.9 Hz, 1H), 2.10 (dddd, *J* = 13.4, 7.9, 4.5, 1.1 Hz, 1H), 1.84 – 1.79 (m, 2H), 1.64 (qt, *J* = 9.1, 3.9 Hz, 1H), 1.60 – 1.54 (m, 1H). **¹³C NMR** (150 MHz, CDCl₃) δ 203.5, 172.5, 147.2, 109.4, 53.7, 51.7, 39.0, 36.3, 33.1, 25.3, 23.5. Clear oil. Purified with 6:4 pentanes:diethyl ether. **HRMS** (ESI-Q-IT) m/z: [M + Na]⁺ calculated for $C_{11}H_{16}O_3Na$ 219.0992; Found 219.0989. (56 mg, 57 %).

23
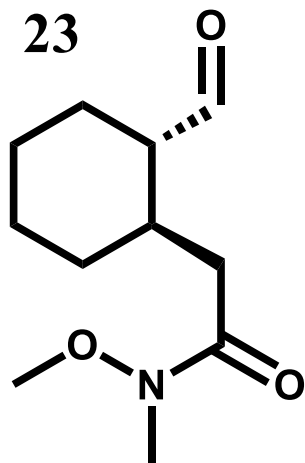
23: ¹H NMR (600 MHz, CDCl₃) δ 9.51 (d, *J* = 3.9 Hz, 1H), 3.66 (s, 3H), 3.16 (s, 3H), 2.46 (dd, *J* = 15.4, 5.1 Hz, 1H), 2.32 (dd, *J* = 15.3, 7.7 Hz, 1H), 2.29 – 2.19 (m, 1H), 2.07 (ddt, *J* = 11.5, 10.3, 3.7 Hz, 1H), 1.87 (dt, *J* = 12.9, 4.0 Hz, 1H), 1.82 – 1.77 (m, 2H), 1.75 – 1.71 (m, 1H), 1.42 (td, *J* = 11.9, 6.6 Hz, 1H), 1.36 – 1.23 (m, 2H), 1.08 (qd, *J* = 11.9, 3.6 Hz, 1H). **¹³C NMR** (150 MHz, CDCl₃) δ 204.7, 172.9, 61.2, 55.6, 36.8, 32.8, 32.0, 31.5, 26.0, 25.1, 24.5. **HRMS** (ESI-Q-IT) m/z: [M + Na] calculated for C₁₁H₁₉NO₃Na 236.1257; Found 236.1254. Clear oil. Purified with 6:4 hexanes:ethyl acetate. (65 mg, 61 %).

Substrate **1** was synthesized via a published procedure. ^{1}H and ^{13}C NMR spectra matched those reported.[48]

20 mol %

20 mol %

0.025 M, Toluene, 4° C, 48 hr

Major diastereomer, major enantiomer shown

ent-3
72 %
12 : 1 d.r., 95 % ee

1
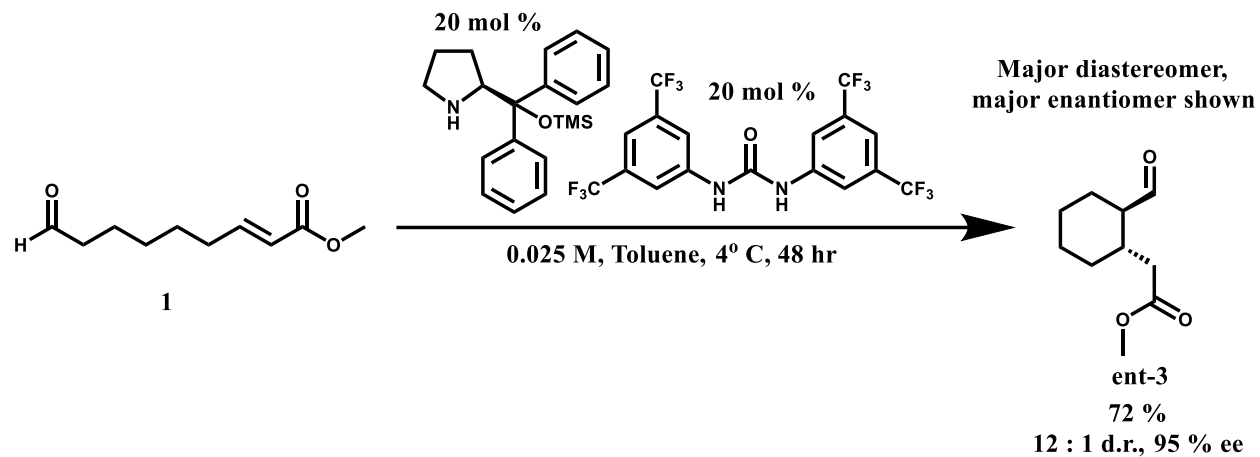
Product **ent-3** was synthesized according to the procedure described above.
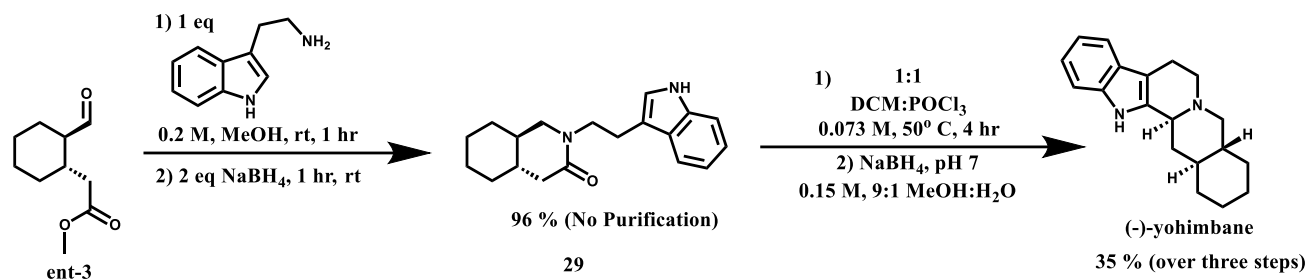
To a 22 mL glass vial equipped with a stir bar were added 98 mg **ent-3** (0.532 mmol) and 2.7 mL of anhydrous methanol. To this solution was added 85.2 mg of tryptamine (0.532 mmol, 1 eq). The reaction mixture was allowed to stir at room temperature for 1 hour, and then 40.4 mg sodium borohydride (1.06 mmol, 2 eq) was added portionwise. The resulting mixture was stirred at room temperature for 1 hour. 5 mL of 1 M aqueous NaOH was then added, followed by 30 mL of ethyl acetate. The organic layer was removed, and the aqueous was extracted again with 30 mL of ethyl acetate. The ethyl acetate layers were combined and washed with brine. The organic layer was dried over magnesium sulfate, filtered and concentrated via rotary evaporation to yield 150 mg **29** as a crude brown solid (150 mg, 96 % yield). A portion of **29** was carried forward without purification.

To an oven-dried 10 mL round bottom flask equipped with a stir bar was added 86 mg **29** (0.29 mmol). Next, 2 mL of anhydrous dichloromethane and 2 mL of $POCl_3$ were added, and the round bottom was fitted with a reflux condenser and put under a nitrogen atmosphere. The flask was placed in a preheated oil bath at 50º C, and the solution was allowed to reflux for 4 hours. The reaction mixture was then cooled to room temperature and concentrated via rotary evaporation. The resulting residue was dissolved in 3.5 mL of 9:1 MeOH:water, which was cooled to 0º C. $NaBH_4$ was then added to the solution until the pH was 7. Next, 2 mL of saturated aqueous ammonium chloride solution was added dropwise, along with a small chunk of ice. The resulting mixture was diluted with 20 mL of dichloromethane and transferred to a

separatory funnel. The organic layer was removed, and the aqueous layer was extracted (3 x 20

mL) with dichloromethane. The organic layers were combined and washed with brine. The

organic layer was then dried over magnesium sulfate, filtered and concentrated via rotary

evaporation to obtain a tan solid. The crude solid was purified via column chromatography,

eluting with 6:4 ethyl acetate: hexanes, visualizing with $KMnO_4$ stain. The column fractions

were then concentrated to obtain a white solid that was recrystallized from a minimal amount of

boiling ethanol to obtain 29.2 mg of (-)-yohimbane as fine white needles (29.2 mg, 35 % yield

over three steps). See subsequent sections for ^{1}H NMR, ^{13}C NMR, melting point, high resolution

mass spectra, and optical rotation data.

(-)-Yohimbane ^{1}H-NMR comparison

Aube, J.; Ghosh, S.; Tanol, M. Symmetry-Driven Synthesis of Indole Alkaloids: Asymmetric Total Syntheses of (+)-Yohimbine, (-)-Yohimbone, (-)-Yohimbane, and (+)-Alloyohimbane. *J. Am. Chem. Soc.*, **1994**, 116, 9009-9018. (-)-Yohimbane, 500 MHz, CDCl$_3$

2020 (-)-Yohimbane, 500 MHz, CDCl$_3$ (This work)

Ghosh, A. K.; Sarkar, A. Enantioselective Syntheses of (-)-Alloyohimbane and (-)-Yohimbane by an Efficient Enzymatic Desymmetrization Process. *Eur. J. Org. Chem.* **2016**, 6001-6009. (-)-Yohimbane, 400 MHz, CDCl$_3$

7.74, 1 H, S	7.71, 1 H, s	7.73, 1 H, s
7.46, 1 H, d, J = 7.4 Hz	7.46, 1 H, d, J = 7.66 Hz	7.47, 1 H, d, J = 7.3 Hz
7.28, 1 H, d, J = 7.5 Hz	7.29, 1 H, d, J = 7.93 Hz	7.30, 1 H, d, J = 7.7 Hz
7.06 - 7.13, 2 H, m	7.04 – 7.15, 2 H, m	7.10, 2 H, dt, J = 14.6, 6.7 Hz
3.27, 1 H, d, J = 10.9 Hz	3.3, 1 H, d, J = 10.6	3.29, 1 H, d, J = 10.7 Hz
2.98 - 3.1, 2 H, m	2.96 – 3.15, 2 H, m	3.09, 1 H, dt, J = 13.2, 6.3 Hz
2.9, 1 H, m	2.91, 1 H, m	2.95-3.04, 1 H, m
2.71, 1 H, d, J = 15 Hz	2.72, 1 H, d, J = 15.4 Hz	2.80-2.95, 1 H, m
2.64, 1 H, m	2.62, 1 H, m	2.72, 1 H, d, J = 15.3 Hz
2.12, 1 H, t, J = 10.9 Hz	2.14, 1 H, t, J = 10.97 Hz	2.62, 1 H, dt, J = 11.0, 5.8 Hz
1.97, 1 H, d, J = 12.1 Hz	2.00, 1 H, dt, J = 12.4, 2.94 Hz	2.13, 1 H, t, J = 10.9 Hz
1.61 – 1.77, 4 H, m	1.60 – 1.80, 4 H, m	2.00, 1 H, d, J = 12.1 Hz
1.02 – 1.47, 7 H, m	0.96 – 1.52, 7 H, m	1.60-1.80, 4 H, m
		1.41-1.51, 1 H, m
		1.31, 4 H, m
		0.99-1.16, 2 H, m

Figure 10. ^{1}H NMR data for our synthetic (-)-yohimbane and comparison to published data for (-)-yohimbane.[56,57] Chemical shifts, splitting patterns, and coupling constants are reported.

(-)-Yohimbane ^{13}C-NMR Comparison

Aube, J.; Ghosh, S.; Tanol, M. Symmetry-Driven Synthesis of Indole Alkaloids: Asymmetric Total Syntheses of (+)-Yohimbine, (-)-Yohimbone, (-)-Yohimbane, and (+)-Alloyohimbane. *J. Am. Chem. Soc.*, **1994**, 116, 9009-9018. (-)-Yohimbane, 125 MHz, CDCl$_3$

2020 (-)-Yohimbane, 125 MHz, CDCl$_3$ (This Work)

21.7	21.7
25.9	26.0
26.4	26.4
30.3	30.3
32.8	32.8
36.9	37.0
41.9	41.9
53.1	53.2
60.2	60.2
62.0	62.0
108.0	108.1
110.7	110.6
118.1	118.1
119.3	119.3
121.2	121.2
127.5	127.5
135.1	135.0
135.9	135.9

Figure 11. ^{13}C NMR data for our synthetic (-)-yohimbane and comparison to published data for (-)-yohimbane.[56] Chemical shifts are reported.

^{1}H-NMR Comparison, (-)-Yohimbane
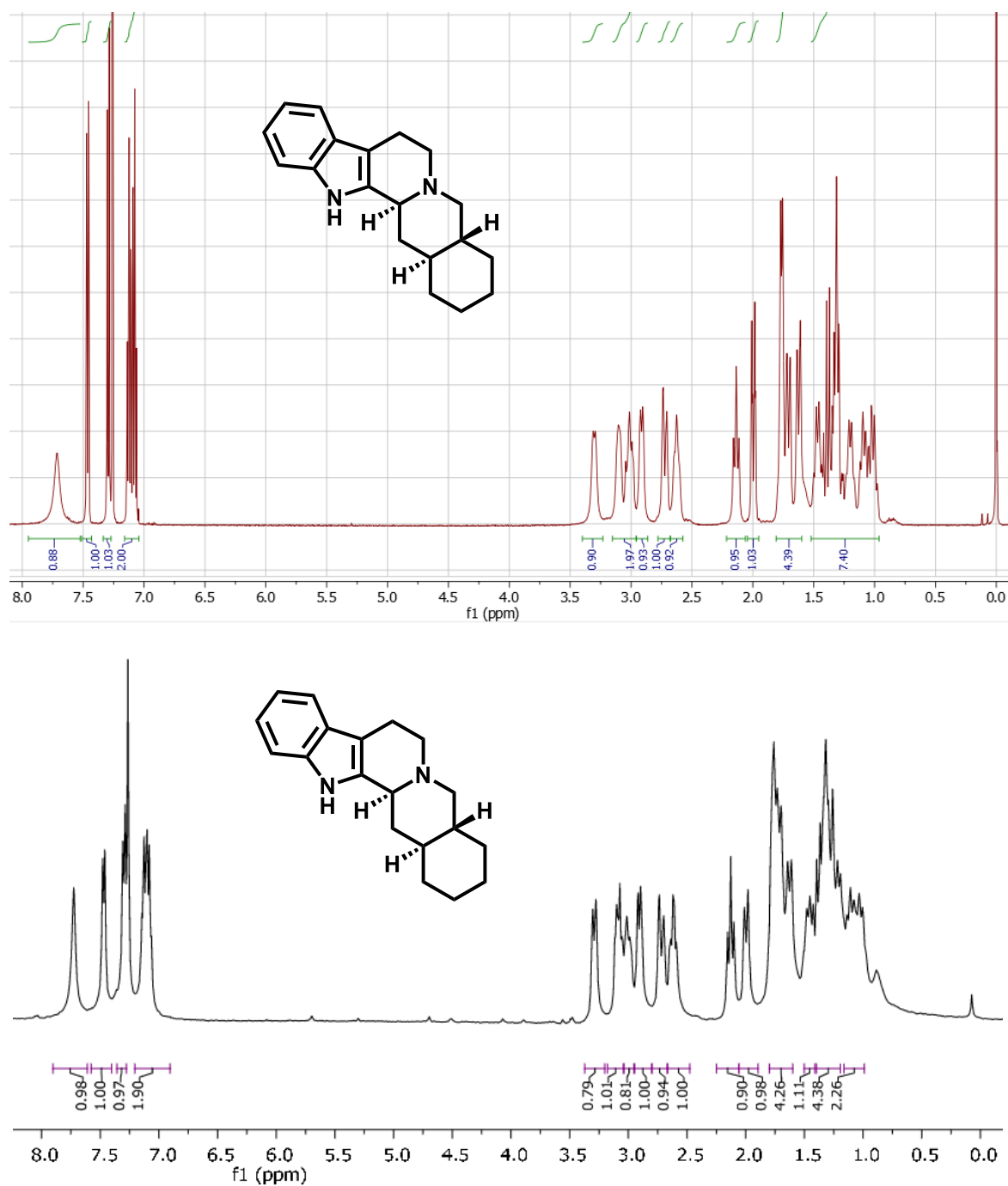
Figure 12. ^{1}H NMR spectra on top: (-)-yohimbane, 500 MHz, CDCl$_3$ (2020, This Work). ^{1}H NMR spectra on bottom: (-)-yohimbane, 400 MHz, CDCl3: Ghosh, A. K.; Sarkar, A. Enantioselective Syntheses of (-)-Alloyohimbane and (-)-Yohimbane by an Efficient Enzymatic Desymmetrization Process. *Eur. J. Org. Chem.* **2016**, 6001-6009.

(-)-Yohimbane Melting Point:

Aube, J.; Ghosh, S.; Tanol, M. Symmetry-Driven Synthesis of Indole Alkaloids: Asymmetric

Total Syntheses of (+)-Yohimbine, (-)-Yohimbone, (-)-Yohimbane, and (+)-Alloyohimbane. *J.

Am. Chem. Soc.*, **1994**, 116, 9009-9018. Melting Point = 204-205 °C

This work, 2020: Melting Point 203-205°C

(-)-Yohimbane Optical Rotation

Ghosh, A. K.; Sarkar, A. Enantioselective Syntheses of (-)-Alloyohimbane and (-)-Yohimbane

by an Efficient Enzymatic Desymmetrization Process. *Eur. J. Org. Chem.* **2016**, 6001-6009.

Optical Rotation: $[\alpha]_D^{20}$ = -77.6 (c = 0.22 M, ethanol)

This work, 2020, Optical Rotation: $[\alpha]_D^{20}$ = -97.5 (c = 0.0069 M, ethanol)

(-)-Yohimbane High Resolution Mass Spectrum

HRMS (ESI-Q-IT) m/z: $[M + H]^+$ calculated for $C_{19}H_{25}N_2$ 281.2012; Found 281.2009.

4.5.4 X-ray Crystallography: Structures of 3A and 21A, Assignment of absolute

stereochemistry of aldehyde products
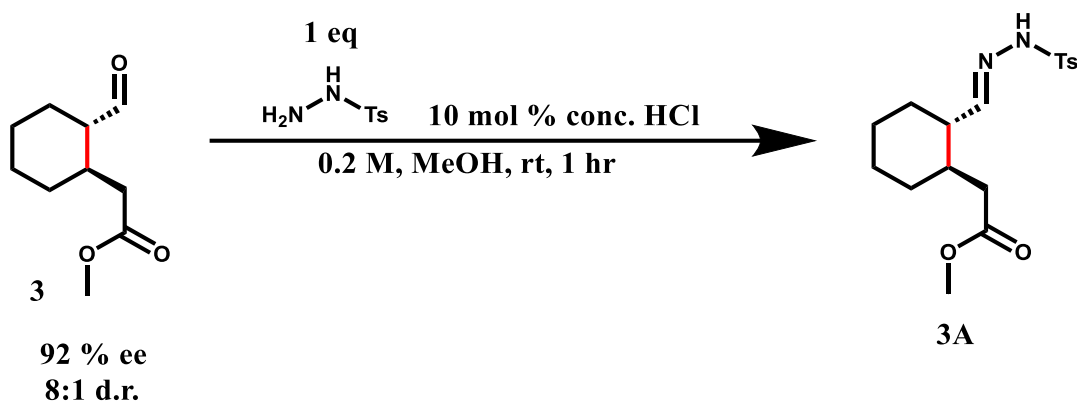
Figure 13. Derivatization of **3** to the p-tosylhydrazone. The p-tosylhydrazone derivative (**3A**) (white solid) was added to a 10 mL glass vial, and 1 mL of diethyl ether was added. The resulting slurry was dissolved by the addition of three drops of methanol. The vial was placed, uncapped, inside a 250 mL glass vial with an inch of diethyl ether inside. The 250 mL vial was capped and allowed to stand at room temperature overnight. Needle-like crystals that were suitable for diffraction grew within 24 hours.
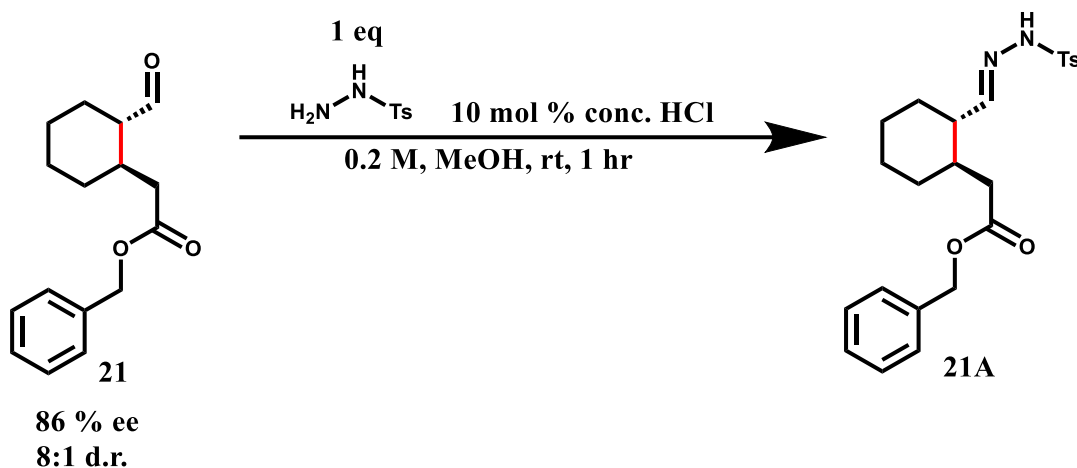
Figure 14. Derivatization of **21** to the p-tosylhydrazone. The p-tosylhydrazone derivative (**21A**) (white solid) was added to a 10 mL glass vial and 1 mL of diethyl ether was added. The resulting slurry was dissolved by the addition of three drops of methanol. The vial was placed, uncapped, inside a 250 mL glass vial with an inch of diethyl ether inside. The 250 mL vial was capped and allowed to stand at room temperature overnight. Needle-like crystals that were suitable for diffraction grew within 72 hours.

Crystallographic Experimental Section

Data Collection of 3A

A colorless crystal with approximate dimensions $0.131 \times 0.054 \times 0.017$ mm^3 was selected under oil under ambient conditions and attached to the tip of a MiTeGen MicroMount©. The crystal was mounted in a stream of cold nitrogen at 100(1) K and centered in the X-ray beam by using a video camera.

The crystal evaluation and data collection were performed on a Bruker DIAMOND PHOTON 3 diffractometer with Cu K$_\alpha$ ($\lambda = 1.54178$ Å) radiation and the diffractometer to crystal distance of 3.5 cm.[58]

The initial cell constants were obtained from a 1-second exposure φ scan. The final cell constants were calculated from a set of 9413 strong reflections from the actual data collection.

The data were collected by using the full sphere data collection routine to survey the reciprocal space to the extent of a full sphere to a resolution of 0.77 Å. A total of 20464 data were harvested by collecting 26 sets of frames with 0.5º scans in ω and φ with exposure times of 1–8 sec per frame. These highly redundant datasets were corrected for Lorentz and polarization effects. The absorption correction was based on fitting a function to the empirical transmission surface as sampled by multiple equivalent measurements.[59]

Structure Solution and Refinement

The systematic absences in the diffraction data were consistent for the space groups $P2_1$ and $P2_1/m$. The E-statistics strongly suggested the non-centrosymmetric space group $P2_1$ that yielded chemically reasonable and computationally stable results of refinement.[60-65]

A successful solution by the direct methods provided most non-hydrogen atoms from the E-map. The remaining non-hydrogen atoms were located in an alternating series of least-squares cycles and difference Fourier maps. All non-hydrogen atoms were refined with anisotropic displacement coefficients. All hydrogen atoms (except H1) were included in the structure factor calculation at idealized positions and were allowed to ride on the neighboring atoms with relative isotropic displacement coefficients.

The absolute configuration was unequivocally established by resonant scattering effects as C9 – S; C14 – R.

The final least-squares refinement of 223 parameters against 3768 data resulted in residuals R (based on F^2 for $I{\geq}2\sigma$) and wR (based on F^2 for all data) of 0.0326 and 0.0851, respectively. The final difference Fourier map was featureless.

Acknowledgement

Summary

Crystal Data for $C_{17}H_{24}N_2O_4S$ (M =352.44 g/mol): monoclinic, space group P2$_1$ (no. 4), a = 11.1577(11) Å, b = 5.0881(7) Å, c = 16.1502(16) Å, β = 96.316(6)°, V = 911.30(18) Å^3, Z =

2, $T = 100.0$ K, μ(Cu Kα) = 1.772 mm^{-1}, $Dcalc$ = 1.284 g/cm^3, 20464 reflections measured

(5.506° $\leq$ 2Θ $\leq$ 160.452°), 3768 unique (R_{int} = 0.0377, R$_{sigma}$ = 0.0295) which were used in all

calculations. The final R_1 was 0.0326 (I > 2σ(I)) and wR_2 was 0.0851 (all data).
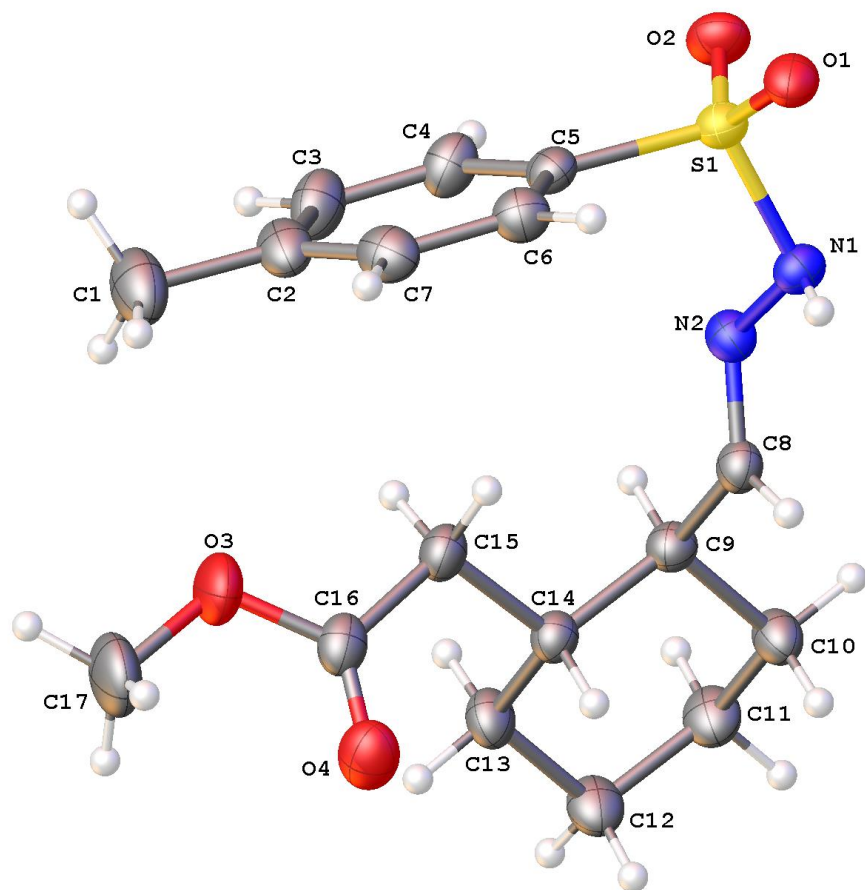
Figure 15. A molecular drawing of **3A** shown with 50% probability ellipsoids.

Figure 16. Crystal data and structure refinement for **3A**.

Identification code	gellman191
Empirical formula	$C_{17}H_{24}N_2O_4S$
Formula weight	352.44
Temperature/K	100.0
Crystal system	monoclinic
Space group	$P2_1$
a/Å	11.1577(11)
b/Å	5.0881(7)
c/Å	16.1502(16)
α/°	90
β/°	96.316(6)
γ/°	90
Volume/Å^3	911.30(18)
Z	2
$\rho_{calc}g/cm^3$	1.284
μ/mm^{-1}	1.772
F(000)	376.0
Crystal size/mm^3	0.131 × 0.054 × 0.017
Radiation	Cu Kα (λ = 1.54178)
2Θ range for data collection/°	5.506 to 160.452
Index ranges	-14 ≤ h ≤ 14, -5 ≤ k ≤ 6, -20 ≤ l ≤ 20
Reflections collected	20464
Independent reflections	3768 [R_{int} = 0.0377, R_{sigma} = 0.0295]
Data/restraints/parameters	3768/1/223
Goodness-of-fit on F^2	1.069

Final R indexes [I>=2σ (I)] $R_1 = 0.0326$, $wR_2 = 0.0850$

Final R indexes [all data] $R_1 = 0.0328$, $wR_2 = 0.0851$

Largest diff. peak/hole / e $Å^{-3}$ 0.23/-0.25

Flack parameter   0.017(9)

Figure 17. Fractional Atomic Coordinates ($\times 10^4$) and Equivalent Isotropic Displacement Parameters ($Å^2 \times 10^3$) for **3A**. U_{eq} is defined as 1/3 of of the trace of the orthogonalised U_{IJ} tensor.

Atom	x	y	z	U(eq)
S1	6147.1(4)	7160.5(10)	8191.3(3)	25.65(14)
O1	7095.7(14)	6027(4)	8741.8(10)	32.7(4)
O2	6258.2(16)	9793(3)	7900.2(11)	36.0(4)
O3	310.5(17)	3834(5)	7655.1(12)	49.6(5)
O4	785.7(18)	229(4)	6993.8(13)	44.4(5)
N1	6010.7(17)	5224(4)	7367.0(12)	26.3(4)
N2	5000.7(16)	5889(4)	6806.3(11)	26.9(4)
C1	1423(3)	6244(8)	9689.1(18)	52.5(8)
C2	2597(2)	6462(6)	9308.5(14)	36.4(6)
C3	2772(2)	8435(7)	8744.4(15)	40.5(6)
C4	3850(2)	8696(5)	8406.0(14)	34.0(5)
C5	4776.5(18)	6923(5)	8635.7(12)	25.9(4)
C6	4622(2)	4909(5)	9191.0(14)	30.9(5)
C7	3532(2)	4683(5)	9520.2(14)	35.2(5)
C8	4499.3(19)	3989(5)	6386.8(13)	26.9(4)
C9	3428(2)	4521(5)	5761.4(13)	27.3(4)
C10	3670(2)	3565(6)	4891.1(13)	32.4(5)
C11	2605(2)	4157(6)	4236.1(14)	36.5(6)
C12	1465(2)	2861(6)	4483.0(14)	36.6(6)

C13	1222.3(19)	3751(6)	5353.3(14)	32.9(5)
C14	2282.1(19)	3202(5)	6014.6(12)	26.1(4)
C15	1969(2)	4125(5)	6871.6(14)	30.3(5)
C16	972(2)	2498(5)	7162.6(13)	31.8(5)
C17	-688(3)	2371(10)	7941(2)	60.7(9)

Figure 18. Anisotropic Displacement Parameters ($Å^2 \times 10^3$) for **3A**. The Anisotropic displacement factor exponent takes the form: $-2\pi^2[h^2a^{*2}U_{11}+2hka^*b^*U_{12}+\ldots]$.

Atom	U_{11}	U_{22}	U_{33}	U_{23}	U_{13}	U_{12}
S1	28.6(2)	24.7(3)	23.5(2)	-1.7(2)	2.07(16)	-1.5(2)
O1	29.1(8)	39.6(9)	28.5(8)	-5.8(7)	-0.9(6)	1.1(7)
O2	43.6(9)	26.1(9)	39.1(9)	-0.8(7)	7.7(7)	-6.6(7)
O3	40.2(10)	63.8(14)	48.7(11)	-12.0(10)	21.9(8)	0.6(9)
O4	45.7(10)	39.1(11)	50.6(11)	3.5(9)	15.2(9)	0.2(8)
N1	29.9(9)	25.2(10)	23.5(9)	-0.7(7)	1.6(7)	2.2(8)
N2	26.6(9)	32.1(10)	22.0(8)	1.4(7)	2.4(7)	-0.9(7)
C1	37.8(14)	85(3)	36.6(13)	-3.7(15)	10.8(11)	-0.6(14)
C2	32.0(11)	54.3(17)	22.8(10)	-6.6(10)	2.1(8)	-1.8(10)
C3	37.2(13)	52.0(15)	31.9(12)	-0.7(11)	2.3(10)	14.4(12)
C4	39.5(12)	35.8(14)	27.2(11)	3.0(10)	5.0(9)	9.7(11)
C5	29.1(9)	27.5(11)	21.2(9)	-4.1(9)	2.8(7)	-0.6(9)
C6	34.0(11)	32.4(13)	25.8(10)	2.0(9)	1.1(8)	0.4(9)
C7	39.9(12)	41.4(14)	24.3(10)	1.5(10)	3.1(9)	-5.7(11)
C8	25.4(10)	31.7(12)	24.0(9)	-1.4(8)	5.1(8)	1.7(8)
C9	27.3(10)	30.1(11)	23.9(10)	-1.7(9)	1.2(8)	0.8(9)
C10	27.0(10)	45.5(14)	25.0(10)	-3.6(10)	4.4(8)	-2.9(10)
C11	35.8(12)	50.7(16)	22.7(10)	-2.0(10)	1.5(9)	0.7(11)

C12	30.2(11)	52.7(18)	25.9(10)	-2.8(10)	-1.8(8)	0.6(10)
C13	24.2(10)	45.6(15)	28.5(11)	-1.1(10)	1.7(8)	4.0(10)
C14	25.4(10)	29.8(11)	23.0(10)	-0.8(8)	2.6(8)	2.9(8)
C15	29.2(10)	34.3(13)	27.9(10)	-3.1(9)	5.6(8)	5.4(9)
C16	29.3(10)	41.1(16)	24.9(9)	1.1(10)	2.6(8)	8.4(10)
C17	40.7(14)	87(3)	59.5(17)	-6.2(19)	26.3(13)	-1.9(18)

Figure 19. Bond Lengths for **3A**.

Atom	Atom	Length/Å	Atom	Atom	Length/Å
S1	O1	1.4270(17)	C4	C5	1.391(3)
S1	O2	1.4297(18)	C5	C6	1.385(3)
S1	N1	1.6499(19)	C6	C7	1.385(4)
S1	C5	1.764(2)	C8	C9	1.502(3)
O3	C16	1.330(3)	C9	C10	1.539(3)
O3	C17	1.457(4)	C9	C14	1.538(3)
O4	C16	1.199(4)	C10	C11	1.531(3)
N1	N2	1.407(3)	C11	C12	1.524(3)
N2	C8	1.274(3)	C12	C13	1.529(3)
C1	C2	1.512(4)	C13	C14	1.529(3)
C2	C3	1.384(4)	C14	C15	1.538(3)
C2	C7	1.395(4)	C15	C16	1.503(3)
C3	C4	1.381(4)			

Figure 20. Bond Angles for **3A**.

Atom	Atom	Atom	Angle/°	Atom	Atom	Atom	Angle/°
O1	S1	O2	119.89(11)	C7	C6	C5	119.2(2)

O1	S1	N1	104.93(10)	C6	C7	C2	121.1(2)
O1	S1	C5	109.62(10)	N2	C8	C9	119.4(2)
O2	S1	N1	107.34(11)	C8	C9	C10	110.49(18)
O2	S1	C5	107.97(11)	C8	C9	C14	111.45(18)
N1	S1	C5	106.28(10)	C14	C9	C10	109.85(18)
C16	O3	C17	115.0(3)	C11	C10	C9	111.57(19)
N2	N1	S1	111.83(15)	C12	C11	C10	109.9(2)
C8	N2	N1	115.7(2)	C11	C12	C13	110.5(2)
C3	C2	C1	120.8(3)	C12	C13	C14	112.72(18)
C3	C2	C7	118.4(2)	C13	C14	C9	109.64(18)
C7	C2	C1	120.7(3)	C13	C14	C15	109.77(17)
C4	C3	C2	121.5(2)	C15	C14	C9	112.56(18)
C3	C4	C5	119.1(2)	C16	C15	C14	111.3(2)
C4	C5	S1	119.95(18)	O3	C16	C15	112.6(2)
C6	C5	S1	119.30(18)	O4	C16	O3	122.3(2)
C6	C5	C4	120.7(2)	O4	C16	C15	125.1(2)

Figure 21. Hydrogen Bonds for **3A**.

D	H	A	d(D-H)/Å	d(H-A)/Å	d(D-A)/Å	D-H-A/°
N1	H1	O2[1]	0.79(4)	2.11(4)	2.898(3)	177(3)

[1]+X,-1+Y,+Z

Figure 22. Torsion Angles for **3A**.

A	B	C	D	Angle/°	A	B	C	D	Angle/°
S1	N1	N2	C8	-149.03(17)	C5	S1	N1	N2	56.26(18)
S1	C5	C6	C7	-178.13(18)	C5	C6	C7	C2	-0.7(4)
O1	S1	N1	N2	172.36(15)	C7	C2	C3	C4	-1.3(4)
O1	S1	C5	C4	154.89(19)	C8	C9	C10	C11	-178.3(2)
O1	S1	C5	C6	-27.3(2)	C8	C9	C14	C13	-178.91(19)
O2	S1	N1	N2	-59.07(17)	C8	C9	C14	C15	58.6(2)
O2	S1	C5	C4	22.7(2)	C9	C10	C11	C12	-58.0(3)
O2	S1	C5	C6	-159.47(18)	C9	C14	C15	C16	-170.82(19)
N1	S1	C5	C4	-92.2(2)	C10	C9	C14	C13	-56.1(3)
N1	S1	C5	C6	85.62(19)	C10	C9	C14	C15	-178.59(19)
N1	N2	C8	C9	-178.90(18)	C10	C11	C12	C13	55.9(3)
N2	C8	C9	C10	122.8(2)	C11	C12	C13	C14	-56.5(3)
N2	C8	C9	C14	-114.7(2)	C12	C13	C14	C9	56.3(3)
C1	C2	C3	C4	178.5(3)	C12	C13	C14	C15	-179.5(2)
C1	C2	C7	C6	-178.3(2)	C13	C14	C15	C16	66.8(3)
C2	C3	C4	C5	0.3(4)	C14	C9	C10	C11	58.3(3)
C3	C2	C7	C6	1.5(4)	C14	C15	C16	O3	-150.8(2)
C3	C4	C5	S1	178.3(2)	C14	C15	C16	O4	30.6(3)
C3	C4	C5	C6	0.5(4)	C17	O3	C16	O4	-2.7(4)
C4	C5	C6	C7	-0.3(3)	C17	O3	C16	C15	178.7(2)

Figure 23. Hydrogen Atom Coordinates ($\mathring{A}\times10^4$) and Isotropic Displacement Parameters ($\mathring{A}^2\times10^3$) for **3A**.

Atom	x	y	z	U(eq)
H1	6110(20)	3740(70)	7512(18)	30(7)
H1A	1390.69	4548.14	9973.57	79
H1B	746.4	6371.99	9249.33	79
H1C	1369.8	7670.2	10091.3	79
H3	2136.79	9637.24	8586.32	49
H4	3957.31	10066.88	8021.66	41
H6	5255.93	3697.62	9343.99	37
H7	3418.85	3292.28	9896.44	42
H8	4800.18	2250.5	6468.75	32
H9	3290.26	6462.74	5734.55	33
H10A	4402.9	4438.98	4730.24	39
H10B	3820.93	1646.99	4909.32	39
H11A	2484.2	6080.55	4188.84	44
H11B	2779.9	3483.07	3686.84	44
H12A	1558.88	926.76	4475.89	44
H12B	771.12	3336.14	4075.09	44
H13A	497.89	2832	5509.28	39
H13B	1049.85	5659.93	5341.44	39
H14	2420.19	1260.65	6040.46	31
H15A	2694.35	3992.38	7281.82	36
H15B	1718.33	5991.6	6836.29	36
H17A	-1237.2	1799.21	7459.89	91
H17B	-1123.19	3499.31	8298.54	91

H17C -373.9	829.03	8258.33	91

Data Collection of 21A

A colorless crystal with approximate dimensions 0.38 x 0.05 x 0.02 mm^3 was selected under oil under ambient conditions and attached to the tip of a MiTeGen MicroMount©. The crystal was mounted in a stream of cold nitrogen at 100(1) K and centered in the X-ray beam by using a video camera.

The crystal evaluation and data collection were performed on a Bruker SMART APEXII diffractometer with Cu K$_\alpha$ (λ = 1.54178 Å) radiation and a diffractometer to crystal distance of 4.03 cm.[58]

The initial cell constants were obtained from three series of ω scans at different starting angles. Each series consisted of 41 frames collected at intervals of 0.6º in a 25º range about ω with the exposure time of 10 seconds per frame. The reflections were successfully indexed by an automated indexing routine built in the APEX3 program. The final cell constants were calculated from a set of 4190 strong reflections from the actual data collection.

The data were collected by using the full sphere data collection routine to survey the reciprocal space to the extent of a full sphere to a resolution of 0.81 Å. A total of 42167 data were harvested by collecting 21 sets of frames with 0.7º scans in ω and φ with an exposure time 20-40 sec per frame. These highly redundant datasets were corrected for Lorentz and polarization effects. The absorption correction was based on fitting a function to the empirical transmission surface as sampled by multiple equivalent measurements.[59]

Structure Solution and Refinement

The systematic absences in the diffraction data were uniquely consistent for the space group $P2_12_12_1$ that yielded chemically reasonable and computationally stable results of refinement.[60-65]

A successful solution by direct methods provided most non-hydrogen atoms from the E-map. The remaining non-hydrogen atoms were located in an alternating series of least-squares cycles and difference Fourier maps. All non-hydrogen atoms were refined with anisotropic displacement coefficients. All hydrogen atoms (apart from H1 atom bound to N1) were included in the structure factor calculation at idealized positions and were allowed to ride on the neighboring atoms with relative isotropic displacement coefficients.

The absolute structure was unequivocally established by anomalous dispersion effects: C9 – S; C14 – R.

The final least-squares refinement of 275 parameters against 4354 data resulted in residuals R (based on F^2 for $I \geq 2\sigma$) and wR (based on F^2 for all data) of 0.0343 and 0.0834, respectively. The final difference Fourier map was featureless.

Summary

Crystal Data for $C_{23}H_{28}N_2O_4S$ ($M = 428.53$ g/mol): orthorhombic, space group $P2_12_12_1$ (no. 19), $a = 4.9569(6)$ Å, $b = 18.1596(15)$ Å, $c = 24.4426(16)$ Å, $V = 2200.2(4)$ Å^3, $Z = 4$, $T = 99.99$ K, μ(Cu Kα) = 1.567 mm^{-1}, $Dcalc = 1.294$ g/cm^3, 42167 reflections measured (6.062° $\leq 2\Theta \leq$ 145.726°), 4354 unique ($R_{int} = 0.0676$, $R_{sigma} = 0.0295$) which were used in all calculations. The final R_1 was 0.0343 (I > 2σ(I)) and wR_2 was 0.0834 (all data).

Figure 24. A molecular drawing of **21A** shown with 50% probability ellipsoids. All H atoms are omitted.
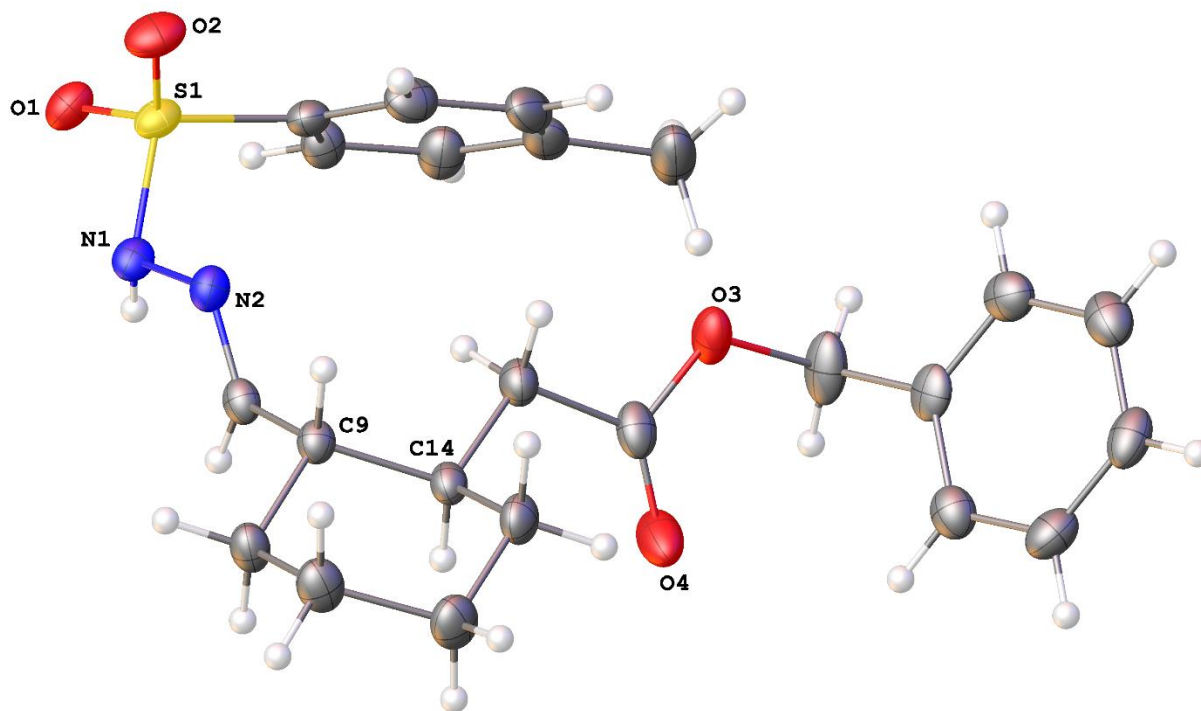
Figure 25. A molecular drawing of **21A** shown with 50% probability ellipsoids and atom labels for heteroatoms.

Figure 26. Crystal data and structure refinement for **21A**.

Identification code	Gellman190
Empirical formula	$C_{23}H_{28}N_2O_4S$
Formula weight	428.53
Temperature/K	99.99
Crystal system	orthorhombic
Space group	$P2_12_12_1$
a/Å	4.9569(6)
b/Å	18.1596(15)
c/Å	24.4426(16)
α/°	90
β/°	90
γ/°	90
Volume/Å^3	2200.2(4)
Z	4
ρ_{calc}g/cm^3	1.294
μ/mm^{-1}	1.567
F(000)	912.0
Crystal size/mm^3	$0.375 \times 0.05 \times 0.02$
Radiation	Cu Kα ($\lambda = 1.54178$)
2Θ range for data collection/°	6.062 to 145.726
Index ranges	$-6 \leq h \leq 5$, $-22 \leq k \leq 22$, $-30 \leq l \leq 30$
Reflections collected	42167
Independent reflections	4354 [$R_{int} = 0.0676$, $R_{sigma} = 0.0295$]

Data/restraints/parameters   4354/0/275

Goodness-of-fit on F^2 1.042

Final R indexes [I>=2σ (I)] $R_1 = 0.0343$, $wR_2 = 0.0803$

Final R indexes [all data] $R_1 = 0.0403$, $wR_2 = 0.0834$

Largest diff. peak/hole / e Å^{-3} 0.33/-0.27

Flack parameter   0.023(9)

Figure 27. Fractional Atomic Coordinates ($\times 10^4$) and Equivalent Isotropic Displacement Parameters ($Å^2 \times 10^3$) for **21A**. U_{eq} is defined as 1/3 of of the trace of the orthogonalised U_{IJ} tensor.

Atom	x	y	z	U(eq)
S1	4857.4(12)	2701.9(3)	7097.1(2)	23.02(14)
O1	3985(4)	2148.9(10)	7473.5(8)	28.1(4)
O2	7613(4)	2726.4(13)	6924.1(8)	35.0(5)
O3	1441(5)	5994.9(10)	6355.1(8)	32.2(5)
O4	-2027(4)	5675.4(12)	5807.0(11)	44.4(6)
N1	3020(5)	2563.5(11)	6543.2(9)	21.3(4)
N2	3650(5)	3046.9(11)	6110.3(9)	22.1(5)
C1	1129(8)	5687.8(17)	7885.3(14)	45.5(8)
C2	2196(7)	4949.6(16)	7710.6(11)	32.8(7)
C3	4221(6)	4890.4(16)	7318.1(13)	35.8(7)
C4	5121(6)	4209.0(16)	7137.2(12)	32.9(6)
C5	3970(5)	3575.7(14)	7354.4(11)	24.0(5)
C6	1991(6)	3621.3(15)	7750.5(11)	26.8(6)
C7	1134(6)	4307.2(16)	7928.3(12)	32.6(6)

C8	1705(5)	3229.4(13)	5803.6(10)	21.4(5)
C9	2238(5)	3703.6(13)	5312.0(10)	21.2(5)
C10	1220(6)	3324.1(14)	4789.9(11)	26.5(6)
C11	1889(7)	3774.0(16)	4279.7(11)	31.4(6)
C12	737(7)	4554.8(15)	4324.5(12)	33.6(7)
C13	1672(6)	4927.4(14)	4850.4(11)	27.7(6)
C14	942(5)	4475.1(13)	5362.4(11)	22.2(5)
C15	1844(6)	4874.7(14)	5880.9(11)	26.0(5)
C16	172(6)	5551.4(14)	5998.8(11)	28.3(6)
C17	-46(8)	6648.8(15)	6535.7(12)	38.5(7)
C18	482(6)	7299.1(15)	6169.6(10)	27.1(6)
C19	2577(6)	7780.1(16)	6286.4(12)	31.9(6)
C20	3021(6)	8393.6(16)	5959.0(13)	34.6(7)
C21	1401(6)	8522.1(16)	5509.0(13)	34.1(7)
C22	-675(6)	8041.7(17)	5387.8(13)	33.7(7)
C23	-1158(6)	7434.2(15)	5715.0(12)	30.3(6)

Figure 28. Anisotropic Displacement Parameters ($\mathring{A}^2 \times 10^3$) for **21A**. The Anisotropic displacement factor exponent takes the form: $-2\pi^2[h^2a^{*2}U_{11}+2hka^*b^*U_{12}+\ldots]$.

Atom	U_{11}	U_{22}	U_{33}	U_{23}	U_{13}	U_{12}
S1	16.8(3)	27.6(3)	24.7(3)	4.8(2)	1.3(3)	3.3(2)
O1	28.1(10)	28.7(10)	27.6(9)	4.9(8)	1.7(7)	7.2(8)
O2	19.7(10)	47.0(13)	38.1(11)	5.8(10)	1.2(8)	5.3(9)
O3	49.7(13)	21.4(10)	25.5(9)	-4.0(7)	-0.6(9)	6.0(9)
O4	23.7(11)	29.6(11)	80.0(17)	-14.7(11)	0.2(11)	2.2(9)

N1	17.2(11)	22.4(11)	24.3(10)	2.6(8)	5.0(9)	0.6(8)
N2	22.9(12)	20.3(10)	23.0(10)	1.4(8)	4.6(9)	1.0(9)
C1	72(2)	26.4(14)	38.0(16)	-1.9(14)	-17.2(17)	2.9(15)
C2	44.1(18)	26.9(14)	27.5(13)	-0.1(11)	-16.1(13)	-1.2(12)
C3	36.3(17)	26.4(14)	44.5(16)	9.7(13)	-13.0(13)	-11.5(12)
C4	25.7(14)	35.7(14)	37.3(14)	8.4(12)	-2.6(14)	-7.4(12)
C5	21.4(13)	24.5(12)	26.1(13)	2.2(10)	-6.1(10)	0.4(10)
C6	32.8(15)	24.6(13)	23.1(12)	2.9(10)	1.3(11)	-2.2(11)
C7	44.1(16)	29.0(14)	24.8(13)	-0.4(12)	-2.2(13)	2.5(12)
C8	22.0(13)	18.4(11)	23.6(12)	-3.1(9)	5.1(10)	-0.8(10)
C9	20.9(13)	18.7(12)	24.1(12)	0.4(10)	3.2(10)	-0.2(9)
C10	34.9(15)	20.4(12)	24.1(13)	-0.4(10)	-0.4(11)	-2.3(10)
C11	41.9(17)	28.7(14)	23.7(13)	2.7(11)	0.9(12)	-4.0(12)
C12	44.4(19)	27.8(14)	28.8(14)	7.1(11)	-2.1(12)	-1.4(12)
C13	30.5(15)	18.8(12)	33.7(14)	4.5(11)	1.7(12)	-1.9(10)
C14	19.8(13)	17.6(12)	29.4(13)	-0.5(10)	1.2(10)	-1.1(9)
C15	26.5(14)	19.8(12)	31.6(13)	-2.2(10)	1.3(11)	0.1(10)
C16	29.8(16)	20.5(12)	34.8(14)	-1.5(10)	11.4(13)	-3.1(11)
C17	65(2)	23.9(13)	26.5(13)	-3.7(11)	15.5(16)	6.6(15)
C18	35.3(16)	22.4(12)	23.6(12)	-5.6(10)	10.6(10)	8.1(12)
C19	33.2(16)	33.4(15)	29.0(13)	-7.7(12)	0.1(12)	6.6(12)
C20	27.7(15)	30.7(15)	45.4(17)	-7.1(13)	6.8(13)	-0.7(11)
C21	30.9(16)	25.8(14)	45.6(17)	6.6(12)	13.2(14)	7.2(12)
C22	29.3(17)	35.7(15)	36.2(15)	6.5(12)	1.0(12)	8.2(12)

| C23 | 30.1(14) | 27.2(14) | 33.5(14) | -4.5(11) | 5.6(11) | -0.2(11) |

Figure 29. Bond Lengths for **21A**.

Atom	Atom	Length/Å	Atom	Atom	Length/Å
S1	O1	1.4290(19)	C8	C9	1.502(3)
S1	O2	1.430(2)	C9	C10	1.536(4)
S1	N1	1.651(2)	C9	C14	1.546(3)
S1	C5	1.763(3)	C10	C11	1.527(4)
O3	C16	1.342(3)	C11	C12	1.532(4)
O3	C17	1.466(3)	C12	C13	1.525(4)
O4	C16	1.208(4)	C13	C14	1.540(4)
N1	N2	1.410(3)	C14	C15	1.527(4)
N2	C8	1.265(3)	C15	C16	1.510(4)
C1	C2	1.503(4)	C17	C18	1.505(4)
C2	C3	1.393(5)	C18	C19	1.387(4)
C2	C7	1.386(4)	C18	C23	1.399(4)
C3	C4	1.388(4)	C19	C20	1.389(4)
C4	C5	1.389(4)	C20	C21	1.382(5)
C5	C6	1.381(4)	C21	C22	1.381(4)
C6	C7	1.386(4)	C22	C23	1.384(4)

Figure 30. Bond Angles for **21A**.

Atom	Atom	Atom	Angle/°	Atom	Atom	Atom	Angle/°
O1	S1	O2	120.08(12)	C10	C9	C14	109.6(2)
O1	S1	N1	104.72(12)	C11	C10	C9	111.5(2)

O1	S1	C5	109.11(12)	C10	C11	C12	110.8(2)
O2	S1	N1	106.80(12)	C13	C12	C11	111.0(2)
O2	S1	C5	108.40(14)	C12	C13	C14	112.1(2)
N1	S1	C5	106.97(11)	C13	C14	C9	108.7(2)
C16	O3	C17	116.5(2)	C15	C14	C9	112.0(2)
N2	N1	S1	113.49(17)	C15	C14	C13	110.6(2)
C8	N2	N1	116.0(2)	C16	C15	C14	112.6(2)
C3	C2	C1	121.2(3)	O3	C16	C15	110.8(3)
C7	C2	C1	120.5(3)	O4	C16	O3	124.2(2)
C7	C2	C3	118.2(3)	O4	C16	C15	124.9(3)
C4	C3	C2	121.3(3)	O3	C17	C18	111.7(2)
C3	C4	C5	119.0(3)	C19	C18	C17	120.1(3)
C4	C5	S1	120.4(2)	C19	C18	C23	119.2(3)
C6	C5	S1	118.8(2)	C23	C18	C17	120.6(3)
C6	C5	C4	120.7(3)	C18	C19	C20	120.3(3)
C5	C6	C7	119.4(3)	C21	C20	C19	120.1(3)
C6	C7	C2	121.3(3)	C22	C21	C20	119.8(3)
N2	C8	C9	119.3(2)	C21	C22	C23	120.6(3)
C8	C9	C10	110.5(2)	C22	C23	C18	119.9(3)
C8	C9	C14	112.5(2)				

Figure 31. Hydrogen Bonds for **21A**.

| D | H | A | d(D-H)/Å | d(H-A)/Å | d(D-A)/Å | D-H-A/° |
| N1 | H1 | O2[1] | 0.81(4) | 2.06(4) | 2.853(3) | 167(3) |

[1]-1+X,+Y,+Z

Figure 32. Torsion Angles for **21A**.

A	B	C	D	Angle/°	A	B	C	D	Angle/°
S1	N1	N2	C8	-147.03(19)	C8	C9	C14	C13	178.2(2)
S1	C5	C6	C7	-175.4(2)	C8	C9	C14	C15	55.6(3)
O1	S1	N1	N2	-178.06(17)	C9	C10	C11	C12	-56.3(3)
O1	S1	C5	C4	164.8(2)	C9	C14	C15	C16	-167.8(2)
O1	S1	C5	C6	-19.2(2)	C10	C9	C14	C13	-58.5(3)
O2	S1	N1	N2	-49.7(2)	C10	C9	C14	C15	179.0(2)
O2	S1	C5	C4	32.4(3)	C10	C11	C12	C13	54.1(3)
O2	S1	C5	C6	-151.6(2)	C11	C12	C13	C14	-56.1(3)
O3	C17	C18	C19	-90.7(3)	C12	C13	C14	C9	58.1(3)
O3	C17	C18	C23	90.5(3)	C12	C13	C14	C15	-178.5(2)
N1	S1	C5	C4	-82.4(2)	C13	C14	C15	C16	70.7(3)
N1	S1	C5	C6	93.5(2)	C14	C9	C10	C11	58.9(3)
N1	N2	C8	C9	-176.1(2)	C14	C15	C16	O3	-162.7(2)
N2	C8	C9	C10	123.8(3)	C14	C15	C16	O4	18.4(4)
N2	C8	C9	C14	-113.3(3)	C16	O3	C17	C18	-90.1(3)
C1	C2	C3	C4	-176.9(3)	C17	O3	C16	O4	3.1(4)
C1	C2	C7	C6	176.5(3)	C17	O3	C16	C15	-175.8(2)
C2	C3	C4	C5	-0.1(4)	C17	C18	C19	C20	-178.0(3)
C3	C2	C7	C6	-2.0(4)	C17	C18	C23	C22	178.9(3)
C3	C4	C5	S1	174.9(2)	C18	C19	C20	C21	-1.0(4)
C3	C4	C5	C6	-1.0(4)	C19	C18	C23	C22	0.1(4)
C4	C5	C6	C7	0.6(4)	C19	C20	C21	C22	0.5(4)

C5 S1 N1 N2 66.2(2)   C20 C21 C22 C23 0.4(4)

C5 C6 C7 C2 1.0(4)   C21 C22 C23 C18 -0.7(4)

C7 C2 C3 C4 1.5(4)   C23 C18 C19 C20 0.7(4)

C8 C9 C10 C11 -176.6(2)

Figure 33. Hydrogen Atom Coordinates ($\text{Å}\times10^4$) and Isotropic Displacement Parameters ($\text{Å}^2\times10^3$) for **21A**.

Atom	x	y	z	U(eq)
H1	1430(70)	2546(17)	6625(12)	26
H1A	-351.13	5834.04	7642.72	68
H1B	2576.86	6054.27	7864.8	68
H1C	465.51	5656.45	8262.27	68
H3	5002.72	5325.28	7171.32	43
H4	6502.21	4176.15	6868.94	40
H6	1223.07	3186.18	7899.87	32
H7	-207.67	4337.64	8204.91	39
H8	-74.91	3068.03	5883.6	26
H9	4234.09	3769.4	5277.83	25
H10A	2058.45	2831.07	4759.19	32
H10B	-758.24	3256.61	4814.42	32
H11A	1125.54	3527.61	3953.2	38
H11B	3870.98	3800.2	4233.91	38
H12A	1331.44	4849.46	4005.82	40
H12B	-1258.39	4532.13	4319.31	40
H13A	826.99	5420.04	4877.33	33

H13B	3651.81	4996.49	4836.44	33
H14	-1062.41	4415.2	5375.15	27
H15A	1713.56	4532.61	6195.16	31
H15B	3758.16	5020.57	5841.34	31
H17A	495.29	6773.02	6914.53	46
H17B	-2001.92	6538.99	6537.04	46
H19	3715.09	7689.69	6591.91	38
H20	4440.84	8725.49	6044.68	42
H21	1713.88	8939.61	5283.59	41
H22	-1781.05	8129.18	5077.01	40
H23	-2602.42	7109.37	5631.12	36

4.5.5   HPLC Traces (Racemic and Enantioenriched)
Conditions shown below the structures of the p-tosylhydrazone derivatives correspond to the reaction conditions used to prepare the cyclic aldehyde products 3, and 20-24.

Note: Some LC-MS chromatograms for the racemic samples have changes in retention time relative to the enantioenriched samples. These differences are due to pressure fluctuations over time.

Note: Products **3**, and **20-24** were purified via column chromatography prior to p-tosylhydrazone formation in order to remove any homo-aldol byproducts and catalysts.

From Racemic 3 (Daicel CHIRALPAK® IF-3, isocratic 85 % Hexane, 15 % iPrOH, 1 mL/min)
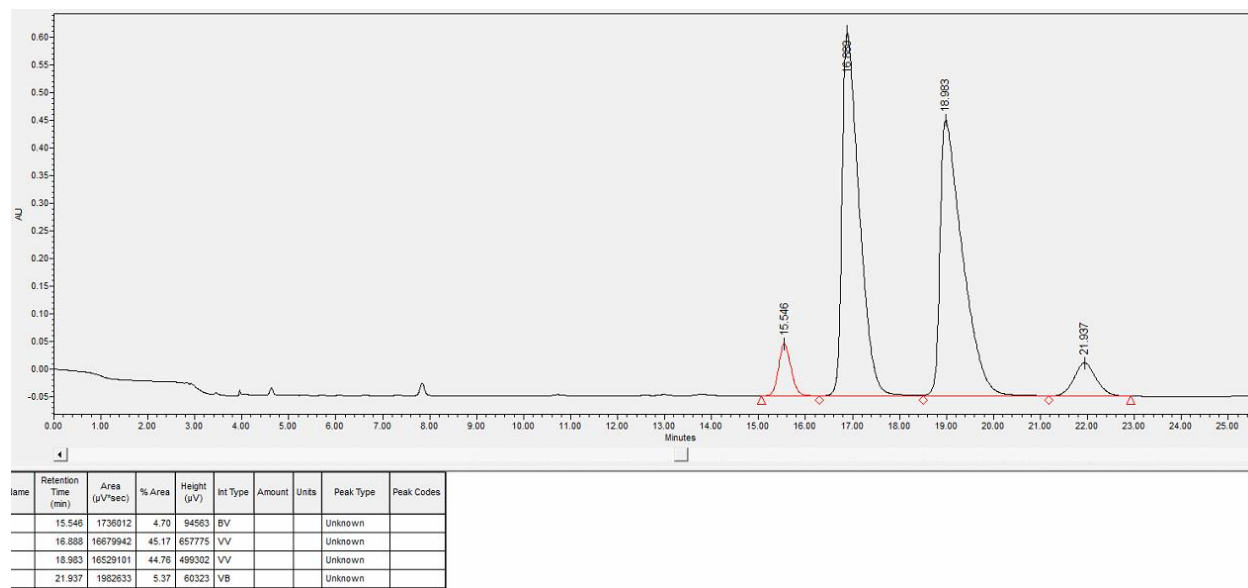
lame	Retention Time (min)	Area (µV*sec)	% Area	Height (µV)	Int Type	Amount	Units	Peak Type	Peak Codes
	15.546	1736012	4.70	94563	BV			Unknown	
	16.888	16679942	45.17	657775	VV			Unknown	
	18.983	16529101	44.76	499302	VV			Unknown	
	21.937	1982633	5.37	60323	VB			Unknown	
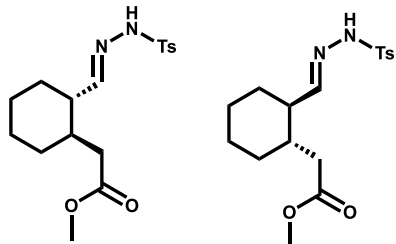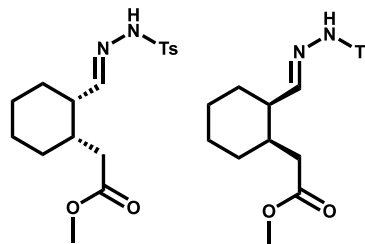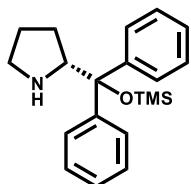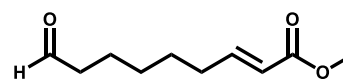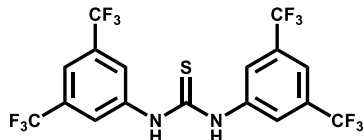
Enantioenriched Trace

From Enantioenriched 3 (Daicel CHIRALPAK® IF-3, isocratic 85 % Hexane, 15 % iPrOH, 1 mL/min)
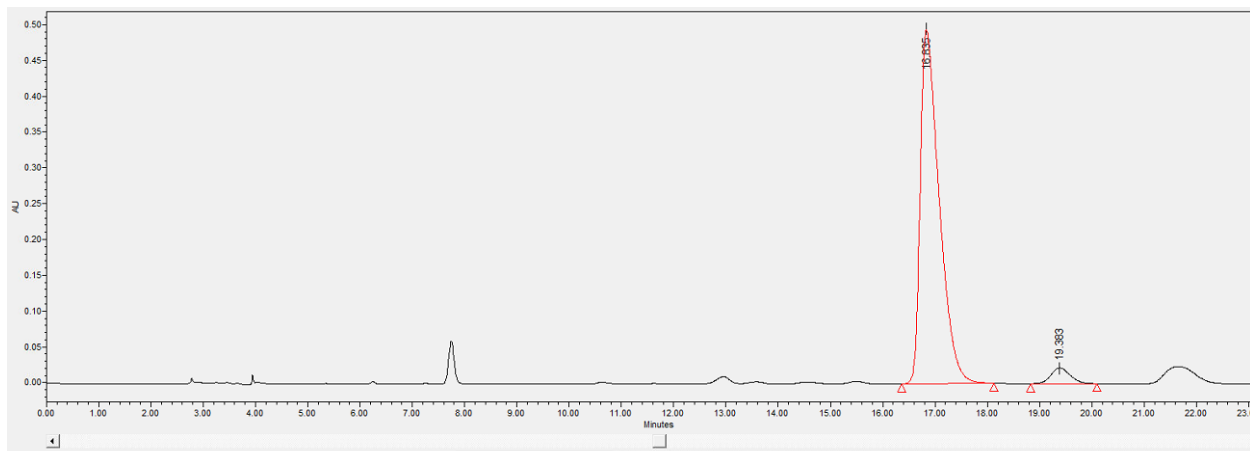
Name	Retention Time (min)	Area (µV*sec)	% Area	Height (µV)	Int Type	Amount	Units	Peak Type	Peak Codes
	16.835	12420232	95.63	494645	BB			Unknown	
	19.383	566941	4.37	21943	BB			Unknown	

Enantioenriched Trace
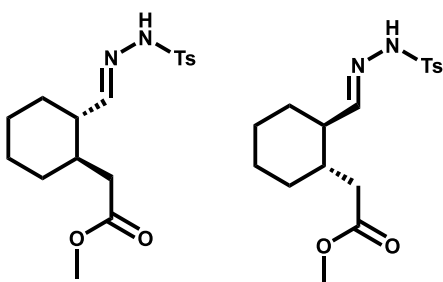
Enantiomers of Major Diastereomer

Enantiomers of Minor Diastereomer
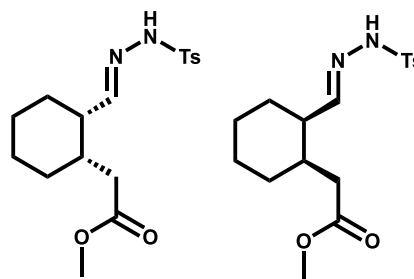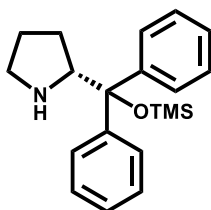
15 mol %

15 mol %
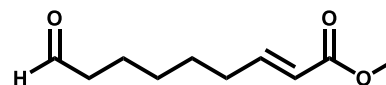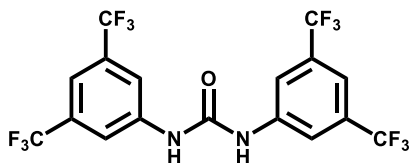
0.05 M, Toluene, 24 hr, rt

From Enantioenriched 3 (Daicel CHIRALPAK® IF-3, isocratic 85 % Hexane, 15 % iPrOH, 1 mL/min)
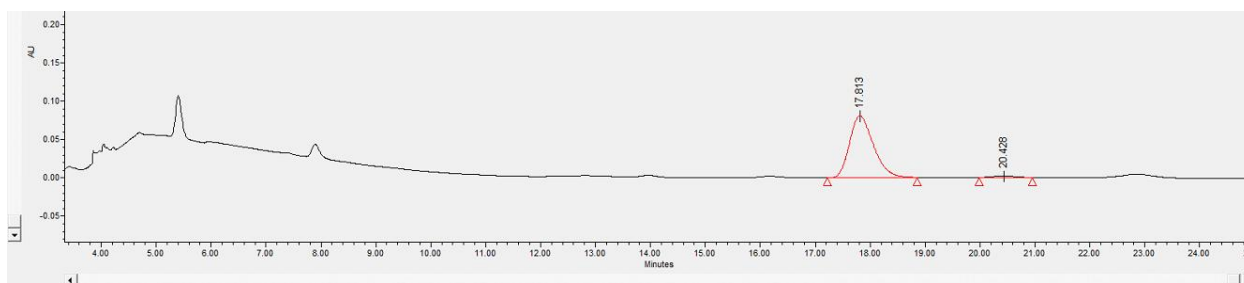
	Name	Retention Time (min)	Area (μV*sec)	% Area	Height (μV)	Int Type	Amount	Units	Peak Type	Peak Codes
1		17.813	2440196	97.57	80536	BB			Unknown	
2		20.428	60783	2.43	2055	BB			Unknown	

Enantioenriched Trace
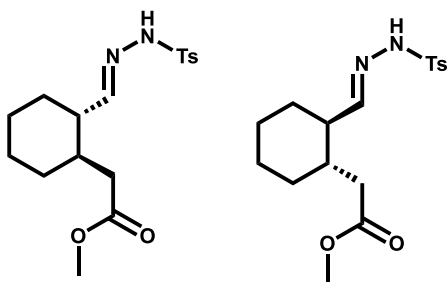
Enantiomers of Major Diastereomer

Enantiomers of Minor Diastereomer
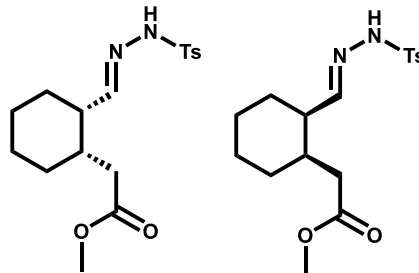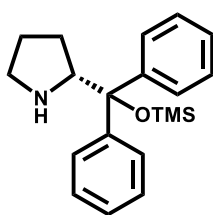
15 mol %

15 mol %
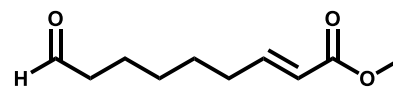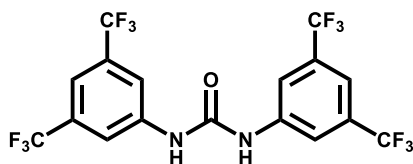
0.05 M, Toluene, 48 hr, 4⁰ C

From Enantioenriched 3 (Daicel CHIRALPAK® IF-3, isocratic 85 % Hexane, 15 % iPrOH, 1 mL/min)
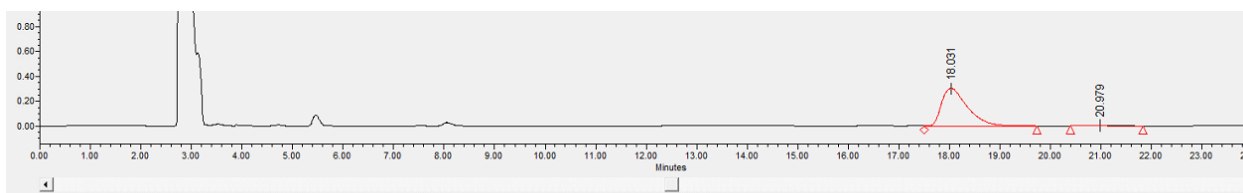
me	Retention Time (min)	Area (µV*sec)	% Area	Height (µV)	Int Type	Amount	Units	Peak Type	Peak Codes
	18.031	10741966	97.60	303017	VB			Unknown	
	20.979	263678	2.40	6865	BB			Unknown	

Enantioenriched Trace

Enantiomers of Major Diastereomer
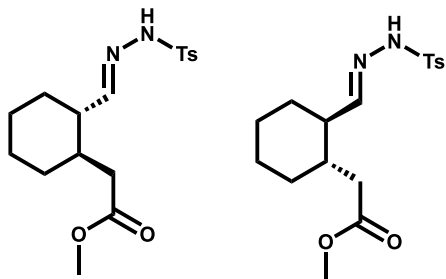
Enantiomers of Minor Diastereomer
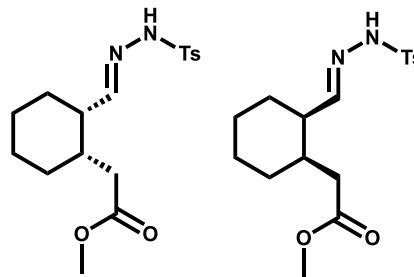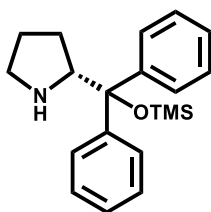
15 mol %

15 mol %
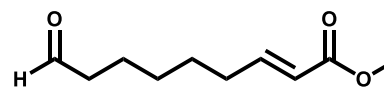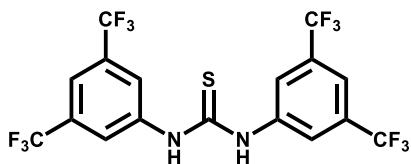
0.05 M, Toluene, 48 hr, 4° C

From Enantioenriched 3 (Daicel CHIRALPAK® IF-3, isocratic 85 % Hexane, 15 % iPrOH, 1 mL/min)
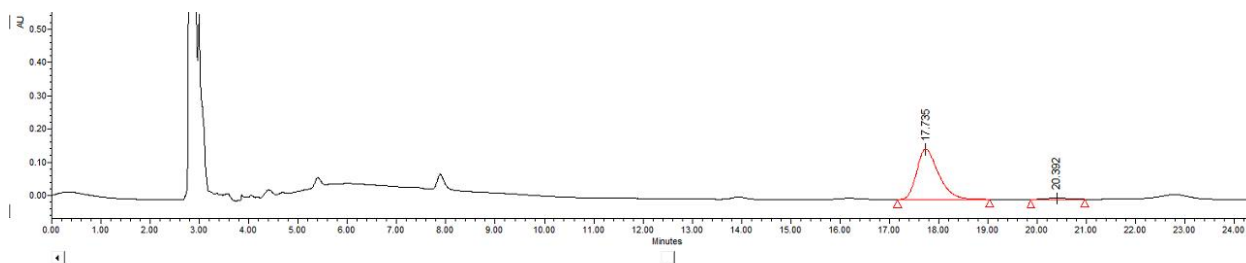
Name	Retention Time (min)	Area (µV*sec)	% Area	Height (µV)	Int Type	Amount	Units	Peak Type	Peak Codes
	17.735	4594110	97.27	150957	BB			Unknown	
	20.392	128742	2.73	4180	BB			Unknown	

Enantioenriched Trace
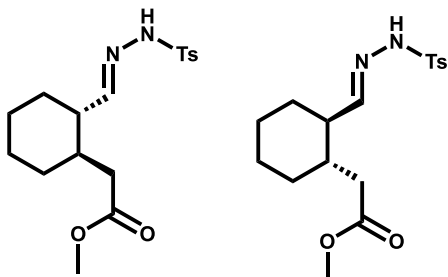
Enantiomers of Major Diastereomer

Enantiomers of Minor Diastereomer

15 mol %

15 mol %
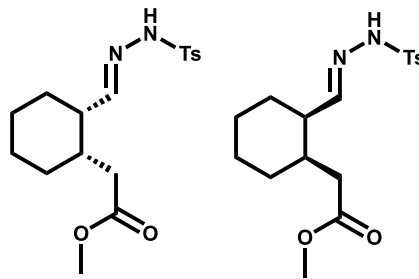
0.05 M, Toluene, 24 hr, rt
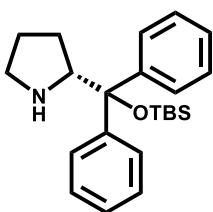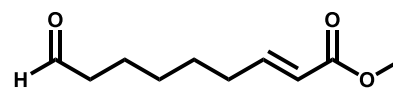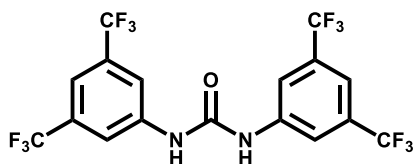
From Enantioenriched 3 (Daicel CHIRALPAK® IF-3, isocratic 85 % Hexane, 15 % iPrOH, 1 mL/min)
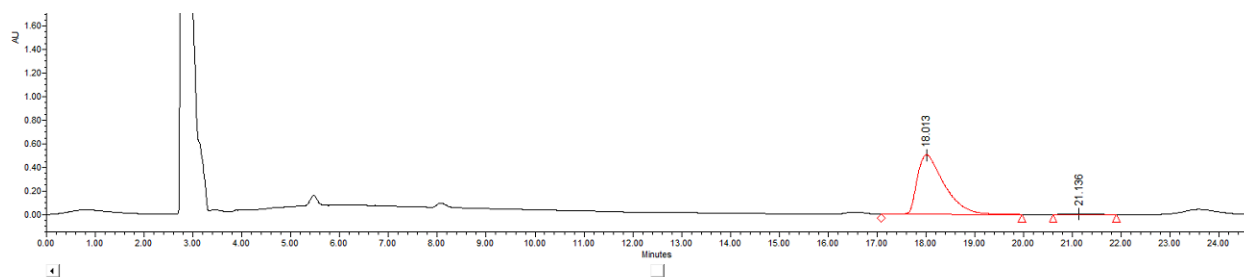
lame	Retention Time (min)	Area (µV*sec)	% Area	Height (µV)	Int Type	Amount	Units	Peak Type	Peak Codes
	18.013	19378794	99.10	504780	VB			Unknown	
	21.136	176590	0.90	4817	BB			Unknown	

Enantioenriched Trace
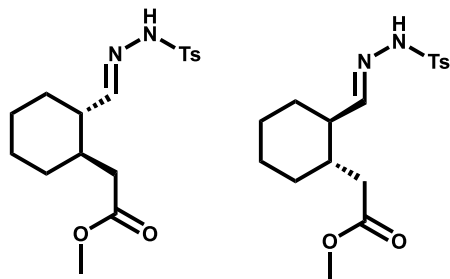
Enantiomers of Major Diastereomer

Enantiomers of Minor Diastereomer
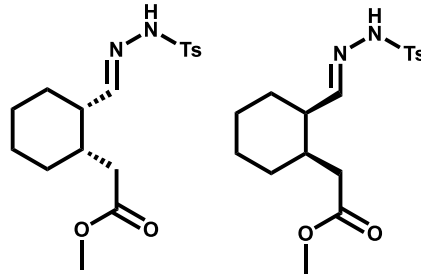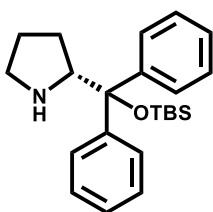
15 mol %

15 mol %
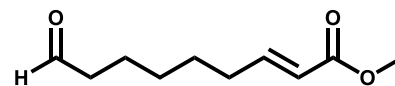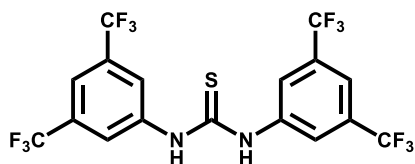
0.05 M, Toluene, 24 hr, rt

From Enantioenriched 3 (Daicel CHIRALPAK® IF-3, isocratic 85 % Hexane, 15 % iPrOH, 1 mL/min)
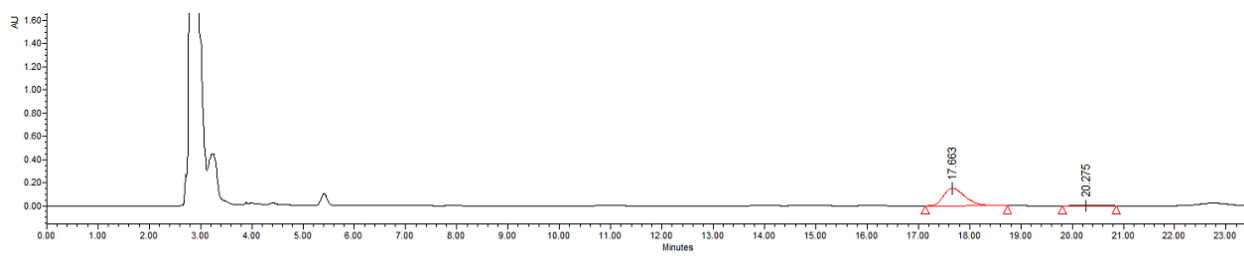
lame	Retention Time (min)	Area (µV*sec)	% Area	Height (µV)	Int Type	Amount	Units	Peak Type	Peak Codes
	17.663	4409939	97.07	152076	BB			Unknown	
	20.275	133217	2.93	4532	BB			Unknown	

Enantioenriched Trace
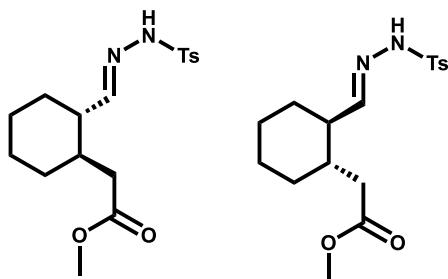
Enantiomers of Major Diastereomer

Enantiomers of Minor Diastereomer

15 mol %

15 mol %

0.05 M, Toluene, 24 hr, rt
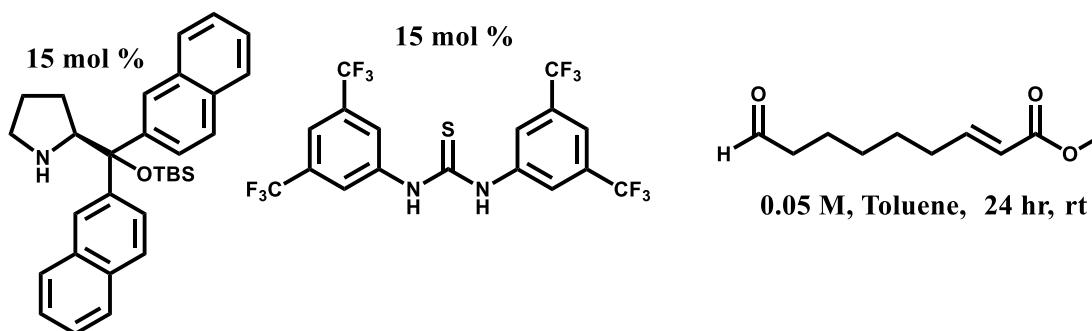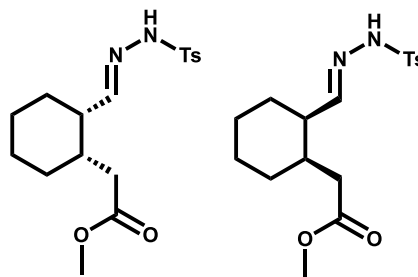
From Enantioenriched 3 (Daicel CHIRALPAK® IF-3, isocratic 85 % Hexane, 15 % iPrOH, 1 mL/min)
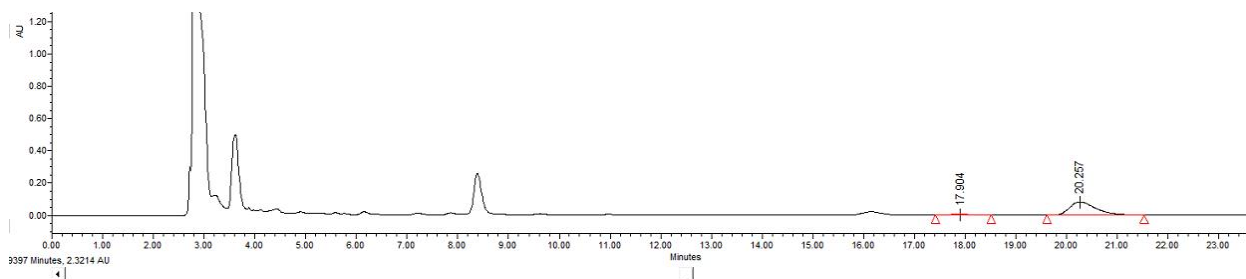
Name	Retention Time (min)	Area (µV*sec)	% Area	Height (µV)	Int Type	Amount	Units	Peak Type	Peak Codes
	17.904	140652	4.59	4820	BB			Unknown	
	20.257	2924144	95.41	82289	BB			Unknown	

Enantioenriched Trace

Enantiomers of Major Diastereomer
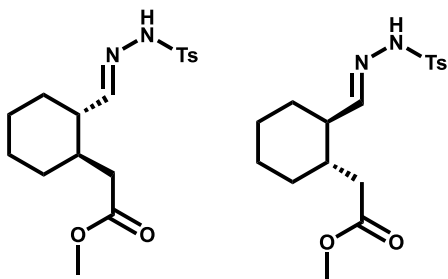
Enantiomers of Minor Diastereomer
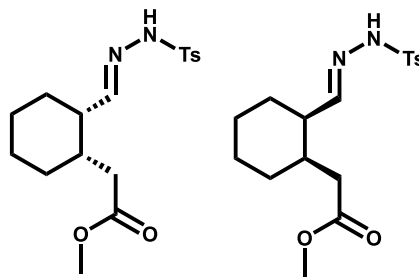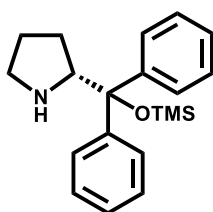
15 mol %

15 mol %
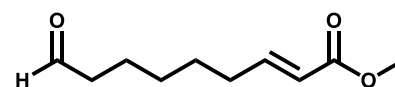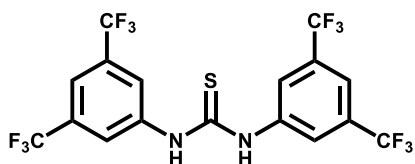
0.05 M, o-xylene, 24 hr, rt

From Enantioenriched 3 (Daicel CHIRALPAK® IF-3, isocratic 85 % Hexane, 15 % iPrOH, 1 mL/min)
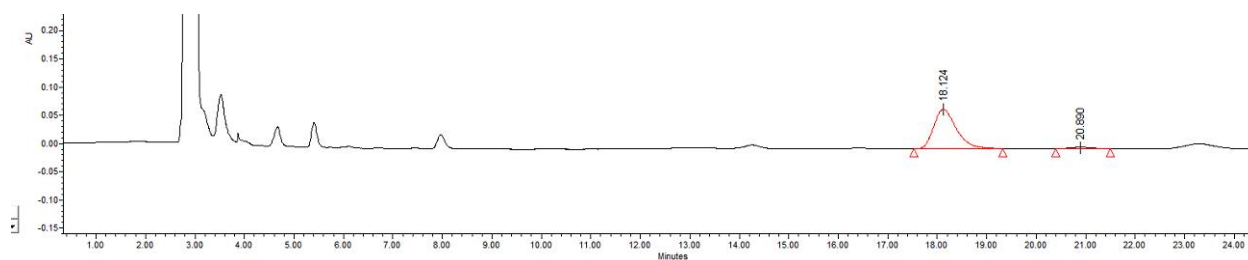
Name	Retention Time (min)	Area (µV*sec)	% Area	Height (µV)	Int Type	Amount	Units	Peak Type	Peak Codes
	18.124	2225646	96.22	70126	BB			Unknown	
	20.890	87351	3.78	2712	BB			Unknown	

Enantioenriched Trace
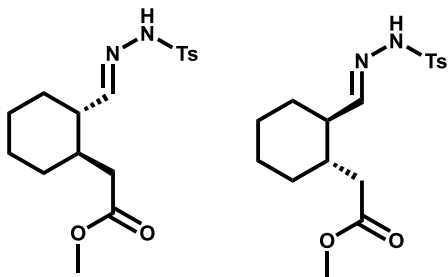
Enantiomers of Major Diastereomer

Enantiomers of Minor Diastereomer

15 mol %

15 mol %

0.05 M, DCM, 24 hr, rt
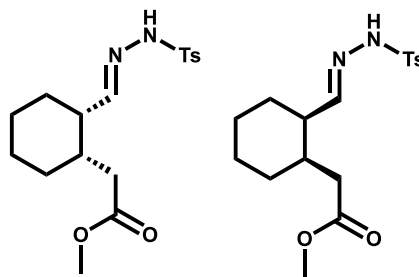
From Enantioenriched 3 (Daicel CHIRALPAK® IF-3, isocratic 85 % Hexane, 15 % iPrOH, 1 mL/min)
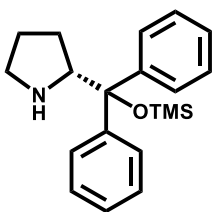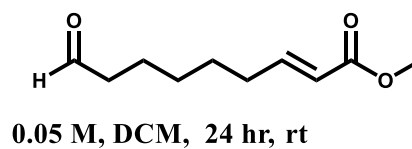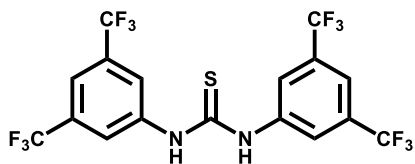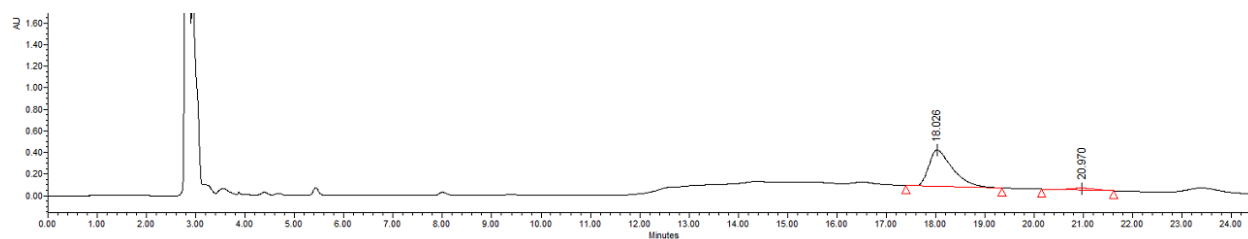
ame	Retention Time (min)	Area (µV*sec)	% Area	Height (µV)	Int Type	Amount	Units	Peak Type	Peak Codes
	18.026	11189778	94.78	337397	bb			Unknown	
	20.970	616349	5.22	18449	bb			Unknown	I08
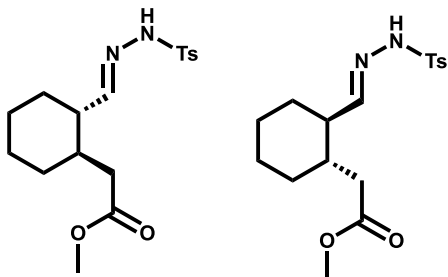
Enantioenriched Trace

Enantiomers of Major Diastereomer

Enantiomers of Minor Diastereomer

15 mol %

15 mol %

0.05 M, CHCl₃, 24 hr, rt
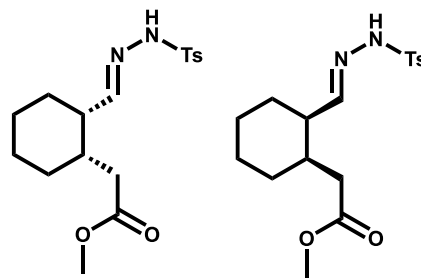
From Enantioenriched 3 (Daicel CHIRALPAK® IF-3, isocratic 85 % Hexane, 15 % iPrOH, 1 mL/min)
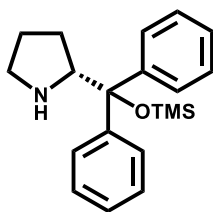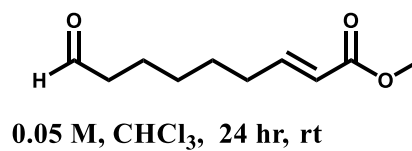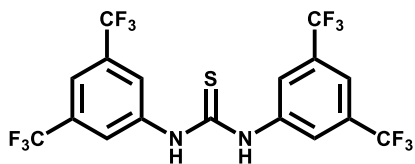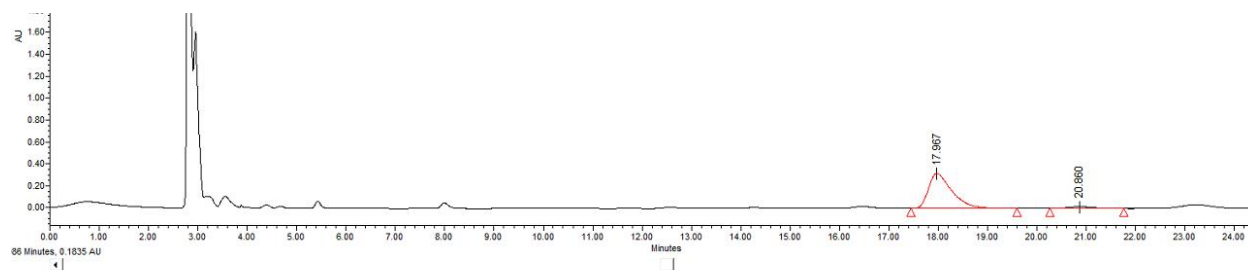
lame	Retention Time (min)	Area (μV*sec)	% Area	Height (μV)	Int Type	Amount	Units	Peak Type	Peak Codes
	17.967	10517545	94.57	321378	BB			Unknown	
	20.860	603726	5.43	17193	BB			Unknown	

Enantioenriched Trace

Enantiomers of Major Diastereomer
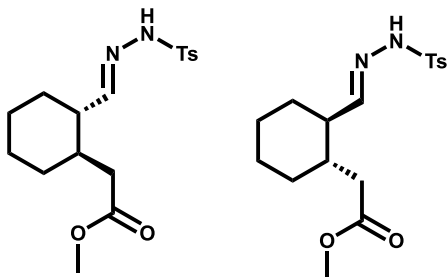
Enantiomers of Minor Diastereomer
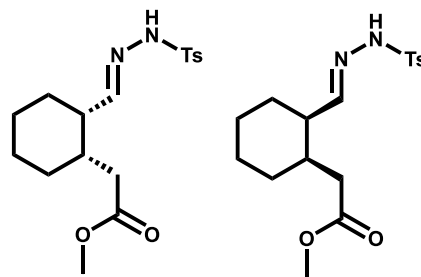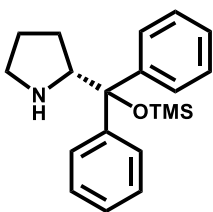
15 mol %

15 mol %
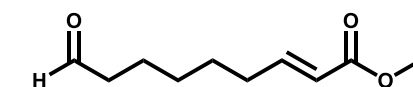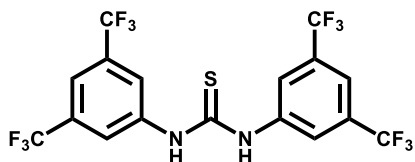
0.05 M, Trifluorotoluene, 24 hr, rt

From Enantioenriched 3 (Daicel CHIRALPAK® IF-3, isocratic 85 % Hexane, 15 % iPrOH, 1 mL/min)
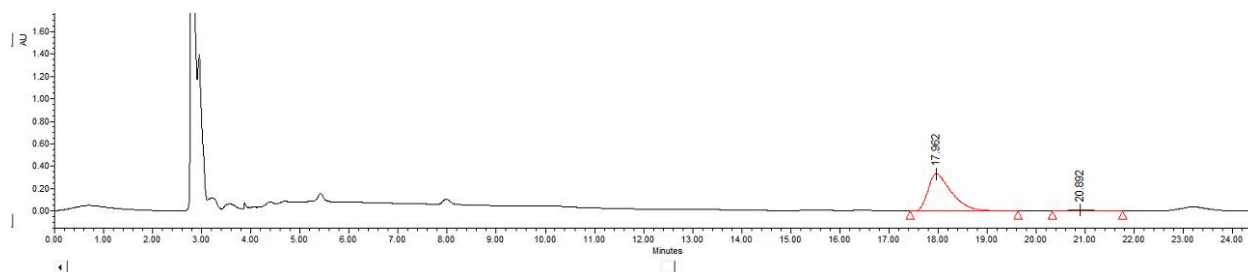
Name	Retention Time (min)	Area (µV*sec)	% Area	Height (µV)	Int Type	Amount	Units	Peak Type	Peak Codes
	17.962	11158562	96.10	335396	BB			Unknown	
	20.892	453359	3.90	12948	BB			Unknown	

Enantioenriched Trace

Enantiomers of Major Diastereomer
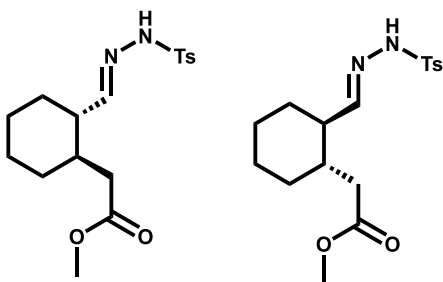
Enantiomers of Minor Diastereomer
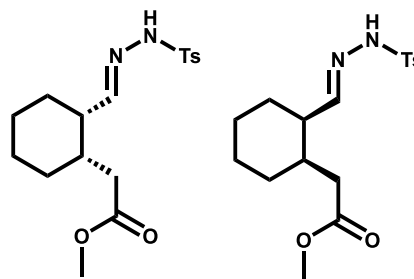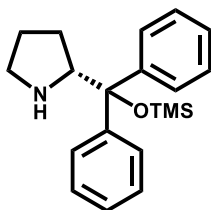
15 mol %

15 mol %
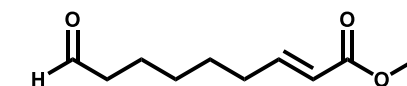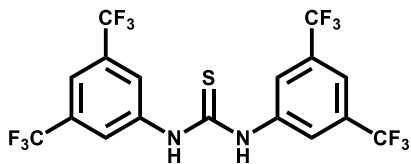
0.05 M, 1,2-dichloroethane, 24 hr, rt

From Enantioenriched 3 (Daicel CHIRALPAK® IF-3, isocratic 85 % Hexane, 15 % iPrOH, 1 mL/min)
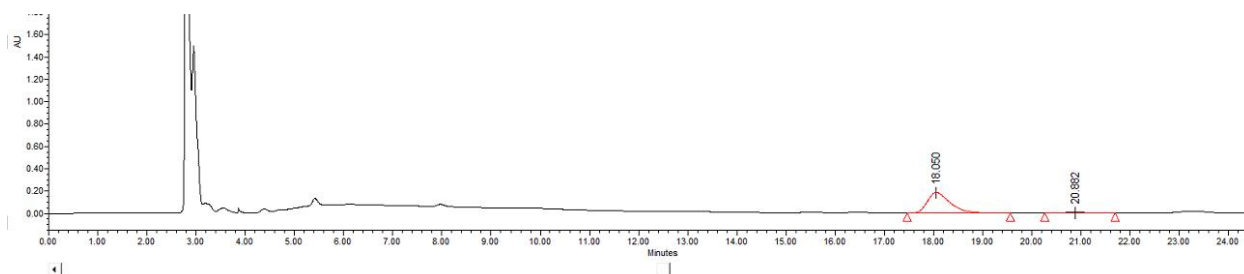
Name	Retention Time (min)	Area (µV*sec)	% Area	Height (µV)	Int Type	Amount	Units	Peak Type	Peak Codes
	18.050	6053330	94.84	186575	BB			Unknown	
	20.882	329099	5.16	9073	BB			Unknown	

Enantioenriched Trace
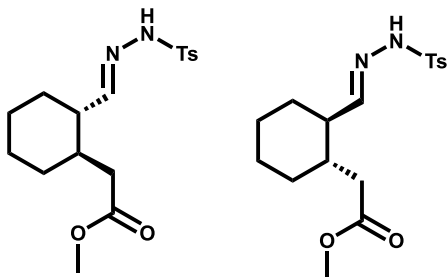
Enantiomers of Major Diastereomer

Enantiomers of Minor Diastereomer
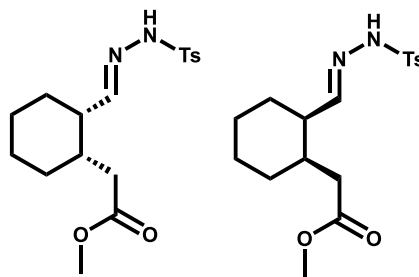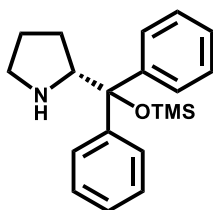
15 mol %

15 mol %
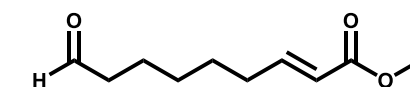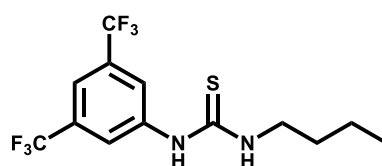
0.05 M, Toluene, 24 hr, rt

From Enantioenriched 3 (Daicel CHIRALPAK® IF-3, isocratic 85 % Hexane, 15 % iPrOH, 1 mL/min)
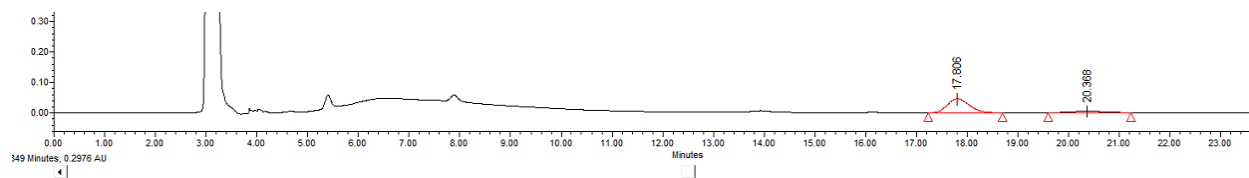
Name	Retention Time (min)	Area (µV*sec)	% Area	Height (µV)	Int Type	Amount	Units	Peak Type	Peak Codes
	17.806	1379056	85.45	46243	BB			Unknown	
	20.368	234874	14.55	5285	BB			Unknown	

Enantioenriched Trace
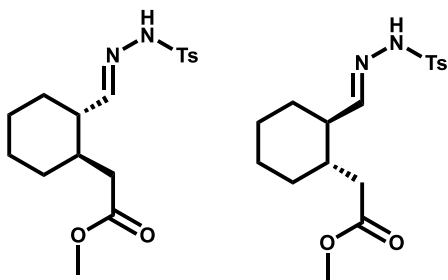
Enantiomers of Major Diastereomer

Enantiomers of Minor Diastereomer
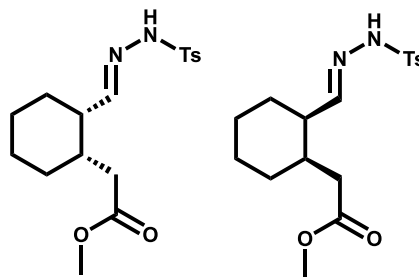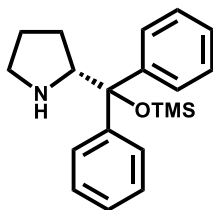
15 mol %

15 mol %
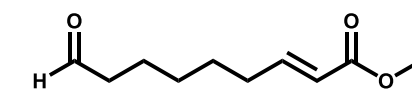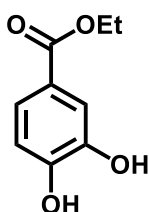
0.05 M, Toluene, 24 hr, rt

From Enantioenriched 3 (Daicel CHIRALPAK® IF-3, isocratic 85 % Hexane, 15 % iPrOH, 1 mL/min)
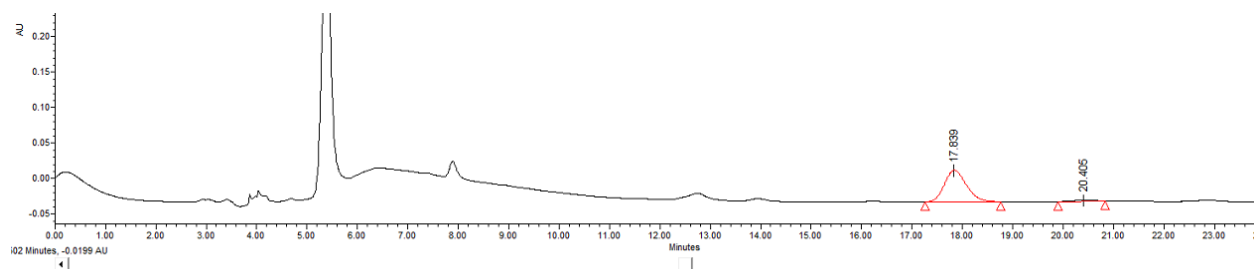
lame	Retention Time (min)	Area (µV*sec)	% Area	Height (µV)	Int Type	Amount	Units	Peak Type	Peak Codes
	17.839	1338514	96.61	44576	BB			Unknown	
	20.405	46929	3.39	1533	BB			Unknown	I08
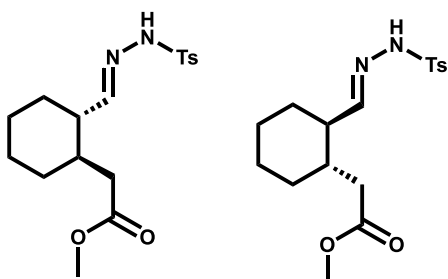
Enantioenriched Trace

Enantiomers of Major Diastereomer

Enantiomers of Minor Diastereomer

15 mol %

15 mol %

0.05 M, Toluene, 24 hr, rt
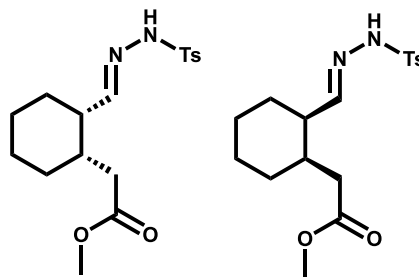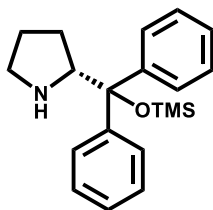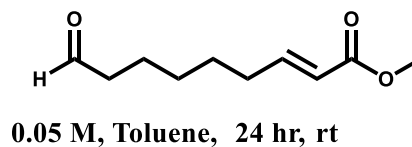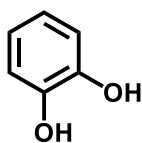
From Enantioenriched 3 (Daicel CHIRALPAK® IF-3, isocratic 85 % Hexane, 15 % iPrOH, 1 mL/min)
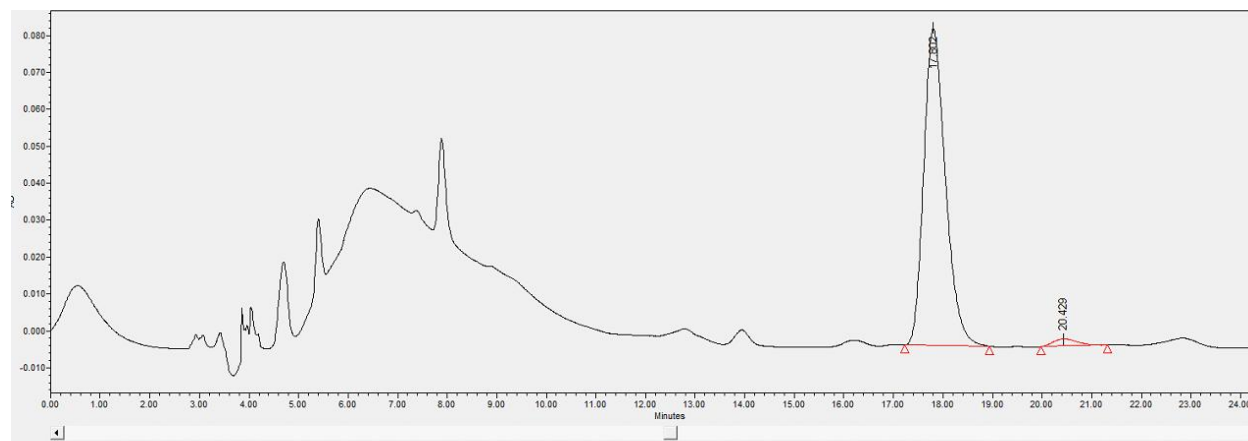
me	Retention Time (min)	Area (µV*sec)	% Area	Height (µV)	Int Type	Amount	Units	Peak Type	Peak Codes
	17.802	2604965	97.52	85807	BB			Unknown	
	20.429	66250	2.48	1966	Bb			Unknown	

Enantioenriched Trace - (-)-Yohimbane Precursor

Enantiomers of Major Diastereomer

Enantiomers of Minor Diastereomer

20 mol %

20 mol %

0.025 M, Toluene, 48 hr, 4° C
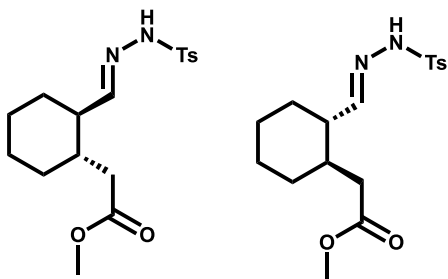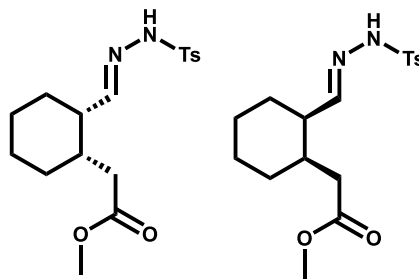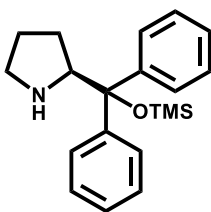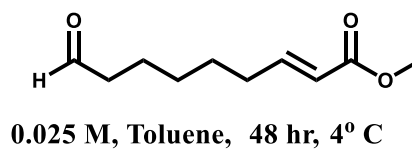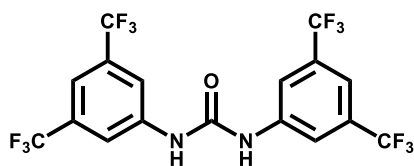
From Enantioenriched ent-3 (Daicel CHIRALPAK® IF-3, isocratic 85 % Hexane, 15 % iPrOH, 1 mL/min)
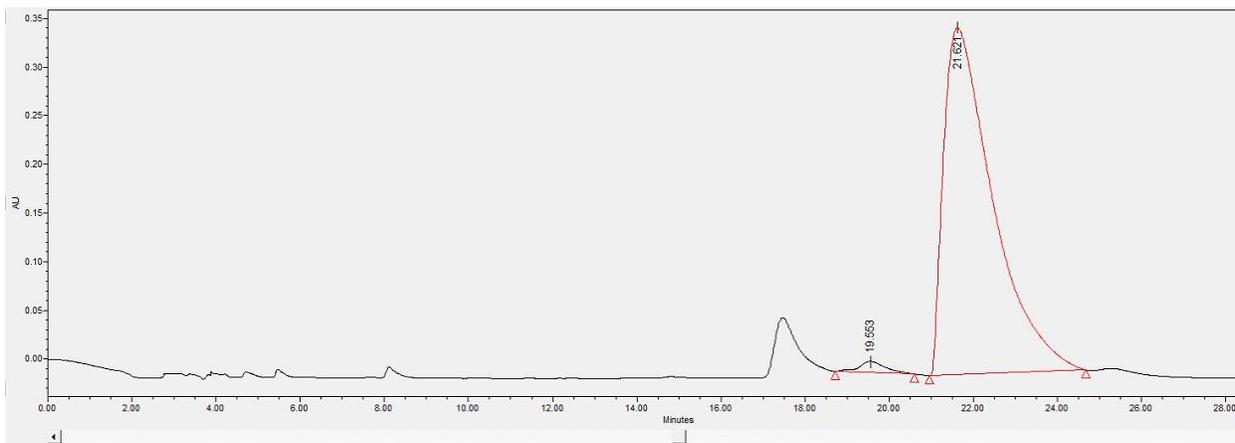
Name	Retention Time (min)	Area (µV*sec)	% Area	Height (µV)	Int Type	Amount	Units	Peak Type	Peak Codes
	19.553	497478	1.69	11360	bb			Unknown	I08
	21.621	28944521	98.31	356338	bb			Unknown	

Racemic Trace

Enantiomers of Major Diastereomer
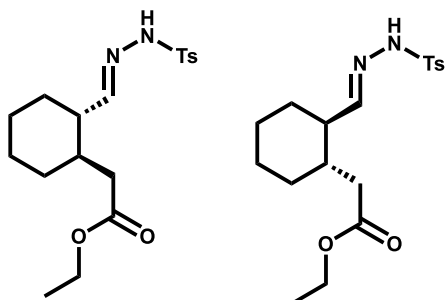
Enantiomers of Minor Diastereomer
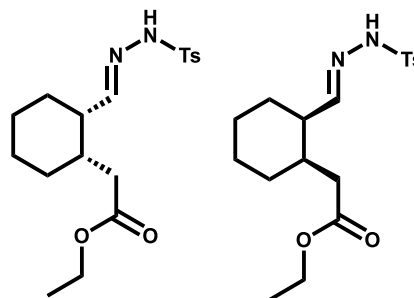
20 mol %
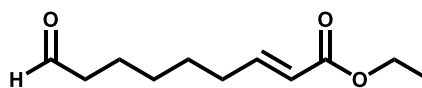
0.1 M, CHCl₃, rt, 24 hr

From Racemic 20 (Daicel CHIRALPAK® IF-3, isocratic 90 % Hexane, 5 % EtOH, 5 % MeOH %, 1 mL/min)
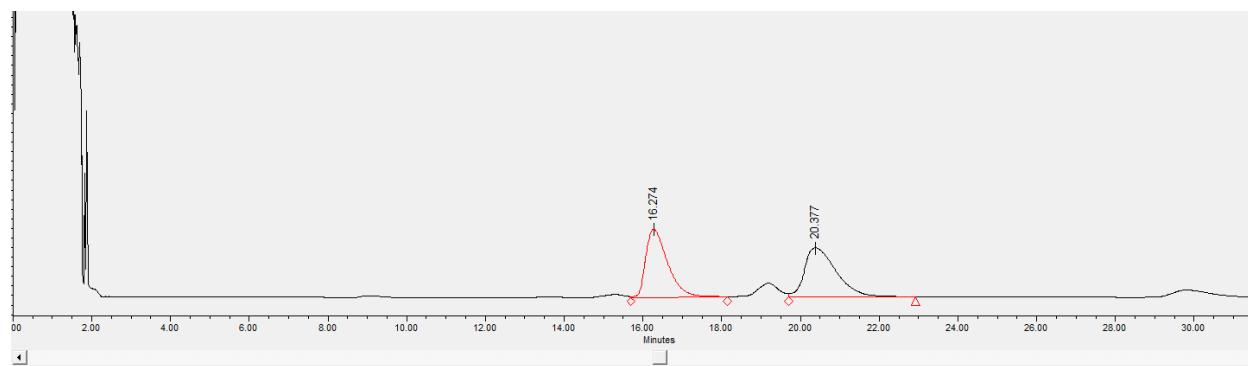
Retention Time (min)	Area (µV*sec)	% Area	Height (µV)	Int Type	Amount	Units	Peak Type	Peak Codes
16.274	13799345	49.08	355120	VV			Unknown	
20.377	14318394	50.92	256402	VB			Unknown	

Enantioenriched Trace

Enantiomers of Major Diastereomer

Enantiomers of Minor Diastereomer

20 mol %

20 mol %

0.025 M, Toluene, 48 hr, 4° C
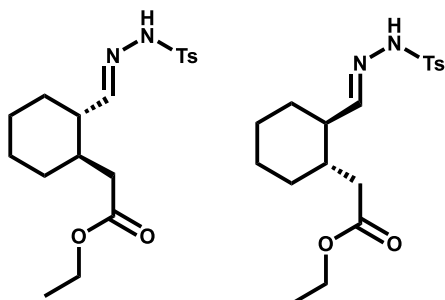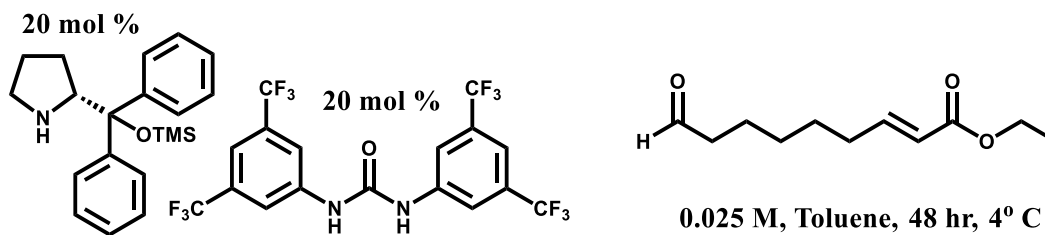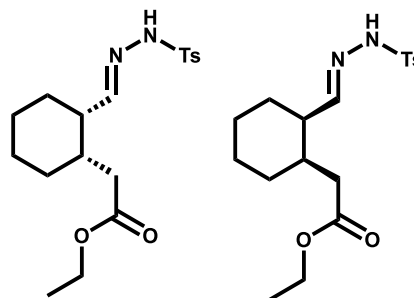
From Enantioenriched 20 (Daicel CHIRALPAK® IF-3, isocratic 90 % Hexane, 5 % EtOH, 5 % MeOH %, 1 mL/min)
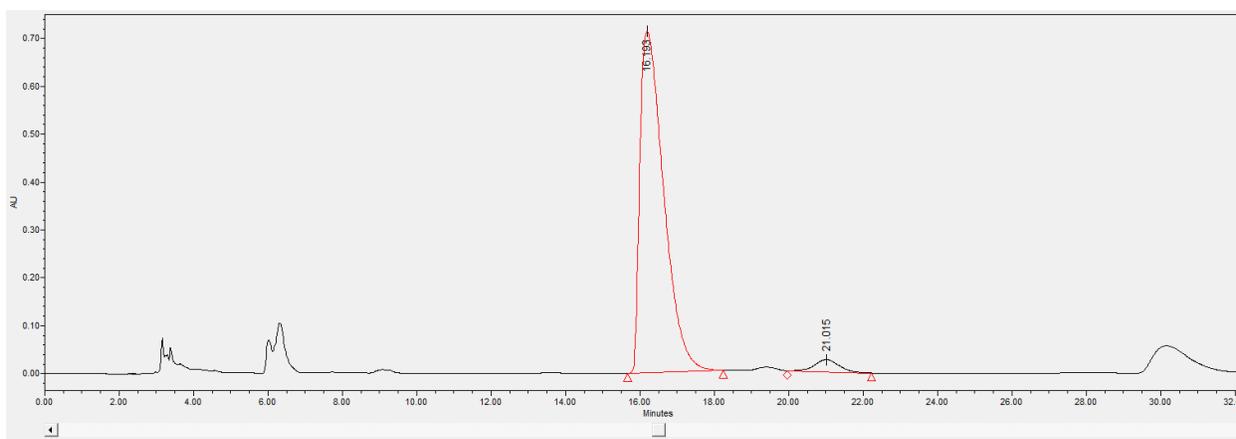
lame	Retention Time (min)	Area (µV*sec)	% Area	Height (µV)	Int Type	Amount	Units	Peak Type	Peak Codes
	16.193	31595701	96.24	712201	BB			Unknown	
	21.015	1233198	3.76	26152	VB			Unknown	

Racemic Trace

Enantiomers of Major Diastereomer
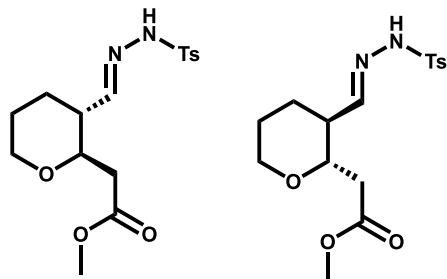
Enantiomers of Minor Diastereomer
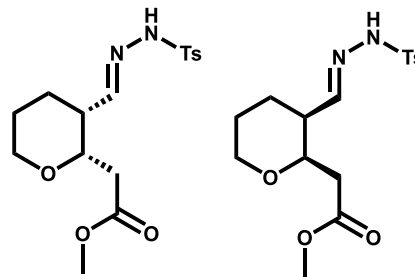
30 mol %

30 mol %
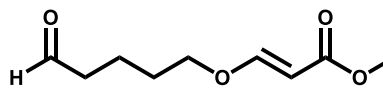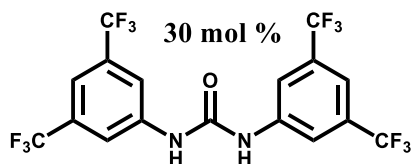
0.05 M, Toluene, 24 hr, rt

From Racemic 22 (Daicel CHIRALPAK® IF-3, isocratic 75 % Hexane, 10 % EtOH, 15 % MeOH %, 1 mL/min)
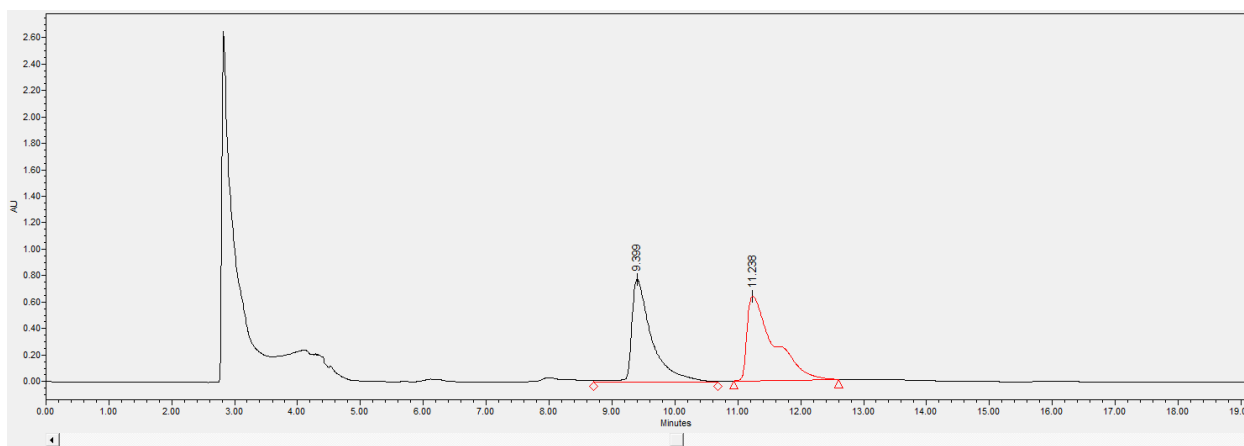
ame	Retention Time (min)	Area (µV*sec)	% Area	Height (µV)	Int Type	Amount	Units	Peak Type	Peak Codes
	9.399	17198441	47.77	776807	VV			Unknown	
	11.238	18806812	52.23	638922	bb			Unknown	

Enantioenriched Trace

Enantiomers of Major Diastereomer

Enantiomers of Minor Diastereomer

30 mol %

30 mol %
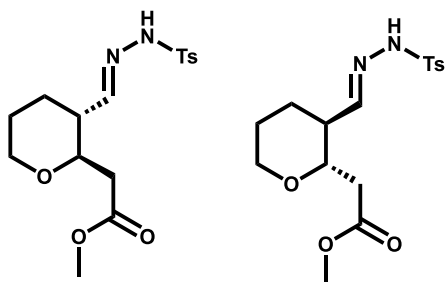
0.025 M, Toluene, rt, 72 hr
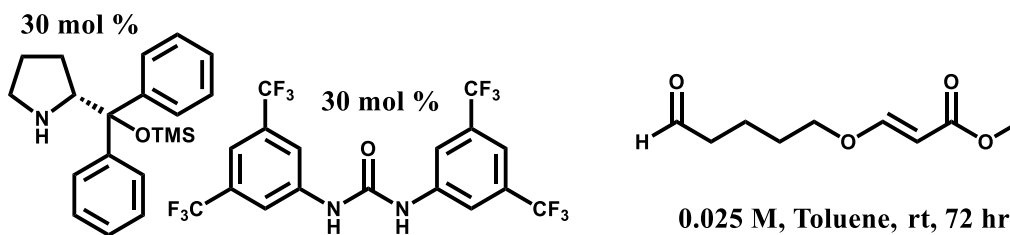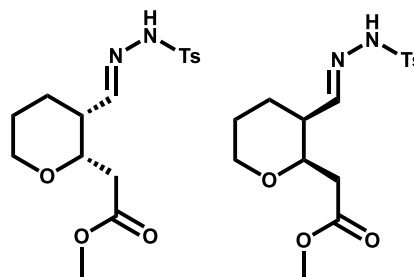
From Enantioenriched 22 (Daicel CHIRALPAK® IF-3, isocratic 75 % Hexane, 10 % EtOH, 15 % MeOH %, 1 mL/min)
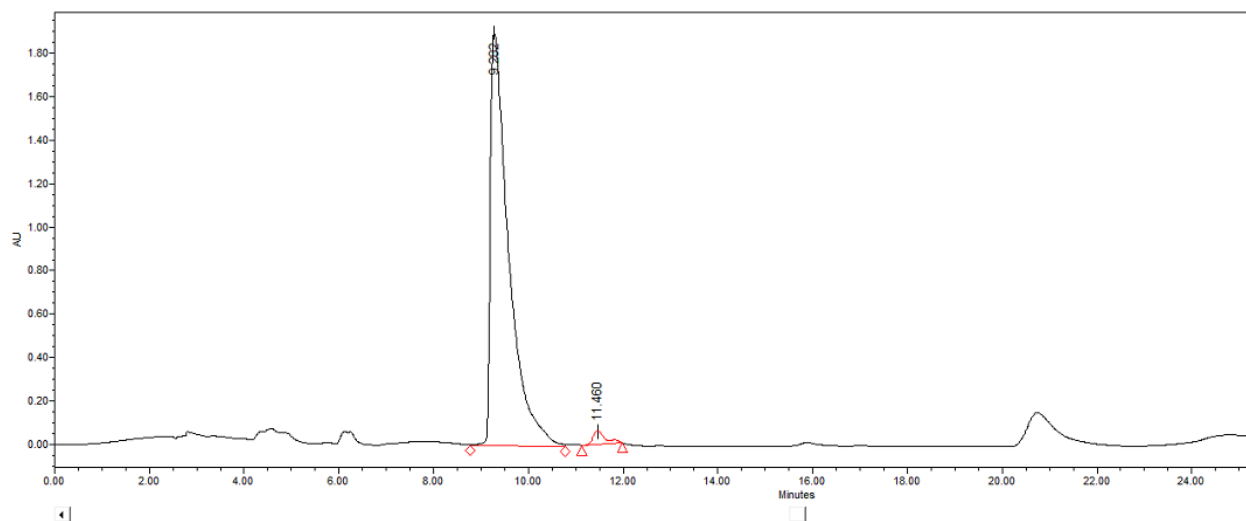
ame	Retention Time (min)	Area (µV*sec)	% Area	Height (µV)	Int Type	Amount	Units	Peak Type	Peak Codes
	9.282	51325397	97.87	1900620	VV			Unknown	
	11.460	1117804	2.13	62251	bb			Unknown	

Racemic Trace

Enantiomers of Major Diastereomer
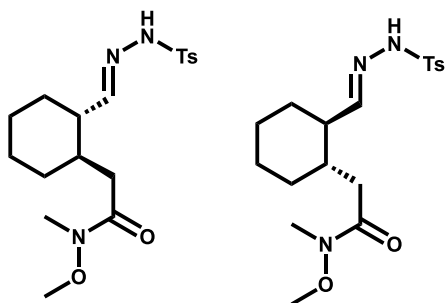
Enantiomers of Minor Diastereomer
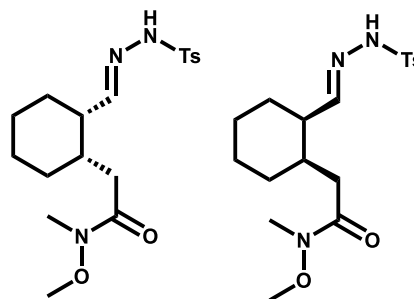
30 mol %

30 mol %
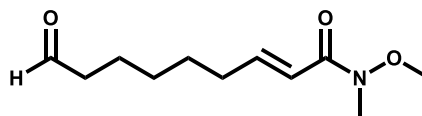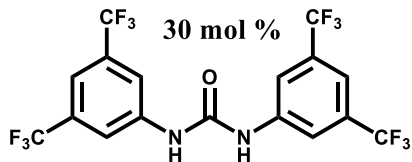
0.025 M, Toluene, 24 hr, rt,

From Racemic 23 (Daicel CHIRALPAK® IF-3, isocratic 90 % Hexane, 5 % EtOH, 5 % MeOH %, 0.75 mL/min)
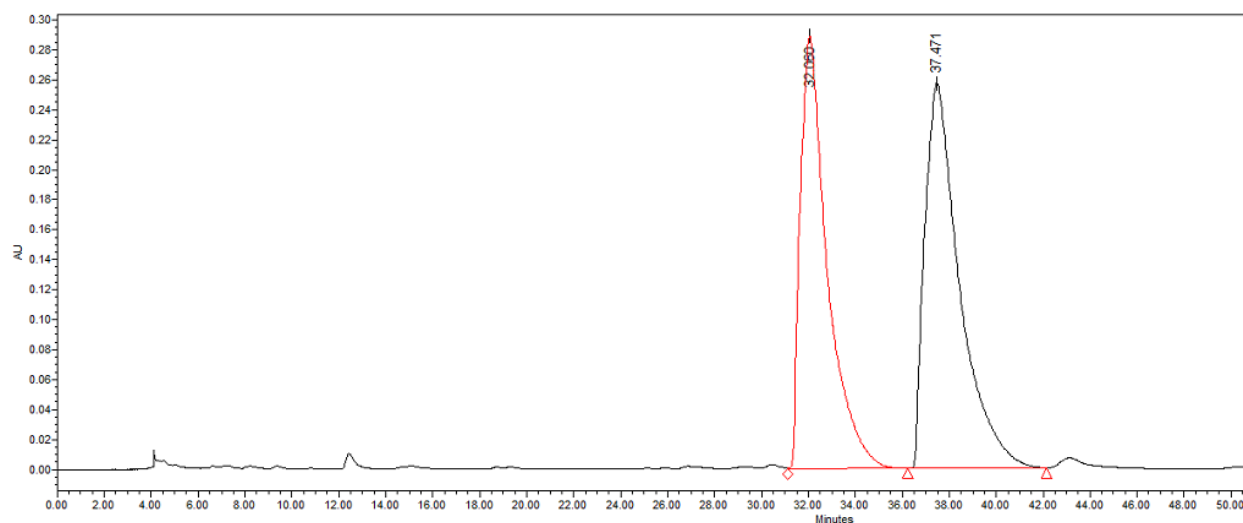
Name	Retention Time (min)	Area (µV*sec)	% Area	Height (µV)	Int Type	Amount	Units	Peak Type	Peak Codes
	32.060	23000417	46.55	288377	VB			Unknown	
	37.471	26411191	53.45	256958	BB			Unknown	

Enantioenriched Trace

Enantiomers of Major Diastereomer
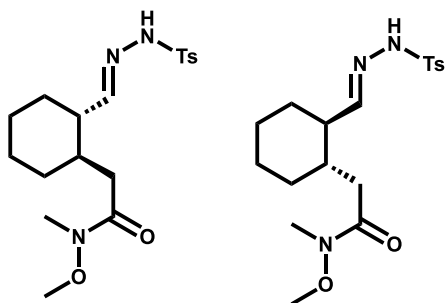
Enantiomers of Minor Diastereomer
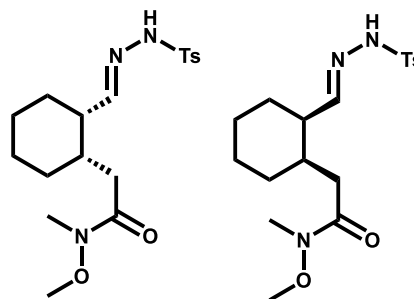
30 mol %

30 mol %
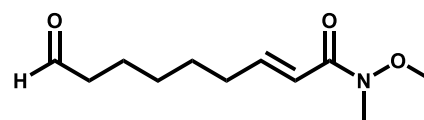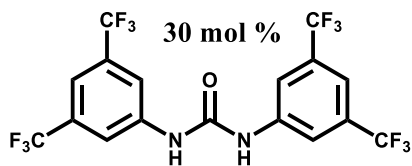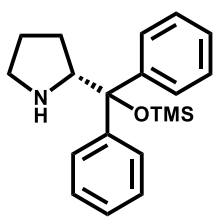
0.025 M, Toluene, 72 hr, 4° C

From Enantioenriched 23 (Daicel CHIRALPAK® IF-3, isocratic 90 % Hexane, 5 % EtOH, 5 % MeOH %, 0.75 mL/min)
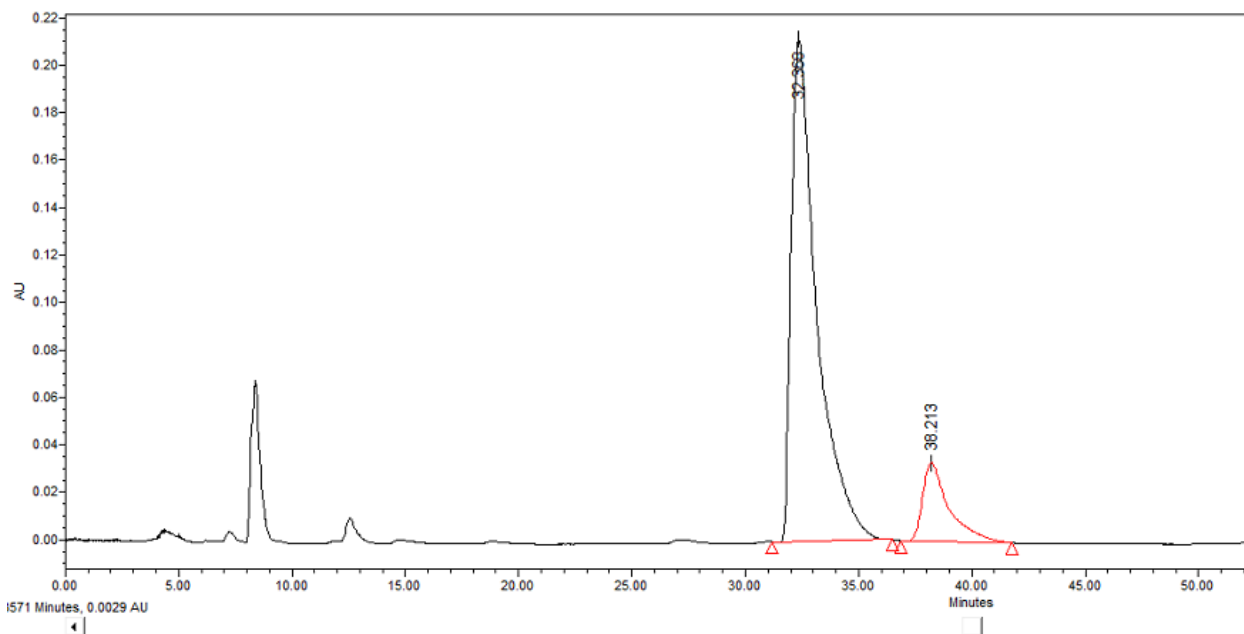
Name	Retention Time (min)	Area (µV*sec)	% Area	Height (µV)	Int Type	Amount	Units	Peak Type	Peak Codes
	32.368	16559998	86.05	211399	bb			Unknown	
	38.213	2684594	13.95	33166	bb			Unknown	

From Racemic 24 (Daicel CHIRALPAK® IF-3, isocratic 80 % Hexane, 20 % iPrOH, 1 mL/min)
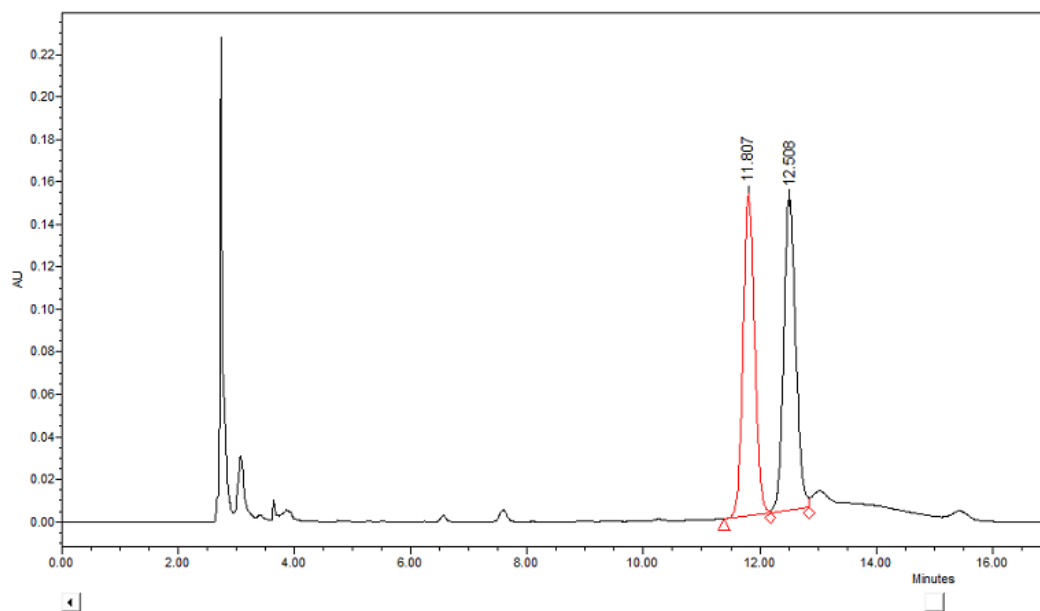
lame	Retention Time (min)	Area (µV*sec)	% Area	Height (µV)	Int Type	Amount	Units	Peak Type	Peak Codes
	11.807	2075342	49.65	151669	BV			Unknown	
	12.508	2104560	50.35	146978	VV			Unknown	

Enantioenriched Trace

Enantiomers of Major Diastereomer
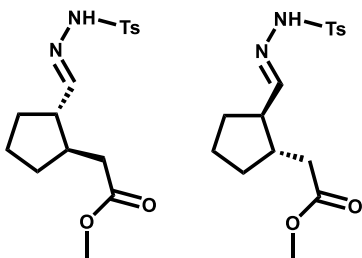
Enantiomers of Minor Diastereomer
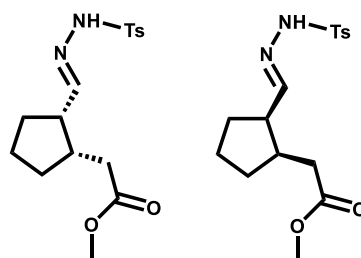
20 mol %

20 mol %
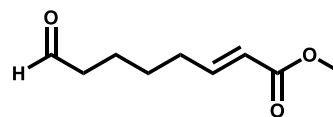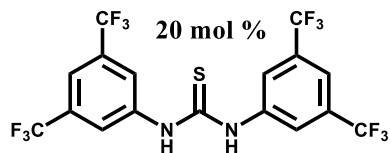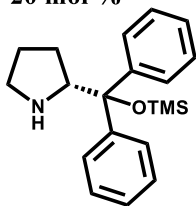
0.05 M, Toluene, rt, 24 hr

Reaction using enantioenriched catalyst to generate 24 (Daicel CHIRALPAK® IF-3, isocratic 80 % Hexane, 20 % iPrOH, 1 mL/min)
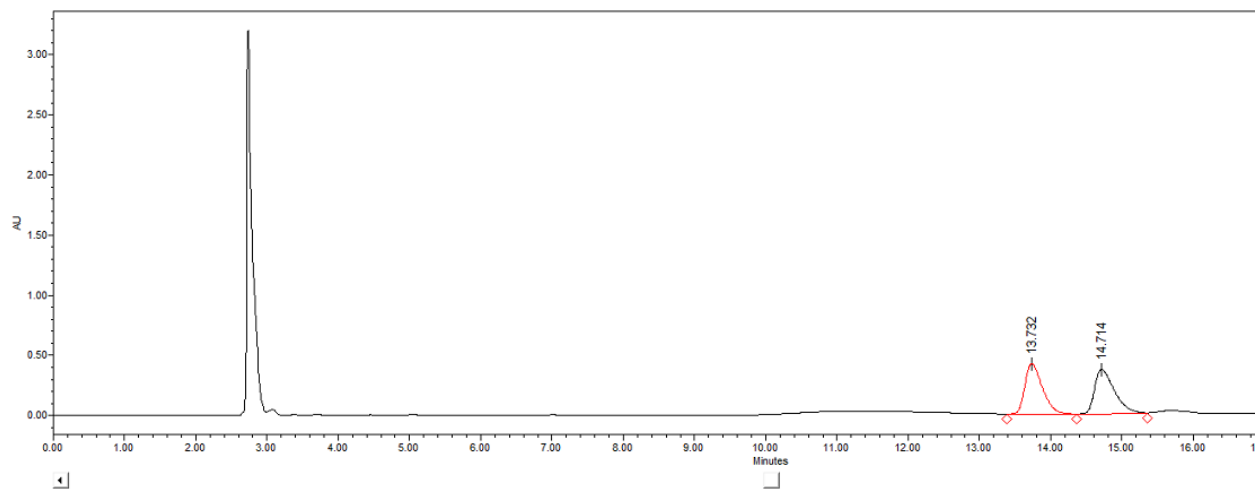
Name	Retention Time (min)	Area (µV*sec)	% Area	Height (µV)	Int Type	Amount	Units	Peak Type	Peak Codes
	13.732	7225233	49.92	421858	VV			Unknown	
	14.714	7249596	50.08	371850	VV			Unknown	

Racemic Trace

Enantiomers of Major Diastereomer
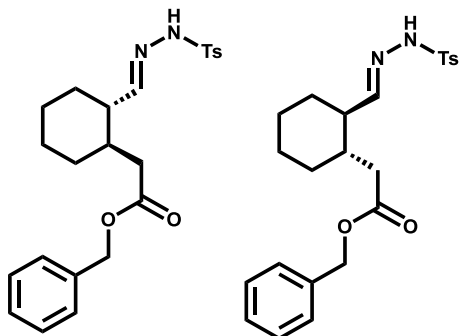
Enantiomers of Minor Diastereomer
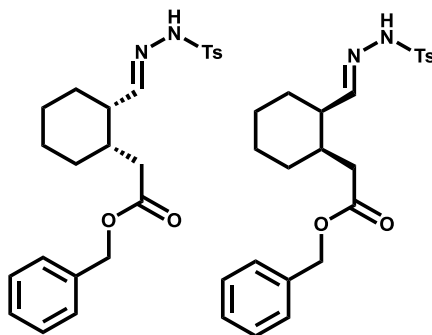
15 mol %
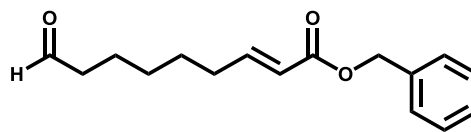
0.05 M, Toluene, rt, 24 hr

From Racemic 21 (Daicel CHIRALPAK® IF-3, isocratic 85 % Hexane, 15 % iPrOH, 1 mL/min)
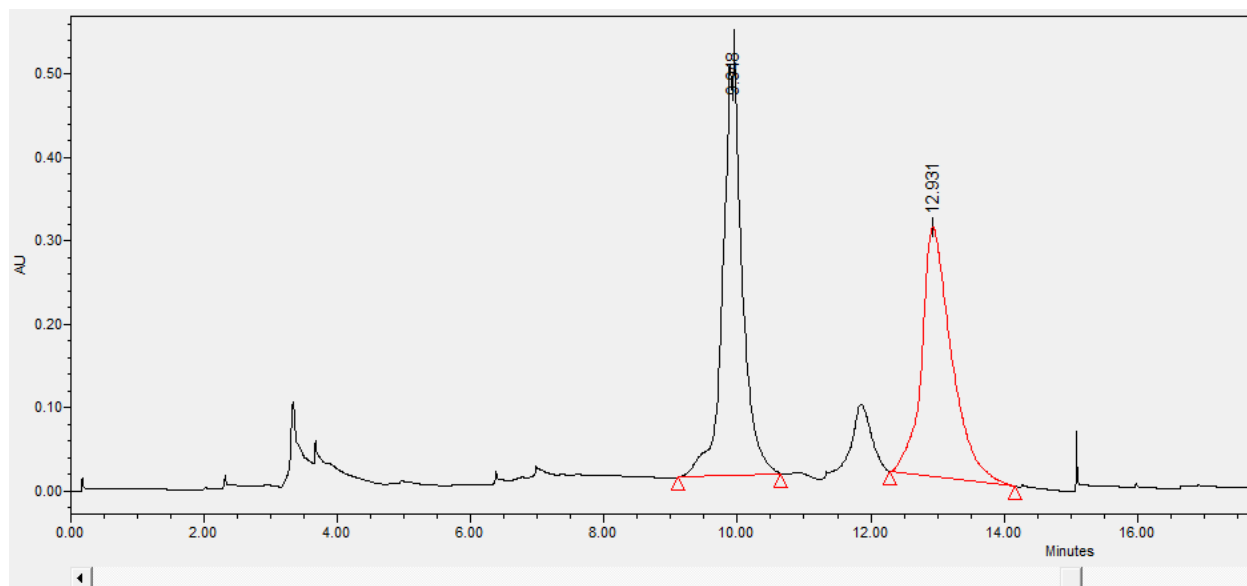
Enantioenriched Trace

Enantiomers of Major Diastereomer

Enantiomers of Minor Diastereomer

20 mol %

20 mol %

0.025 M, Toluene, 48 hr, 4° C

From Enantioenriched 21 (Daicel CHIRALPAK® IF-3, isocratic 85 % Hexane, 15 % iPrOH, 1 mL/min)

ame	Retention Time (min)	Area (µV*sec)	% Area	Height (µV)	Int Type	Amount	Units	Peak Type	Peak Codes
	9.948	10170777	52.19	523194	bb			Unknown	
	12.931	9318773	47.81	299018	bb			Unknown	

ame	Retention Time (min)	Area (µV*sec)	% Area	Height (µV)	Int Type	Amount	Units	Peak Type	Peak Codes
	9.797	17686263	93.17	808401	BV			Unknown	
	13.402	1295991	6.83	46170	VV			Unknown	
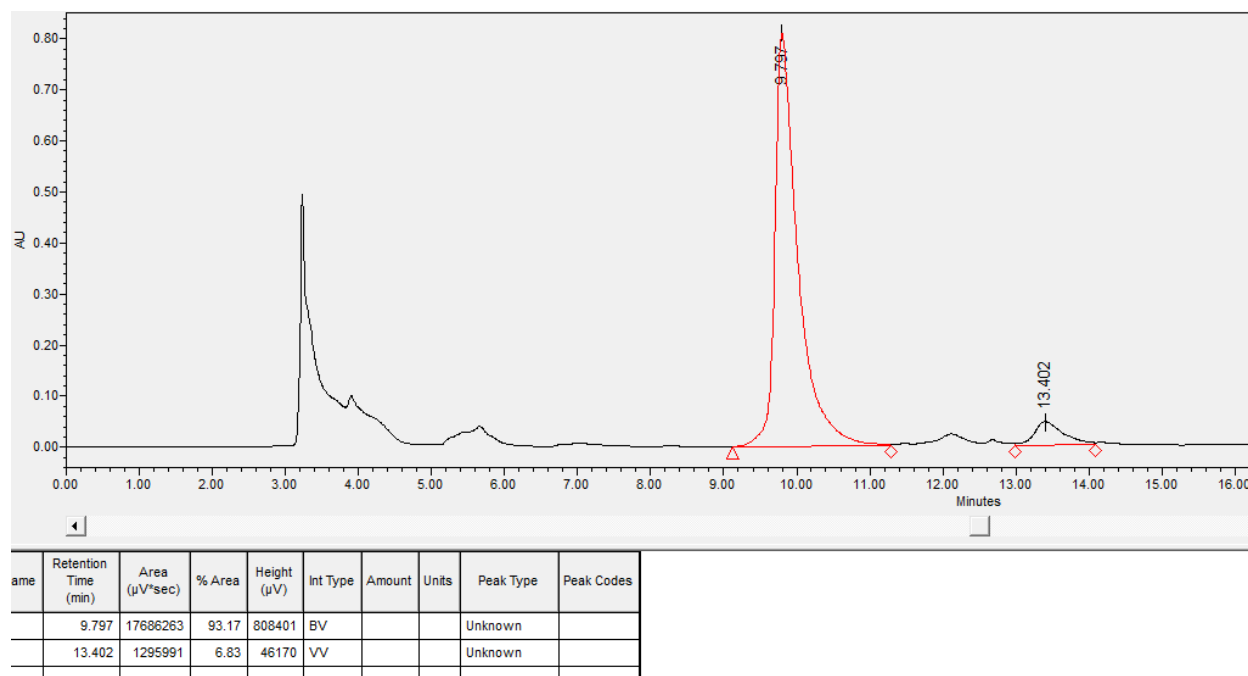
1. ^{1}H NMR Determination of Enantiomeric excess of 28
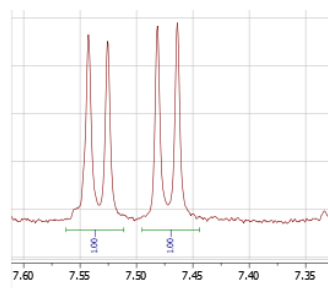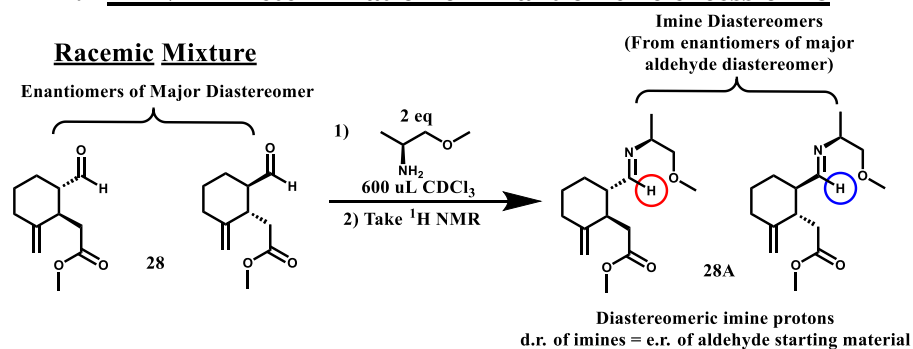
Figure 34. Zoom in of ^{1}H NMR taken after diastereomeric imines were formed from a racemic mixture of aldehyde **28**. 1:1 d.r. based on integration of resoances for imine protons circled above. See section **4.2.2** for analysis and determination of enantiomeric excess.[47]
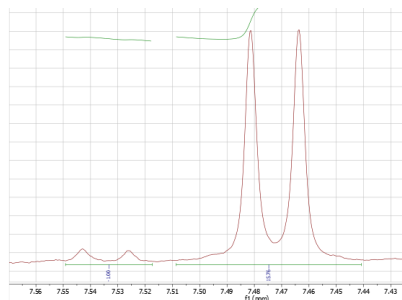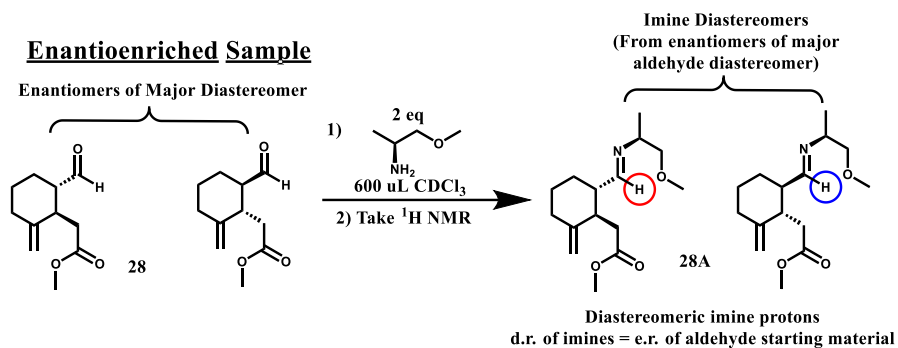
Figure 35. Zoom in of ^{1}H NMR taken after diastereomeric imines were formed from an enantioenriched mixture of aldehyde **28**. 15.76:1 d.r. based on integration of resoances for imine protons circled above (88 % ee). See section **4.2.2** for analysis and determination of enantiomeric excess.[48]

4.5.6 Spectra Data: ¹H NMR, ¹³C NMR, and 2D spectra

5

NB4_P132_Fr 16-18.10.fid
H1_standard.UW CDCl3 /home/zgirvin/callisto zgirvin 15

¹H NMR (500 MHz, Chloroform-*d*)

1 (t) 9.77
9 (dt) 6.95
10 (dt) 5.82
14 (s) 3.73
8 (qd) 2.22
7 (m) 1.37
4 (td) 2.44
5 (p) 1.65
6 (p) 1.49

NB4_P132_Fr 16-18.11.fid
C13_H1dec.UW CDCl3 /home/zgirvin/callisto zgirvin 15

¹³C NMR (126 MHz, Chloroform-*d*)

2 (s) 202.46
11 (s) 167.07
9 (s) 149.16
10 (s) 121.12
14 (s) 51.41
4 (s) 43.73
5 (s) 21.76
7 (s) 28.59
8 (s) 31.92
6 (s) 27.75

Substrate 1

NB4_P296.10.fid
H1_standard.UW CDCl3 /home/zgirvin/callisto zgirvin 7

¹H NMR (500 MHz, Chloroform-*d*)

1 (t)
9.77

9 (dt)
6.96

10 (dt)
6.40

16 (s)
3.70

15 (s)
3.24

4 (td)
2.44

8 (qd)
2.25

6 (p)
1.51

5 (p)
1.65

7 (m)
1.38

NB4_P296.11.fid
C13_H1dec.UW CDCl3 /home/zgirvin/callisto zgirvin

¹³C NMR (126 MHz, Chloroform-*d*)

2 (s)
202.60

11 (s)
166.97

9 (s)
147.40

10 (s)
118.92

16 (s)
61.69

4 (s)
43.79

A (s)
28.65

B (s)
28.06

15 (s)
32.36

8 (s)
32.23

C (s)
21.82

f1 (ppm)

Substrate S1

NB4_P126_C8 HWE Purification Fr 51-60.10.fid
H1_standard.UW CDCl3 /home/zgirvin/callisto zgirvin 34

1H NMR (500 MHz, Chloroform-d)

1 (t)
9.77

10 (dt)
6.96

11 (dt)
5.82

15 (s)
3.73

9 (qd)
2.20

B (dq)
1.47

4 (td)
2.43

5 (m)
1.62

C (m)
1.34

126 MHz, CDCl₃

Substrate S6.

Substrate 27. ¹H NMR (500 MHz), ¹³C NMR (126 MHz), CDCl₃

NB1PG015 C2001152226 frac5-10 pure pump.10.fid — H1_standard.UW CDCl3 /home/plampkin/callisto plampkin 24 —

¹H NMR (500 MHz, Chloroform-d)

NB1PG015 C2001152226 frac5-10 pure pump.12.fid — C13_H1dec.UW CDCl3 /home/plampkin/callisto plampkin 24 —

¹³C NMR (126 MHz, Chloroform-d)
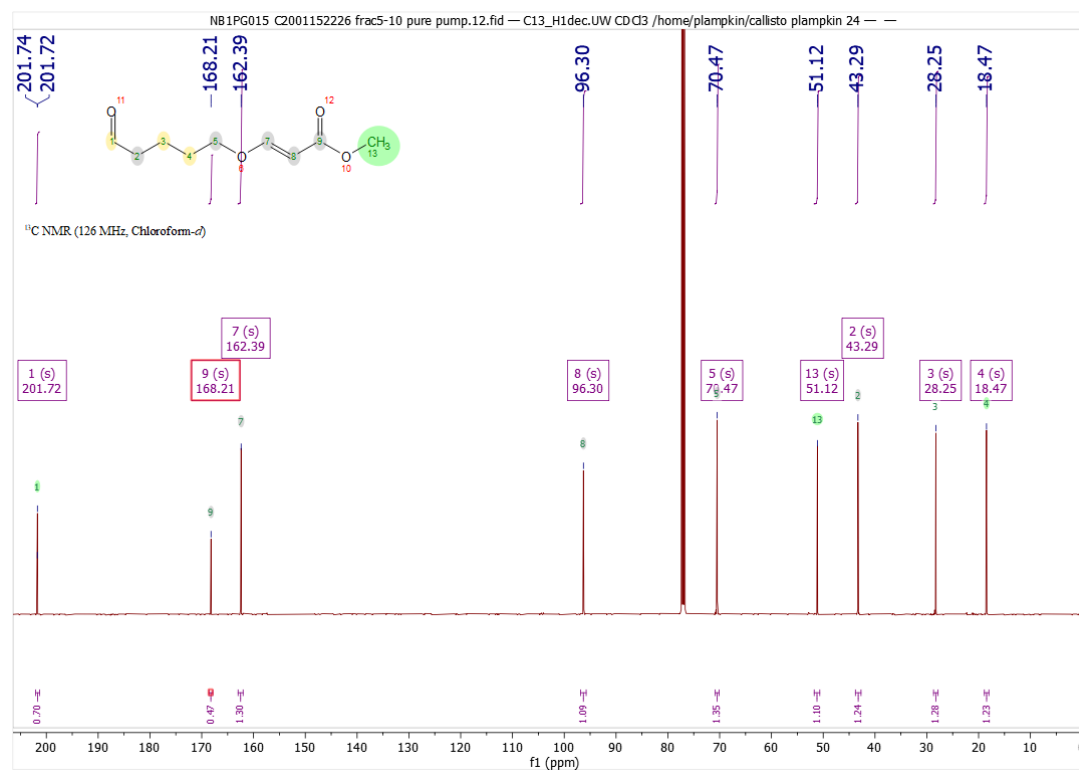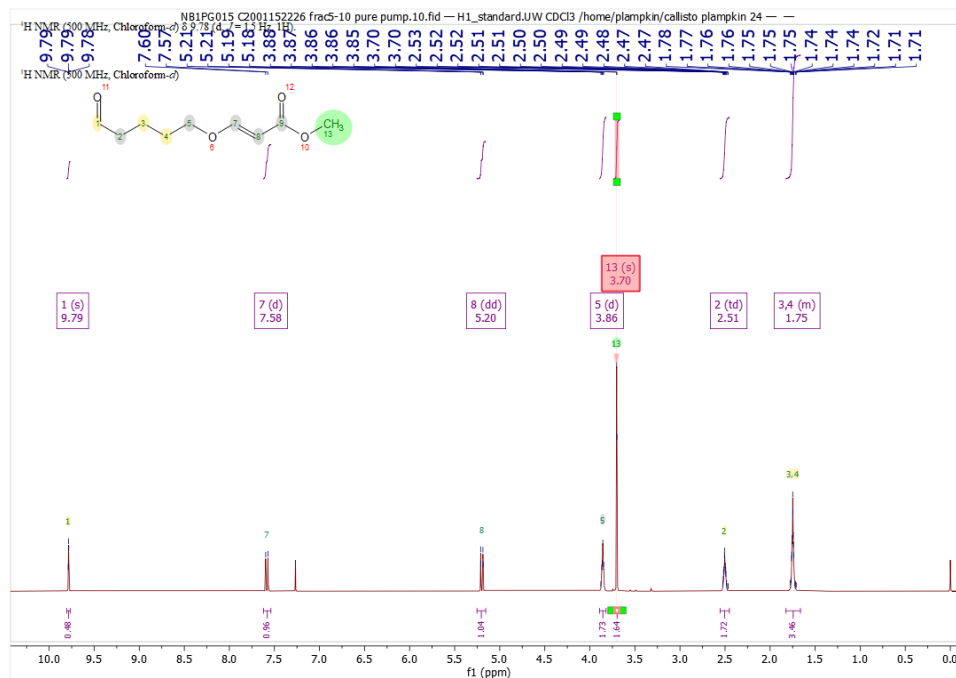
Substrate S9.

Product Spectra: Products **3**, **20**-**24**, and **28** were each obtained as an inseparable mixture of diastereomers. The NMR spectra below contain mixtures of the major and minor diastereomer of each product. Numerous 2D NMR techniques described below were used to assign the major diastereomer of each product, and obtain coupling constants.

All the spectra were obtained using a Bruker Avance 600 MHz spectrometer equipped with a 5 mm, z-axis gradient, triple resonance, cryogenic probe at 24°C. The following standard Avance pulse programs were employed: 1D ^{1}H NMR (zg30), 1D ^{13}C NMR (zgpg30), 1D ^{13}C attached proton test (APT) (jmod), 2D COSY (cosygp45ppqf), 2D edited [^{1}H, ^{13}C] HSQC (hsqcedetgpsisp2p3), and selective 1D TOCSY (tocsy1dzq). Selective 1D TOCSY experiments used mixing times of 10 ms, 30 ms, 50ms, 70ms, and/or 100ms. Data were processed using TopSpin 3.6.1. Data were analyzed using MestReNova.
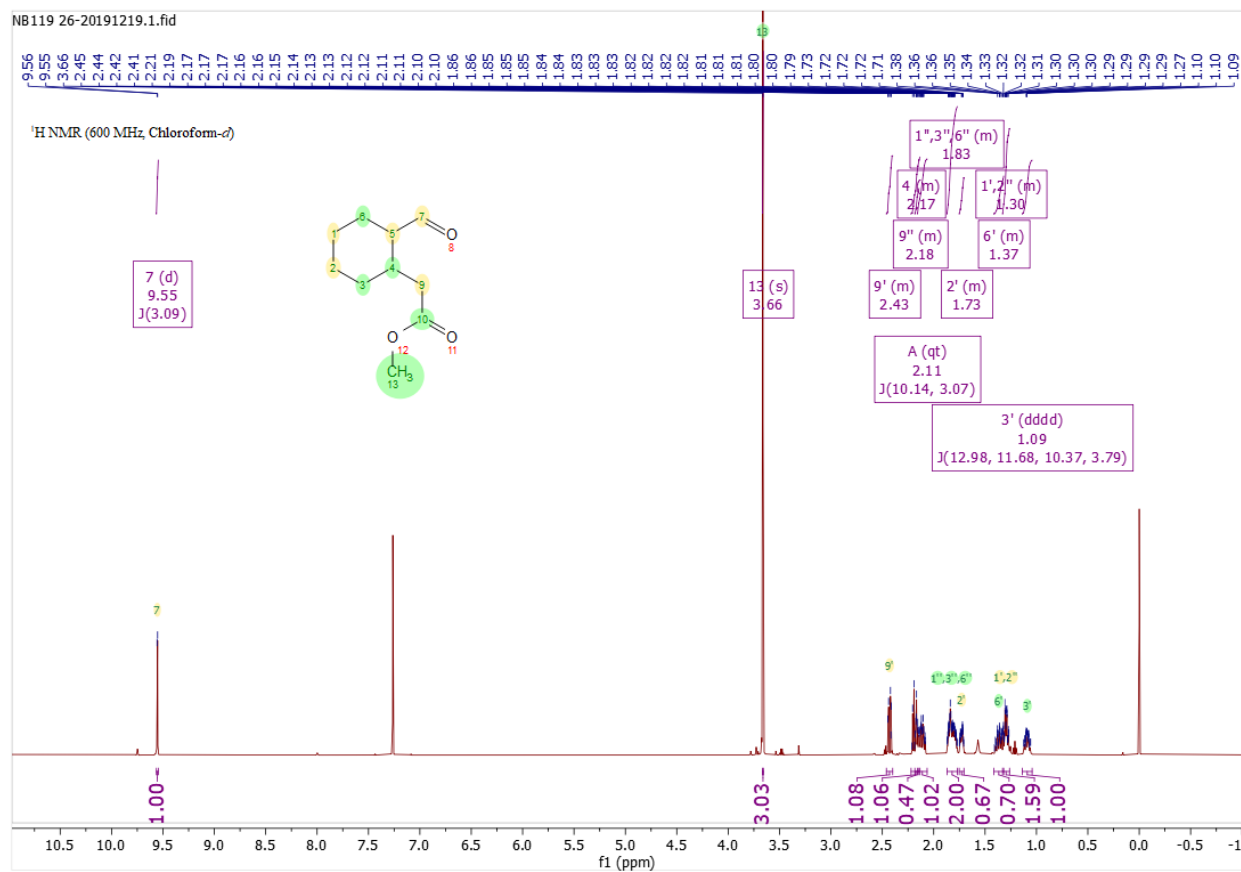
¹H NMR of compound 3 in CDCl₃.
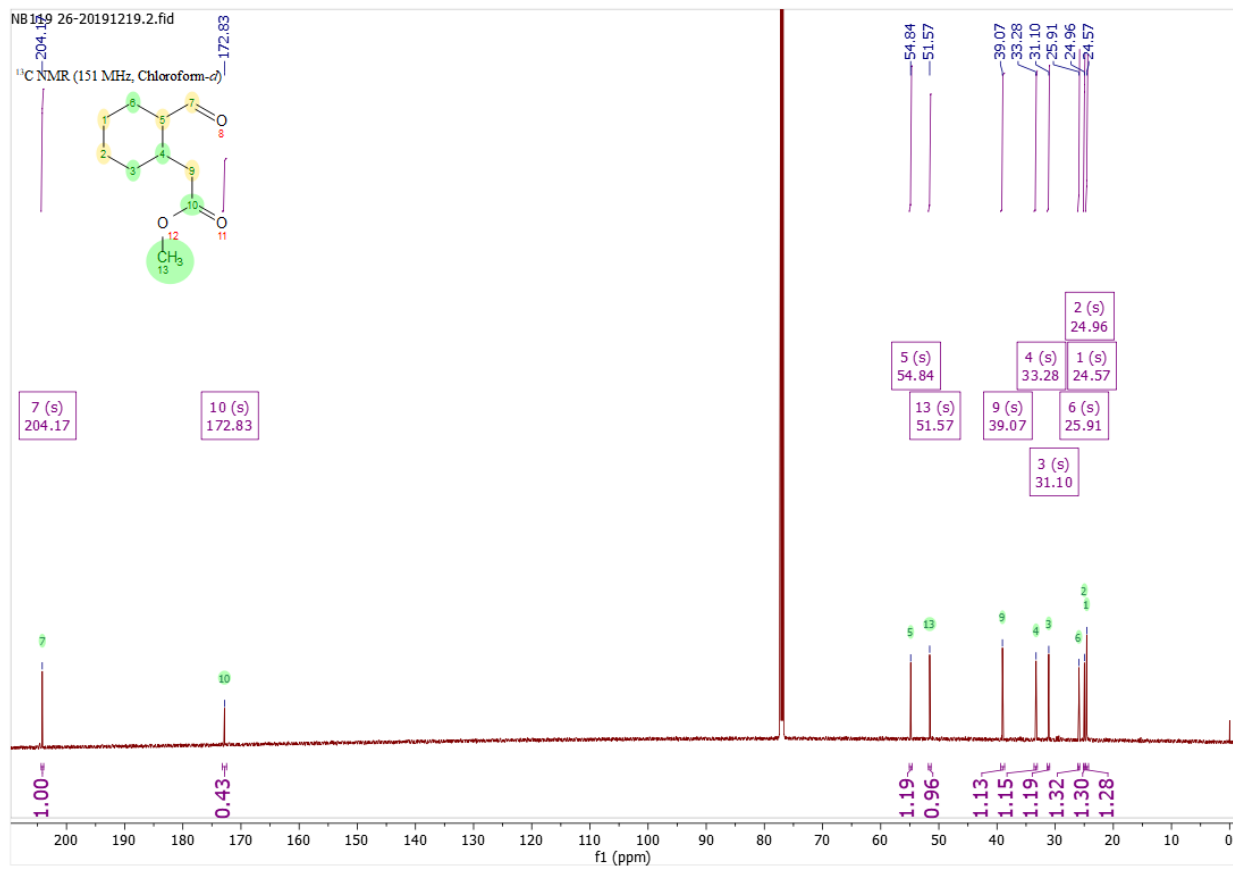
13C NMR of compound 3 in CDCl3.
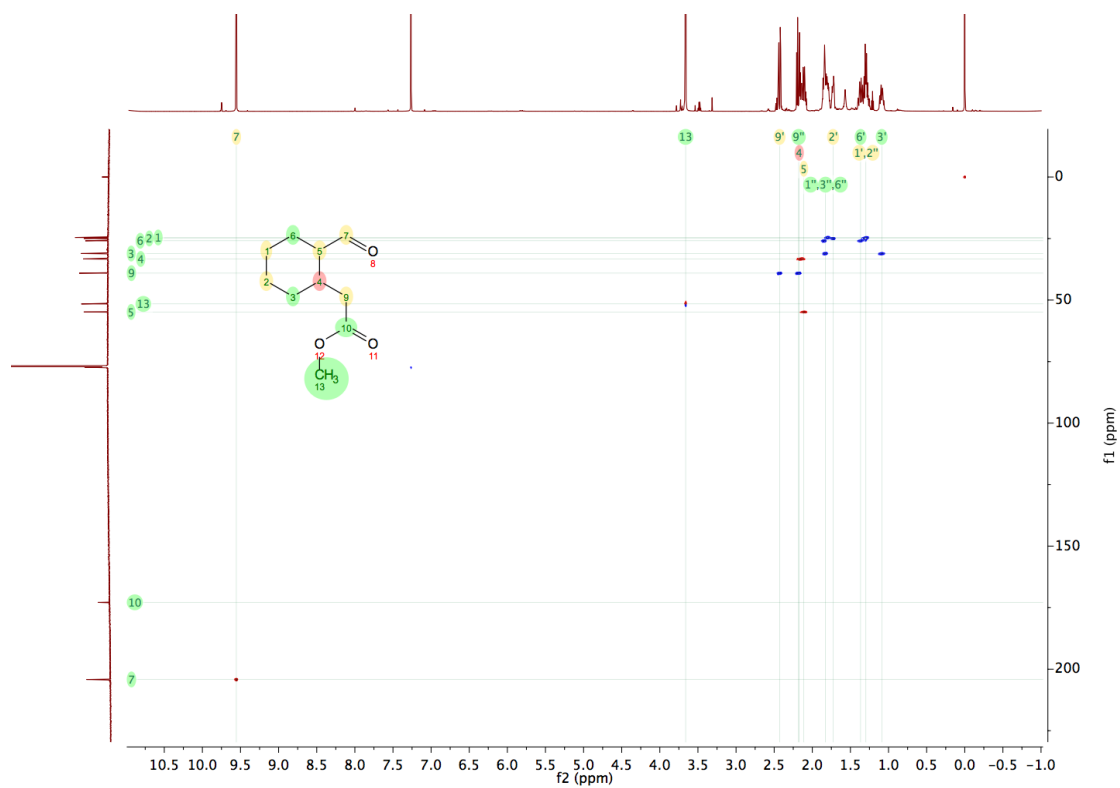
Figure 36. 2D edited [^{1}H, ^{13}C] HSQC NMR of compound 3 in CDCl$_3$.

Figure 37. 2D COSY NMR of compound 3 in CDCl₃.
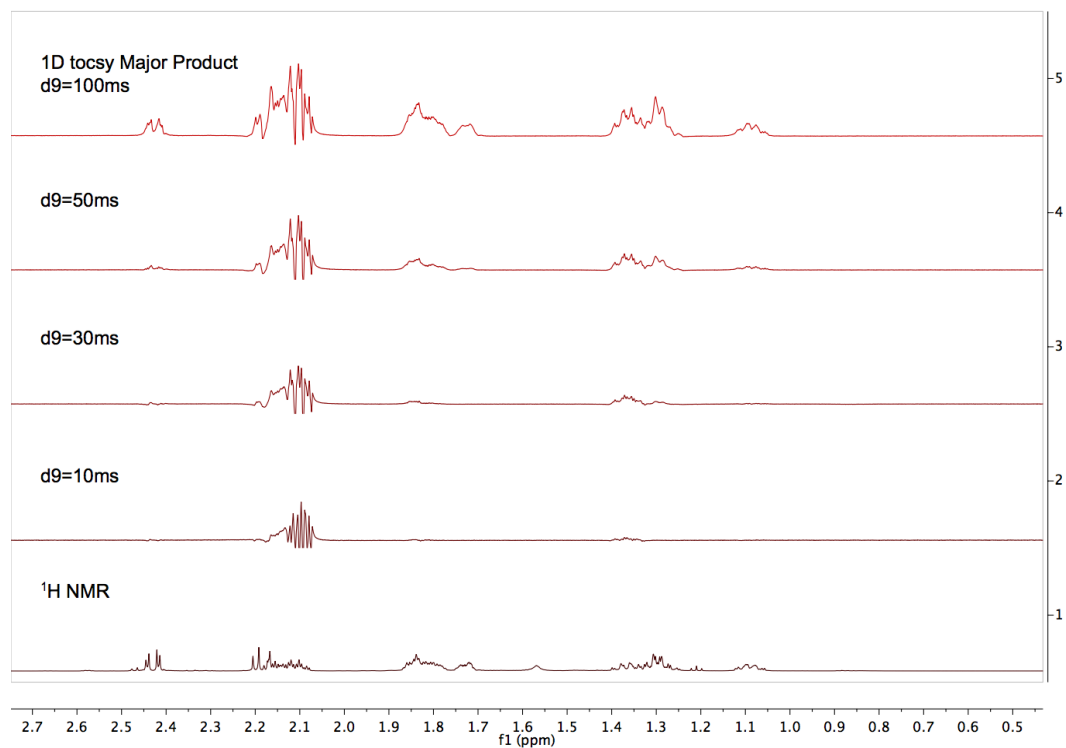
Figure 38. Selective 1D TOCSY NMR with excitation of the aldehyde resonance at 9.55 ppm for the major product 3 in CDCl₃.
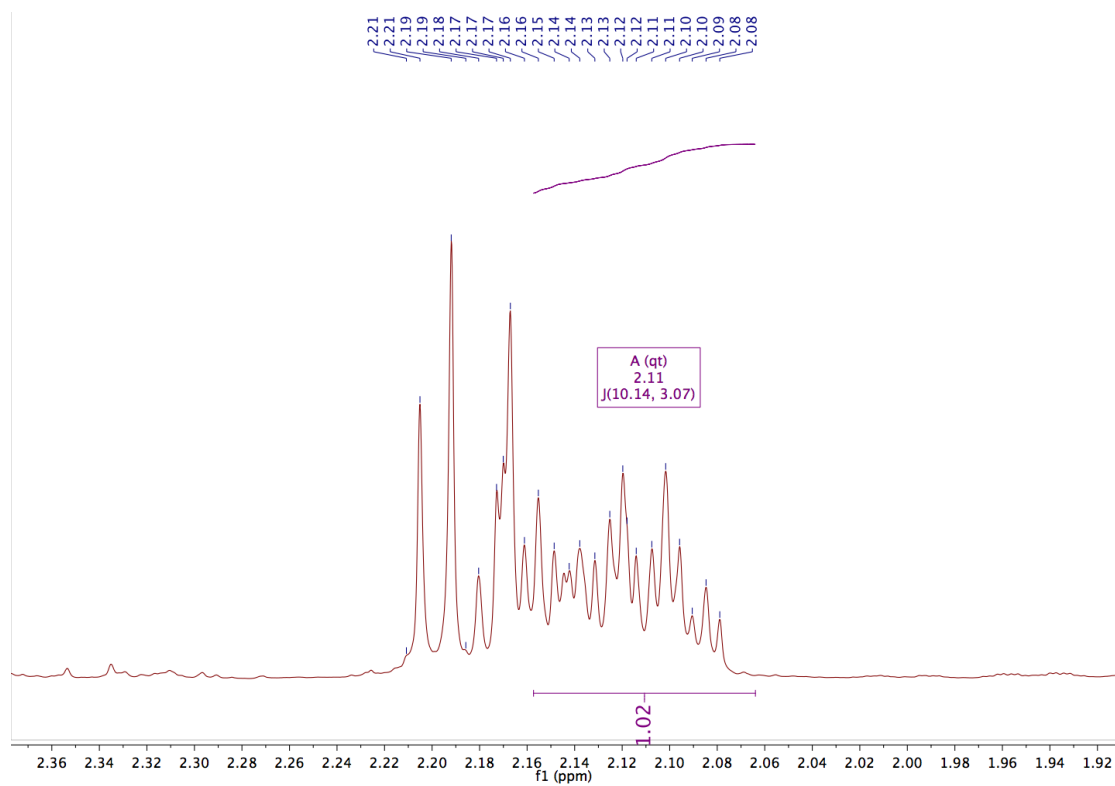
Figure 39. Multiplicity analysis of the proton adjacent to the aldehyde in the major product 3.
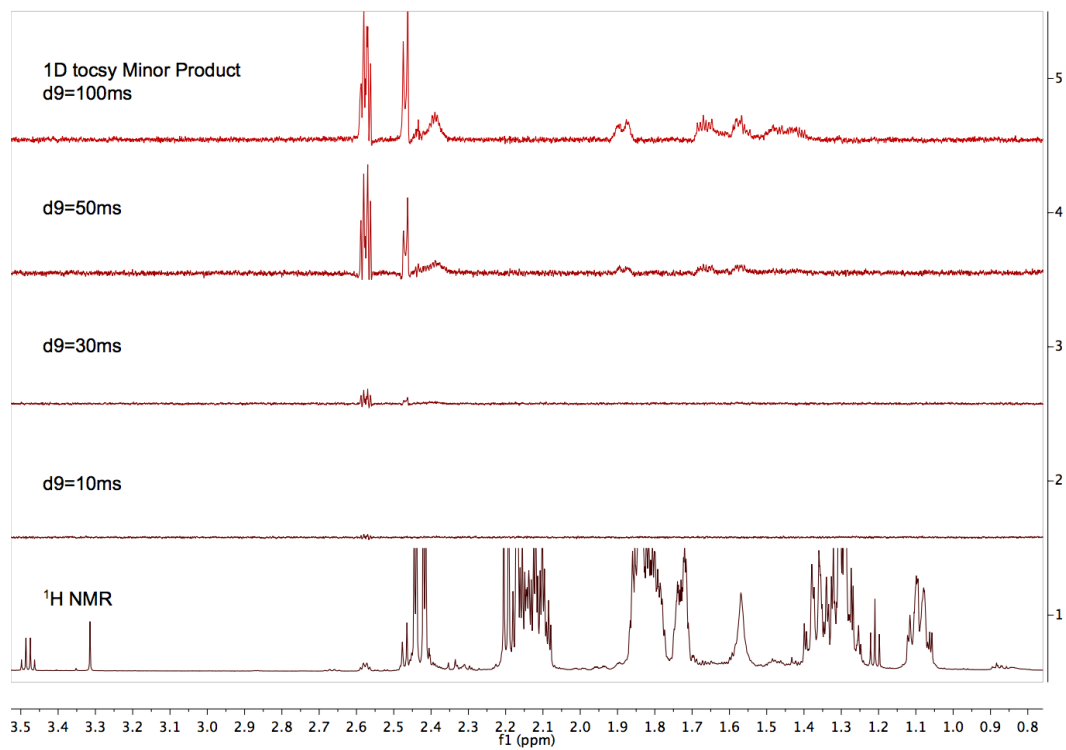
Figure 40. Selective 1D TOCSY NMR with excitation of the aldehyde resonance at 9.75 ppm for the minor product 3 in CDCl₃.
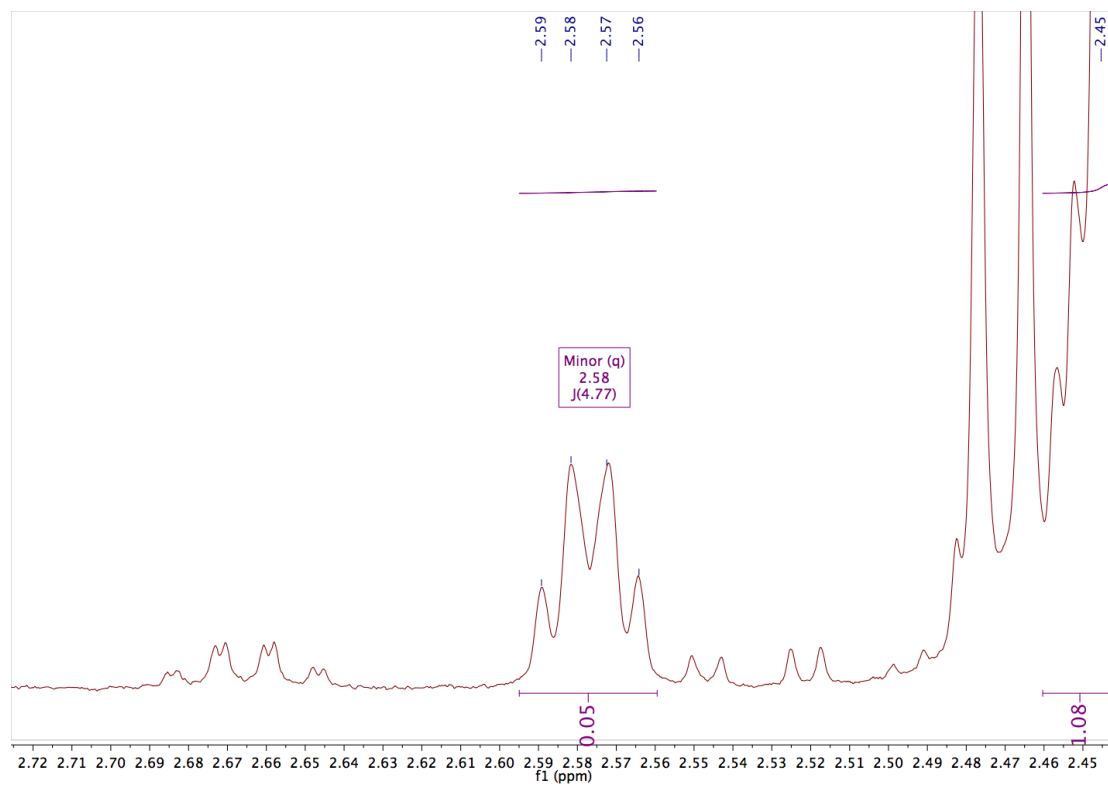
Figure 41. Multiplicity analysis of the proton adjacent to the aldehyde in the minor product 3.
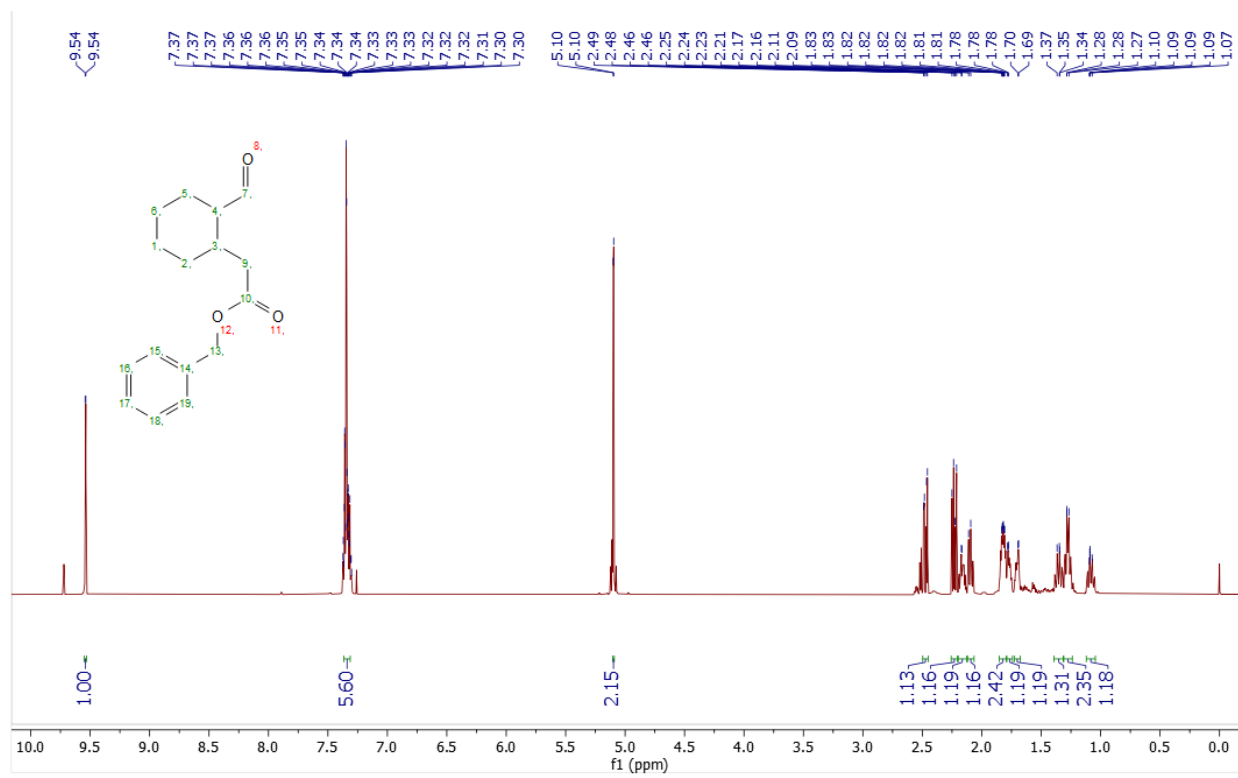
^{1}H NMR of compound 21 in CDCl$_3$, 600 MHz.
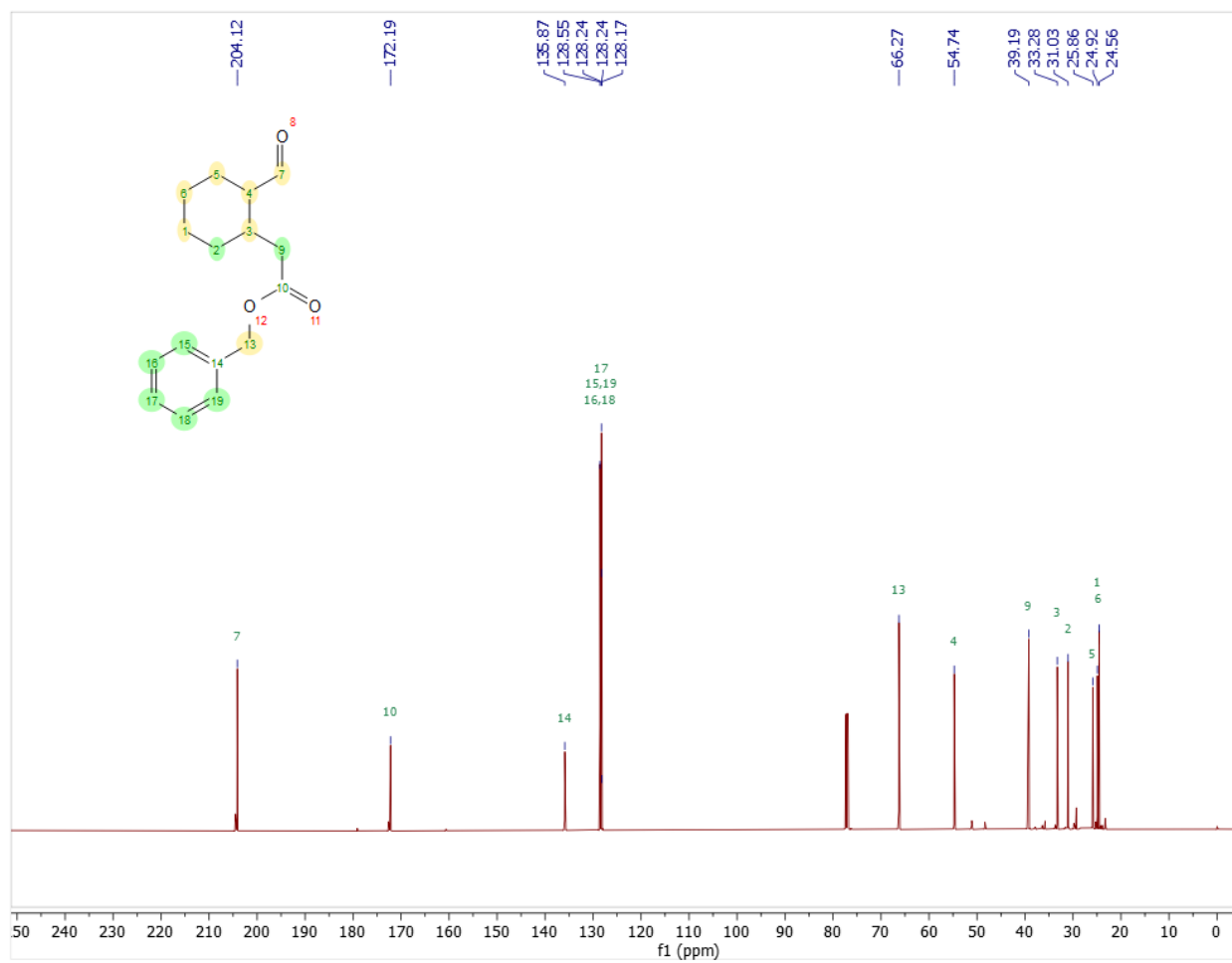
^{13}C NMR of compound 21 in CDCl$_3$, 151 Mhz.
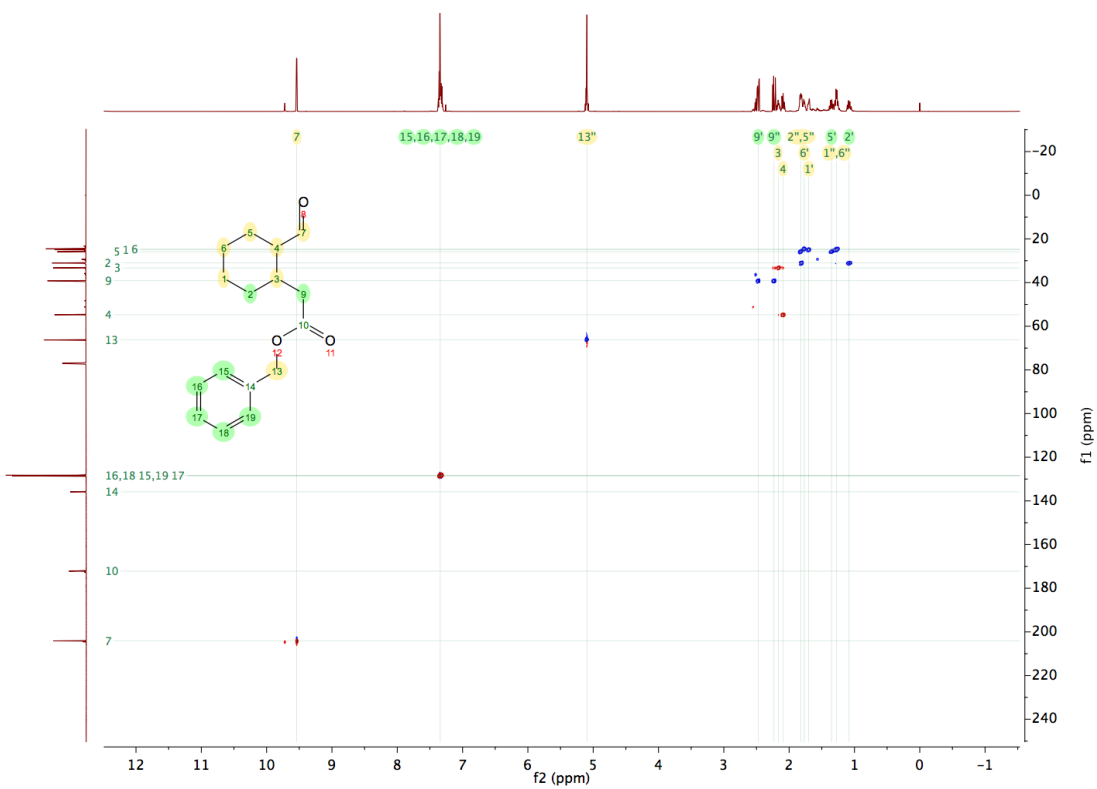
Figure 42. 2D edited [^{1}H, ^{13}C] HSQC NMR of compound 21 in CDCl$_3$.
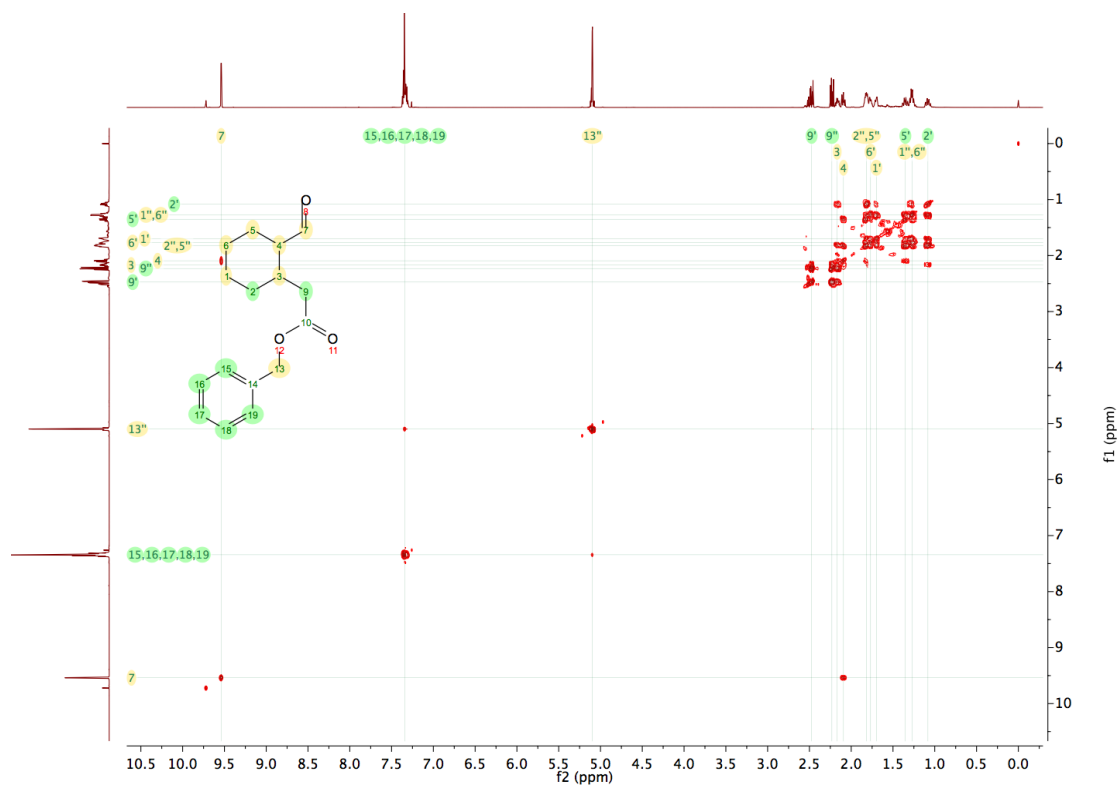
Figure 43. 2D COSY NMR of compound 21 in CDCl₃.
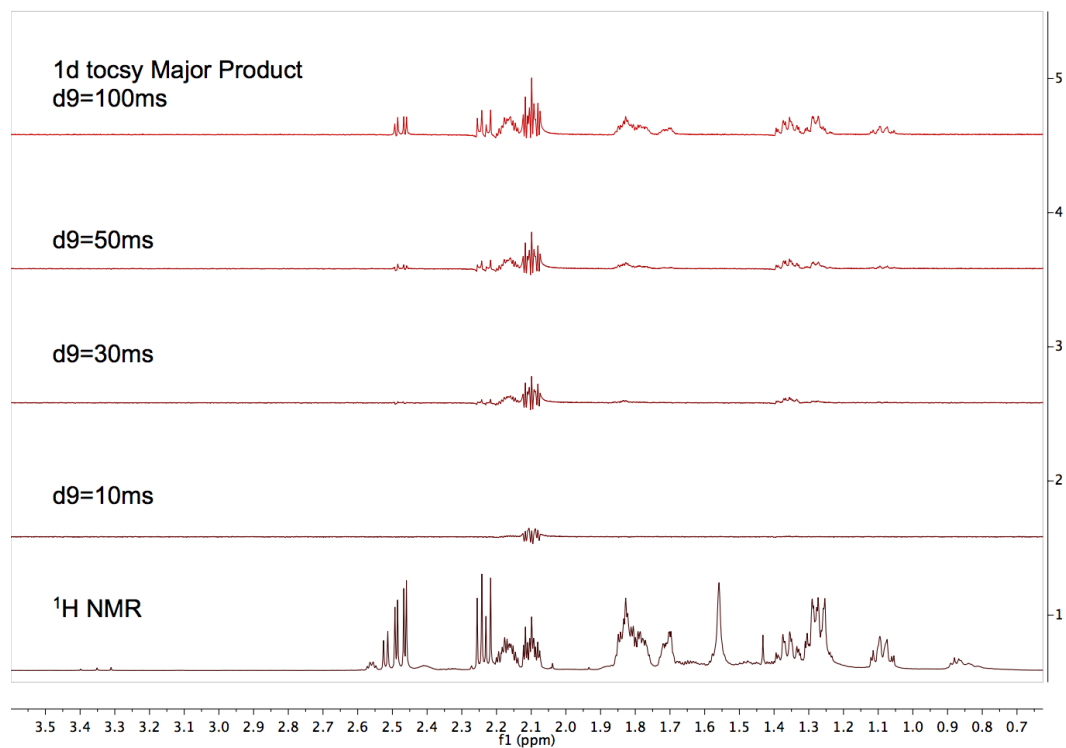
Figure 44. Selective 1D TOCSY NMR with excitation of the aldehyde resonance at 9.54 ppm for the major product 21 in CDCl₃.
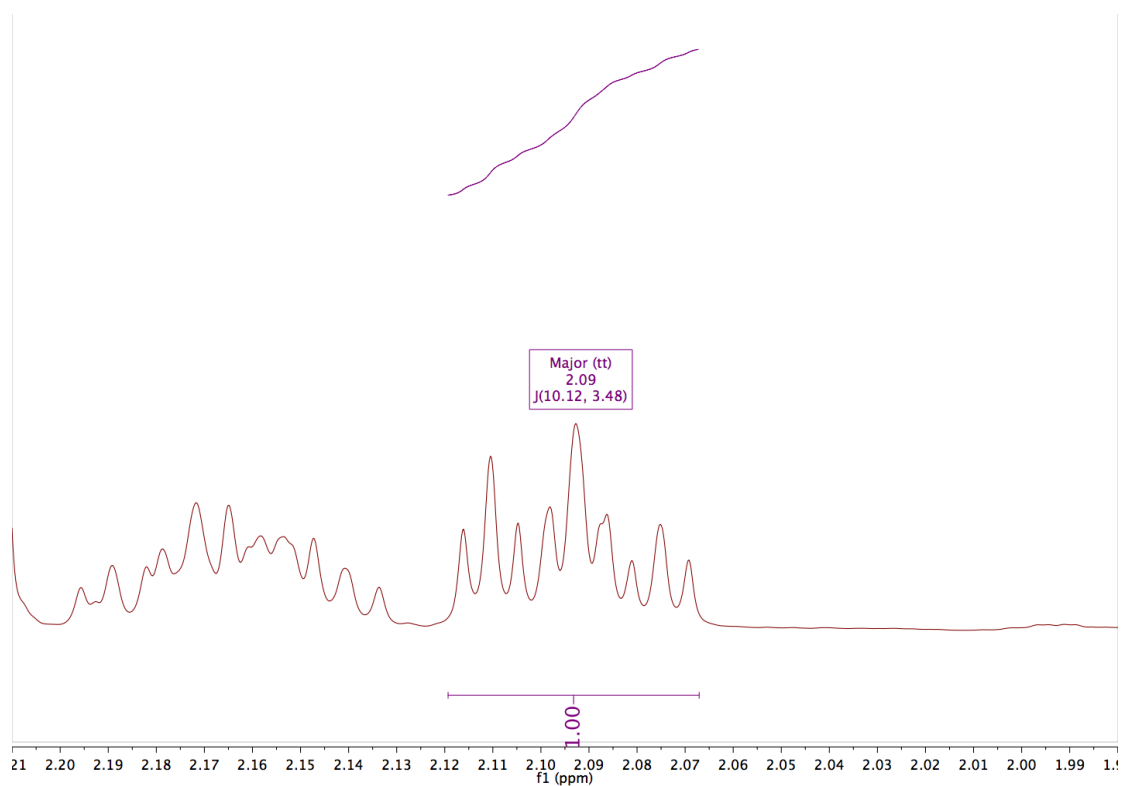
Figure 45. Multiplicity analysis of the proton adjacent to the aldehyde in the major product 21.
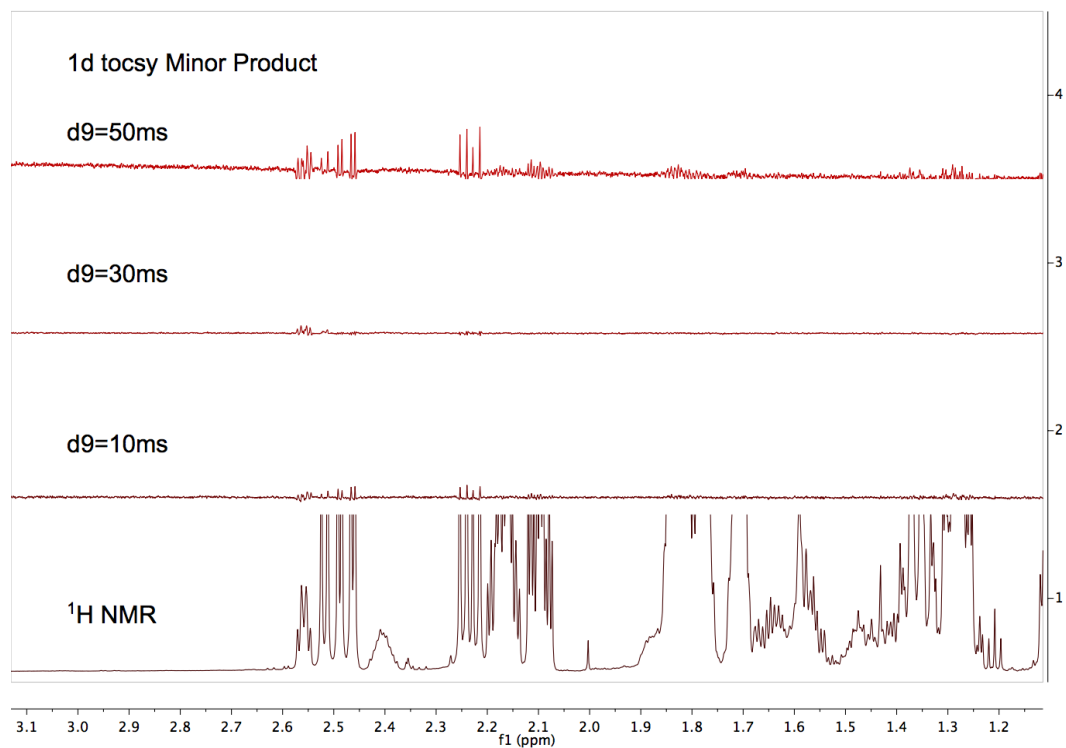
Figure 46. Selective 1D TOCSY NMR with excitation of the aldehyde resonance at 9.73 ppm for the minor product 21 in CDCl₃.
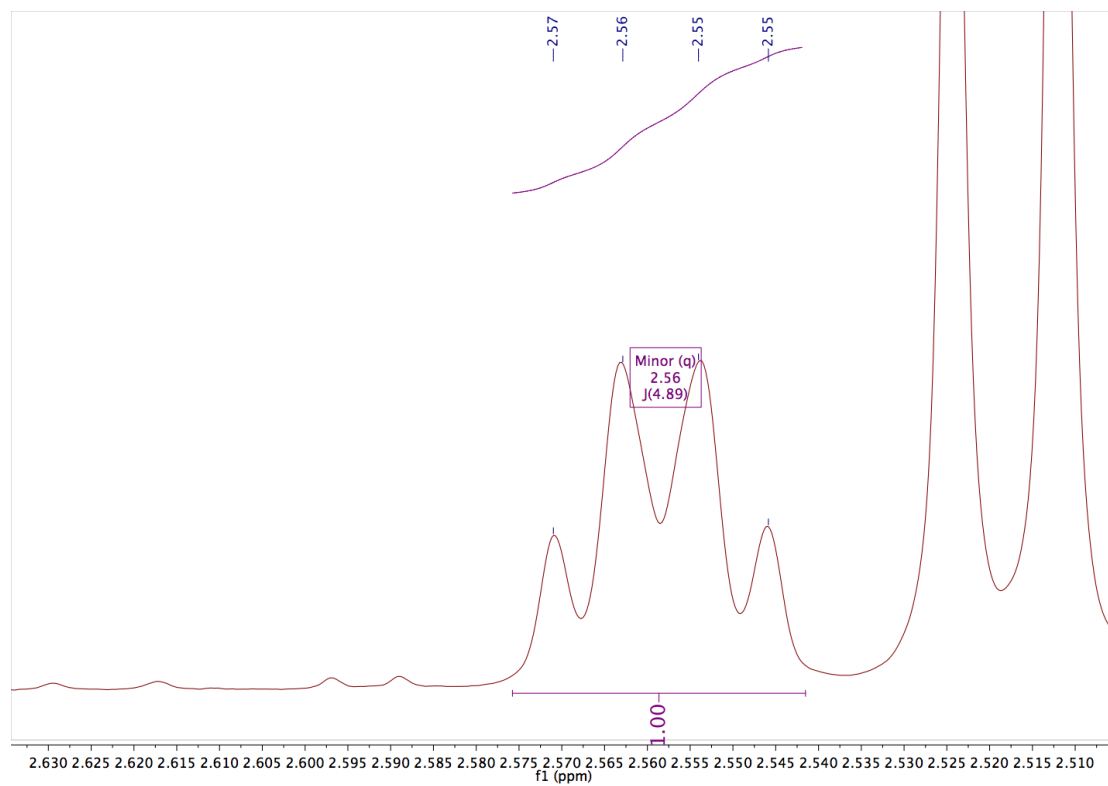
Figure 47. Multiplicity analysis of the proton adjacent to the aldehyde in the minor product 21.
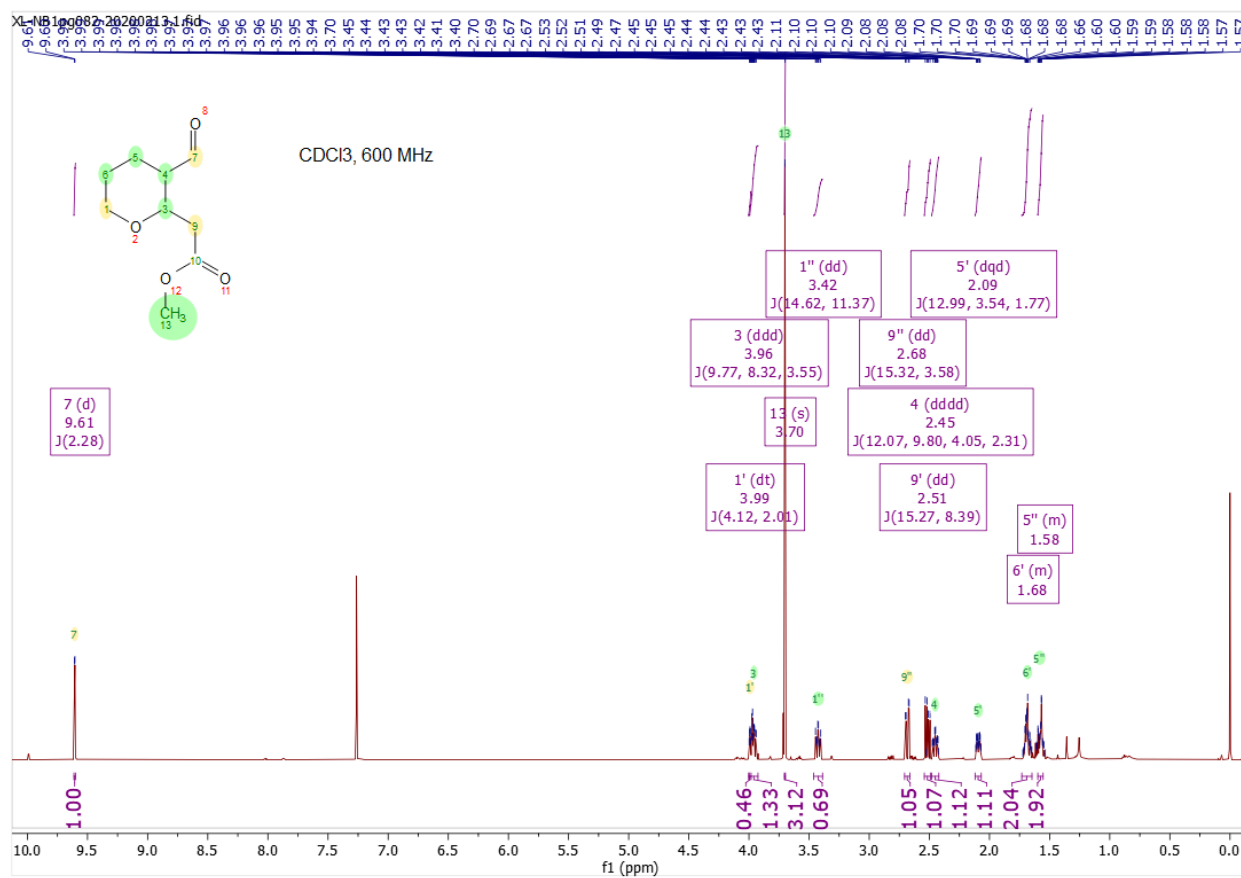
¹H NMR of compound 22 in CDCl₃.
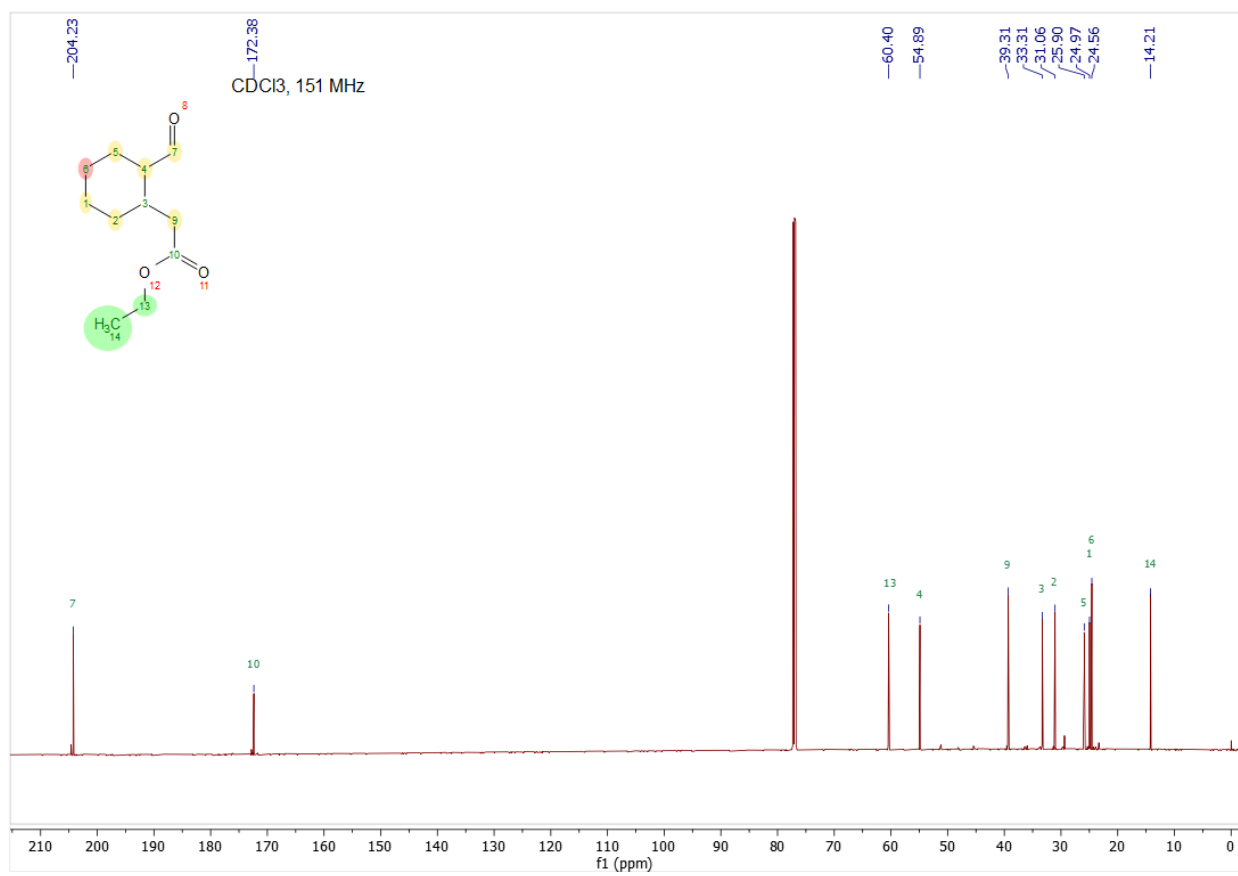
¹³C NMR of compound **22** in CDCl₃.
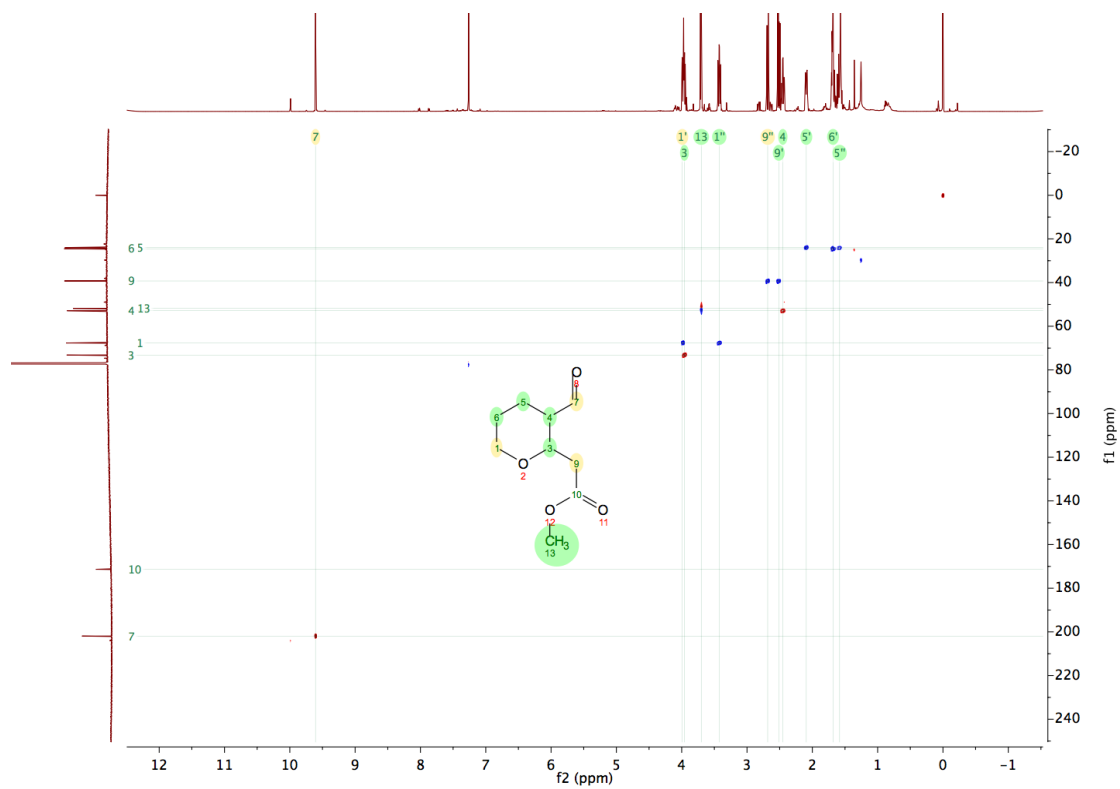
Figure 48. 2D edited [^{1}H, ^{13}C] HSQC NMR of compound 22 in CDCl$_3$.
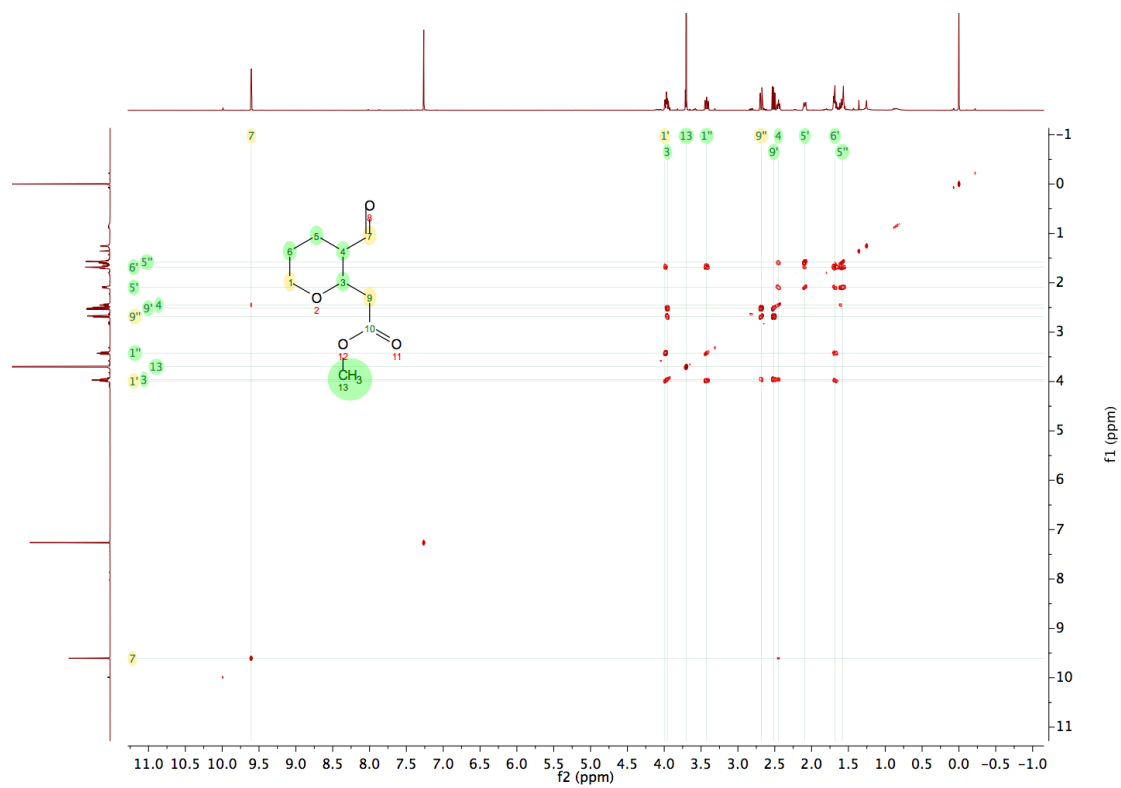
Figure 49. 2D COSY NMR of compound 22 in CDCl₃.
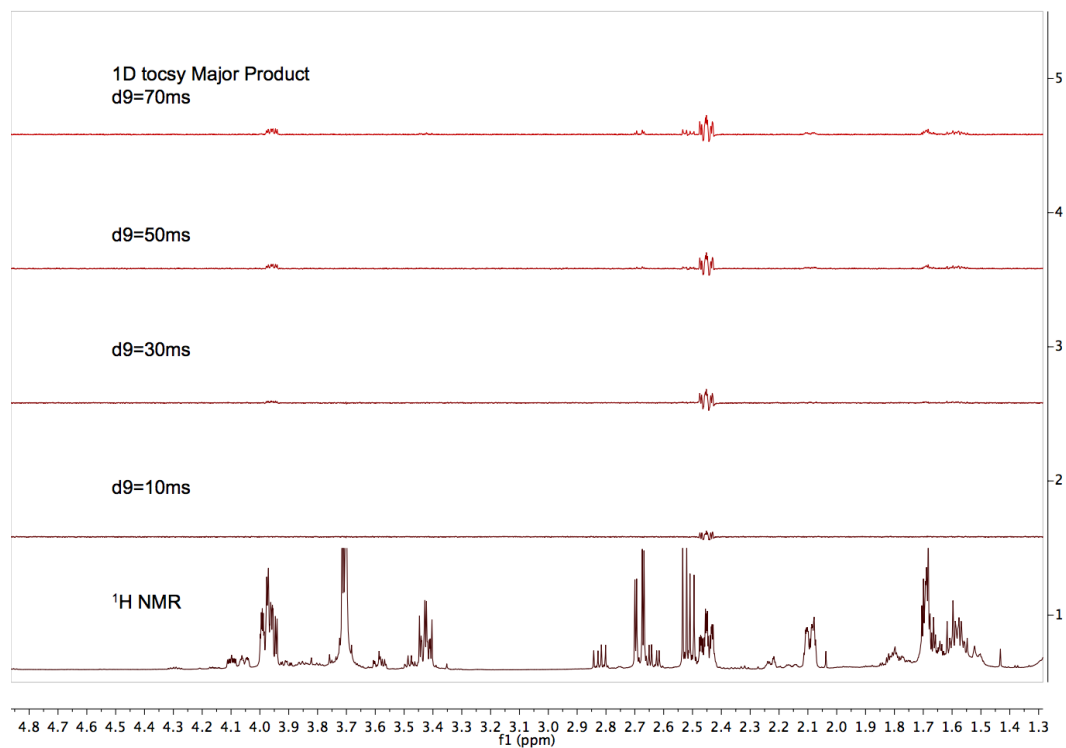
Figure 50. Selective 1D TOCSY NMR with excitation of the aldehyde resonance at 9.61 ppm for the major product 22 in CDCl$_3$.
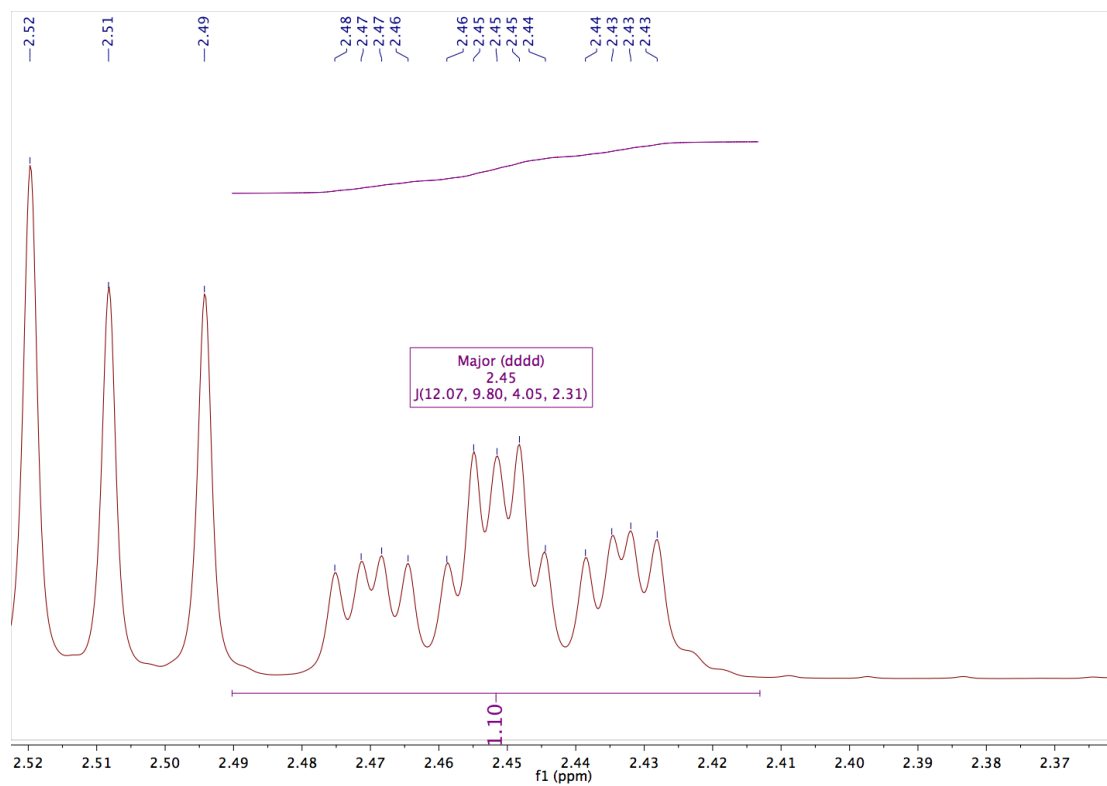
Figure 51. Multiplicity analysis of the proton adjacent to the aldehyde in the major product 22.
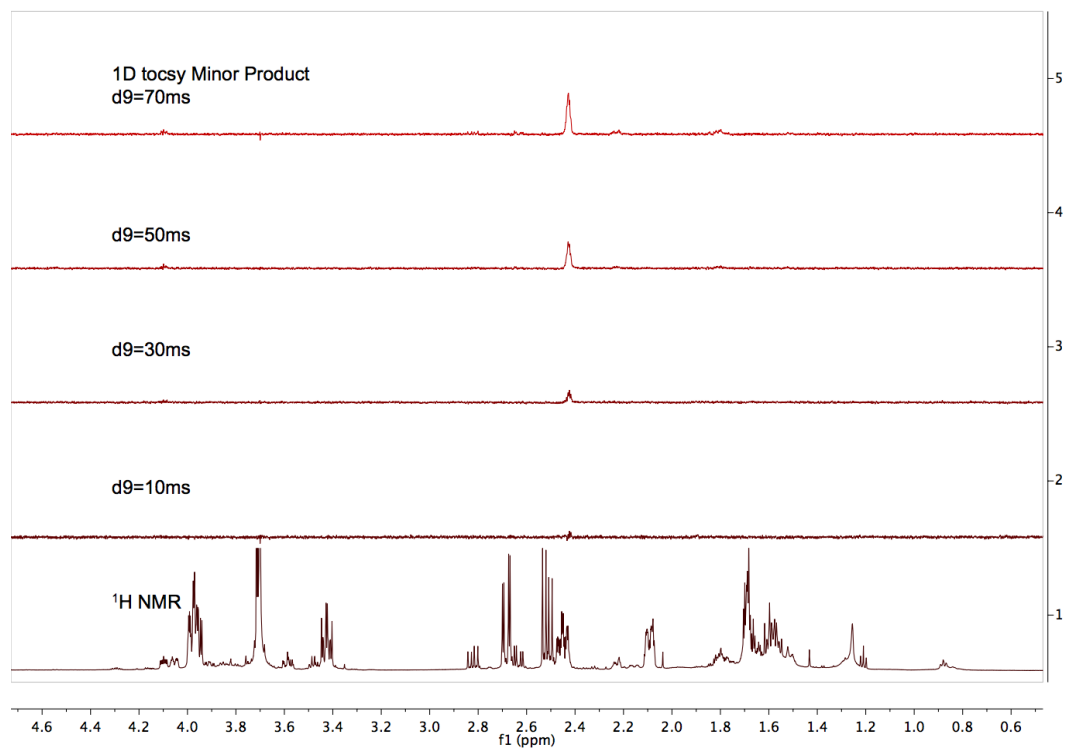
Figure 52. Selective 1D TOCSY NMR with excitation of the aldehyde resonance at 9.99 ppm for the minor product 22 in CDCl₃.
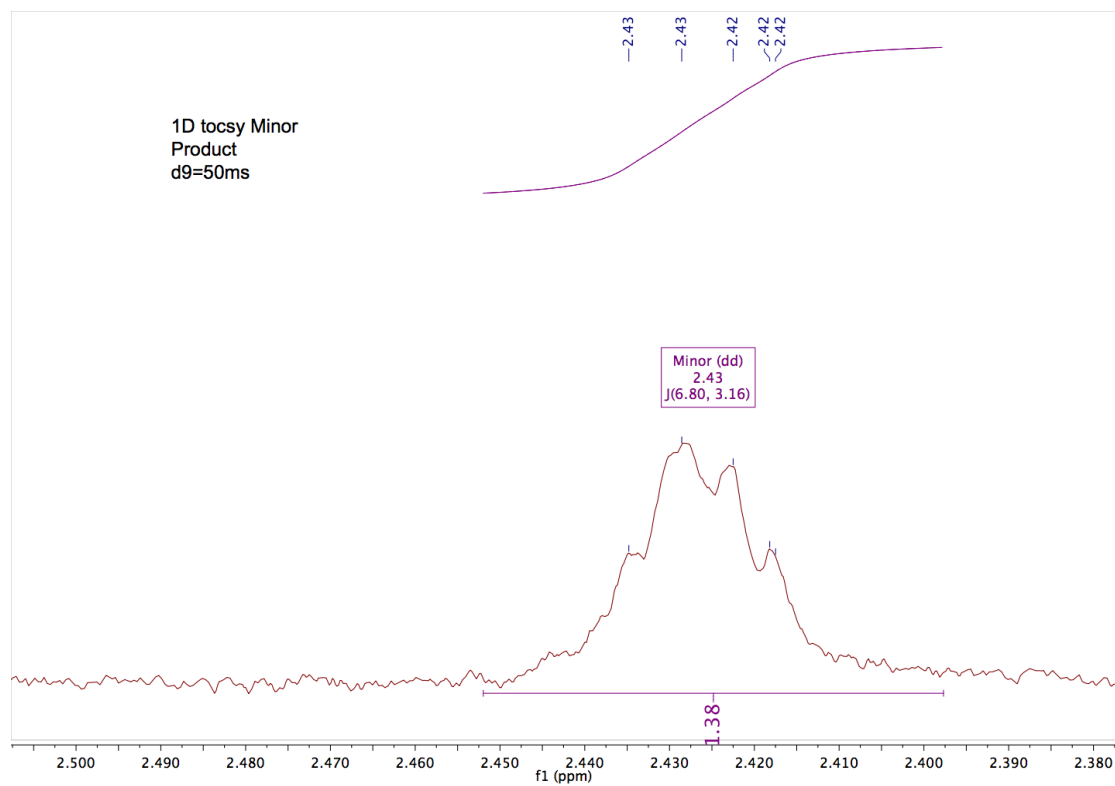
Figure 53. Multiplicity analysis of the proton adjacent to the aldehyde in the minor product 22 using selective 1D TOCSY spectrum, since the peak was buried in ^{1}H NMR.
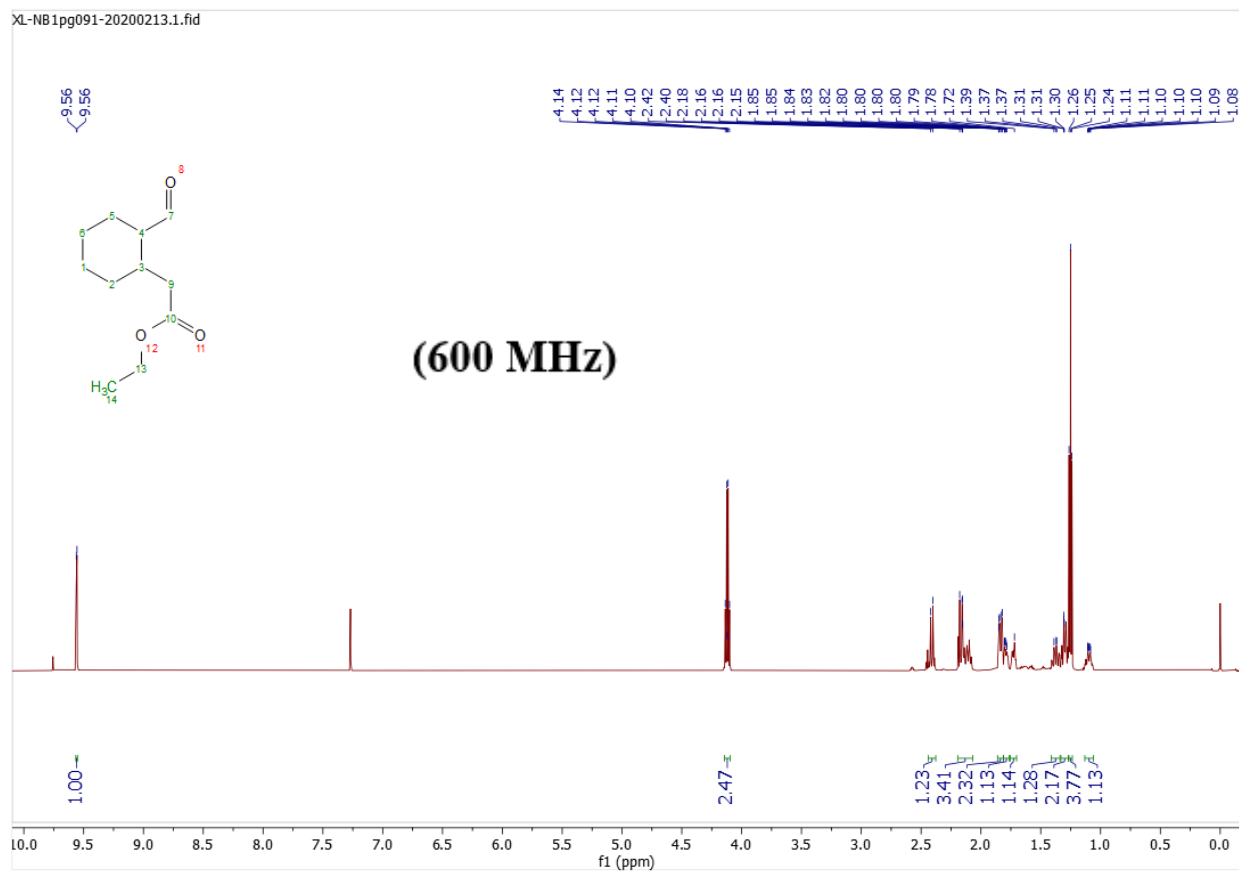
¹H NMR of compound 20 in CDCl₃.

13C NMR of compound 20 in CDCl3.
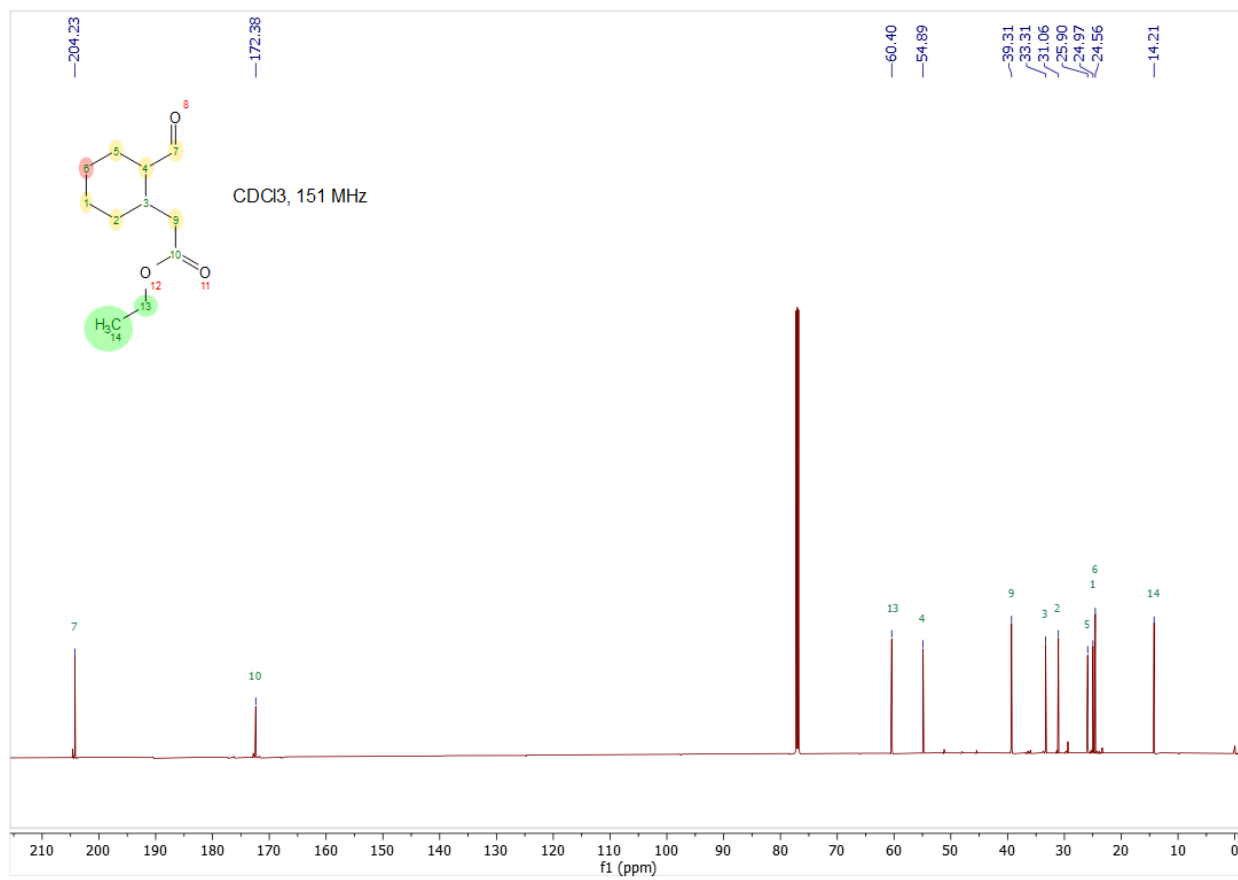
Figure 54. 2D edited [^{1}H, ^{13}C] HSQC NMR of compound 20 in CDCl$_3$.
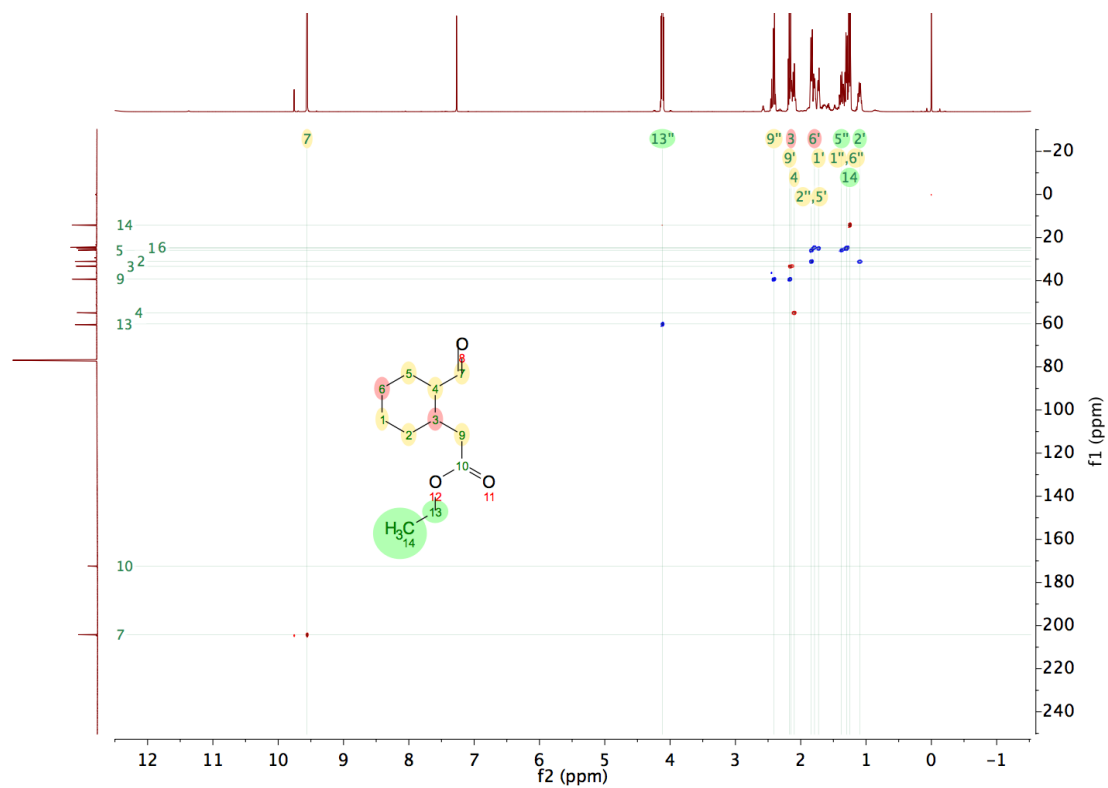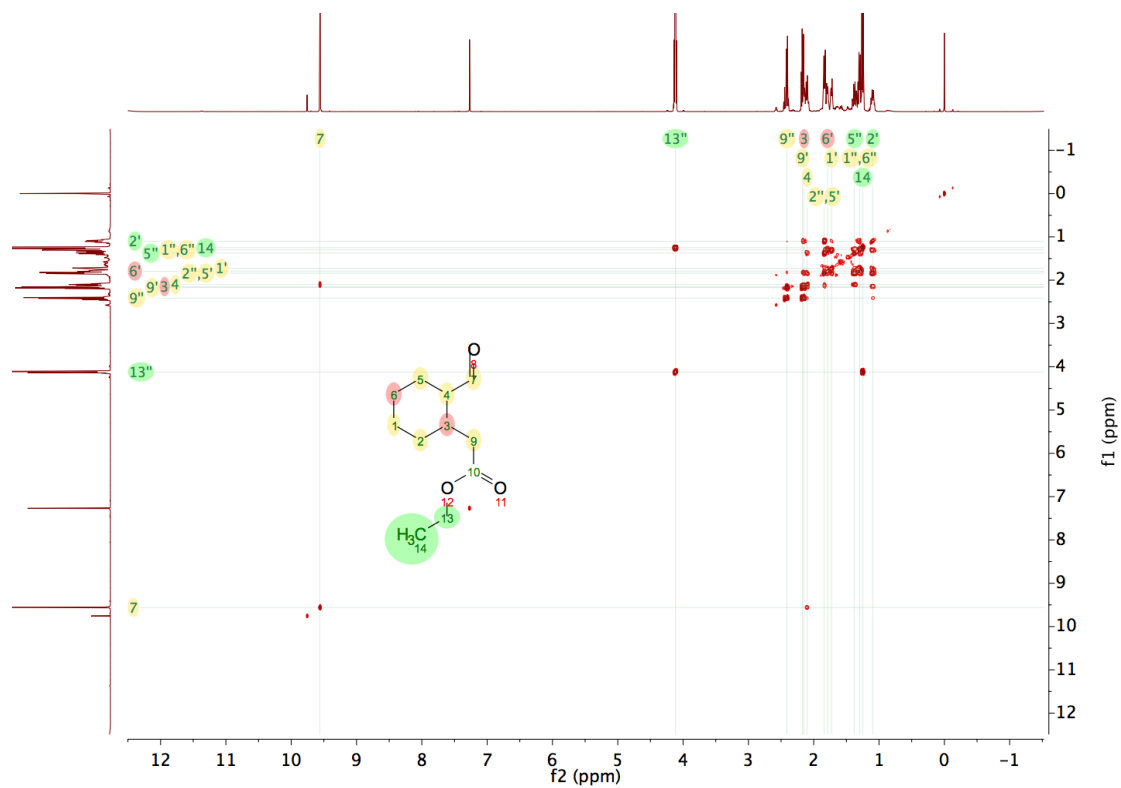
Figure 55. 2D COSY NMR of compound 20 in CDCl₃.
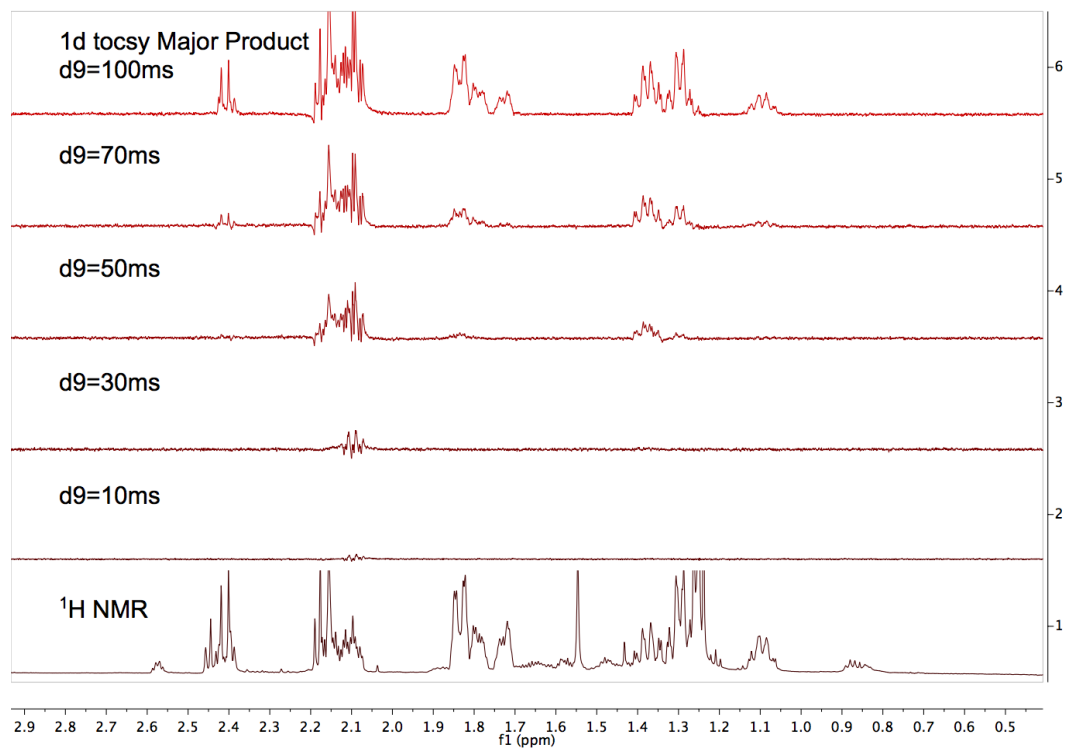
Figure 56. Selective 1D TOCSY NMR with excitation of the aldehyde resonance at 9.56 ppm for the major product 20 in CDCl₃.
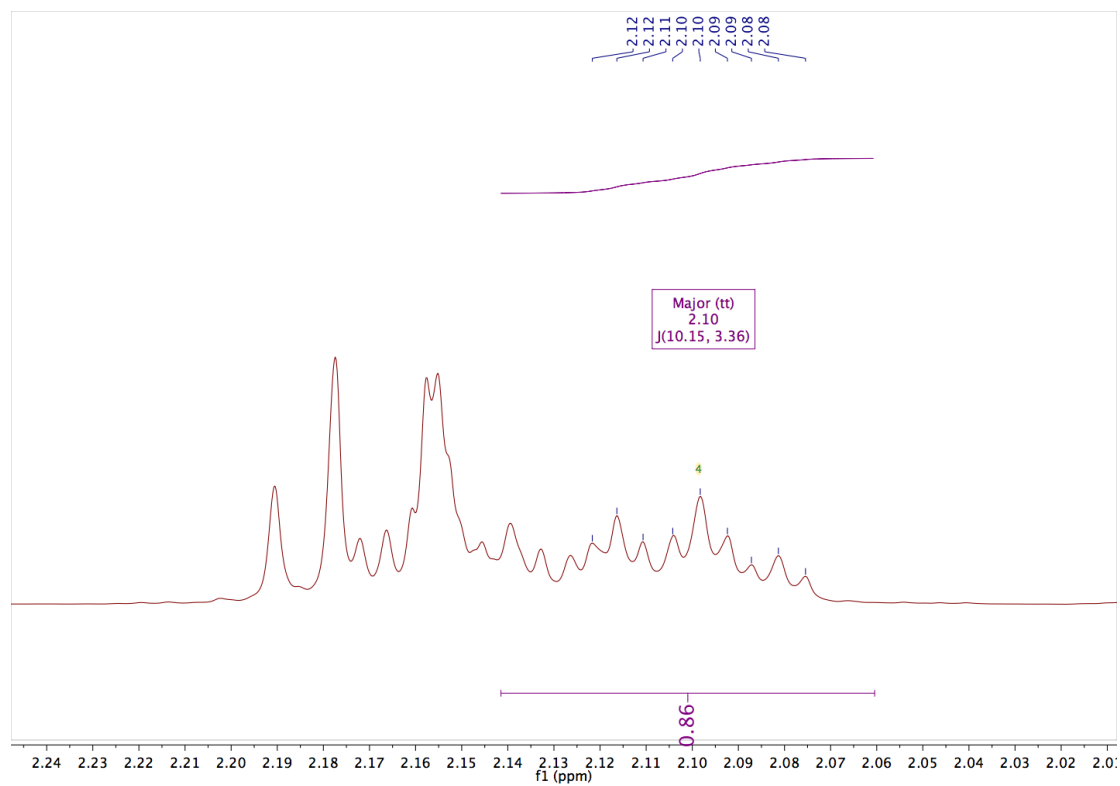
Figure 57. Multiplicity analysis of the proton adjacent to the aldehyde in the major product 20.
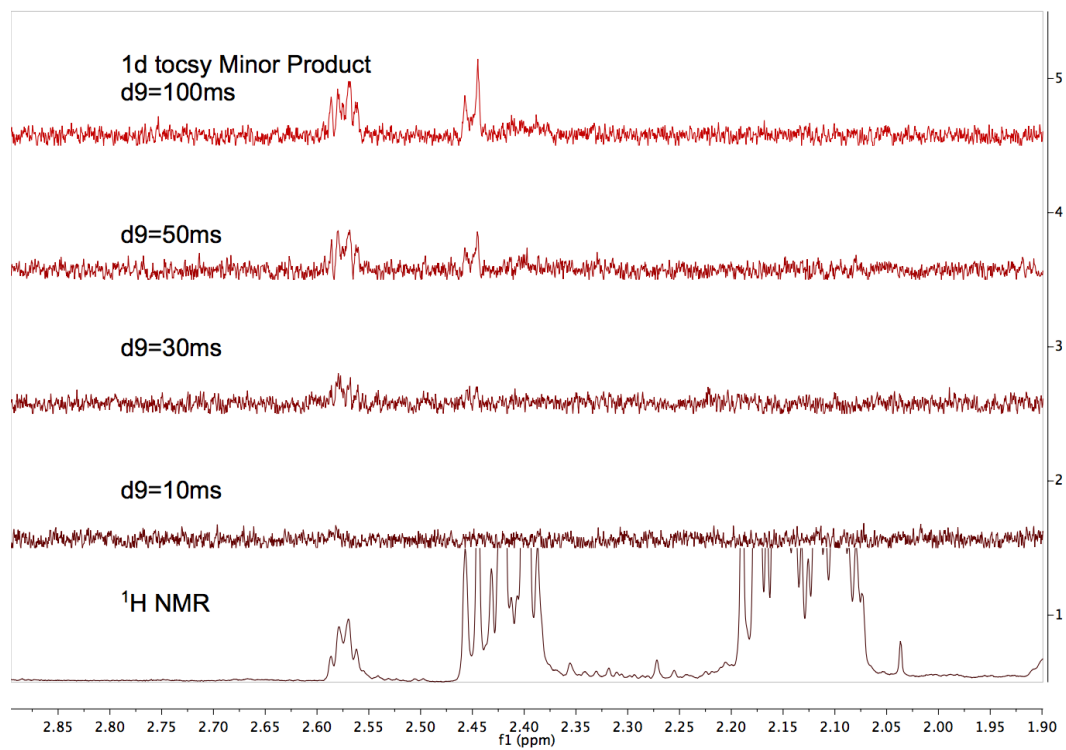
Figure 58. Selective 1D TOCSY NMR with excitation of the aldehyde resonance at 9.76 ppm for the minor product 20 in CDCl$_3$.
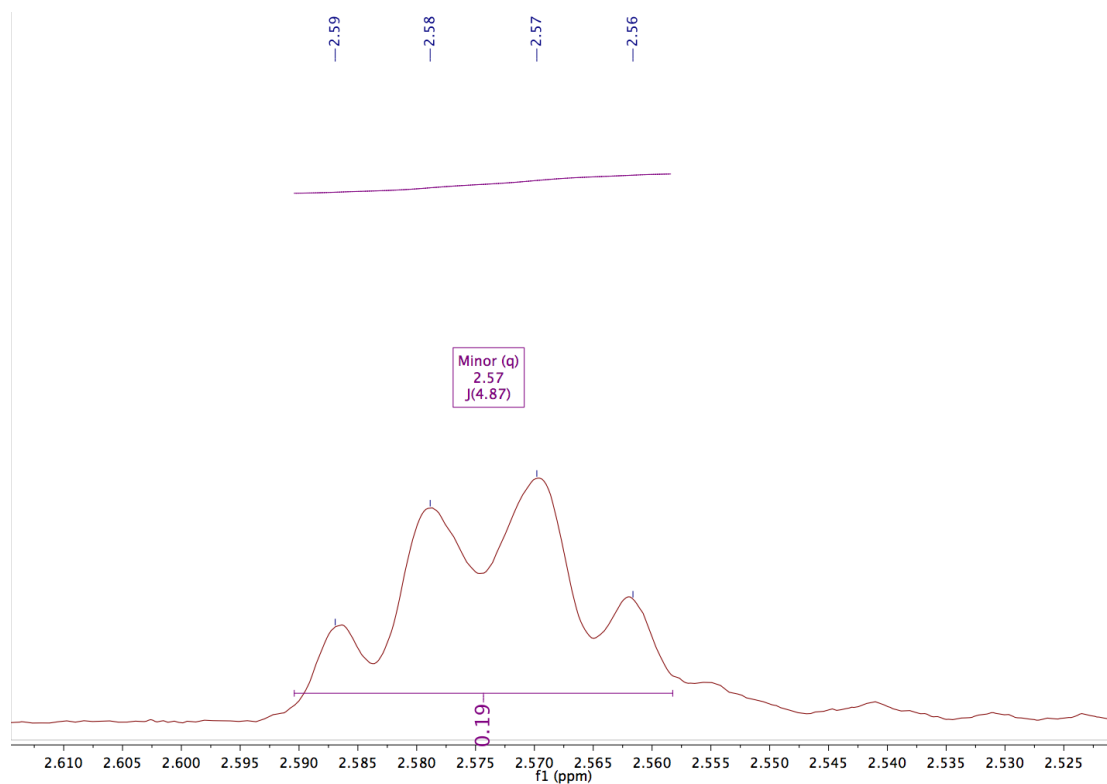
Figure 59. Multiplicity analysis of the proton adjacent to the aldehyde in the minor product 20.

Product 24: **¹H NMR (600 MHz, CDCl₃)** δ 9.61 (d, *J* = 3.3 Hz, 1H), 3.66 (s, 3H), 2.58 (h, *J* = 7.7 Hz, 1H), 2.44 – 2.41 (m, 3H), 2.02 – 1.94 (m, 1H), 1.89 (td, *J* = 7.8, 6.6 Hz, 2H), 1.78 – 1.69 (m, 1H), 1.63 (ddt, *J* = 15.7, 13.0, 7.8 Hz, 1H), 1.34 (dq, *J* = 12.7, 8.4 Hz, 1H). **¹³C NMR (150 MHz, CDCl₃)** δ 203.13, 172.85, 57.37, 51.60, 38.91, 37.15, 32.82, 26.73, 24.69. Clear oil.

(Little, 2005)[54] compound 24 NMR (CDCl3, 400 MHz) 9.61 (d, J) 3.1 Hz, 1H), 3.65 (s,3H), 2.58 (m, 1H), 2.45 (m, 2H), 1.98 (m, 1 H), 1.9 (m, 2H), 1.7(m, 2H), 1.3-1.2 (m, 2H); **13C NMR (CDCl3, 100 MHz)** 203.4,173.1, 57.6, 51.8, 39.1, 37.3, 33.0, 26.9, 24.9.

Multiplicity analysis is less reliable in case of cyclopentanes.

https://www.chem.wisc.edu/areas/reich/nmr/05-hmr-05-3j.htm[56]

"In most cyclopentanes… The *cis* couplings (8-10 Hz) are usually larger than *trans* (2-9 Hz). However the Karplus curves for cyclopentane have a region where the *cis* and *trans* lines cross (Figure above, at ca 20° dihedral angle), so there are many cases where *J*trans > *J*cis. There are also cases where *cis* and *trans* couplings are identical, as on the compound below, where the allylic proton is a quartet of doublets, arising from accidental equivalence of three vicinal couplings."
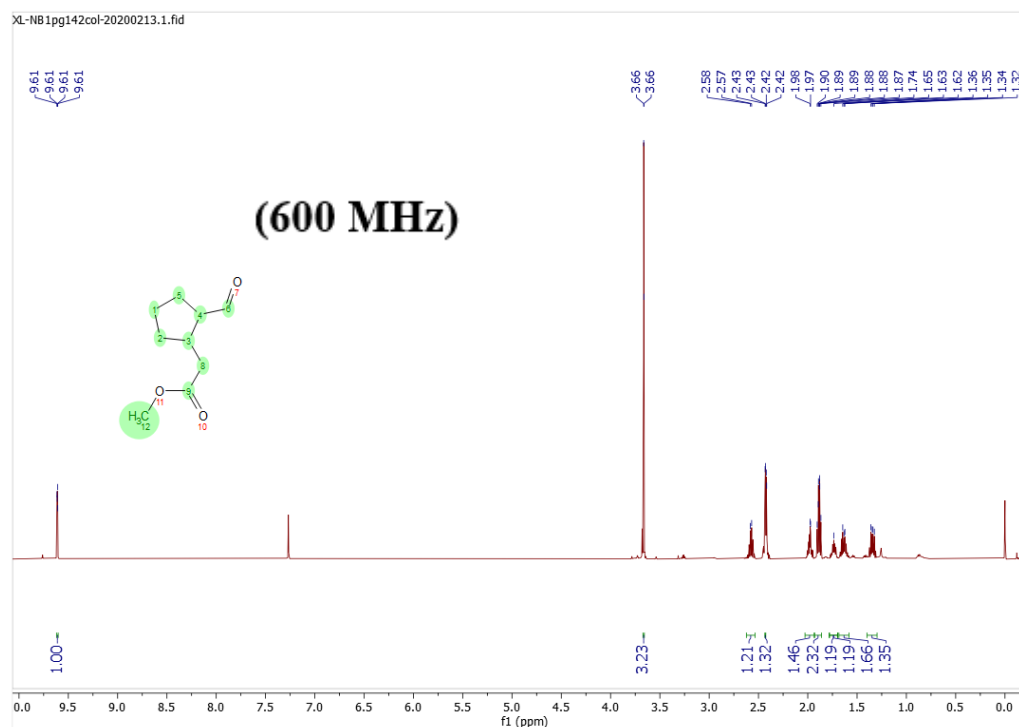
¹H NMR of compound 24 in CDCl₃.
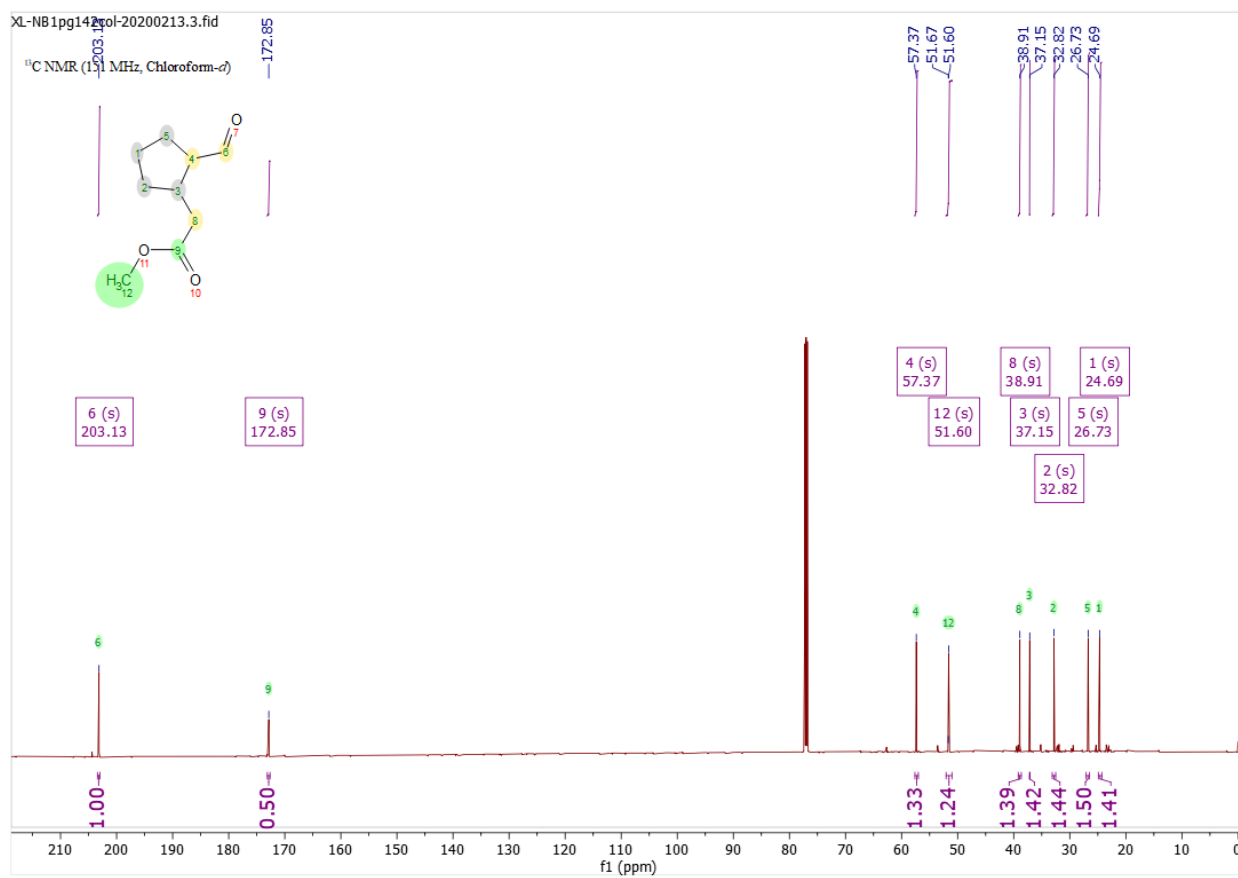
^{13}C NMR of compound 24 in CDCl$_3$.
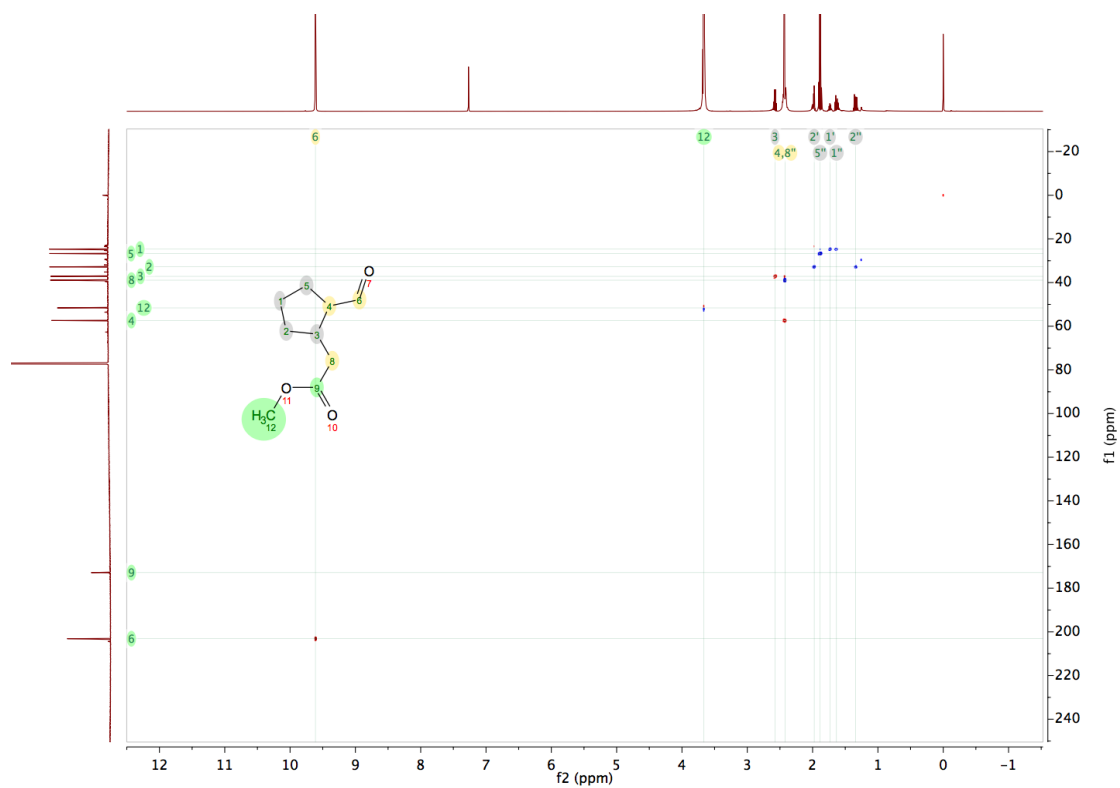
Figure 60. 2D edited [¹H, ¹³C] HSQC NMR of compound 24 in CDCl₃.
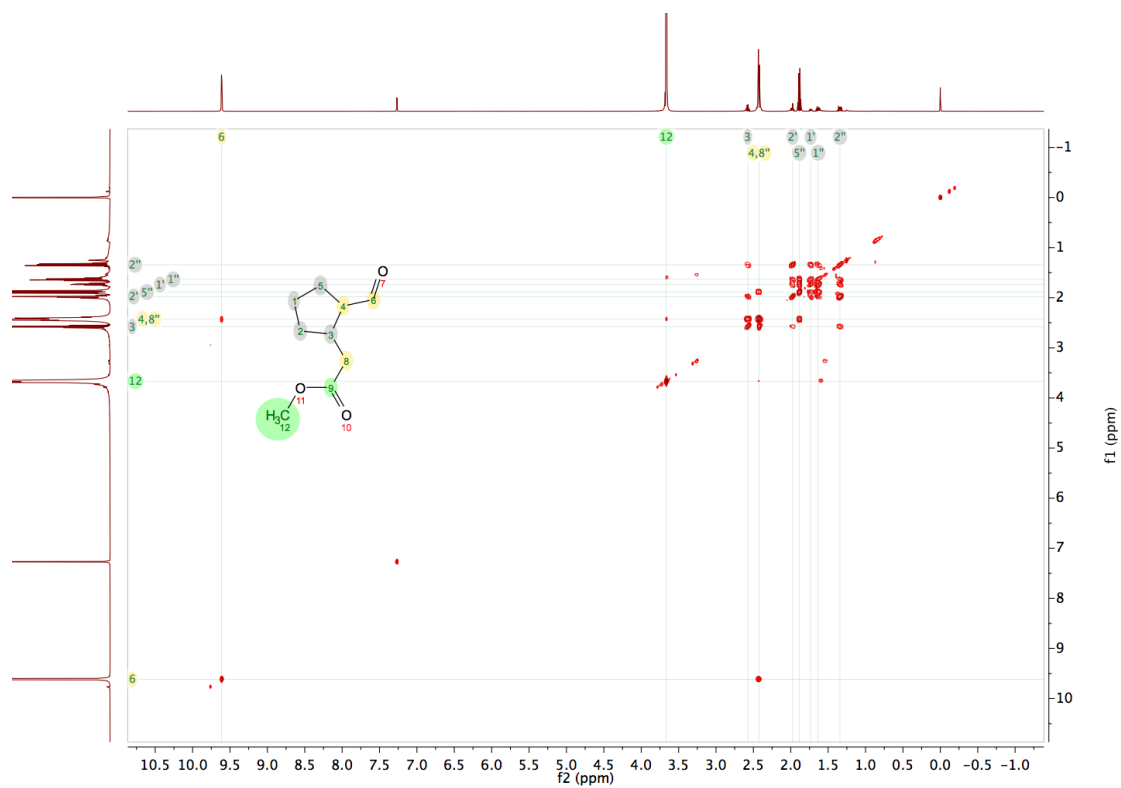
Figure 61. 2D COSY NMR of compound 24 in CDCl₃.

(600 MHz)
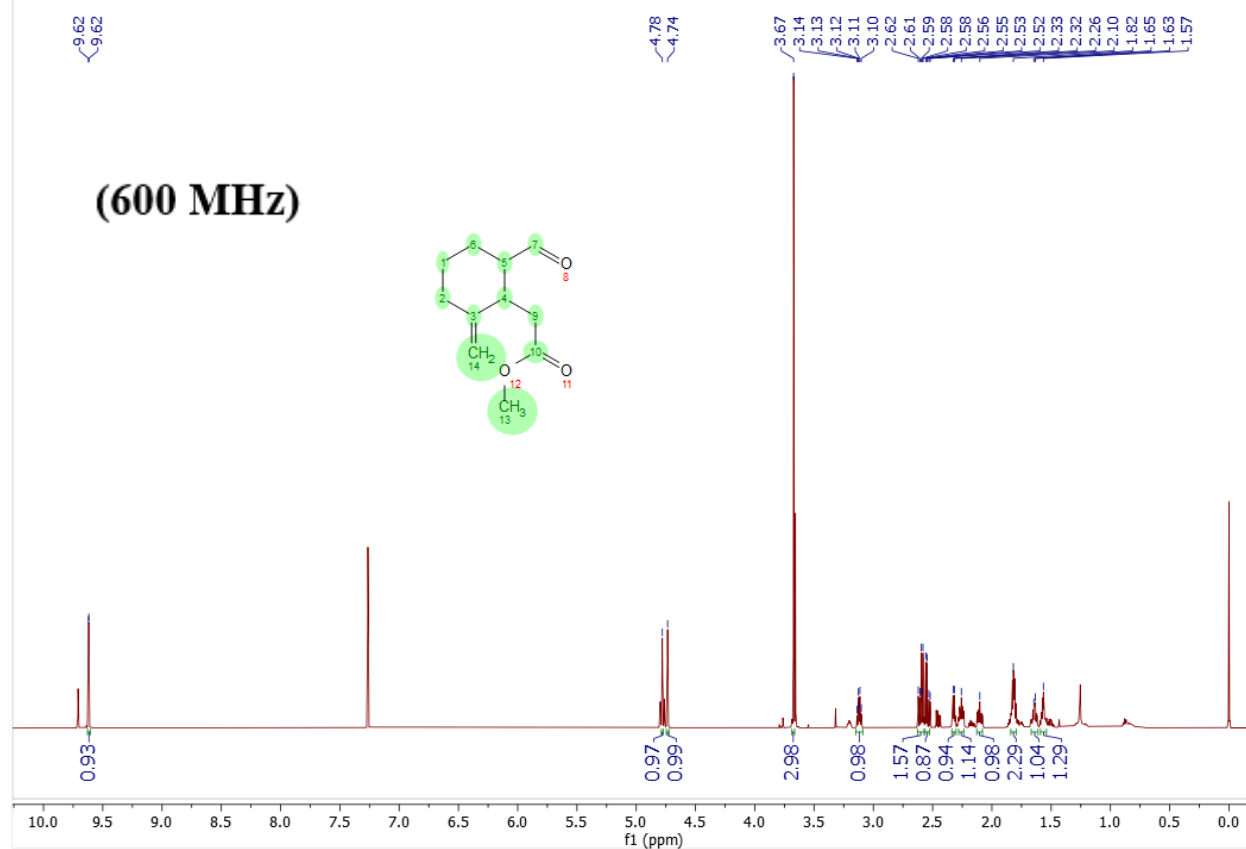
^{1}H NMR of compound 28 in CDCl$_3$.

^{13}C NMR of compound 28 in CDCl$_3$.
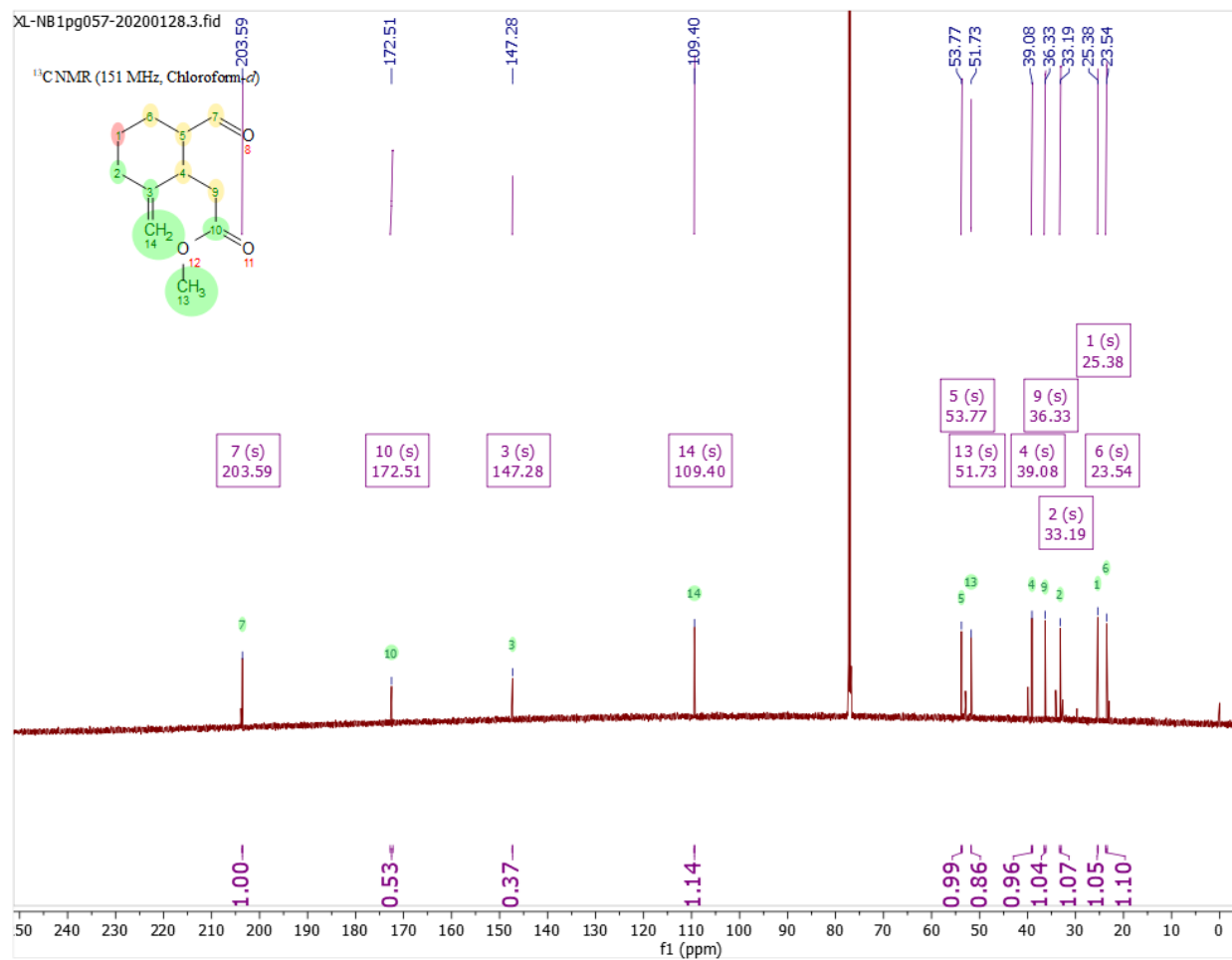
Figure 62. 2D edited [^{1}H, ^{13}C] HSQC NMR of compound 28 in CDCl$_3$.
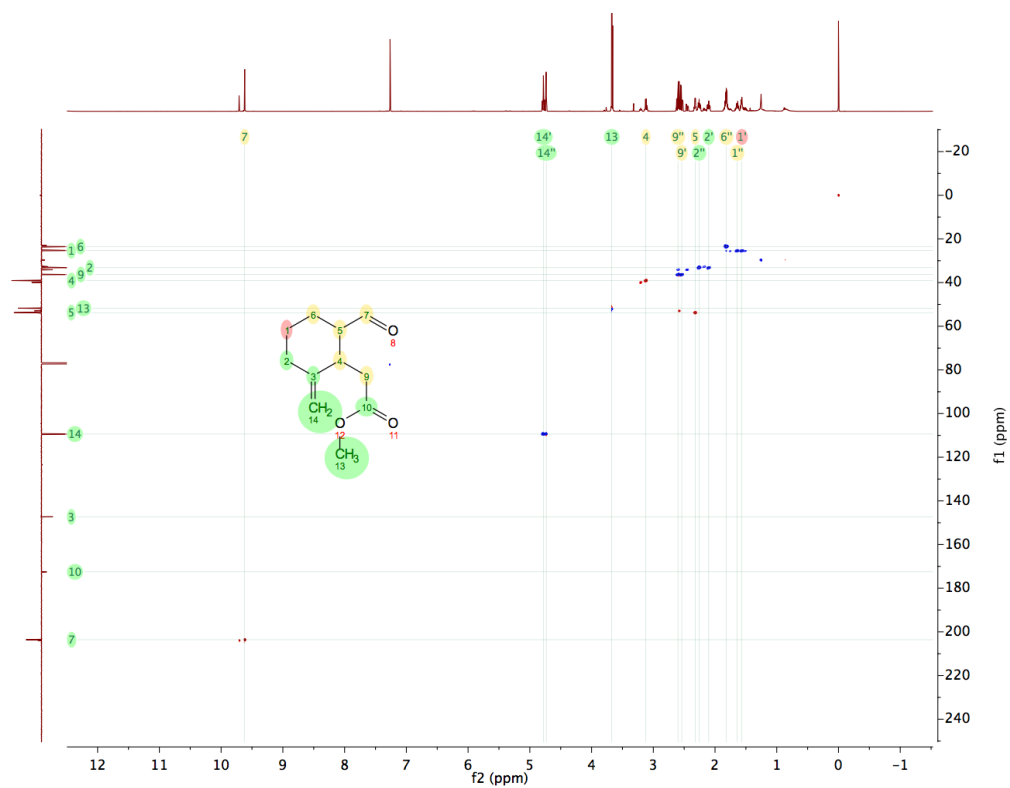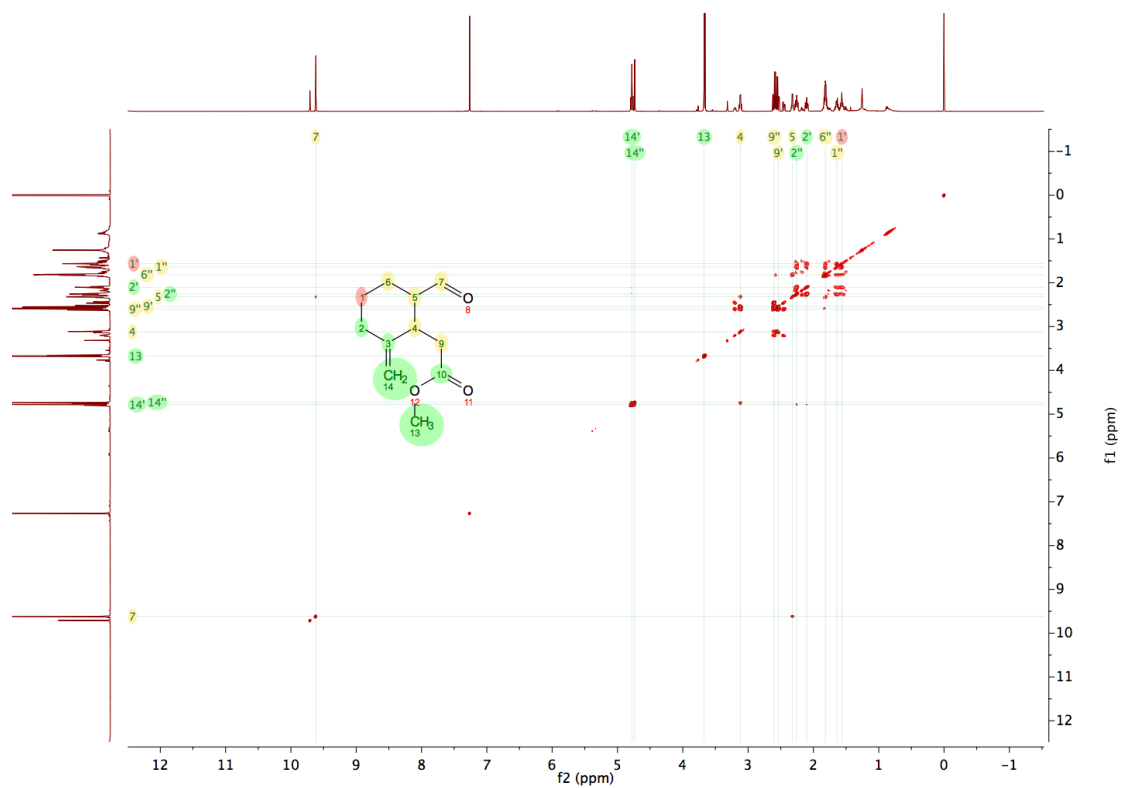
Figure 63. 2D COSY NMR of compound 28 in CDCl$_3$.
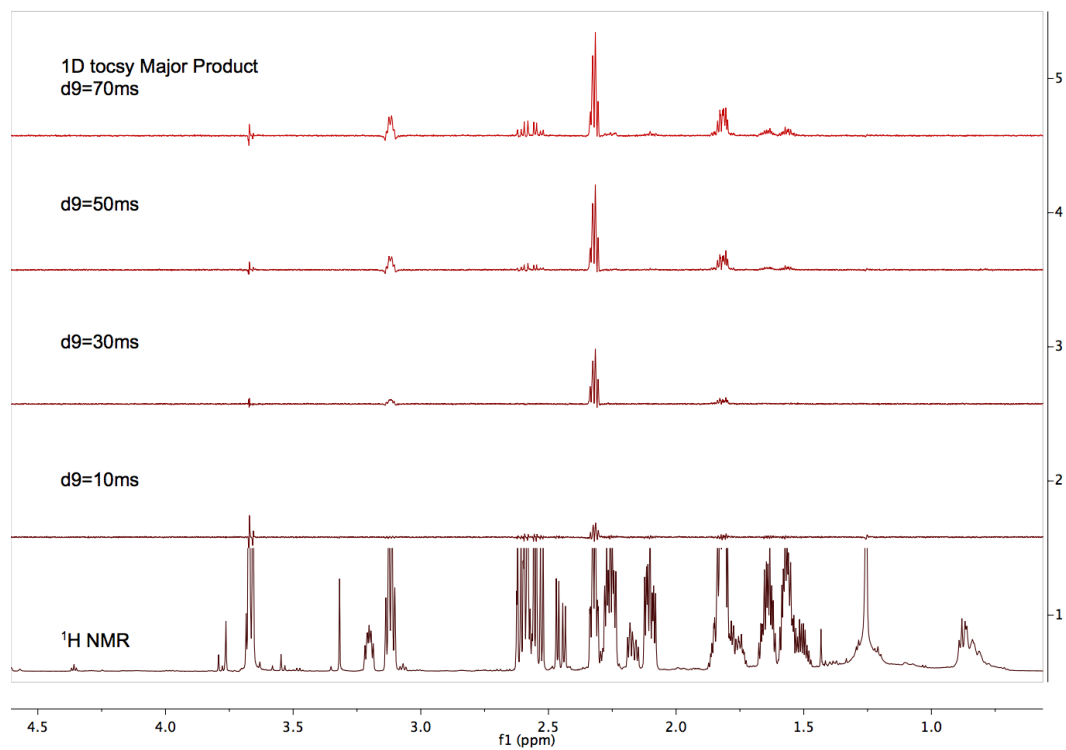
Figure 64. Selective 1D TOCSY NMR with excitation of the aldehyde resonance at 9.62 ppm for the major product 28 in CDCl3.
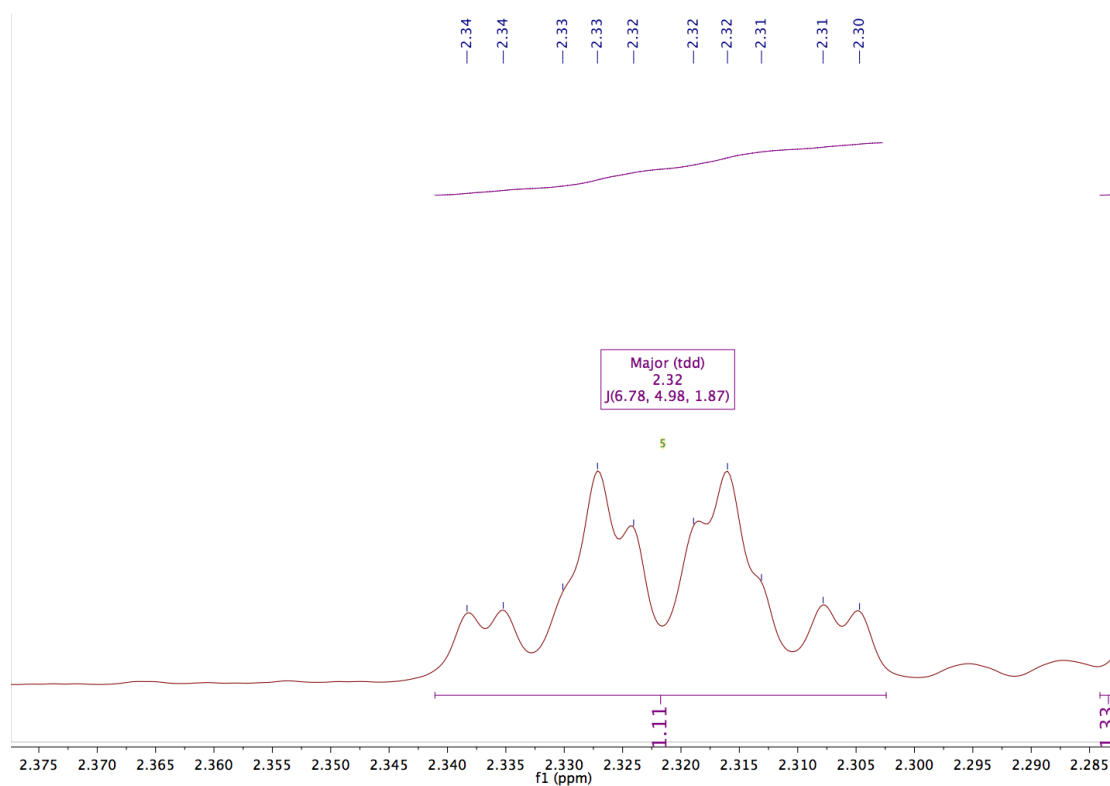
Figure 65. Multiplicity analysis of the proton adjacent to the aldehyde in the major product 28.
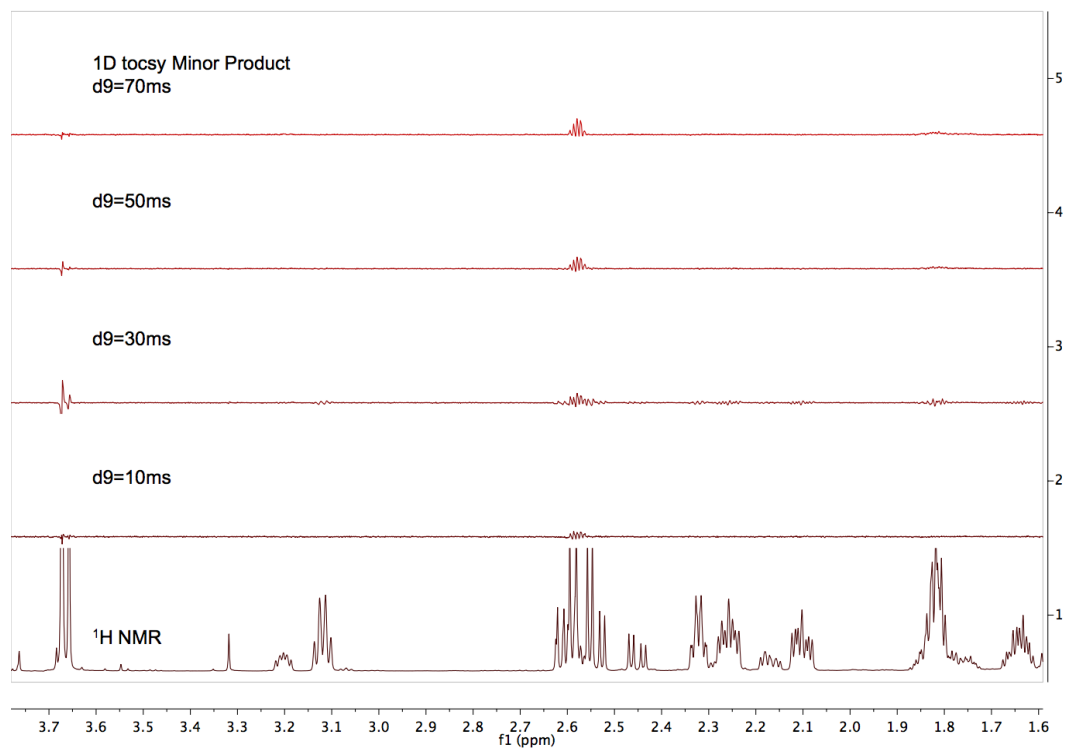
Figure 66. Selective 1D TOCSY NMR with excitation of the aldehyde resonance at 9.71 ppm for the minor product 28 in CDCl₃.
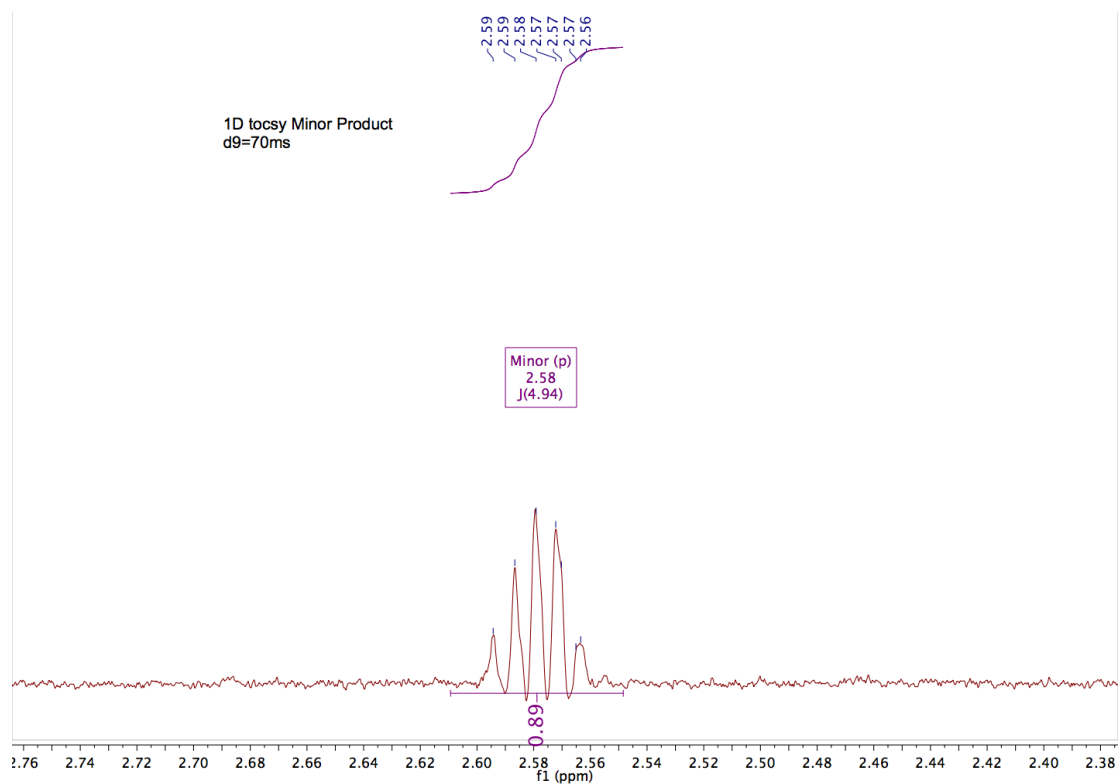
Figure 67. Multiplicity analysis of the proton adjacent to the aldehyde in the minor product 28 using selective 1D TOCSY spectrum, since the peak was buried in ^{1}H NMR.
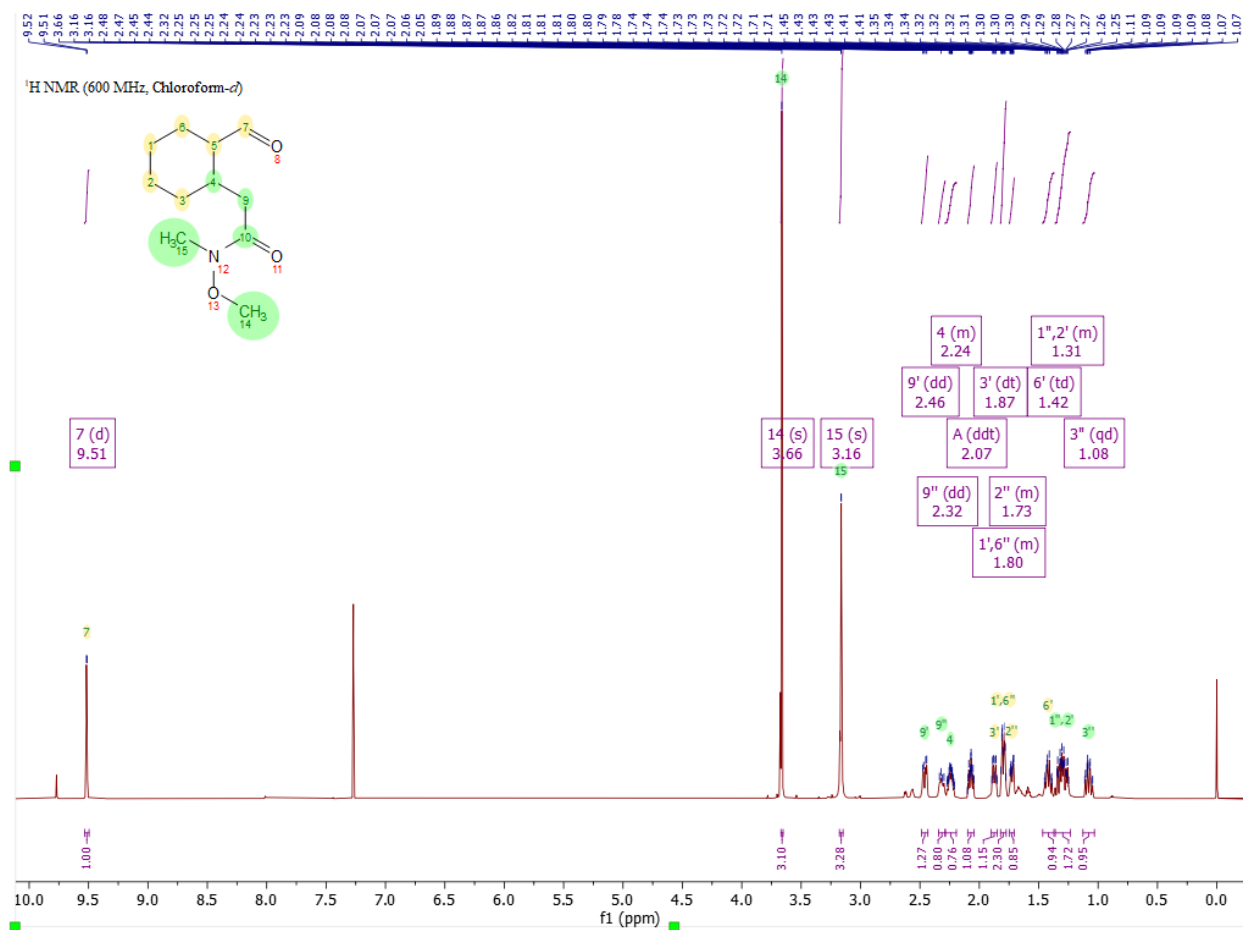
^{1}H NMR of compound 23 in CDCl$_3$.

^{13}C NMR (151 MHz, Chloroform-*d*)

7 (s) 204.74

10 (s) 172.98

5 (s) 55.65

14 (s) 61.25

9 (s) 36.80

6 (s) 26.01

1 (s) 24.53

15 (s) 32.05

3 (s) 31.50

4 (s) 32.89

2 (s) 25.13
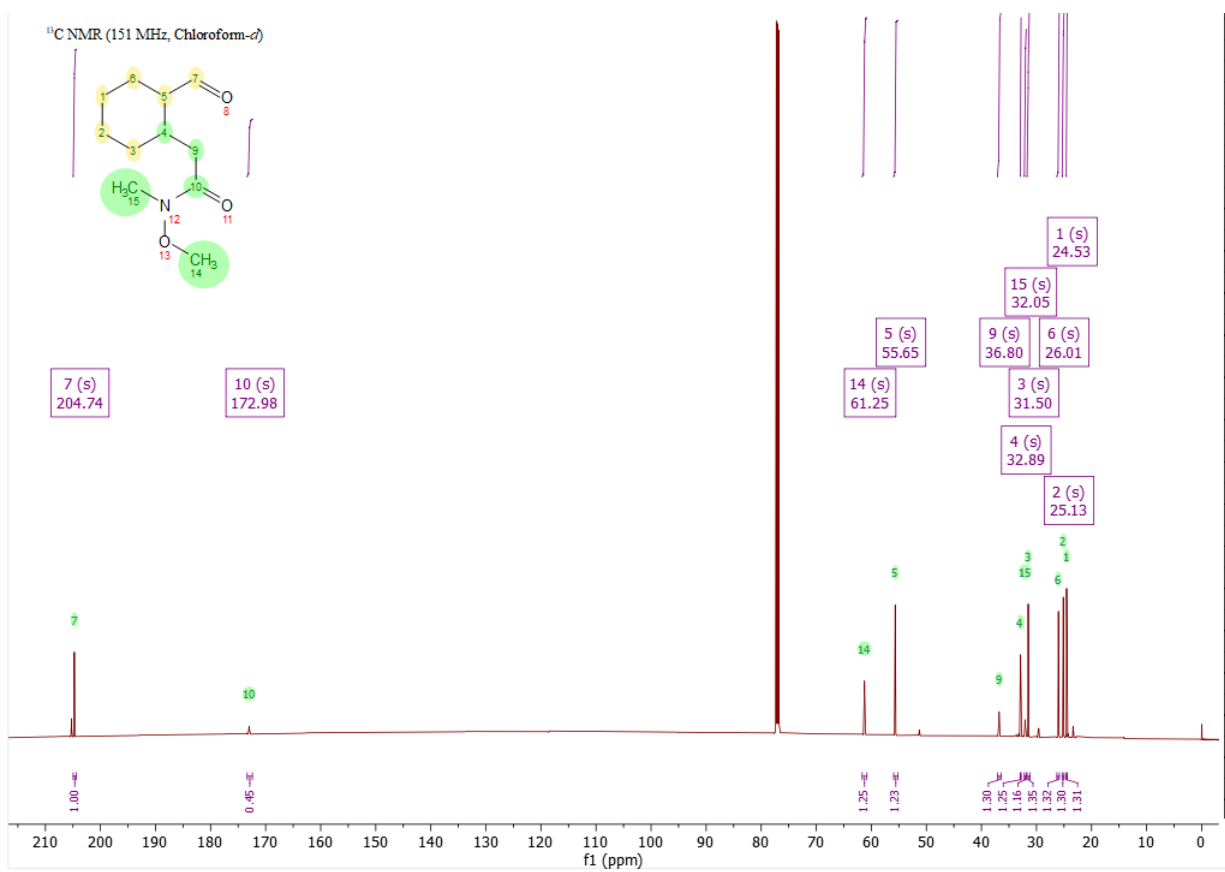
^{13}C NMR of compound 23 in CDCl$_3$.
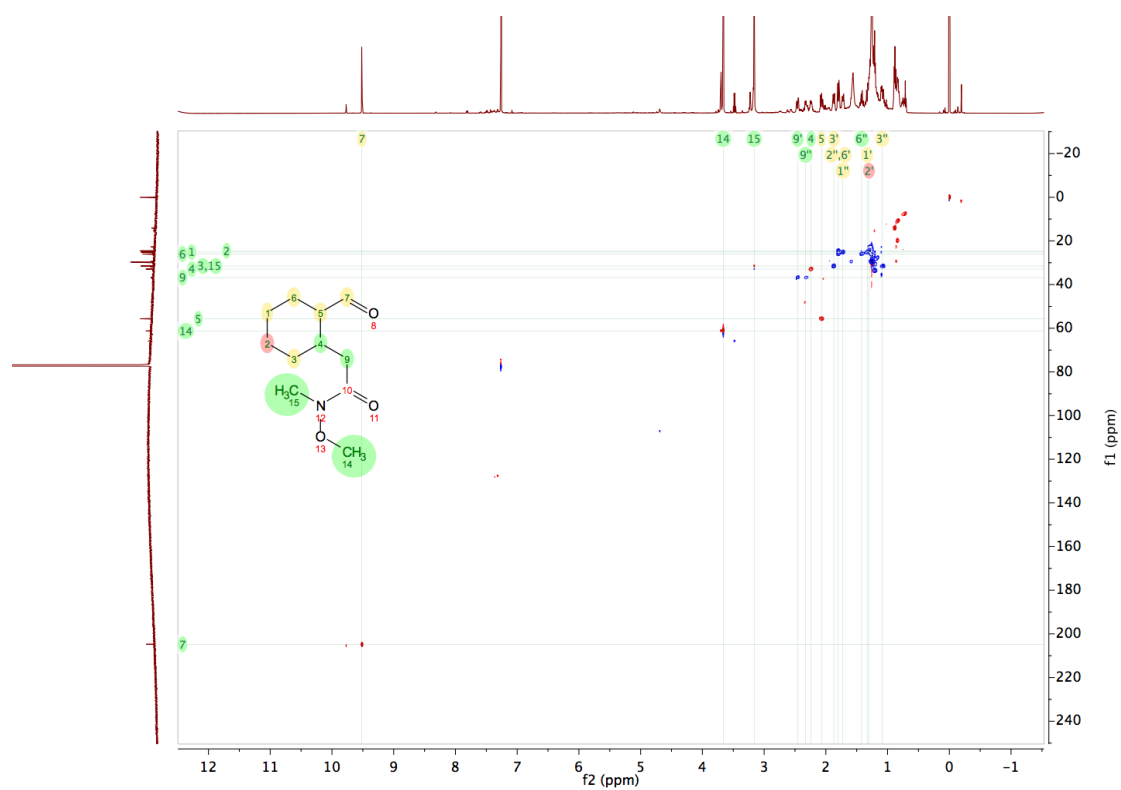
Figure 68. 2D edited [^{1}H, ^{13}C] HSQC NMR of compound 23 in CDCl$_3$.
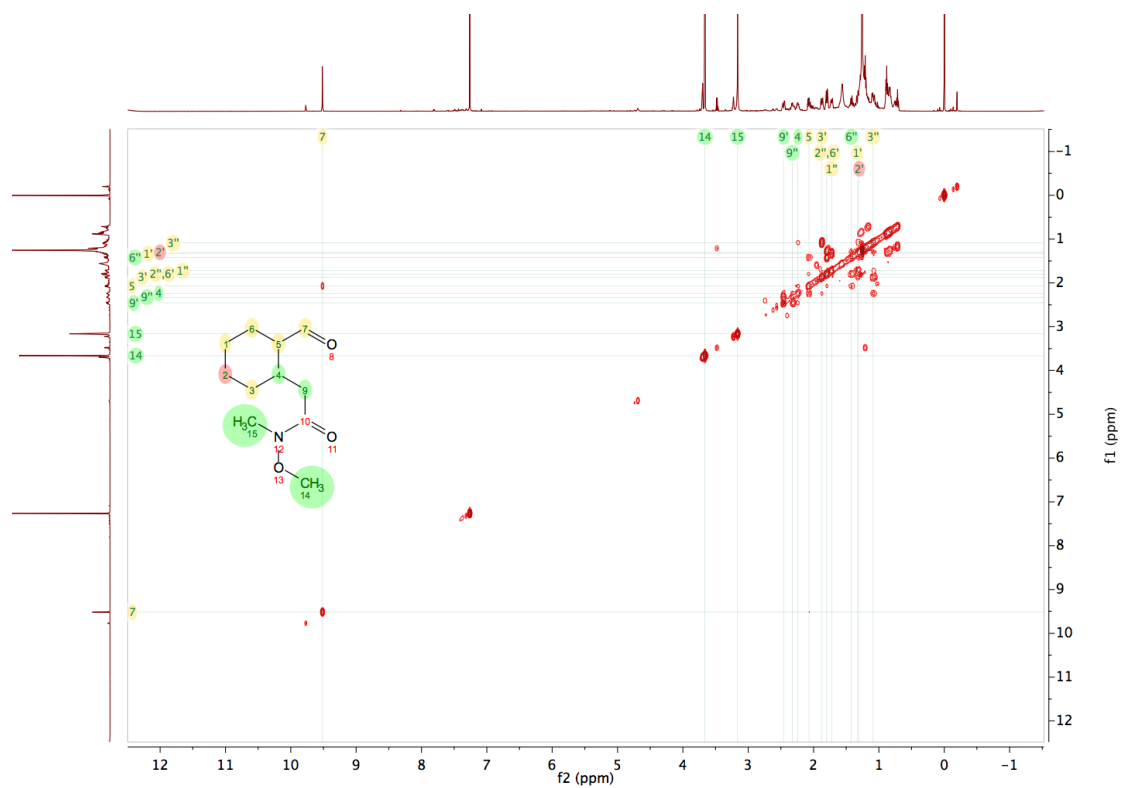
Figure 69. 2D COSY NMR of compound 23 in CDCl₃.
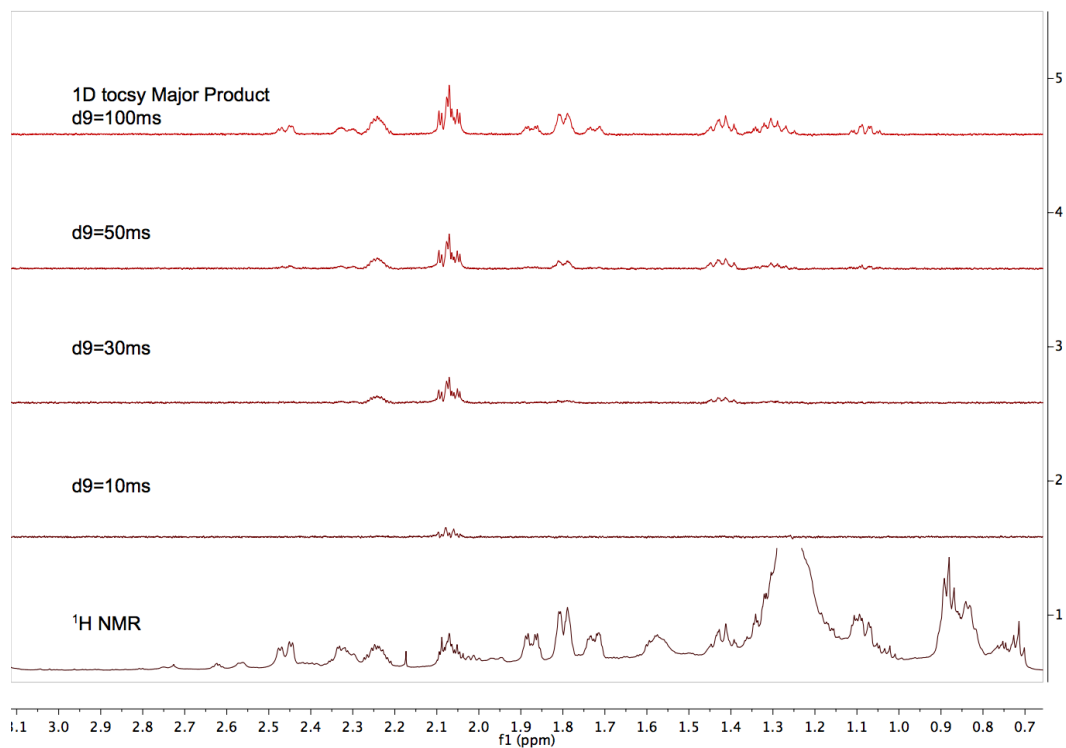
Figure 70. Selective 1D TOCSY NMR with excitation of the aldehyde resonance at 9.51 ppm for the major product 23 in CDCl₃.
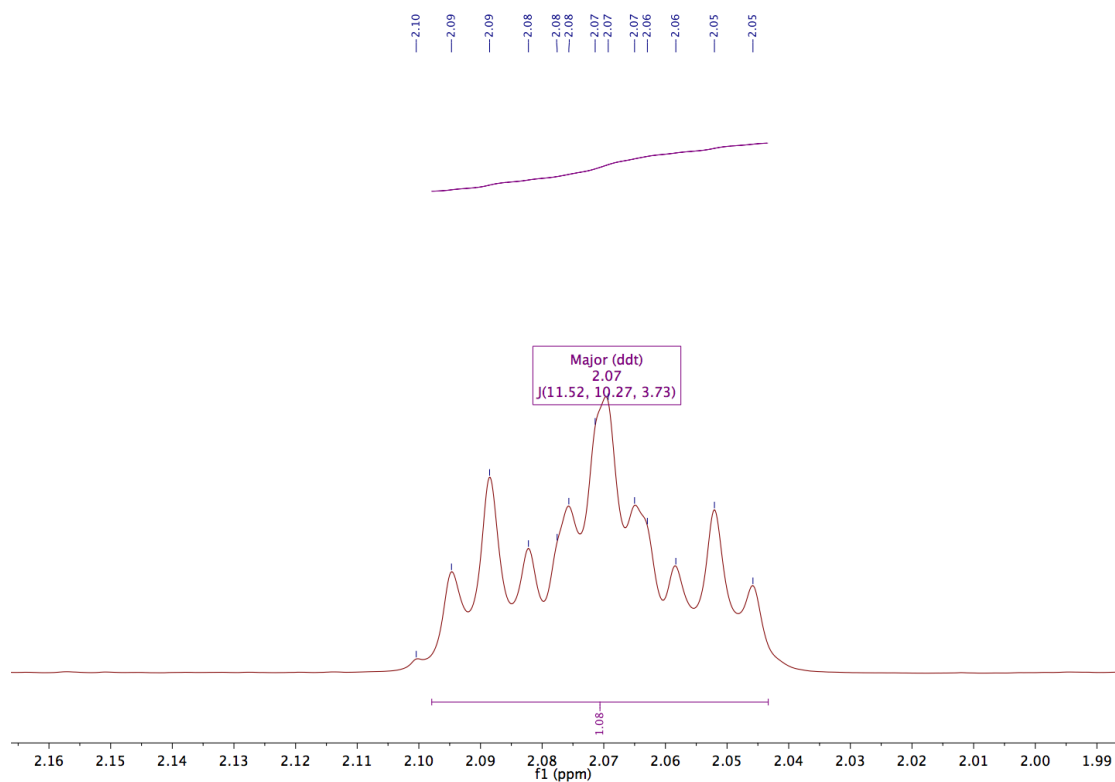
Figure 71. Multiplicity analysis of the proton adjacent to the aldehyde in the major product 23.

Selective 1D TOCSY NMR with excitation of the aldehyde resonance at 9.77 ppm for the minor product showed no peaks at NS=1024, thus the multiplicity analysis of the proton adjacent to the aldehyde in the minor product 23-minor diastereomer is not available.
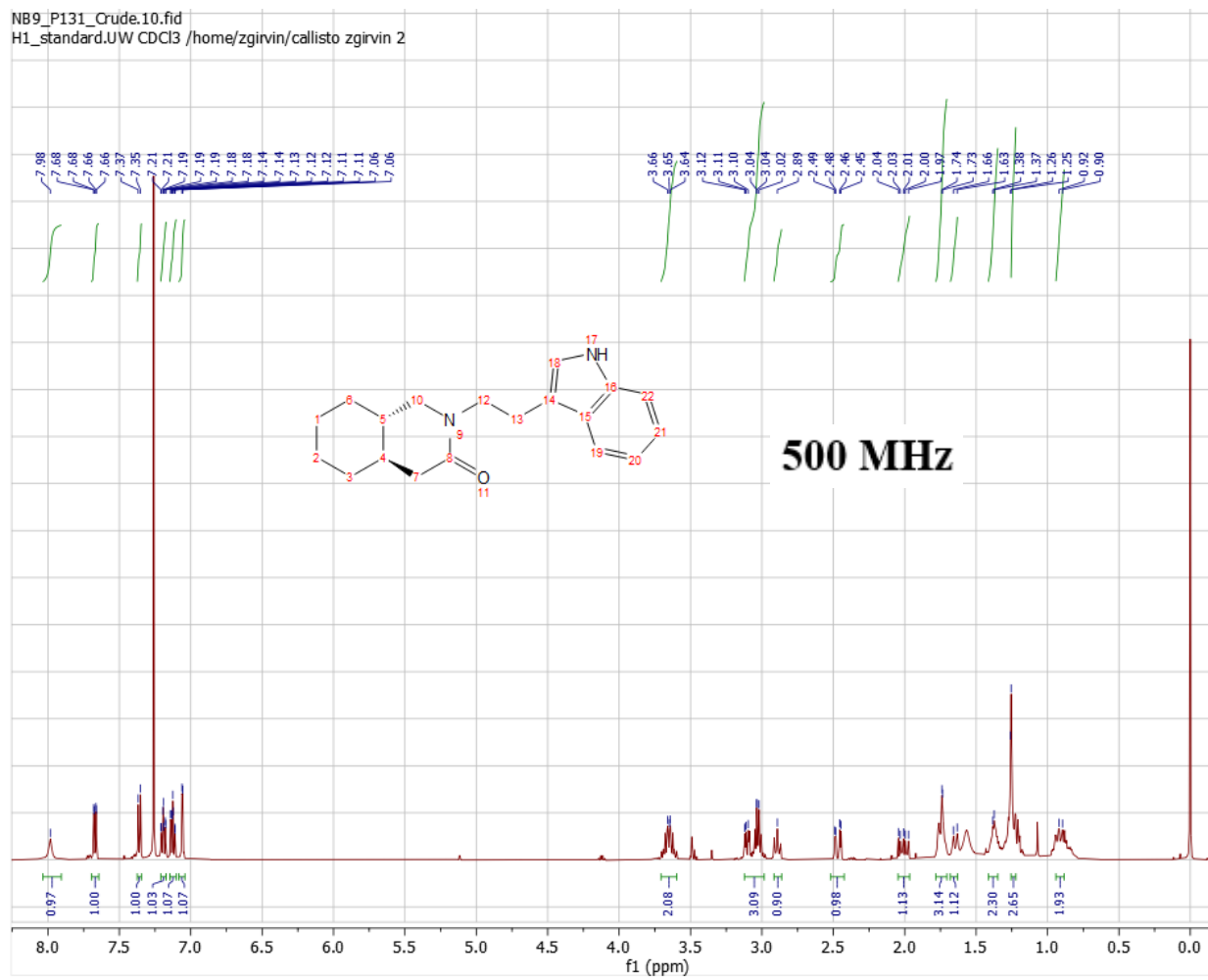
Crude ^{1}H NMR of compound 29 in CDCl$_3$.

NB9_P131_Crude.11.fid
C13_H1dec.UW CDCl3 /home/zgirvin/callisto zgirvin 2

169.63

136.25

127.57
122.05
121.82
119.36
118.88
113.50
111.08

54.46

47.93

39.52
38.43
37.12
32.64
29.74
25.42
25.41
22.94

126 MHz

f1 (ppm)
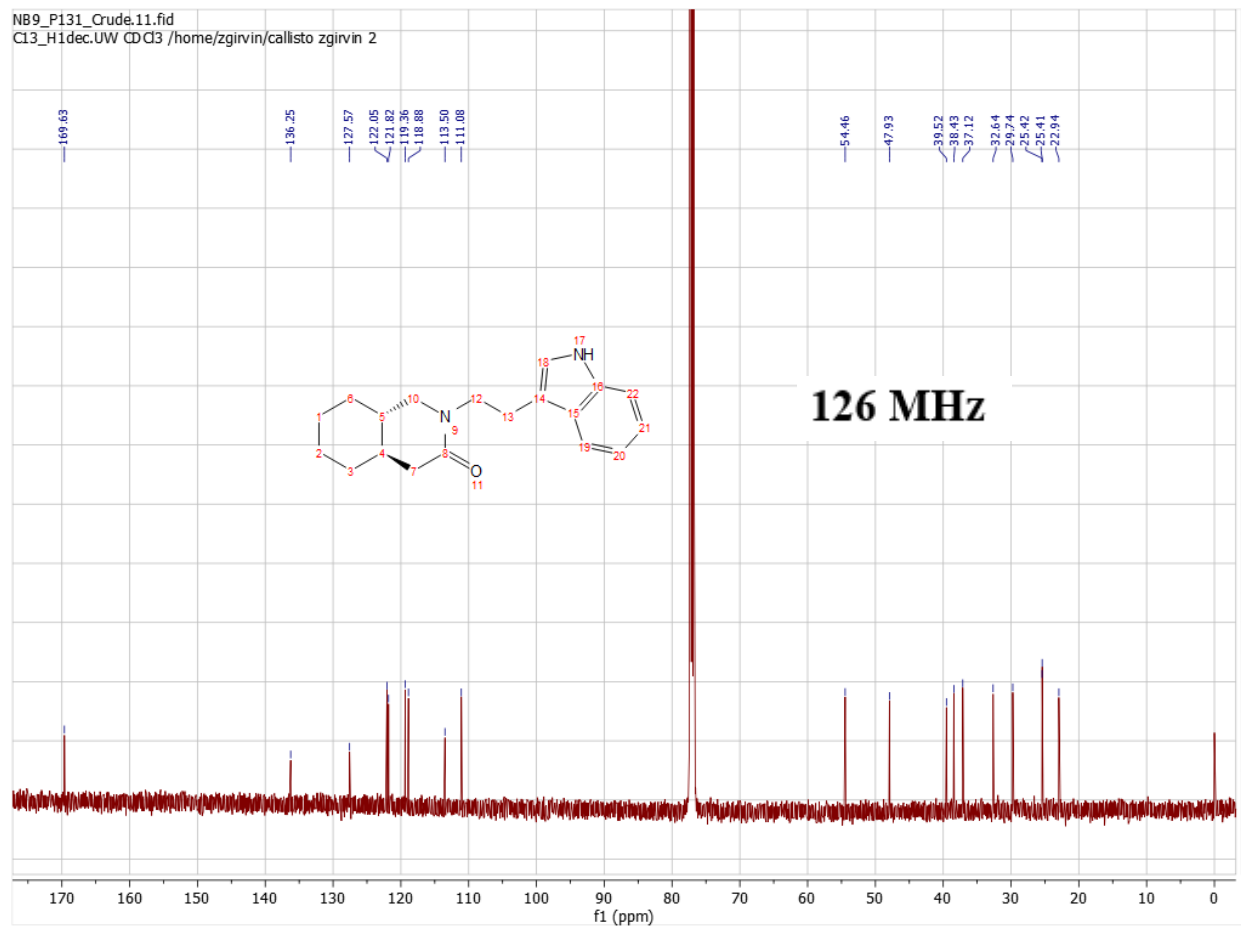
Crude ^{13}C spectra of 29 in CDCl$_3$.

NB9_P137_(-)-Yohimbane_Recyrst_High Vac.10.fid
H1_standard.UW CDCl3 /home/zgirvin/callisto zgirvin 52

500 MHz
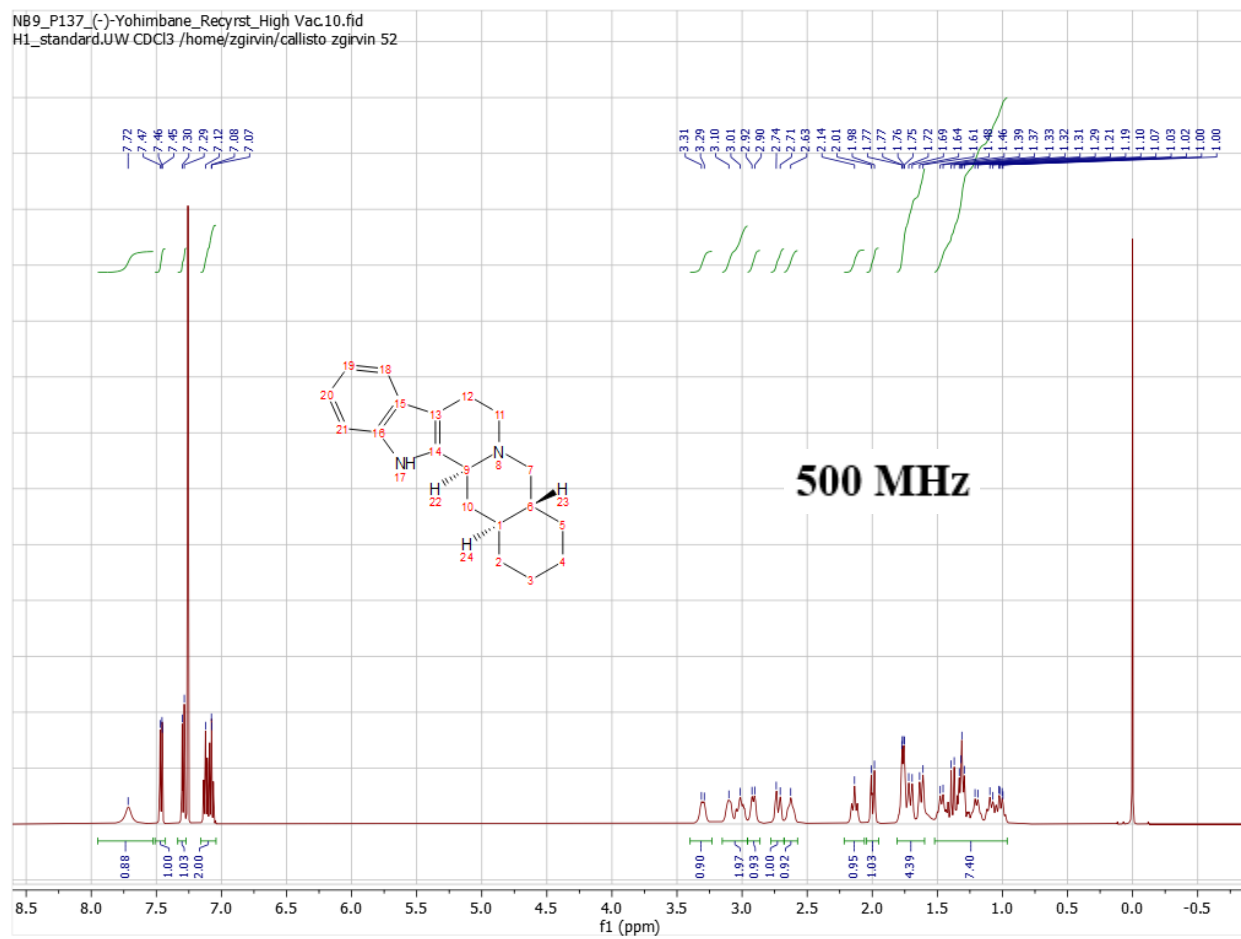
¹H NMR spectra of (-)-yohimbane in CDCl₃.
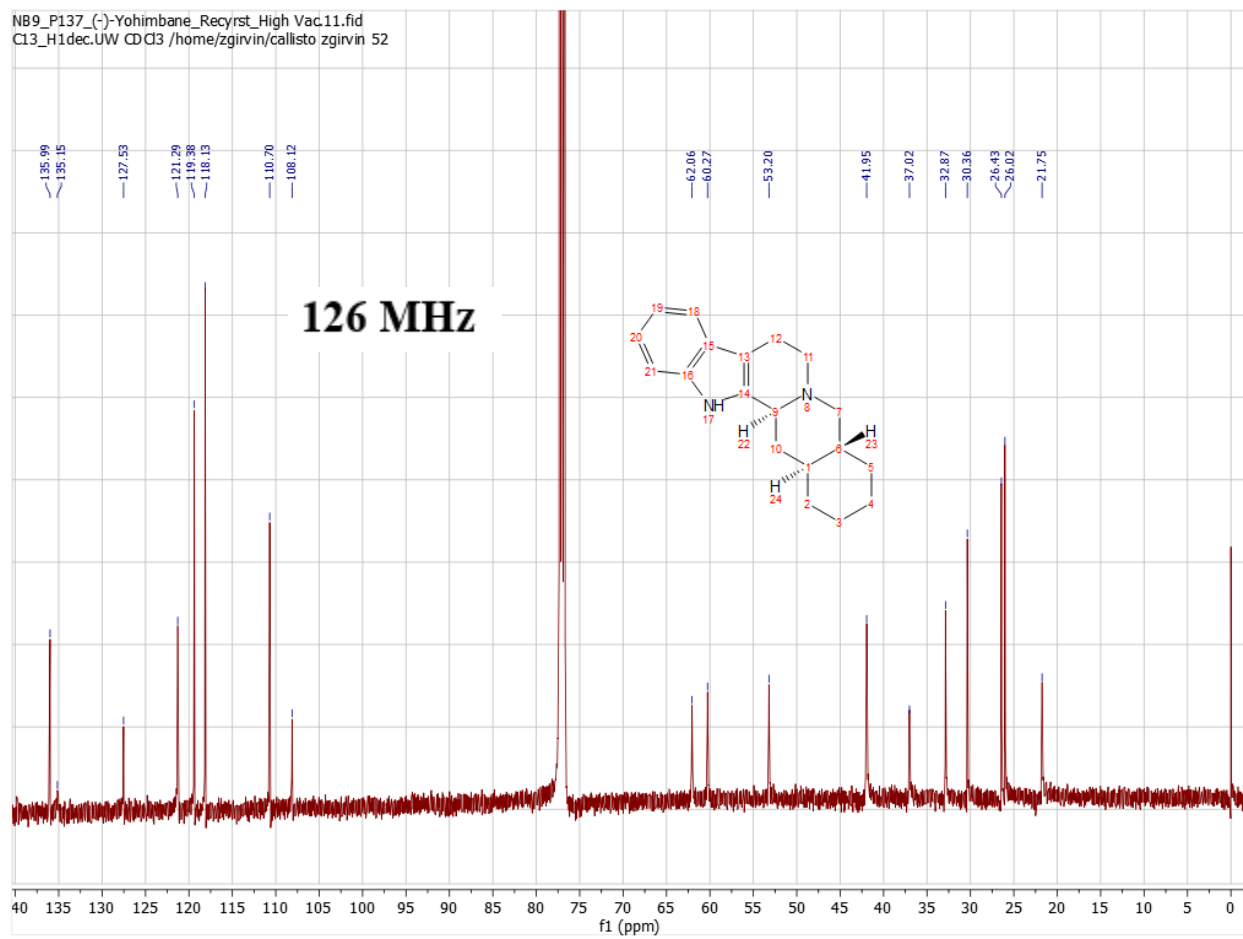
^{13}C NMR spectra of (-)-yohimbane in CDCl[3].

4.6 References

Brown, D. G.; Bostrom, J. Analysis of Past and Present Synthetic Methodologies on Medicinal Chemistry: Where Have All the New Reactions Gone? *J. Med. Chem.* **2016**, 59, 4483-4458.

Bostrom, J.; Brown, D. G.; Young, R. J.; Keseru, G. M. Expanding the medicinal chemistry synthetic toolbox. *Nature Reviews Drug Discovery* **2018**, 17, 709-727.

Campos, K. R.; Coleman, P. J.; Alvarez, J. C.; Dreher, S. D.; Garbaccio, R. M.; Terrett, N. K.; Tillyer, R. D.; Truppo, M. D.; Parmee, E. R. The importance of synthetic chemistry in the pharmaceutical industry. *Science* **2019**, 363, eaat805.

Troshin, K.; Hartwig, J. F. Snap deconvolution: An informatics approach to high-throughput discovery of catalytic reactions. *Science* **2017**, 357, 175-181.

McNally, A.; Prier, C. K.; MacMillan, D. W. C. Discovery of an α-Amino C-H Arylation Reaction Using the Strategy of Accelerated Serendipity. *Science* **2011**, 334, 1114-1117.

Anslyn, E. V.; Dougherty, D. A. *Modern Physical Organic Chemistry*. University Science Books: **2006**.

Fleming, I. *Molecular Orbitals and Organic Chemistry Reactions – student edition*. Wiley, **2009**.

(a) Norman, M. H.; Heathcock, C. H. Improved Synthesis of N-Benzyl-5-ethyl-1,2,3,4-tetrahydropyridine. *J. Org. Chem.* **1988**, 53, 3371-3373. (b) Ahmad, Z.; Goswami, P.; Venkateswaran, R. V. A Formal Stereocontrolled Synthesis of (±) Isoclovene. *Tetrahedron* **1989**, 45, 6833-6840. (c) Costello, G.; Saxton, J. E. Approaches to the Synthesis of Asidosperma Alkaloids, Part 1, Preliminary Studies in the Vincadifformine Group. *Tetrahedron* **1986**, 42, 6047-6069.

For an example of aldehyde-derived enamines adding to activated α,β-unsaturated esters see: Kano, T.; Shirozu, F.; Akakura, M.; Maruoka, K. Powerful Amino Diol Catalyst for Effecting the Direct Asymmetric Conjugate Addition of Aldehydes to Acrylates. *J. Am. Chem. Soc.* **2012**, 134, 16068-16073.

Michael, A. On the addition of sodium acetoacetate- and sodium malonic acid esters to the esters of unsaturated acids. *Journal fur Praktische Chemie* **1887**, 35, 349-356.

(a) Alonso, D. A.; Baeza, A.; Chinchilla, R.; Gomez, C.; Guillena, G.; Pastor, I. M.; Ramon, D. J. Recent Advances in Asymmetric Organocatalyzed Conjugate Additions to Nitroalkenes. *Molecules* **2017**, 22, 895. (b) Betancort, J. M.; Barbas III, C. F. Catalytic Direct Asymmetric Michael Reactions: Taming Naked Aldehyde Donors, *Org. Lett.* **2001**, 3, 3737-3740. (c) Melchiorre, P.; Jorgensen, K. A. Direct Enantioselective Michael Additions of Aldehydes to Vinyl Ketones Catalyzed by Chiral Amines. *J. Org. Chem.* **2003**, 68, 4151-4157. (d) Hechavarria Fonseca, M. T.; List, B. Catalytic asymmetric intramolecular Michael reaction of aldehydes. *Angew. Chem. Int. Ed.* **2004**, 43, 3958-3960. (e) Peelen, T. J.; Chi, Y.; Gellman, S. H. Enantioselective Organocatalytic Michael Additions of Aldehydes to Enones with Imidazolidinones: Cocatalyst Effects and Evidence for an Enamine Intermediate. *J. Am. Chem. Soc.* **2005**, 127, 11598-11599. (f) Krause, N., Hoffmann-Rober, A. Recent Advances in Catalytic Enantioselective Michael Additions. *Synthesis* **2001**, 2, 171-196. (g) Hayashi, Y.; Itoh, T.; Ohkubo, M.; Ishikawa, H. Asymmetric Michael Reaction of Acetaldehyde Catalyzed by Diphenylprolinol Silyl Ether. *Ang. Chem. Int. Ed.* **2008**, 47, 4722-4724. (h) Bournaud, C.; Marchal, E.; Quintard, A.; Sulzer-Mosse, S.; Alexakis, A. Organocatalyst-mediated enantioselective intramolecular Michael addition of aldehydes to vinyl sulfones. *Tetrahedron: Asymmetry* **2010**, 21, 1666-

1673. (i) Seebach, D.; Sun, X.; Ebert, M.; Bernd Schweizer, W.; Purkayastha, N.; Beck, A. K.; Duschmale, J.; Wennemers, H. Stoichiometric Reactions of Enamines Derived from Diphenylprolinol Silyl Ethers with Nitro Olefins and Lessons for the Corresponding Organocatalytic Conversions – a Survey. *Helvetica Chimica Acta*. **2013**, 96, 799-852.

Allgauer, D. S.; Jangra, H.; Asahara, H.; Li, Z.; Chen, Q.; Zipse, H.; Ofial, A. R.; Mayr, H. Quantification and Theoretical Analysis of the Electrophilicities of Michael Acceptors. *J. Am. Chem. Soc.* **2017**, 139, 13318-13329.

Mayr, H. **2015**, Available at: https://www.cup.lmu.de/oc/mayr/ReactScalesPoster.pdf. Accessed March 2, 2020.

Appel, R.; Mayr, H. Quantification of the Electrophilic Reactivities of Aldehydes, Imines, and Enones. *J. Am. Chem. Soc.* **2011**, 133, 8240-8251.

Gatzenmeier, T.; Kaib, P. S. J.; Lingnau, J. B.; Goddard, R.; List, B. The Catalytic Asymmetric Mukaiyama-Michael Reaction of Silyl Ketene Acetals with α,β-Unsaturated Methyl Esters. *Angew. Chem. Int. Ed.* **2018**, 57, 2464-2468.

Younai, A.; Zeng, B.; Meltzer, H. Y.; Scheidt, K. A. Enantioselective Syntheses of Heteroyohimbine Natural Products: A Unified Approach through Cooperative Catalysis. *Angew. Chem. Int. Ed.* **2015**, 54, 6900-6904.

Gammack Yamagata, A. D.; Datta, S.; Jackson, K. E.; Stegbauer, L.; Paton, R. S.; Dixon, D. J. Enantioselective Desymmetrization of Prochiral Cyclohexanones by Organocatalytic Intramolecular Michael Additions to α,β-Unsaturated Esters. *Angew. Chem. Int. Ed.* **2015**, 54, 4899-4903.

Leonov, A. I.; Timofeeva, D. S.; Ofial, A. R.; Mayr, H. Metal Enolates – Enamines – Enol Ethers: How Do Enolate Equivalents Differ in Nucleophilic Reactivity? *Synthesis* **2019**, 51, 1157-1170.

Hirai, Y.; Terada, T.; Yamazaki, T.; Momose, T. Heterocycles in asymmetric synthesis. Part 1. Construction of the chiral building blocks for enantioselective alkaloid synthesis *via* an asymmetric intramolecular Michael reaction. *J. Chem. Soc., Perkin Trans. 1.* **1992**, 509-516.

Kang, J. Y.; Carter, R. G. Primary Amine, Thiourea-Based Dual Catalysis Motif for Synthesis of Stereogenic, All-Carbon Quaternary Center-Containing Cycloalkanones. *Org. Lett*. **2012**, 14, 3178-3181.

Mukherjee, S.; Yang, J. W.; Hoffmann, S.; List, B. Asymmetric Enamine Catalysis. *Chem. Rev.* **2007**, 107, 5471-5569.

Marigo, M.; Jorgensen, K. A. Enantioselective Organocatalysis: Reactions and Experimental Procedures; Wiley, 2007.

Frazen, J.; Marigo, M.; Fielenbach, D.; Wabnitz, T., C.; Kjaersgaard, A.; Jorgensen, K. A. A General Organocatalyst for Direct α-Functionalization of Aldehydes: Stereoselective C-C, C-N, C-F, C-Br, and C-S Bond-Forming Reactions. Scope and Mechanistic Insights. *J. Am. Chem. Soc.* **2005**, 127, 18296-18304.

Donslund, B. S.; Johansen, T. K.; Poulsen, P. H.; Halskov, K. S.; Jorgensen, K. A. The Diarylprolinol Silyl Ethers: Ten Years After. *Angew. Chem. Int. Ed.* **2015**, 54, 13860-13874.

Chi, Y.; Guo, L.; Kopf, N. A.; Gellman, S. H. Enantioselective Organocatalytic Michael Addition of Aldehydes to Nitroethylene: Efficient Access to γ^2-Amino Acids. *J. Am. Chem. Soc.* **2008**, 130, 5608-5609.

Akiyama, T.; Mori, K. Stronger Bronsted Acids: Recent Progress. *Chem. Rev.* **2015**, 115, 9277-9306.

(a) Doyle, A. G.; Jacobsen, E. N. Small-Molecule H-Bond Donors in Asymmetric Catalysis. *Chem. Rev.* **2007**, 107, 5713-5743. (b) Taylor, M. S.; Jacobsen, E. N. Asymmetric Catalysis by Chiral Hydrogen-Bond Donors. *Angew. Chem. Int. Ed.* **2006**, 45, 1520-1543.

(a) Yamamoto, H.; Futatsugi, K. "Designer Acids": Combined Acid Catalysis for Asymmetric Synthesis. *Angew. Chem., Int. Ed.* **2005**, 44, 1924-1942. (b) Saito, S.; Yamamoto, H. Designer Lewis acid catalysts – bulky aluminum reagents for selective organic synthesis. *Chem. Commun.* **1997**, 1585-1592.

Chi, Y.; Gellman, S. H. Diphenylprolinol Methyl Ether: A Highly Enantioselective Catalyst for Michael Addition of Aldehydes to Simple Enones. *Org. Lett.* **2005**, 7, 4253-4256.

Chung, C. K.; Liu, Z.; Lexa, K. W.; Andreani, T.; Xu, Y.; Ji, Y.; DiRocco, D. A.; Humphrey, G. R.; Ruck, Rebecca, T. Asymmetric Hydrogen Bonding Catalysis for the Synthesis of Dihydroquinazoline-Containing Antiviral, Letermovir. *J. Am. Chem. Soc.* **2017**, 139, 10637-10640.

(a) Schreiner, P. R.; Wittkopp, A. H-Bonding Additives Act Like Lewis Acid Catalysts. *Org. Lett.* **2002**, 4, 217-220. (b) Schreiner, P. R. Metal-free organocatalysis through explicit hydrogen bonding interactions. *Chem. Soc. Rev.* **2003**, 32, 289-296. (c) Etter, M.; Panunto, T. W. 1,3-Bis(m-nitrophenyl)urea: An Exceptionally Good Complexing Agent for Proton Acceptors. *J. Am. Chem. Soc.* **1988**, 110, 5896-5897. (d) Curran, D. P.; Kuo, L. H. Altering the Stereochemistry of Allylation Reactions of Cyclic α-Sulfinyl Radicals with Diarylureas. *J. Org. Chem.* **1994**, 59, 3259-3261.

Jakab, G.; Tancon, C.; Zhang, Z.; Lippert, K. M.; Schreiner, P. R. (Thio)urea Organocatalyst Equilibrium Acidities in DMSO. *Org. Lett.* **2012**, 14, 1724-1727.

Toste, D. F.; Sigman, M. S.; Miller, S. J. Pursuit of Noncovalent Interactions for Strategic Site-Selective Catalysis. *Acc. Chem. Res.* **2017**, 50, 609-615.

Erkkila, A.; Majander, I.; Pihko, P. M. Iminium Catalysis, *Chem. Rev.* **2007**, 107, 5416-5470.

Nahm, S.; Weinreb. S. M. N-methoxy-n-methylamides as effective acylating agents. *Tetrahedron Letters* **1981**, 22, 3815-3818.

Sakai, K.; Inouye, K.; Nakamura, N. Synthesis of (+)-Prostanoic Acid. *Prostaglandins* **1976**, 12, 399-401.

Crabbe, P.; Cervantes, A.; Guzman, A. Synthesis of a 9,11-Bis-desoxy-prostaglandin. *Tetrahedron Letters,* **1972**, 12, 1123-1125. (b) Corey, E. J.; Schaaf, T. K.; Huber, W.; Koelliker, U.; Weinshenker, N. M. Total Synthesis of Prostaglandins $F_{2\alpha}$ and E_2 as the Naturally Occurring Forms. *J. Am. Chem. Soc.*, **1970**, 92, 397-398.

(a) Baldwin, J. Rules for Ring Closure, *J. Chem. Soc. Chem. Commun*. **1976**, 18, 734-736. (b) Baldwin, J. E.; Thomas, R. C.; Kruse, L. I.; Silberman, L. Rules for ring closure: ring formation by conjugate addition of oxygen nucleophiles. *J. Org. Chem.* **1977**, 42, 3846-3852.

Szantay, C.; Blasko, G.; Honty, K.; Dornye, G. *The Alkaloids*; Academic: New York; 1986, Vol. 27.

Aube, J.; Ghosh, S.; Tanol, M. Symmetry-Driven Synthesis of Indole Alkaloids: Asymmetric Total Syntheses of (+)-Yohimbine, (-)-Yohimbone, (-)-Yohimbane, and (+)-Alloyohimbane. *J. Am. Chem. Soc.* **1994**, 116, 9009-9018.

Ghosh, A. K.; Sarkar, A. Enantioselective Syntheses of (-)-Alloyohimbane and (-)-Yohimbane by an Efficient Enzymatic Desymmetrization Process. *Eur. J. Org. Chem.* **2016**, 6001-6009.

Xie, C.; Luo, J.; Zhang, L.; Hong, R. A Chiral Pentenolide-Based Unified Strategy toward Dihydrocorynantheal, Dihydrocorynantheol, Protoemetine, Protoemetinol, and Yohimbane., *Org. Lett.* **2017**, 19, 3592-3595.

Claus, R. E.; Schreiber, S. L. Ozonolytic Cleavage of Cyclohexene to Terminally Differentiated Products: Methyl 6-Oxohexanoate, 6,6-Dimethoxyhexanal, Methyl 6,6-Dimethoxyhexanoate. *Org. Synth.* **1986**, 64, 150.

(a) Van Tamelen, E. E.; Shamma, M.; Aldrich, P. The Stereospecific Synthesis of dl-Yohimbane. Stereochemistry of Tohimbine. *J. Am. Chem. Soc.* **1956**, 78, 4628-4632. (b) Allin, S. M.; Duffy, L. J.; Bulman Page, P. C.; McKee, V.; McKenzie, M. J. Towards a total synthesis of the manadomanzamine alkaloids: the first asymmetric construction of the pentacyclic indole core. *Tetrahedron Letters* **2007**, 48, 4711-4714. (c) Yang, V.; Hong, B.; Kao, H.; Tu, T.; Chen, C.; Lee, G.; Chou, P. One-Pot Dichotomous Construction of Inside-Azayohimban and Pro-Azayohimban Systems via an Enantioselective Organocatalytic Cascade; Their Use as a Model to Probe the (Aza-)Indole Local Solvent Environment. *Org. Lett.* **2015**, 17, 5816-5819.

Bischler, A.; Napieralski, B. A new method for the synthesis of isoquinolines. *Ber. Dtsch. Chem. Ges.* **1893**, 26, 1903-1908.

(a) Alford, J. S.; Abascal, N. C.; Shugrue, C. R.; Colvin, S. M.; Romney, R. K.; Miller, S. J. Aspartyl Oxidation Catalysts That Dial in Functional Group Selectivity, along with Regio- and Stereoselectivity. *ACS Cent. Sci.* **2016**, 2, 733-739. (b) Liu, W.; Ren, Z.; Bosse, A. T.;

Liao, K.; Goldstein, E. L.; Bacsa, J.; Musaev, D. G.; Stoltz, B. M.; Davies, H. M. L. Catalyst-Controlled Selective Functionalization of Unactivated C-H Bonds in the Presence of Electronically Activated C-H Bonds. *J. Am. Chem. Soc.* **2018**, 140, 12247-12255. (c) Cook, A. K.; Schimler, S. D.; Matzger, A. J.; Sanford, M. S. Catalyst-controlled selectivity in the C-H borylation of methane and ethane. *Science* **2016**, 351, 1421-1424. (d) Hartwig, J. Catalyst-Controlled Site-Selective Bond Activation. *Acc. Chem. Res.* **2017**, 50, 549-555. (e) Jung, S. T.; Lauchli, R.; Arnold, F. H. Cytochrome P450: taming a wild type enzyme. *Current Opinion in Biotechnology* **2011**, 22, 809-817.

Chi, Y.; Peelen, T. J.; Gellman, S. H. A Rapid ^{1}H NMR Assay for Enantioenriched Excess of α-substituted Aldehdyes. *Org. Lett.*, **2005**, 7, 3469-3472.

Schreiber, S. L.; Kelly, S. E.; Porco Jr., J. A.; Sammakia, T.; Suh, E. M. Structural Studies and Synthetic Studies of the Spore Germination Autoinhibitor Gloeosporone. *J. Am. Chem. Soc.*, **1988**, 110, 6210-6218.

Pawar, A. S.; S, S.; Chattopadhyay, S. Chemoenzymatic Synthesis of Ferrulactone II and (2E)-9-Hydroxydecenoic Acid, *Tetrahedron: Asymmetry*, **1995**, 6, 2219-2226.

Terrett, J. A.; Clift, M. D.; MacMillan, D. W. C. Direct β-Alkylation of Aldehydes via Photoredox Organocatalysis, *J. Am. Chem. Soc.*, **2014**, 136, 6858-6861.

De Miguel, I.; Herradon, B.; Mann, E. Intramolecular Azide-Alkene 1,3-Dipolar Cycloaddition/Enamine Addition(s) Cascade Reaction: Synthesis of Nitrogen-Containing Heterocycles, *Adv. Synth. Catal.*, **2012**, 354, 1731-1736.

Douelle, F.; Capes, A. S.; Greaney, M. F. Highly Diastereoselective Synthesis of vicinal Quaternary and Tertiary Stereocenters Using the Iodo-aldol Cyclization. *Org. Lett.*, **2007**, 9, 1931-1934.

Tran, V.; Minehan, T. G., Lewis Acid Catalyzed Intramolecular Condensation of Ynol Ether-Acetals. Synthesis of Alkoxycycloalkene Carboxylates. *Org. Lett.*, **2012**, 14, 6100-6103.

Miranda, J. A.; Wade, C. J.; Little, R. D., Indirect Electroreductive Cyclization and Electrohydrocyclization Using Catalytic Reduced Nickel(II) Salen. *J. Org. Chem.,* **2005**, 70, 8017-8026.

Crabbe, P.; Cervantes, A.; Guzman, A. Synthesis of A 9,11-Bis-Desoxy-Prostaglandin, *Tetrahedron Letters*, **1972**, 12, 1123-1125.

Aube, J.; Ghosh, S.; Tanol, M. Symmetry-Driven Synthesis of Indole Alkaloids: Asymmetric Total Syntheses of (+)-Yohimbane, (-)-Yohimbane, and (+)-Alloyohimbane. *J. Am. Chem. Soc.,* **1994**, 116, 9009-9018.

Ghosh, A. K.; Sarkar, A. Enantioselective Syntheses of (-)-Alloyohimbane and (-)-Yohimbane by an Efficient Enzymatic Desymmetrization Process. *Eur. J. Org. Chem.,* **2016**, 6001-6009.

Bruker-AXS, Version 2018.1-0. http://bruker.com (2018).

L. Krause, R. Herbst-Irmer, G. M. Sheldrick, D. Stalke, Comparison of silver and molybdenum microfocus X-ray sources for single-crystal structure determination. *J. Appl. Crystallogr.* 48, 3–10 (2015).

G. M. Sheldrick, XPREP, Version 1 (Georg-August-Universitat Gottingen, 2013).

G. M. Sheldrick, The SHELX homepage (2013); http://shelx.uni-ac.gwdg.de/SHELX/.

G. M. Sheldrick, SHELXT - integrated space-group and crystal-structure determination. *Acta Crystallogr. A Found. Adv.* 71, 3–8 (2015).

G. M. Sheldrick, Crystal structure refinement with SHELXL. *Acta Crystallogr. C Struct. Chem.* 71, 3–8 (2015).

O. V. Dolomanov, L. J. Bourhis, R. J. Gildea, J. A. K. Howard, H. Puschmann, OLEX2: A complete structure solution, refinement and analysis program. *J. Appl. Cryst.* 42, 339– 341 (2009).

Chapter 5

Large-scale Synthesis of Orthogonally Protected (3*R*, 4*S*)-trans-3-aminopyrrolidine-4-carboxylic acid: A Valuable Catalytic Residue
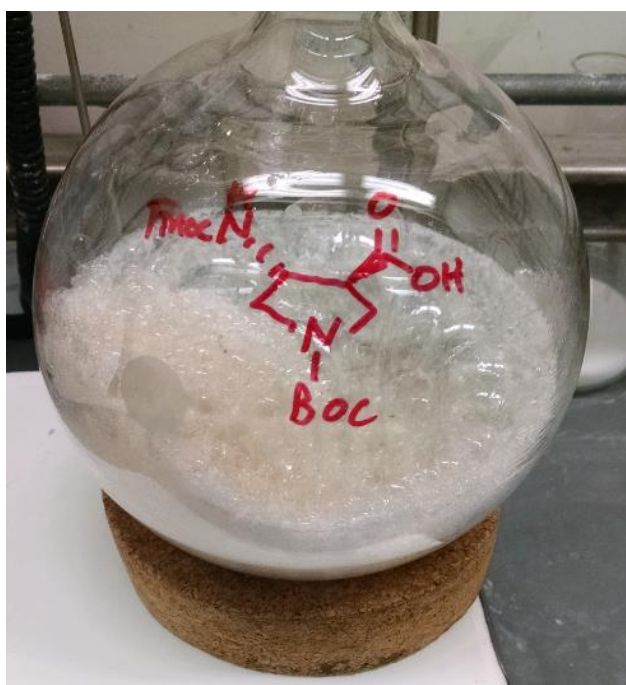
For Publications Detailing Original Synthesis Please See:

Lee, H- S.; LePlae, P. R.; Porter, E. A.; Gellman, S. H. An Efficient Route to Either Enantiomer of Orthogonally Protected *trans*-3-Aminopyrrolidine-4-carboxylic Acid, *J. Org. Chem.*, **2001,** *66*, 3597-3599.

Wang, X.; Espinosa, J. F.; Gellman, S. H. 12-Helix Formation in Aqueous Solution with Short β-Peptides Containing Pyrrolidine-Based Residues, *I. Am. Chem. Soc.*, **2000**, *122*, 4821-4822.

Note: Experimental protocols described in this chapter were all run by Zebediah Girvin. Mary Katherine Andrews replicated all experiments in reproducible yields, which are reported elsewhere.

5.1 Introduction

Foldamers, which are oligomers or polymers that are strongly disposed to adopt specific conformations, have found uses in various applications, including as ligands for protein receptors, as ion binders, and as catalysts.[1-6] Detailed solution- and solid-state studies of foldamers with diverse backbones have revealed a number of distinct helical secondary structures.[7] The ability to predict an oligomer's conformational propensity based on primary sequence can enable the use of rational design to generate foldamers that are tailored to specific functions.

Foldamers can have homogenous backbones (all subunits derived from the same class of molecules, such a β-amino acids) or heterogeneous backbones (different types of subunits, such as those derived from α- and β-amino acids). Early studies focused on foldamers containing exclusively β-amino acids.[7a,7b] β-amino acids containing a cyclic structure were found to be particularly advantageous, as conformational rigidification at the residue level was found to promote helical folding in short oligomers.[7a,7c]

In 2001, Lee et al. disclosed the enantiospecific synthesis of an orthogonally protected derivative of *trans*-3-aminopyrrolidine-carboxylic acid (APC) in each enantiomeric form (Figure 1). This building block can be used to introduce a cationic, cyclic β-amino acid residue into foldamers.[8] Initial interest in the residue was driven by a desire to understand novel secondary structures, as well as biological activities of β-peptides. Protonation of the ring nitrogen generates positive charge that support solubility in water. The cyclic constraint favors formation of helices in oligomers containing only a few residues.[9,10]
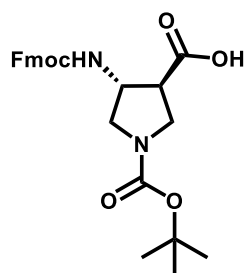
Orthoganally Protected
(3*R*, 4*S*)-*trans*-3-aminopyrrolidine-4-carboxylic acid
(APC)

Figure 1. Orthogonally protected (3*R, 4*S)-*trans*-3-aminopyrrolidine-4-carboxylic acid, APC.

Almost twenty years later, our group remains reliant on APC for a variety of uses, including the backbone-modification of GLP-1 analogues,[11] and most recently, to introduce a reactive secondary amine group into catalytically active foldamers (Figure 2).[12,13] Commercial acquisition of protected APC is prohibited by the high price ($3,500-4,260/gram, from (Combi-Blocks, Matrix Scientific). Therefore, research projects that require this unit also require enantioselective synthesis of the protected precursor.[14] The synthesis of APC can be time-consuming; therefore, a protocol that supports large-scale production is critical for efficient research.[15] Here, we present an updated protocol based on the route reported in 2001.[8]

Non-haemolytic, APC-cotaining β-peptide (ref. 10)
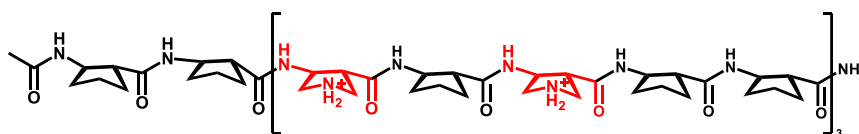
Catalytically Active, APC-containing 1:2 α/β-peptides (ref. 11, 12)
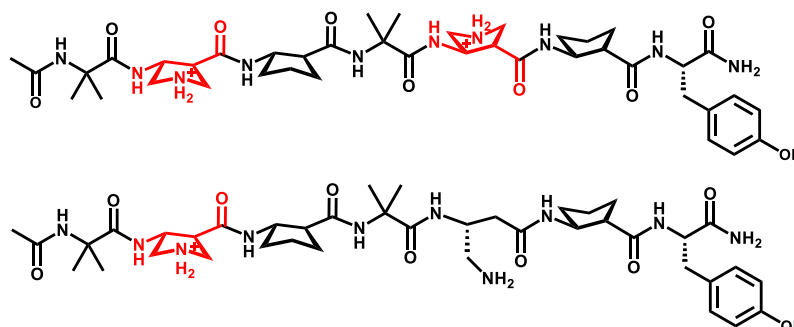
Figure 2. Structures of foldamers with antibiotic or catalytic activity containing the (3*S*, 4*R*)- or (3*R*, 4*S*)-APC building block, highlighted in red.

5.2 Results and Discussion

Over the years, members of our group carrying out the synthesis of protected APC, have encountered inconsistencies in yield and low yields of the final product. In this work, numerous key observations have resulted in a more reliable protocol. The updated synthetic procedure described below can provide more than 25 grams of protected APC within one week. While the synthetic route remains largely consistent with the initial report,[8] key procedural differences lead to an improved and more consistent overall yield. The synthetic route is summarized in figure 3.
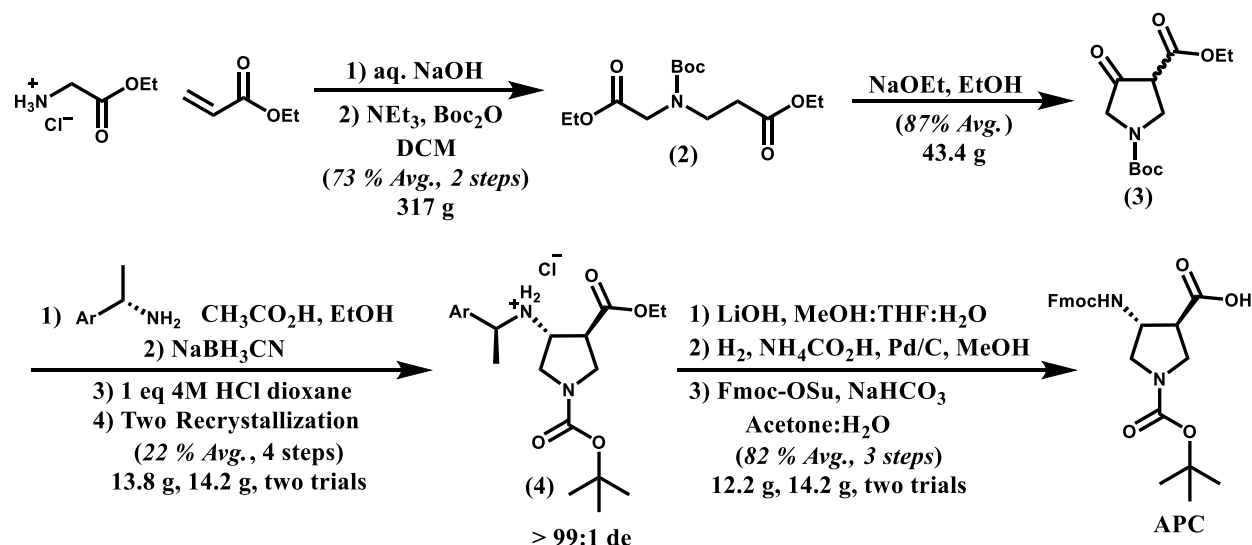
Figure 3. Synthetic route for protected **APC**. For full experimental protocols and procedures see the experimental section.

The route commences with the aza-Michael addition of glycine ethyl ester hydrochloride to ethyl acrylate, followed by boc-protection via with di-tert-butyl dicarbonate to yield 317 grams of diester **2** after simple extraction (73 %, from 1.43 mol glycine ethyl ester hydrochloride).[16,17] This two-step sequence takes < 48 hours and can be carried out routinely on hundreds of grams of starting material.[18] Size limitations of common laboratory glassware (i.e., it

is challenging to work with vessels larger than 2 L) make dividing intermediate **2** into portions

necessary prior to the Claisen-condensation that generates β-ketoester **3**.[19,20] Dry glassware is

critical for a high yield in this reaction; the glassware should be flame-dried. The sodium

ethoxide must be added to a vigorously stirring solution of **2** in ethanol to prevent clumping of

the base on the sides of the round bottom flask, which results in low yield. Compound **3** can be

isolated over three steps in high purity and yield with simple extractions (64 % yield). The

critical reductive amination involves initial imine/enamine formation between **3** and (*S*)-(-)-α-

methylbenzylamine. The imine is selectively reduced in the presence the ethyl ester with sodium

cyanoborohydride,[21] producing a mixture of four amine diastereomers. Column chromatography

of the crude reaction mixture is necessary to remove excess (*S*)-(-)-α-methylbenzylamine, which

appears on the baseline of the TLC plate (eluted with 9:1 DCM:MeOH).

We have found that failure to remove (*S*)-(-)-α-methylbenzylamine interferes with HCl

salt formation of the product mixture. Formation of the diastereomeric mixture of HCl salts in

the original publication occurs by slow addition of a 4 M HCl dioxane to the amine mixture in

ethyl acetate at 0° C.[8] However, we have observed that partial removal of the Boc protecting

group can occur under these conditions. As an alternative, we have found that HCl salt formation

occurs readily if 4 M HCl in dioxane is added slowly to a 0.1 M solution of the amine

diastereomers in diethyl ether at 0° C. Under these conditions, boc-deprotection has not been

observed over multiple trials. We have observed what appears to be an initiation period for HCl

salt formation. After the first ≈ 10 % of the 4 M HCl dioxane solution has been added dropwise

with vigorous stirring, it is important to wait for five minutes before more HCl solution is added.

Typically, this approach results in the formation of a white precipitate that seems to aid the

formation of further HCl salt. Addition of 4 M HCl dioxane rapidly, or omission of this waiting period, can cause diminished yields.

Upon complete addition of HCl solution, the thick white slurry was allowed to stir for an additional 10 minutes at 0° C, and then subjected to vacuum filtration. The crude white solid was recrystallized from acetonitrile. LC-MS analysis of the filtrate revealed that some of the desired diastereomer remained in this liquid. For this reason, the filtrate was concentrated via rotary evaporation, and the residue was recrystallized, resulting in additional diastereomerically pure **4**. LC-MS analysis again revealed a small amount of the desired diastereomer in the filtrate, and the concentration-recrystallization sequence was repeated, but no further HCl salt was obtained. A total of 14.2 grams of diastereomerically pure product was obtained. It should be noted that facile LC-MS analysis is of critical importance for two reasons: 1) LC-MS establishes the purity of **4** carried forward, and 2) LC-MS facilitates isolation of the maximum quantity of **4** is obtained after reductive amination.

Intermediate **4** is subjected to saponification with lithium hydroxide monohydrate in a three-solvent system. After the reaction is complete, as confirmed by TLC,[8] the base is quenched by addition of 1 eq 1 M aq. HCl. Prior to concentration, an excess of toluene (relative to the volume of 1 M aq. HCl that was used) should be added in order to ensure azeotropic removal of water. It is critical to thoroughly dry the crude saponification product prior to hydrogenation. Often rotary evaporation at 70° C for 45 minutes is sufficient, followed by pumping under high vacuum for 1-2 hours.

Hydrogenolytic removal of the α-methylbenzyl group generates the free amine. It is important for the hydrogenation step that Pd/C and ammonium formate are added to the crude saponification product prior to solvent addition. Once all solids have been combined, and the

round bottom flask has been purged with nitrogen, methanol can be safely added via cannula. (CAUTION: Addition of Pd/C to a round bottom flask containing methanol can result in sparking at the ground glass joint and ignition of the solvent/vapors.) Reflux of the solution for 24 hours is sufficient to ensure full removal of the α-methylbenzyl group, as confirmed via TLC. Caution must be taken during workup of the hydrogenation. Filtration of the reaction mixture through methanol-wetted celite, to removed Pd/C, should be accomplished while purging the aparatus with nitrogen. CAUTION: the celite pad must not be aspirated to dryness, which can result in ignition of the Pd/C. Concentration of the crude hydrogenation product yields a light pink oil, which can be carried forward to the final Fmoc-protection.

Protection of the free amine is accomplished with Fmoc-OSu under basic conditions. The purification of Fmoc-(Boc)APC-OH is reported by Lee et al. to occur via crystallization from *n*-heptane/ethyl acetate;[8] however, we have found this procedure to be irreproducible. Instead, the crude oil obtained after workup (see experimental section for full details) is dissolved in a minimal amount of ethyl acetate (just enough to decrease the viscosity of the oil and allow this material to be easily removed via pipette). The solution of crude product is added dropwise to vigorously stirring hexanes at 0°C, which results in the precipitation of a white/light tan solid. After the addition is complete, the precipitate is filtered and rinsed with portions of hexanes that had been pre-cooled to 0°C. After the precipitate has been dried via aspiration, the solid obtained typically forms a gum. To obtain an easily manipulated crystalline solid, the gum is dissolved in DCM and concentrated via rotary evaporation. The residue is then placed under high vacuum for a few hours, resulting in analytically pure Fmoc-(Boc)APC-OH. It should be noted, that this triturated procedure avoids tedious and time-consuming column chromatography of the final product, which can be accomplished using 7:3 hexanes: ethyl acetate + 3 % acetic acid. Not only

is the chromatographic separation nonideal, but also this approach requires azeotropic removal of acetic acid with toluene. If acetic acid remains in the final Fmoc-(Boc)APC-OH, this contaminant will cause failure in future solid-phase synthesis because the carboxylic acid will be activated and cause peptide acetylation. The trituration avoids any contact with acetic acid and is highly preferable to chromatography.

5.3 Conclusion

In conclusion, we report on critical procedural improvements relative to the original publication of Lee et al. on the synthesis of Fmoc-(Boc)APC-OH.[8] These improvements enable reproducible large-scale synthesis of enantiomerically pureFmoc-(Boc)APC-OH. The APC residue has been valuable in research efforts aimed at developing ligands for protein receptors, and APC has provided catalytic amine groups in foldamer-based catalysts. A facile, streamlined route to large quantities of Fmoc-(Boc)APC-OH is essential because this critical building block is not commercial available.

5.4 Experimental

5.4.1 Materials and Reagents

All solvents were obtained from Sigma-Aldrich. Glycine ethyl ester hydrochloride, di-tert-butyl decarbonate, (S)-(-)-alpha-methylbenzylamine, sodium cyanoborohydride, and *N*-(9-Fluorenylmethoxycarbonyloxy)succinimide were obtained from Chem-Impex International, Inc. Ethyl acrylate, sodium ethoxide, lithium hydroxide monohydrate, palladium on carbon, and sodium bicarbonate were obtained from Sigma-Aldrich. Filtered Millipore water was used in reactions requiring water. Chromatography was performed on silica gel (200-425 mesh) using standard techniques. Products were visualized by UV or Ninhydrin stain.

5.4.2 Instrumentation

Diastereomeric purity for the reductive amination step was assayed using a Waters Acquity Arc® LC-MS instrument. ^{1}H and ^{13}C NMR spectra were acquired on 400, and 500 MHz Bruker NMR instruments. NMR chemical shifts are reported in ppm and are referenced to tetramethylsilane (TMS, = 0.00 ppm) for ^{1}H NMR. For ^{13}C NMR, chemical shifts are reported in ppm and are referenced to the residual solvent peak for $CDCl_3$ (= 77.16 ppm). Coupling constants (*J*) are reported in Hz.

Instrument Acknowledgements

Bruker Advance III-400, NMR Spectrometer, NSF CHE-1048642 2010

Bruker Advance III-500, NMR Spectrometer, Generous gift from Paul J. Bender 2012

5.4.3 Synthetic Procedures
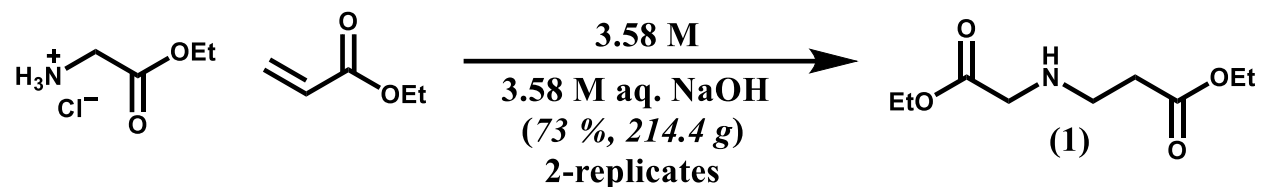
To a 2 L round bottom flask equipped with a stir bar was added 200 g of glycine ethyl ester

hydrochloride (1.43 mol) and 250 mL of Millipore water. Next, 150 mL of 9.55 M aqueous

sodium hydroxide was added, portion wise, to obtain a clear solution. Ethyl acrylate (1.46 mol,

155 mL) was then added dropwise, and the reaction mixture was allowed to stir at room

temperature for 24 hours. (Ethyl acrylate is a known carcinogen and quite pungent and should be

carefully handled within a fume hood).

After 24 hours, the reaction mixture was transferred to a separatory funnel and the organic layer

was separated. The organic layer was then washed with 1 M aqueous sodium hydroxide, and

brine, and dried over $MgSO_4$. The organic layer was then dried with magnesium sulfate, filtered,

and concentrated under vacuum. The light-yellow oil obtained (214.4 g, 74 %) was carried

forward without further purification.

1 is a known compound and our ^{1}H and ^{13}C spectra match those reported.[17]
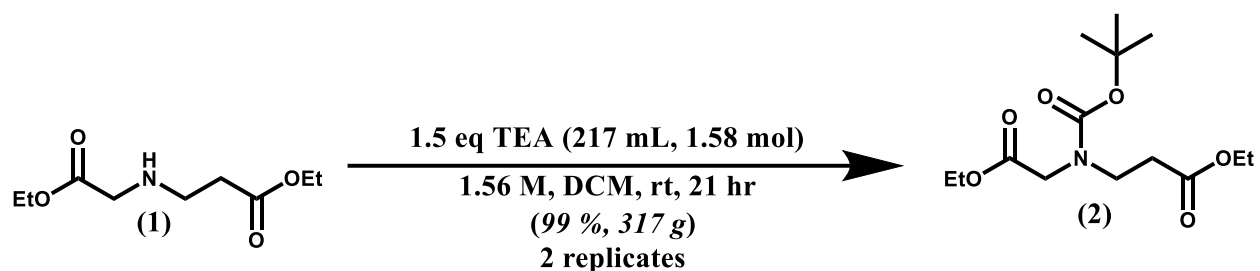
To a 2 L round bottom flask equipped with a stir bar was added 276.3 g boc anhydride (1.27 mol, 1.2 eq), followed by 467 mL DCM. In a separate flask, diester **2** was dissolved in 214 mL DCM and 214 mL triethylamine. The resulting diester solution was added dropwise to the round bottom flask containing boc anhydride over 20 minutes. (Caution: exotherm occurs, as well as gas generation (carbon dioxide). If the diester is added too fast, the dichloromethane solvent can boil over.) After complete addition of the diester, the reaction mixture was light yellow. After stirring at room temperature for 21 hours, a color change to dark brown occurred.

After stirring for 21 hours at room temperature, the reaction mixture was concentrated under vacuum. The crude oil was dissolved in 600 mL ethyl acetate and washed with 1 M aq. HCl (2X), and brine. The organic layer was then dried with magnesium sulfate, filtered, and concentrated under vacuum. **2** was obtained as a dark-brown oil (317 g, 99 %), and was carried forward without further purification.

2 is a known compound and our ^{1}H and ^{13}C spectra match those reported.[17]
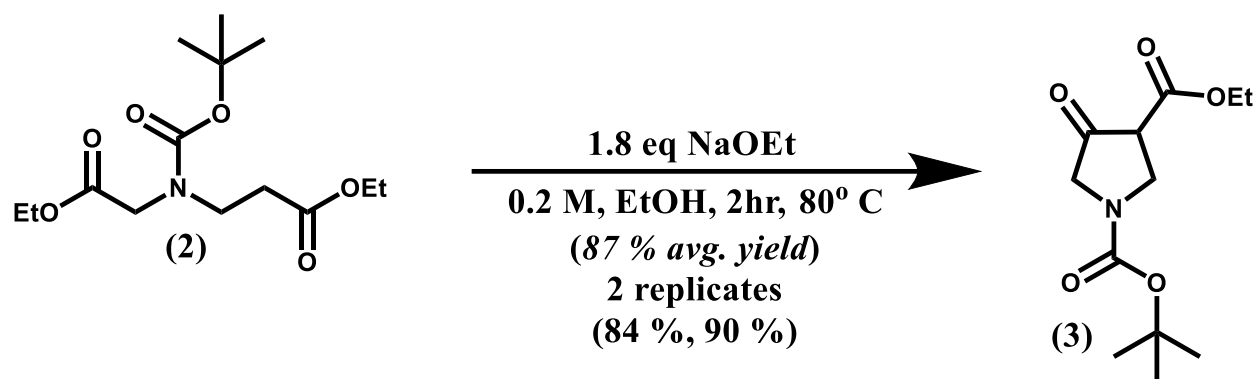
Note: Due to limitations in oil-bath capacity, 2 (from the previous step) cannot be carried forward in totality. Around 60 grams of 2 have routinely been carried forward.

To a flame dried 2 L round bottom flask equipped with a stir bar under a nitrogen atmosphere was added **1** (61 g, 0.201 mol) and 1 L of anhydrous ethanol. While this solution was vigorously stirring at room temperature, sodium ethoxide (24.6 g, 0.362 mol, 1.8 eq) was added portion wise. Addition of sodium ethoxide all at once, or without vigorous stirring can cause clumping of the base to the sides of the round bottom flask, resulting in poor yield. Following addition of sodium ethoxide, the round bottom flask was fitted with a reflux condenser and purged with nitrogen gas. The round bottom was then submerged in a preheated oil bath at 80° C – 95° C, and the reaction mixture was allowed to stir for 2 hours. For the two replicates of this reaction yields of 84 % and 90 % were obtained. For the reaction yielding 90 % product, the temperature was held at 80° C, while the reaction yielding 84 % product was allowed to reach 95° C.

After stirring at 80° C for two hours, the reaction mixture was removed from the oil bath and cooled to room temperature. After cooling to room temperature, acetic acid (0.362 mol, 20.7 mL, 1 eq) wad added dropwise to the reaction mixture while stirring. The reaction mixture was then concentrated under vacuum, and the crude residue was dissolved in 400 mL ethyl acetate. The organic layer was added to a separatory funnel and washed with 200 mL of 2 M NaH_2PO_4 (2X),

and brine. The organic layer was then dried with magnesium sulfate, filtered, and concentrated under vacuum, yielding 43.4 g **3** (84 %) as a dark brown oil. **3** was carried forward without further purification.

3 is a known compound and our ^{1}H and ^{13}C spectra match those reported.[18,19]
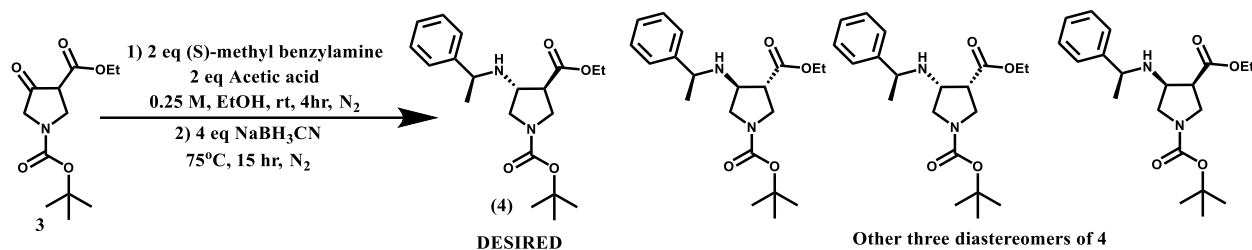
To a 2 L round bottom flask equipped with a stir bar was added **3** (43.4 g, 0.169 mol), and 676 mL of anhydrous ethanol. To the solution of **3** was then added (*S*)-(-)-alpha-methylbenzlamine (0.338 mol, 43 mL, 2 eq), followed by acetic acid (0.338 mol, 19.3 mL, 2 eq). The round bottom was sealed with a septum and the reaction mixture was purged with nitrogen and allowed to stir for 4 hours at room temperature.

After the mixture had stirred for 4 hours at room temperature, sodium cyanoborohydride (0.676 mol, 42.5 g, 4 eq) was added, and the round bottom was fitted with a reflux condenser, purged with nitrogen, and submerged in a preheated oil bath at 75°C. After stirring for 15 hours the reaction mixture was removed from the oil bath and allowed to cool to room temperature. The reaction mixture was then concentrated under vacuum. **Caution:** potential evolution of hydrogen cyanide gas (HCN). Reaction of sodium cyanoborohydride with acid can evolve hydrogen cyanide gas. The crude reaction mixture was then dissolved in 1 L of 50:50 diethyl ether: water and transferred to a separatory funnel. The organic layer was removed and the aqueous layer was re-extracted with diethyl ether (2X, 200 mL). The organic layers were combined, and washed with brine, dried over magnesium sulfate, filtered, and concentrated under vacuum, yielding 37.8 g (62 %) of a diastereomeric mixture of amines.

The crude diastereomeric mixture was then partially purified via column chromatography. The column is used to mainly to remove excess (*S*)-(-)-alpha-methylbenzylamine, while the diastereomers coelute using a mobile phase of 7:3 → 1:1 hexanes:ethyl acetate. Visualization of

the products via TLC is achieved by ninhydrin stain followed by heating for about 30 seconds. (*S*)-(-)-alpha-methylbenzylamine appears on the baseline of the TLC plate and is visualized by staining with ninhydrin and mild heating. The difference in time that it takes for the product diastereomers to be visualized versus methylbenzylamine is useful in determining separation of the two. After completion of the column, fractions containing the product diastereomers were concentrated under vacuum to yield 37.8 g (62 %) of a light yellow oil. **Note:** Multiple columns may be required if the crude material surpasses the amount of material the column can handle without bleeding through. For example, instead of running a column on 40 g of crude material, two 20 g columns can be run.

The light-yellow oil (37.8 g, 0.104 mol) was then dissolved in 1 L of anhydrous diethyl ether (0.1 M) and cooled to 0° C. Once the solution was cooled, a 4 M HCl solution in dioxane (26 mL, 0.104 mol, 1 eq) was added dropwise, while the amine solution was stirred vigorously. **Important:** Over several replicates, I have observed what appears to be an initiation period of HCl salt formation. Once about 10 % of the 4 M HCl solution has been added dropwise (2.6 mL), allow the solution to stir at 0° C for ten minutes before any more has been added. This results in the precipitation of HCl salt, which seems to aid in further precipitation. (If all the 4 M HCl solution is added at once, low yields of HCl salt formation have occurred, and there is a potential for boc-deprotection.) Once this ten-minute period has finished, the remaining 4 M HCl solution is added dropwise. Upon complete addition of the HCl solution, the white slurry was allowed to stir at 0° C for an additional ten minutes. The slurry was then filtered via vacuum aspiration to give a white powder, which was washed with two 100 mL portions of cold diethyl ether.

After the initial HCl salt had been aspirated to dryness, it was transferred to a 1 L Erlenmeyer flask equipped with a stir bar. 400 mL of acetonitrile was then added and brought to a boil while vigorously stirring on a hot plate. After the solid had fully dissolved, the solution was allowed to boil until precipitation occurred. Once precipitation occurred, a minimal amount of acetonitrile was added and the mixture was returned to a boil ensuring all of the solid had dissolved. The Erlenmeyer flask was removed from the hot plate and allowed to cool to room temperature. Within 15 minutes after removal from the hot plate, fine white needles began to form. The flask was left to sit for a total of 3 hours. After 3 hours, the white needles were filtered via vacuum aspiration and dried to give 12.8 g of product. The diastereopurity of this material was assayed via LC-MS to be > 99 % de. LC-MS analysis of the mother liquor from the first recrystallization revealed some of the desired diastereomer remained. The mother liquor was concentrated under vacuum and the recrystallization was repeated yielding 1.0 g of product (> 99 % de). Analysis of the mother liquor revealed a small portion of desired product still remained; however, a third recrystallization yielded no material. Overall, 13.8 g of diastereomerically pure HCl salt were obtained (21 % from **3**). A second replicate of the procedure gave a 24 % yield from **4**. (Average yield = 22 %).

4 and its **ent-4** are known compounds, and our ^{1}H and ^{13}C spectra match those reported.[8,21]

Experimental/Technical Differences from *J. Org. Chem.*, **2001**, *66*, 3597-3599:

Original: "*Upon addition of sodium cyanoborohydride the reaction mixture is heated for 14 hours.*"

Updated: Upon addition of sodium cyanoborohydride the reaction mixture is heated for 15 hours.

Original: Upon concentration of the diethyl ether extracts from the crude reaction mixture the following procedure was followed: "*The oil was applied to a plug of silica gel and washed with 2:1 hexane/ethyl acetate. The filtrate was concentrated to obtain a colorless oil. The oil was dissolved in ethyl acetate (250 mL), and 4 N HCl in dioxane (15.6 mL) was added dropwise at room temperature. The resulting solution was cooled to 0 °C and allowed to stand for 3 h at 0 °C. A precipitate formed during this time. The solid was filtered and washed two times with 100 mL portions of ethyl acetate to provide the desired material in 42% crude yield (98% de) from 1.*"

Updated: The initial separation of the product diastereomers from (*S*)-(-)-alpha-methylbenzylamine requires a full flash column, rather than a silica plug. Elution with 7:3 → 1:1 hexanes:ethyl acetate is used. In my hands, utilization of the original procedure for HCl salt formation has led to boc-deprotection of the diastereomeric products. When I have utilized the alternative diethyl ether procedure described above, I have never observed boc-deprotection.

Original: Regarding the recrystallization of diastereomerically pure HCl salt, the original procedure is described as: "*This crude product could be purified by recrystallization from acetonitrile. The solid was suspended in acetonitrile (200 mL) and heated to reflux for 1 h. The mixture was then cooled to 0 °C for 3 h. The resulting precipitate was isolated by filtration and washed two times with 30 mL portions of acetonitrile. The solid was further dried under vacuum to give 9.4 g of 2 as a white crystalline solid (99.0% de, 38% yield from 1...*"

Updated: As described in detail above, purification of the diastereomeric mixture of HCl salts is achieved through two recrystallizations yielding an average of 22 % **4**. In my hands I have never been able to reproduce the originally reported 38 % yield. Additionally, as described above, the product is cooled to room temperature, not 0° C.

4 and its enantiomer) are known compounds, and our ^{1}H and ^{13}C spectra match those reported.[8]

Light yellow reaction mixture after heating reaction mixture with sodium cyanoborohydride for 15 hours at 75° C.

Flash column packed with silica utilized for removal of (*S*)-(-)-alpha-methylbenzylamine from the product amine diastereomeric mixture.

A replicate of the flash column utilized for removal of (*S*)-(-)-alpha-methylbenzylamine from the product amine diastereomeric mixture, during the separation. 150 mL fractions were taken.
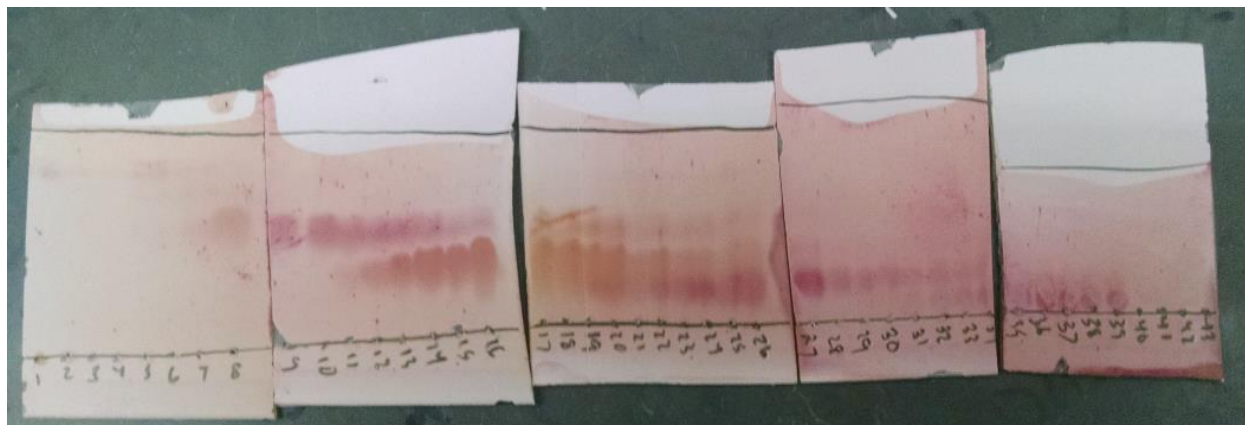
TLC plates from depicting each fraction from flash column seen in previous image. Fractions 7-40 were concentrated under vacuum. Faint spots in 1-6 at top of TLC plate are not combined. (*S*)-(-)-alpha-methylbenzylamine was easily separated from product diastereomers and eluted sometime after fraction 43.
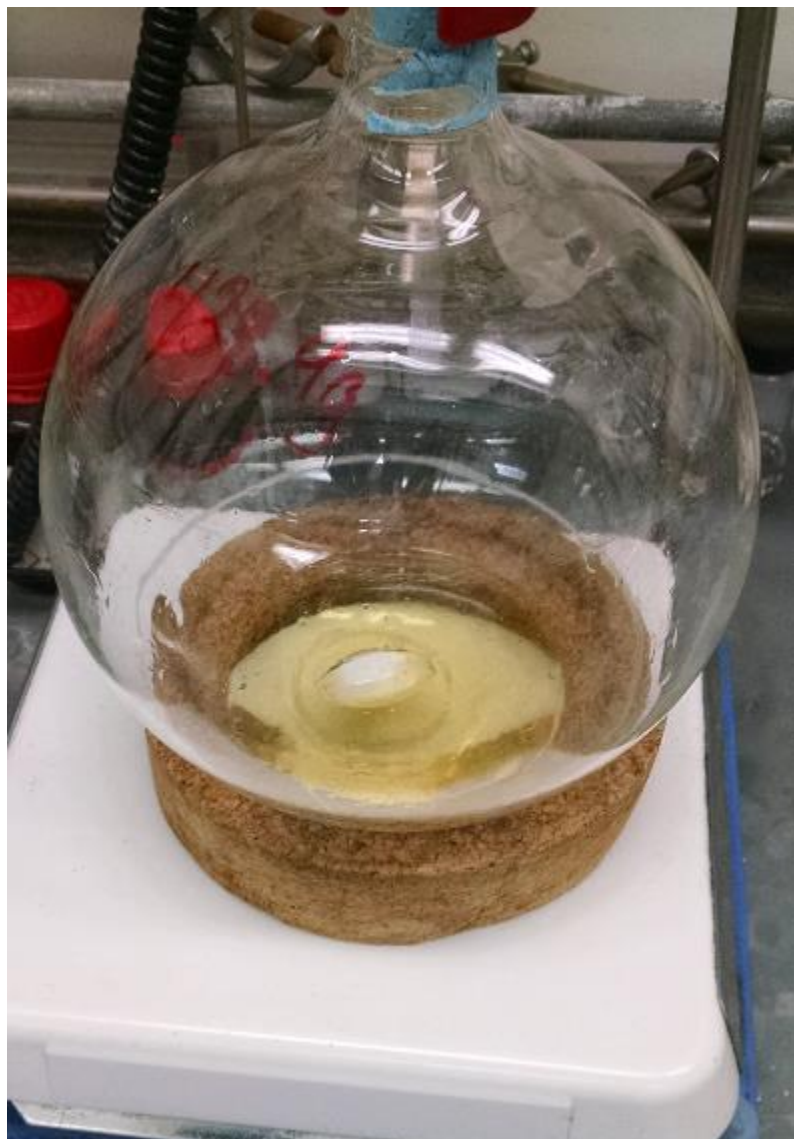
Crude light-yellow oil of **4 + diastereomers** (all 4 amine diastereomers) obtained after

concentrating fractions 7-40 of reductive amination flash column.

0.1 M solution of **4 + diastereomers** from column in 0° C, diethyl ether, on stir plate

(background), and syringe of 4 M HCl solution in dioxane to be added dropwise

(foreground).

Initial formation of HCl salt during ten-minute period after about 10 % of 4 M HCl dioxane
solution has been added. The cloudy slurry often takes ten minutes to form after initial addition
of the first 10 % of 4 M HCl dioxane solution.

HCl salt precipitated after complete addition of 4 M HCl dioxane solution.

Fritted filter used for filtration of HCl salt from diethyl ether:dioxane solution, equipped to an Erlenmeyer flask, connected to a vacuum aspirator. Use of a clamp to secure the flask is recommended.
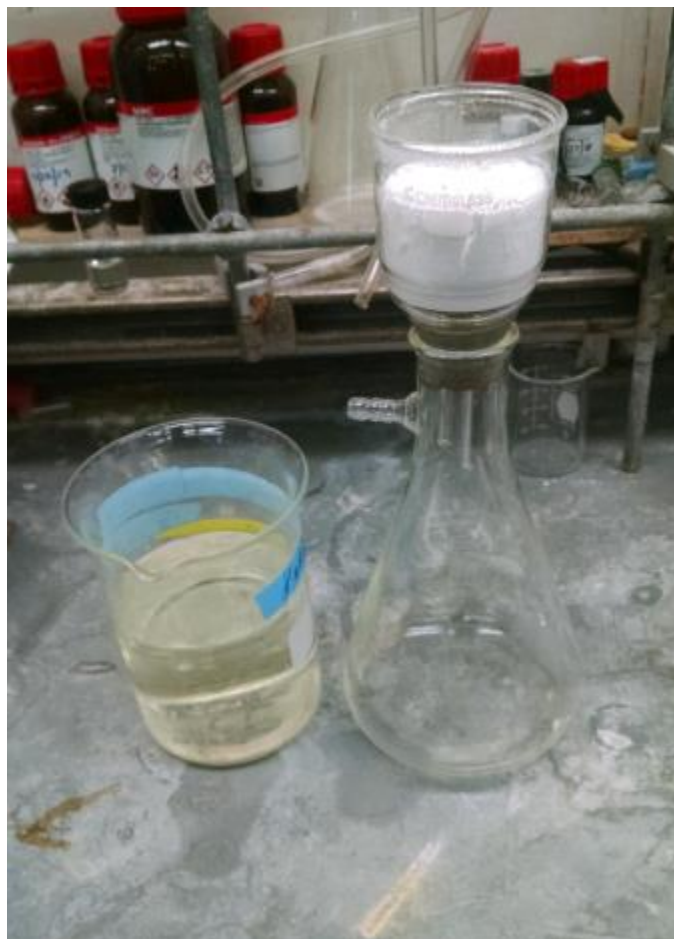
Diethyl ether and dioxane solution after filtration of HCl salt (Left). Diastereomeric mixture of

HCl salt after filtration and vacuum aspiration (right).

Powder of diastereomeric mixture of HCl salts prior to recrystallization (granular appearance).
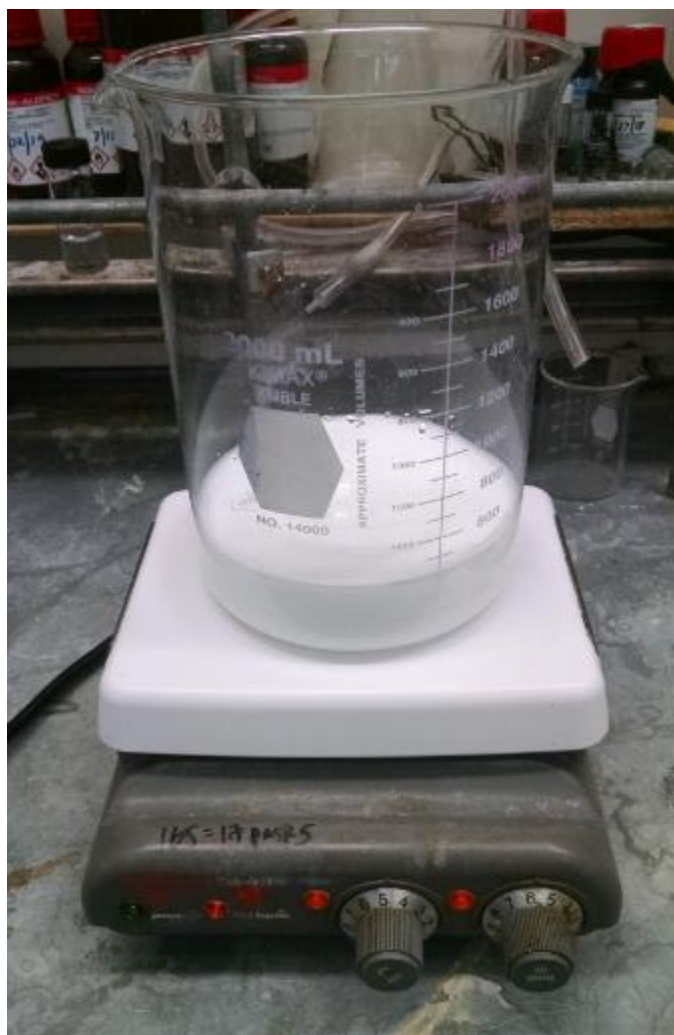
Diastereomeric HCl salts as a slurry in acetonitrile prior to boiling (Insoluble, white slurry).

Diastereomeric HCl salts partially solubilized as acetonitrile is heated (cloudy solution).
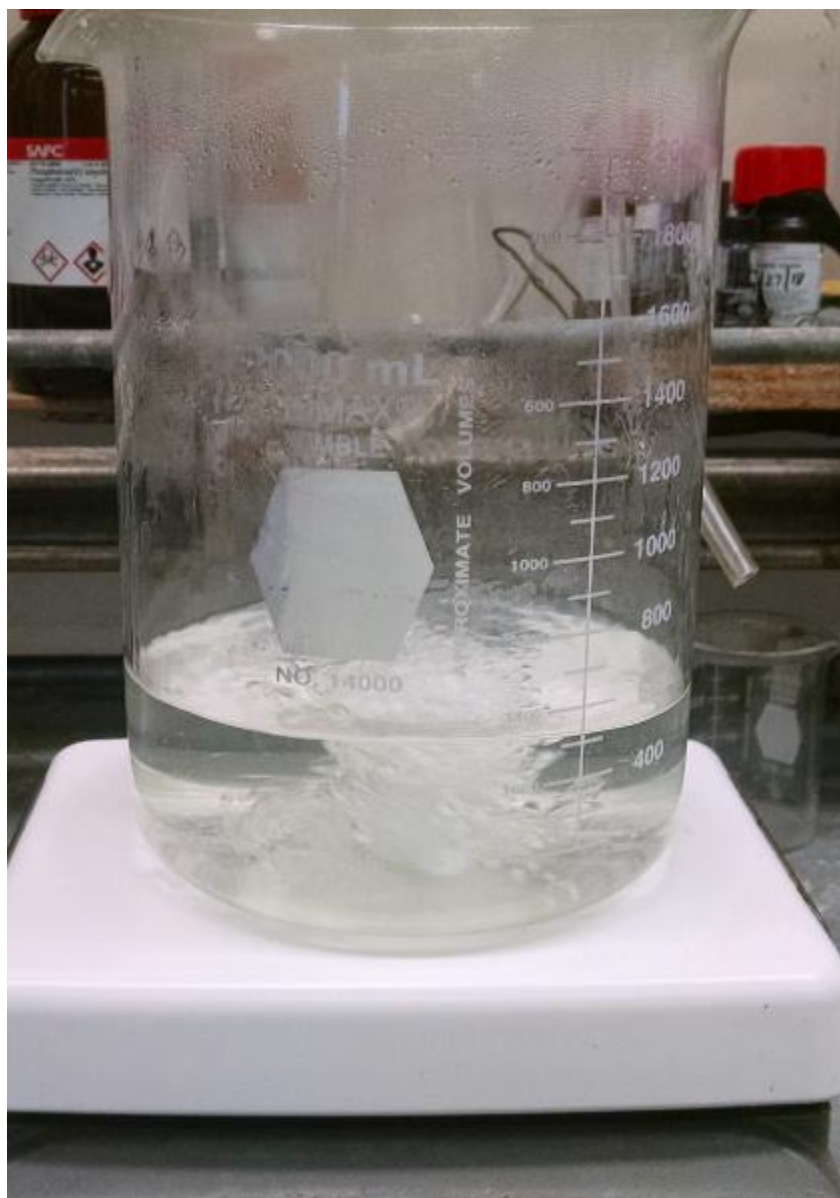
Diastereomeric HCl salts fully dissolved in boiling acetonitrile, while vigorously stirring. Once this clear solution is obtained, the beaker is removed from the hot plate and allowed to cool to room temperature.

Acetonitrile solution of diastereomeric HCl salts less than one minute after removal from hot plate (no crystals).

Top down view of diastereomerically pure **4** crystallizing out of the cooling acetonitrile solution (about 10 minutes after removal from hot plate). They will appear as fine white needles that clump into plates.
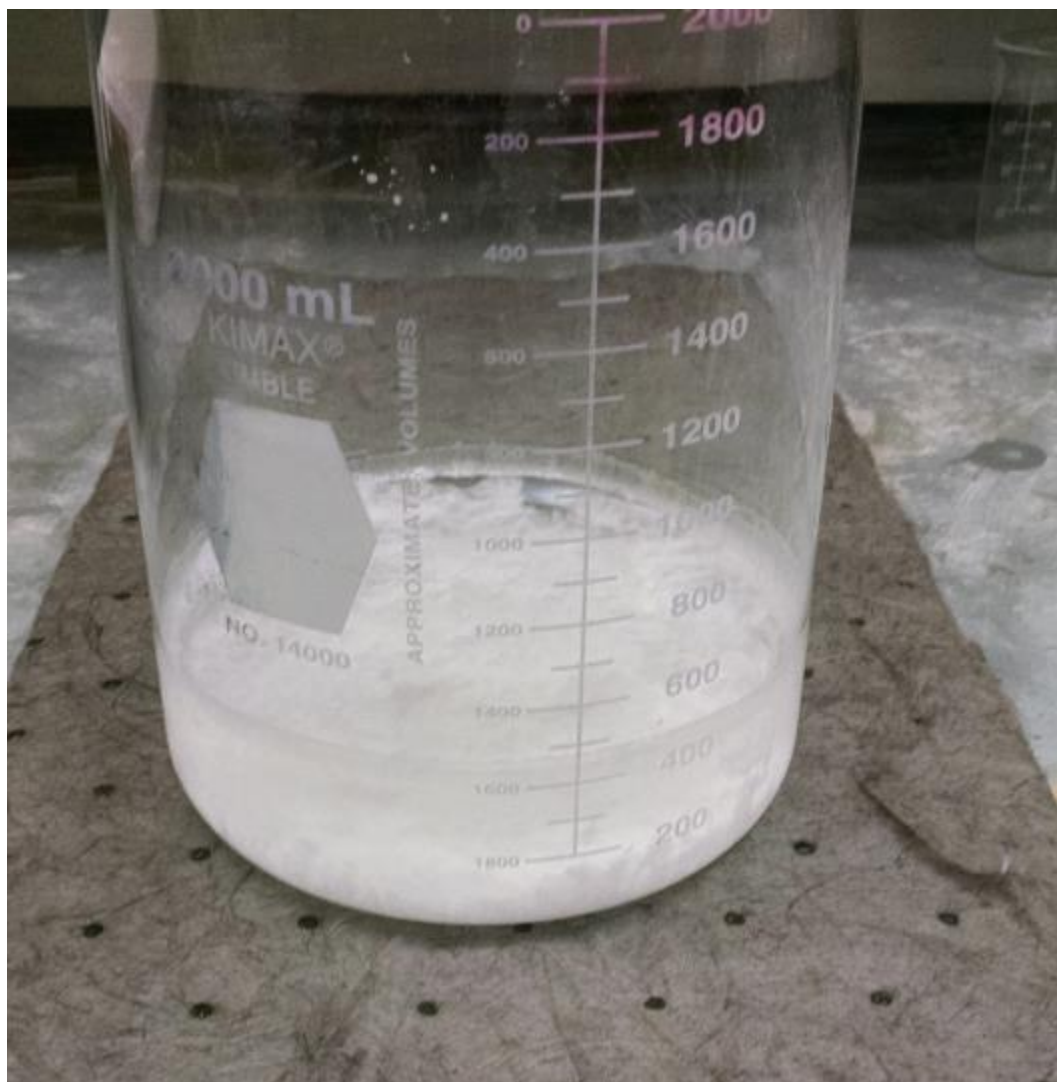
Diastereomerically pure **4** after crystallizing out of the acetonitrile solution upon cooling to room temperature over three hours. **4** appears as fine white needles.
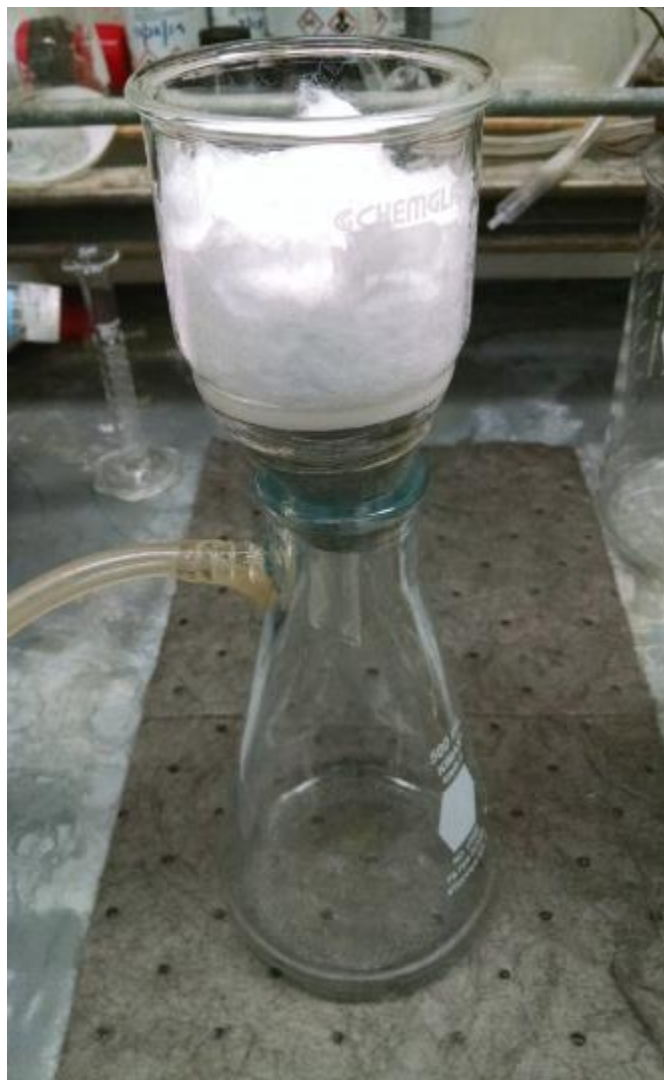
Diastereomerically pure **4** after filtration of acetonitrile mother liquor. Use of a clamp to secure the flask is recommended.
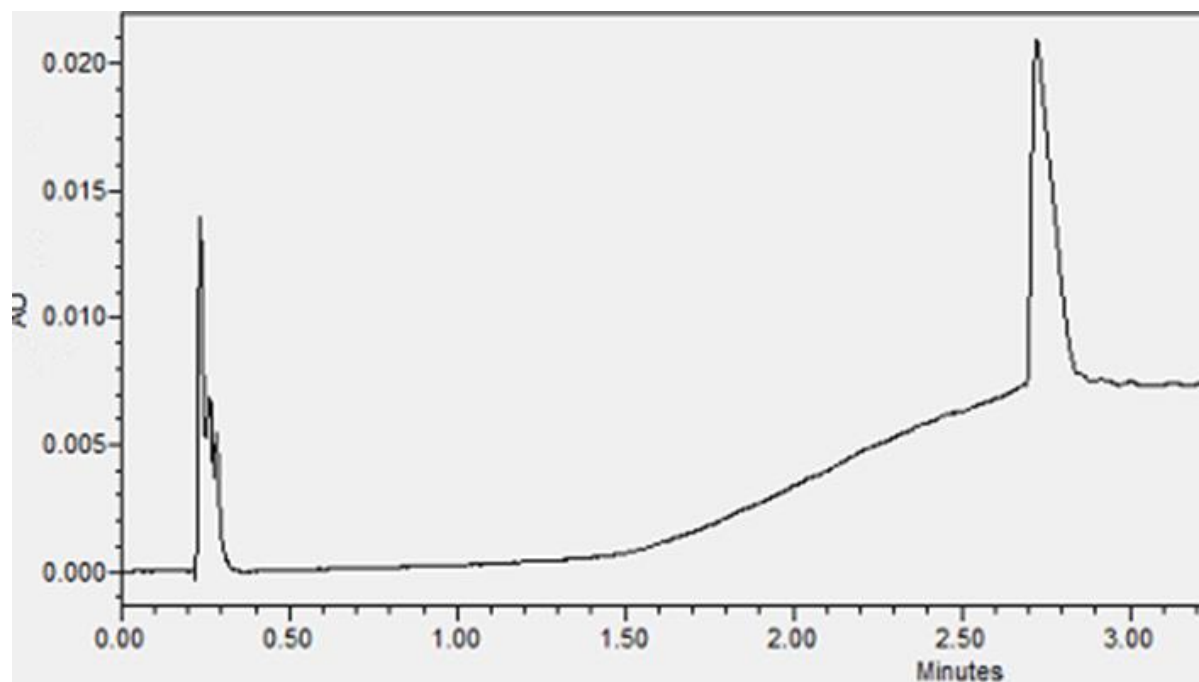
Zoom in of the LC-MS trace for analysis of the diastereomerically pure HCl salt after first recrystallization (254 nm channel). The LC-MS method for analysis of **4** and other diastereomers is: 10-95 % B over 4 minutes, A = water + 0.1 % formic acid, B = acetonitrile + 0.1 % formic acid. 0.75 mL/min, C18 5 cm, XBridge column.
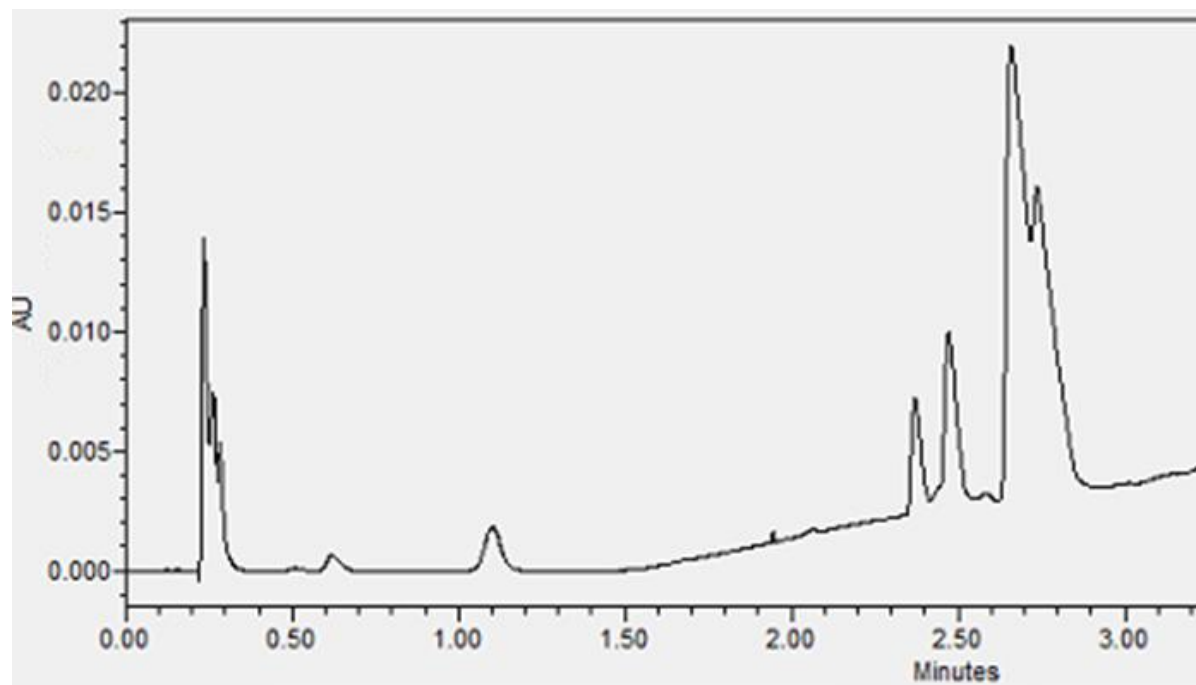
Zoom in of LC-MS trace of mother liquor after the first recrystallization. 4 diastereomers are observed, including the desired product (254 nm channel).
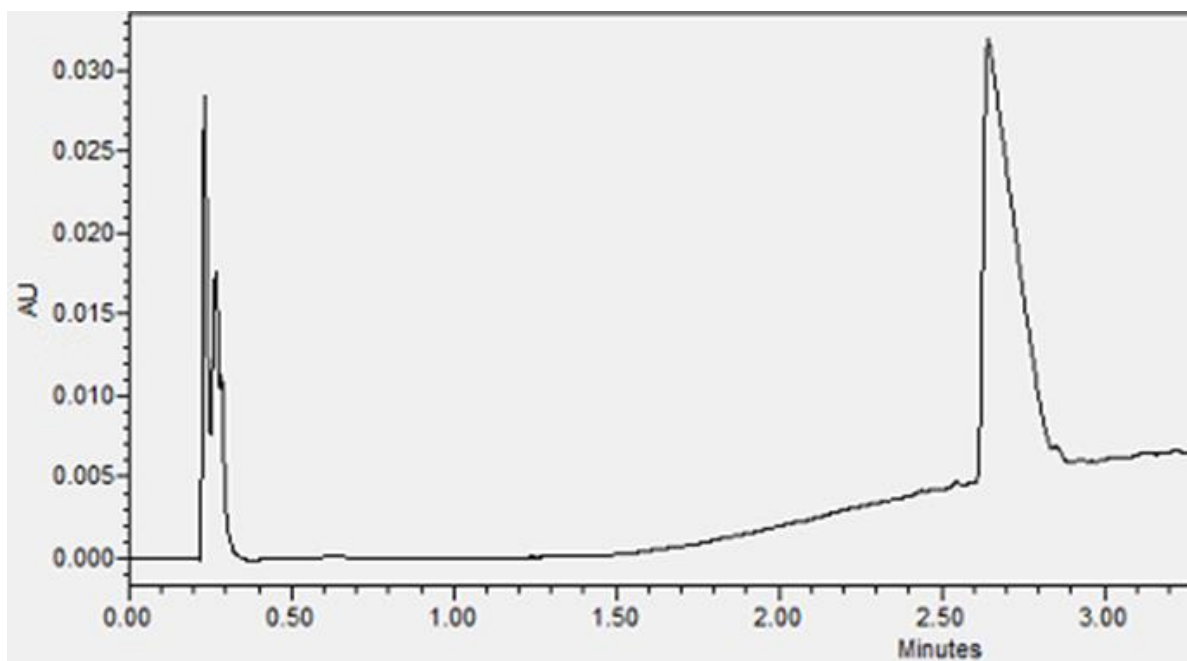
Zoom in of LC-MS trace of diastereomerically pure **4** after second recrystallization (254 nm channel).
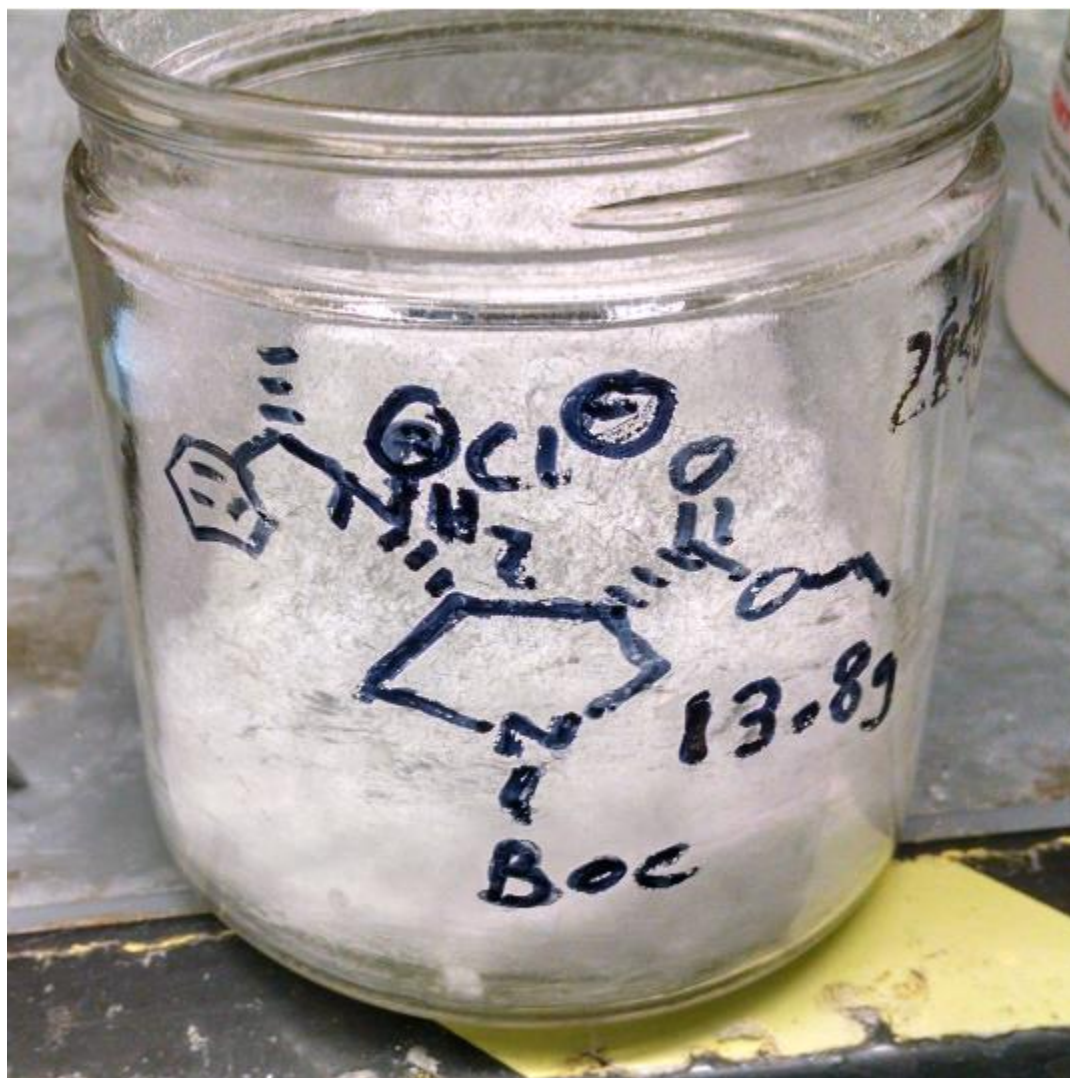
13.8 g of **4** obtained after two recrystallizations.
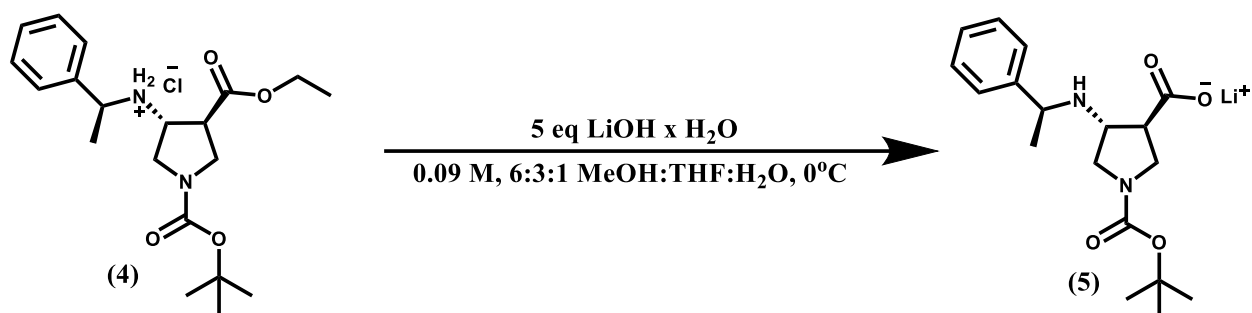
To a 1 L round bottom flask equipped with a stir bar was added 13.7 g (0.0343 mol) of **4**, followed by 229 mL methanol, 114 mL THF, and 38 mL Millipore water (0.09 M overall, 6:3:1 MeOH:THF:Water). The solution was then cooled to $0°$ C. Once the solution had cooled, lithium hydroxide monohydrate (0.172 mol, 7.22 g, 5 eq) was added and the reaction mixture was stirred at $0°$ C for 4 hours.

After the mixture had stirred for 4 hours, 1 M aqueous HCl was added (0.172 mol, 172 mL, 1 eq), along with 200 mL toluene. The reaction mixture was concentrated under vacuum, heating to $75°$ C. After all solvent had been removed, the white solid obtained was pumped on the high vacuum for a few hours to ensure complete dryness. The crude saponified product, **5** was carried forward without purification.

Experimental/Technical Differences from *J. Org. Chem.*, **2001**, *66*, 3597-3599:

Original: Reaction mixture stirred at $0°$ C for 3 hours.

Updated: Reaction mixture stirred at $0°$ C for 4 hours.

Original: Regarding reaction mixture concentration the original procedure is described as "*The mixture was stirred at 0 °C for 3 h. Aqueous HCl (1 N, 18 mL) was added at 0 °C. The solvent was then removed on a vacuum rotary evaporator to give a white solid…*"

Updated: After quenching the reaction mixture with 1 M HCl, toluene is added as well to allow for azeotropic removal of water. This eliminated the need for a high-vacuum rotary evaporator.
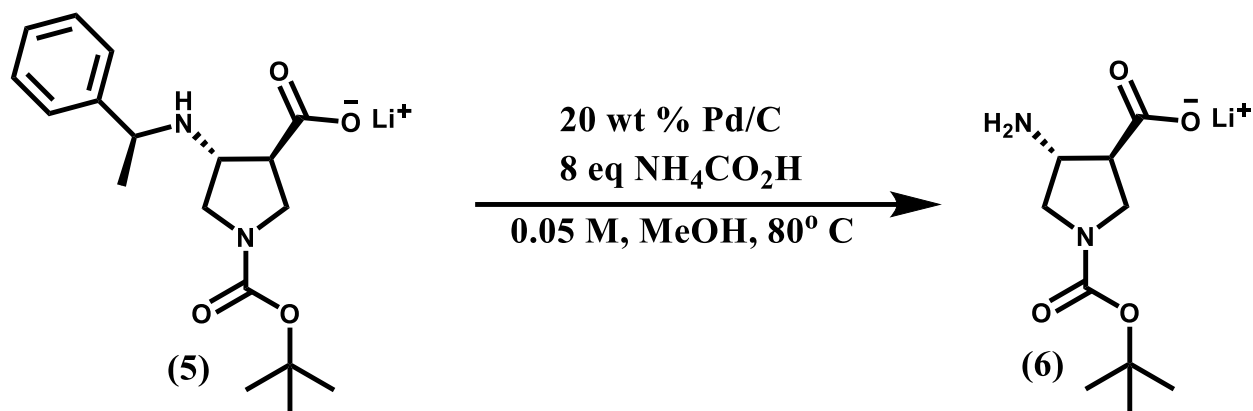
To a 2 L round bottom containing the saponified product was added a stir bar. Next, Pd/C (2.74 g, 20 wt % calculated from the original 13.7 g of HCl salt), and ammonium formate (0.274 mol, 17.3 g, 8 eq) were added. The round bottom was sealed with a septum and purged with nitrogen gas. Next, 686 mL of methanol was added via cannula. The round bottom flask was fitted with a reflux condenser and purged with nitrogen gas, and then submerged in a preheated oil bath at 80° C. The reaction mixture was allowed to reflux for 24 hours.

After the mixture had refluxed for 24 hours, the round bottom flask was removed from the oil bath and allowed to cool to room temperature. During the cooling period, a fritted filter was packed with methanol-wetted celite and on a Erlenmeyer flask with a side arm going to a vacuum aspirator. The setup was placed under a nitrogen gas line to purge any atmospheric oxygen. Once cooled, the contents of the reaction flask were carefully filtered over the celtite plug. The round bottom flask was washed with 300 mL of additional methanol and passed through the celite plug. The filtrate was concentrated under vacuum, yielding a light pink oil. The pink oil was carried forward without further purification. Note: If celite is not wet-packed on the filter, upon pouring the reaction mixture onto the plug, Pd/C may bleed through resulting in a grey-black oil. If this occurs, the reaction mixture must be re-filtered.

Experimental/Technical Differences from *J. Org. Chem.*, **2001**, *66*, 3597-3599:

Original: Reaction setup for hydrogenation of the crude product obtained via saponification is described as "*The white solid was dissolved in 150 mL of 95% ethanol in a hydrogenation flask. Pd-C (10%, 1.1 g) was added. The resulting mixture was shaken under H_2 (45 psi) for 24 h.*"

Updated: To avoid using a pressurized reaction vessel, which requires special glassware and added risk, the updated procedure as described above, utilizes ammonium formate, which produces hydrogen gas in situ. The reaction proceeds at atmospheric pressure. Methanol is used instead of ethanol as the reaction solvent in the updated procedure.

Crude saponification product **5**, ammonium formate, and Pd/C in a 2 L round bottom equipped with a stir bar, with MeOH being transferred in via cannula.
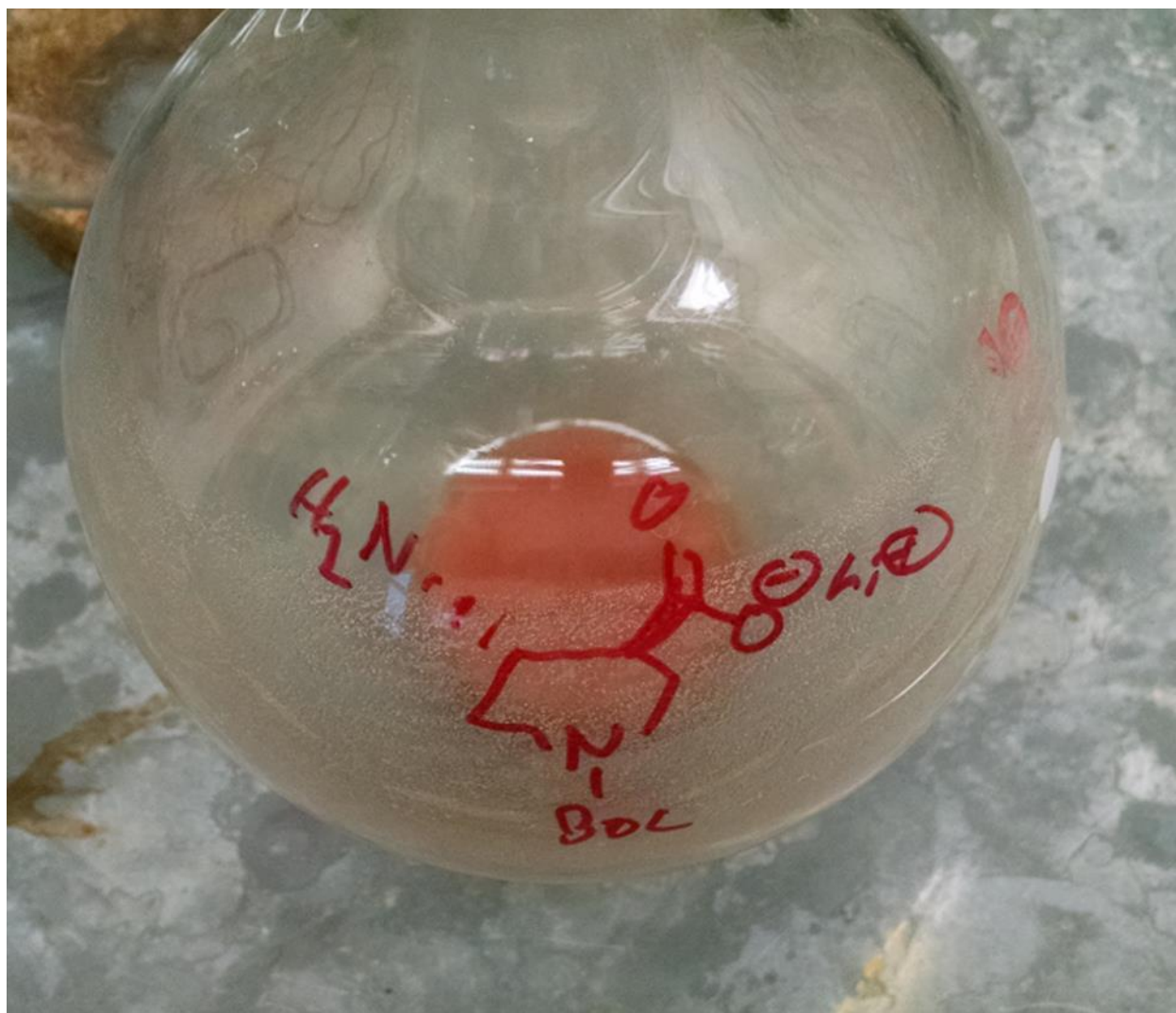
Crude light-pink oil, **6** obtained after filtration of hydrogenation reaction mixture through a celite plug with methanol, followed by concentration under vacuum.
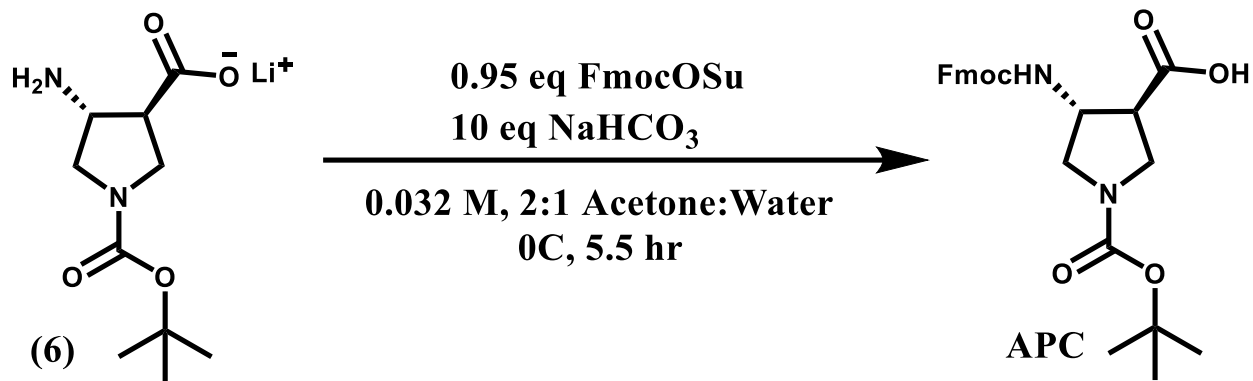
To a 2 L round bottom flask was added the crude oil from the hydrogenation, 707 mL acetone, and 353 mL of water. The solution was then cooled to 0° C. Sodium bicarbonate (0.343 mol, 10 eq, 28.83 g) and Fmoc-OSu (0.0326 mol, 0.95 eq, 11 g) were then added all at once. (Note: The equivalents of sodium bicarbonate and Fmoc-OSu are calculated based on the mole amount of **4** used for the saponification.) The resulting slurry was vigorously stirred for 5.5 hours at 0° C. Upon reaction completion, as monitored by TLC (9:1 DCM:MeOH), the reaction mixture was concentrated to $\approx$ 353 mL (acetone removed) under vacuum. The reaction mixture was transferred to a separatory funnel, rinsing with 200 mL water. The aqueous layer was washed with diethyl ether (2 X, 300 mL). After the ether wash, the aqueous layer was transferred to a 2L beaker equipped with a stir bar. While the mixture was vigorously stirring, aqueous 1 M HCl was slowly added until pH 4 was reached (dark red on litmus paper). (Note: evolution of CO_2 occurs through sodium bicarbonate quenching; make sure to not add 1 M HCl too rapidly, which can cause the reaction mixture to overflow the beaker.) As the aqueous layer was acidified, the precipitation of a tan solid occured. To allow easy monitoring of pH, ethyl acetate can be added to solubilize the precipitate. Once the aqueous layer reached pH 4, 400 mL of additional ethyl acetate was added, and the biphasic mixture was transferred to a separatory funnel. (Note: do not

allow the residue to sit in pH 4 for an extended period of time, as boc-deprotection may occur). The ethyl acetate layer was removed, and the aqueous layer was again extracted with ethyl acetate (2 X, 250 mL). The organic layers were then combined and dried with magnesium sulfate, filtered, and concentrated under vacuum to obtain a light brown oil.

The light brown oil was dissolved in a minimal amount of ethyl acetate (just enough so that the resulting solution could easily be taken up in a Pasteur pipette). To a 2 L beaker, equipped with a stir bar was added 1 L of hexanes, and the beaker was cooled to 0° C in an ice bath. The ethyl acetate solution was then added dropwise to the cooled hexanes while stirring rapidly. As the ethyl acetate was added, a white/tan solid precipitated o. Upon complete addition of the ethyl acetate solution, the solid was filtered and washed with 100 mL of cold hexanes. Upon drying, the solid often turned to a gum. This gum was dissolved in dichloromethane, and the solution was transferred to a round bottom flask. The solution was then concentrated under vacuum. The sequence of adding dichloromethane and then concentrating under vacuum was repeated (2X). The round bottom flask was then pumped on the high vacuum, resulting in removal of residual dichloromethane to leave a white/tan foamy solid. After pumping for 2 hours, the foam was crushed into an easily workable powder of pure **APC** (12.2 g, 79 % over 3 steps). A second replicate of the saponification-hydrogenation-Fmoc protection procedure resulted in pure **APC** (14.2 g, 84 % over 3 steps). Average yield = 82 %. [***NOTE: The phrase "analytically pure" means that the purity is established via elemental analysis, which is not true here.***]

APC (and its enantiomer) is a known compound and our ^{1}H and ^{13}C spectra match those reported.[8]

Experimental/Technical Differences from *J. Org. Chem.*, **2001**, *66*, 3597-3599:

Original: For purification of the **APC**, the original procedure is described as "*The crude product was purified by crystallization from n-heptane/ethyl acetate…*"

Updated: As described above, a trituration procedure with the crude product involving 0° C hexanes is utilized.

Original: The original procedure reports the isolation of 1.13 g of **ent-APC**, in 72 % yield over the final three steps.

Updated: Over two replicates, 26.4 g (average of 13.2 g, 82 % average yield over the final three steps) of **APC** was obtained.
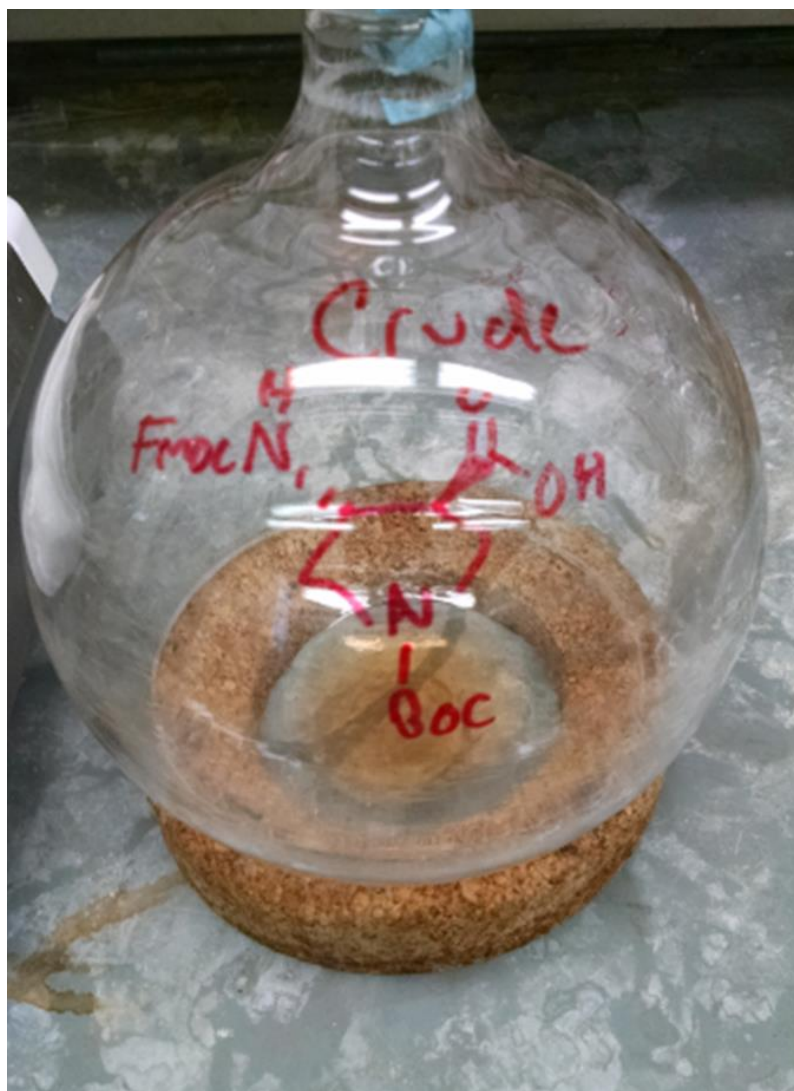
Crude light-brown oil obtained after workup of Fmoc-protection, prior to trituration.
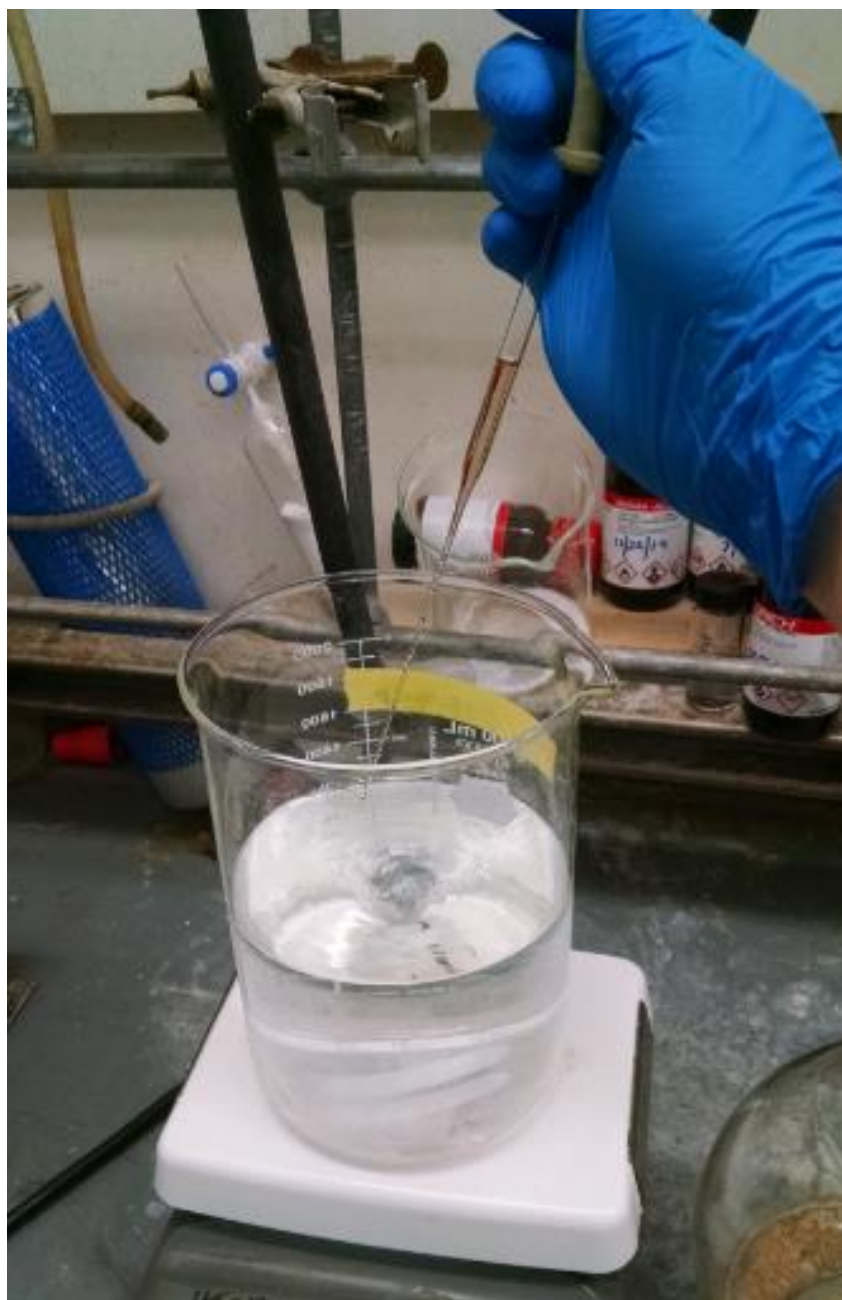
Ethyl acetate solution of crude **APC** added dropwise via Pasteur pipette to a 2 L beaker equipped with a stir bar, containing 1 L of 0º C hexanes.

After complete addition of the ethyl acetate layer containing crude **APC**, a white/tan precipitate appears.

Vacuum filtration of the precipitated **APC**. Use of a clamp to secure the flask is recommended.

White/tan gum obtained after filtration.
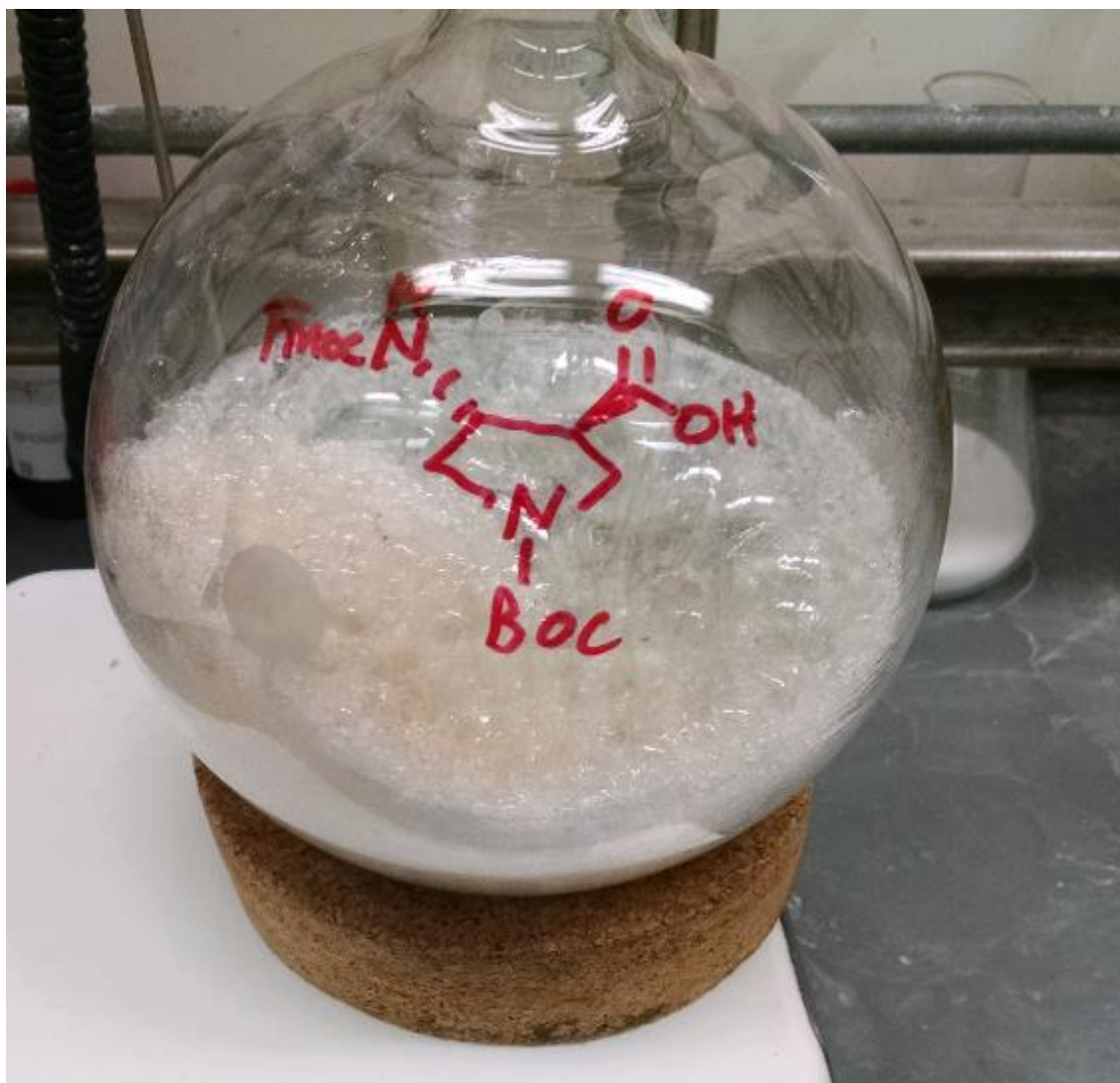
Pure **APC**, obtained after dissolving the gum in dichloromethane, concentrating under vacuum (3 X), and subsequently pumping on high vacuum.
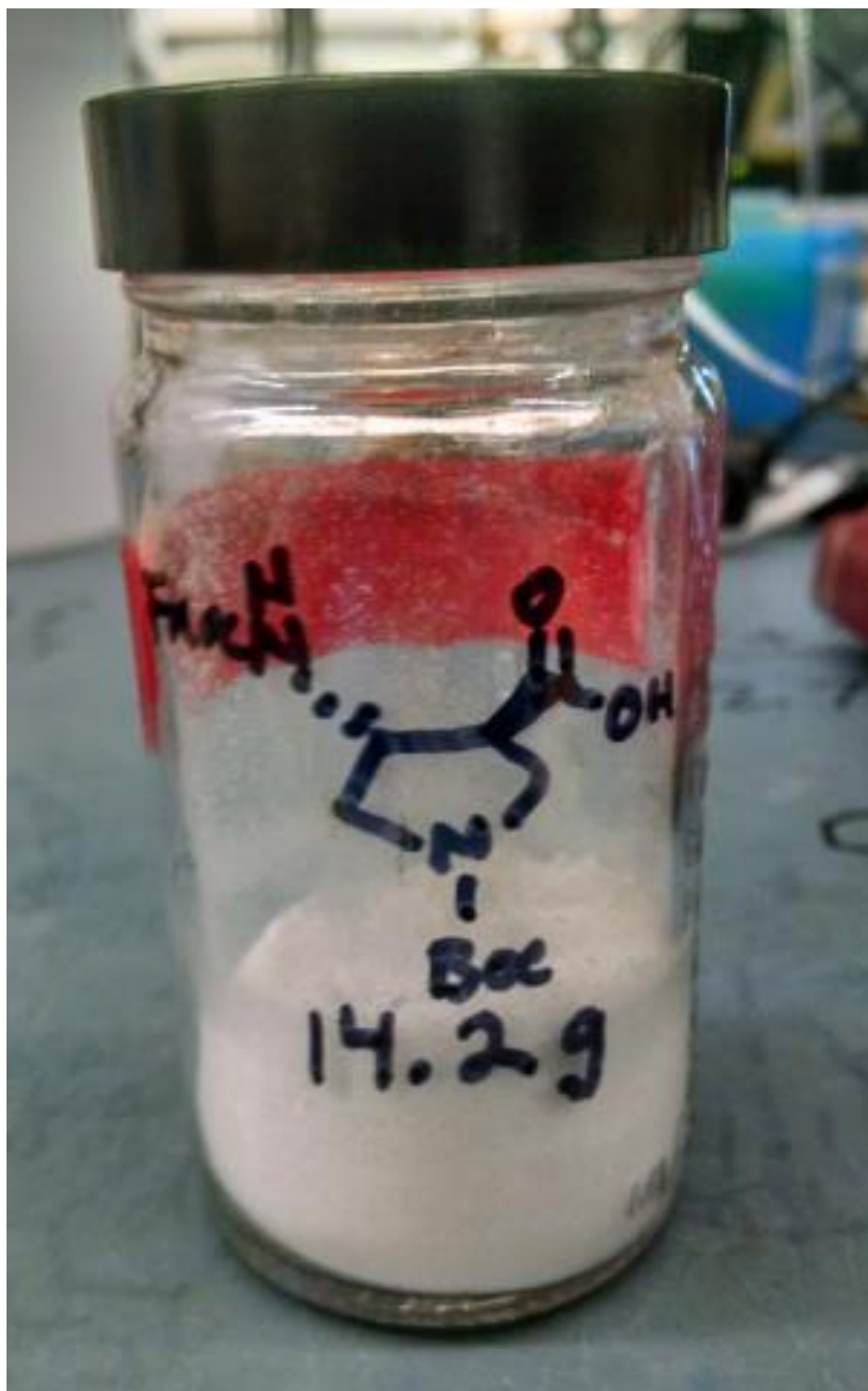
14.2 grams of pure **APC** after white/tan foam was crushed into a fine powder.

5.5 References

1. Gellman, S.H.; *Acc. Chem. Res.*, **1998**, *31*, 173-180.

2. Hecht, S.; Huc, I. *Foldamers: Structure, Properties, and Applications*, Wiley-VCH, Weinheim, **2007**, pp.1-435.

3. Hill, D. J.; Mio, M. J.; Prince, R. B.; Hughes, T. S.; Moore, J. S. *Chem. Rev.* **2001**, *101*, 3893-4011.

4. Guichard, D.; Huc, I. *Chem. Commun.* **2011**, *47*, 5933-5941.

5. Martinek, T. A.; Fulop, F. *Chem. Soc. Rev.* **2012**, *41*, 687-702.

6. Cheng, R. P.; Gellman, S. H.; DeGrado, W. F. *Chem. Rev.* **2011**, *101*, 3219-3252.

7. a) Appella, D. H.; Christianson, L. A.; Karle, I. L.; Powell, D. R.; Gellman, S. H. *J. Am. Chem. Soc.* **1996**, *118*, 13071-13072. b) Seebach, D.; Overhand, M.; Kuhnle, F. N. M.; Martinoni, B.; Oberer, L.; Hommel, U.; Widmer, H. *Helv. Chim. Acta.*, **1996**, 79, 913-941. c) Appella, D. H.; Christianson, L. A.; Klein, D. A.; Powell, D. R.; Huang, X.; Barchi Jr., J. J.; Gellman, S. H. *Nature*, **1997**, 387, 381-384 d) Schmitt, M. A.; Choi, S. H.; Guzei, I. A.; Gellman, S. H. *J. Am. Chem. Soc.*, **2006**, 128, 4538-4539. e) Choi, S. H.; Guzei, I. A.; Spencer, L.; Gellman, S. H. *J. Am. Chem. Soc.*, **2009**, 131, 2917-2924. f) Guo, L.; Chi, Y.; Almeida, A. M.; Guzei, I. A.; Parker, B. K.; Gellman, S. H. *J. Am. Chem. Soc.*, 2009, 131, 16018-16020. g) Shin, H. Y.; Gellman, S. H. *J. Am. Chem. Soc.*, **2018**, 140, 1394-1400. f) Fisher, B. F.; Gellman, S. H. *J. Am. Chem. Soc.*, **2016**, 138, 10766-10769. g) Giuliano, M. W.; Maynard, S. J.; Almeida, A. M.; Guo, L.; Guzei, I. A.; Spencer, L. C.; Gellman, S. H. *J. Am. Chem. Soc.*, **2014**, 136, 15046-15053. h) Shin, Y. H.; Mortenson, D. E.; Satyshur, K. A.; Forest, K. T.; Gellman, S. H. *J.*

Am. Chem. Soc., **2013**, 135, 8149-8152. i) Guo, L.; Zhang, W.; Reidenbach, A.; Giuliano, M. W.; Guzei, I. A.; Spencer, L. C.; Gellman, S. H. *Angew. Chem. Int. Ed.*, **2011**, 50, 5843-5846. j) Fisher, B. F.; Guo, L.; Dolinar, B. S.; Guzei, I. A.; Gellman, S. H. *J. Am. Chem. Soc.*, **2015**, 137, 6484-6487. k) Guo, L.; Almeida, A. M.; Zhang, W.; Reidenbach, A. G.; Choi, S. H.; Guzei, I. A.; Gellman, S. H. *J. Am. Chem. Soc.*, **2010**, 132, 7868-7869.

8. Lee, H.S.; LePlae, P. R.; Porter, E. A.; Gellman, S. H. *J. Org. Chem.*, **2001**, *66*, 3597-3599.

9. a) Appella, D. H.; Barchi, Jr. J. J.; Durell, S. R.; Gellman, S. H. *J. Am. Chem. Soc.*, **1999**, *121*, 2309-2310. b) Wang, X.; Espinosa, J. F.; Gellman, S. H. *J. Am. Chem. Soc.*, **2000**, *122*, 4821-4822.

10. Porter, E. A.; Wang, X.; Lee, H- S.; Weisblum, B.; Gellman, S. H. *Nature*, **2000**, *404*, 565.

11. Hager, M. V.; Johnson, L. M.; Wooten, D.; Sexton, P. M.; Gellman, S. H. *J. Am. Chem. Soc.*, **2016**, *138*, 14970-14979.

12. Girvin, Z. C.; Gellman, S. H. *J. Am. Chem. Soc.*, **2018**, *140*, 12476-12483.

13. Girvin, Z. C.; Andrews, M. K.; Liu, X.; Gellman, S. H. *Science*, **2019**, *366*, 1528-1531.

14. A Scifinder® structure search of **X** comes back with prices of: $2130 for 0.5 g from Combi-Blocks catalog, and $3564/gram from Matrix Scientific.

15. Newhouse, T.; Baran, P. S.; Hoffmann, R. W. *Chem. Soc. Rev.*, **2009**, *38*, 3010-3021.

16. Michael, A. *J. Prakt. Chem.* **1887**, *35*, 349-356.

17. Rene, A.; Quilan, M.; Deng, Y.; Cheng, Y.; Teleha, C. A.; Raboisson, P.; Bonfanti, J- F.' Fortin, J.; Charette, A. B.; Pannecouke, X.; Poisson, T.; Jubault, P. *Org. Process Res. Dev.*, **2020**, *24*, 792-801.

18. Ethyl glycinate hydrochloride from Chem-Impex international ($0.07/gram, 10 KG - $655). Ethyl acrylate from Sigma-Aldrich ($0.06/gram, 2 L - $118). Di-tert-butyl pyrocarbonate ($0.07/gram, 25 KG - $1,790). Prices obtained on July 20, 2020.

19. Brogi, S.; Brindisi, M.; Butini, S.; Kshirsagar, G. U.; Maramai, S.; Chemi, G.; Gemma, S.; Campiani, G.; Novellino, E.; Fiorenzani, P.; Pinassi, J.; Aloisi, A. M.; Gynther, M.; Venkutonyte, R.; Han, L.; Frydenvang, K.; Kastrup, J. S.; Pickering, D. S. *J. Med. Chem.*, **2018**, *61*, 2124-2130.

20. Blake, J.; Wilson, C. D.; Rapoport, H. *J. Am. Chem. Soc.*, **1964**, *86*, 5293-5299.

21. Borch, R. F.; Bernstein, M. D.; Dupont Durst, H. *J. Am. Chem. Soc.* **1971**, *93*, 2897-2904.

22. Reenabthue, N.; Boonlua, C.; Vilaivan, C.; Vilaivan, T.; Suprarpprom, C. *Bioorg. Med. Chem. Lett.*, **2011**, *21*, 6465-6469.

Chapter 6

Moving Forward
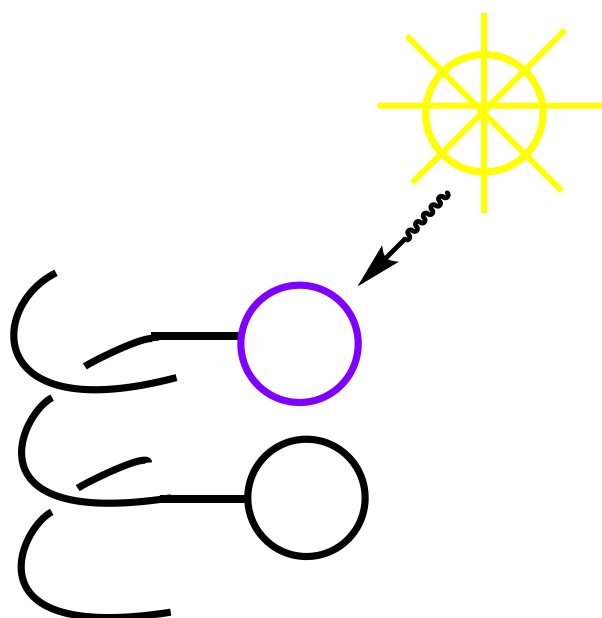
6.1 Foldamers: Opportunities in Photochemistry?

The diverse secondary structures available to foldamers and preexisting knowledge of foldamer conformational propensities dependent upon primary sequence allow for the programable arrangement of reactive groups in three-dimensions.[1-6] Compared to the natural α-helix,[7] foldamer scaffolds offer additional levels of diversification at the backbone and side chain level, along with the capability to incorporate a large set of functional units and to generate a broad range of molecular shapes (Figure 1).
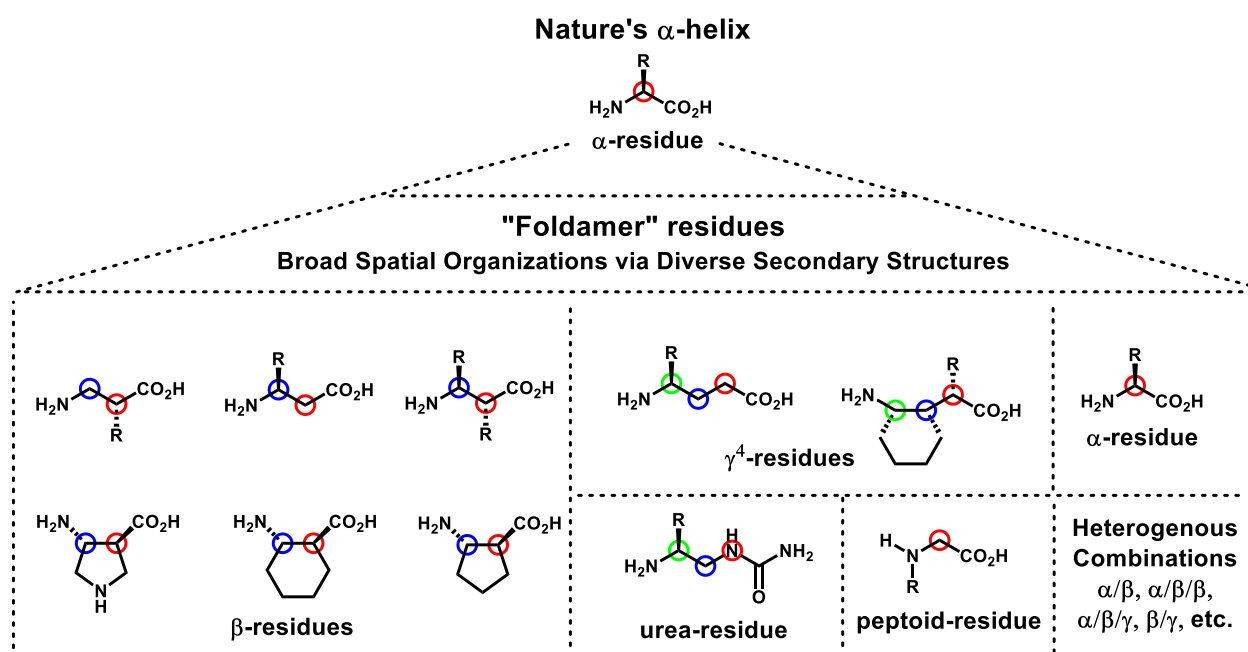
Figure 1. Generic α-residue that makes up the α-helix found in nature. Selected, non-natural residues, known to adopt diverse helical secondary structures via homo- and heterogenous backbones. Circled in red, blue, and green, are the backbone carbon atom(s) composing each residue. R = generic side chain residue

These features are attractive for many reasons, but perhaps none is more important than the ability to rationally predict the orientations of reactive groups presented from well-characterized foldamer scaffolds. Proteins adopt complex tertiary structures that organize reactive residues within the active site, in geometries optimized through evolution. The chemist has long sought

mimicry of nature, though mastery of protein design has yet to be accomplished. Foldamers, offer a "middle ground", between conventional small molecule catalysts and proteins, because short oligomers containing α- and/or β- and/or γ-amino acid residues, and other subunits, fold into predictable and diverse helical secondary structures.[8-12] Foldamers are attractive as catalysts since they may employ lessons learned from nature, while invoking new strategies created in the laboratory.

What features might make foldamer-derived catalysts superior to traditional and widely-studied small-molecule catalysts? This question must have a compelling answer if the chemist is to invest his or her time in the synthesis of foldamers for evaluation as catalysts. Pioneering examples from the groups of Miller and Jacobsen show that oligomers containing amino acid residues and related subunits can catalyze reactions with impressive stereo- or regiochemical control.[13,14] Miller et al. have shown, for example, that site-selective modification of a polyfunctional molecule can be achieved through careful design of peptide-based catalysts. In one case, Miller et al. showed that the well-known peroxyacid *m*CPBA preferred epoxidation at one of the five olefin sites within the naturally occurring polyene geldanamycin.[13] Through the iterative design of a five-residue peptide, regioselective epoxidation of an alternative site was achieved. Here, the molecular complexity of the peptide is justified because the selectivity cannot be achieved in any other way.

In my opinion, a particularly fruitful avenue forward for foldamer catalysis is photochemistry.[15] In recent years, photochemistry has emerged as an extremely powerful approach for the construction of molecular complexity in novel ways. Mild radical generation, driving what would be energetically uphill processes in the ground state, and minimal environmental toll represent attractive features.[16,17]

Despite considerable recent progress in the design of photocatalysts for organic transformations, significant knowledge gaps remain, several which may be addressed with a foldamer-based approach. For example, foldamer-based photocatalysts could promote transformations with very high quantum yields. The quantum yield of a chemical reaction refers to the number of product molecules produced from the absorption of a single photon. A quantum yield of one means that for each photon that is absorbed, one reaction takes place. Though such efficiencies would be highly desirable, most photochemical reactions occur with quantum yields < 1.[18-20] A major reason that low quantum yields occur is common catalysts have short-lived excited states,[21] which means that many excitation events are unproductive. For a given energy-transfer photochemical reaction, initiation occurs when a photocatalyst (PC) absorbs a photon, which causes promotion of a ground-state electron and formation of a spin-paired excited singlet state. From this singlet state a variety of processes can occur, including non-radiative internal conversion to lower singlet states via vibrational relaxation, or radiative fluorescence upon relaxation to the ground state. Excited singlet states are typically short lived. Although some reactions are known to occur from the singlet manifold, most photocatalyzed reactions occur via excited triplet states, which are generally longer-lived that excited singlet states. Formation of an excited triplet state from an excited singlet state is achieved through spin-forbidden intersystem crossing, where the excited electron switches its spin state. The rate of intersystem crossing is highly dependent on the nature of the molecular orbitals involved. El-Sayed's rule states that non-radiative intersystem crossing of an electron from a molecular orbital to another of the same type (i.e. $\pi,\pi^* \rightarrow \pi,\pi^*$) is slow compared to intersystem crossing involving different orbital types (i.e. $n,\pi^* \rightarrow \pi,\pi^*$).[22] Once an excited triplet state is populated, several pathways may operate. Like singlet excited states, excited triplet states can dissipate

through non-radiative internal conversion involving vibrational relaxation. Additionally,

radiative decay to the ground state can occur, which leads to phosphorescence. This simple

overview of photocatalyst excited states (PC*) provides a framework for considering triplet

sensitization, a process of great importance in photocatalysis.

Once the excited triplet state of a PC has been achieved (PC*), an energy-

transfer mechanism or an electron-transfer mechanism, or both, can be operative. To simplify the

discussion, we will focus on energy transfer. For effective energy transfer to occur from a PC* to

an acceptor (A) in the ground state, sufficient orbital overlap must occur.[23] For the requisite

orbital overlap to occur, the PC* and A must find each other in solution, generating an

association complex (PC*-A) (Figure 2).
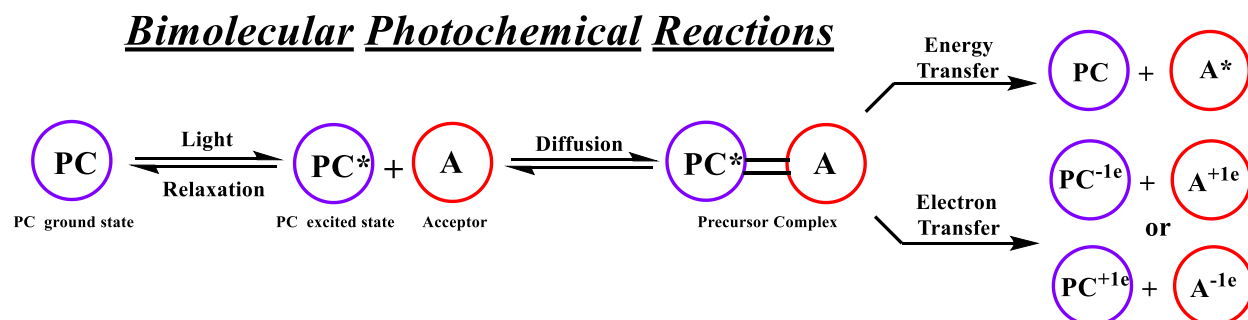
Figure 2. Simplified mechanism for energy/electron transfer.

Formation of this association complex requires diffusion, and thus is not instantaneous. If the

association complex fails to form, PC* relaxes back to the ground state, which is non-productive.

For this reason, chemists often favor photocatalysts with long-lived excited states, to provide

time for the substrate and PC* to find one another.[21] Increasing substrate concentration can also

promote formation of the precursor complex. However, for biomolecular reactions, increasing

the concentration of just one component can be wasteful. For macrocyclization reactions,

increasing the concentration may not viable as oligomeric products can predominate due to the

large entropic cost of ring closure.

One possible strategy for increasing the efficiency of energy transfer from PC* to a substrate would be through accelerated formation of the association complex. A well-established strategy in the realm of polar chemistry for increasing rates of intermolecular reactions is based on temporary intramolecularity,[24] whereby a bifunctional catalyst is employed to utilize covalent/non-covalent activation of two reactants and enable a bond formation step to be "intramolecular". This strategy has been adopted by the photochemistry community; a number of groups have relied on bifunctional catalysts that contain a photocatalytic group and a substrate-binding group. Selected examples of this strategy have been reported by the groups of Yoon,[25] Bach,[26] and Xiao.[27] These three examples are of particular interest due to the utilization of a chiral architecture, which allows asymmetric transformations.

Achieving stereocontrol in photocatalytic reactions is a widely sought goal. Unfortunately, designing novel photocatalysts in non-trivial as photophysical properties can be difficult to predict.[28] The emergence of a class of sensitizers that could be attached to a readily diversified chiral backbone could be very useful in this regard. Bach has demonstrated that incorporation of a photocatalytic thioxanthone unit into a chiral scaffold derived from Kemp's triacid allows for a variety of asymmetric transformations.[29,30] These accomplishments represent landmark discoveries; however, this strategy requires that nearly all of the substrates contain a lactam or other amide group, which limits scope. This requirement arises from the need for hydrogen bonding of the substrate to the lactam in the catalyst.

Foldamers seem to offer an alternative approach, which is potentially very versatile, for combining a photocatalyic unit and a substrate-binding unit into a single molecule. For example, foldamers can readily incorporate an acid-substituted thioxanthone photocatalyst via amide bond formation on a specific helical face, with a substrate-binding domain presented

nearby. Figure 3 depicts components of foldamers that might mimic the photocatalytic prowess of the Bach systems.
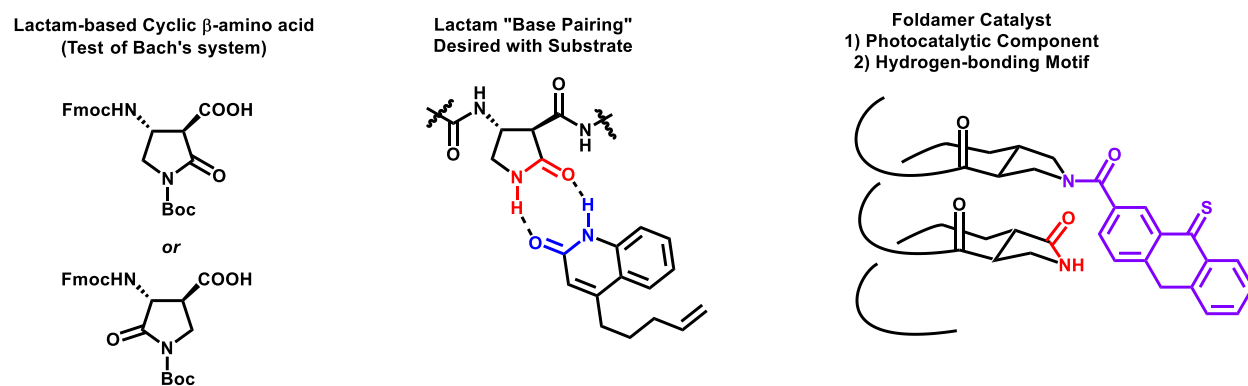
Figure 3. Proposed lactam containing β-amino acids, lactam hydrogen bonding, and cartoon of potential bifunctional foldamer containing a photosensitizer and lactam.

A foldamer approach might prove advantageous if one sought to catalyze the cyclization of an acrylate-tethered olefin. In the case of Bach's system, the chiral lactam sensitizer may not hydrogen bond as well to an acrylate, which would preclude effective catalysis. The foldamer architecture might enable incorporation of H-bonding units that would be more effective than a lactam for H-bonding to an acrylate. For example, a thiourea or urea functional group could be incorporated to occupy the same helix face that displays the sensitizer. Below, a series of figures depict ideas that may be of use in foldamer-based photochemistry.

Potential Synthetic Route
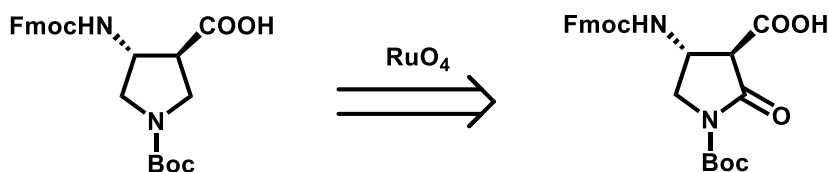
- **Route based on APC eliminates need to set stereochemistry another way.**
- **Ensures scalability. APC can be made on > 20 gram scale.**
- **Time cost is minimal as APC synthesis is always needed.**
- **Potential for regioisomers, as well as over oxidation to imide. Is separation possible?**

β-**amino acid synthesis may proove difficult.**
(*L*)-**pyroglutamic Acid instead?)**
Commerically Available $0.40/gram
(*R*) **enantiomer also available**

Incorporate Helical segment + β-**turn (Miller/Kudo)**
- **two chiral elements, binding pocket?**

Helix + β-turn motif

**Any Helical
Secondary Structure**
β, α/β, αββ, γ, **etc.**

β-**turn with terminal
lactam motif**

HELIX

◯ **= Photocatalyst**

- **trifunctional catalysis?**
- **additional chiral information**
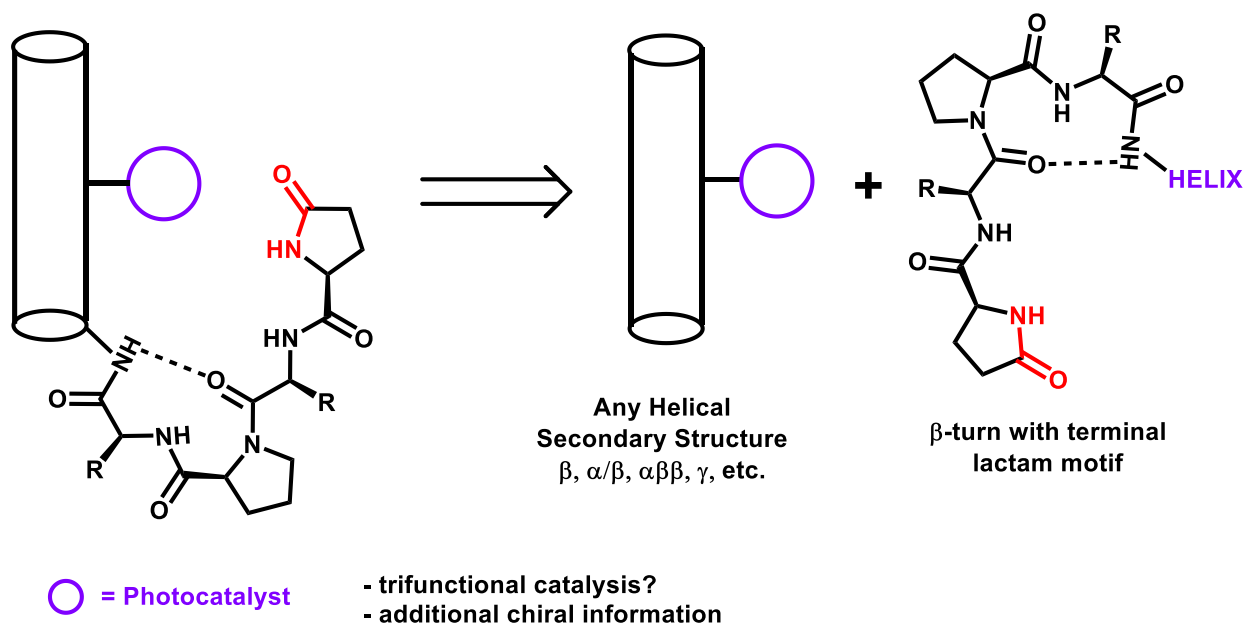
Figure 4. Potential synthetic route to chiral, lactam-based β-amino acid. Alternative strategy employing (L)-pyroglutamic acid, and a turn motif at the N-terminus of the helix.

**Potential Access
to 3 electron electrophilic radical
on Foldamer**

**Potential Access
to 5 electron nucleophilic radical
on Foldamer**
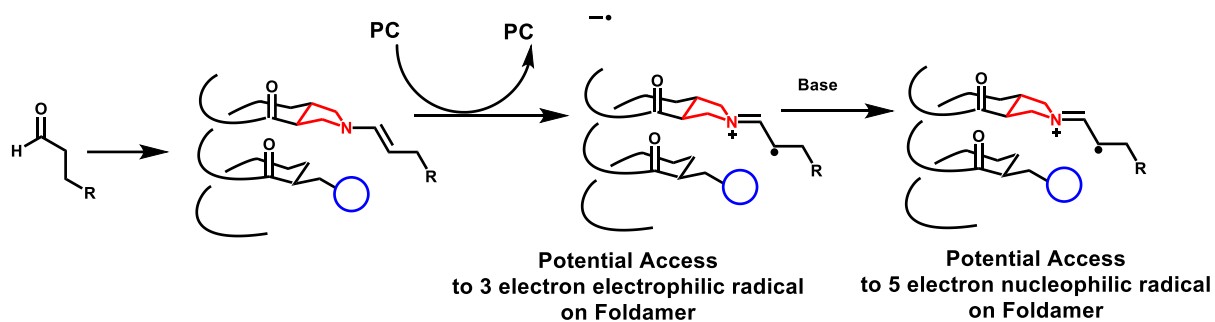
Potential Minisci Chemistry on Foldamer?
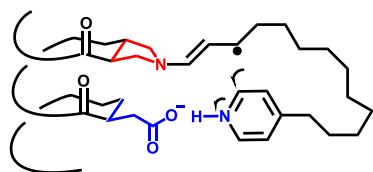
- access nucleophilic radical via photochemistry
- Protonation of pyridine via aspartic acid/glutamic acid side chain
- Chiral Ion pair
- Would need to reduce PC after intial enamine oxidation so that pyridyl radical could be oxidized (rearomatization)

Figure 5. Through covalent enamine formation, and known SOMO/ 5 π electron activation modes, reactive radicals could be generated on-foldamer. Carboxylic acid side chain groups could allow for coulombic interactions to hold substrate on-catalyst. Potential Minisci-type macrocyclization via nucleophilic radical addition into a protonated pyridine.

Melchiorre's EDA complex on Foldamer?
Direct Excitation, only when
Donor/Acceptor
Proximal AND in Chiral Environment
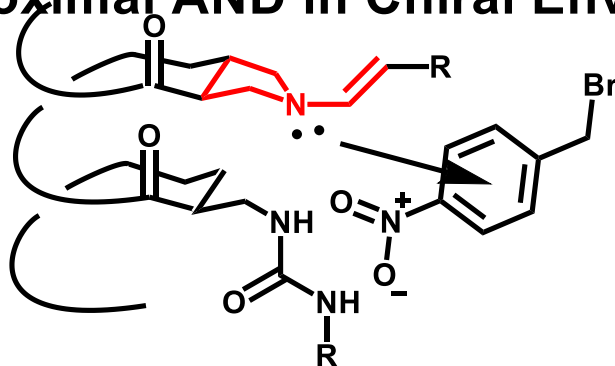
- **Way to control background reactions**
- **Chiral Ion Pair on Foldamer**
- **Macrocyclizations**

Figure 6. Formation of photo excitable EDA complex on foldamer?[31]

Figure 7. Proposed 2+2/Macrocyclization via iminium sensitization.

6.2 Foldamer Approach to the Synthesis of Medium-Sized Rings

The synthesis medium and large rings remains a substantial challenge. Rings of medium size are classified as those containing 8-11 atoms, and macrocycles are rings of 12 atoms or more. While the synthesis of macrocyclic compounds remains challenging in terms of entropy, the enthalpic cost is manageable, as the large ring structures are conformationally mobile (i.e., no strain develops upon ring closure). Construction of medium-sized rings suffers from both entropic and enthalpic difficulties. Figure 8 shows the heats of combustion for cycloalkanes of various sizes, highlighting the strain released upon combustion for rings of 8-11 atoms. This strain in medium-sized rings is a combination of Pitzer strain (due to unfavorable eclipsing interactions), bond-angle distortion (a major component of ring strain in 3- and 4-membered rings), and transannular steric interactions (Figure 9).
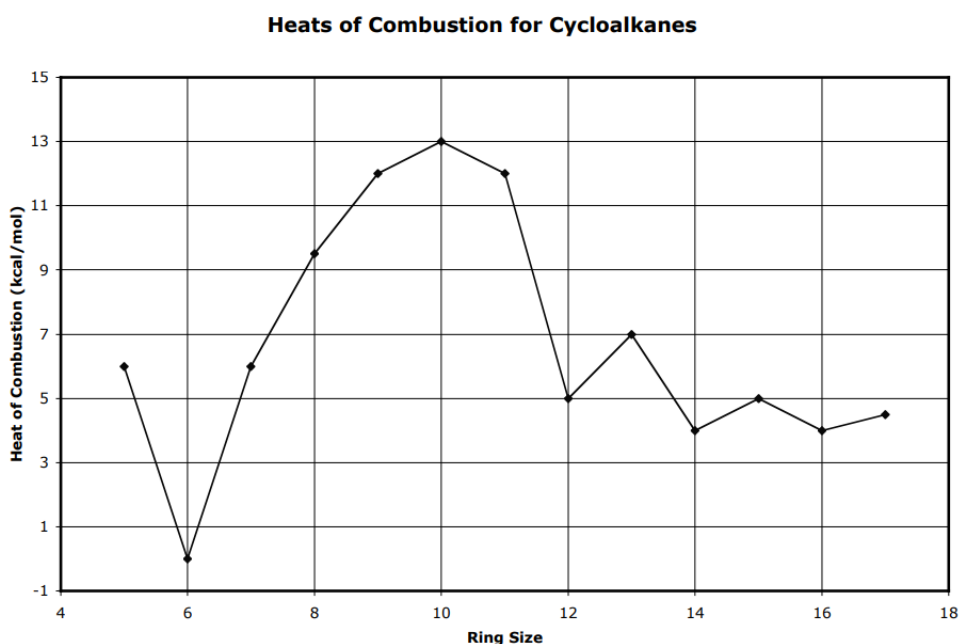
Figure 8. Heats of Combustion for cycloalkanes. From Tadross, P., Stoltz literature group meeting, *Strategies for the Construction of Medium-Sized Rings*, **2008**.
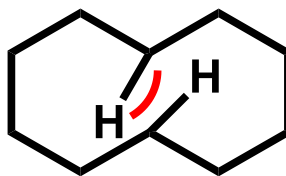
**Transannular Strain
in cyclodecane**

Figure 9. Example of transannular repulsions in a ten-membered ring.

Recently, we have demonstrated the use of a foldamer-templated macrocyclization strategy for the aldol-based ring closure of dialdehydes to efficiently form rings of 14-22 atoms.[32] Activation of both aldehyde groups via iminium/enamine formation on a helical foldamer scaffold minimizes the entropic cost of ring closure. However, this strategy proved ineffective in the formation of medium sized rings, and even 12-membered ring formation was accompanied by production of cyclo-dimers and cyclo-trimers.

One particularly interesting strategy for the construction of medium-sized rings could rely on the simultaneous formation of additional rings, of favorable size. Formation of a favorable ring size may offset some of the entropic/enthalpic cost for formation of a ring of less favorable size. Transannular reactions often involve macrocyclic substrates and lead to the formation of one or more rings. Balskus and Jacobsen have accomplished an enantioselective transannular Diels-Alder reaction via Lewis-acid catalysis (Figure 10A). The Diels-Alder reaction is very important in organic synthesis, because it forges multiple bonds and stereocenters in a single step. Substrate activation strategies have involved both Lewis acids (coordination) and catalytic amines (iminium activation) (Figure 10B). Due to our group's recent interest in amine-based catalytic foldamers, iminium activation is particularly attractive to us.

Iminium activation is a known strategy for the intramolecular Diels-Alder reaction of an enal

tethered to a diene (Figure 10C).
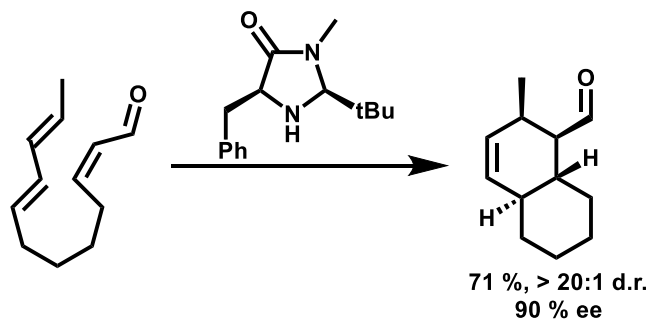
Figure 10. A) Asymmetric transannular Diels-Alder reaction. B) Iminium activation. C) Iminium catalyzed Diels-Alder reaction.

One avenue that may be fruitful in the construction of medium-sized rings catalyzed by a foldamer scaffold could involve a transannular Diels-Alder reaction, similar to that of Jacobsen, but utilizing transient iminium activation. Figure 11 outlines a general strategy for merging a transannular Diels-Alder reaction with our foldamer-catalyzed macrocyclization.

Foldamer-catalyzed Macrocyclization-Transannular Cascade
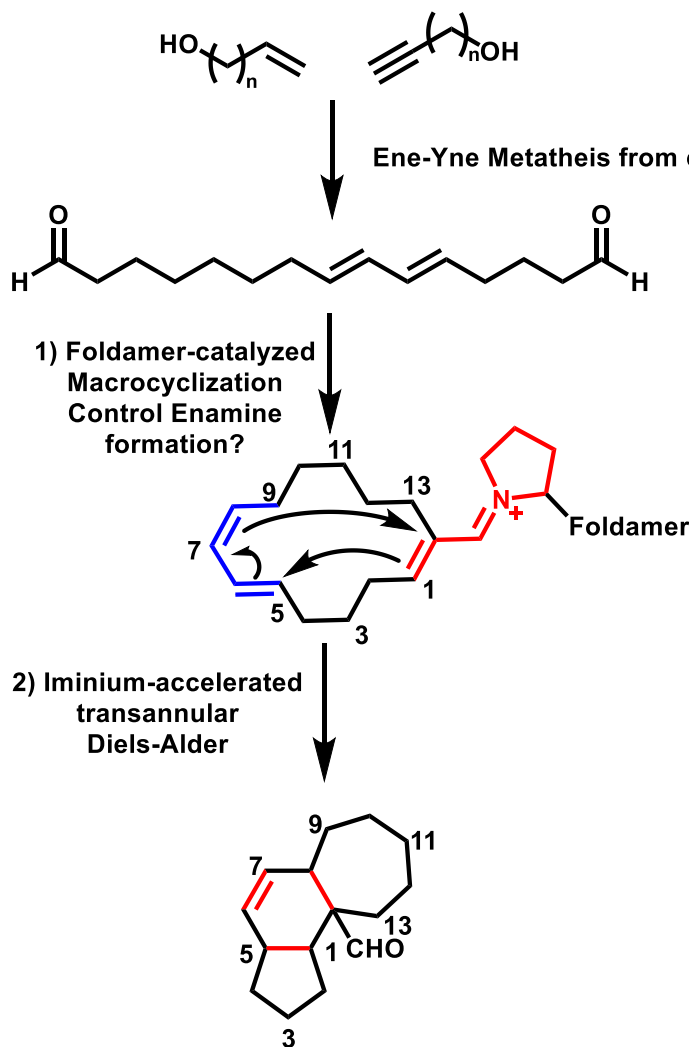
Figure 11. Foldamer-catalyzed macrocyclization-transannular cascade.

Ene-yne metathesis of commercial alcohols, followed by Dess-Martin oxidation would provide access to diene-substituted dialdehydes. The dialdehyde substrates could then participate in the known foldamer-catalyzed macrocyclization to generate a macrocyclic enal. This

macrocyclization would produce regioisomeric enals due to the unsymmetrical nature of the substrate, unless enamine formation could be controlled at one aldehyde over the other. The catalytic cycle for macrocycle formation requires the formation of an iminium ion prior to hydrolysis to the branched enal. This iminium may occur on a primary or secondary amine, though due to the well-known ability of secondary amines to participate in enamine catalysis over primary amines,[33] the iminium will likely form on the secondary amine. However, this iminium ion is likely short-lived since secondary amines rarely participate in iminium formation with branched enals due to $A_{1,3}$-strain. However, if this iminium ion persists long enough, the tethered diene could undergo a transannular Diels-Alder reaction, generating a tricyclic skeleton. Achieving such a cascade would be remarkable in that it would represent a one-pot reaction sequence that forms four rings and five bonds (via a transient macrocycle) from a linear precursor.

If utilization of a secondary amine-containing scaffold proves ineffective, a bis-primary amine scaffold can be examined. Although we have previously reported foldamers with a bis-primary amine diad to be less catalytically active for aldol reactions than those with a primary-secondary diad, the bis-primary amine diad does support the desired reactivity.[32] Primary amines are much more effective in forming iminium ions with alpha-branched enals relative to secondary amines, and may allow a better chance for the transannular Diels-Alder reaction to occur.

Construction of doubly strained bicyclic rings?
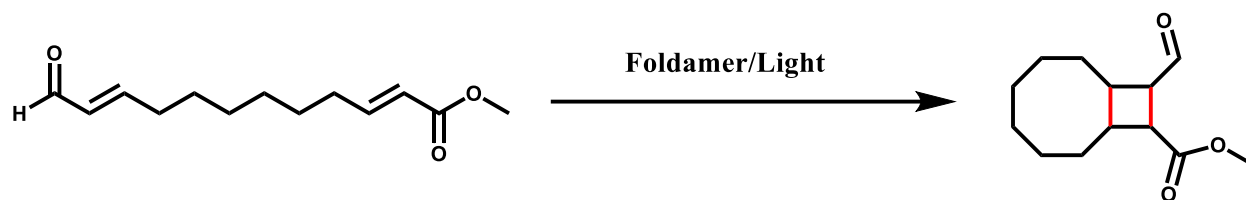
Figure 12. Synthesis of medium/small ring bicyclic systems utilizing high reactivity of excited state intermediates. Triplet sensitization of the iminium ion on the foldamer can react with the urea group (non-covalent interactions with a urea or thiourea). The subsequent radical recombination to form the four-membered ring is known and fast. The high energy triplet intermediates may compensate for the high energetic cost of ring formation.

6.3. Cascade Reactivity: Reactivity on Multiple Faces of a Foldamer Helix

The marvelous reactivity exhibited by enzymes has long inspired organic chemists. The principles of enzymatic catalysis that enable the remarkable selectivity and control over reaction pathway suggest strategies for the design of organic catalysts. Biocatalytic cascades represent a strategy that would be of unrivaled value in the lab, saving time and cost. Recently, Merck & Co. have demonstrated a biocatalytic cascade for the synthesis of islatravir, a potential drug for HIV treatment. Through iterative rounds of enzymatic evolution, they achieved the stereoselective synthesis of islatravir from achiral building blocks while cutting the step-count in half.

I wonder whether foldamers could be designed to promote catalytic cascade reactions. The tertiary structures adopted by enzymes are composed of hundreds of amino acids residues; however, typically only a few participate in catalysis (i.e. catalytic triad). Foldamers that adopt stable conformations at short chain lengths might enable a much larger percentage of the residues to participate in catalysis. Figure 13 depicts our macrocyclization catalyst,[32] which utilizes two catalytic amine residues. The other five residues promote conformational stability (and the β^3-hTyr residue allows detection via UV absorbance). Upon folding, a foldamer backbone with a 1:2 α:β repeat will adopt a helix with almost a exactly three residues per turn. This results in three distinct helical faces. One could imagine a cascade reaction where one reaction occurs on a

first face, and another on a second helix face. This would result in a foldamer catalyst that has a

very high percentage of catalytically active residues.

Foldamer-based Macrocyclization Catalyst
(Gellman, *Science*, 2019)

**29 % of residues
are involved in catalysis
(2 of 7)**
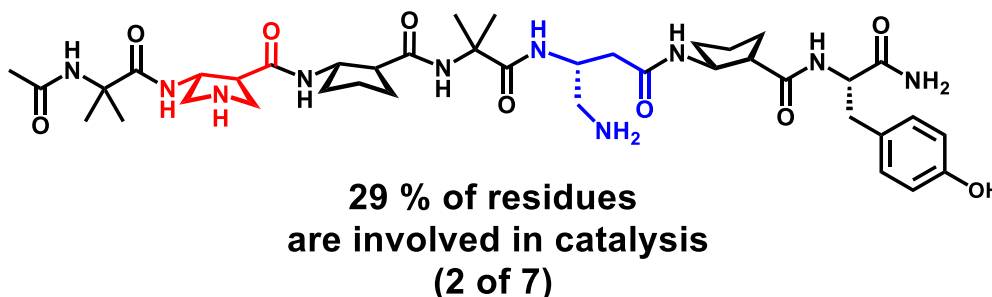
Cartoon Depiction of 1:2 α/β-foldamer (top down view)
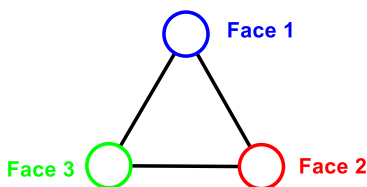
Helix provides stable scaffold with 3 distinct faces

Can Catalytic Diads Exist on Multiple Faces to Accomplish A Cascade?
Reaction 1 - Face 1 --> Reaction 2 - Face 2

Figure 13. Foldamer-based macrocyclization catalyst, with catalytic amine diad highlighted in red and blue. Cartoon depiction of the helical secondary structure, highlighting the three possible faces of the helix in red, blue, and green.

One example of a potential cascade reaction that could occur would involve the α-methylenation-

Diels Alder cascade shown in figure 14.
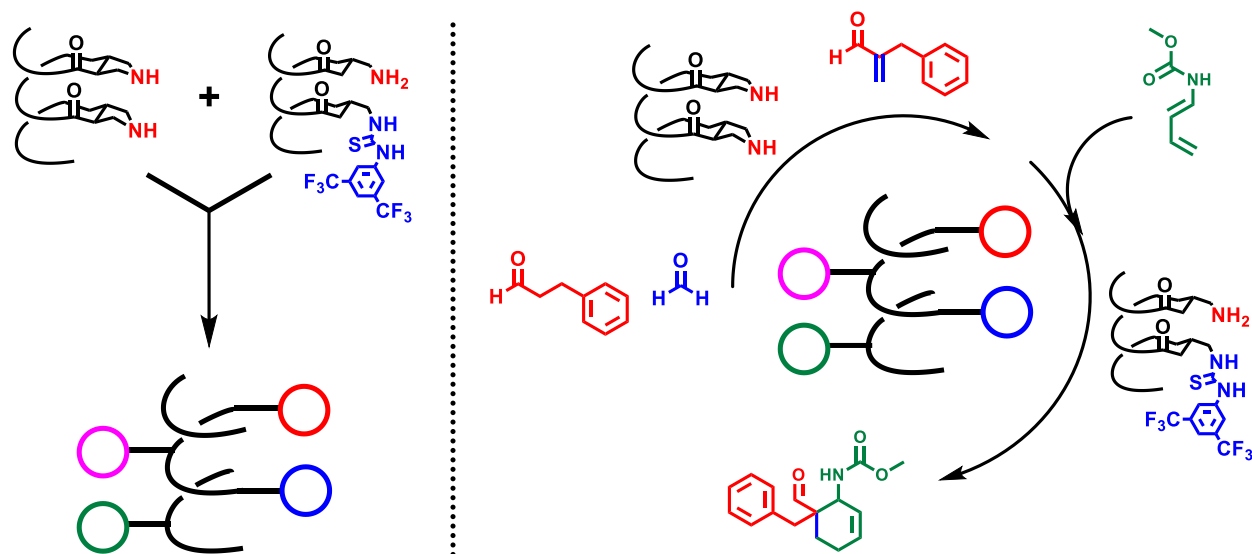
Figure 14. Proposed α-methylenation-Diels-Alder cascade reaction employing a tetra-functionalized foldamer.

6.4. Miscellaneous

Intermolecular addition of aldehyde-derived enamines to α/β-unsaturated esters?

Gellman, *Org. Lett.*, 2020, *22*, 4568-4573

96 % conversion
2 % homo-aldol
98 % ee, 8.1 : 1 d.r.
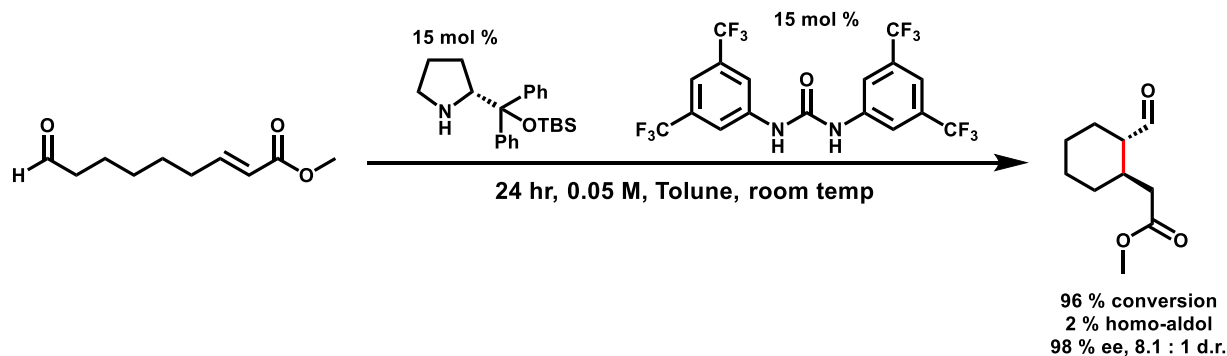
Intermolecular Examples = NONE
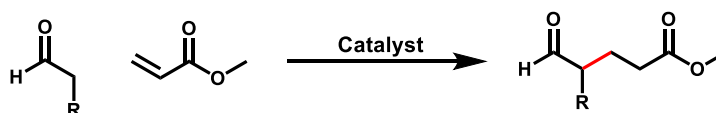
- Bulky group on chiral amine provides high facial selection
&
mimimizes aza-Michael addition to deactivate catalyst
- Use excess methyl acrylate (not ideal, however its a commodity chemical)
$0.02/gram from Sigma (18 L)
- Utilize both commerical catalyst from intramolecular varient
-Syring pump in aldehyde to minimize homo aldol formation.
- Dilute conditions further minimize homol aldol formation.

Although design of a catalyst that could accomplish intermolecular version with 1:1 substrate equivalents is ideal, the reaction in general is more important.

**Small Molecule Catalyzed Addition of Aldehydes
to 4-vinylpyridines
(Wang, *JACS*, 2015, *137*, 2303-2310)**

Bronsted Acid

- -
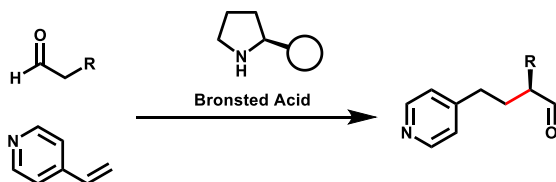
**Bifunctional Foldamers Covalent/Coulombic Activation
Macrocyclic Michael Addition to Vinyl-heterocycles**

Foldamer

14

Enamine - Covalent Activation
Chiral Ion Pair - Bronsted Acid Activation (Pseudo-iminium)
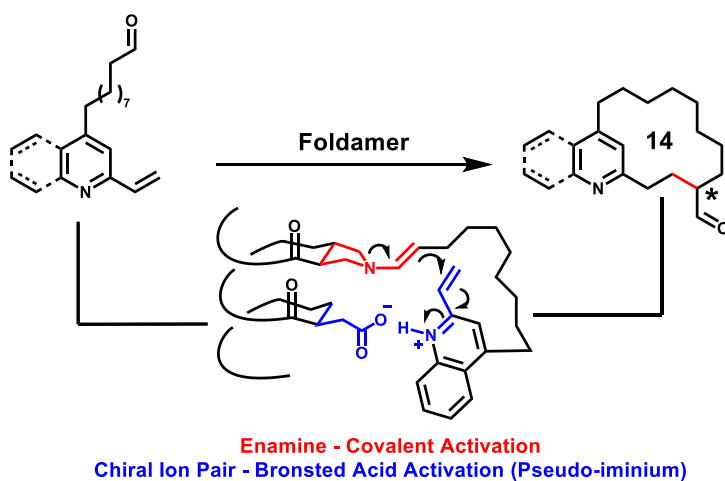
- Extension of Bifunctional
 Activation
to Coulombic Interactions

- Chiral Ion pair = Potential for
asymmetric reaction

- Proximal orientation of
pseudo-iminium ion,
good Michael
acceptor.

- Foldamer scaffold organizes
reactive diad proximal
 in space
lowering entropic cost of
macrocyclization

- Wang's system works well
in DMF/H_2O, solvent system
which readilly dissolves
foldamer

6.5 References

1. Gellman, S. H. *Acc. Chem. Res.* **1998**, *31*, 173-180.

2. Hecht, S.; Huc, I. *Foldamers: Structure, Properties, and Applications*, Wiley-VCH, Weinheim, **2007**, pp.1-435

3. Hill, D. J.; Mio, M. J.; Prince, R. B.; Hughes, T. S.; Moore, J. S. *Chem. Rev.* **2001**, *101*, 3893-4011.

4. Guichard, D.; Huc, I. *Chem. Commun.* **2011**, *47*, 5933-5941.

5. Martinek, T. A.; Fulop, F. *Chem. Soc. Rev.* **2012**, *41*, 687-702.

6. Cheng, R. P.; Gellman, S. H.; DeGrado, W. F. *Chem. Rev.* **2011**, *101*, 3219-3252.

7. Pauling, L.; Corey, R. B.; Branson, H. R. *PNAS*, **1951**, 37, 205-211.

8. Appella, D. H.; Christianson, L. A.; Karle, I. L.; Powell, D. R.; Gellman, S. H. *J. Am. Chem. Soc.* **1996**, *118*, 13071-13072. b) Seebach, D.; Overhand, M.; Kuhnle, F. N. M.; Martinoni, B.; Oberer, L.; Hommel, U.; Widmer, H. *Helv. Chim. Acta.*, **1996**, 79, 913-941.

9. Raguse, T. L.; Lai, J. R.; Gellman, S. H. *J. Am. Chem. Soc.*, **2003**, 125, 5592-5593.

10. Appella, D. H.; Christianson, L. A.; Klein, D. A.; Powell, D. R.; Huang, X.; Barchi Jr., J. J.; Gellman, S. H. *Nature*, **1997**, 387, 381-384.

11. a) Schmitt, M. A.; Choi, S. H.; Guzei, I. A.; Gellman, S. H. *J. Am. Chem. Soc.*, **2006**, 128, 4538-4539. b) Choi, S. H.; Guzei, I. A.; Spencer, L.; Gellman, S. H. *J. Am. Chem. Soc.*, **2009**, 131, 2917-2924.

12. a) Guo, L.; Chi, Y.; Almeida, A. M.; Guzei, I. A.; Parker, B. K.; Gellman, S. H. *J. Am. Chem. Soc.*, 2009, 131, 16018-16020. b) Shin, H. Y.; Gellman, S. H. *J. Am. Chem. Soc.*, **2018**, 140, 1394-1400. c) Fisher, B. F.; Gellman, S. H. *J. Am. Chem. Soc.*, **2016**, 138,

10766-10769. d) Giuliano, M. W.; Maynard, S. J.; Almeida, A. M.; Guo, L.; Guzei, I. A.; Spencer, L. C.; Gellman, S. H. *J. Am. Chem. Soc.*, **2014**, 136, 15046-15053. e) Shin, Y. H.; Mortenson, D. E.; Satyshur, K. A.; Forest, K. T.; Gellman, S. H. *J. Am. Chem. Soc.*, **2013**, 135, 8149-8152. f) Guo, L.; Zhang, W.; Reidenbach, A.; Giuliano, M. W.; Guzei, I. A.; Spencer, L. C.; Gellman, S. H. *Angew. Chem. Int. Ed.*, **2011**, 50, 5843-5846. g) Fisher, B. F.; Guo, L.; Dolinar, B. S.; Guzei, I. A.; Gellman, S. H. *J. Am. Chem. Soc.*, **2015**, 137, 6484-6487. h) Guo, L.; Almeida, A. M.; Zhang, W.; Reidenbach, A. G.; Choi, S. H.; Guzei, I. A.; Gellman, S. H. *J. Am. Chem. Soc.*, **2010**, 132, 7868-7869.

13. Hilton, M. J.; Brackett, C. M.; Mercado, B. Q.; Blagg, B. S. J.; Miller, S. J. *ACS Cent. Sci.*, **2020**, *6*, 426-435.

14. Mayfield, A. B.; Metternich, J. B.; Trotta, A. H.; Jacobsen, E. N. *J. Am. Chem. Soc.*, **2020**, *142*, 4061-4069.

15. a) Yoon, T. P.; Ischay, M. A.; Du, J. *Nature Chemistry,* **2010**, *2*, 527-532. b) Prier, C. K.; Rankic, D. A.; MacMillan D. W. C. *Chem. Rev.* **2013**, *113*, 5322-5363. c) Romero, N. A.; Nicewicz, D. A. *Chem Rev.* **2016**, *116*, 10075-10166. d) Narayanam, J. M. R.; Stephenson, C. R. J. *Chem. Soc. Rev.* **2011**, *40*, 102-113.

16. Shin, N. Y.; Ryss, J. M.; Zhang, X.; Miller, S. J.; Knowles, R. R. *Science*, **2019**, *366*, 364-369.

17. Edwards, J. T.; Merchant, R. R.; McClymont, K. S.; Knouse, K. W.; Qin, T.; Malins, L. R.; Vokits, B.; Shaw, S. A.; Bao, D- H.; Wei, F- L.; Eastgate, M. D.; Baran, P. S. *Nature,* **2017**, *545*, 213-218.

18. Tagami, T.; Arakawa, Y.; Minagawa, K.; Imada, Y. *Org. Lett.* **2019**, *21*, 6978-6982.

19. Neumann, M.; Fuldner, S.; Konig, B.; Zeitler, K. *Angew. Chem. Int. Ed.*, **2011**, *50*, 951-954

20. Nacsa, E. D.; MacMillan, D. W. C. *J. Am. Chem. Soc.* **2018**, *140*, 3322-3330.

21. Arias-Rotondo, D. M.; McCusker, J. K. *Chem. Soc. Rev.* **2016**, *45*, 5803-5820.

22. Burda, C.; Chen, X.; Narayanan, R.; El-Sayed, M. A. *Chem. Rev.* **2005**, *105*, 1025-1102.

23. Dexter, D. L. *J. Chem. Phys.* **1953**, *21*, 836-850.

24. Tan, K. L. *ACS Catal.* **2011**, *8*, 877-886.

25. Zheng, J.; Swords, W. B.; Jung, H.; Skubi, K. L.; Kidd, J. B.; Meyer, G. J.; Baik, M- H.; Yoon, T. P. *J. Am. Chem. Soc.*, **2019**, *141*, 13625-13634.

26. Holzl-Hobmeier, A.; Bauer, A.; Silva, A. V.; Huber, S. M.; Bannwarth, C.; Bach, T. *Nature*, **2018**, *564*, 240-243.

27. Ding, W.; Lu, L- Q.; Zhou, Q- Q.; Wei, Y.; Chen, J- R.; Xiao, W- J. *J. Am. Chem. Soc.* **2017**, *139*, 63-66.

28. Singh, V. S. et. al. *Nature Catalysis*, **2018**, *1*, 794-804.

29. Burg, F.; Bach, T. *J. Org. Chem.* **2019**, *84*, 8815-8836.

30. Kemp, D. S.; Petrakis, K. S.; *J. Org. Chem.* **1981**, *46*, 5140-5143.

31. Crisenza, G. E. M.; Mazzarella, D.; Melchiorre, P. *J. Am. Chem. Soc.*, **2020**, *142*, 5461-5476.

32. Girvin, Z. C.; Andrews, M. K.; Liu, X.; Gellman S. H. *Science*, **2019**, *366*, 1528-1531.

33. Mukherjee, S.; Yang, J- W.; Hoffmann, S.; List, B. *Chem. Rev.* **2007**, *107*, 5471-5569.

Thank you for everything, Boss. Especially for your unconditional support.

The best is yet to come.